

兰州理工大学

科研成果汇总

学 号：221081101008

研 究 生：郭奕彤

导 师：马军 教授

研究方向：复杂系统的建模、优化与控制

论文题目：一类神经元电路及网络动力学与机械臂控制

学 科：控制理论与控制工程

学 院：电气工程与信息工程学院

入学时间：2022 年 9 月

目 录

论文检索报告.....	1
Biophysical mechanism of signal encoding in an auditory neuron	5
Control the stability in chaotic circuit coupled by memristor in different branch circuits	17
Nonlinear responses in a neural network under spatial electromagnetic radiation.....	30
Physical approach of a neuron model with memristive membranes.....	45
How to define energy function for memristive oscillator and map	61
Energy controls wave propagation in a neural network with spatial stimuli	74
Energy and synchronization between two neurons with nonlinear coupling.....	87
Model approach of electromechanical arm interacted with neural circuit, a minireview	100
Memristive oscillator to memristive map, energy characteristic	108
Control electromechanical arms by using a neural circuit.....	120
Model approach of artificial muscle and leg movements	138
Jointed pendulums driven by a neural circuit, electromechanical arm model approach	147
An electromechanical arm model controlled by artificial muscle	161



机构: 兰州理工大学

姓名: 郭奕彤 [221081101008]

著者要求对其在国内外学术出版物所发表的科技论著被以下数据库收录情况进行查证。

检索范围:

- 科学引文索引 (Science Citation Index Expanded): 1900年-2025年

检索结果:

检索类型	数据库	年份范围	总篇数	第一作者篇数	第二作者篇数
SCI-E 收录	SCI-EXPANDED	2021 - 2025	13	12	1

End



委托人声明:

本人委托兰州理工大学图书馆查询论著被指定检索工具收录情况, 经核对检索结果, 附件中所列文献均为本人论著, 特此声明。

作者 (签字): 郭奕彤

完成人 (签字): 安宗玉

完成日期: 2025年3月24日

完成单位 (盖章): 兰州理工大学图书馆信息咨询与学科服务部

(本检索报告仅限校内使用)



图书馆

文献检索报告 SCI-E 收录



兰州理工大学图书馆 LUTLIB

报告编号: R2025-0240 SCI-E 收录


数据库: 科学引文索引 (Science Citation Index Expanded) 时间范围: 2021年至2025年			作者姓名: 郭奕彤 作者单位: 兰州理工大学		检索人员: 李宇玉 检索日期: 2025年3月24日	
检索结果: 被 SCI-E 收录文献 13 篇						
#	作者	地址	标题	来源出版物	文献类型	入藏号
1	Guo, YT; Zhou, P; Yao, Z; Ma, J	[Guo, Yitong; Zhou, Ping; Yao, Zhao; Ma, Jun] Lanzhou Univ Technol, Dept Phys, Lanzhou 730050, Peoples R China.; [Zhou, Ping; Ma, Jun] Chongqing Univ Posts & Telecommunicat, Sch Sci, Chongqing 430065, Peoples R China.	Biophysical mechanism of signal encoding in an auditory neuron	NONLINEAR DYNAMICS 2021, 105 (4): 3603-3614.	J Article	WOS:0006 815497000 06
2	Guo, YT; Yao, Z; Xu, Y; Ma, J	[Guo, Yitong; Yao, Zhao; Ma, Jun] Lanzhou Univ Technol, Dept Phys, Lanzhou 73005, Peoples R China.; [Xu, Ying] Shandong Normal Univ, Sch Math & Stat, Jinan 250014, Peoples R China.; [Ma, Jun] Chongqing Univ Posts & Telecommun, Sch Sci, Chongqing 430065, Peoples R China.	Control the stability in chaotic circuit coupled by memristor in different branch circuits	AEU-INTERNATIONAL JOURNAL OF ELECTRONICS AND COMMUNICATIONS 2022, 145: 154074.	J Article	WOS:0007 957660000 02
3	Guo, YT; Xie, Y; Ma, J	[Guo, Yitong; Ma, Jun] Lanzhou Univ Technol, Coll Elect & Informat Engn, Lanzhou 730050, Peoples R China.; [Xie, Ying; Ma, Jun] Lanzhou Univ Technol, Dept Phys, Lanzhou 730050, Peoples R China.; [Ma, Jun] Chongqing Univ Posts & Telecommun, Sch Sci, Chongqing 430065, Peoples R China.	Nonlinear responses in a neural network under spatial electromagnetic radiation	PHYSICA A-STATISTICAL MECHANICS AND ITS APPLICATIONS 2023, 626: 129120.	J Article	WOS:0010 716097000 01
4	Guo, YT; Wu, FQ; Yang, FF; Ma, J	[Guo, Yitong; Yang, Feifei; Ma, Jun] Lanzhou Univ Technol, Coll Elect & Informat Engn, Lanzhou 730050, Peoples R China.; [Wu, Fuqiang] Ningxia Univ, Sch Math & Stat, Yinchuan 750021, Peoples R China.; [Ma, Jun] Lanzhou Univ Technol, Dept Phys, Lanzhou 730050, Peoples R China.	Physical approach of a neuron model with memristive membranes	CHAOS 2023, 33 (11): 113106.	J Article	WOS:0010 966806000 08

5	Guo, YT; Xie, Y; Ma, J	[Guo, Yitong; Ma, Jun] Lanzhou Univ Technol, Coll Elect & Informat Engn, Lanzhou 730050, Peoples R China.; [Guo, Yitong; Ma, Jun] Lanzhou Univ Technol, Dept Phys, Lanzhou 730050, Peoples R China.; [Xie, Ying; Ma, Jun] Chongqing Univ Posts & Telecommun, Sch Sci, Chongqing 430065, Peoples R China.	How to define energy function for memristive oscillator and map	<i>NONLINEAR DYNAMICS</i> 2023, 111 (23): 21903-21915.	J Article	WOS:0010 932638000 04
6	Guo, YT; Lv, M; Wang, CN; Ma, J	[Guo, Yitong; Ma, Jun] Lanzhou Univ Technol, Coll Elect & Informat Engn, Lanzhou 730050, Gansu, Peoples R China.; [Lv, Mi] China Univ Petr Beijing Karamay, Fac Engn, Karamay 834000, Xinjiang, Peoples R China.; [Wang, Chunni; Ma, Jun] Lanzhou Univ Technol, Dept Phys, Lanzhou 730050, Gansu, Peoples R China.	Energy controls wave propagation in a neural network with spatial stimuli	<i>NEURAL NETWORKS</i> 2024, 171: 1-13.	J Article	WOS:0011 396303000 01
7	Guo, YT; Xie, Y; Wang, CN; Ma, J	[Guo, Yitong] Lanzhou Univ Technol, Coll Elect & Informat Engn, Lanzhou 730050, Peoples R China.; [Xie, Ying; Wang, Chunni; Ma, Jun] Lanzhou Univ Technol, Dept Phys, Lanzhou 730050, Peoples R China.; [Ma, Jun] Chongqing Univ Posts & Telecommun, Sch Sci, Chongqing 430065, Peoples R China.	Energy and synchronization between two neurons with nonlinear coupling	<i>COGNITIVE NEURODYNAMICS</i> 2024, 18 (4): 1835-1847.	J Article	WOS:0011 316486000 01
8	Guo, YT; Ma, J; Zhang, XF; Hu, XK	[Guo, YiTong; Ma, Jun] Lanzhou Univ Technol, Coll Elect & Informat Engn, Lanzhou 730050, Peoples R China.; [Guo, YiTong; Ma, Jun; Zhang, XiaoFeng] Lanzhou Univ Technol, Dept Phys, Lanzhou 730050, Peoples R China.; [Ma, Jun; Hu, XiKui] Chongqing Univ Posts & Telecommun, Sch Sci, Chongqing 400065, Peoples R China.	Memristive oscillator to memristive map, energy characteristic	<i>SCIENCE CHINA-TECHNOLOGICAL SCIENCES</i> 2024, 67 (5): 1567-1578.	J Article	WOS:0012 076276000 02
9	Ma, J; Guo, YT	[Ma, Jun; Guo, Yitong] Lanzhou Univ Technol, Coll Elect & Informat Engn, Lanzhou 730050, Peoples R China.; [Ma, Jun; Guo, Yitong]	Model approach of electromechanical arm interacted with neural circuit, a minireview	<i>CHAOS SOLITONS & FRACTALS</i> 2024, 183: 8.	J Review	WOS:0012 205691000 01

		Lanzhou Univ Technol, Dept Phys, Lanzhou 730050, Peoples R China.; [Ma, Jun] Chongqing Univ Posts & Telecommun, Sch Sci, Chongqing 430065, Peoples R China.				
10	Guo, YT; Song, XL; Ma, J	[Guo, Yitong; Ma, Jun] Lanzhou Univ Technol, Coll Elect & Informat Engn, Lanzhou 730050, Peoples R China.; [Song, Xinlin] Xian Univ Sci & Technol, Sch Sci, Xian 710054, Peoples R China.; [Ma, Jun] Lanzhou Univ Technol, Dept Phys, Lanzhou 730050, Peoples R China.	Control electromechanical arms by using a neural circuit	<i>NONLINEAR DYNAMICS</i> 2025, 113 (2): 1605- 1622.	J Article	WOS:0013 030333000 01
11	Guo, YT; Wang, CN; Ma, J	[Guo, Yitong; Ma, Jun] Lanzhou Univ Technol, Coll Elect & Informat Engn, Lanzhou 730050, Peoples R China.; [Wang, Chunni; Ma, Jun] Lanzhou Univ Technol, Dept Phys, Lanzhou 730050, Peoples R China.	Model approach of artificial muscle and leg movements	<i>PHYSICS LETTERS A</i> 2025, 529: 130069.	J Article	WOS:0013 618019000 01
12	Guo, YT; Wang, CN; Ma, J	[Guo, Yitong; Ma, Jun] Lanzhou Univ Technol, Coll Elect & Informat Engn, Lanzhou 730050, Peoples R China.; [Wang, Chunni; Ma, Jun] Lanzhou Univ Technol, Dept Phys, Lanzhou 730050, Peoples R China.; [Guo, Yitong] North Univ China, Dept Math, Taiyuan 030051, Shanxi, Peoples R China.	Jointed pendulums driven by a neural circuit, electromechanical arm model approach	<i>CHAOS SOLITONS & FRACTALS</i> 2024, 189: 115739.	J Article	WOS:0013 606658000 01
13	Guo, YT; Ma, J	[Guo, Yitong; Ma, Jun] Lanzhou Univ Technol, Coll Elect & Informat Engn, Lanzhou 730050, Peoples R China.; [Guo, Yitong; Ma, Jun] Lanzhou Univ Technol, Dept Phys, Lanzhou 730050, Peoples R China.; [Guo, Yitong] North Univ China, Dept Math, Taiyuan 030051, Peoples R China.	An electromechanical arm model controlled by artificial muscles	<i>SCIENCE CHINA- TECHNOLOGICAL SCIENCES</i> 2025, 68 (4): 1420403.	J Article	WOS:0014 398899000 04
合计						13



Biophysical mechanism of signal encoding in an auditory neuron

Yitong Guo · Ping Zhou · Zhao Yao · Jun Ma 

Received: 20 April 2021 / Accepted: 24 July 2021 / Published online: 5 August 2021
© The Author(s), under exclusive licence to Springer Nature B.V. 2021

Abstract Auditory system in animals can capture external sound signals, which can be converted into biophysical electric signals, and then the auditory neurons are activated to generate kinds of firing patterns. Bats can detect signals with ultrahigh frequency while human auditory system is sensitive to sound and voice within the frequency range 20 to 20,000 Hertz. In this paper, a piezoelectric neuron is proposed to investigate the physical mechanism for selection of frequency and filtering in auditory wave, and filtering wave function is designed to simulate the mode selection in the electrical activities of auditory neuron. Sound signals with multiple frequencies are imposed to drive the auditory neuron and mode selection is analyzed in detail. A decay factor is introduced to control the wave filter and frequency selection, and the amplitude is decreased sharply within transient period when the frequency is beyond or below the threshold. Furthermore, additive noise is accompanied by the sound signals and the mode selection is investigated by taming the noise intensity carefully. It is found that intermediate noise intensity can enhance nonlinear resonance and the auditory

wave is encoded to induce regularity in the neural activities. The results can be helpful for further designing smart sensor and wave filter in signal processing, and the biophysical mechanism for signal processing in auditory system is clarified.

Keywords Piezoelectric neuron · Wave filter · Frequency selection · Mode selection

1 Introduction

Auditory neurons [1–5] are sensitive to certain auditory wave within appropriate frequency, and the nonlinear vibrations from acoustic source can be propagated and converted into electrophysiological signal for activating kinds of firing modes in the auditory system. From the biophysical viewpoint, the vibration energy from the acoustic source can be absorbed partially and then is exchanged in the nervous system. The realistic voice and sound often present combination of signals with multiple frequencies, and the tympanic membrane and other structures will be forced with nonlinear vibration propagated to the spiral organ to the cochlea. Spirochetes are auditory receptors that sense acoustic stimulation, and it is composed of supporting cells and hair cells which can encode and transmit sound signals to neural electric signals, and then spiral ganglion neurons are

Y. Guo · Z. Yao · J. Ma (✉)
Department of Physics, Lanzhou University of
Technology, Lanzhou 730050, China
e-mail: hyperchaos@163.com

P. Zhou · J. Ma
School of Science, Chongqing University of Posts and
Telecommunications, Chongqing 430065, China

activated to propagate these electric signals to the brain and the sound signals are decoded completely.

During the encoding and decoding of sound signals, vibration energy is captured and transferred to electric field energy in the nervous system. The sampled time series for sounds and voice can present complex and nonlinear rhythm, and thus the multiple frequency even chaos can be detected via nonlinear analysis. As is well known, piezoelectric ceramics can transmit vibration signal to electric signals when acoustic wave and mechanical pressures are imposed on these functional components. The authors in Ref. [6] suggested that piezoelectric ceramics can be incorporated into the simple neural circuit for possible repairing the hearing impairment, and the dynamics in the functional auditory neuron is investigated carefully. For potential application in artificial intelligence and neuroscience, more physical electric components can be embedded into the neural circuits for detecting and encoding the external optical signal, electromagnetic field and thermal signals. For example, thermistor [7–9] can be connected to the neural circuit and its ability to percept temperature effect can be realized in the biophysical thermosensitive neuron [10–12]. Phototube can be coupled with most of the neural circuits, and photocurrent is generated to excite the neuron for presenting kinds of firing modes, and this light-dependent neuron model [13–15] can show potential application in designing artificial eyes. The channel current across the Josephson junction [16–18] can be regulated by changing the external magnetic field, and the functional neuron [19, 20] can estimate the effect of magnetic field when a Josephson junction is connected to any branch of the neural circuits [21–24]. Memristor connected to the neural circuits enables realization of reliable memristive synapses [25–27] and estimating the effect of electromagnetic induction in neurons [28, 29]. For most of the generic and functional neural circuits, some intrinsic parameters can be tamed to present sole firing modes such as spiking, bursting and even chaotic states, while the activation of electromagnetic radiation [30–34] can induce multiple firing modes and different firing modes are induced intermittently. For reliable bifurcation analysis and synchronization control in neuron and neural network [35–39], these neural circuits can be expressed by applying appropriate scale transformation [40] on the physical variables and parameters in the equations for the neural circuits [41–44].

In fact, the emitted signals from the realistic signal source seldom present sole frequency, while most of the works about dynamics in neurons are used to discuss the nonlinear analysis and mode selection in neurons by applying periodical stimuli and noise [45–49]. That is, the external current on neuron models is considered as equivalent transmembrane current than realistic external current. On the other hand, these functional electric components have finite parameter response range and then wave filter occurs to block possible activation and response for some signal bands. For example, the photocurrent can be generated only when the frequency in the external illumination should be beyond the threshold of frequency for the cathode material in the phototube. For animals, the wavelength should be within the range of visible light and thus the eyes can see the objects completely. For human ears, the frequency in acoustic wave within 20 to 20,000 Hertz can be heard while bats ears are more sensitive to ultrasonic waves.

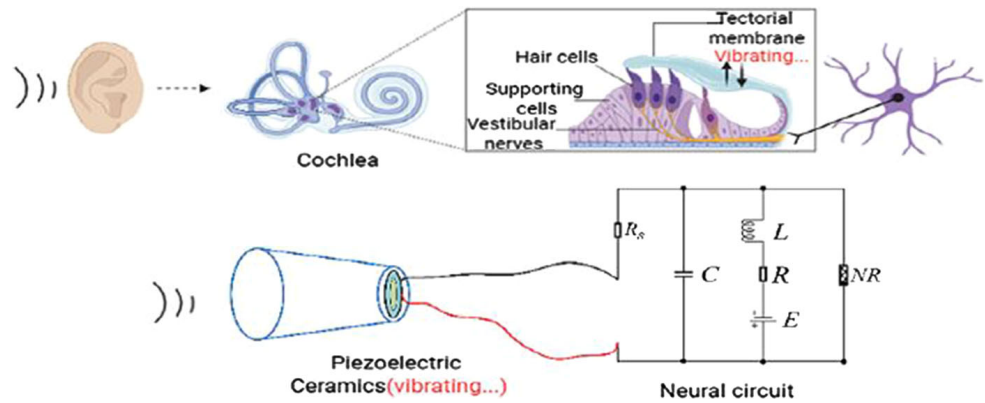
In this paper, a piezoelectric neuron [6] is used to percept and encode the sound signals by activating the wave filter. The sound signals from the signal source present multiple frequencies and some acoustic waves are blocked in the piezoelectric ceramic device in the functional neuron, and the encoding mechanism is explained to confirm the mode selection in the electric activities in this piezoelectric neuron.

2 Model and scheme

From physical viewpoint, distinct mechanical deformation can be induced when the acoustic wave and mechanical force are imposed on the media surface, and the polarity of molecules can be changed to regulate distribution of inner field of the media. As a result, transverse voltage is generated and changed in the piezoelectric materials. Constant mechanical pressure can generate stable output voltage while nonlinear vibration can induce time-varying voltage in the piezoelectric devices. In Fig. 1, a piezoelectric component is connected to a neural circuit [50] for receiving sound voice, and the processing of auditory signal is presented.

The physical relation for external pressure F and voltage V_{PC} on the piezoelectric ceramics in Fig. 1 can be approached by

Fig. 1 Schematic diagram for auditory neuron and artificial neural circuit coupled by piezoelectric ceramics. The voltage for the capacitor describes the membrane potential for the neuron, R_s, R, L, E, R_{non} represents linear resistors, induction coil, constant voltage and nonlinear resistor, respectively



$$V_{PC} = \frac{F d_0}{S \varepsilon} h = P g h = V(F, \mu); \quad P = \frac{F}{S}; \quad g = \frac{d_0}{\varepsilon} \quad (1)$$

where $F, \varepsilon, S, h, d_0$ denote the external mechanical force, dielectric constant, cross-sectional area, thickness of the piezoelectric ceramics and dependence on the physical property of the material, respectively. That is, the output voltage V_{PC} can estimate the effect of external vibration and mechanical force on this piezoelectric device. The current i_{NR} across the nonlinear resistor in Fig. 1 can be estimated [50, 51] as follows

$$i_{NR} = -\frac{1}{\rho} \left(V - \frac{1}{3} \frac{V^3}{V_0^2} \right) \quad (2)$$

where the parameters ρ, V_0 and V describe the conductance, reverse voltage and across voltage for the nonlinear resistor R_{non} , respectively. Based on the physical Kirchhoff's law, the circuit equation for the piezoelectric neuron circuit can be obtained by

$$\begin{cases} C \frac{dV_C}{dt} = \frac{V_{PC} - V_C}{R_s} - i_L - i_{NR} \\ L \frac{di_L}{dt} = V_C - R i_L + E \end{cases} \quad (3)$$

Furthermore, the physical variables and parameters in Eq. (3) are mapped into dimensionless variables and normalized parameters by starting the scale transformation [40] as follows

$$\begin{cases} x = \frac{V_C}{V_0}, y = \frac{\rho i_L}{V_0}, \tau = \frac{t}{\rho C}, u_{pc} = \frac{V_{PC}}{V_0} \\ \xi = \frac{\rho}{R_s}, a = \frac{E}{V_0}, b = \frac{R}{\rho}, c = \frac{\rho^2 C}{L} \end{cases} \quad (4)$$

Therefore, the dynamics and firing modes of the piezoelectric neuron can be calculated by

$$\begin{cases} \frac{dx}{d\tau} = x(1 - \xi) - \frac{1}{3} x^3 - y + \xi u_{pc} \\ \frac{dy}{d\tau} = c[x + a - by] \end{cases} \quad (5)$$

From dynamical viewpoint, the equivalent voltage-controlled current ξu_{pc} estimates the piezoelectric effect, and possible mode selection in neural activities induced by external acoustic wave or mechanical force can be well addressed by presenting the sampled time series for membrane potential x . In the neural circuit, the involvement of linear resistor R_s can stabilize and balance the function of piezoelectric ceramics which can be used as time-varying voltage source or current source by regulating the channel current across this branch circuit. In fact, the acoustic wave is encoded by the piezoelectric ceramics and some wave bands are blocked to prevent generating further response and mode transition in neural activities. That is, the voltage-controlled current ξu_{pc} can present more frequency than sole periodical current completely. In a practical way, some bands in the acoustic wave can be decreased soon or absorbed by the media completely. Here, we suggest that the mapped current can be described by signals with variant angular frequency as follows

$$\xi u_{pc} = A(\omega, \tau) \cos \omega \tau + \zeta(\tau) \quad (6)$$

where the stochastic disturbance $\zeta(\tau)$ can be estimated by Gaussian white noise with zero average $\langle \zeta(\tau) \rangle = 0$, and its statistical correlation is represented by $\langle \zeta(\tau) \zeta(\tau') \rangle = 2D\delta(\tau - \tau')$ with

any noise intensity D . The amplitude in the experimental signal can be dependent on the angular frequency, and it is defined by

$$A(\omega, \tau) = \begin{cases} A_0 \exp(-\tau/\lambda), & \omega \geq \omega_{\max}; \\ A_0, & \omega_{\min} < \omega < \omega_{\max} \\ A_0 \exp(-\tau/\lambda), & \omega \leq \omega_{\min}; \end{cases} \quad (7)$$

where A_0 is the amplitude value for the current under piezoelectric effect, the positive parameter λ denotes the decay factor and it is decided by the piezoelectric material. For setting smaller value for λ , the acoustic wave out of the suggested bands will be filtered quickly, otherwise, the filtered wave will be accompanied by additive weak wave beyond the suggested thresholds. ω_{\max} and ω_{\min} , respectively, define the upper and lower threshold for angular frequency, as a result, the output voltage from the piezoelectric device will be decreased quickly within finite transient period, otherwise, the output voltage of this functional neural circuit will be controlled by the acoustic wave completely because the stimulus generated from the piezoelectric ceramics is controlled by external vibration. In the practice of circuit realization, similar filter wave control can be applied as follows

$$\begin{aligned} \xi u_{pc} = A(\omega) \cos \omega \tau = & [H(\omega - \omega_{\max}) + H(\omega_{\min} \\ & - \omega)] A_0 \exp(-\tau/\lambda) \cos \omega \tau \\ & + A_0 [H(\omega_{\max} - \omega) + H(\omega - \omega_{\min}) - 1] \cos \omega \tau; \end{aligned} \quad (8)$$

where $H(*)$ represents the Heaviside function, and $H(x) = 1$ at $x \geq 0$, otherwise, $H(x) = 0$. As is well known, the neural activities can present possible stochastic resonance when the noise intensity is tamed carefully in the presence of certain periodical exciting, and the signal-to-noise ratio (SNR) reaches a peak value for generating higher regularity in the firing patterns. On the other hand, coherence resonance can be induced in the absence of periodical exciting, and the coefficient variability (CV) of interspike interval (ISI) series is calculated to show the coherence degree [52–54] as follows

$$CV = \frac{\sqrt{\langle T^2 \rangle - \langle T \rangle^2}}{\langle T \rangle} \quad (9)$$

where the period for adjacent peaks in the sampled time series for membrane potentials is calculated for the ISI with T value. The intrinsic parameters and amplitude in the auditory wave can be adjusted to induce better coherence with smaller CV value.

In experiment and practice, most nonlinear circuits can be controlled and used as signal source with single or multiple frequency. For example, the output voltage from chaotic circuits can be used to drive a piezoelectric device and sounds are induced as voice source, which will generate kinds of sound signals by taming the intrinsic parameters and the external stimuli. Surely, the same simple neural circuit [50] can be used and a piezoelectric is connected in parallel for building an artificial sound source, and the emitted acoustic wave will drive our proposed neural circuit considering piezoelectric effect. That is, the acoustic wave will induce complex vibration on the piezoelectric device and voltage-controlled current ξu_{pc} will present different angular frequencies. For simplicity, the regulation and adjustment of angular frequency in the voltage-controlled current can be encoded from the outputs voltage of the known chaotic Chua circuit [55, 56]. Indeed, the output voltage in chaotic state can contain signals with wide frequency band, and the Chua oscillator is described by

$$\begin{cases} \dot{x}' = \alpha(y' - x') - \alpha f(x') \\ \dot{y}' = x' - y' + z' \\ \dot{z}' = -\beta y' - \gamma z' \end{cases} \quad (10)$$

where x' , y' , z' are dimensionless variables mapped from the output voltages for two capacitors and the channel current across the induction coil, and the normalized parameters α , β , γ are associated with the physical values for the resistors, capacitors and inductor. While the nonlinear function $f(x')$ is mapped from the channel current across the Chua diode for the Chua circuit, and it is obtained by

$$f(x') = m_1 x' + 0.5(m_0 - m_1)(|x' + 1| - |x' - 1|) \quad (11)$$

It is confirmed that chaos can be induced in Eq. (10) by setting parameters as $\alpha = 10$, $\beta = 16$, $\gamma = 0.01$, $m_0 = -1.296$, $m_1 = -0.7364$, and the initial values for the three variables can be selected as (0.01, 0.1, 1.0). In the following section, the sampled time series for variable x' will be used as signal source.

3 Numerical results and discussion

For getting numerical solutions for the neuron oscillator driven by variant acoustic wave, the fourth-order Runge–Kutta algorithm is applied and the time step is fixed at $h = 0.01$ and the transient period is about 1000 time units. In generic way, the chaotic signals can present wide band and frequency range, and they can be used as signal source. As mentioned above, the chaotic voltage from the Chua circuit can be used as acoustic signal before being absorbed by the piezoelectric ceramics, which can generate variant voltage and current across this branch circuit, and then the neural circuit is excited effectively. At first, chaotic outputs signal from Eq. (10) are filtered according to the criterion shown in Eq. (7), and the original signals and the spectrum after frequency selection are plotted in Fig. 2.

That is, the thresholds ω_{max} , ω_{min} control the frequency band in the filtered signal. As shown in Fig. 2, acoustic signal within high frequency and low frequency can be filtered. For clear illustration, Fig. 3 shows the selection of frequency by applying different threshold for ω_{max} , ω_{min} .

In fact, decreasing the distance between ω_{max} , ω_{min} enables the filtered signal present sole frequency and period, and the functional neuron can be excited by

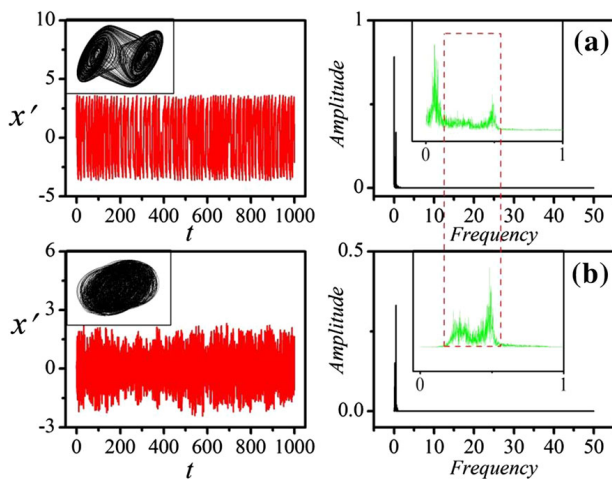


Fig. 2 Acoustic signal (sampled from Chua system) and the filtered acoustic signal are calculated in the time domain and frequency domain. (a) Original acoustic signal and its spectrum after FFT; (b) filtered acoustic signal and its spectrum after FFT. The threshold for frequency selection is activated at $\omega_{max} = 0.75$, $\omega_{min} = 0.25$, and the parameters are selected as $a = 0.7$, $b = 0.8$, $c = 0.1$, $\xi = 0.15$ with initials (0.2, 0.1) in the neuron. The inserted subfigure is an enlarged one within the region [0, 1]

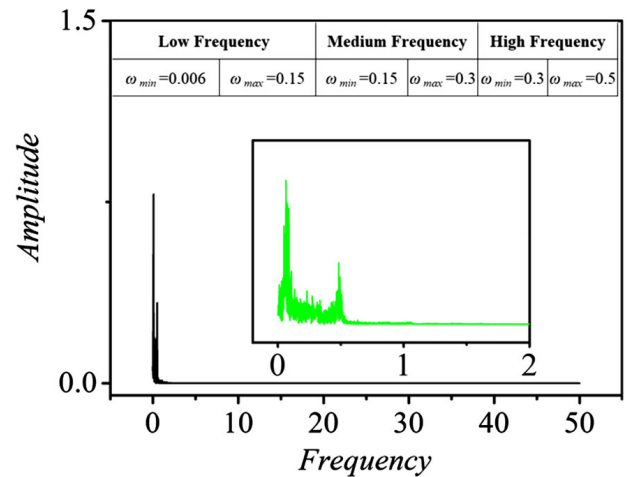


Fig. 3 Setting thresholds ω_{max} , ω_{min} for filtering acoustic signals from the signal source in Eq. (10). The inserted subfigure is an enlarged one within the region [0, 2]

distinct periodical stimulus for generating certain firing modes. In the absence of noise, when the amplitude of periodical stimulus is fixed, the angular frequency in Eq. (6) is changed to trigger different firing modes in the electrical activities, and the results are plotted in Fig. 4.

The excitability of the neuron can be controlled by changing the external stimulus, and a variety of firing modes can be induced in the neural activities when the frequency is changed carefully even within small region. In practical way, the filtered acoustic signal can be used to excite this functional neuron, and the

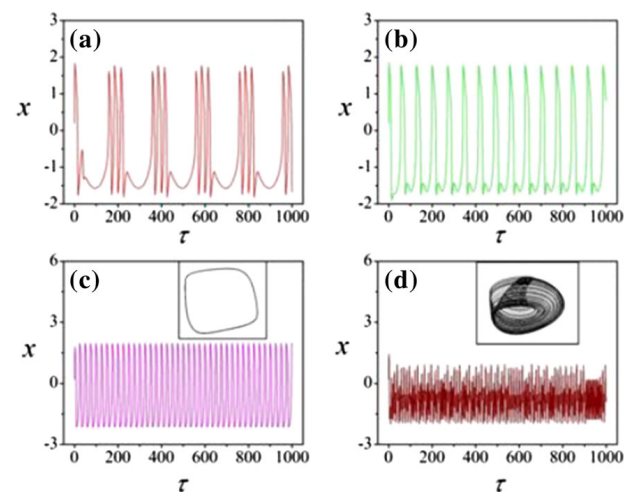


Fig. 4 Sampled time series for the membrane potential in the functional neuron is calculated by changing the angular frequency in the external stimulus. For **a** $\omega = 0.004$; **b** $\omega = 0.012$; **c** $\omega = 0.05$; **d** $\omega = 0.15$. The parameters are fixed at $a = 0.7$, $b = 0.8$, $c = 0.1$, $\xi = 0.15$, $A = 1.0$

electric activities in the neuron driven by low-frequency signals are presented in Fig. 5.

From Fig. 5, it is demonstrated that the filter signal within low-frequency band can excite the neuron for generating continuous firing patterns with multiple frequency and mixed modes are induced effectively. Furthermore, the effect of noise accompanied with low frequency in the filtered signals is estimated by calculating the signal-to-noise ratio (SNR) [10] and CV derived from the interspike interval (ISI) series in Fig. 6, respectively.

$$SNR = 10 \log_{10} \frac{S}{B}, \quad B = \frac{\Delta\omega}{\omega_p} \quad (12)$$

where S represents the height of the signal peak (values of the output power spectrum density at the peak) and B denotes the amplitude of the background noise measured at the base of the signal peak (the base of the signal feature). $\Delta\omega$ is the width for half height of signal peak, and ω_p is the frequency located to the peak frequency. The coherence degree is described by the CV value and it indicates higher regularity in the signal at lower CV value. When stochastic resonance and coherence resonance occur, the firing patterns show distinct regularity and the distribution for SNR and CV is, respectively, calculated in Fig. 6 by changing the noise intensities carefully.

It is confirmed that SNR can reach peak value while CV gets smallest value when intermediate noise intensity is applied to excite the functional neuron accompanied driving by signals with low-frequency bands. And the peak value locates the appropriate noise intensity $D = 7.0$. For better illustration, the firing patterns in the neuron are presented in Fig. 7 by applying different noise intensities.

That is, the involvement of noise can enhance the disturbance on the firing patterns and multiple modes can be induced in the neural activities. Furthermore, we investigate the case when the filtered signals within medium frequency band and the electrical activities are presented in Fig. 8.

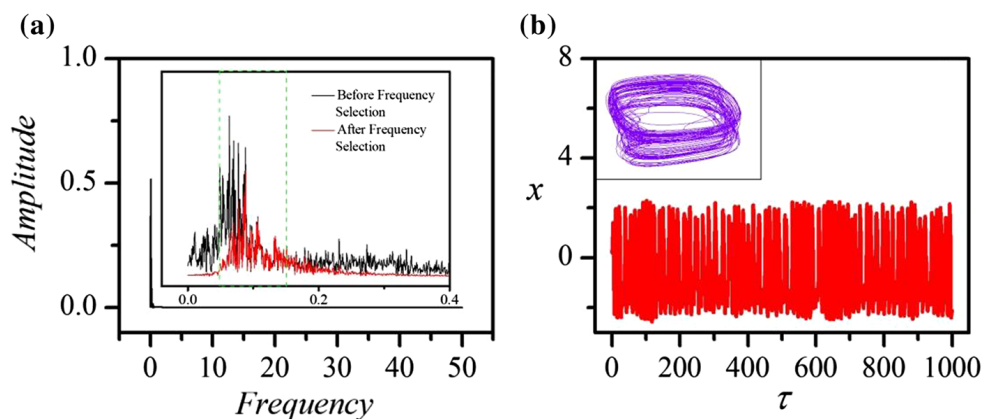
When the filtered signal within medium frequency band is applied, the neural circuit is excited by external stimuli with multiple frequencies. As a result, the firing patterns become more complex than presenting sole firing modes. It indicates that this functional neural circuit keeps sensitive response to the realistic stimuli and generates appropriate mode selection in the electrical activities. By the way, the noise effect is also estimated by calculating the SNR and CV in Fig. 9 when the noise intensity is adjusted in wider range.

It is confirmed that SNR can reach the peak value at noise intensity $D = 26$, and similar stochastic resonance is induced completely. Furthermore, noise intensity is changed to trigger different firing patterns in Fig. 10.

With the increasing of noise intensity, the chaotic firing is enhanced in the neuron driven by the filtered signals within medium frequency band, and the neuron can give appropriate response in electrical activities in time. For the high-frequency band, the mode selection in the neuron and the filtered signals are presented in Fig. 11.

It indicates that the neuron tends to generate chaotic firing patterns when filtered signal with higher frequency is applied to excite the neuron. It is interesting to judge whether similar nonlinear resonance can be induced when noise is accompanied with this filtered signal in high frequency, and the SNR, CV distribution dependence on the noise intensity is estimated, respectively, in Fig. 12.

Fig. 5 Filtered acoustic signal (a) and the sampled time series (b) for the neuron driven by the filtered signal. The parameters are fixed at $a = 0.7$, $b = 0.8$, $c = 0.1$, $\xi = 0.15$, $\omega_{max} = 0.15$, $\omega_{min} = 0.006$



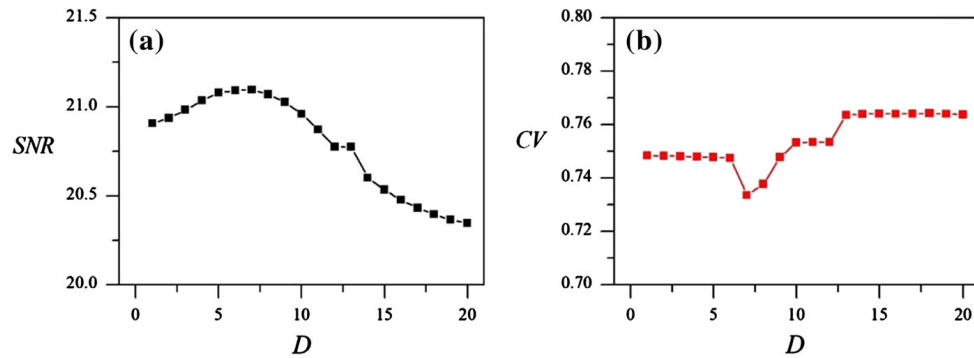


Fig. 6 SNR and CV dependence on the noise intensity. The parameters are selected as $a = 0.7$, $b = 0.8$, $c = 0.1$, $\xi = 0.15$, $\omega_{max} = 0.15$, $\omega_{min} = 0.006$. The threshold for peak value is

selected with 1.0 for detecting ISI value, which measures the period between two successive peaks in the sampled time series for membrane potential x

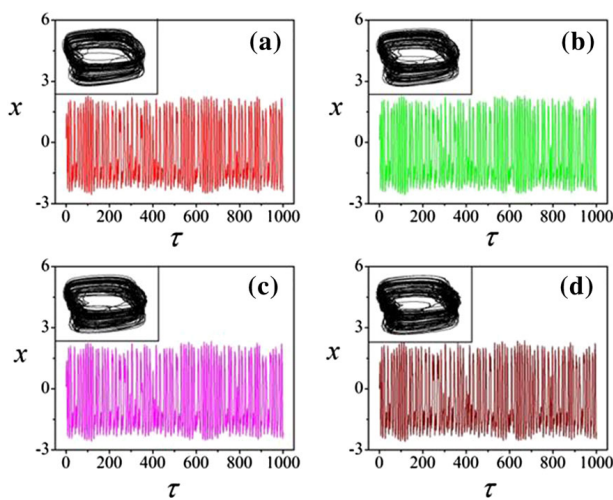


Fig. 7 Firing patterns and attractors in the neuron by applying different noise intensities. For (a) $D = 1$; (b) $D = 7$; (c) $D = 12$; (d) $D = 18$. The parameters are selected as $a = 0.7$, $b = 0.8$, $c = 0.1$, $\xi = 0.15$, $\omega_{max} = 0.15$, $\omega_{min} = 0.006$

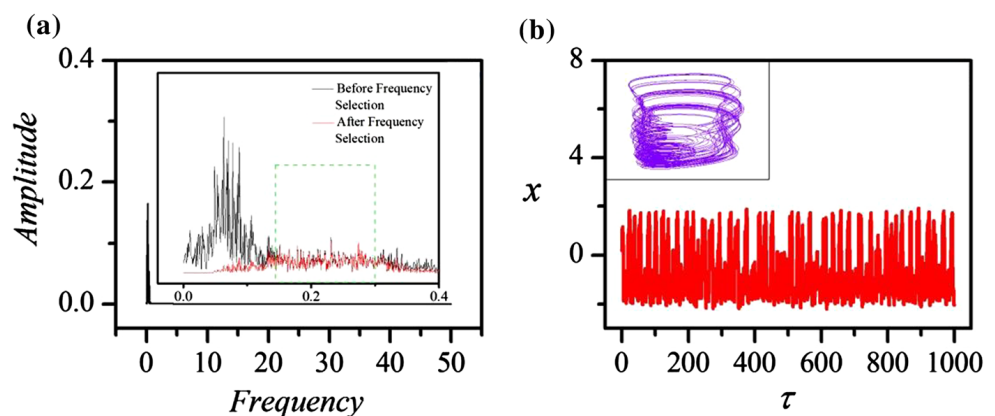
A peak value is stabilized for SNR at $D = 0.4$, and further increase of the noise intensity will corrupt the regularity in the neural activities of this functional

neuron. That is, appropriate noise setting in the intensity will enhance the auditory effect and the signal is discerned clearly. In addition, the firing patterns are plotted by applying noise disturbance in the filtered signals with high frequency, and the results are presented in Fig. 13.

Indeed, it indicates that decoded sound voice becomes unclear when the electrical activities in this functional neuron becomes more chaotic and decomposition of the sound signal becomes difficult. In this way, the ear function is destroyed and noisy condition makes the capacity of discernment in auditory system breakdown.

Indeed, the function of tympanic membrane and spiral organ to the cochlea are reproduced by the piezoelectric device coupled with the neural circuit, and acoustic wave is captured and encoded for inducing different firing patterns and action potentials. Some bands of the acoustic wave are absorbed and decayed soon while appropriate bands of the acoustic wave are effective to realize piezoelectric effect for generating electric signal and the neural circuit is

Fig. 8 Filtered acoustic signal **a** and the sampled time series **b** for the neuron driven by the filtered signal. The parameters are selected as $a = 0.7$, $b = 0.8$, $c = 0.1$, $\xi = 0.15$, $\omega_{max} = 0.3$, $\omega_{min} = 0.15$



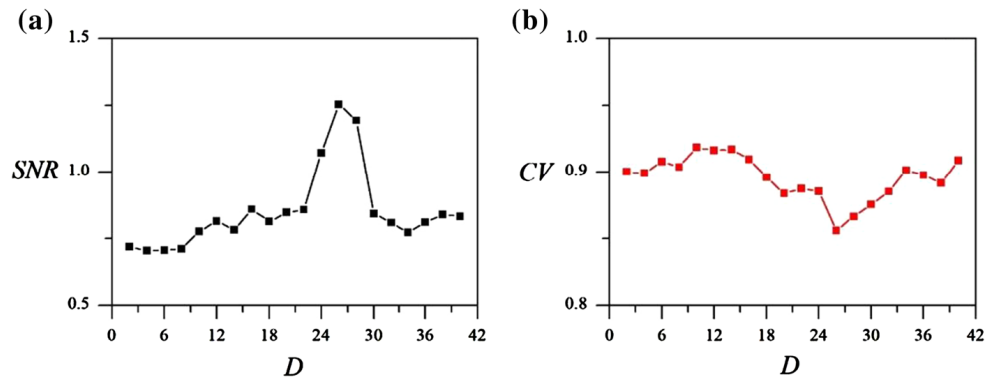


Fig. 9 SNR and CV dependence on the noise intensity. The parameters are fixed at $a = 0.7$, $b = 0.8$, $c = 0.1$, $\xi = 0.15$, $\omega_{max} = 0.3$, $\omega_{min} = 0.15$. The threshold for peak value is

selected with 1.0 for detecting ISI value, which measures the period between two successive peaks in the sampled time series for membrane potential x

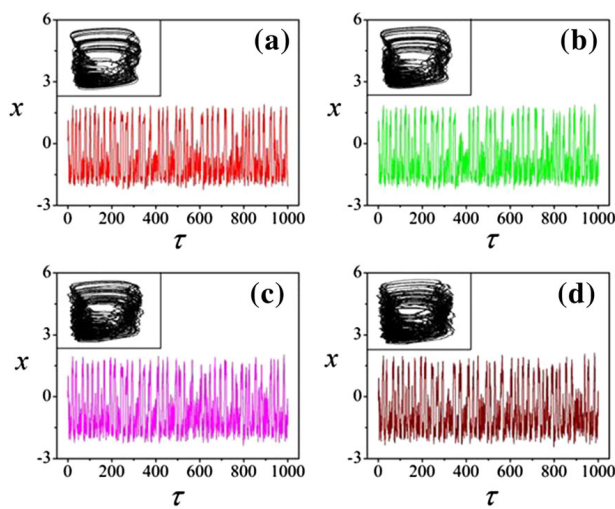
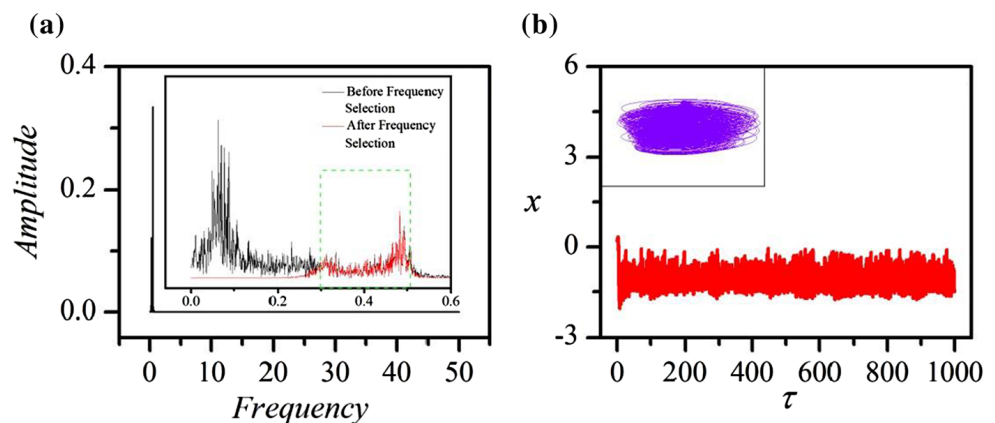


Fig. 10 Firing patterns and attractors in the neuron by applying different noise intensities. For **a** $D = 8.0$; **b** $D = 12.0$; **c** $D = 26$; **d** $D = 36$. The parameters are kept as $a = 0.7$, $b = 0.8$, $c = 0.1$, $\xi = 0.15$, $\omega_{max} = 0.3$, $\omega_{min} = 0.15$

Fig. 11 Filtered acoustic signal **a** and the sampled time series **b** for the neuron driven by the filtered signal. The parameters are fixed at $a = 0.7$, $b = 0.8$, $c = 0.1$, $\xi = 0.15$, $\omega_{max} = 0.5$, $\omega_{min} = 0.3$



excited. In fact, for better detection of the acoustic waves in noisy condition, more piezoelectric devices can be used to couple the neural circuit, and more artificial auditory neural circuits can be connected in array and the sensitivity for wider bands can be enhanced. Also, the similar algorithm for the wave filter and frequency selection can be further used for detection of ultrasonic in bats and optical filter in visual systems for animals.

4 Open problems

The biological tissue and nervous system develop certain self-adaption function for blocking noise and stochastic disturbance, and thus signal can be well detected and encoded. For example, all ears can be strained and cocked to hear slight sounds voice.

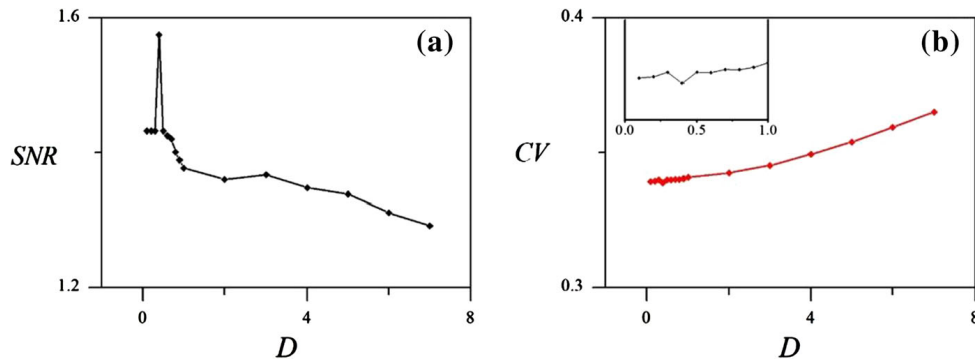


Fig. 12 SNR and CV dependence on the noise intensity. The parameters for neuron are fixed at $a = 0.7$, $b = 0.8$, $c = 0.1$, $\xi = 0.15$, $\omega_{max} = 0.5$, $\omega_{min} = 0.3$. The threshold for peak value

is selected with 1.0 for detecting ISI value, which measures the period between two successive peaks in the sampled time series for membrane potential x

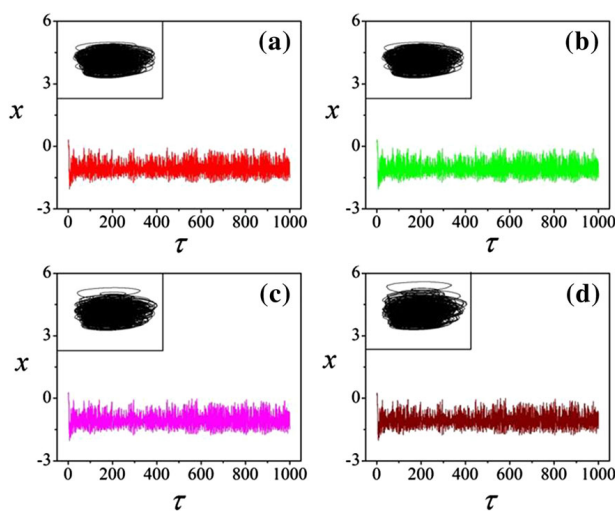


Fig. 13 Firing patterns and attractors in the neuron by applying different noise intensities. For **a** $D = 0.2$; **b** $D = 0.4$; **c** $D = 4.0$; **d** $D = 6.0$. The parameters are selected as $a = 0.7$, $b = 0.8$, $c = 0.1$, $\xi = 0.15$, $\omega_{max} = 0.5$, $\omega_{min} = 0.3$

Squinting the eyes enable possible capturing the blurry images and objects in the distance. Therefore, the signal source comes from this neural circuit, the frequency selection mechanism can be helpful for selecting the most suitable firing patterns and modes. For example, the output signals from this functional neural circuit can control its frequency as follows

$$\frac{d\omega}{d\tau} = f(x) = k \sin x \quad (13)$$

where the coefficient k can be carefully selected within appropriate range and then the acoustic wave will cover larger band. The variable x can be obtained from the functional neuron defined in Eq. (5), and other appropriate forms for $f(*)$ in Eq. (12) can be selected to approach acoustic wave with different bands. For

example, the sound signals can be recorded series or generated from another signal source, and the frequency selection is controlled under the criterion shown in Eq. (7). Accompanied with Eq. (13), after wave filter and frequency selection, the voltage-controlled current ξu_{pc} will be controlled in the amplitude and frequency with time, and then the auditory neuron is excited for generating kinds of firing modes and then the electrical signals are propagated to the brain for further processing with the gaits. As reported in some of the previous works, the biophysical energy accounts for the mode selection when the neuron is excited to propagate different electrical signals, and the Hamilton energy mapped from the physical field energy in these electric components can be obtained by

$$W = \frac{1}{2} CV^2 + \frac{1}{2} Li_L^2; \quad H = \frac{W}{CV_0^2} = \frac{1}{2} x^2 + \frac{1}{2c} y^2 \quad (14)$$

where the variable V , i_L describes the output voltage across the capacitor and channel current across the induction coil, respectively. The Hamilton energy H measures the equivalent field energy in the neural circuit, and it is effective to estimate the correlation and dependence between channel current and membrane potential. In fact, any slight changes in the Hamilton energy indicate the occurrence of mode selection and transition in the firing patterns, and fast firing means quick release of energy and lower average Hamilton energy is approached. As is well known, both electric and chemical synapses can enable effective signal processing and encoding in biophysical signals, and the energy is absorbed to

regulate the distribution and propagation of intracellular and extracellular ions of the cell. Then a lot of firing modes can be activated and selected effectively. The biophysical mechanism for frequency selection in the neural circuit can filter some wave bands and appropriate firing modes can be selected. Furthermore, the collective electrical activities of neural networks can be optimized and synchronized under field coupling [57–59], which can enhance signal and energy exchange even synapse coupling is suppressed. For these functional neurons and neural circuits under hybrid synapse connection or field coupling (connected via capacitor, induction coil, memristor, Josephson junction), continuous regulation and controllability in the coupling channels can explain the biophysical mechanism of synaptic plasticity and activation of chemical synapse. Therefore, for forthcoming study on pattern selection and control of synchronization stability in neural networks, the effect of frequency selection should be considered than applying any external stimuli on the neurons and networks.

5 Conclusions

In this paper, an artificial auditory neural circuit is proposed by incorporating piezoelectric device into a feasible neural circuit, and reliable algorithm for wave filtering is presented to discern the acoustic wave via the piezoelectric ceramics. In a noisy condition, this functional neural circuit can be effective to discern and encode the acoustic wave and trigger effective action potentials, and then appropriate firing modes are triggered in the artificial neuron. As a result, the brain is informed to guide the body to behave suitable gaits. The results well addressed the biophysical function of auditory neurons and the mechanism for wave filtering and frequency selection in the sound signals. Readers in this field can further explore the collective behaviors of functional network composed of auditory neurons driven by more acoustic waves.

Acknowledgements This project is partially supported by the National Natural Science Foundation of China under Grant No. 12072139.

Data availability statement The datasets generated during and/or analyzed during the current study are available from the corresponding author on reasonable request.

Declarations

Conflict of interest The authors declare that they have no conflict of interest.

References

1. Karak, S., Jacobs, J.S., Kittelmann, M., et al.: Diverse roles of axonemal dyneins in *Drosophila* auditory neuron function and mechanical amplification in hearing. *Sci. Rep.* **5**, 17085 (2015)
2. Cody, A.R., Johnstone, B.M.: Single auditory neuron response during acute acoustic trauma. *Hear. Res.* **3**(1), 3–16 (1980)
3. Tritsch, N.X., Rodríguez-Contreras, A., Crins, T.T., et al.: Calcium action potentials in hair cells pattern auditory neuron activity before hearing onset. *Nat. Neurosci.* **13**(9), 1050–1052 (2010)
4. Venail F, Mura T, Akkari M, et al. Modeling of auditory neuron response thresholds with cochlear implants. *BioMed Research International* 2015, 2015:398647.
5. Mizrahi, A., Shalev, A., Nelken, I.: Single neuron and population coding of natural sounds in auditory cortex. *Curr. Opin. Neurobiol.* **24**, 103–110 (2014)
6. Zhou P, Yao Z, Ma J, et al. A piezoelectric sensing neuron and resonance synchronization between auditory neurons under stimulus. *Chaos, Solitons & Fractals* 2021, 145:110751.
7. Lukić, J., Denić, D.: A novel design of an NTC thermistor linearization circuit. *Metrol. Measurement Syst.* **22**(3), 351–362 (2015)
8. Zhang, X., Wang, C., Ma, J., et al.: Control and synchronization in nonlinear circuits by using a thermistor. *Mod. Phys. Lett. B* **34**(25), 2050267 (2020)
9. Ibrahim, O., Hassan, S.M., Abdulkarim, A., et al.: Design of wheatstone bridge based thermistor signal conditioning circuit for temperature measurement. *J. Eng. Sci. Technol. Rev.* **12**, 12–17 (2019)
10. Xu Y, Guo Y, Ren G, et al. Dynamics and stochastic resonance in a thermosensitive neuron. *Applied Mathematics and Computation* 2020, 385:125427.
11. Xu Y, Liu M, Zhu Z, et al. Dynamics and coherence resonance in a thermosensitive neuron driven by photocurrent. *Chinese Physics B* 2020, 29:098704.
12. Nakayama, T.: Thermosensitive neurons in the brain. *Jpn. J. Physiol.* **35**, 375–389 (1985)
13. Liu, Y., Xu, W., Ma, J., et al.: A new photosensitive neuron model and its dynamics. *Front. Inform. Technol. Electron. Eng.* **21**, 1387–1396 (2020)
14. Liu Y, Xu Y, Ma J.: Synchronization and spatial patterns in a light-dependent neural network. *Commun. Nonlinear Sci. Numer. Simul.* **89**, 105297 (2020)
15. Guo Y, Zhu Z, Wang C, et al. Coupling synchronization between photoelectric neurons by using memristive synapse. *Optik* 2020, 218:164993.
16. Saira O P, Zgirski M, Viisanen K L, et al. Dispersive thermometry with a Josephson junction coupled to a resonator. *Phys. Rev. Appl.* 2016, 6:024005.

17. Koudafokê G N, Hinvì L A, Miwadinou C H, et al. Passive sensor with Josephson junction coupled to an electric resonator and a nanobeam. *Sens Actuat A: Phys.* 2021, 318:112509.
18. Pountounigni O V, Yamapi R, Filatrella G, et al. Noise and disorder effects in a series of birhythmic Josephson junctions coupled to a resonator. *Phys. Rev. E* 2019, 99:032220.
19. Zhang, Y., Zhou, P., Tang, J., et al.: Mode selection in a neuron driven by Josephson junction current in presence of magnetic field. *Chin. J. Phys.* **71**, 72–84 (2020)
20. Zhang, Y., Xu, Y., Yao, Z., et al.: A feasible neuron for estimating the magnetic field effect. *Nonlinear Dyn.* **102**, 1849–1867 (2020)
21. Lin, H., Wang, C., Sun, Y., et al.: Firing multistability in a locally active memristive neuron model. *Nonlinear Dyn.* **100**, 3667–3683 (2020)
22. Chen, M., Qi, J.W., Wu, H.G., et al.: Bifurcation analyses and hardware experiments for bursting dynamics in non-autonomous memristive FitzHugh-Nagumo circuit. *Sci. China Technol. Sci.* **63**, 1035–1044 (2020)
23. Bao, B., Zhu, Y., Ma, J., et al.: Memristive neuron model with an adapting synapse and its hardware experiments. *Sci. China Technol. Sci.* **64**, 1107–1117 (2021)
24. Kwon M W, Baek M H, Hwang S, et al. Integrate-and-fire neuron circuit using positive feedback field effect transistor for low power operation. *J. Appl. Phys.* **124**(15), 152107 (2018)
25. Yang, Z., Zhang, Y., Wu, F.: Memristive magnetic coupling feedback induces wave-pattern transition. *Nonlinear Dyn.* **100**, 647–658 (2020)
26. Juzekaeva, E., Nasretidinov, A., Battistoni, S., et al.: Coupling cortical neurons through electronic memristive synapse. *Advanced Materials Technologies* **4**(1), 1800350 (2019)
27. Wu, F., Zhang, Y., Zhang, X.: Regulating firing rates in a neural circuit by activating memristive synapse with magnetic coupling. *Nonlinear Dyn.* **98**, 971–984 (2019)
28. Jin, W., Wang, A., Ma, J., et al.: Effects of electromagnetic induction and noise on the regulation of sleep wake cycle. *Sci China Technol. Sci.* **62**(12), 2113–2119 (2019)
29. Lu, L., Jia, Y., Xu, Y., et al.: Energy dependence on modes of electric activities of neuron driven by different external mixed signals under electromagnetic induction. *Sci. China Technol. Sci.* **62**, 427–440 (2019)
30. Rajagopal, K., Nazarimehr, F., Karthikeyan, A., et al.: Dynamics of a neuron exposed to integer-and fractional-order discontinuous external magnetic flux. *Front. Inform. Technol. Electron. Eng.* **20**(4), 584–590 (2019)
31. Parastesh, F., Rajagopal, K., Karthikeyan, A., et al.: Complex dynamics of a neuron model with discontinuous magnetic induction and exposed to external radiation. *Cogn. Neurodyn.* **12**, 607–614 (2018)
32. Mondal, A., Upadhyay, R.K., Ma, J., et al.: Bifurcation analysis and diverse firing activities of a modified excitable neuron model. *Cogn. Neurodyn.* **13**, 393–407 (2019)
33. Ge, M.Y., Wang, G.W., Jia, Y., et al.: Influence of the Gaussian colored noise and electromagnetic radiation on the propagation of subthreshold signals in feedforward neural networks. *Sci. China Technol. Sci.* **64**, 847–857 (2021)
34. Zhan, F., Liu, S.: Response of electrical activity in an improved neuron model under electromagnetic radiation and noise. *Front. Comput. Neurosci.* **11**, 107 (2017)
35. Ma, J., Yang, Z., Yang, L., et al.: A physical view of computational neurodynamics. *J. Zhejiang Univ.-Sci. A* **20**(9), 639–659 (2019)
36. Shi, S., Xiao, M., Rong, L., et al.: Stability and bifurcation control of a neuron system under a novel fractional-order PD controller. *Sci. China Technol. Sci.* **62**, 2120–2129 (2019)
37. Wu, F., Ma, J., Zhang, G.: Energy estimation and coupling synchronization between biophysical neurons. *Sci. China Technol. Sci.* **63**, 625–636 (2020)
38. He, Z.W., Yao, C.G.: The effect of oxygen concentration on the coupled neurons: rich spiking patterns and synchronization. *Sci. China Technol. Sci.* **63**(11), 2339–2348 (2020)
39. Xiao, W., Gu, H., Liu, M.R.: Spatiotemporal dynamics in a network composed of neurons with different excitabilities and excitatory coupling. *Sci. China Technol. Sci.* **59**(12), 1943–1952 (2016)
40. Wang, C., Tang, J., Ma, J.: Minireview on signal exchange between nonlinear circuits and neurons via field coupling. *Eur. Phys. J. Special Topics* **228**(10), 1907–1924 (2019)
41. Feller, M.B.: Spontaneous correlated activity in developing neural circuits. *Neuron* **22**(4), 653–656 (1999)
42. Sussillo, D.: Neural circuits as computational dynamical systems. *Curr. Opin. Neurobiol.* **25**, 156–163 (2014)
43. Mercer, A.J., Hentges, S.T., Meshul, C.K., et al.: Unraveling the central proopiomelanocortin neural circuits. *Front. Neurosci.* **7**, 19 (2013)
44. Bokinec, P., Zampieri, N., Lewin, G.R., et al.: The neural circuits of thermal perception. *Curr. Opin. Neurobiol.* **52**, 98–106 (2018)
45. Wang, H., Chen, Y.: Response of autaptic Hodgkin-Huxley neuron with noise to subthreshold sinusoidal signals. *Phys. A* **462**, 321–329 (2016)
46. Hilborn, R.C., Erwin, R.J.: Coherence resonance in models of an excitable neuron with noise in both the fast and slow dynamics. *Phys. Lett. A* **322**(1–2), 19–24 (2004)
47. Hauschildt B, Janson N B, Balanov A, et al. Noise-induced cooperative dynamics and its control in coupled neuron models. *Phys. Rev. E* 2006, 74:051906.
48. Wang, Z., Shi, X.: Electric activities of time-delay memristive neuron disturbed by Gaussian white noise. *Cogn. Neurodyn.* **14**, 115–124 (2020)
49. Kafraj M S, Parastesh F, Jafari S. Firing patterns of an improved Izhikevich neuron model under the effect of electromagnetic induction and noise. *Chaos, Solitons & Fractals* 2020, 137:109782.
50. Kyprianidis, I.M., Papachristou, V., Stouboulos, I.N., et al.: Dynamics of coupled chaotic Bonhoeffer–van der Pol oscillators. *WSEAS Trans. Syst.* **11**(9), 516–526 (2012)
51. Rajasekar, S., Lakshmanan, M.: Period-doubling bifurcations, chaos, phase-locking and devil’s staircase in a Bonhoeffer–van der Pol oscillator. *Physica D* **32**, 146–152 (1988)
52. Gu, H., Zhang, H., Wei, C., et al.: Coherence resonance–induced stochastic neural firing at a saddle-node bifurcation. *Int. J. Mod. Phys. B* **25**(29), 3977–3986 (2011)

53. Yu, H., Galán, R.F., Wang, J., et al.: Stochastic resonance, coherence resonance, and spike timing reliability of Hodgkin-Huxley neurons with ion-channel noise. *Phys. A* **471**, 263–275 (2017)
54. Song, X., Wang, H., Chen, Y.: Coherence resonance in an autaptic Hodgkin-Huxley neuron with time delay. *Nonlinear Dyn.* **94**, 141–150 (2018)
55. Chua, L.O.: Chua's circuit: an overview ten years later. *J Circuits, Syst. Comput.* **4**(2), 117–159 (1994)
56. Chua, L.O., Kocarev, L., Eckert, K., et al.: Experimental chaos synchronization in Chua's circuit. *Int. J. Bifurcation and Chaos* **2**(3), 705–708 (1992)
57. Lv, M., Ma, J., Yao, Y.G., et al.: Synchronization and wave propagation in neuronal network under field coupling. *Sci. China Technol. Sci.* **62**(3), 448–457 (2019)
58. Xu, Y., Jia, Y., Wang, H., et al.: Spiking activities in chain neural network driven by channel noise with field coupling. *Nonlinear Dyn.* **95**, 3237–3247 (2019)
59. Zhang, Y., Wang, C., Tang, J., et al.: Phase coupling synchronization of FHN neurons connected by a Josephson junction. *Sci. China Technol. Sci.* **63**, 2328–2338 (2020)

Publisher's Note Springer Nature remains neutral with regard to jurisdictional claims in published maps and institutional affiliations.



Control the stability in chaotic circuit coupled by memristor in different branch circuits

Yitong Guo^a, Zhao Yao^a, Ying Xu^b, Jun Ma^{a,c,*}

^a Department of Physics, Lanzhou University of Technology, Lanzhou 73005, China

^b School of Mathematics and Statistics, Shandong Normal University, Ji'nan 250014, China

^c School of Science, Chongqing University of Posts and Telecommunications, Chongqing 430065, China

ARTICLE INFO

Keywords:
Memristor
Bifurcation
Hamilton energy
Chaotic circuit

ABSTRACT

A memristor is incorporated into one branch circuit, and the effect of electromagnetic induction in the chaotic circuit is discussed. The involvement of memristor into different branch circuit just changes the energy exchange and balance in the chaotic circuit and then the dynamics and Hamilton energy can be adjusted completely. The magnetic field energy in the memristor can compensate and suppress the pumping and exchange of electric field energy in the capacitor along the same branch circuit. Therefore, the energy pumping is terminated, and then the chaotic circuit is controlled completely when the memristor is connected to the capacitor in the branch circuit. When memristor is connected to the induction coil in series, the current across the memristor has slight impacts on changing the chaotic states even stochastic disturbance is applied because the magnetic field energy can be shared between the memristor and induction coil. Additive branch circuit composed of isolated memristor can be connected to chaotic circuits for enhancing its memory effect. The connection of memristor to capacitor along any branch circuits of chaotic circuits will control the chaos, while connection to induction coil in series can change the dissipation and chaos is kept well.

1. Introduction

Nonlinear circuits can be controlled to present a variety of firing modes in the sampled series for output voltage, and some chaotic circuits [1–4] can be used as reliable signal generator for producing stable output voltage and continuous periodical signals as well. Some of the chaotic systems have potential application in the field of secure communication and image encryption [5–9]. The realization and activation of nonlinear circuits depend on the intrinsic physical properties of nonlinear electric components and external stimuli as well. For building generic chaotic and hyperchaotic circuits, the capacitor, induction coil, nonlinear resistor and/or channel diode, linear resistors are often connected in parallel and in series for completing more close loops and nodes. For further dynamical analysis and control, scale transformation [10] is applied for the variables and physical parameters of electric components and then dimensionless nonlinear oscillators are obtained. Furthermore, two or more chaotic oscillators are coupled to stabilize synchronization control [11–14], and parameter estimation [15–18], pattern selection and control [19–22] by applying more feasible schemes.

Memristor is a specific electric component, and its memristive property can enhance the release and activation of specific biophysical function when it is incorporated into neural circuits. The collective behaviors of networks and coupled oscillators are dependent on the physical properties of coupling channels, local kinetics of nodes, and topological connection between nodes in the network [23–25]. The direct variable coupling results from the voltage coupling via linear resistor, and continuous consumption of Joule heat will change the energy exchange and propagation and thus chaotic circuits can be controlled completely. In practical way, the coupling channel should be controllable so that the coupling intensity can be adjusted and the most suitable coupling intensity is confirmed with lower control cost (shorter transient period, lower energy cost). For example, when the parameters are unknown, the saturation gain method [26,27] becomes available and effective for synchronization stabilization between chaotic and neural circuits because the coupling intensity can be increased with slight step before reaching complete synchronization even all the parameters of the coupled chaotic systems are unknown. On the other hand, adaptive synchronization [28–30] can be applied for estimating unknown parameters in the chaotic systems when the parameter

* Corresponding author at: Department of Physics, Lanzhou University of Technology, Lanzhou 73005, China.
E-mail address: hyperchaos@163.com (J. Ma).

<https://doi.org/10.1016/j.aue.2021.154074>

Received 3 November 2021; Accepted 12 December 2021

Available online 20 December 2021

1434-8411/© 2021 Elsevier GmbH. All rights reserved.

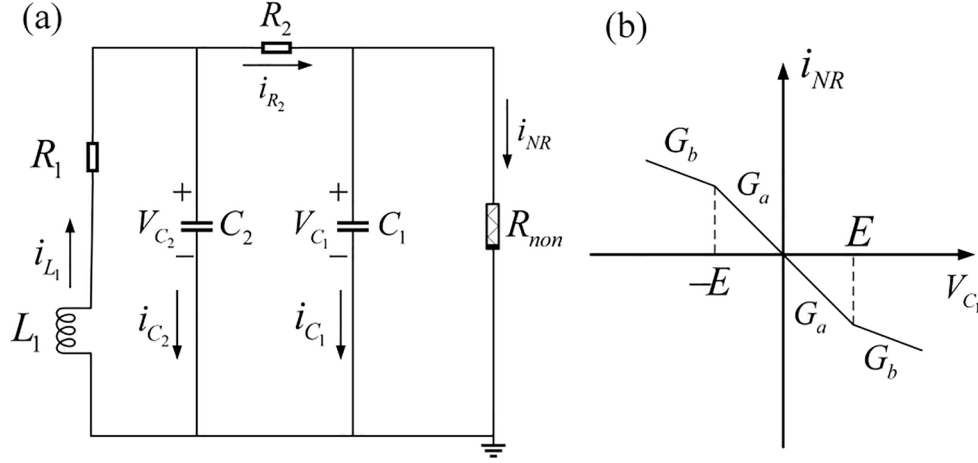


Fig. 1. Schematic diagram for Chua circuit. R_{non} denotes the Chua diode.

observers are controllable. In fact, the involvement of specific electric components coupled to the nonlinear circuits can utilize some physical abilities by changing the channel current in practical way. For example, Josephson junction [31–33] has the physical property as induction coil and it can estimate the effect of magnetic field [34,35] when it is coupled with some nonlinear circuits. Electric field is activated in the coupling channel when capacitor is used to couple chaotic circuits, and complete synchronization can be stabilized when energy pumping and exchange are controlled for balance along the coupling channel [36–38]. Magnetic field is induced in the coupling channel when induction coil is used to bridge connection between neural circuits, and it explains the biophysical mechanism for chemical synapse coupling between biological neurons [39,40]. Memristor is a new specific electric component and bridges connection to magnetic flux and charge [41–44], and its distinct memory property shows that the memductance is dependent on the passed current and propagated charges along the channel. From dynamical viewpoint, the involvement of time delay and fractional calculus [45,46] can introduce and estimate the memory effect. Memristive synapse [47–50] is designed when memristor is connected to neural circuits, and synaptic plasticity is reproduced when memristor is used to couple neural circuits and the coupling channels become changeable. These memristor-coupled nonlinear circuits can be mapped and developed to get a variety of memristive systems [51–53], which the dynamics is dependent on the initial value for the memristive variable, and the synchronization stability is also changed when the memristive variable is disturbed even the coupling intensity and parameters are fixed [54,55]. In particular, the effect of electromagnetic induction and radiation on biological neurons can be explained when magnetic flux and induction current are considered according to the Faraday's law of electromagnetic induction and the principle of dimensional consistency [56].

In fact, the current balance between different branch circuits can control the energy exchange and dynamics in the nonlinear circuits. As a result, the branch circuit current becomes changeable and memristive when a memristor is incorporated into this branch circuit. In presence of external magnetic field, the propagation of charges and fluctuation of the magnetic flux will be affected because the channel current across the memristor is dependent on external magnetic flux. Therefore, the memristor-coupled nonlinear circuit will present different sensitivities and dynamics dependence on the initial value for memristive variable [57–59] when memristor is connected to different branch circuits in parallel. When memristor is coupled with the Chua circuit in an additive branch circuit, the shunted current across this memristor can excite the memristive Chua circuit in possible way [60–64]. However, the channel current will be controlled completely when a memristor is incorporated into any branch circuits by connecting to the capacitor, induction coil in

series, respectively. In this paper, a memristor is respectively connected to the capacitor, and induction coil in series for estimating the dynamics and stability, and the energy balance is also discussed. Bifurcation analysis and Lyapunov exponents are calculated when the memristor is connected to different electric components in Chua circuit, respectively. Furthermore, the external magnetic field is applied to estimate the stability in the memristive circuit by regulating the magnetic flux with noisy signal, and nonlinear resonance is investigated. These results could provide possible guidance for building more memristive circuits by placing the memristors into the most appropriate branch circuit and the memory effect is enhanced greatly.

2. Model and scheme

The original Chua circuit is composed of two capacitors, two linear resistors, one induction coil and one nonlinear resistor, and it can be controlled to present chaos by taming the intrinsic parameters for the electric components even any initial values are applied. In practical way, piecewise linear and Jerk functions for nonlinear electric devices can be applied to obtain multi-scroll attractors, and memristor can be coupled in an additive branch circuit to enhance its multistability and initials dependence. In Fig. 1, the original Chua circuit is presented, and the output voltages from the two capacitors can be tracked for further series analysis.

The circuit equations for an isolated Chua circuit can be described by

$$\begin{cases} C_1 \frac{dV_{C1}}{dt} = \frac{V_{C2} - V_{C1}}{R_2} - i_{NR} \\ C_2 \frac{dV_{C2}}{dt} = i_{L1} - \frac{V_{C2} - V_{C1}}{R_2}; \\ L_1 \frac{di_{L1}}{dt} = -i_{L1}R_1 - V_{C2} \end{cases} \quad (1a)$$

$$i_{NR} = f(V_{C1}) = G_b V_{C1} + 0.5(G_a - G_b)(|V_{C1} + E| - |V_{C1} - E|) \quad (1b)$$

where i_{NR} denotes the current across the nonlinear resistor (Chua diode), and V_{C1} , V_{C2} , i_{L1} represents the output voltage from capacitors and induction coil, respectively. Standard scale transformation shown in Eq.(2) is applied for all variables and parameters in the Eq.(1) as follows

$$\begin{cases} x = \frac{V_{C1}}{E}, y = \frac{V_{C2}}{E}, z = \frac{i_{L1}R_2}{E}, \tau = \frac{t}{R_2C_2}, \alpha = \frac{C_2}{C_1}, \\ \beta = \frac{C_2R_2^2}{L_1}, m_0 = R_2G_a, m_1 = R_2G_b, \gamma = \frac{R_1R_2C_2}{L_1}; \end{cases} \quad (2)$$

As a consequence, the dimensionless Chua system is obtained by

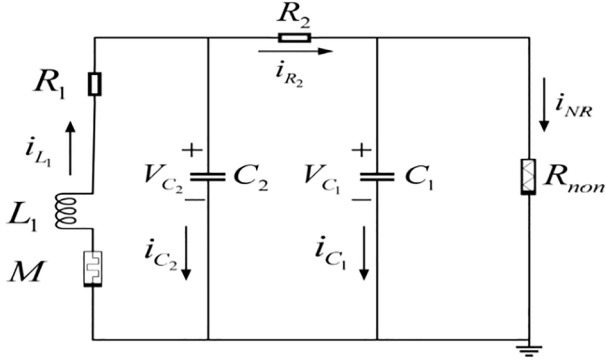


Fig. 2. Case 1: Memristive Chua circuit in which the memristor is connected to the induction coil L_1 in series. M and R_{non} describe the memristor and Chua diode. R_1 and R_2 represent the linear resistors.

$$\begin{cases} \dot{x} = \alpha(y - x) - \alpha f(x) \\ \dot{y} = x - y + z \\ \dot{z} = -\beta y - \gamma z \end{cases} \quad (3a)$$

$$f(x) = m_1 x + 0.5(m_0 - m_1)(|x + 1| - |x - 1|); \quad (3b)$$

where the nonlinear function $f(x)$ denotes the dimensionless current across the Chua diode (nonlinear resistor), and the variable x, y, z represents the variables mapped from the voltage, current across the two capacitors, and induction coil, respectively. The coefficients $\alpha, \beta, \gamma, m_0, m_1$ are normalized parameters for the electric components. As is well known, memristor is a specific physical component, and it bridges connection to the physical variables between magnetic flux and charge. The memory effect of memristor indicates that its memductance is relative to the propagated charges/current or exchange of magnetic flux, as a result, the variant current across the magnetic flux-controlled memristor can be estimated by

$$i_M = \frac{dq(\phi)}{dt} = \frac{dq(\phi)}{d\phi} \frac{d\phi}{dt} = M(\phi) \frac{d\phi}{dt} = M(\phi) V_M = (a + 3b\phi^2) V_M; \quad (4)$$

Here, ϕ describes the magnetic flux, $M(\phi)$ is memductance, and V_M denotes the voltage across the memristor. The magnetic flux across the memristor will be controlled when it is exposed to external magnetic field, as a result, the channel current will be controlled by external magnetic field when the memristor is incorporated into any branch circuit in the nonlinear circuit. Three cases are investigated, the memristor is used to connect to the capacitors and induction coil in series, respectively. The memristor is connected to the induction coil (Case 1), memristor connects the capacitor C_2 (Case 2), and memristor is bridged to capacitor C_2 (Case 3), and the physical parameters can be adjusted to discuss the dynamics dependence on the memristive variable. At first, we discuss the case when a magnetic flux-controlled memristor is connected to the induction coil in the Chua circuit, and the memristive circuit is plotted in Fig. 2.

According to the physical Kirchhoff theorem, the circuit equations for Fig. 2 can be obtained by

$$\begin{cases} C_1 \frac{dV_{C1}}{dt} = \frac{V_{C2} - V_{C1}}{R_2} - i_{NR} \\ C_2 \frac{dV_{C2}}{dt} = i_{L1} - \frac{V_{C2} - V_{C1}}{R_2} \\ L_1 \frac{di_{L1}}{dt} = -i_{L1} R_1 - V_{C2} - V_M \\ \frac{d\phi}{dt} = V_M \end{cases} \Rightarrow \begin{cases} i_{L1} = i_M \\ V_M = \frac{i_M}{a + 3b\phi^2} \end{cases} \Rightarrow \begin{cases} C_1 \frac{dV_{C1}}{dt} = \frac{V_{C2} - V_{C1}}{R_2} - i_{NR} \\ C_2 \frac{dV_{C2}}{dt} = i_M - \frac{V_{C2} - V_{C1}}{R_2} \\ L_1 \frac{di_M}{dt} = -i_M R_1 - V_{C2} - \frac{i_M}{a + 3b\phi^2} \\ \frac{d\phi}{dt} = \frac{i_M}{a + 3b\phi^2} \end{cases} \quad (5)$$

In addition, the current across the Chua diode is also described by Eq. (1b). V_M, ϕ represents the voltage across the memristor and magnetic flux for the memristor, while G_a, G_b, E denotes the conductance value, and cut-off voltage in the V - I curve for Chua diode, respectively. When the memristor is connected to the induction coil in series, both the induction coil and memristor are controlled by the same channel current. Therefore, the channel current along this branch circuit is described by the memristive current. For further nonlinear analysis, scale transformation as shown in Eq. (6) is applied for the physical variables and parameters in the circuit equation defined in Eq. (5), it meets as follows

$$\begin{cases} x = \frac{V_{C1}}{E}, y = \frac{V_{C2}}{E}, z = \frac{i_M R_2}{E}, \tau = \frac{t}{R_2 C_2}, \phi' = \frac{\phi(R_1 + R_2)}{EL_1}, \\ m_0 = R_2 G_a, m_1 = R_2 G_b, \alpha = \frac{C_2}{C_1}, \beta = \frac{C_2 R_2^2}{L_1}, \gamma = \frac{R_1 R_2 C_2}{L_1}, \end{cases} \quad (6)$$

As a consequence, the memristive Chua system for Case 1 can be represented by

$$\begin{cases} \dot{x} = \alpha(y - x) - \alpha f(x); \\ \dot{y} = x - y + z; \\ \dot{z} = -\gamma z - \beta y - \beta \frac{z}{(a' + b'\phi'^2)}; \\ \dot{\phi}' = (\beta + \gamma) \frac{z}{(a' + b'\phi'^2)}; \end{cases} \quad (7)$$

where the normalized parameters are defined as $a' = R_2 a$, $b' = 3b R_2 (EL_1)^2 / (R_1 + R_2)^2$, and they are relative to the selection of intrinsic parameters in the memristor. The normalized current across the Chua diode of Chua circuit is estimated in Eq. (3b). For further knowing the effect of memristor connection to different branch circuits, the physical energy in these components and the Hamilton energy is respectively calculated for three cases. The energy unit is estimated as $W_0 = C_2 E^2$, and the field energy in the memristor can be calculated as well when it is regarded as an equivalent inductor with appropriate inductance L_M . For Case 1, the field energy in the capacitors, induction coil and memristor are respectively obtained by

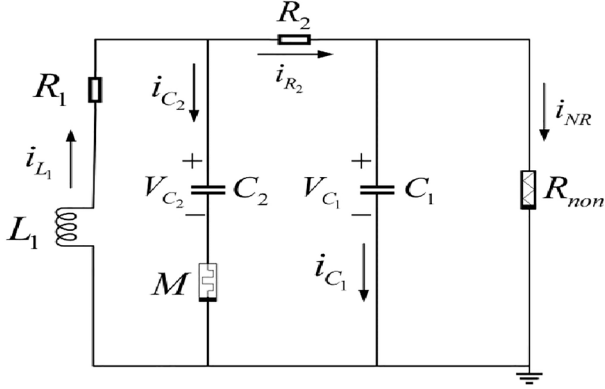


Fig. 3. Case 2 Memristive Chua circuit in which the memristor is connected to the capacitor C_2 in series. M and R_{non} describe the memristor and Chua diode. R_1 and R_2 represent the linear resistors.

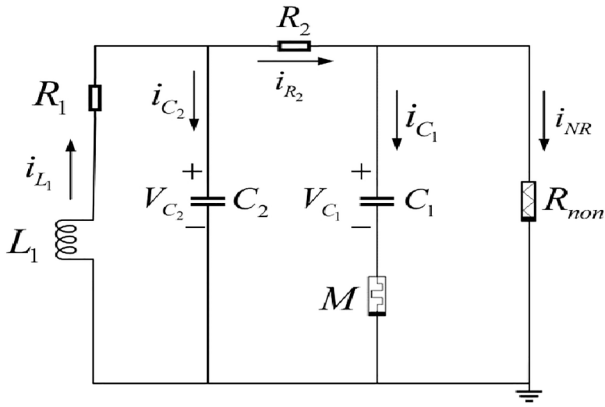


Fig. 4. Case 3 Memristive Chua circuit in which the memristor is connected to the capacitor C_1 in series. M and R_{non} describe the memristor and Chua diode. R_1 and R_2 represent the linear resistors.

$$\begin{cases} W_{C_1} = \frac{1}{2}C_1 V_{C_1}^2 = \frac{1}{2}C_1 E^2 x^2 = \frac{1}{2} \frac{C_1}{C_2} C_2 E^2 x^2 = \frac{1}{2\alpha} W_0 x^2; \\ W_{C_2} = \frac{1}{2}C_2 V_{C_2}^2 = \frac{1}{2}C_2 E^2 y^2 = \frac{1}{2} W_0 y^2; \\ W_{L_1} = \frac{1}{2}L_1 i_{L_1}^2 = \frac{1}{2}L_1 i_M^2 = \frac{1}{2} \frac{L_1}{C_2 R_2^2} C_2 E^2 z^2 = \frac{1}{2\beta} W_0 z^2; \\ W_M = \frac{1}{2}L_M i_M^2 = \frac{1}{2}\phi i_M = \frac{1}{2} \frac{EL_1 \phi'}{(R_1 + R_2)} \frac{E}{R_2} z = \frac{1}{2} \frac{1}{\beta + \gamma} W_0 \phi' z; \end{cases} \quad (8)$$

For the memristive system in Case 1, the Hamilton energy for each component can be replaced by

$$\begin{cases} H_{C_1} = \frac{1}{2\alpha} x^2; H_{C_2} = \frac{1}{2} y^2; H_{L_1} = \frac{1}{2\beta} z^2; H_M = \frac{1}{2} \frac{1}{\beta + \gamma} \phi' z; \\ H = -\frac{1}{2\alpha} x^2 + \frac{1}{2} y^2 + \frac{1}{2\beta} z^2 + \frac{1}{2} \frac{1}{\beta + \gamma} \phi' z; \end{cases} \quad (9)$$

Where the symbol “-” indicates that the capacitor C_1 used to release electric field energy while another capacitor C_2 prefers to absorb and pump field energy. Indeed, according to the Helmholtz theorem [65], the Hamilton energy function for generic dynamical system accounts for the intrinsic field energy. It is claimed that the most Lyapunov function should be consistent with the sole Hamilton energy function [66]. In addition, when this memristive circuit is exposed to magnetic field, the charge propagation and magnetic flux across the memristor will be

changed. In case of stochastic disturbance, the memristive system is regulated by

$$\begin{cases} \dot{x} = \alpha(y - x) - \alpha f(x); \\ \dot{y} = x - y + z; \\ \dot{z} = -\gamma z - \beta y - \beta \frac{z}{(a + b\phi'^2)}; \\ \dot{\phi} = (\beta + \gamma) \frac{z}{(a + b\phi'^2)} + \xi(\tau); \end{cases} \quad (10)$$

When external stochastic disturbance $\xi(\tau)$ is applied, the magnetic flux is regulated to change the output voltage across the capacitor in nonlinear way, and the dynamics becomes dependent on the memristive variable because of memory effect. As shown in Fig. 2, the memristive current across the memristor estimates the current across the induction coil, and the electromagnetic induction in this branch is controlled by the memristor completely. Therefore, it is interesting to discuss the case when memristor is connected to the capacitor C_2 , and the memristive circuit is shown in Fig. 3.

The channel current across the memristor will regulate the charge and discharge on the capacitor C_2 , and the circuit equations can be approached by

$$\begin{cases} C_1 \frac{dV_{C_1}}{dt} = i_{L_1} - i_M - i_{NR} \\ C_2 \frac{dV_{C_2}}{dt} = i_M \\ L_1 \frac{di_{L_1}}{dt} = -i_{L_1} R_1 - V_{C_1} - (i_{L_1} - i_M) R_2 \\ \frac{d\phi}{dt} = V_M \end{cases} \Rightarrow V_{C_2} \quad (11)$$

$$= V_{C_1} - V_M \Rightarrow \begin{cases} C_1 \frac{dV_{C_1}}{dt} = i_{L_1} - i_M - i_{NR} \\ C_2 \frac{dV_M}{dt} = C_2 \frac{dV_{C_1}}{dt} - i_M \\ L_1 \frac{di_{L_1}}{dt} = -i_{L_1} R_1 - V_{C_1} - (i_{L_1} - i_M) R_2 \\ \frac{d\phi}{dt} = V_M \end{cases}$$

Considering the induction current across the memristor shown in Eq. (4), and then the Eq.(11) is updated by applying similar scale transformation as follows

$$\begin{cases} x = \frac{V_{C_1}}{E}, w = \frac{V_M}{E}, z = \frac{i_{L_1} R_2}{E}, \phi' = \frac{\phi(R_1 + R_2)}{EL_1}, \tau = \frac{t}{R_2 C_2}, \\ m_0 = R_2 G_a, m_1 = R_2 G_b, \alpha = \frac{C_2}{C_1}, \beta = \frac{C_2 R_2^2}{L_1}, \gamma = \frac{R_1 R_2 C_2}{L_1}; \end{cases} \quad (12)$$

In addition, the improved memristive system for Case 2 can be rewritten by

$$\begin{cases} \dot{x} = \alpha z' - \alpha f(x) - \alpha(a' + b'\phi'^2)w \\ \dot{w} = -\alpha z' + \alpha f(x) - (\alpha - 1)(a' + b'\phi'^2)w \\ \dot{z} = \gamma z_1 - \beta x - \beta z' - \beta(a' + b'\phi'^2)w \\ \dot{\phi}' = (\beta + \gamma)w \end{cases} \quad (13)$$

The normalized parameters a' , b' are the same as shown in Eq.(6), and Eq.(7), and the normalized current $f(x)$ for case 2 is still estimated in Eq.(1b). Considering the third term in the second formula in Eq.(13), it will induce rapid increase of the variable w and thus the system becomes more convergent at $\alpha > 1$. By the same way, the field energy saved in these electric components and corresponding Hamilton energy can be estimated by

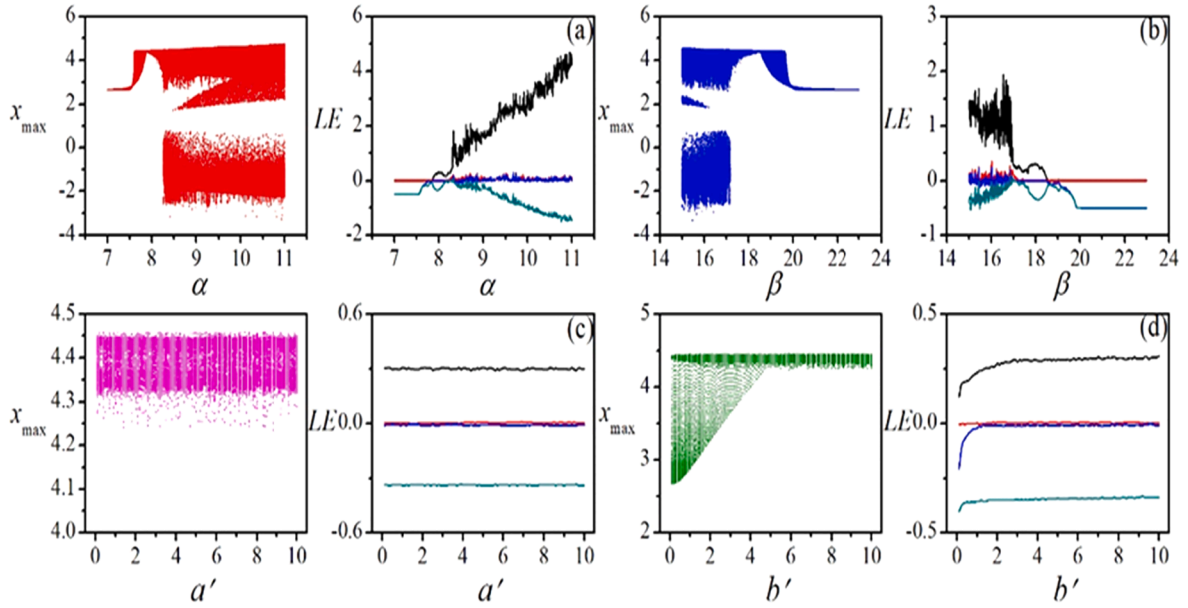


Fig. 5. Bifurcation diagram and distribution of three larger Lyapunov exponents for Case 1. For (a) $\beta = 18, \gamma = 0, m_0 = -1.664, m_1 = -0.598, a' = 1, b' = 10$; (b) $\alpha = 8, \gamma = 0, m_0 = -1.664, m_1 = -0.598, a' = 1, b' = 10$; (c) $\alpha = 8, \beta = 18, \gamma = 0, m_0 = -1.664, m_1 = -0.598, b' = 10$; (d) $\alpha = 8, \beta = 18, \gamma = 0, m_0 = -1.664, m_1 = -0.598, a' = 1$. The parameters are fixed at $m_0 = -1.664, m_1 = -0.598, \gamma = 0.0, b' = 0.25$, and the initial values for Eq.(7) are selected as $(x_0, y_0, z_0, w_0) = (0.1, 0.1, 1.0, 0.1)$.

$$\left\{ \begin{array}{l} W_{C_1} = \frac{1}{2} C_1 V_{C_1}^2 = \frac{1}{2} \frac{C_1}{C_2} C_2 E^2 x^2 = \frac{1}{2\alpha} W_0 x^2; \\ W_{C_2} = \frac{1}{2} C_2 V_{C_2}^2 = \frac{1}{2} C_2 (V_{C_1} - V_M)^2 = \frac{1}{2} C_2 E^2 (x - w)^2 = \frac{1}{2} W_0 (x - w)^2; \\ W_{L_1} = \frac{1}{2} L_1 i_{L_1}^2 = \frac{1}{2} L_1 \frac{E^2}{R_2^2} z^2 = \frac{1}{2\beta} W_0 z^2; \\ W_M = \frac{1}{2} L_M i_M^2 = \frac{1}{2} \phi i_M = \frac{1}{2} \phi (a + 3b\phi^2) V_M = \frac{1}{2} W_0 \left(\frac{a'}{\beta + \gamma} \phi' + \frac{b'}{\beta + \gamma} \phi'^3 \right) w = W_M^J + W_M^F; \end{array} \right. \quad (14)$$

The superscript J and F represents the Joule heat and field symbol, respectively, and the terms indicate that the average Joule heat consumed and magnetic field energy in the memristor. Therefore, the Hamilton energy in the four electric components can be rewritten by

$$\left\{ \begin{array}{l} H_{C_1} = \frac{1}{2\alpha} x^2; \quad H_{C_2} = \frac{1}{2} (x - w)^2; \quad H_{L_1} = \frac{1}{2\beta} z^2; \\ H_M = H_M^J + \boxed{H_M^F} = \frac{1}{2} \frac{a'}{\beta + \gamma} \phi' w + \boxed{\frac{1}{2} \frac{b'}{\beta + \gamma} \phi'^3 w} \\ H = -\frac{1}{2\alpha} x^2 + \frac{1}{2} (x - w)^2 + \frac{1}{2\beta} z^2 + \frac{1}{2} \frac{b'}{\beta + \gamma} \phi'^3 w \end{array} \right. \quad (15)$$

The Hamilton energy for the memristor contains two parts, one account for the Joule heat and another term means the pumping of field energy. This energy is dependent on the intrinsic parameters in memristor and other parameters for the capacitor and induction coil in the

Chua circuit as well. In addition, external magnetic field can change the channel current and thus the dynamics of the memristive system can be controlled. The magnetic flux is controlled by magnetic field in presence of stochastic disturbance as follows

$$\left\{ \begin{array}{l} \dot{x} = \alpha z' - \alpha f(x) - \alpha (a' + b' \phi'^2) w \\ \dot{w} = -\alpha z' + \alpha f(x) - (\alpha - 1) (a' + b' \phi'^2) w; \\ \dot{z} = \gamma z_1 - \beta x - \beta z - \beta (a' + b' \phi'^2) w \\ \dot{\phi} = (\beta + \gamma) w + \xi(\tau) \end{array} \right. \quad (16)$$

In fact, the memristor can also be connected to the capacitor C_1 , and the memristive circuit is plotted in Fig. 4.

According to Fig. 4 and the Kirchhoff theorem, the voltage changes along the close loop connected the capacitor C_1, C_2 , and memristor M follow $V_{C_1} + V_M - V_{C_2} + R_2 i_{R_2} = 0$, and the equivalent circuit equations are obtained by

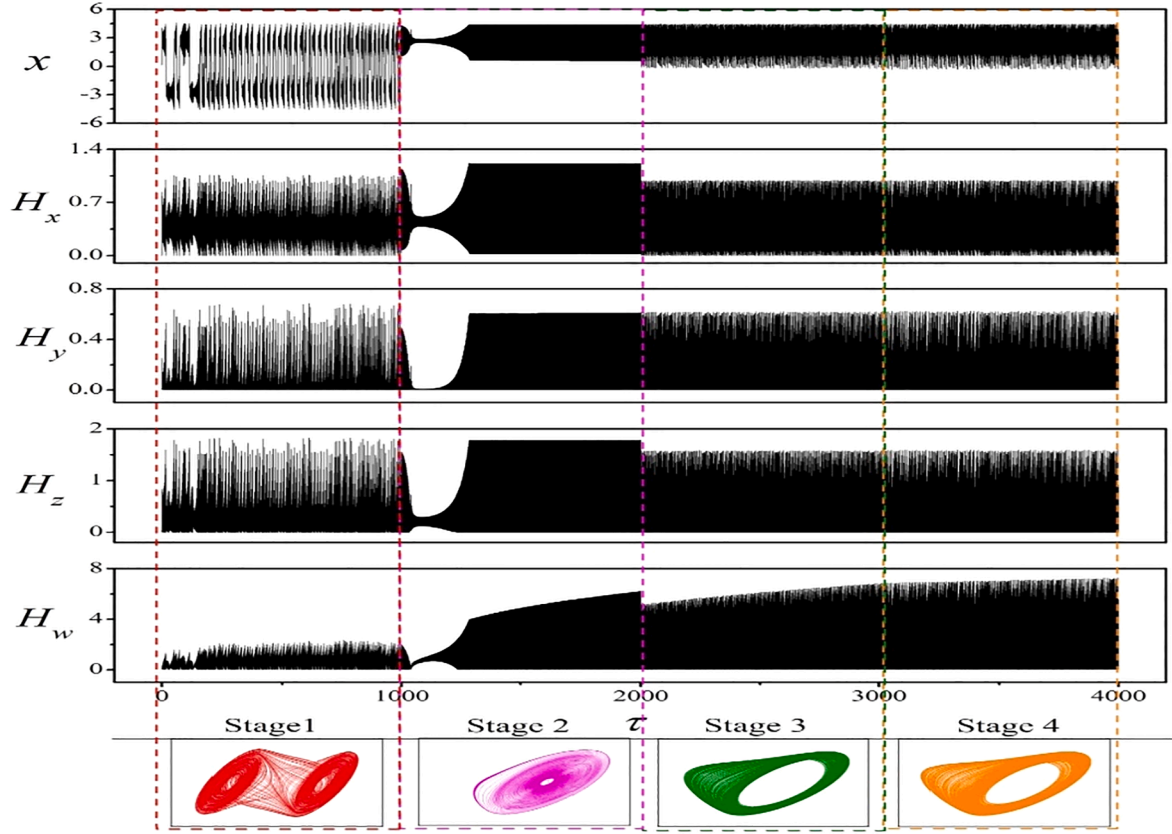


Fig. 6. Developed attractors, evolution of variable and transition in the Hamilton energy in different electrical components are plotted by changing one parameter for Case 1. For stage 1, $\alpha = 10, \beta = 18, \gamma = 0, m_0 = -1.664, m_1 = -0.598, a' = 5, b' = 2$; stage 2, $\alpha = 8, \beta = 18, \gamma = 0, m_0 = -1.664, m_1 = -0.598, a' = 5, b' = 2$; stage 3, $\alpha = 10, \beta = 24, \gamma = 0, m_0 = -1.664, m_1 = -0.598, a' = 5, b' = 2$; stage 4, $\alpha = 10, \beta = 24, \gamma = 0, m_0 = -1.664, m_1 = -0.598, a' = 5, b' = 6$.

$$\left\{ \begin{array}{l} C_1 \frac{dV_{C_1}}{dt} = i_M \\ C_1 \frac{dV_M}{dt} = -i_M + C_1 \frac{dV_{C_2}}{dt} - C_1 R_2 \frac{di_{R_2}}{dt} \\ C_2 \frac{dV_{C_2}}{dt} = i_{L_1} - i_M - i_{NR} \\ L_1 \frac{di_{L_1}}{dt} = -i_{L_1} R_1 - V_{C_2} \\ \frac{d\phi}{dt} = V_M \end{array} \right. ; \quad (17)$$

$$\left\{ \begin{array}{l} x = \frac{V_{C_1}}{E}, w = \frac{V_M}{E}, y = \frac{V_{C_2}}{E}, z = \frac{i_{L_1} R_2}{E}, \phi' = \frac{\phi(R_1 + R_2)}{EL_1}, \tau = \frac{t}{R_2 C_2}, m_0 = R_2 G_a, \\ m_1 = R_2 G_b, \alpha = \frac{C_2}{C_1}, \beta = \frac{C_2 R_2^2}{L_1}, \gamma = \frac{R_1 R_2 C_2}{L_1}, a' = R_2 a, b' = \frac{3bR_2(EL_1)^2}{(R_1 + R_2)^2} \end{array} \right. ; \quad (18)$$

In particular, the normalized current across the nonlinear resistor (Chua diode) is updated by

$$f'(x) = m_1(x + w) + 0.5(m_0 - m_1)(|(x + w) + 1| - |(x + w) - 1|); \quad (19)$$

In addition, the memristive system for Case 3 can be represented by

Similar scale transformation in Eq.(18) is applied for variables and parameters in Eq.(17),

$$\left\{ \begin{array}{l} \dot{x} = \alpha(a' + b'\phi'^2)w \\ \dot{w} = \frac{1}{1 + (a' + b'\phi'^2) + m_1} [-2b'\phi'(\beta + \gamma)w^2 - (m_1\alpha + 1 + \alpha)(a' + b'\phi'^2)w + z' - f'(x)] \\ \dot{y} = z' - (a' + b'\phi'^2)w - f'(x) \\ \dot{z}' = -\beta y - \gamma z' \\ \dot{\phi}' = (\beta + \gamma)w \end{array} \right. ; \quad (20)$$

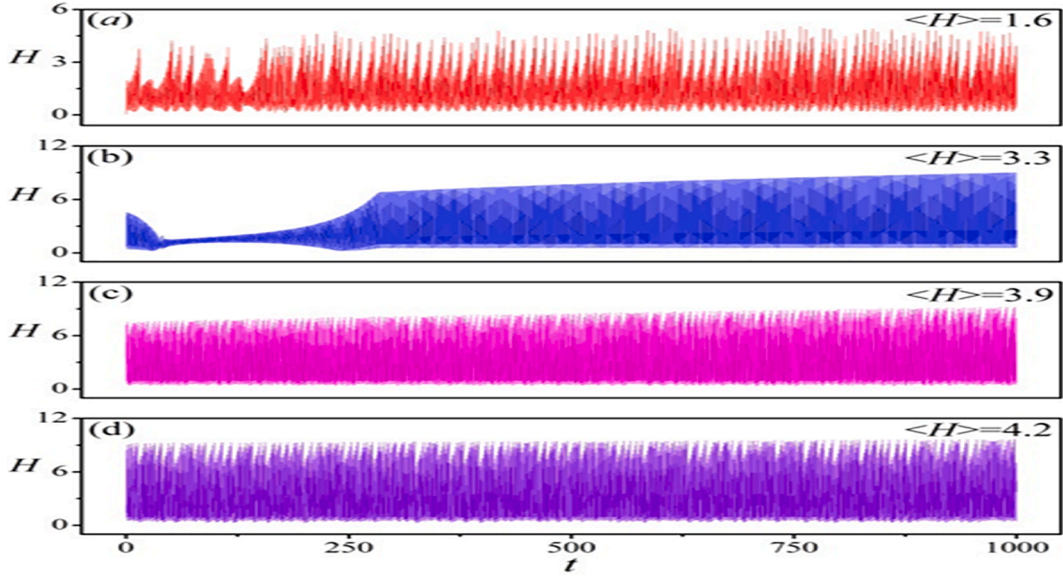


Fig. 7. Evolution of the Hamilton energy H in this memristive circuit. For (a) $\alpha = 10, \beta = 18, b' = 2$; (b) $\alpha = 8, \beta = 18, b' = 2$; (c) $\alpha = 10, \beta = 24, b' = 2$; (d) $\alpha = 10, \beta = 24, \gamma = 0, b' = 6$, the other parameters are fixed at $\gamma = 0, m_0 = -1.664, m_1 = -0.598, a' = 5$.

Compared the dynamical equations for Case 3 with the Case 1 and Case 2, more normalized parameters are involved. As a result, the dynamics becomes more sensitive and dependent on these parameters. Similar field energy and Hamilton energy are also estimated for the Case 3.

$$\left\{ \begin{array}{l} W_{C_1} = \frac{1}{2} C_1 V_{C_1}^2 = \frac{1}{2} C_1 (V_{C_2} - V_M)^2 = \frac{1}{2} C_1 E^2 (y-w)^2 = \frac{1}{2\alpha} W_0 (y-w)^2; \\ W_{C_2} = \frac{1}{2} C_2 V_{C_2}^2 = \frac{1}{2} C_2 E^2 y^2 = \frac{1}{2} W_0 y^2; \\ W_{L_1} = \frac{1}{2} L_1 i_{L_1}^2 = \frac{1}{2} L_1 \frac{E^2}{R_2^2} z'^2 = \frac{1}{2\beta} W_0 z'^2; \\ W_M = \frac{1}{2} L_M i_M^2 = \frac{1}{2} \phi i_M = \frac{1}{2} \phi (a + 3b\phi^2) V_M = \frac{1}{2} W_0 \left(\frac{a'}{\beta + \gamma} \phi' + \frac{b'}{\beta + \gamma} \phi'^3 \right) w = W_M^J + W_M^F; \end{array} \right. \quad (21)$$

Furthermore, the equivalent Hamilton energy for case 3 can be updated as follows

$$\left\{ \begin{array}{l} H_{C_1} = \frac{1}{2\alpha} (y-w)^2; \quad H_{C_2} = \frac{1}{2} y^2; \quad H_{L_1} = \frac{1}{2\beta} z'^2; \\ H_M = H_M^J + \boxed{H_M^F} = \frac{1}{2} \frac{a'}{\beta + \gamma} \phi' w + \boxed{\frac{1}{2} \frac{b'}{\beta + \gamma} \phi'^3 w}; \\ H = -\frac{1}{2\alpha} (y-w)^2 + \frac{1}{2} y^2 + \frac{1}{2\beta} z'^2 + \frac{1}{2} \frac{b'}{\beta + \gamma} \phi'^3 w; \end{array} \right. \quad (22)$$

$$\left\{ \begin{array}{l} \dot{x} = a(a' + b'\phi'^2)w \\ \dot{w} = \frac{1}{1 + (a' + b'\phi'^2) + m_1} [-2b'\phi'(\beta + \gamma)w^2 - (m_1\alpha + 1 + \alpha)(a' + b'\phi'^2)w + z' - f'(x)] \\ \dot{y} = z' - (a' + b'\phi'^2)w - f'(x) \\ \dot{z}' = -\beta y - \gamma z' \\ \dot{\phi}' = (\beta + \gamma)w + \xi(\tau) \end{array} \right. ; \quad (23)$$

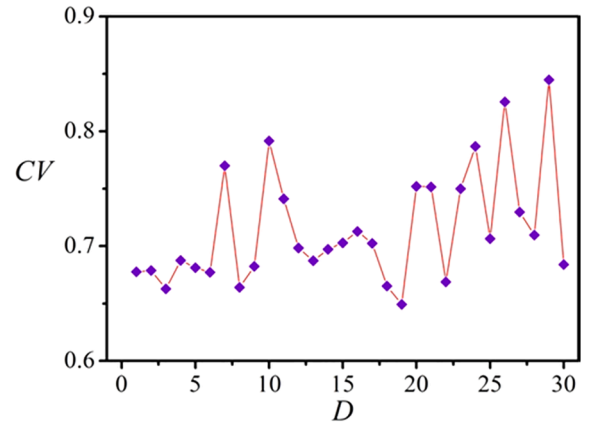


Fig. 8. Distribution of CV by changing the noise intensity for Case 1. The parameters are fixed at $\alpha = 10, \beta = 18, \gamma = 0, m_0 = -1.664, m_1 = -0.598, a' = 5, b' = 10$, initial values are selected as (0.1, 0.1, 1.0, 0.1).

From dynamical viewpoint, taming the normalized parameters in the memristor and electric components can change the dynamics of the memristive oscillator, and similar firing patterns (spiking, bursting) can be induced besides the chaotic or periodical firing modes. Furthermore, stochastic external magnetic field can be applied to control the channel current across the memristor, and then the dynamics of this memristive circuit can be regulated as follows

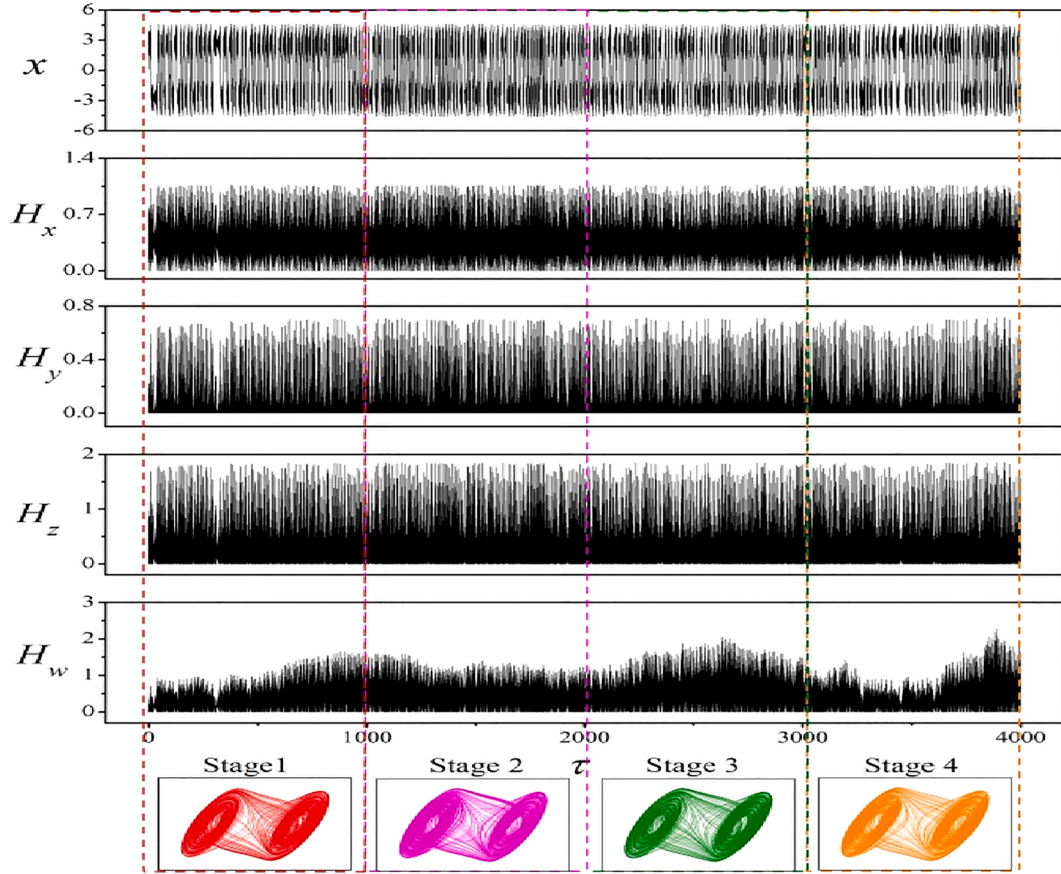


Fig. 9. Developed attractors, evolution of variable and transition in the Hamilton energy in different electrical components are plotted by changing noise intensity for Case 1. For stage 1, $D = 5$; stage 2, $D = 10$, stage 3, $D = 19$; stage 4, $D = 29$, and the parameters are fixed at $\alpha = 10$, $\beta = 18$, $\gamma = 0$, $m_0 = -1.664$, $m_1 = -0.598$, $a' = 5$, $b' = 10$, initial values are selected as (0.1, 0.1, 1.0, 0.1).

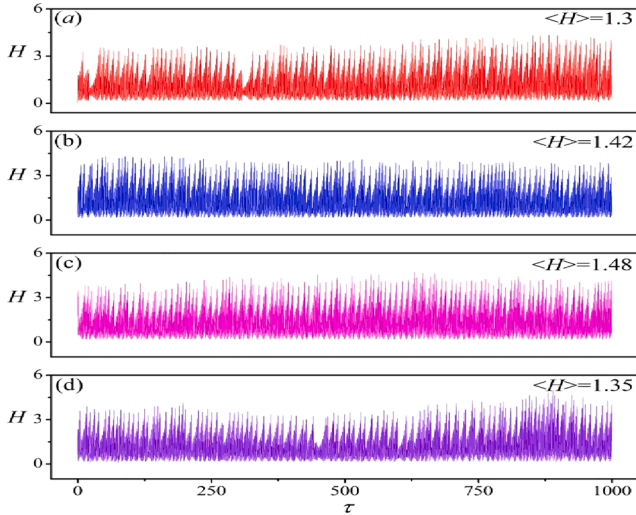


Fig. 10. Evolution of the Hamilton energy H in this memristive circuit driven by noise for Case 1. For noise intensity (a) $D = 5$; (b) $D = 10$; (c) $D = 19$; (d) $D = 29$, the parameters are fixed at $\alpha = 10$, $\beta = 18$, $\gamma = 0$, $m_0 = -1.664$, $m_1 = -0.598$, $a' = 5$, $b' = 10$.

In generic way, Gaussian white noise with zero average is often considered for describing the stochastic disturbance and its physical statistical properties are defined as $\langle \xi(\tau) \rangle = 0$, $\langle \xi(\tau) \xi(\tau') \rangle = 2D\delta(\tau - \tau')$, where D denotes the noise intensity and $\delta(*)$ means Dirac- δ function. From physical viewpoint, the electric components in the circuit will pump and store field energy when the capacitors are charged and current passed across the induction coil. Electric field energy and magnetic field energy can be injected and released from the capacitor and induction coil, respectively. On the other hand, the memristor can consume Joule heat and absorb magnetic field as well. For further nonlinear analysis and potential application in neurodynamics, the coherence degree can be estimated by calculating the coefficient variability (CV) of interspike interval (ISI) series as follows

$$CV = \frac{\sqrt{\langle T^2 \rangle - \langle T \rangle^2}}{\langle T \rangle}; \quad (24)$$

where the T represents the denotes the period for two adjacent peaks (ISI) in the sampled time series for membrane potentials or output variables. In this paper, the ISI can be reduced from the sampled time series for the variable x directly.

3. Numerical results and discussion

When memristor is incorporated into different branches of the Chua circuit, the channel current across the memristor can regulate the outputs voltage of the memristive circuit with different scales. As a result, the profile and firing modes of this memristive circuit will be controlled by the memristive variable even all the parameters are fixed. For

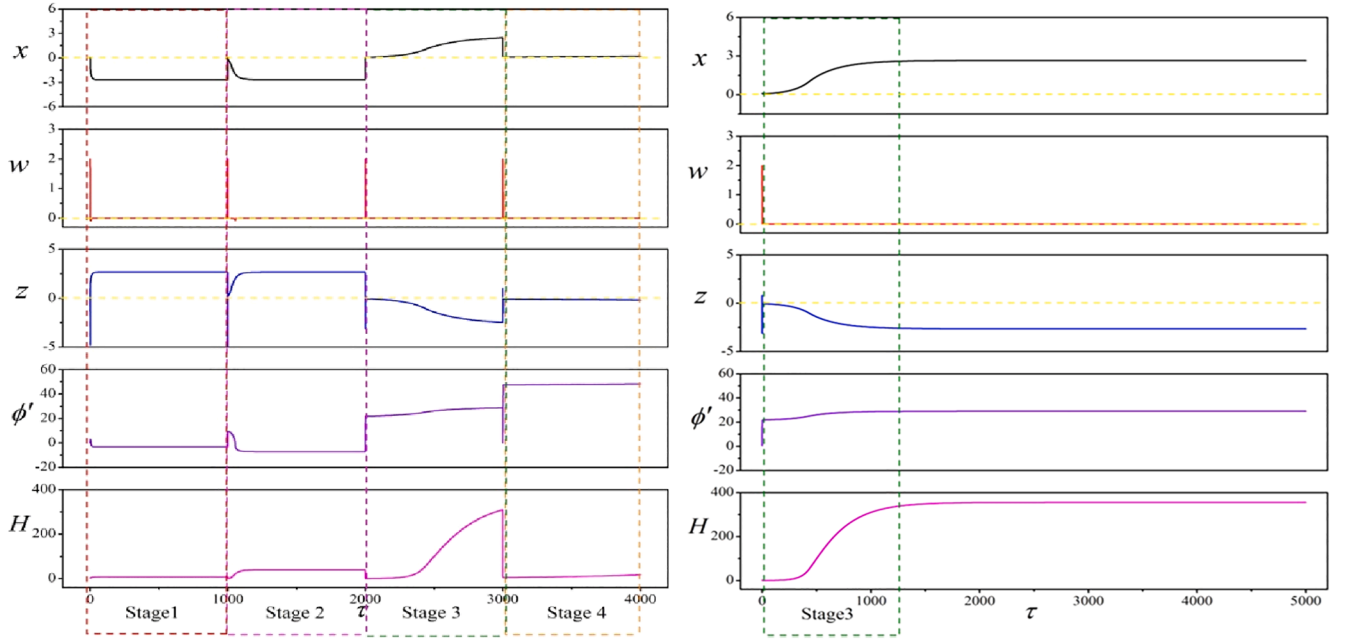


Fig. 11. Evolution of variables and Hamilton energy are changed by switching one of the intrinsic parameters in different stages (Case 2). For stage 1, $\alpha = 1$, $a' = 1$, $b' = 1$; stage 2, $\alpha = 0.1$, $a' = 0.1$, $b' = 0.1$; stage 3, $\alpha = 0.01$, $a' = 0.01$, $b' = 0.01$; stage 4, $\alpha = 0.001$, $a' = 0.001$, $b' = 0.001$, the other parameters are fixed at $\beta = 24$, $\gamma = 0$, $m_0 = -1.664$, $m_1 = -0.598$.

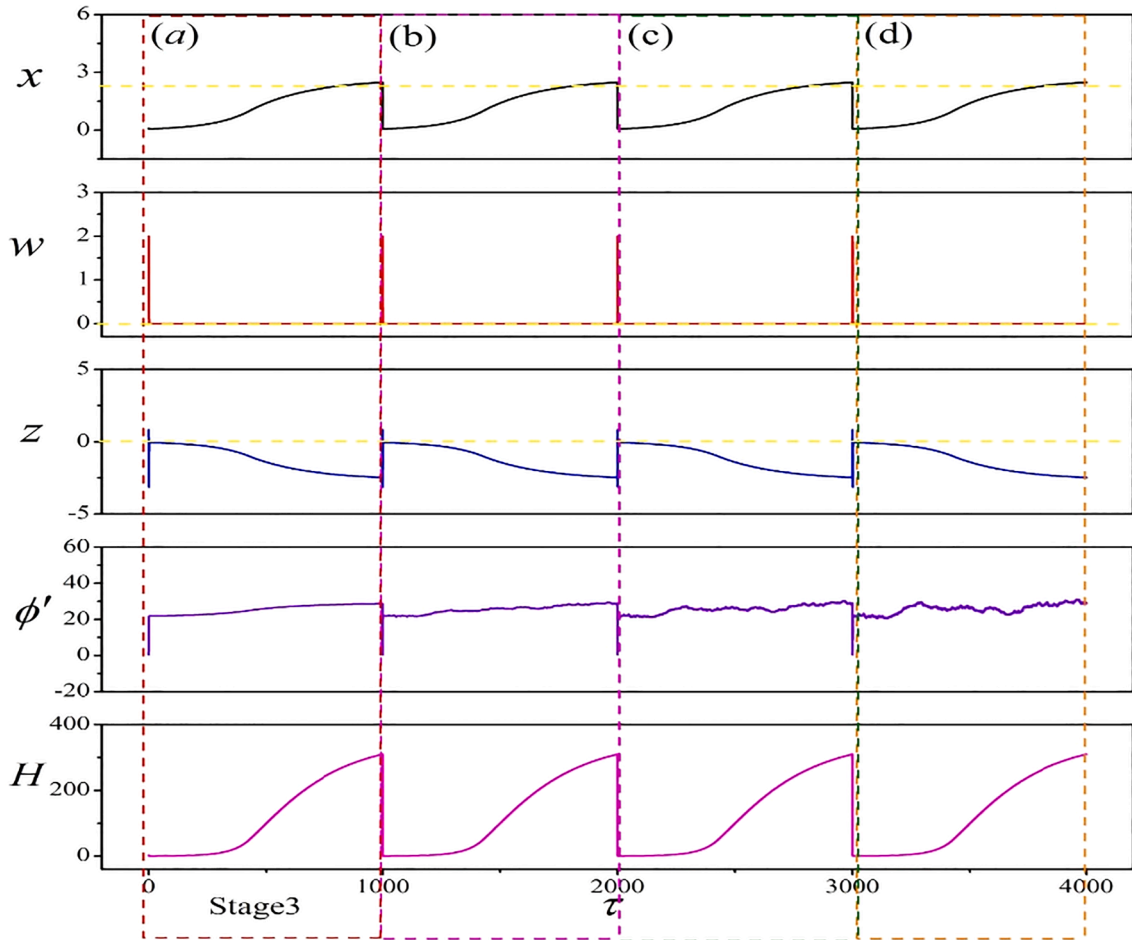


Fig. 12. Evolution of variables and the Hamilton energy H in this memristive circuit driven by noise (Case 2). For noise intensity (a) $D = 0$; (b) $D = 10$; (c) $D = 20$; (d) $D = 30$, the parameters for stage 3 are fixed at $\alpha = 0.01$, $\beta = 24$, $\gamma = 0$, $m_0 = -1.664$, $m_1 = -0.598$, $a' = 0.01$, $b' = 0.01$.

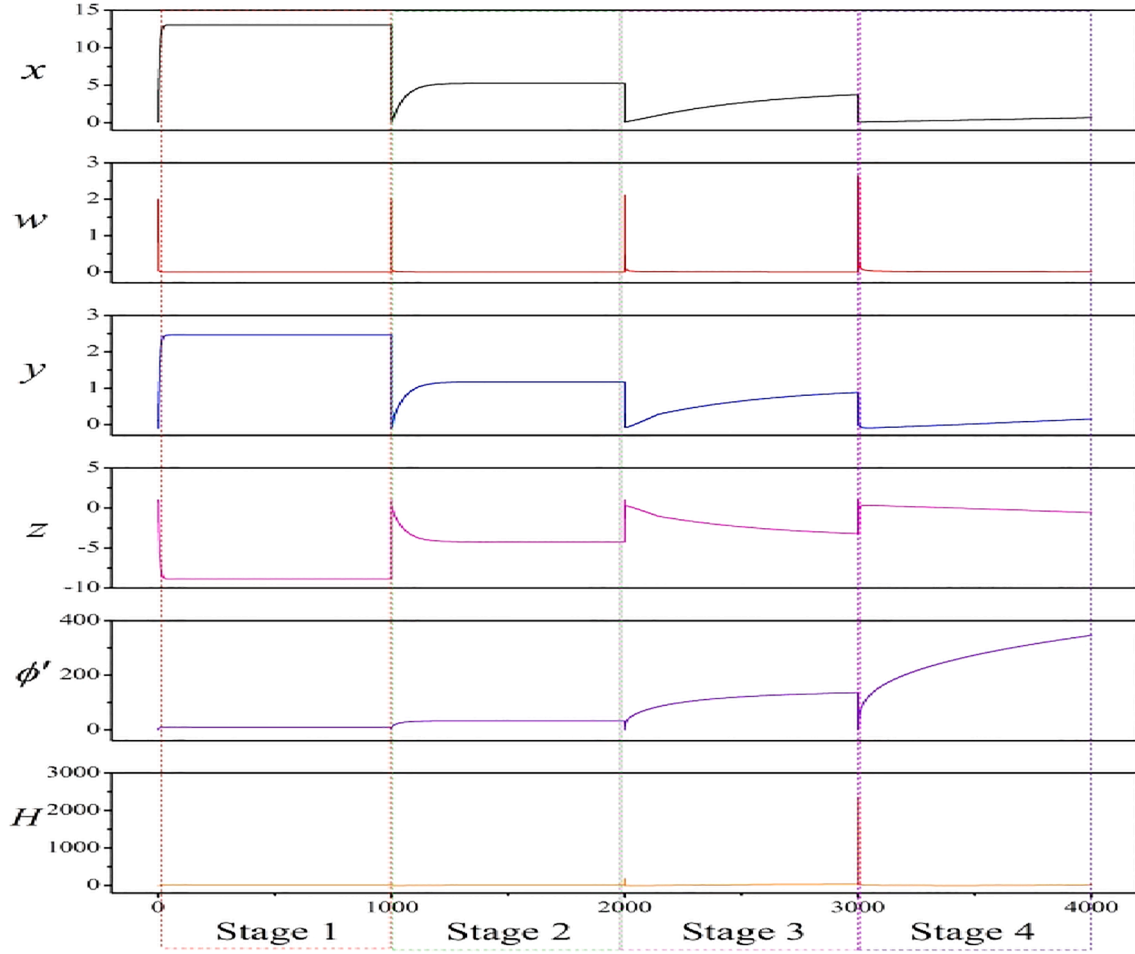


Fig. 13. Evolution of variables and Hamilton energy are changed by switching one of the intrinsic parameters in different stages (Case 3). For stage 1, $\alpha = 1$, $\alpha' = 1$, $b' = 1$; stage 2, $\alpha = 0.1$, $\alpha' = 0.1$, $b' = 0.1$; stage 3, $\alpha = 0.01$, $\alpha' = 0.01$, $b' = 0.01$; stage 4, $\alpha = 0.001$, $\alpha' = 0.001$, $b' = 0.001$, the other parameters are fixed at $\beta = 24$, $\gamma = 5$, $m_0 = -1.664$, $m_1 = -0.598$.

simplicity, the resistance for resistor R_1 is removed and then the parameter $\gamma = 0$ without special statement. The fourth order Runge-Kutta algorithm is applied to find numerical solutions of these memristive systems with time step $h = 0.01$. For the case 1, the memristive current is relative to the channel current and induction current across the induction coil, and the dynamics dependence on the intrinsic parameters (α , β , α' , b') is estimated by calculating the Lyapunov exponents and supplying the bifurcation analysis in Fig. 5.

It is confirmed that slight changes in the parameters (α , β) mapped from capacitance and inductance can induce distinct mode transition from periodic to chaotic states, while the changes in the normalized parameters (α' , b') in the memristor seldom changes the chaotic state effectively. Furthermore, the formation of attractors and evolution of Hamilton energy in this memristive circuit are calculated in Fig. 6 by changing one parameter.

As presented in Fig. 6, the output voltages from the memristive circuit and chaotic attractors are changed completely, in addition, the energy pumping in each electric component is also changed when the intrinsic parameters for capacitor and induction coil (α , β) are adjusted. However, the Hamilton energy for these components, chaotic attractors and output voltages seldom show distinct changes. The total Hamilton energy in this memristive circuit is also calculated in Fig. 7 when one of the intrinsic parameters is changed.

The results in Fig. 7 are consistent with the presentation shown in Fig. 6, the memristive circuit used to hold lower average Hamilton energy when double scroll attractors are developed, while single scroll attractor enables higher Hamilton energy in this circuit.

Noise is often applied on the nonlinear systems and excitable media for estimating the effect of stochastic disturbance. Nonlinear resonance such as stochastic resonance and coherence resonance can be induced and the disturbed systems often present distinct periodicity in the output variables by adjusting the noise intensity carefully. For the memristive system without external periodic stimulus, stochastic electromagnetic radiation can change the channel current across the memristor, and the other branch circuits can be controlled by the memristive current effectively when the intensity of electromagnetic radiation is changed. In Fig. 8, the noise intensity is changed to detect the nonlinear response from Eq.(10) when external electromagnetic radiation is applied with different intensities. The CV value shows distinct fluctuations with the increase of noise intensity, and it reaches a lowest value at $D = 19$ while the attractors show chaotic than periodic type. Furthermore, the evolution and transition in the output variable and Hamilton energy are calculated by changing the noise intensity, and the results are shown in Fig. 9.

It is confirmed that the profile of double scroll attractors keep robustness to the noise even its intensity is further increased. The potential mechanism could be that the memristor is activated completely and its field energy is increased and then is pumped to the induction coil L_1 for possible balance along this branch circuit. By the way, the evolution of total Hamilton energy in this memristive circuit is also calculated in Fig. 10.

In presence of double scroll attractors, the average Hamilton energy is much close to a lower value even the noise intensity is changed in wide range. It indicates that chaotic attractors are kept alive even noisy

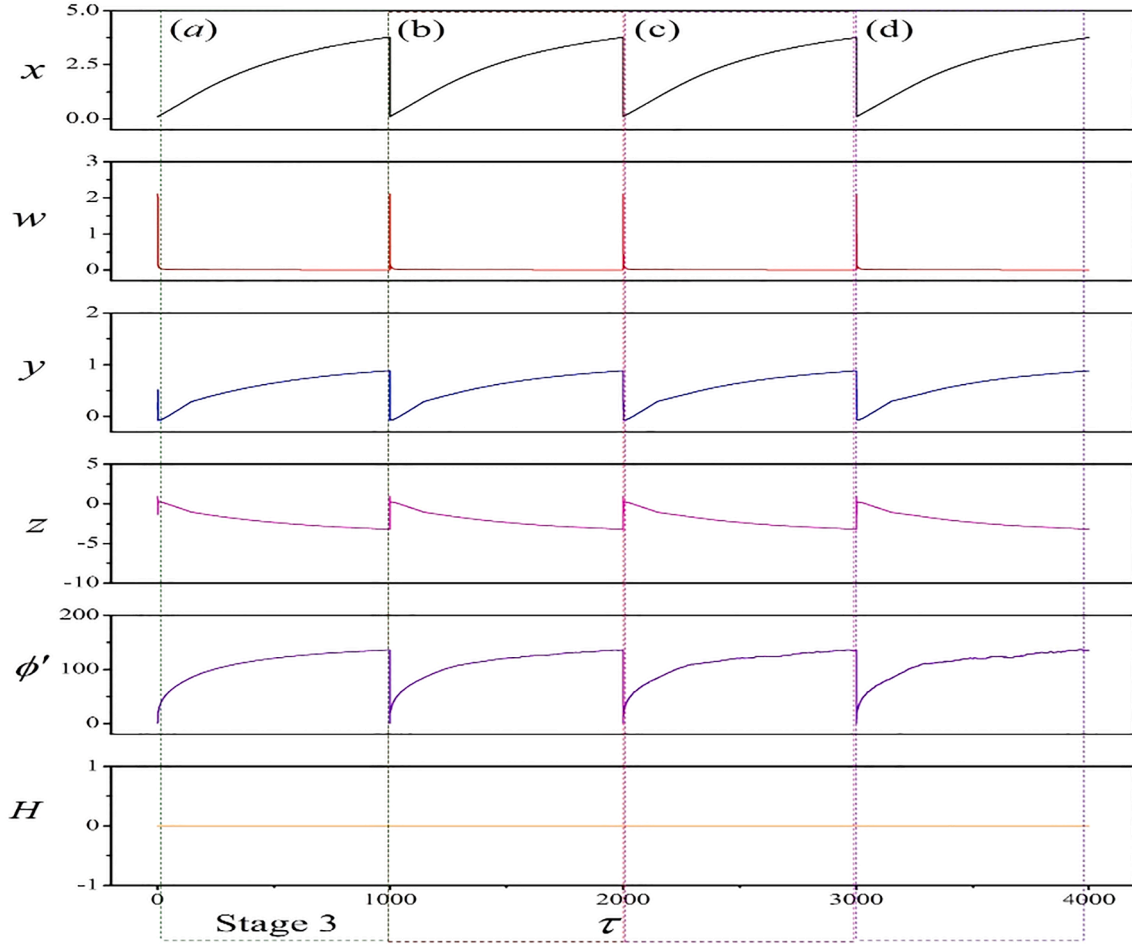


Fig. 14. Evolution of variables and the Hamilton energy H in this memristive circuit driven by noise. For noise intensity (a), $D = 0$; (b), $D = 10$; (c), $D = 20$; (d) $D = 30$, the parameters for stage 3 are fixed at $\alpha = 0.01$, $\beta = 24$, $\gamma = 5$, $m_0 = -1.664$, $m_1 = -0.598$, $a' = 0.01$, $b' = 0.01$.

disturbance via the memristor is further increased. In fact, for the condition described in Case 1, the memristive current and field energy across the memristor are changed by external magnetic field, which is estimated by changing the magnetic flux variable. As a result, magnetic field energy is pumped into the induction coil. Therefore, the chaotic attractors keep alive to the changes of parameters for memristor, and external magnetic field has slight impact on the stability of chaotic attractors. It is also interesting to discuss the Case 2, from physical viewpoint, magnetic field energy can coexist with the electric field energy along the same branch circuit. For Case 2, the firing mode, evolution of Hamilton energy in the memristive circuit are plotted in Fig. 11. It is found that the involvement of memristor connected to capacitor C_2 can calm down the chaotic circuit, and the Hamilton energy is decreased to stable value. Furthermore, the stage 3 in Fig. 11 is extended to 5000 time units, and it is confirmed that all the variables and Hamilton energy reach stable value finally. Because of the magnetic field effect in the magnetic flux-controlled memristor, the excitation of channel current can be converted to magnetic field energy and then the capacitor connected to this memristor is seldom excited. As a result, the processing of charge and discharge becomes discontinuous, and then the output voltage from the capacitor becomes stable within finite transient period. By the same way, external electromagnetic radiation is applied with different intensities, and the results are plotted in Fig. 12.

Extensive numerical results confirmed that the chaos and oscillation in the memristor-coupled circuit is suppressed, and the Hamilton energy is stabilized because the variables become stable accompanied by the termination of energy pumping. We also investigate the same problem for Case 3, and the evolution of variable and transition of Hamilton

energy are plotted in Fig. 13.

Similar to the results approached for Case 2, the variables developed to a stable and certain saturation value when the memristor is connected to the capacitor C_1 , as a result, the oscillation in the memristive circuit is suppressed completely. Furthermore, external electromagnetic radiation is applied to discuss the stability and transition in the variable by applying the same parameters for stage 3, and the results are plotted in Fig. 14.

The chaotic circuit began to reach stable state within certain transient period and the oscillation is suppressed even external electromagnetic radiation on this nonlinear circuit is further increased. According to Eq.(20), the variable w will be stabilized to stable value with large negative gain, and then the output voltage from capacitor C_1 will be kept balance. As a result, the channel current along this branch circuit becomes stable, and then the energy pumping and exchange are blocked. Therefore, continuous oscillation is terminated effectively.

In the previous works, an additive branch circuit composed of isolated memristor is built to couple many chaotic circuits [67–70], and then the memristive current across the memristor will be considered as external stimulus, which has distinct excitation to the original chaotic circuit. In particular, the involvement of memristive function associated with memristor can induce multistability [71,72] in some nonlinear circuits. The dynamics becomes richer and complex in fractional order systems [73] composed of memristor, and hidden attractors [74,75] with different shapes of equilibrium points can be induced in some memristive systems. The channel current across the memristor and its field energy have effective impacts on mode transition and energy transition in the memristive circuits. However, the connection of memristor to

capacitor or induction coil along the same branch circuit may induce extreme state (death in oscillation, keeps chaotic) because of the balance and compensation of field energy between two electric components. On the other hand, memristor coupling is effective to realize synchronization [76–79], incorporation of memristor in the coupling channel just activates an equivalent additive branch circuit, and thus two chaotic circuits (neural circuits) can be guided and controlled to reach possible consensus in the states. Our results in this paper remind that the involvement of memristor to different electric components in the nonlinear circuit will has distinct effect on the dynamics and mode selection. Therefore, when more physical electric components such as phototube, thermistor, Josephson junction, piezoelectric device are used to couple resonators and nonlinear circuits, the effect of incorporation position and connection to which electric component should be discussed.

4. Conclusions

As is well known, the dynamics of nonlinear circuits becomes dependent of initial values even all the parameters are fixed, and this circuit is improved as memristive when a memristor is coupled to a nonlinear circuit by adding an additive branch circuit. That is, a connection of isolated memristor to the nonlinear circuit along an additive branch circuit in parallel will activate the memristive effect effectively because the memristive current across the memristor will regulate the nonlinear circuit as external stimulus. In this paper, a memristor is connected to the induction coil, capacitors in series along three different branch circuits, the energy pumping in each electric components and Hamilton energy in this improved circuit is calculated, respectively. It is confirmed that the chaotic circuit keeps alive when memristor is connected to the induction coil along the branch circuit, and the two components can share and exchange magnetic field energy continuously, therefore, this circuit still keeps alive even external magnetic radiation is applied. However, when memristor is connected to the capacitor along another two branch circuits, the magnetic field energy in the memristor can compensate and keep balance the energy in the capacitor, as a result, continuous oscillation is suppressed and the nonlinear circuit tends to reach stable state within finite transient period. These results confirmed that connection of memristor to different electric components will have different impact on the stability of nonlinear circuits.

Declaration of Competing Interest

The authors declare that they have no known competing financial interests or personal relationships that could have appeared to influence the work reported in this paper.

Acknowledgements

This project is partially supported by the National Natural Science Foundation of China under Grant Nos. 12062009, 12072139.

References

- [1] Muthuswamy B, Chua L O. Simplest chaotic circuit. *International Journal of Bifurcation and Chaos* 2010; 20(05):1567–1580.
- [2] Lao S-K, Shekofteh Y, Jafari S, Sprott JC. Cost function based on Gaussian mixture model for parameter estimation of a chaotic circuit with a hidden attractor. *Int J Bifurcation Chaos* 2014;24(01):1450010. <https://doi.org/10.1142/S0218127414500102>.
- [3] Minati L, Gambuzza LV, Thio WJ, Sprott JC, Frasca M. A chaotic circuit based on a physical memristor. *Chaos, Solitons Fractals* 2020;138:109990. <https://doi.org/10.1016/j.chaos.2020.109990>.
- [4] Pham VT, Ali DS, Al-Saidi NMG, Rajagopal K, Alsaadi FE, Jafari S. A novel megastable chaotic circuit. *Radioengineering* 2020;29(1):140–6.
- [5] Peng G, Min F. Multistability analysis, circuit implementations and application in image encryption of a novel memristive chaotic circuit. *Nonlinear Dyn* 2017;90(3):1607–25.

- [6] Ye X, Wang X, Gao S, Mou J, Wang Z, Yang F. A new chaotic circuit with multiple memristors and its application in image encryption. *Nonlinear Dyn* 2020;99(2):1489–506.
- [7] Tsafack N, Kengne J, Abd-El-Atty B, Ilyasu AM, Hirota K, Abd EL-Latif AA. Design and implementation of a simple dynamical 4-D chaotic circuit with applications in image encryption. *Inf Sci* 2020;515:191–217.
- [8] Kamal FM, Elsonbaty A, Elsaid A. A novel fractional nonautonomous chaotic circuit model and its application to image encryption. *Chaos, Solitons Fractals* 2021;144:110686. <https://doi.org/10.1016/j.chaos.2021.110686>.
- [9] Çavuşoğlu Ü, Panahi S, Akgül A, Jafari S, Kaçar S. A new chaotic system with hidden attractor and its engineering applications: analog circuit realization and image encryption. *Analog Integr Circ Sig Process* 2019;98(1):85–99.
- [10] Wang C, Tang J, Ma J. Minireview on signal exchange between nonlinear circuits and neurons via field coupling. *European Physical Journal Special Topics* 2019;228(10):1907–24.
- [11] Chen M, Shao S-Y, Shi P, Shi Y. Disturbance-observer-based robust synchronization control for a class of fractional-order chaotic systems. *IEEE Trans Circuits Syst II Express Briefs* 2017;64(4):417–21.
- [12] Lai Q, Wan Z, Kamdem Kuete PD, Fotsin H. Coexisting attractors, circuit implementation and synchronization control of a new chaotic system evolved from the simplest memristor chaotic circuit. *Commun Nonlinear Sci Numer Simul* 2020;89:105341. <https://doi.org/10.1016/j.cnsns.2020.105341>.
- [13] Sundarapandian V, Pehlivan I. Analysis, control, synchronization, and circuit design of a novel chaotic system. *Math Comput Modell* 2012;55(7-8):1904–15.
- [14] Dadras S, Momeni HR. Adaptive sliding mode control of chaotic dynamical systems with application to synchronization. *Math Comput Simul* 2010;80(12):2245–57.
- [15] Peng Bo, Liu Bo, Zhang F-Y, Wang L. Differential evolution algorithm-based parameter estimation for chaotic systems. *Chaos, Solitons Fractals* 2009;39(5):2110–8.
- [16] Wang L, Xu Ye. An effective hybrid biogeography-based optimization algorithm for parameter estimation of chaotic systems. *Expert Syst Appl* 2011;38(12):15103–9.
- [17] Jafari S, Sprott JC, Pham V-T, Golpayegani SMRH, Jafari AH. A new cost function for parameter estimation of chaotic systems using return maps as fingerprints. *Int J Bifurcation Chaos* 2014;24(10):1450134. <https://doi.org/10.1142/S021812741450134X>.
- [18] Kapitaniak T, Mohammadi S, Mekhilef S, Alsaadi F, Hayat T, Pham V-T. A new chaotic system with stable equilibrium: Entropy analysis, parameter estimation, and circuit design. *Entropy* 2018;20(9):670. <https://doi.org/10.3390/e20090670>.
- [19] Wang C, Ma J. A review and guidance for pattern selection in spatiotemporal system. *Int J Mod Phys B* 2018;32(06):1830003. <https://doi.org/10.1142/S0217979218300037>.
- [20] Wu N, Ying H. The dynamic of repulsion of spiral waves from excitable regions. *Nonlinear Dyn* 2021;103(1):979–86.
- [21] Lv M, Ma J, Yao YG, et al. Synchronization and wave propagation in neuronal network under field coupling. *Science China Technological Sciences* 2019;62:448–57.
- [22] Yang KL, Zhuo XJ, Wang CJ, et al. Traveling wave induced periodic synchronous patterns in coupled discontinuous systems and its potential application. *Nonlinear Dyn* 2020;102:2783–92.
- [23] Wang G, Ge M, Lu L, et al. Study on propagation efficiency and fidelity of subthreshold signal in feed-forward hybrid neural network under electromagnetic radiation. *Nonlinear Dyn* 2021;103:2627–43.
- [24] Qu L, Du L, Hu H, et al. Pattern control of external electromagnetic stimulation to neuronal networks. *Nonlinear Dyn* 2020;102:2739–57.
- [25] Njougouo T, Simo GR, Louodop P, et al. Dynamics of Rössler oscillators in a star network with the central node controlled by an external system. *Nonlinear Dyn* 2020;102:2875–85.
- [26] Ma S, Zhou P, Ma J, et al. Phase synchronization of memristive systems by using saturation gain method. *Int J Mod Phys B* 2020;34:2050074.
- [27] Liu Z, Zhou P, Ma J, et al. Autonomic learning via saturation gain method, and synchronization between neurons. *Chaos, Solitons Fractals* 2020;131:109533.
- [28] Elabbasy EM, Agiza HN, El-Dessoky M. Adaptive synchronization of a hyperchaotic system with uncertain parameter. *Chaos, Solitons Fractals* 2006;30:1133–42.
- [29] Zhang F, Sun K, Chen Y, et al. Parameters identification and adaptive tracking control of uncertain complex-variable chaotic systems with complex parameters. *Nonlinear Dyn* 2019;95:3161–76.
- [30] Fan D, Zhang L, Wang Q. Transition dynamics and adaptive synchronization of time-delay interconnected corticothalamic systems via nonlinear control. *Nonlinear Dyn* 2018;94:2807–25.
- [31] Levi M, Hoppensteadt FC, Miranker WL. Dynamics of the Josephson junction. *Q Appl Math* 1978;36:167–98.
- [32] Sickinger H, Lipman A, Weides M, et al. Experimental evidence of a φ Josephson junction. *Phys Rev Lett* 2012;109:107002.
- [33] Dana SK, Sengupta DC, Edoh KD. Chaotic dynamics in Josephson junction. *IEEE Transactions on Circuits and Systems I: Fundamental Theory and Applications* 2001;48(8):990–6.
- [34] Zhang Y, Zhou P, Tang J, et al. Mode selection in a neuron driven by Josephson junction current in presence of magnetic field. *Chin J Phys* 2021;71:72–84.
- [35] Zhang Y, Xu Y, Yao Z, et al. A feasible neuron for estimating the magnetic field effect. *Nonlinear Dyn* 2020;102:1849–67.
- [36] Liu Z, Ma J, Zhang G, et al. Synchronization control between two Chua's circuits via capacitive coupling. *Appl Math Comput* 2019;360:94–106.
- [37] Yao Z, Zhou P, Alsaedi A, et al. Energy flow-guided synchronization between chaotic circuits. *Appl Math Comput* 2020;374:124998.
- [38] Mandal K, Banerjee S. Synchronization phenomena in microgrids with capacitive coupling. *IEEE J Emerging Sel Top Circuits Syst* 2015;5:364–71.

- [39] Liu Z, Wang C, Zhang G, et al. Synchronization between neural circuits connected by hybrid synapse. *Int J Mod Phys B* 2019;33:1950170.
- [40] Xu YM, Yao Z, Hobiny A, et al. Differential coupling contributes to synchronization via a capacitor connection between chaotic circuits. *Frontiers of Information Technology & Electronic Engineering* 2019;20:571–83.
- [41] Yakopcic C, Taha TM, Subramanyam G, et al. A memristor device model. *IEEE Electron Device Lett* 2011;32(10):1436–8.
- [42] Ascoli A, Corinto F, Senger V, et al. Memristor model comparison. *IEEE Circuits Syst Mag* 2013;13:89–105.
- [43] Zidan MA, Fahmy HAH, Hussain M, et al. Memristor-based memory: The sneak paths problem and solutions. *Microelectron J* 2013;44:176–83.
- [44] Valsa J, Biolek D, Biolek Z. An analogue model of the memristor. *Int J Numer Model Electron Networks Devices Fields* 2011;24:400–8.
- [45] Zhou P, Ma J, Tang J. Clarify the physical process for fractional dynamical systems. *Nonlinear Dyn* 2020;100:2353–64.
- [46] Wu GC, Luo M, Huang L, et al. Short memory fractional differential equations for new memristor and neural network design. *Nonlinear Dyn* 2020;100:3611–23.
- [47] Yamakou ME. Chaotic synchronization of memristive neurons: Lyapunov function versus Hamilton function. *Nonlinear Dyn* 2020;101:487–500.
- [48] Bao H, Zhang Y, Liu W, et al. Memristor synapse-coupled memristive neuron network: synchronization transition and occurrence of chimera. *Nonlinear Dyn* 2020;93:7–50.
- [49] Wu F, Zhang Y, Zhang X. Regulating firing rates in a neural circuit by activating memristive synapse with magnetic coupling. *Nonlinear Dyn* 2019;98:971–84.
- [50] Nair MV, Muller LK, Indiveri G. A differential memristive synapse circuit for on-line learning in neuromorphic computing systems. *Nano Futures* 2017;1(3): 035003.
- [51] Yang Y, Zhang X, Qin L, et al. Probing nanoscale oxygen ion motion in memristive systems. *Nat Commun* 2017;8:15173.
- [52] Di Ventra M, Pershin YV. On the physical properties of memristive, memcapacitive and meminductive systems. *Nanotechnology* 2013;24(25):255201.
- [53] Wedig A, Luebben M, Cho DY, et al. Nanoscale cation motion in TaO_x, HfO_x and TiO_x memristive systems. *Nat Nanotechnol* 2016;11:67–74.
- [54] Wu F, Ma J, Ren G. Synchronization stability between initial-dependent oscillators with periodical and chaotic oscillation. *Journal of Zhejiang University-Science A* 2018;19:889–903.
- [55] Wu F, Zhou P, Alsaedi A, et al. Synchronization dependence on initial setting of chaotic systems without equilibria. *Chaos, Solitons Fractals* 2018;110:124–32.
- [56] Ma J, Tang J. A review for dynamics of collective behaviors of network of neurons. *Science China Technological Sciences* 2015;58(12):2038–45.
- [57] Yu D, Ju HC, Liang Y, et al. Dynamic behavior of coupled memristor circuits. *IEEE Trans Circuits Syst I Regul Pap* 2015;62:1607–16.
- [58] Zhang J, Liao X. Effects of initial conditions on the synchronization of the coupled memristor neural circuits. *Nonlinear Dyn* 2019;95:1269–82.
- [59] Corinto F, Forti M. Complex dynamics in arrays of memristor oscillators via the flux-charge method. *IEEE Trans Circuits Syst I Regul Pap* 2017;65:1040–50.
- [60] Bao B, Jiang P, Wu H, et al. Complex transient dynamics in periodically forced memristive Chua's circuit. *Nonlinear Dyn* 2015;79:2333–43.
- [61] Chen M, Yu J, Bao BC. Finding hidden attractors in improved memristor-based Chua's circuit. *Electron Lett* 2015;51:462–4.
- [62] Chua LO, Kang SM. Memristive devices and systems. *Proc IEEE* 1976;64:209–23.
- [63] Ishaq Ahamed A, Lakshmanan M. Nonsmooth bifurcations, transient hyperchaos and hyperchaotic beats in a memristive Murali–Lakshmanan–Chua circuit. *Int J Bifurcation Chaos* 2013;23:1350098.
- [64] Rocha R, Ruthiramoorthy J, Kathamuthu T. Memristive oscillator based on Chua's circuit: stability analysis and hidden dynamics. *Nonlinear Dyn* 2017;88:2577–87.
- [65] Kobe DH. Helmholtz's theorem revisited. *Am J Phys* 1986;54:552–4.
- [66] Zhou P, Hu XK, Zhu ZG, et al. What is the most suitable Lyapunov function? *Chaos, Solitons Fractals* 2021;150:111154.
- [67] Ramadoss J, Kengne J, Telem ANK, et al. Broken symmetry and dynamics of a memristive diodes bridge-based Shinriki oscillator. *Physica A* 2021;588:126562.
- [68] Karthikeyan A, Rajagopal K, Kamdoun Tamba V, et al. A Simple Chaotic Wien Bridge Oscillator with a Fractional-Order Memristor and Its Combination Synchronization for Efficient Antiattack Capability. *Complexity* 2021;2021: 8857075.
- [69] Kingston SL, Suresh K, Thamilaran K, et al. Extreme and critical transition events in the memristor based Liénard system. *European Physical Journal Special Topics* 2020;229:1033–44.
- [70] Singh JP, Koley J, Akgül A, et al. A new chaotic oscillator containing generalised memristor, single op-amp and RLC with chaos suppression and an application for the random number generation. *European Physical Journal Special Topics* 2019; 228(10):2233–45.
- [71] Chen CY, Rajagopal K, Hamarash II, et al. Antimonotonicity and multistability in a fractional order memristive chaotic oscillator. *European Physical Journal Special Topics* 2019;228(10):1969–81.
- [72] Singh JP, Roy BK, Kuznetsov NV. Multistability and hidden attractors in the dynamics of permanent magnet synchronous motor. *Int J Bifurcation Chaos* 2019; 29:1950056.
- [73] Akgül A, Rajagopal K, Durdu A, et al. A simple fractional-order chaotic system based on memristor and memcapacitor and its synchronization application. *Chaos, Solitons Fractals* 2021;152:111306.
- [74] Singh JP, Roy BK. Crisis and inverse crisis route to chaos in a new 3-D chaotic system with saddle, saddle foci and stable node foci nature of equilibria. *Optik* 2016;127(24):11982–2002.
- [75] Singh JP, Roy BK. The simplest 4-D chaotic system with line of equilibria, chaotic 2-torus and 3-torus behaviour. *Nonlinear Dyn* 2017;89:1845–62.
- [76] Gambuzza LV, Buscarino A, Fortuna L, et al. Memristor-based adaptive coupling for consensus and synchronization. *IEEE Trans Circuits Syst I Regul Pap* 2015;62: 1175–84.
- [77] Zhang J, Liao X. Synchronization and chaos in coupled memristor-based FitzHugh-Nagumo circuits with memristor synapse. *Aeu-international journal of electronics and communications* 2017;75:82–90.
- [78] Zhang X, Wu F, Ma J, et al. Field coupling synchronization between chaotic circuits via a memristor. *AEU-International Journal of Electronics and Communications* 2020;115:153050.
- [79] Korneev IA, Semenov V, Vadivasova TE. Synchronization of periodic self-oscillators interacting via memristor-based coupling. *Int J Bifurcation Chaos* 2020; 30:2050096.



Nonlinear responses in a neural network under spatial electromagnetic radiation

Yitong Guo^a, Ying Xie^b, Jun Ma^{a,b,c,*}

^a College of Electrical and Information Engineering, Lanzhou University of Technology, Lanzhou 730050, China

^b Department of Physics, Lanzhou University of Technology, Lanzhou 730050, China

^c School of Science, Chongqing University of Posts and Telecommunications, Chongqing 430065, China

ARTICLE INFO

Article history:

Received 8 May 2023

Received in revised form 29 July 2023

Available online 2 August 2023

Keywords:

Memristive neuron

Field coupling

Non-uniform radiation

Stochastic resonance

ABSTRACT

Biological neurons are clustered and functional synapses are created to propagate electric signals accompanying with formation of spatial patterns in the neural network. From physical aspect, fast synaptic connections to neurons provide an effective shortcut for energy exchange and keeping energy balance between neurons. In fact, field coupling behaves effective bridge connections to neurons and then neural activities can be controlled by spatial induction currents in the neural network. In this paper, memristive neurons are controlled by magnetic flux by inducing gradient induction current in presence of electromagnetic radiation without synaptic connections. Differed from the previous uniform radiation, spatial radiation is imposed on the neural network and the stability of spatial patterns is explored by imposing a spatiotemporal disturbance on the network. Memristive neurons developed from Hindmarsh–Rose neurons by involving memristive term and magnetic flux variable are used to build a chain network and a lattice network under field coupling rather than using synaptic coupling. Synchronization factors are calculated to discern the synchronization dependence on noise, amplitude and frequency in the spatial electromagnetic radiation. An isolated neuron can present stochastic resonance under noise and radiation with diversity. Field coupling enhances energy exchange and local energy balance, and then synchronous patterns are controlled in absence of synaptic coupling. External noise and spatial disturbance can induce certain diversity in induction current and excitability, therefore, approach of complete synchronization and development of regular patterns are blocked because of local energy balance under field coupling. These results indicate that energy injection and control of energy flow are effective to prevent the occurrence of bursting synchronization and coexistence of multiple firing modes is formed in neural network composed of memristive neurons under spatial radiation.

© 2023 Elsevier B.V. All rights reserved.

1. Introduction

Biological neurons present intrinsic self-adaption to external stimuli and thus appropriate firing patterns can be guided and controlled completely. Indeed, any external physical stimuli used to inject energy into the media while chemical stimuli will change the ions flow and shape deformation, and then energy flow is guided to regulate the neural activities [1–5]. During continuous pumping and diffusion of intracellular ions and exchange with extracellular

* Corresponding author at: College of Electrical and Information Engineering, Lanzhou University of Technology, Lanzhou 730050, China.

E-mail addresses: hyperchaos@lut.edu.cn, hyperchaos@163.com (J. Ma).

ions, the inner field energy is changed accompanying with the propagation of energy flow in/out of the cells. Sampled data for membrane potentials are detected for nonlinear analysis, and then some theoretical models are proposed to reproduce similar output series and then these models are handled as biological or mathematical neurons. From dynamical aspect, continuous models [6–10] described by ordinary differential equations containing nonlinear terms and discrete models [11–14] presented in maps can be controlled in the external stimulus and intrinsic parameters for showing similar firing patterns including quiescent, spiking, bursting and even chaotic patterns, which can also be detected from biological neurons in nervous system by using patch clamp technology [15,16].

In fact, the physical effect in the biological neurons becomes important for further predicting and control of the neural activities of neurons and network in complex electromagnetic environments. It is also worthy of investigating the intrinsic biophysical property of biological neurons for designing more artificial neural circuits [17–22] and intelligent networks. For example, Yamakou et al. [18] calculated the nonlinear resonance in a memristive neuron under noise. Sayari et al. [19] explored the effect of structural connectivity matrix of a human brain on bursting synchronization in presence of stimulus. Kusbeyzi et al. [20] suggested a scheme for improving the biophysical function of mathematical neuron models by supplying memristive terms associated with memristor [21]. Hansen et al. [22] demonstrated the role of time delay on synchronization stability in a neural network. The inner and outer cell membranes of biological neurons discern the capacitive property and the channel currents show the inductance characteristics of neurons. Therefore, both capacitor and inductor are necessary electric components for building an equivalent neural circuit. Because of the stochastic diffusion of inner ions and complex exchange between field energy (magnetic field and electric field), nonlinear electric components including negative resistor, memristor, piezoelectric element are often incorporated into the ion channels to control the energy flow [23–27]. In addition, external voltage source is applied as external stimulus and constant voltage source added to the ion channels for proper measurement of inverse/resting potentials. These neural circuits can be approached by using equivalent biophysical models [28–32] when scale transformation is applied on the physical variables and parameters for the neural circuits. In this way, more biophysical neuron models can be obtained to discern external illumination, acoustic wave, temperature changes and external magnetic field as well by embedding photocell, piezoelectric ceramics, thermistor, Josephson junction into one of the branch circuits [33–35]. For example, Zhang et al. [33] built a new neural circuit by connecting Josephson junction and external magnetic field can be perceived effectively. Zhao et al. [35] proposed a neural circuit by incorporating memristor into one branch and a spiking neuron model is obtained. In particular, the involvement of memristor can make a memristive system, which its dynamics can be controlled by the initial value for the memristive variable even other parameters are fixed, and the inner effect of electromagnetic induction can be addressed well by involving additive magnetic flux variable and induction current into the neuron models [36–40].

Based on these mathematical and biophysical neuron models, complete bifurcation analysis, nonlinear resonance, synchronization and anti-synchronization can be explored well [41–45]. For example, Lian et al. [41] investigated the stability of antiphase synchronization in nonlinear circuits under field coupling. Zhang et al. [42] suggested a scheme for estimating complexity by analyzing the order patterns. Li et al. [43] claimed that frequency analysis can be used to identify the parameters of nonlinear structural systems. Palabas et al. [46] confirmed the regulation on double coherence resonance in neuron coupled by astrocyte. Klinshov et al. [47] discovered the occurrence of rate chaos and memory life time in neural network composed of spiking neurons. Parastesh et al. [48] confirmed that blinking coupling is helpful to synchronization enhancement. Sar et al. [49] found that time-varying phase interactions have impacts on swarming and synchronization. For more guidance about collective self-organization in networks, clues can be found in the review [50]. Besides the external stimulus, adjacent synaptic currents also have important role in regulating the electric activities of neurons in the networks. For two or more neurons, the synchronous firing patterns are mainly dependent on the biophysical properties of the coupling channels including electric synapse, chemical synapse, hybrid synapse and memristive synapse [51–53]. For biological neurons, the activation and modulation of synaptic connections are effective to propagate energy flow and then the firing pattern in each neuron can be adjusted to show appropriate firing modes, and the adjacent neurons will reach energy balance and possible synchronization or phase lock [54–56].

The collective electric behaviors of neural networks are mainly estimated by developing spatial patterns [57–63] including spiral waves, Turing patterns and even spatiotemporal patterns and stabilizing synchronization in one-layer or multi-layer networks. For example, Wu et al. [61] explored the repulsion dynamics of spiral waves near the unexcitable zone and clarified that repulsion behavior results from any changes in the natural frequency of the spiral wave near the unexcitable boundary. In a practical way, external noisy and periodic stimuli can be applied to control the pattern formation and synchronization stability of networks. For neural circuits and biological neurons, the EMR (electromagnetic radiation) can enhance the effect of electromagnetic induction [64–68] by injecting field energy because the propagation of intracellular ions can be affected by electromagnetic field. Considering the controllability in realistic systems, the characteristic of self-adaption and robustness should be considered by applying optimization algorithm [69,70] should be confirmed for obtaining reliable controllers. In fact, biophysical models are enhanced in this self-adaptive property and the self-organization of biological neurons can be discerned under field coupling, which enhances the signal processing via energy exchange.

In this paper, based on a memristive neuron model, neurons are clustered under field coupling [71–74] and the pattern formation under noise and EMR is discussed in the neural networks in absence of synaptic connections. Considering the inner diversity of neurons and radiation emitted from more sources, spatial EMR is applied to investigate the wave propagation and pattern stability. The scientific contribution of this work can be summarized as follows. Based on a

memristive neuron including the electromagnetic induction effect, field coupling is activated without direct synaptic coupling for discerning the synchronization approach and pattern formation in the memristive network. In particular, EMR with non-uniform spatial distribution is considered by imposing spatial disturbance on the magnetic flux variable for each neuron in the network, and diversity of induction current can further induce the diversity in excitability and changes in firing modes. This scheme is useful to discern the neural activities in realistic biological media and nervous system including cardiac tissue under inhomogeneous electromagnetic radiation [75]. It also explains why neurons can present coexistent multiple firing modes in the electric activities because of diversity in excitability and some intrinsic parameters.

2. Model and scheme

As is known, continuous pumping and stochastic diffusion of intracellular and extracellular ions can induce electromagnetic field in cells. On the other hand, external electromagnetic field has distinct impact on the distribution of inner field of the cell due to uncertain polarization and magnetization. The involvement of magnetic flux can well estimate the effect of magnetic field on the membrane potential of neuron. Firstly, magnetic flux variable and memristive term for induction current [36,37] are introduced into the Hindmarsh–Rose neuron and a memristive neuron model is obtained to describe the effect of electromagnetic induction and EMR on neuron and neural networks [76].

$$\begin{cases} \frac{dx}{dt} = y - ax^3 + bx^2 - z + I_{ext} - k_1 W(\varphi)x; \\ \frac{dy}{dt} = c - dx^2 - y; \\ \frac{dz}{dt} = r[s(x + 1.56) - z]; \\ \frac{d\varphi}{dt} = kx_i - k_2\varphi_i + \varphi_{ext}; \end{cases} \quad (1)$$

where the variables (x, y, z, φ) denote the membrane potential, recovery variable for slow current, adaption current, and magnetic flux, respectively. I_{ext} represents external electric stimulus and it can be adjusted to trigger different firing patterns in the neuron. The normalized parameters (a, b, c, d, r, s) are the same as the original Hindmarsh–Rose neuron, the coefficient k_1 for the memristive term (induction current) is relative to the intrinsic property of the media and the intensity of induction current across the cell membrane is controlled by the gain k_1 . Considering the magnetic field effect in the cell, an equivalent induction coil with N turns is suggested to estimate the magnetic field as $1/N = k$, and so equivalent neural circuits can be designed to reproduce similar dynamical property in biological neurons. Therefore, an equivalent capacitor is often introduced into neural circuit for discerning the capacitance of cell membrane. Considering the stochastic diffusion of ions in the direction, the coefficient k_2 is introduced to estimate the apposite diffusion of magnetic flux and leakage. The memristive term $W(\varphi)x$ calculates the current in the memristive synapse/channel with memductance $W(\varphi) = dq(\varphi)/d\varphi = \alpha + 3\beta\varphi^2$, (α, β) are normalized parameters for the memristive channel, good explanation can found in Refs. [77,78]. When neurons are exposed to external electromagnetic field, the propagation and diffusion of intracellular ions will be changed greatly because of magnetization and driving/blocking from electric field. Therefore, the magnetic flux across the cell membrane will be changed and then φ_{ext} is often applied with different forms to match with low-frequency, high-frequency and stochastic radiation on the neuron and neural networks.

For a chain neural network clustered with N neurons under field coupling without synaptic connection, the magnetic flux is affected by the other $N - 1$ neurons and then the induction current for each neuron shows certain diversity. Indeed, the spatial induction currents induce diversity in the excitability, and wave fronts are induced for stochastic collision and interaction, which symmetric breaking can occur for developing specific regular patterns in the neural network. Furthermore, the involvement of additive noise $\xi(t)$ can estimate the effect of stochastic fluctuation of electric field on the membrane potential of neurons, and continuous exposure to EMR (φ_{ext}) also regulates the firing modes in neurons. Considering the inner diversity in neurons, external EMR often induces spatial diversity on the magnetic field and induction current, therefore, φ_{ext} can be selected with spatial form for discerning the non-uniform EMR on neural networks. The neural activities in a chain network under field coupling [74] in presence of additive noise and EMR can be described by

$$\begin{cases} \frac{dx_i}{dt} = y_i - ax_i^3 + bx_i^2 - z_i + I_{ext} - k_1 W(\varphi_i)x_i + \xi(t); \\ \frac{dy_i}{dt} = c - dx_i^2 - y_i; \\ \frac{dz_i}{dt} = r[s(x_i + 1.56) - z_i]; \\ \frac{d\varphi_i}{dt} = kx_i - k_2\varphi_i - k_3 \sum_{\substack{j=1 \\ i \neq j}}^N (\varphi_j - \varphi_i) + \varphi_{ext}^i; \end{cases} \quad (2)$$

The subscripts/superscripts (i, j) represents the node position of the network, and the third term in the right side of the four formula describes the superposition of magnetic field on the i th neuron. The EMR (φ_{ext}) is selected as spatial form given in $\varphi_{ext}^i = A \cos(\omega t + i^* \lambda)$, λ is a constant relative to the intrinsic property of the media and the intrinsic parameters (A, ω) can be adjusted to describe the EMR on the neuron. $\xi(t)$ represent noise. For estimating the synchronization stability and formation of spatial patterns, a statistical synchronization factor R for a chain network is defined according to the mean field theory as follows [36]

$$F = \frac{1}{N} \sum_{i=1}^N x_i; \quad R = \frac{\langle F^2 \rangle - \langle F \rangle^2}{\frac{1}{N} \sum_{i=1}^N (\langle x_i^2 \rangle - \langle x_i \rangle^2)}; \quad (3)$$

For a chain network composed of N neurons, the noise intensity and EMR can be regulated to control the collective neural activities. When all neurons become synchronous firing completely, the network becomes homogeneous and no pattern is developed because of perfect synchronization with higher value in the synchronization factor R . On the other hand, distinct spatial patterns can be developed when synchronization is corrupted with lower value for R .

For neural network in two-dimensional space on a lattice, the collective firing patterns under field coupling can be controlled by noise and EMR as well, and the dynamics can be calculated by [76]

$$\begin{cases} \frac{dx_{ij}}{dt} = y_{ij} - ax_{ij}^3 + bx_{ij}^2 - z_{ij} + I_{ext} - k_1 W(\varphi_{ij}) x_{ij} + \xi(t); \\ \frac{dy_{ij}}{dt} = c - dx_{ij}^2 - y_{ij}; \\ \frac{dz_{ij}}{dt} = r[s(x_{ij} + 1.56) - z_{ij}]; \\ \frac{d\varphi_{ij}}{dt} = kx_{ij} - k_2 \varphi_{ij} - k_3 \sum_{\substack{m=1, n=1 \\ m \neq i, n \neq j}}^N (\varphi_{mn} - \varphi_{ij}) + \varphi_{ext}^{ij}; \end{cases} \quad (4)$$

Similar to the case for chain network, all neurons are connected via field coupling and synaptic connections are removed. The subscripts/superscripts (ij, mn) mark the node position for neurons, and spatial patterns will be dependent on the EMR (φ_{ext}^{ij}), external stimuli and stochastic excitation on the membrane potentials. The spatial radiation φ_{ext}^{ij} on each node is different when the node position (ij) is changed. Similar definition for synchronization factor R [72] on lattice is defined as follows

$$F = \frac{1}{N^2} \sum_{j=1}^N \sum_{i=1}^N x_{ij}; \quad R = \frac{\langle F^2 \rangle - \langle F \rangle^2}{\frac{1}{N^2} \sum_{j=1}^N \sum_{i=1}^N (\langle x_{ij}^2 \rangle - \langle x_{ij} \rangle^2)}; \quad (5)$$

Within certain transient period, a higher value for R indicates that perfect synchronization is obtained and formation of regular patterns is suppressed. A lower value for R is helpful to develop regular patterns in the neural network. The symbol $\langle * \rangle$ means an average estimation of variables within finite transient period or running times for numerical calculation. In addition, the EMR on neurons in the square array is updated as $\varphi_{ext}^{ij} = A \cos(\omega t + i^* \lambda_1 + j^* \lambda_2)$, λ_1, λ_2 are constants. The additive Gaussian white noise with zero average value and its statistical property is estimated by $\langle \xi(t) \xi(t') \rangle = 2D \delta(t - t')$, D is the noise intensity and $\delta(*)$ represents Dirac- δ function.

On the other hand, the memristive current considers the consumption and storage of field energy when memristive channel is involved to estimate the effect of electromagnetic induction. The energy in the memristive channel is estimated by [79]

$$\begin{aligned} E &= \frac{1}{2} L_m i_m^2 = \frac{1}{2} (L_m \cdot i_m) i_m = \frac{1}{2} \varphi \cdot i_m = \frac{1}{2} \varphi \frac{dq(\varphi)}{dt} \\ &= \frac{1}{2} \varphi \frac{dq(\varphi)}{d\varphi} \frac{d\varphi}{dt} = \frac{1}{2} k_1 \varphi W(\varphi) x \\ &= \frac{1}{2} k_1 \alpha x \varphi + \frac{3}{2} k_1 \beta x \varphi^3; \end{aligned} \quad (6)$$

The first term in Eq. (6) discerns the consumption of Joule heat and the second term estimates the energy savage of magnetic field in the memristive channel developed from magnetic flux-controlled memristor. In presence of stochastic disturbance as noisy driving, distinct regularity can be induced and detected in the sampled time series for membrane potentials by taming the noise intensity. In practical way, statistical functions including signal-to-noise ratio (SNR) and coefficient variability (CV) of ISI series are often calculated for predicting the occurrence of nonlinear resonance [80–82].

$$\begin{cases} SNR = 10 \log 10 \left(\frac{S}{B} \right) = P_{peak} \frac{f_{peak}}{\Delta f}; \\ CV = \frac{\sqrt{(\langle T^2 \rangle - \langle T \rangle^2)}}{\langle T \rangle}; \end{cases} \quad (7)$$

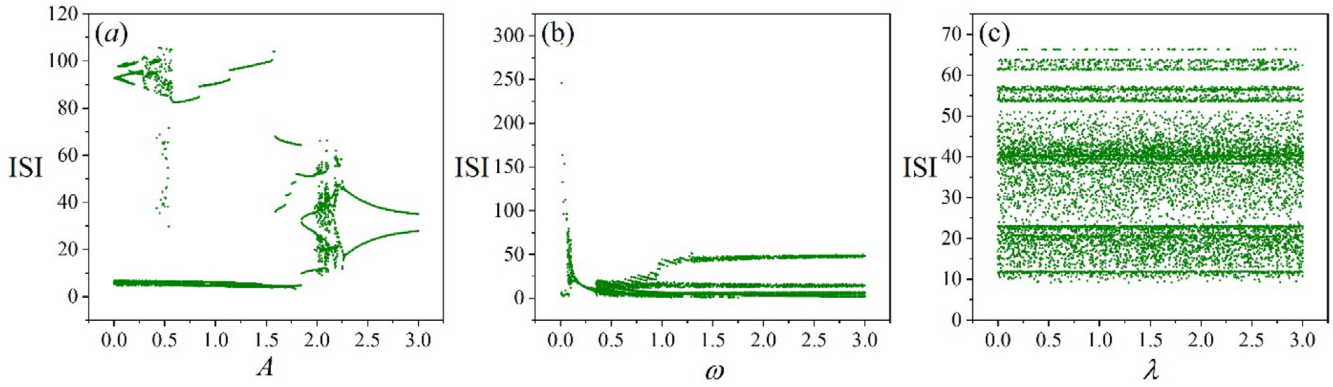


Fig. 1. Bifurcation of ISI for membrane potential x vs. parameters A , ω , λ . For (a) $\omega = 0.1$, $\lambda = 0.2$; (b) $A = 2.1$, $\lambda = 0.2$; (c) $A = 2.1$, $\omega = 0.1$. Setting parameters $I_{ext} = I = 4.0$, $\alpha = 0.4$, $\beta = 0.02$, $k = 0.5$, $k_1 = 0.9$, $k_2 = 0.4$, $a = 1.0$, $b = 3.0$, $c = 1.0$, $d = 5.0$, $r = 0.006$, $s = 4.0$, $\varphi_{ext} = A\cos(\omega\tau + \lambda)$, and initial values for variables in single neuron are selected as (0.02, 0.03, 0.01, 0.1).

where S and B represent the values of the output power spectrum density (PSD) at the peak (height of the signal peak) and the base of the signal feature (the amplitude of the background noise measured at the base of the signal peak), respectively. P_{peak} denotes the peak height of power spectrum, Δf represents the peak width at half-height and f_{peak} estimates the frequency for peak value in the power spectrum. The value for T discerns its value as interspike interval (ISI), and appearance of lower value for CV means higher coherence degree in the neural activities under noise.

3. Numerical results and discussion

In this section, reliable algorithm as fourth order Runge–Kutta algorithm is applied to find numerical solutions of the neuron model and neural network with time step $h = 0.01$ when no noisy excitation is applied. In presence of noisy disturbance on the membrane potentials, the neuron model and network may show mode transition in neural activities but distinct firing patterns are developed as well, the Euler forward algorithm [83] can be effective to obtain reliable statistical analysis including distribution of SNR, CV and synchronization factors. It is believed that the Langzhiwan method is suitable for finding numerical solutions of the stochastic dynamical systems. In Refs. [84,85], extensive suggestions are provided to find exact solutions for stochastic differential equations. In fact, mode selection in neuron models is mainly controlled by the nonlinear terms including channel currents, and noisy excitation just can optimize and induce transition of firing modes and then distinct firing patterns are developed. Therefore, stochastic effect is suppressed by nonlinearity and Euler algorithm and even multi-step (Runge–Kutta like) numerical methods are suitable for the program implementation because they can be expressed as a sequence of explicit formulas [85]. The parameters for the memristive neuron model are fixed at $(a, b, c, d, r, s) = (1.0, 3.0, 1.0, 5.0, 0.006, 4.0)$ and $\alpha = 0.4$, $\beta = 0.02$. For simplicity, $k = 0.5$, $k_1 = 0.9$, $k_2 = 0.4$, $k_3 = 0.0001, 0.00001$, and external stimulus $I_{ext} = 4.0$. No-flux boundary condition is applied and initials are selected with certain diversity for the neural network. In mathematical definition for continuous media, $\partial u / \partial n = 0$ is applied on the boundary of the media. For chain networks, $u(N) = u(N+1)$, $u(1) = u(2)$ can be used to mimic the setting for no-flux boundary condition in numerical results. The initial values for neurons in the network can be uniform in which each neuron has the same initials as other neurons. Surely, diversity in the initials can be considered by selecting random values 0.0~1.0 for each neuron in the network. At first, the bifurcation of ISI (interspike intervals) for sampled membrane potentials is calculated in Fig. 1 by changing the amplitude, frequency and initial phase in the radiation $\varphi_{ext}^i = A\cos(\omega t + i\lambda) = A\cos(\omega\tau + i\lambda)$, $i = 1$, respectively. The parameter λ introduces diversity in the initial phases for different nodes in the neural network. In the following numerical approach, evolution of membrane potentials, energy and spatial patterns are presented within finite transient period ($t = \tau = 1000$ time units).

For a single memristive HR neuron excited by $\varphi_{ext} = A\cos(\omega\tau + \lambda)$, distinct firing mode in the neural activity can be controlled effectively by taming one of the intrinsic parameters (A , ω) for the EMR when the external stimulus is fixed in Fig. 1. In particular, the neuron prefers to present chaotic patterns at $I_{ext} = 4.0$, and chaotic states keep alive for different initial phases in the EMR by exploring the phase portraits and confirming positive Lyapunov exponents. For better showing, the firing patterns and energy growth in an isolated neuron under EMR are calculated in Fig. 2 without external noise being consideration.

From Fig. 2, it is demonstrated that spiking neuron often keeps higher energy than bursting neurons. In particular, periodic firing in neuron enables its much higher energy than spiking neuron because of higher regularity in the neural activities. When membrane potential becomes negative, the energy in the memristive synapse also shows negative value with time, it means that this memristive channel can absorb external field energy and then energy flow is emitted to excite the neuron. As is known, neural activities can be controlled by noisy disturbance, and specific noise with moderate intensity can enhance the regularity and coherence in the electric activities accompanied with stochastic resonance by discerning the SNR (signal to noise ratio) in Fig. 3.

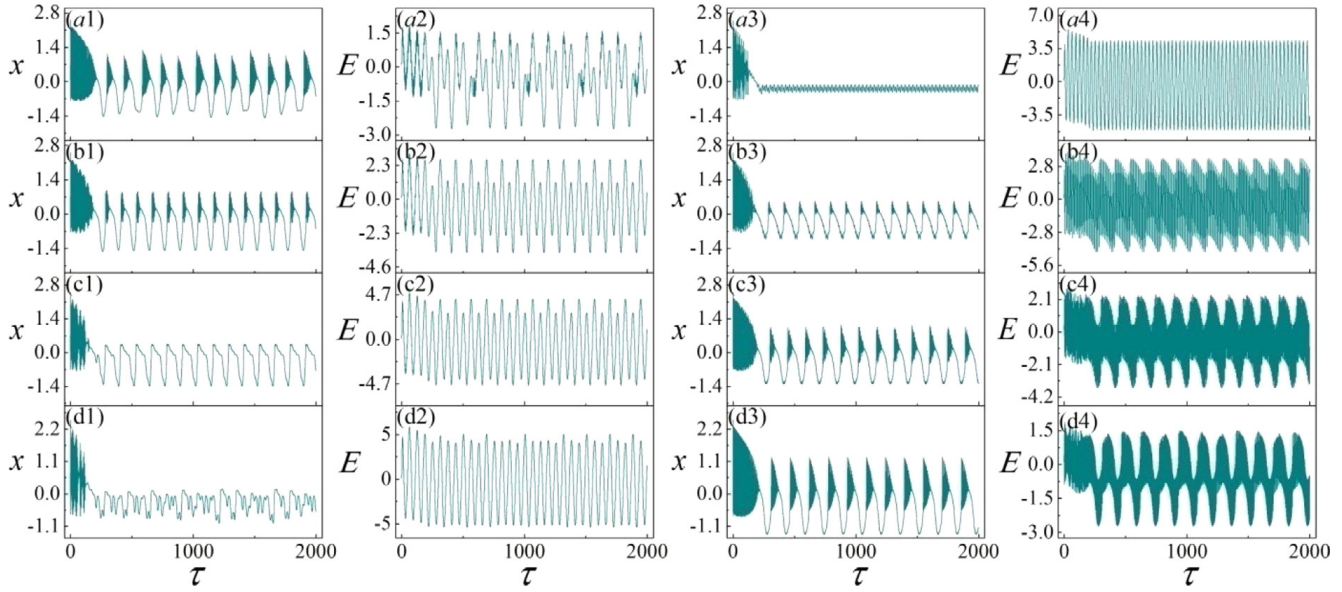


Fig. 2. Evolution of membrane potential and energy level in the memristive channel. For (a1, a2) $A = 0.48$, $\omega = 0.1$; (b1, b2) $A = 1.0$, $\omega = 0.1$; (c1, c2) $A = 1.7$, $\omega = 0.1$; (d1, d2) $A = 2.1$, $\omega = 0.1$; (a3, a4) $A = 2.1$, $\omega = 0.2$; (b3, b4) $A = 2.1$, $\omega = 0.5$; (c3, c3) $A = 2.1$, $\omega = 0.96$; (d4, d4) $A = 2.1$, $\omega = 2.0$. The rest parameters are set as $I = 4.0$, $\alpha = 0.4$, $\beta = 0.02$, $k = 0.5$, $k_1 = 0.9$, $k_2 = 0.4$, $a = 1.0$, $b = 3.0$, $c = 1.0$, $d = 5.0$, $r = 0.006$, $s = 4.0$, $\lambda = 0.02$, and the initial values for variables in single neuron are selected as (0.02, 0.03, 0.01, 0.1).

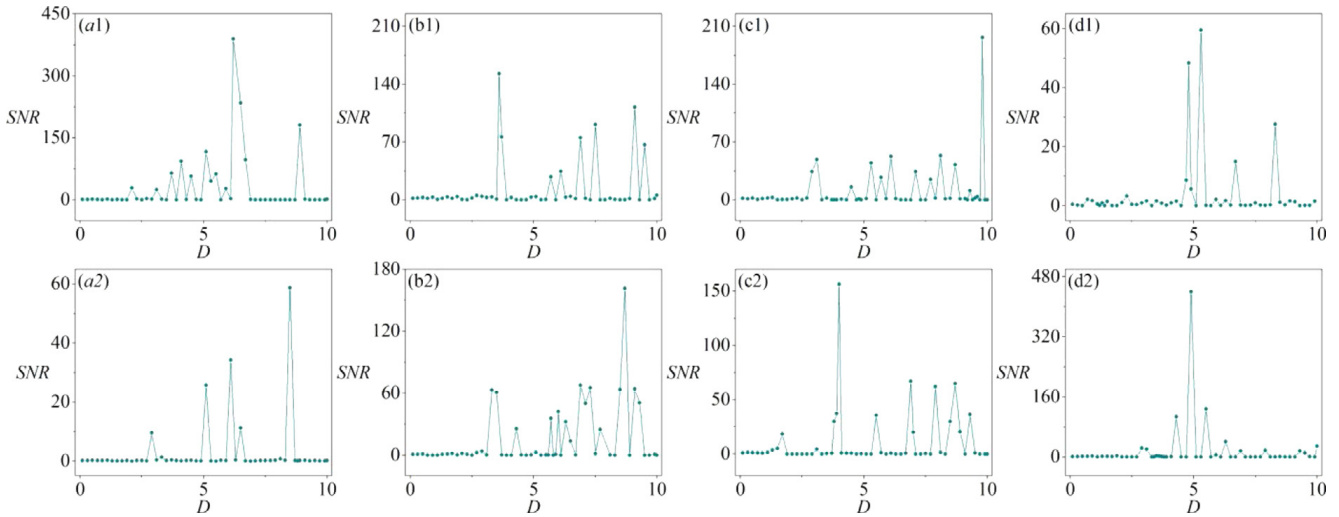


Fig. 3. Distribution of SNR is plotted by changing noise intensity D . For (a1) $A = 0.48$, $\omega = 0.1$; (b1) $A = 1.0$, $\omega = 0.1$; (c1) $A = 1.7$, $\omega = 0.1$; (d1) $A = 2.1$, $\omega = 0.1$; (a2) $A = 2.1$, $\omega = 0.2$; (b2) $A = 2.1$, $\omega = 0.5$; (c2) $A = 2.1$, $\omega = 0.96$; (d2) $A = 2.1$, $\omega = 2.0$. Setting $I_{\text{ext}} = 4.0$, $\alpha = 0.4$, $\beta = 0.02$, $k = 0.5$, $k_1 = 0.9$, $k_2 = 0.4$, $a = 1.0$, $b = 3.0$, $c = 1.0$, $d = 5.0$, $r = 0.006$, $s = 4.0$, $\lambda = 0.02$, and the initial values for variables in single neuron are selected as (0.02, 0.03, 0.01, 0.1).

In presence of EMR with different amplitudes and frequencies, similar stochastic resonance can be induced and discerned even the noise intensity for peak value for the SNR is different. Peak value is detected in the curve for SNR, and stochastic resonance occurs in this memristive neuron under EMR. It also indicates that careful setting in the noise intensity can control the effect of EMR on a single neuron and the distinct firing patterns can be induced with high regularity under coherence. For discerning the synchronization stability of chain network excited by EMR, the synchronization factors are estimated in Fig. 4 when EMR is changed in the amplitude and frequency, respectively.

The synchronization factor shows distinct decrease when external EMR is increased in the amplitude. On the other hand, further increase of the frequency of external EMR also has impact on the synchronization factors in the chain network, and fast frequency in EMR will induce quick change in induction current and the excitability synchronously. In fact, when external EMR is enhanced, magnetic flux and corresponding equivalent induction current show more difference and neurons become more different in induction current. As a result, diversity in excitability is generated and synchronization approach becomes difficult in the chain network composed of memristive neurons. According to Eq. (2), the membrane potential for each neuron in the chain network is calculated and the spatial distribution at any times is

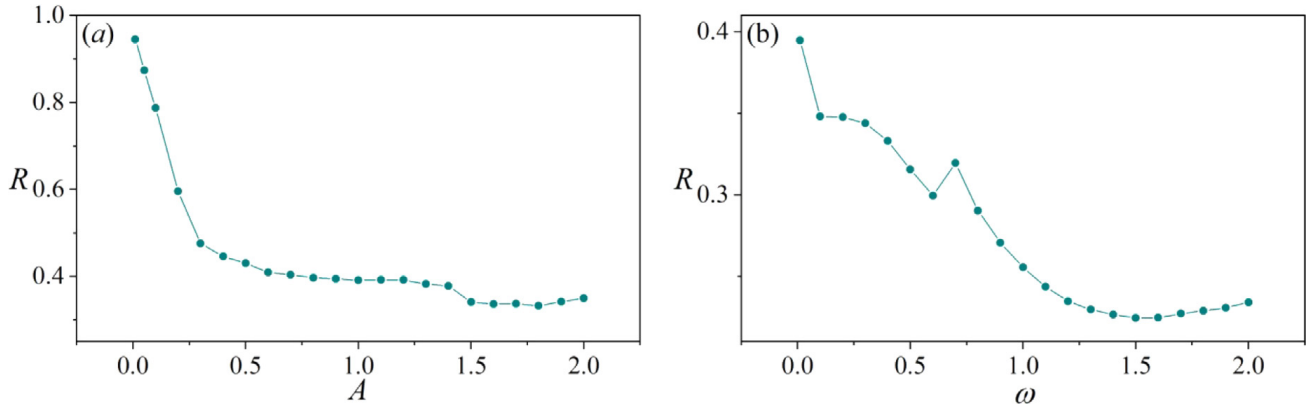


Fig. 4. Distribution of synchronization factors R is estimated by changing the amplitude A or ω for $\varphi_{ext}^i = A \cos(\omega t + i^* \lambda)$. For (a) $\omega = 0.1$; (b) $A = 2.1$. Setting $I_{ext} = 4.0$, $\alpha = 0.4$, $\beta = 0.02$, $k = 0.5$, $k_1 = 0.9$, $k_2 = 0.4$, $a = 1.0$, $b = 3.0$, $c = 1.0$, $d = 5.0$, $r = 0.006$, $s = 4.0$, $k_3 = 0.0001$, $\lambda = 0.02$, and the initial values for variables in single neuron are selected as (0.02, 0.03, 0.01, 0.1).

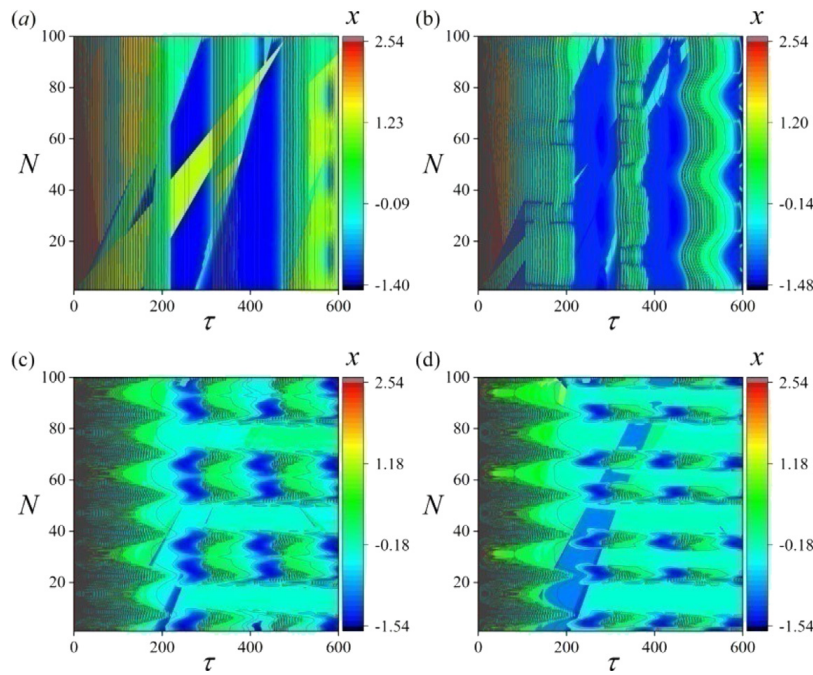


Fig. 5. Development of spatial pattern is plotted at different amplitudes A for $\varphi_{ext}^i = A \cos(\omega t + i^* \lambda)$ in chain network composed of 100 neurons. For (a) $A = 0.01$; (b) $A = 0.2$; (c) $A = 1.4$; (d) $A = 1.8$. Setting $I_{ext} = 4.0$, $\alpha = 0.4$, $\beta = 0.02$, $k = 0.5$, $k_1 = 0.9$, $k_2 = 0.4$, $a = 1.0$, $b = 3.0$, $c = 1.0$, $d = 5.0$, $r = 0.006$, $s = 4.0$, $k_3 = 0.0001$, $\lambda = 0.02$, and the initial values for variables in single neuron are selected as (0.02, 0.03, 0.01, 0.1). Snapshots are plotted in color scale and the spatial patterns discern the distribution of membrane potentials for neurons.

plotted to show the coherence under EMR. In Fig. 5, the wave propagation in the chain network is explored by applying EMR with different amplitudes.

With the increase of amplitude in the EMR, spatial induction currents are enhanced in the diversity of induction currents for all memristive neurons, and synchronization stability under field coupling is corrupted completely. As a result, spatial patterns become irregular and wave propagation becomes uncertain in the network. In addition, external noise is applied to predict whether spatial regularity can be induced to aid the wave propagation in the network, and synchronization factors are obtained in Fig. 6 by applying membrane noise with different intensities.

In presence of EMR, the involvement of noise on the cell membrane can decrease the synchronization factors and synchronization is destroyed in the chain network. It means that additive noise on the membrane potential is helpful for wave propagation along the chain network. Therefore, the spatial patterns for membrane potentials are calculated to discern whether wave propagation can be controlled by noise in Fig. 7.

Wave fronts are induced while no regular wave propagation is continued along the chain network even the noisy disturbance on membrane potential is further increased. That is, continuous collision between these wave fronts can be helpful to excite all the neurons but no regular wave profiles can be developed in presence of noise. We also explored the similar case on wave propagation and patterns formation in neural network on a lattice under field coupling accompanied

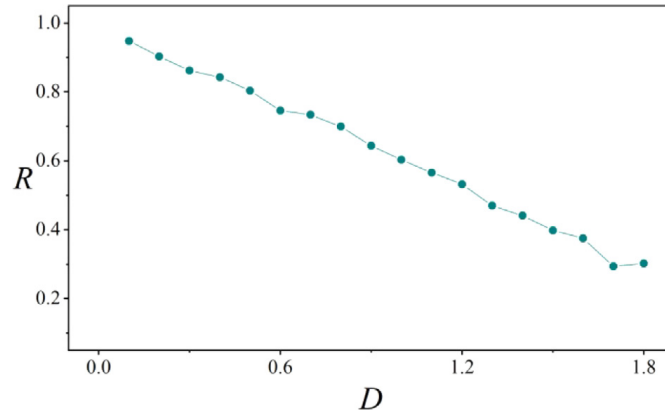


Fig. 6. Distribution of synchronization factors R is estimated by changing noise intensity D . Setting $A = 0.01$, $\omega = 0.1$, $I_{\text{ext}} = 4.0$, $\alpha = 0.4$, $\beta = 0.02$, $k = 0.5$, $k_1 = 0.9$, $k_2 = 0.4$, $a = 1.0$, $b = 3.0$, $c = 1.0$, $d = 5.0$, $r = 0.006$, $s = 4.0$, $k_3 = 0.0001$, $\lambda = 0.02$, and initials of each neuron in the chain network are selected as (0.02, 0.03, 0.01, 0.1).

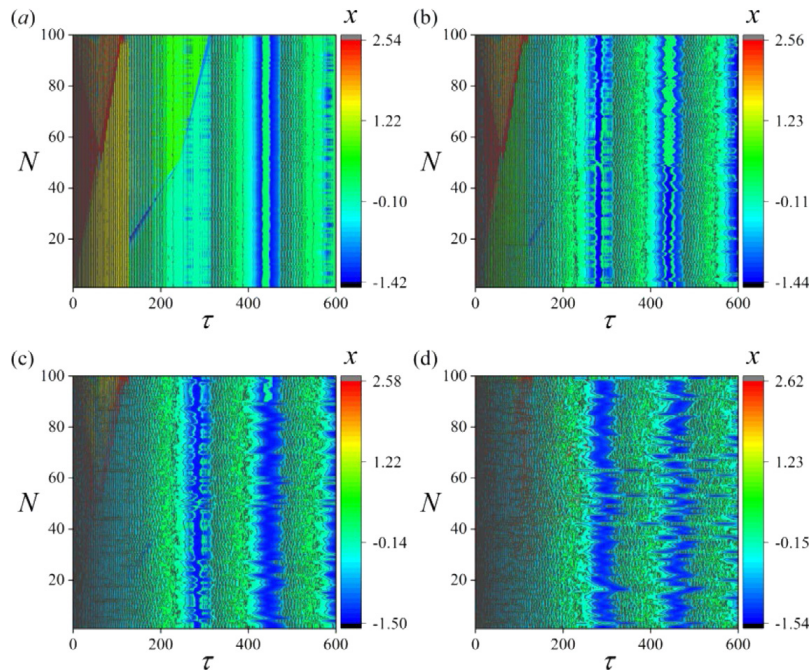


Fig. 7. Development of spatial pattern is plotted under different noise intensities D . For (a) $D = 0.1$; (b) $D = 0.4$; (c) $D = 0.8$; (d) $D = 1.3$. Setting $A = 0.01$, $\omega = 0.1$, $I_{\text{ext}} = 4.0$, $\alpha = 0.4$, $\beta = 0.02$, $k = 0.5$, $k_1 = 0.9$, $k_2 = 0.4$, $a = 1.0$, $b = 3.0$, $c = 1.0$, $d = 5.0$, $r = 0.006$, $s = 4.0$, $k_3 = 0.0001$, $\lambda = 0.02$, and initials of each neuron in the chain network are selected as (0.02, 0.03, 0.01, 0.1). Snapshots are plotted in color scale and the spatial patterns discern the distribution of membrane potentials for neurons.

with EMR, and the synchronization factors for the two-dimensional neural network are obtained in Fig. 8 by taming the external EMR in the intensity and phase, respectively.

Similar to the case for chain network composed of memristive neurons, the synchronization factors are lessened when EMR is increased in the amplitude or angular frequency. For better showing, the formation of spatial patterns is also explored in Fig. 9.

Most area of the network shows homogeneous state and the spatial patterns show distinct symmetry with further increase of the amplitude of external EMR. That is, horizontal and vertical disturbance from EMR can enhance the synchronization degree and more memristive neurons become synchronous in absence of noise. Furthermore, the synchronization stability is explored in presence of noise by estimating the synchronization factors in Fig. 10.

When noisy disturbance applied on membrane potential is activated, synchronization degree is decreased under higher noise intensity. For better illumination, the formation of spatial patterns in the lattice under noise is plotted in Fig. 11.

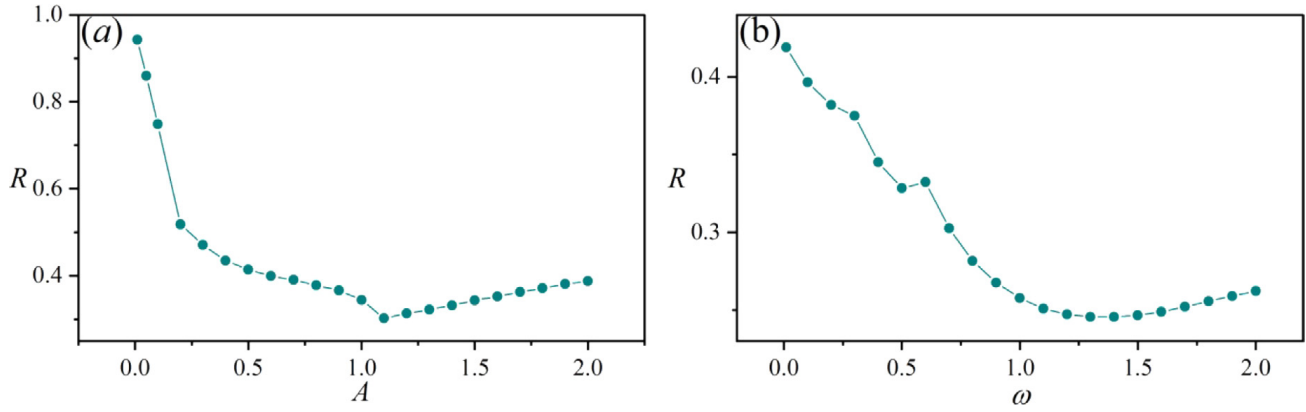


Fig. 8. Distribution of synchronization factors R is estimated by changing the amplitude A or ω frequency in $\varphi_{ext}^{ij} = A \cos(\omega t + i^* \lambda_1 + j^* \lambda_2)$. For (a) $\omega = 0.1$; (b) $A = 2.1$. Setting $I_{ext} = 4.0$, $\alpha = 0.4$, $\beta = 0.02$, $k = 0.5$, $k_1 = 0.9$, $k_2 = 0.4$, $a = 1.0$, $b = 3.0$, $c = 1.0$, $d = 5.0$, $r = 0.006$, $s = 4.0$, $k_3 = 0.00001$, $\lambda_1 = \lambda_2 = \lambda = 0.02$, and initials of each neuron in the 2D regular network are selected as (0.02, 0.03, 0.01, 0.1).

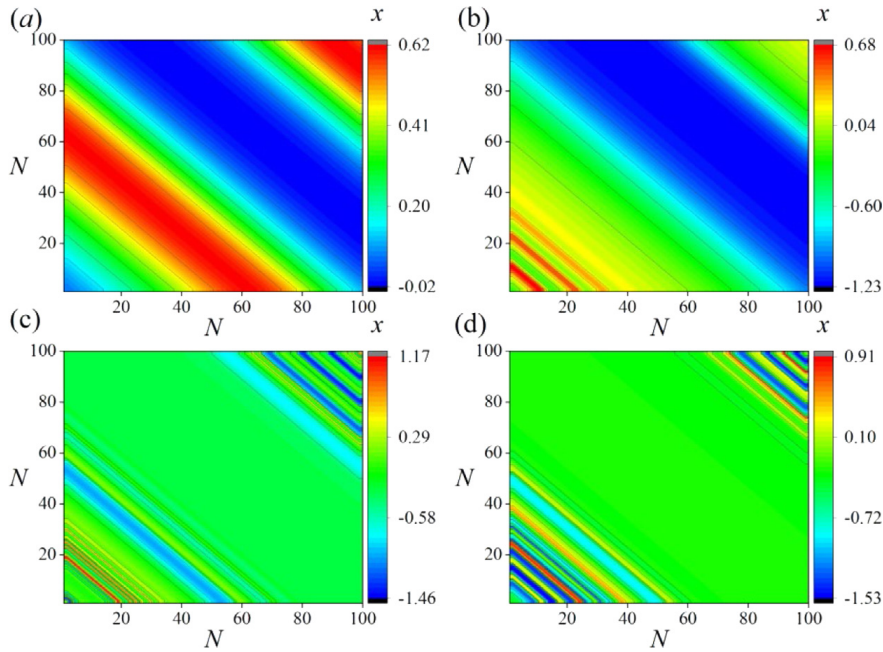


Fig. 9. Developed spatial patterns in the neural network on lattice at $\tau = 1000$ time units by applying different amplitudes A for $\varphi_{ext}^{ij} = A \cos(\omega t + i^* \lambda_1 + j^* \lambda_2)$. For (a) $A = 0.01$; (b) $A = 0.2$; (c) $A = 1.1$; (d) $A = 1.6$. Setting $I_{ext} = 4.0$, $\alpha = 0.4$, $\beta = 0.02$, $k = 0.5$, $k_1 = 0.9$, $k_2 = 0.4$, $a = 1.0$, $b = 3.0$, $c = 1.0$, $d = 5.0$, $r = 0.006$, $s = 4.0$, $k_3 = 0.00001$, $\lambda_1 = \lambda_2 = \lambda = 0.02$, and initials of each neuron in the 2D regular network are selected as (0.02, 0.03, 0.01, 0.1). Snapshots are plotted in color scale and the spatial patterns discern the distribution of membrane potentials for neurons.

The results in Fig. 11 are consistent with the results in Fig. 10, and synchronization degree is suppressed to develop possible spatial patterns under noise. The neural network shows spatiotemporal chaos and regular patterns are corrupted under noise accompanied by spatial EMR. It is interesting to discuss the case that EMR is not symmetrical along the horizontal and vertical direction ($\lambda_1 \neq \lambda_2$). In Fig. 12, the synchronization factors are calculated under non-uniform EMR and transition of spatial patterns are plotted as well.

The synchronization factor becomes to present a lower value when EMR is increased the amplitude, the spatial patterns show distinct symmetry when the EMR is applied asymmetrically. Finally, external noise is imposed with different intensities, and the selection of spatial patterns accompanying with changes in synchronization factors is plotted in Fig. 13.

Indeed, the regular spatial patterns are corrupted when noise is imposed on the neural network and the synchronization factors show distinct decrease with further increasing the noise intensity. From dynamical viewpoint, the involvement of spatial disturbance from non-uniform EMR just introduces spatial-dependent excitation on the neural network, and its

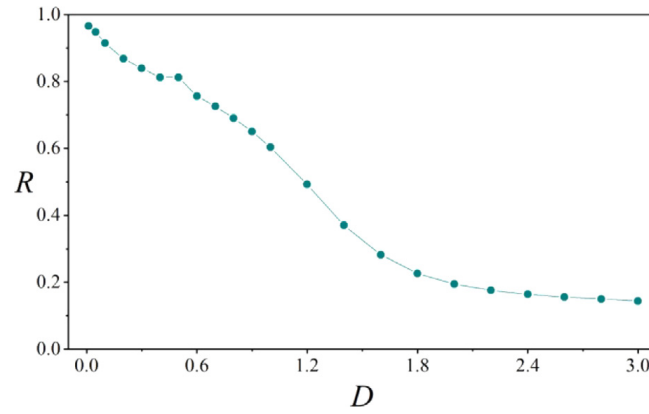


Fig. 10. Distribution of synchronization factors R is estimated by changing noise intensity D . Setting $A = 0.01$, $\omega = 0.1$, $I_{\text{ext}} = 4.0$, $\alpha = 0.4$, $\beta = 0.02$, $k = 0.5$, $k_1 = 0.9$, $k_2 = 0.4$, $a = 1.0$, $b = 3.0$, $c = 1.0$, $d = 5.0$, $r = 0.006$, $s = 4.0$, $k_3 = 0.00001$, $\lambda_1 = \lambda_2 = 0.2$, and initials of each neuron in the 2D regular network are selected as (0.02, 0.03, 0.01, 0.1).

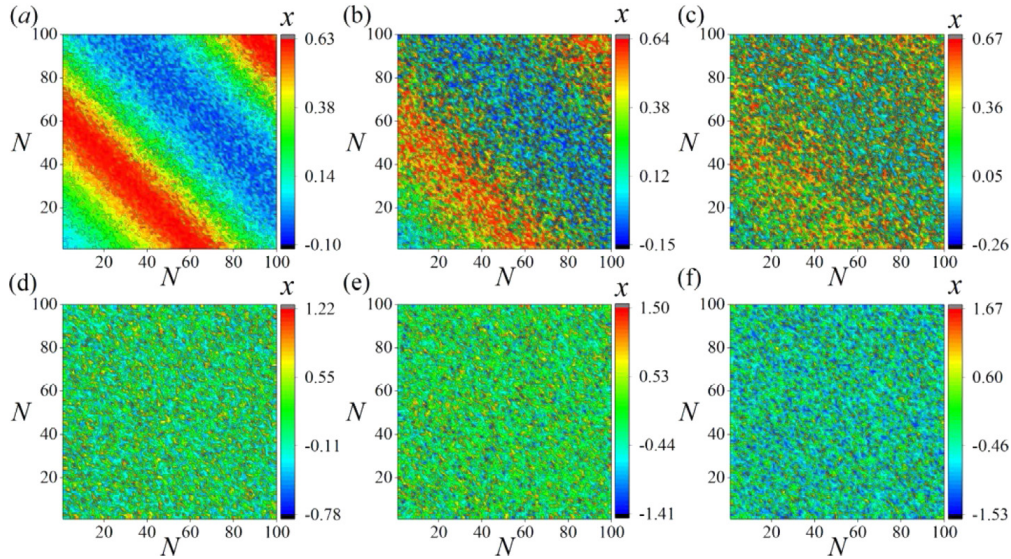


Fig. 11. Developed spatial patterns are plotted at $\tau = 1000$ time units in presence of noise. For noise intensity (a) $D = 0.01$; (b) $D = 0.05$; (c) $D = 0.1$; (d) $D = 0.7$; (e) $D = 1.2$; (f) $D = 2.0$. Setting $A = 0.01$, $\omega = 0.1$, $I_{\text{ext}} = 4.0$, $\alpha = 0.4$, $\beta = 0.02$, $k = 0.5$, $k_1 = 0.9$, $k_2 = 0.4$, $a = 1.0$, $b = 3.0$, $c = 1.0$, $d = 5.0$, $r = 0.006$, $s = 4.0$, $k_3 = 0.00001$, $\lambda_1 = \lambda_2 = 0.2$, and initials of each neuron in the lattice are selected as (0.02, 0.03, 0.01, 0.1).

dynamics can be approached by using similar stochastic network under field coupling as follows

$$\begin{cases} \frac{dx_i}{dt} = y_i - ax_i^3 + bx_i^2 - z_i + I_{\text{ext}} - k_1 W(\varphi_i)x_i + \xi_i(t); \\ \frac{dy_i}{dt} = c - dx_i^2 - y_i; \\ \frac{dz_i}{dt} = r[s(x_i + 1.56) - z_i]; \\ \frac{d\varphi_i}{dt} = kx_i - k_2\varphi_i - k_3 \sum_{\substack{j=1 \\ i \neq j}}^N (\varphi_j - \varphi_i); \end{cases} \quad (8a)$$

The last term in the fourth formula activates exchange of magnetic flux and field coupling becomes active in the networks. As a result, each neuron will receive memristive current (induction current) with diversity, and the effect stochastic diffusion of magnetic field will change the induction current, so the membrane potential is excited with noisy

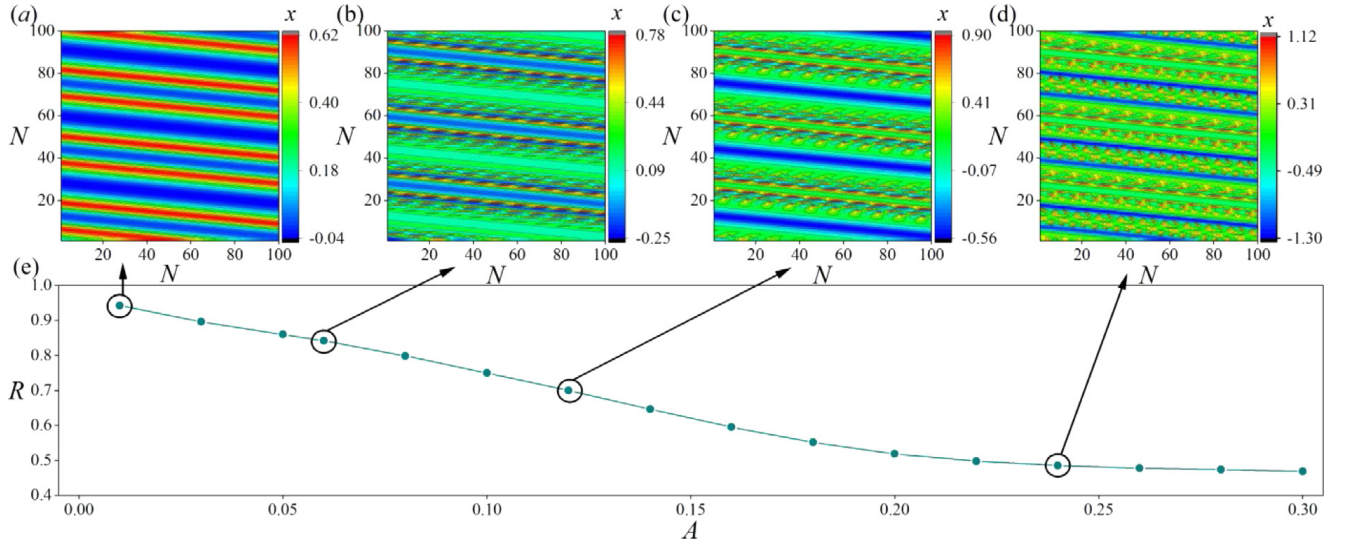


Fig. 12. Developed spatial patterns are plotted at $\tau = 1000$ time units by changing the amplitude A for $\varphi_{ext}^{ij} = A \cos(\omega t + i^* \lambda_1 + j^* \lambda_2)$. For (a) $A = 0.01$; (b) $A = 0.06$; (c) $A = 0.12$; (d) $A = 0.24$; (e) distribution for synchronization factors R vs. amplitude A in EMR. Setting $\omega = 0.1$, $I_{ext} = 4.0$, $\alpha = 0.4$, $\beta = 0.02$, $k = 0.5$, $k_1 = 0.9$, $k_2 = 0.4$, $a = 1.0$, $b = 3.0$, $c = 1.0$, $d = 5.0$, $r = 0.006$, $s = 4.0$, $k_3 = 0.00001$, $\lambda_1 = 0.2$, $\lambda_2 = 0.02$, and initials of each neuron in the 2D regular network are selected as (0.02, 0.03, 0.01, 0.1).

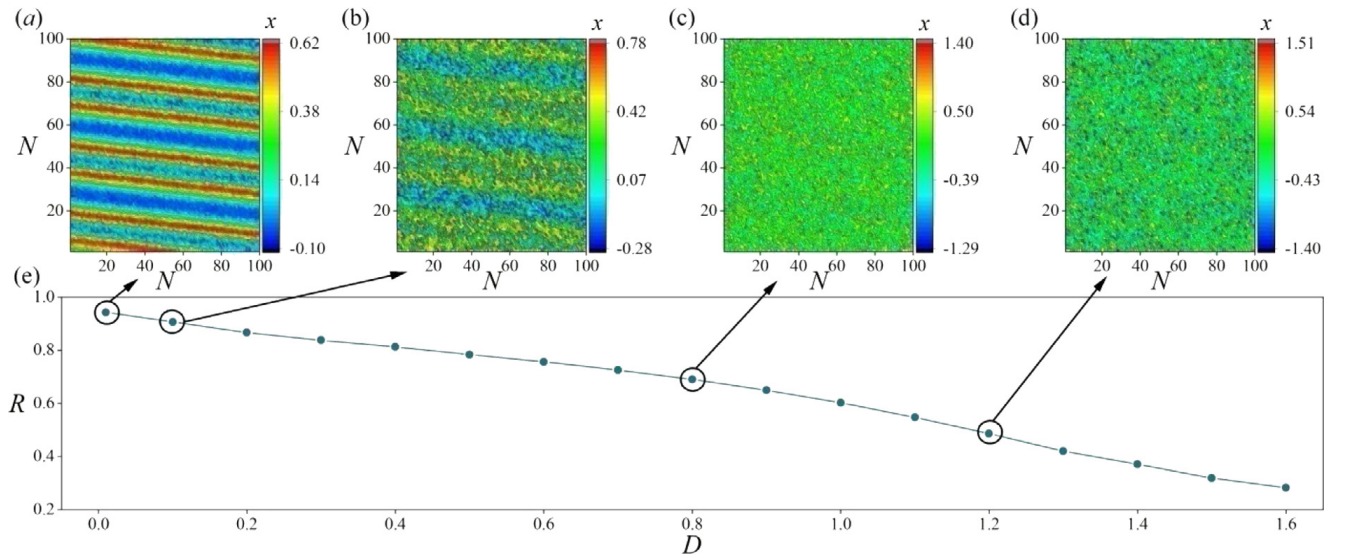


Fig. 13. Developed spatial patterns in presence of non-uniform EMR are plotted at $\tau = 1000$ time units by changing the noise intensity D . For (a) $D = 0.01$; (b) $D = 0.1$; (c) $D = 0.8$; (d) $D = 1.2$; (e) distribution for synchronization factors R vs. noise intensity D . Setting $A = 0.01$, $\omega = 0.1$, $I_{ext} = 4.0$, $\alpha = 0.4$, $\beta = 0.02$, $k = 0.5$, $k_1 = 0.9$, $k_2 = 0.4$, $a = 1.0$, $b = 3.0$, $c = 1.0$, $d = 5.0$, $r = 0.006$, $s = 4.0$, $k_3 = 0.00001$, $\lambda_1 = 0.2$, $\lambda_2 = 0.02$, and initials of each neuron in the 2D regular network are selected as (0.02, 0.03, 0.01, 0.1).

excitation.

$$\begin{cases} \frac{dx_{ij}}{dt} = y_{ij} - ax_{ij}^3 + bx_{ij}^2 - z_{ij} + I_{ext} - k_1 W(\varphi_{ij}) x_{ij} + \xi_{ij}(t); \\ \frac{dy_{ij}}{dt} = c - dx_{ij}^2 - y_{ij}; \\ \frac{dz_{ij}}{dt} = r[s(x_{ij} + 1.56) - z_{ij}]; \\ \frac{d\varphi_{ij}}{dt} = kx_{ij} - k_2 \varphi_{ij} - k_3 \sum_{\substack{n=1 \\ n \neq j}}^N \sum_{\substack{m=1 \\ m \neq i}}^N (\varphi_{mn} - \varphi_{ij}); \end{cases} \quad (8b)$$

That is, the spatial disturbance from EMR can be approached by applying equivalent spatial correlated noise on the membrane potentials of neurons. The noise disturbance on each neuron is different and it is dependent on the biophysical

property of each neuron in the network under field coupling. In absence of noisy disturbance, it can be considered as the similar case under uniform EMR. In feasible way, the energy for each neuron can be estimated. Considered the recent work about energy in Hindmarsh–Rose (HR) neuron [86], additive energy in memristive synapse shown in Eq. (6), and then the total energy in the memristive HR neuron can be obtained by

$$H = \frac{1}{2} \left[\frac{2}{3} dx^3 + rsx^2 + (y - z)^2 \right] + \frac{1}{2} k_1 \alpha x \varphi + \frac{3}{2} k_1 \beta x \varphi^3; \quad (9)$$

For the neural network under field coupling, energy is kept in each neuron of the network. Any external EMR or disturbance on the membrane potential will change the energy distribution in the network, as a result, energy flow is guided to control the collective behaviors of the neurons under field coupling. By imposing different forms for EMR, the distribution of energy in the neural network can be calculated in numerical way and the pattern formation of membrane potentials can be understood because different energy levels support different firing patterns in the neurons. Readers can extend this study in more memristive neural networks by calculating the energy distribution under noisy and EMR, and similar discussion can be applied for discerning the wave stability in cardiac tissue by detecting the spiral waves or Turing patterns.

Above all, we discussed the pattern formation and synchronization approach in neural networks composed of memristive neurons under field coupling and EMR. The involvement of spatial EMR introduces spatial diversity in induction currents, and excitability diversity occurs for exciting neurons in presenting different firing modes. Additive noisy disturbance on the membrane potentials of memristive neurons enhances the diversity of excitability and then these neurons are excited under field coupling. The activation of spatial EMR induces continuous polarization and magnetization in these neurons of the network accompanied by energy exchange and propagation, and the synchronization approach and formation of regular patterns become difficult because of distinct diversity in the induction current and excitability. Indeed, the creation of synapses connection and further growth of synaptic coupling can be effective to reach synchronization and energy balance.

As mentioned in the recent works [54–57,87,88], distinct energy diversity is helpful to create synapse connection for reaching local energy balance because these flexible synapses can be guided to build bridge connections to neurons for exchanging energy quickly. In fact, field coupling is enhanced when more biological neurons are clustered in a functional region and energy diversity is decreased. Therefore, adaptive creation of synapse connection and growth of synaptic coupling will be blocked. In presence of spatial EMR and noisy disturbance, local energy balance occurs accompanying with local homogeneous state in the neural network. By further increasing the noise intensity, these memristive neurons become different in the excitability and firing patterns, complete synchronization is blocked and local energy balance is reached to prevent the activation of synapses to neurons in the network. That is, appropriate spatial EMR is helpful to prevent the occurrence of bursting synchronization and seizure in the neural network because synaptic function is suppressed under field coupling.

4. Conclusions

In this work, memristive neurons are regulated in the collective behaviors of networks under field coupling rather than creating any synaptic connections. The isolated memristive neuron can present stochastic resonance under noise and EMR. The effect of electromagnetic induction can be discerned in the local kinetics of a memristive neuron, and the interaction between neurons without synapses coupling is estimated by field coupling, which controls the magnetic flux on each neuron. Considering the intrinsic diversity between these memristive neurons, external spatial EMR will induce non-uniform regulation on the magnetic flux and induction current on each neuron. Therefore, spatial EMR is applied to investigate the pattern stability and synchronization degree in the neural network. It is confirmed that the local spatial patterns can be developed and further noisy driving on the membrane potential can break spatial regularity in the network. The activation of field coupling among more neurons in the network can be helpful to suppress the energy diversity and then the growth of synaptic coupling is suppressed due to local energy balance. Furthermore, these memristive neurons show distinct diversity in excitability accompanied with slight difference in energy and local energy balance is stabilized. Therefore, synchronization approach becomes difficult and bursting synchronization will be prevented effectively. These results predict that appropriate spatial EMR is helpful to control neural activities and prevent the occurrence of seizure in nervous system.

In the present work, no synaptic connections are considered in the neural network and local kinetics considers no ion channel noise. According to our recent works, synaptic connection can be created during the field coupling because of local energy diversity, therefore, some neurons in the network can also be connected via electric, chemical or memristive synapses under energy flow. In the forthcoming works, the researchers can consider the creation of synapse connection under field coupling when energy flow is propagated under non-uniform radiation. The scheme can also be considered in the biological neuron models containing ion channels, and then the effect of channel noise can be considered synchronously. The suggestions are helpful to know the potential mechanism for developing heterogeneity in the neural networks.

CRediT authorship contribution statement

Yitong Guo: Finished the model approach, Numerical results, Formal analysis. **Ying Xie:** Finished the model approach, Numerical results, Formal analysis. **Jun Ma:** Suggested this investigation, Wrote the draft, Edited the final version of this work.

Declaration of competing interest

The authors declare that they have no known competing financial interests or personal relationships that could have appeared to influence the work reported in this paper.

Data availability

Data will be made available on request.

Acknowledgments

This project is partially supported by National Natural Science Foundation of China under Grant Nos. 12072139.

References

- [1] L. Xu, G. Qi, J. Ma, Modeling of memristor-based Hindmarsh-Rose neuron and its dynamical analyses using energy method, *Appl. Math. Model.* 101 (2022) 503–516.
- [2] R.K. Upadhyay, S.K. Sharma, A. Mondal, et al., Emergence of hidden dynamics in different neuronal network architecture with injected electromagnetic induction, *Appl. Math. Model.* 111 (2022) 288–309.
- [3] Z. Rostami, S. Jafari, Defects formation and spiral waves in a network of neurons in presence of electromagnetic induction, *Cogn. Neurodyn.* 12 (2018) 235–254.
- [4] N. Zandi-Mehran, S. Jafari, S.M.R. Hashemi Golpayegani, et al., Different synaptic connections evoke different firing patterns in neurons subject to an electromagnetic field, *Nonlinear Dynam.* 100 (2020) 1809–1824.
- [5] B. Ramakrishnan, M. Mehrabbeik, F. Parastesh, et al., A new memristive neuron map model and its network's dynamics under electrochemical coupling, *Electronics* 11 (2022) 153.
- [6] M. Desroches, P. Kowalczyk, S. Rodrigues, Spike-adding and reset-induced canard cycles in adaptive integrate and fire models, *Nonlinear Dynam.* 104 (2021) 2451–2470.
- [7] B.A. Santos, R.M. Gomes, P. Husbands, The role of rebound spikes in the maintenance of self-sustained neural spiking activity, *Nonlinear Dynam.* 105 (2021) 767–784.
- [8] A. Mondal, A. Mondal, S.K. Sharma, et al., Analysis of spatially extended excitable Izhikevich neuron model near instability, *Nonlinear Dynam.* 105 (2021) 3515–3527.
- [9] B. Ramakrishnan, I. Moroz, C. Li, et al., Effects of noise on the wave propagation in an excitable media with magnetic induction, *Eur. Phys. J. Spec. Top.* 230 (2021) 3369–3379.
- [10] S.Y. Kim, W. Lim, Disynaptic effect of hilar cells on pattern separation in a spiking neural network of hippocampal dentate gyrus, *Cogn. Neurodyn.* 16 (2022) 1427–1447.
- [11] S. He, K. Rajagopal, A. Karthikeyan, et al., A discrete Huber-Braun neuron model: From nodal properties to network performance, *Cogn. Neurodyn.* 17 (2022) 301–310.
- [12] S.S. Muni, K. Rajagopal, A. Karthikeyan, et al., Discrete hybrid Izhikevich neuron model: Nodal and network behaviours considering electromagnetic flux coupling, *Chaos Solitons Fractals* 155 (2022) 111759.
- [13] B. Ibarz, J.M. Casado, M.A.F. Sanjuán, Map-based models in neuronal dynamics, *Phys. Rep.* 501 (2011) 1–74.
- [14] S. Kumarasamy, A. Srinivasan, M. Ramasamy, et al., Strange nonchaotic dynamics in a discrete FitzHugh–Nagumo neuron model with sigmoidal recovery variable, *Chaos* 32 (2022) 073106.
- [15] H.J. Suk, E.S. Boyden, I. van Welie, Advances in the automation of whole-cell patch clamp technology, *J. Neurosci. Methods* 326 (2019) 108357.
- [16] T.J. Dale, C. Townsend, E.C. Hollands, et al., Population patch clamp electrophysiology: a breakthrough technology for ion channel screening, *Mol. Biosyst.* 3 (2007) 714–722.
- [17] H.A. Elkaranshaw, N.M. Aboukelila, H.M. Elabsy, Suppressing the spiking of a synchronized array of Izhikevich neurons, *Nonlinear Dynam.* 104 (2021) 2653–2670.
- [18] M.E. Yamakou, T.D. Tran, Levy noise-induced self-induced stochastic resonance in a memristive neuron, *Nonlinear Dynam.* 107 (2022) 2847–2865.
- [19] E. Sayari, E.C. Gabrick, F.S. Borges, et al., Analyzing bursting synchronization in structural connectivity matrix of a human brain under external pulsed currents, *Chaos* 33 (2023) 033131.
- [20] I. Kusbeyzi Aybar, Memristor-based oscillatory behavior in the FitzHugh–Nagumo and Hindmarsh-Rose models, *Nonlinear Dynam.* 103 (2021) 2917–2929.
- [21] K.M. Kim, J.J. Yang, E. Merced, et al., Low variability resistor–memristor circuit masking the actual memristor states, *Adv. Electron. Mater.* 1 (2015) 1500095.
- [22] M. Hansen, P.R. Protachevich, K.C. Iarosz, et al., The effect of time delay for synchronisation suppression in neuronal networks, *Chaos Solitons Fractals* 164 (2022) 112690.
- [23] J. Ma, Z. Yang, L. Yang, et al., A physical view of computational neurodynamics, *J. Zhejiang Univ. Sci. A* 20 (2019) 639–659.
- [24] Z. Yao, P. Zhou, A. Alsaedi, et al., Energy flow-guided synchronization between chaotic circuits, *Appl. Math. Comput.* 374 (2020) 124998.
- [25] Y. Xu, Z. Yao, A. Hobiny, et al., Differential coupling contributes to synchronization via a capacitor connection between chaotic circuits, *Front. Inf. Technol. Electron. Eng.* 20 (2019) 571–583.
- [26] X. Zhang, F. Wu, J. Ma, et al., Field coupling synchronization between chaotic circuits via a memristor, *AEU-Int. J. Electron. Commun.* 115 (2020) 153050.

- [27] A. Moujahid, A. d'Anjou, F.J. Torrealdea, et al., Efficient synchronization of structurally adaptive coupled Hindmarsh–Rose neurons, *Chaos Solitons Fractals* 44 (2011) 929–933.
- [28] Y. Xie, Z. Yao, X. Hu, et al., Enhance sensitivity to illumination and synchronization in light-dependent neurons, *Chin. Phys. B* 30 (2021) 120510.
- [29] Y. Zhang, Y. Xu, Z. Yao, et al., A feasible neuron for estimating the magnetic field effect, *Nonlinear Dynam.* 102 (2020) 1849–1867.
- [30] F. Wu, J. Ma, G. Zhang, Energy estimation and coupling synchronization between biophysical neurons, *Sci. China Technol. Sci.* 63 (2020) 625–636.
- [31] Y. Liu, W. Xu, J. Ma, et al., A new photosensitive neuron model and its dynamics, *Front. Inf. Technol. Electron. Eng.* 21 (2020) 1387–1396.
- [32] Y. Xu, M. Liu, Z. Zhu, et al., Dynamics and coherence resonance in a thermosensitive neuron driven by photocurrent, *Chin. Phys. B* 29 (2020) 098704.
- [33] Y. Zhang, P. Zhou, J. Tang, et al., Mode selection in a neuron driven by Josephson junction current in presence of magnetic field, *Chinese J. Phys.* 71 (2021) 72–84.
- [34] X. Zhang, J. Ma, Wave filtering and firing modes in a light-sensitive neural circuit, *J. Zhejiang Univ. Sci. A* 22 (2021) 707–720.
- [35] L. Zhao, Q. Hong, X. Wang, Novel designs of spiking neuron circuit and STDP learning circuit based on memristor, *Neurocomputing* 314 (2018) 207–214.
- [36] J. Ma, J. Tang, A review for dynamics of collective behaviors of network of neurons, *Sci. China Technol. Sci.* 58 (2015) 2038–2045.
- [37] M. Lv, C. Wang, G. Ren, et al., Model of electrical activity in a neuron under magnetic flow effect, *Nonlinear Dynam.* 85 (2016) 1479–1490.
- [38] F. Wu, C. Wang, W. Jin, et al., Dynamical responses in a new neuron model subjected to electromagnetic induction and phase noise, *Physica A* 469 (2017) 81–88.
- [39] J. Ma, F. Wu, T. Hayat, et al., Electromagnetic induction and radiation-induced abnormality of wave propagation in excitable media, *Physica A* 486 (2017) 508–516.
- [40] Y. Xu, J. Ma, Control of firing activities in thermosensitive neuron by activating excitatory autapse, *Chin. Phys. B* 30 (2021) 100501.
- [41] K. Lian, X. Zhou, W. Liu, et al., Antiphase synchronization and central symmetrical antiphase synchronization in magnetic field coupled circuits, *Nonlinear Dynam.* 99 (2020) 3217–3229.
- [42] Y. Zhang, P. Shang, J. He, et al., A measure of complexity based on the order patterns, *Nonlinear Dynam.* 102 (2020) 1925–1938.
- [43] W. Li, Y. Chen, Z.R. Lu, et al., Parameter identification of nonlinear structural systems through frequency response sensitivity analysis, *Nonlinear Dynam.* 104 (2021) 3975–3990.
- [44] P.R. Protachevich, C.A. Bonin, K.C. Iarosz, et al., Large coefficient of variation of inter-spike intervals induced by noise current in the resonate-and-fire model neuron, *Cogn. Neurodyn.* 16 (2022) 1461–1470.
- [45] K. Rajagopal, F. Nazarimehr, A. Karthikeyan, et al., Dynamics of a neuron exposed to integer-and fractional-order discontinuous external magnetic flux, *Front. Inf. Technol. Electron. Eng.* 20 (2019) 584–590.
- [46] T. Palabas, J.J. Torres, M. Perc, et al., Double stochastic resonance in neuronal dynamics due to astrocytes, *Chaos Solitons Fractals* 168 (2023) 113140.
- [47] V.V. Klinshov, A.V. Kovalchuk, I. Franović, et al., Rate chaos and memory lifetime in spiking neural networks, *Chaos Solitons Fractals* 158 (2022) 112011.
- [48] F. Parastesh, K. Rajagopal, S. Jafari, et al., Blinking coupling enhances network synchronization, *Phys. Rev. E* 105 (2022) 054304.
- [49] G.K. Sar, S.N. Chowdhury, M. Perc, et al., Swarmalators under competitive time-varying phase interactions, *New J. Phys.* 24 (2022) 043004.
- [50] P. Ji, J. Ye, Y. Mu, et al., Signal propagation in complex networks, *Phys. Rep.* 1017 (2023) 1–96.
- [51] M. Chen, Q. Zheng, R. Wu, et al., Spatiotemporal patterns in a general networked activator-substrate model, *Nonlinear Dynam.* 106 (2021) 3521–3538.
- [52] H. Bao, Z.G. Chen, J.M. Cai, et al., Memristive cyclic three-neuron-based neural network with chaos and global coexisting attractors, *Sci. China Technol. Sci.* 65 (2022) 2582–2592.
- [53] K. Xu, J.P. Maidana, P. Orio, Diversity of neuronal activity is provided by hybrid synapses, *Nonlinear Dynam.* 105 (2021) 2693–2710.
- [54] Y. Wang, G. Sun, G. Ren, Diffusive field coupling induced synchronization between neural circuits under energy balance, *Chin. Phys. B* 32 (2023) 040504.
- [55] C. Wang, G. Sun, F. Yang, et al., Capacitive coupling memristive systems for energy balance, *AEU- Int. J. Electron. Commun.* 153 (2022) 154280.
- [56] X. Ma, Y. Xu, Taming the hybrid synapse under energy balance between neurons, *Chaos Solitons Fractals* 159 (2022) 112149.
- [57] Y. Kang, Y. Chen, Y. Fu, et al., Formation of spiral wave in Hodgkin–Huxley neuron networks with Gamma-distributed synaptic input, *Commun. Nonlinear Sci. Numer. Simul.* 83 (2020) 105112.
- [58] G. Yuan, Z. Gao, S. Yan, et al., Termination of a pinned spiral wave by the wave train with a free defect, *Nonlinear Dynam.* 104 (2021) 2583–2597.
- [59] M. Paul Asir, A. Prasad, N.V. Kuznetsov, et al., Chimera states in a class of hidden oscillatory networks, *Nonlinear Dynam.* 104 (2021) 1645–1655.
- [60] L. Lü, L. Ge, L. Gao, et al., Synchronization transmission of spiral wave and turbulence in uncertain time-delay neuronal networks, *Physica A* 525 (2019) 64–71.
- [61] N. Wu, H. Ying, The dynamic of repulsion of spiral waves from excitable regions, *Nonlinear Dynam.* 103 (2021) 979–986.
- [62] K. Rajagopal, I. Hussain, Z. Rostami, et al., Magnetic induction can control the effect of external electrical stimuli on the spiral wave, *Appl. Math. Comput.* 390 (2021) 125608.
- [63] K. Rajagopal, A. Karthikeyan, Spiral waves and their characterization through spatioperiod and spatioenergy under distinct excitable media, *Chaos Solitons Fractals* 158 (2022) 112105.
- [64] C.B. Tabi, A.S. Etémé, T.C. Kofané, Unstable cardiac multi-spiral waves in a FitzHugh–Nagumo soliton model under magnetic flow effect, *Nonlinear Dynam.* 100 (2020) 3799–3814.
- [65] M.S. Kafraj, F. Parastesh, S. Jafari, Firing patterns of an improved Izhikevich neuron model under the effect of electromagnetic induction and noise, *Chaos Solitons Fractals* 137 (2020) 109782.
- [66] L. Lu, Y. Jia, Y. Xu, et al., Energy dependence on modes of electric activities of neuron driven by different external mixed signals under electromagnetic induction, *Sci. China Technol. Sci.* 62 (2019) 427–440.
- [67] V. Baysal, E. Yilmaz, Effects of electromagnetic induction on vibrational resonance in single neurons and neuronal networks, *Physica A* 537 (2020) 122733.
- [68] K. Rajagopal, I. Moroz, A. Karthikeyan, et al., Wave propagation in a network of extended Morris–Lecar neurons with electromagnetic induction and its local kinetics, *Nonlinear Dynam.* 100 (2020) 3625–3644.
- [69] S. He, H. Fang, M. Zhang, et al., Adaptive optimal control for a class of nonlinear systems: The online policy iteration approach, *IEEE Trans. Neural Netw. Learn. Syst.* 31 (2019) 549–558.
- [70] S. He, H. Fang, M. Zhang, et al., Online policy iterative-based H_∞ optimization algorithm for a class of nonlinear systems, *Inform. Sci.* 495 (2019) 1–13.
- [71] Y. Liu, Z. Sun, X. Yang, et al., Rhythmicity and firing modes in modular neuronal network under electromagnetic field, *Nonlinear Dynam.* 104 (2021) 4391–4400.
- [72] C. Wang, J. Tang, J. Ma, Minireview on signal exchange between nonlinear circuits and neurons via field coupling, *Eur. Phys. J. Spec. Top.* 228 (2019) 1907–1924.

- [73] Z. Yao, C. Wang, P. Zhou, et al., Regulating synchronous patterns in neurons and networks via field coupling, *Commun. Nonlinear Sci. Numer. Simul.* 95 (2021) 105583.
- [74] J. Ma, F. Wu, A. Alsaedi, et al., Crack synchronization of chaotic circuits under field coupling, *Nonlinear Dynam.* 93 (2018) 2057–2069.
- [75] Y. Xu, G. Ren, J. Ma, Patterns stability in cardiac tissue under spatial electromagnetic radiation, *Chaos Solitons Fractals* 171 (2023) 113522.
- [76] M. Lv, J. Ma, Y.G. Yao, et al., Synchronization and wave propagation in neuronal network under field coupling, *Sci. China Technol. Sci.* 62 (2019) 448–457.
- [77] F. Wu, X. Hu, J. Ma, Estimation of the effect of magnetic field on a memristive neuron, *Appl. Math. Comput.* 432 (2022) 127366.
- [78] F. Wu, Y. Guo, J. Ma, Reproduce the biophysical function of chemical synapse by using a memristive synapse, *Nonlinear Dynam.* 109 (2022) 2063–2084.
- [79] Y. Guo, Z. Yao, Y. Xu, et al., Control the stability in chaotic circuit coupled by memristor in different branch circuits, *AEU-Int. J. Electron. Commun.* 145 (2022) 154074.
- [80] A.V. Andreev, V.V. Makarov, A.E. Runnova, et al., Coherence resonance in stimulated neuronal network, *Chaos Solitons Fractals* 106 (2018) 80–85.
- [81] Y. Jia, H. Gu, Y. Li, et al., Inhibitory autapses enhance coherence resonance of a neuronal network, *Commun. Nonlinear Sci. Numer. Simul.* 95 (2021) 105643.
- [82] L. Lu, C. Bao, M. Ge, et al., Phase noise-induced coherence resonance in three dimension memristive Hindmarsh-Rose neuron model, *Eur. Phys. J. Spec. Top.* 228 (2019) 2101–2110.
- [83] M. Bayram, T. Partal, G. Orucova Buyukoz, Numerical methods for simulation of stochastic differential equations, *Adv. Difference Equ.* 2018 (2018) 17.
- [84] M.N. Gevorkyan, T.R. Velieva, A.V. Korolkova, et al., Stochastic Runge–Kutta software package for stochastic differential equations, in: *Dependability Engineering and Complex Systems: Proceedings of the Eleventh International Conference on Dependability and Complex Systems, DepCoS-RELCOMEX. June 27–July 1, 2016, Brunów, Poland, Springer International Publishing, 2016*, pp. 169–179.
- [85] Y. Xie, Z. Yao, G.D. Ren, et al., Estimate physical reliability in Hindmarsh-Rose neuron, *Phys. Lett. A* 24 (2023) 109–129.
- [86] Y. Xie, Z. Yao, J. Ma, Formation of local heterogeneity under energy collection in neural networks, *Sci. China Technol. Sci.* 66 (2023) 439–455.
- [87] Y. Xie, Z. Yao, J. Ma, Phase synchronization and energy balance between neurons, *Front. Inf. Technol. Electron. Eng.* 23 (2022) 1407–1420.
- [88] R.F. Fox, I.R. Gatland, R. Roy, et al., Fast, accurate algorithm for numerical simulation of exponentially correlated colored noise, *Phys. Rev. A* 38 (1988) 5938.

RESEARCH ARTICLE | NOVEMBER 01 2023

Physical approach of a neuron model with memristive membranes

Yitong Guo ; Fuqiang Wu ; Feifei Yang ; Jun Ma  



Chaos 33, 113106 (2023)

<https://doi.org/10.1063/5.0170121>



CrossMark



AIP Advances

Why Publish With Us?

**25 DAYS**
average time
to 1st decision

**740+ DOWNLOADS**
average per article

**INCLUSIVE**
scope

[Learn More](#)

 AIP
Publishing

Physical approach of a neuron model with memristive membranes

Cite as: Chaos 33, 113106 (2023); doi: 10.1063/5.0170121

Submitted: 31 July 2023 · Accepted: 13 October 2023 ·

Published Online: 1 November 2023



View Online



Export Citation



CrossMark

Yitong Guo,¹ Fuqiang Wu,² Feifei Yang,¹ and Jun Ma^{1,3,a)}

AFFILIATIONS

¹College of Electrical and Information Engineering, Lanzhou University of Technology, Lanzhou 730050, China

²School of Mathematics and Statistics, Ningxia University, Yinchuan 750021, China

³Department of Physics, Lanzhou University of Technology, Lanzhou 730050, China

^{a)}Author to whom correspondence should be addressed: hyperchaos@163.com

ABSTRACT

The membrane potential of a neuron is mainly controlled by the gradient distribution of electromagnetic field and concentration diversity between intracellular and extracellular ions. Without considering the thickness and material property, the electric characteristic of cell membrane is described by a capacitive variable and output voltage in an equivalent neural circuit. The flexible property of cell membrane enables controllability of endomembrane and outer membrane, and the capacitive properties and gradient field can be approached by double membranes connected by a memristor in an equivalent neural circuit. In this work, two capacitors connected by a memristor are used to mimic the physical property of two-layer membranes, and an inductive channel is added to the neural circuit. A biophysical neuron is obtained and the energy characteristic, dynamics, self-adaption is discussed, respectively. Coherence resonance and mode selection in adaptive way are detected under noisy excitation. The distribution of average energy function is effective to predict the appearance of coherence resonance. An adaptive law is proposed to control the capacitive parameters, and the controllability of cell membrane under external stimulus can be explained in theoretical way. The neuron with memristive membranes explains the self-adaptive mechanism of parameter changes and mode transition from energy viewpoint.

Published under an exclusive license by AIP Publishing. <https://doi.org/10.1063/5.0170121>

The cell membrane is located on the surface of the cell, with a thickness of usually 7–8 nm, and is composed of lipids and proteins. Its most important characteristic is semipermeability, also known as selective permeability, which has strong selective permeability for substances entering and exiting cells. The electrophysiological environment inside and outside of the cell membrane is different, two capacitive terms are effective to mimic the physical energy characteristic, and exact description of controllability and flexibility in the cell membrane needs controllable physical definition and description. A memristive connection to two-layer cell membranes is suggested, and its equivalent circuit combination is expressed by connecting two capacitors via memristor in the equivalent neural circuits. Shape deformation of cell membrane and external energy injection will regulate the capacitive parameter under energy flow, and then suitable firing modes are induced under external stimulus. From physical viewpoint,

the energy diversity for capacitive field is adjusted with the change of membrane parameter ratio.

I. INTRODUCTION

Biological neurons show distinct controllability and the mode selection in the firing patterns is induced under external stimuli and noisy disturbance.^{1–5} When electric stimuli and physical field are applied, the media suffers from continuous polarization and magnetization because of energy injection. As a result, the injected energy flow is shunted into different ion channels for regulating energy balance^{6–10} and local synchronization stability between adjacent neurons. For a single neuron, continuous energy injection and larger stimulus may induce local shape deformation and some intrinsic parameters are forced with possible shift accompanying

with synchronous mode transition in the electric activities and firing patterns.¹¹ For two identical neurons, diversity in energy can induce adaptive parameter jump, and desynchronization¹² appears to keep energy balance between two non-identical neurons. For more neurons, non-uniform energy distribution can induce formation of local defects or heterogeneity for keeping local energy balance in the neural network.^{13,14}

In fact, membrane potential is a detectable variable and the sampled time series are often obtained for further signal analysis due to the application of patch clamp technology. Based on electromagnetic field theory, the membrane potential depends on the distribution of electromagnetic field in a neuron can be calculated theoretically and in experimental way. The effect of external field¹⁵ on neural activities can be recognized by using nonlinear analysis. Most of the generic neuron models contain variables for membrane potential, slow variable for channel current or gate variable, and external stimuli are mapped into an equivalent transmembrane current imposed on the cell membrane. In fact, biological neurons are considered as artificial signal processors, therefore, a variety of electric components are connected to build different neural circuits,^{16–20} which can produce similar firing patterns observed in the biological neurons, and, thus, more physical effect can be considered and explained. The physical basis is that the inner electromagnetic field in the biological neurons can be reproduced in the capacitive and inductive components; therefore, equivalent neural circuits can be designed to mimic the neural activities in neurons.

Biological neurons can perceive external signals synchronously and an isolated neuron prefers to trigger suitable firing patterns induced by external stimulus with higher energy density.^{21,22} For more neurons in a network, multi-channel stimuli will be perceived by different neurons and the collective responses in electrical activities will depend on the cooperation and self-organization of neurons, and coexistence of multiple firing modes can be developed in the network by creating different spatial patterns.^{23–28} The energy characteristic of biological neurons can be expressed and discussed in some equivalent neural circuits by combining a few specific electronic components including memristor,^{29–32} Josephson junction,^{33,34} piezoelectric device,^{35,36} and phototube^{37–39} into the branch circuits of some nonlinear circuits. In particular, memristor-based artificial synapse^{40–44} can quantify the electromagnetic effect induced by continuous diffusion of intracellular ions, and the controllability of synapses in neurons can be realized in practice. Distinct spatial patterns and chimera states can be developed in these memristive networks^{45–49} and external noisy disturbance can control these patterns and synchronization stability. The main characteristic of memristive synapse can be its biophysical property for reproducing similar functional regulation as chemical synapse,^{50–52} and external field is applied to control the firing modes in electrical activities. Based on some generic neuron models, bifurcation analysis^{53–59} and pattern selection can provide possible clues to explain the potential mechanism for seizure occurrence,^{60–63} and then reliable schemes can be used to suppress the occurrence of some neural disease. For more comments on neurodynamics, readers can refer to the recent review in 2023.⁶⁴

For simplicity, a variety of nonlinear oscillators and nonlinear circuits are tamed to produce similar firing patterns as those observed in biological neurons by generating spiking, bursting, and

even chaotic patterns. Furthermore, specific terms such as memristive function are used to describe the physical effect during release of action potential in the excitable media. Bifurcation analysis and Lyapunov exponents provide easy way for detecting the transition between chaos and periodic oscillation. As claimed in 2016,⁶⁵ introducing memristive current and magnetic flux variable can describe the effect of electromagnetic induction and radiation in a neuron. Furthermore, more researchers designed different neural circuits to mimic the nonlinear response in physical neurons and some memristive neurons are guided to develop collective cooperation and spatial patterns under field coupling. The involvement of memristor into nonlinear circuits can induce multistability and coexistence of chaos. However, most of the works about memristive circuits^{66–70} keep eyes on the regulation from memristive current across the additive channel composed of memristor. The most important application of memristor into artificial neural circuits is relative to morphological calculation and setting reliable signal processors with distinct self-adaption. In fact, a single neuron can process finite information and understanding the cooperation between neurons requires investigation on collective behaviors in neural networks, and synchronization stability. Pattern formation shows the cooperation and self-organization in the network, and it can be affected by the interaction and self-adaptive property in the neurons and synaptic channels completely.^{71–73} In presence of noisy excitation, appropriate intensity can induce nonlinear resonance including stochastic resonance and coherence resonance^{74,75} in the media, and regular oscillation can be detected in the variables.

The field distribution inner and outer of the cell/neuron is different, and two capacitive variables are useful to describe the physical characteristics of cell membrane, which is considered as two-layer form. That is, the cell membrane with certain thickness can also be considered with double layers, and the filler materials are considered as a kind of memristor. The memristive membrane can regulate the energy diversity between in and out of the neuron/media in adaptive way. Furthermore, this neuron with memristive membrane can be mimicked by an equivalent circuit. In this paper, two capacitors are connected via a magnetic flux-controlled memristor for mimicking a flexible two-layer membrane of a biophysical neuron; inductor and nonlinear resistor are combined to build a feasible neural circuit considering the electromagnetic induction effect. Intrinsic energy function for the neural circuit is defined and its equivalent Hamilton energy for the neuron is obtained in theoretical way. The energy function can affect the firing mode and patterns, and noisy disturbance is applied to detect the occurrence of coherence resonance in the neuron. In particular, the adaptive mechanism for parameter shift is explained under energy flow.

II. MODEL AND SCHEME

Cell membrane has two sides and its field properties can be described by capacitive terms. Its flexibility means that the connection between capacitors is controllable in the neural circuit. Therefore, a memristor is used to connect two capacitors and the effect of channel current is described by adding an inductor in parallel with the capacitors. Furthermore, a nonlinear resistor with cubic relation for the channel current and voltage are used to regulate the energy exchange between magnetic field and electric field in Fig. 1.

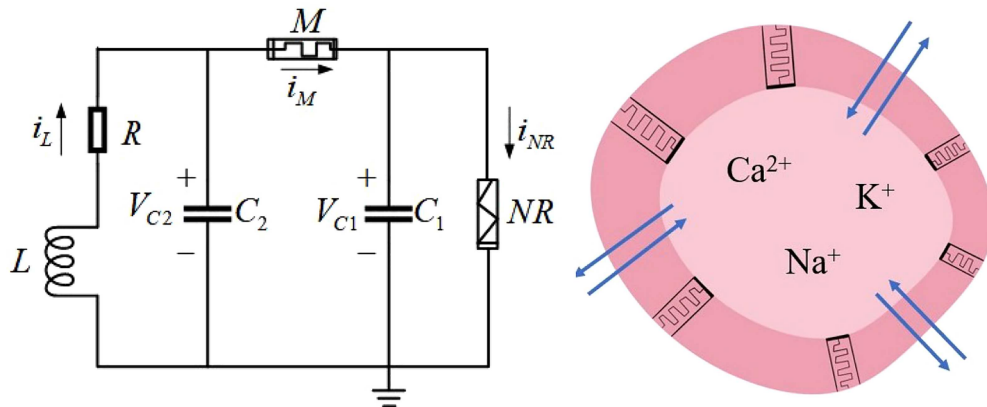


FIG. 1. Schematic diagram for a neural circuit with memristive connection and memristive membrane. i_M denotes the channel current across the memristor, and i_{NR} estimates the current along the nonlinear resistor NR . Double arrows indicate the exchange and propagation of intracellular and extracellular ions, the filler material between two-layer membranes has similar property in memristor.

Based on Kirchhoff's theorem, the correlation between the physical variables is expressed by

$$\begin{cases} C_1 \frac{dV_{C1}}{dt} = M(\varphi)(V_{C2} - V_{C1}) - i_{NR}, \\ C_2 \frac{dV_{C2}}{dt} = M(\varphi)(V_{C1} - V_{C2}) + i_L, \\ L \frac{di_L}{dt} = -V_{C2} - Ri_L, \\ \frac{d\varphi}{dt} = V_{C2} - V_{C1}, M(\varphi) = \frac{dq(\varphi)}{d\varphi} = a + 3b\varphi^2, \\ i_{NR} = -\frac{1}{\rho} \left(V_{C1} - \frac{1}{3} \frac{V_{C1}^3}{V_0^2} \right), \end{cases} \quad (1)$$

where the physical parameters (C_1 , C_2 , L , a , b , V_0 , ρ) are selected with suitable values, and this neural circuit can be adjusted for presenting similar bursting, spiking, and even chaotic patterns. These physical variables are replaced with dimensionless variables under scale transformation,⁷⁶

$$\begin{cases} x = \frac{V_{C1}}{V_0}, y = \frac{V_{C2}}{V_0}, z = \frac{i_L \rho}{V_0}, \varphi' = \frac{\varphi}{\rho C_2 V_0}, \tau = \frac{t}{\rho C_2}, \\ \alpha = \frac{C_2}{C_1}, \beta = \frac{\rho^2 C_2}{L}, \gamma = \frac{\rho R C_2}{L}, a' = a\rho, b' = 3b\rho^3 C_2^2 V_0^2. \end{cases} \quad (2)$$

The dynamics of this memristive neuron with two capacitive terms/double membranes is described by

$$\begin{cases} \frac{dx}{d\tau} = \alpha \left[(a' + b'\varphi'^2)(y - x) + x - \frac{1}{3}x^3 \right], \\ \frac{dy}{d\tau} = (a' + b'\varphi'^2)(x - y) + z, \\ \frac{dz}{d\tau} = -\beta y - \gamma z, \\ \frac{d\varphi'}{d\tau} = y - x. \end{cases} \quad (3)$$

The appearance of memristive term introduces more adjustable parameters into the biophysical neuron model, and the normalized parameters (a' , b') are relative to the property of cell membrane. Continuous diffusion and exchange of intracellular and extracellular ions induce time-varying electromagnetic field accompanying with certain distribution of field energy, and the inner energy in the memristive neural circuit is estimated by

$$\begin{aligned} W_E &= -\frac{1}{2}C_1 V_{C1}^2 + \frac{1}{2}C_2 V_{C2}^2 + \frac{1}{2}L i_L^2 + \frac{1}{2}L_M i_M^2 \\ &= C_2 V_0^2 \left[-\frac{1}{2\alpha}x^2 + \frac{1}{2}y^2 + \frac{1}{2\beta}z^2 + \frac{1}{2}(a'\varphi' + b'\varphi'^3)(y - x) \right]. \end{aligned} \quad (4)$$

The energy is kept in the media (neuron) by introducing electromagnetic field. For neural circuits, energy is saved in these electric components, while resistor just consumes Joule heat and the injected energy from external stimuli will be shunted and saved in different forms. The physical field energy is replaced by an equivalent Hamilton energy H as follows

$$H = \frac{W_E}{C_2 V_0^2} = -\frac{1}{2\alpha}x^2 + \frac{1}{2}y^2 + \frac{1}{2\beta}z^2 + \frac{1}{2}(a'\varphi' + b'\varphi'^3)(y - x). \quad (5)$$

The normalized parameters (a' , b' , α , β , γ) are mapped from the physical parameters for the capacitors, inductor, and memristor, and any changes of these dimensionless parameters have direct impact on the energy level and then mode transition in neural activities is also switched effectively. It is important for neurons to select some firing patterns rather than keeping silent or resting states. Therefore, the energy function in Eq. (5) can be considered as a reliable Lyapunov function, and the neuron terminates its firing states at $dH/d\tau < 0$. When one or more parameters are changed, mode transition and stability in the neuron will be switched, and this confirmation can be solved in numerical way by fixing some parameters. On the other hand, Jacobi matrix for Eq. (3) can also be obtained by

using stability analysis, and then the firing stability of the neuron can be carried out. Furthermore, the energy function in Eq. (5) can be obtained and confirmed by using the Helmholtz theorem,^{12,31,64} detailed proof can refer to the Appendix,

$$\begin{aligned} \dot{X} &= F_c(X) + F_d(x), \quad \nabla H^T F_c(X) = 0, \quad dH/dt = \nabla H^T F_d(X), \\ X &= \{x_1, x_2, \dots, x_n\}. \end{aligned} \quad (6)$$

Realistic neurons can perceive external signals and appropriate noise intensity enhances the signal detection under stochastic resonance in noisy condition. Electric stimulus shows distinct penetrability and energy is injected to change the distribution and propagation of intracellular ions. That is, these stimuli will be converted into equivalent transmembrane current and then the membrane potential is changed synchronously. A generic neuron model can present distinct mode transition from spiking to bursting and even chaotic patterns when the parameters or external stimulus is changed, respectively. In particular, noisy excitation can induce coherence resonance in the neuron, and the dependence of coefficient variability (CV) of ISI series on noise intensity is often

calculated to predict the occurrence of coherence,

$$CV = \frac{\sqrt{\langle T^2 \rangle - \langle T \rangle^2}}{\langle T \rangle}, \quad (7)$$

where T measures value for each ISI and $\langle * \rangle$ detects the average value within a running time or transient period. A lowest value for CV means that the sampled time series for membrane potential show distinct periodicity under moderate noise intensity. When additive noise is imposed on the formula for membrane potential, it means that noisy electric field has important impact on the neural activities. On the other hand, it means that the noisy magnetic field with fluctuation controls the neural activities when additive noise is imposed on the formula for the channel current or recovery variable. The mainly energy in the neuron is kept in the form of magnetic field and electric field, and similar energy function in Eq. (5) is obtained for the neuron driven by external physical signals even in presence of noisy disturbance. Indeed, the average value for the energy function $\langle H \rangle$ is effective to predict the appearance of coherence resonance when external noise or radiation is adjusted. The membrane potential will present perfect periodicity and the $\langle H \rangle$ reaches a highest value when the neuron is driven by noise. In the presence of noisy disturbance, the electric activities of the memristive neuron

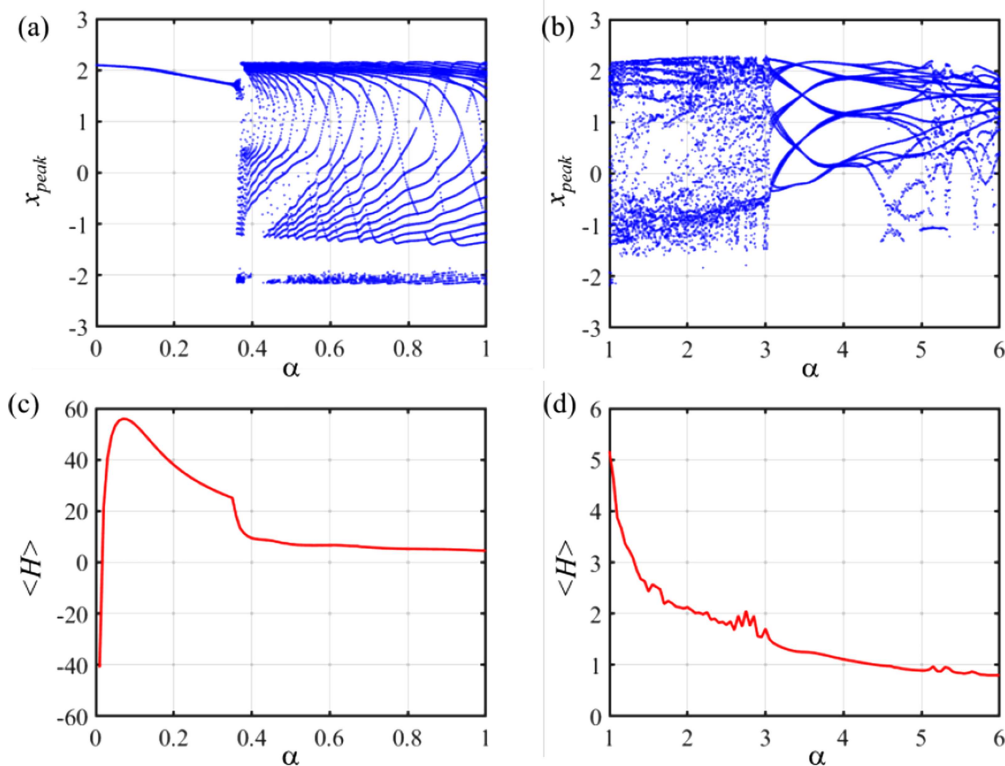


FIG. 2. Bifurcation of ISI (interspike interval) of membrane potentials and average energy. (a) and (c) $\alpha < 1$, periodic stimulus controls first variable and (b) and (d) $\alpha > 1$, periodic stimulus regulates the second variable.

in Eq. (3) can be expressed by

$$\begin{cases} \frac{dx}{d\tau} = \alpha \left[(a' + b'\varphi^2)(y - x) + x - \frac{1}{3}x^3 \right], \\ \frac{dy}{d\tau} = (a' + b'\varphi^2)(x - y) + z + \xi(\tau), \\ \frac{dz}{d\tau} = -\beta y - \gamma z + \zeta(\tau), \\ \frac{d\varphi'}{d\tau} = y - x + \eta(\tau). \end{cases} \quad (8)$$

The last term for the second, third, and fourth formula in Eq. (8) can be considered as Gaussian white noise, and the statistical properties with intensity D are defined by

$$\begin{cases} \langle \xi(\tau) \rangle = 0, & \langle \xi(\tau)\xi(s) \rangle = 2D\delta(\tau - s), \\ \langle \zeta(\tau) \rangle = 0, & \langle \zeta(\tau)\zeta(s) \rangle = 2D\delta(\tau - s), \\ \langle \eta(\tau) \rangle = 0, & \langle \eta(\tau)\eta(s) \rangle = 2D\delta(\tau - s). \end{cases} \quad (9)$$

From physical viewpoint, external noisy disturbance also changes the energy flow in the neural circuits and biological neurons. When the energy flow is beyond threshold, local shape deformation is induced in the cell and some intrinsic parameters can show possible jumps. For a capacitive neuron, shape deformation of

cell membrane can control the parameter α when the electric field energy is beyond certain threshold as follows:

$$\begin{cases} \frac{d\alpha}{d\tau} = \sigma \cdot \alpha \cdot \vartheta(H_{C2} - \lambda), \\ \vartheta(P) = 1, P \geq 0, \vartheta(P) = 0, P < 0, \\ H_{C2} = \frac{1}{2}y^2, \end{cases} \quad (10)$$

where λ measures the energy threshold and σ denotes the gain for increasing parameter α . The outer membrane often holds higher capacitance value than the inner membrane and shape deformation due to energy injection and accommodation will adjust the parameter α effectively. On the other hand, the energy H_{C1} can also be used to adjust the growth of the parameter α or one memristive parameter for the double membranes of the neuron, and suitable threshold in the Heaviside function in Eq. (10) can be selected to express the self-adaptive growth of intrinsic parameters under energy flow.

III. NUMERICAL RESULTS AND DISCUSSION

A fourth order Runge-Kutta algorithm can be applied to detect numerical solutions for the memristive oscillator in Eqs. (3) and (8) under Gaussian white noise. For simplicity, the parameters are fixed at $a' = 0.07$, $b' = 0.03$, $\beta = 0.01$, $\gamma = 0.01$,

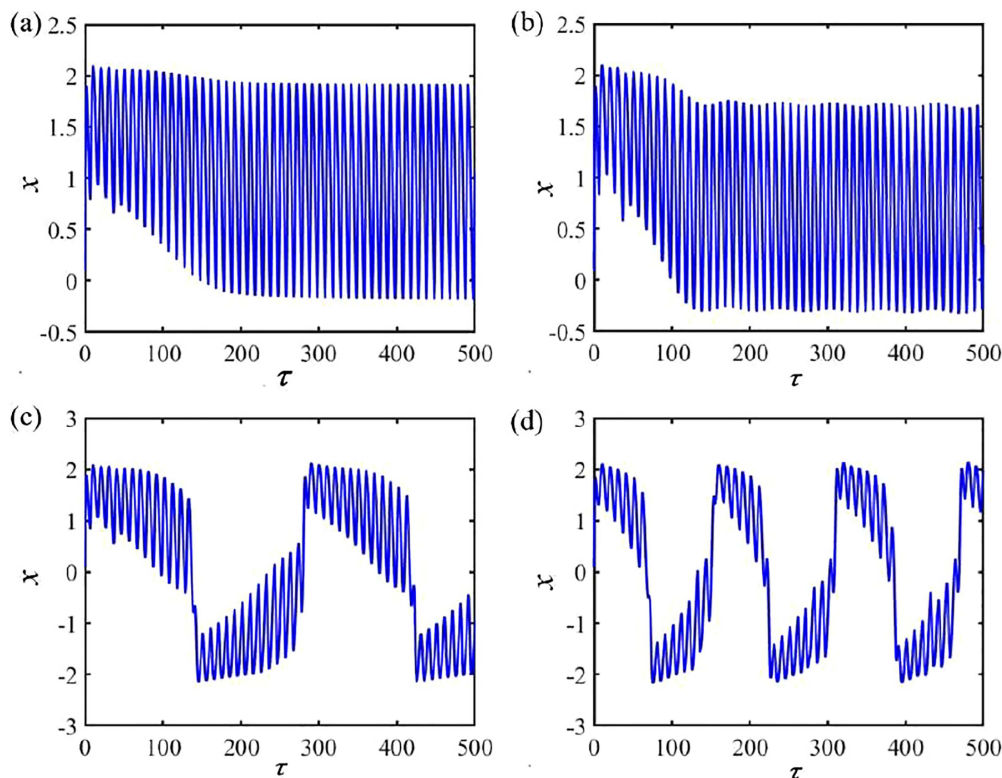


FIG. 3. Membrane potential at $\alpha < 1$ under periodic stimulus. For (a) $\alpha = 0.2$; (b) $\alpha = 0.35$; (c) $\alpha = 0.4$; and (d) $\alpha = 0.98$.

$u_s = A \cos(2\pi f\tau) = \cos(0.2\pi\tau)$, and the membrane parameter α can be adjusted to trigger different firing patterns in the neural activities. The initial values for the four variables are selected with (0.1, 0.2, 0.3, and 0.1). Surely, these intrinsic parameters can also be selected with another group of values and similar bifurcation analysis can be carried out. In Fig. 2, the peak values for the membrane potential and average Hamilton energy are calculated to predict mode transition when parameter α is adjusted carefully.

From Fig. 2, the increase of the average energy level is crucial to keep continuous firing activities. In case of $\alpha < 1$, the Hamilton energy prefers to keep negative value and energy flow mainly pumps into the inner cell membrane by capturing energy from external periodic stimulus. According to the definition for the capacitive ratio $\alpha = C_2/C_1$, the value for α describes the physical property of the memristive membrane because outer membrane has higher capacitance value than inner membrane. The outer and inner cell membranes are connected by a kind of memristive media, and the ratio for α can switch the definition of outer membrane and inner membrane. For $\alpha < 1$, capacitor C_1 behaves similar outer membrane and these channels pumps extracellular ions into the inner membrane. For $\alpha > 1$, C_2 behaves similar outer membrane and C_1 behaves as inner membrane to pump intracellular ions out. In fact, the energy level becomes positive at $\alpha > 1$ and external stimulus applied on the outer membrane is effective to excite the memristive

neuron for presenting different firing modes. In Fig. 3, the firing patterns are plotted for $\alpha < 1$, and transition in the energy level is plotted in Fig. 4 when external forcing is imposed to excite the first variable x .

The firing patterns are affected by the energy level of the memristive neuron, and changes of parameter α will induce mode transition for keeping suitable energy level in the neuron. We also investigate the case for $\alpha > 1$ and periodic signal is applied to control the second variable, and evolution of firing patterns is plotted in Fig. 5.

The value for parameter α is further increased; the bursting neuron will be regulated to present chaotic series because of continuous periodic exciting on the membrane potential. In addition, energy transition is plotted in Fig. 6.

The energy for the memristive neuron presents chaotic characteristic when the neural activities are discerned with chaotic behaviors. Both noisy disturbance and periodic stimulus can regulate the energy level and energy shunting between capacitive and inductive forms because external excitation can inject energy flow into the media. To discern the self-regulation in the neuron, bifurcation parameter α is adjusted to predict the energy level without applying noise and periodic forcing on neuron, and the average energy is calculated in Fig. 7 by showing the evolution of membrane potential as well.

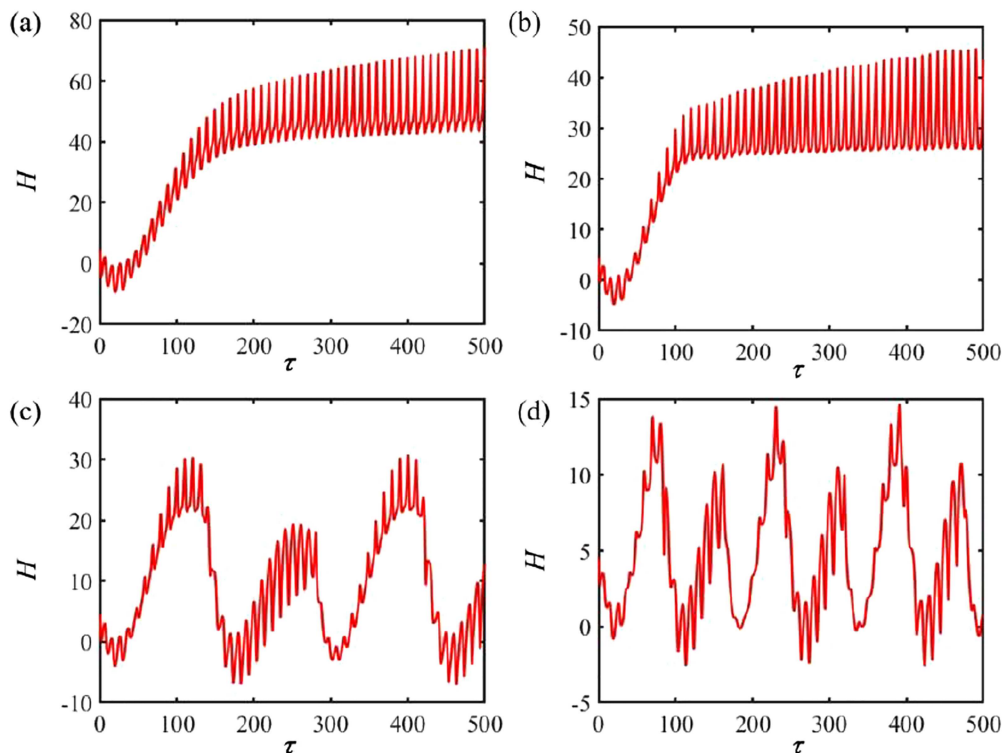


FIG. 4. Hamilton energy at $\alpha < 1$ under periodic stimulus. (a) $\alpha = 0.2$; (b) $\alpha = 0.35$; (c) $\alpha = 0.4$; and (d) $\alpha = 0.98$.

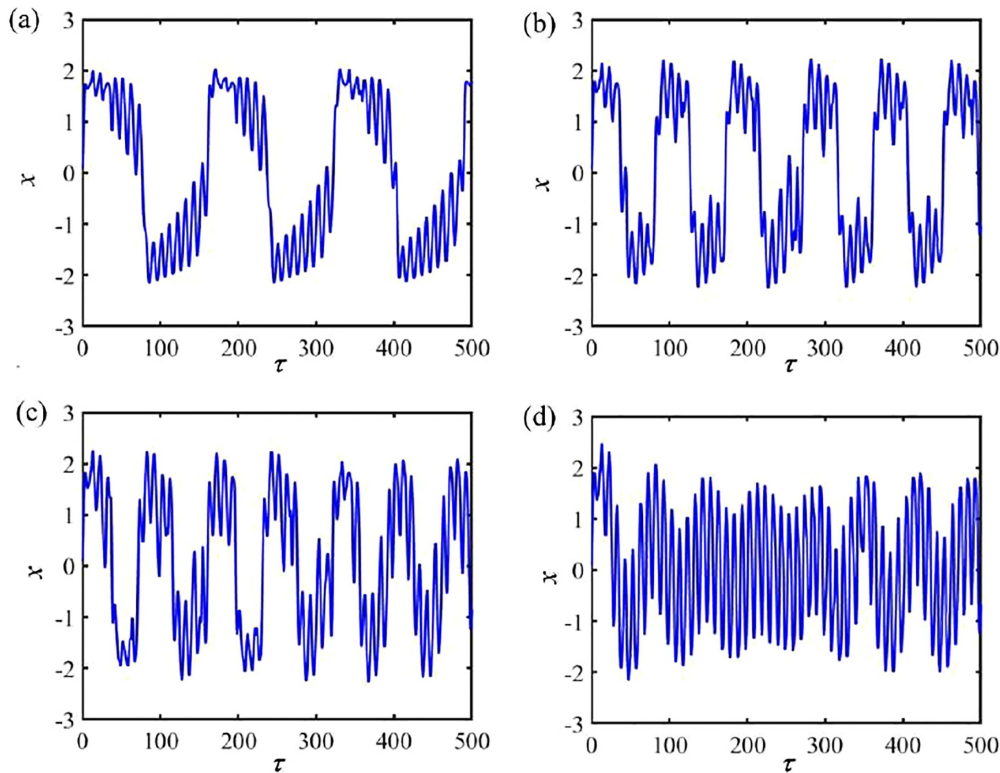


FIG. 5. Membrane potential at $\alpha > 1$ under periodic stimulus. For (a) $\alpha = 1$; (b) $\alpha = 2$; (c) $\alpha = 3$; and (d) $\alpha = 6$.

Without external exciting and disturbance, the neuron presents distinct periodic patterns and the average energy level is also increased slightly by applying larger parameter α , and the neuron fires with shorter period in electric activities. For a generic neuron model, additive noise can induce coherence resonance. For simplicity, only Gaussian white noise is considered in Eq. (8) and no periodic stimulus is applied to estimate the distribution of CV and average Hamilton energy. The parameters are used for the memristive neuron, which can also present spiking, bursting, chaotic patterns when parameter α is changed in Fig. 8.

Indeed, both external periodic forcing and noisy disturbance have direct impact on the mode transition of neural activities because external energy flow can break the energy balance between capacitive and inductive channels. As shown in Eq. (8), when noisy disturbance is applied on different channels/variables, energy flow is shunted with different ways and the energy flow is controlled to keep suitable energy level. To predict the emergence of coherence resonance, distribution for CV values is calculated when noise is imposed on channel shown in Eq. (8). In Fig. 9, noisy disturbance is applied to regulate the variable y .

The CV value decreases with time while the average energy keeps further increase with time, it means large noise intensity will be helpful to induce distinct periodic patterns, and regularity is enhanced under higher energy level. For example, CV gets lowest

value 0.0967 and average energy reaches highest value 0.0017 at noise intensity $D = 1.8$, and it means this neuron presents distinct regularity in electric activities because of coherence resonance under this noise intensity. In fact, the outer membrane captures energy flow under noisy disturbance when electric field is fluctuated with time (capacitor C_2 is excited by external forcing). The same noisy disturbance is applied to excite memristive channel under noisy electric field, and the transition of CV and average energy are plotted in Fig. 10.

Similar to the case presented in Fig. 9, the average energy is kept with lower value, and the memristive neuron will keep chaotic patterns when stochastic electric field is applied to affect the memristive channel. At noise intensity $D = 1.95$, coherence resonance is induced with lowest CV value 0.3764 and highest average energy level 0.2246, the neuron is excited to present periodic firing patterns. Noisy exciting is also imposed to regulate the fourth variable in Eq. (8), it can mimic the effect of noisy radiation on the neural circuit due to fluctuation of magnetic field, and the results are shown in Fig. 11.

Distinct peak (1.5484) is found in the curve for average energy when noise intensity is tamed carefully, and CV also finds lowest value at 0.0062 synchronously at noise intensity $D = 1.4$, it means that this neuron is guided to keep regularity in the electric activities under coherence resonance. That is, noisy disturbance from external

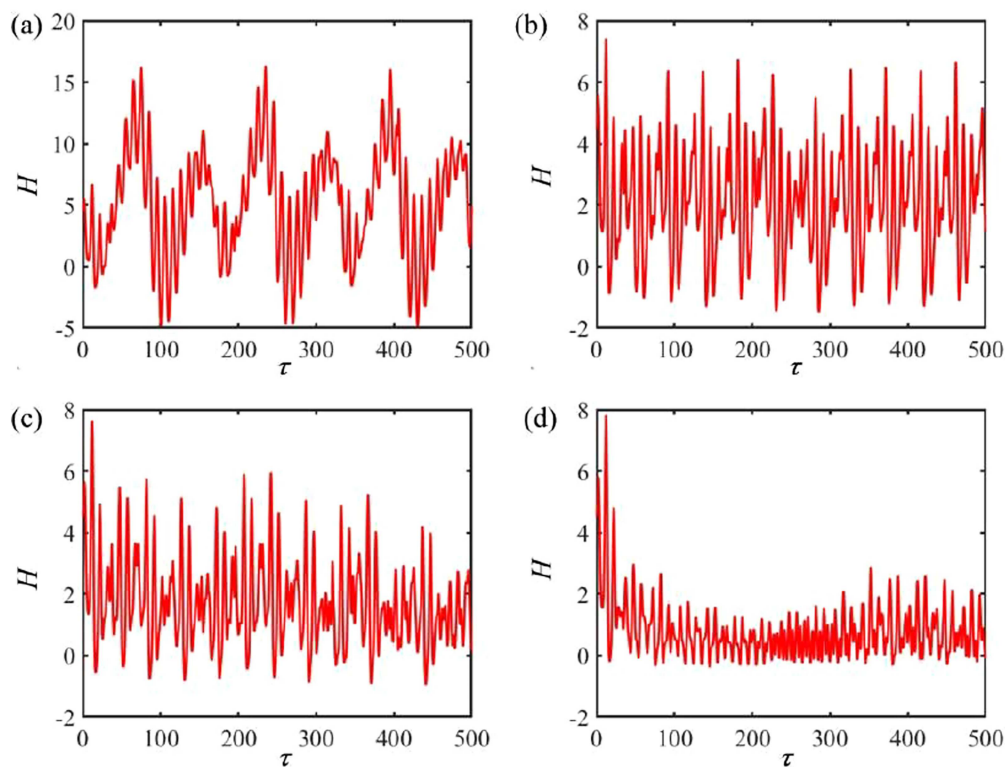


FIG. 6. Hamilton energy at $\alpha > 1$ under periodic stimulus. (a) $\alpha = 1$; (b) $\alpha = 2$; (c) $\alpha = 3$; and (d) $\alpha = 6$.

field has different impacts on the membrane potential, channel currents, and then the mode transition and occurrence of coherence resonance will be induced with different noise intensities.

External energy injection due to electric stimulus and electromagnetic radiation, shape deformation of media and components will change some intrinsic parameters. The parameter α suffers from certain jump and shift when energy flow is accumulated beyond the capacitive ability. According to Eq. (10), parameter shift is controlled by the energy threshold λ , and continuous increase of parameter α is controlled with a Heaviside function. In Fig. 12, different thresholds for λ are applied to predict the mode transition and changes of the ratio for two capacitive comments α with time.

With higher energy threshold, the membrane ratio can increase to be close saturation value and chaotic patterns can be suppressed to present bursting patterns. As a result, capacitive energy for the outer membrane can keep higher energy value and the electric activities for inner membrane can be controlled by the energy flow. The effect of gain σ is considered in Fig. 13.

It is found that higher gain for σ can be effective to suppress chaotic states and the membrane ratio parameter α will increase to certain saturation value within finite transient period, and the neuron will present periodic firing patterns. By the way, similar adaptive growth of membrane ratio is considered when external noise is

added to affect the outer membrane (output voltage on capacitor C_2), and the changes of CV values are calculated in Fig. 14.

The involvement of noise on outer cell membrane can induce similar coherence resonance and distinct bottom values are detected. Make a contrast with the results in Fig. 13 with Fig. 9, the curve for CV values is changed but the threshold of noise for developing distinct regularity in electric activities under noise is decreased. In fact, the membrane ratio parameter α begins its growth from a larger value, and it is helpful to keep against external noisy disturbance because of its capacitive energy level keeps high value. In addition, the bursting and chaotic neurons are able to develop regular firing patterns with lower noise intensity under coherence resonance.

In this memristive neuron considering double membranes and biophysical properties are much dependent on the membrane ratio α . In fact, at $\alpha > 1$, the variable y is suitable to describe the characteristic of outer membrane and ion channels have direct impact on the electric activities of inner membrane described by variable x . On the other hand, in case of $\alpha < 1$, variable x describes the characteristic of outer membrane and channel ions are embedded into the outer membrane rather than into the inner membrane described by y . Therefore, noisy disturbance on the mode transition and energy level are relative to the selection of membrane ratio α because the regulation and energy shunting in the ion channels have different scales of impact on the membrane potentials.

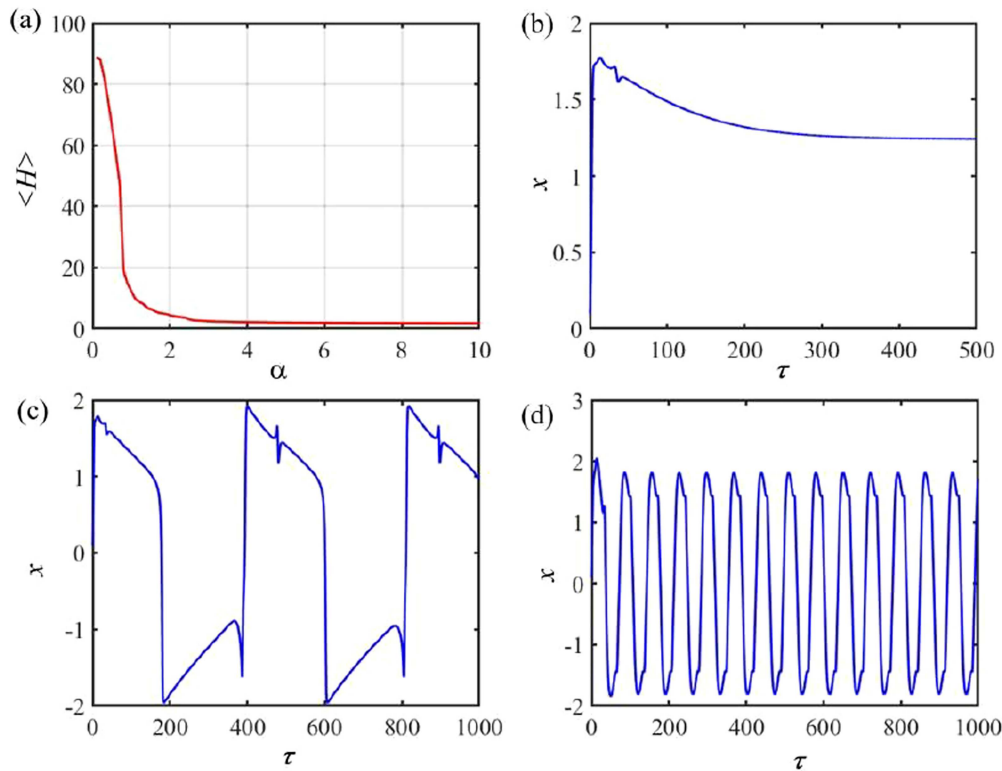


FIG. 7. Dependence of average energy on membrane ratio α and firing patterns. (b) $\alpha = 0.5$; (c) $\alpha = 0.78$; and (d) $\alpha = 8$.

IV. OPEN PROBLEMS

Each ion channel has certain reverse potential, and external stimulus can break the balance to activate exchange between intracellular and extracellular ions. To implement an equivalent neural circuit, constant voltage connected in the branch circuits will be mapped into constant parameter in the improved neuron models. As shown in Fig. 1(a), two different constant voltage sources E_1 and E_2 can be connected to the inductor and nonlinear resistor, respectively. By using the same reference voltage, the memristive neuron is updated as follows:

$$\begin{cases} \frac{dx}{d\tau} = \alpha \left[(a' + b'\varphi'^2)(y - x) + x - \frac{1}{3}x^3 \right], \\ \frac{dy}{d\tau} = (a' + b'\varphi'^2)(x - y) + z, \\ \frac{dz}{d\tau} = -\beta y - \gamma z + d, \\ \frac{d\varphi'}{d\tau} = y - x; \quad d = \frac{E_1 \rho^2 C_2}{LV_0} = \beta \frac{E_1}{V_0}. \end{cases} \quad (11)$$

That is, the involvement of constant voltage in the branch circuit composed of NR seldom changes the circuit equations directly. By the way, noisy disturbance and external stimuli can be applied to

explore the mode transition and jump between energy levels, readers can further discuss this case and dynamics in networks.

In a summary, a simple memristor is used to connect two capacitors for regulating energy balance, and inductive channel can shunt the field energy. The Chua circuit also has two capacitors, and the connection to memristor in additive branch circuits can regulate the dynamics of the memristive Chua systems.^{77–81} In this work, memristor is used to regulate the energy difference between inner and outer fields separated by two membranes, and the filler media between two-layer membranes is considered with memristor property. Therefore, the memristive membrane is suitable to mimic the flexibility and controllability of cell membrane for biological neurons. In the recent work,⁸² a linear resistor is used to couple two capacitors in a memristive circuit, and a memristive neuron with two capacitive membranes is suggested. The membrane property is described by resistive form, which two capacitors are connected via a resistor, and the energy diversity between inner membrane and outer membrane is controlled by Joule Heat across the resistor. This work is some different from the model in Ref. 82, which double membranes are connected with resistive channel, and an adaptive law is presented to explain the regulation of energy level on the capacitive property. In addition, a smooth function is applied for the nonlinear resistor and its intrinsic parameters are used as reference values during scale transition. In practical way, external field

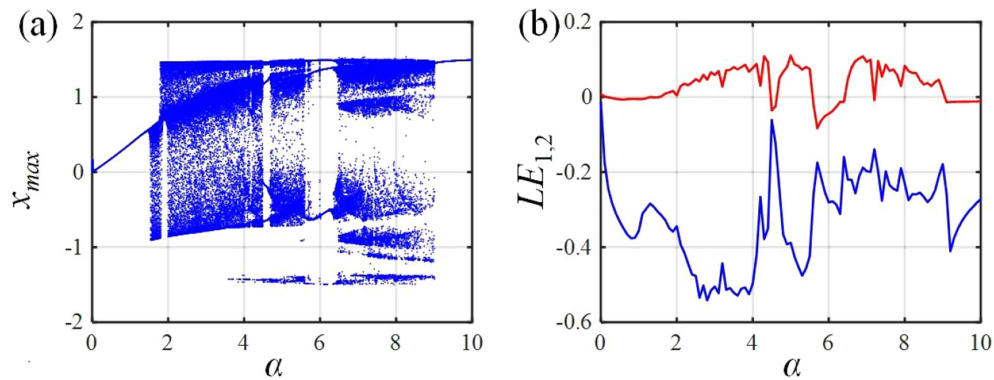


FIG. 8. (a) Bifurcation of peak value x_{\max} for membrane potential vs parameter α and (b) distribution of two larger Lyapunov exponents. Setting parameters $a' = 0.48$, $b' = 0.001$, $\beta = 11.0$, $\gamma = 0.001$, $A = 0.3$, $\omega = 0.9$, and external periodic forcing $u_s = A\cos(\omega\tau)$ is used to drive the first variable x .

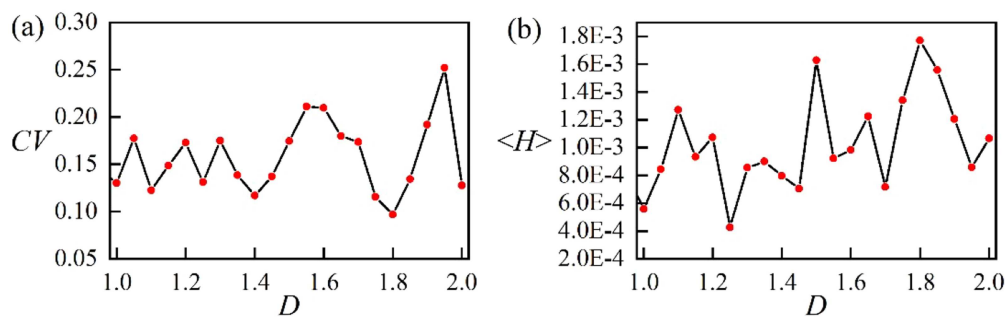


FIG. 9. Dependence of CV value (a) and average energy (b) on noise intensity D when noise is added to excite the second variable in Eq. (8). Setting parameters $\alpha = 5.0$, $\beta = 8.55$, $\gamma = 0.01$, $a' = 0.1$, $b' = 0.01$, and $A = 0.0$. CV minima is 0.0967.

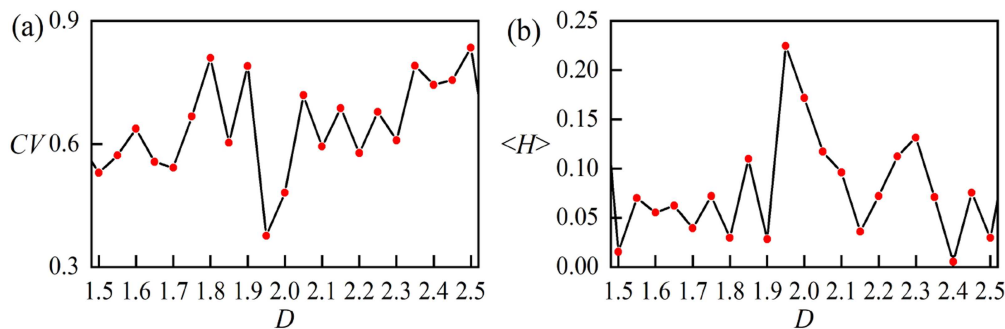


FIG. 10. Dependence of CV value (a) and average energy (b) on noise intensity D when noise is added to excite the third variable in Eq. (8). Setting parameters $\alpha = 5.0$, $\beta = 8.55$, $\gamma = 0.01$, $a' = 0.1$, $b' = 0.01$, and $A = 0.0$. CV minima is 0.3764.

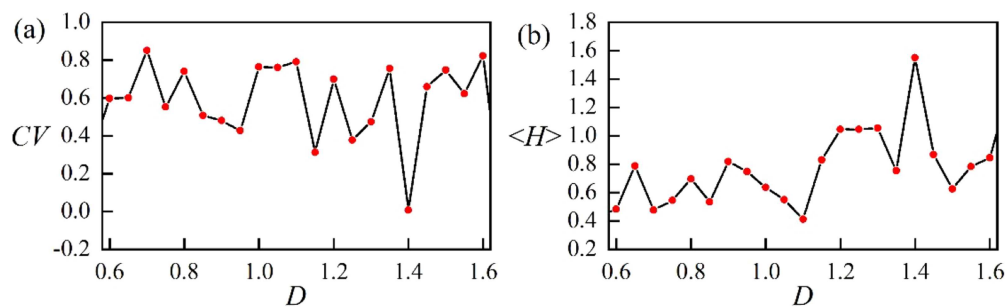


FIG. 11. Dependence of CV value (a) and average energy (b) on noise intensity D when noise is added to excite the fourth variable in Eq. (8). Setting parameters $\alpha = 5.0$, $\beta = 8.55$, $\gamma = 0.01$, $a' = 0.1$, $b' = 0.01$, $A = 0.0$. CV minima is 0.0062.

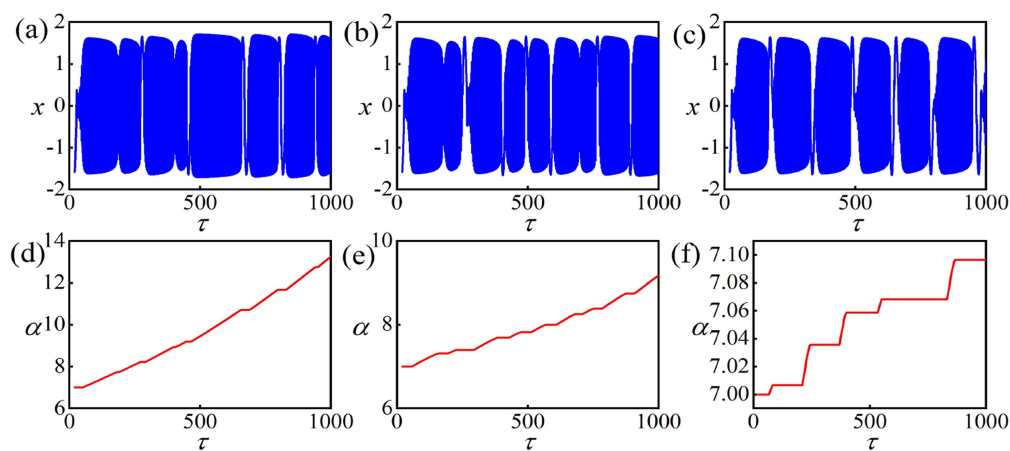


FIG. 12. Evolution of membrane potential and increase of membrane ratio α with initial value $\alpha_0 = 7.0$. Setting parameters $\beta = 8.55$, $a' = 0.1$, $b' = 0.01$, $\gamma = 0.01$, $\sigma = 0.001$. For (a) (d) $\lambda = 0.5$; (b), (e) $\lambda = 0.8$; (c), (f) $\lambda = 1.0$.

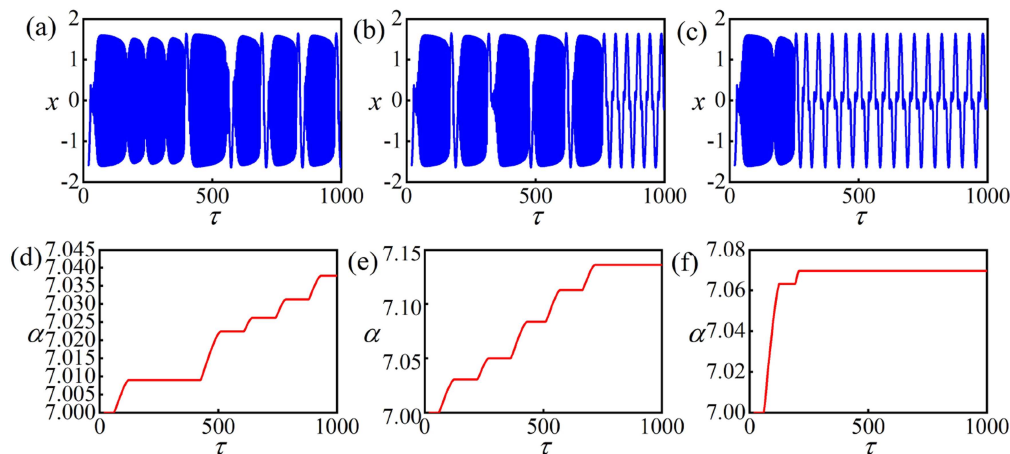


FIG. 13. Evolution of membrane potential and increase of membrane ratio α with initial value $\alpha_0 = 7.0$. Setting parameters $\beta = 8.55$, $a' = 0.1$, $b' = 0.01$, $\gamma = 0.01$, and $\lambda = 0.8$. For (a) and (d) $\sigma = 0.00009$; (b) and (e) $\sigma = 0.0003$; and (c) and (f) $\sigma = 0.0006$.

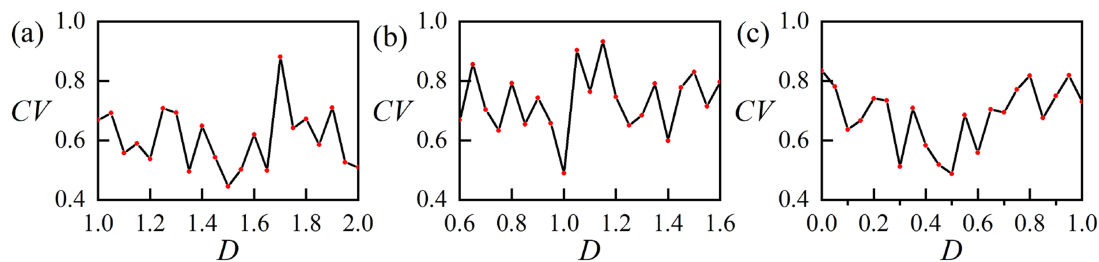


FIG. 14. Distribution of CV under noisy disturbance imposed to regulate the second variable. Setting parameters $\beta = 8.55$, $a' = 0.1$, $b' = 0.01$, $\gamma = 0.01$, $\lambda = 0.8$, and $\sigma = 0.001$. (a) $\alpha_0 = 8$; (b) $\alpha_0 = 9$; and (c) $\alpha_0 = 10$.

has direct impact on the membrane potential and continuous energy accommodation will induce parameter shift because of local shape deformation in non-uniform radiation or stimuli. From dynamical viewpoint, this memristive neuron can be more suitable to produce the biophysical property of biological neurons, and it can be used to build neural networks considering the self-organization under external electromagnetic radiation and noisy disturbance. This neuron model is much different from most of the neuron models with only one capacitive variable, and it provides good clues to design artificial membrane and understand the application of memristor in neural circuits.

The most contribution of this work is that memristor is used to mimic the controllability of cell membrane with two capacitive variables, while most of the previous works confirmed that memristors in different forms of memductance are effective to describe the effect of ion channels. In particular, the involvement of memristors into nonlinear circuits can induce multistability, and these memristive circuits are useful in neuromorphic computing.^{83–85}

V. CONCLUSIONS

Bi-directional propagation and exchange of ions and stochastic diffusion of intracellular ions induce complex electromagnetic field in the media and then membrane potential is regulated synchronously to present suitable firing modes and keep appropriate energy level. Each coin (or membrane) has two sides, the physical characteristic of cell membrane is considered as double-layer forms because the inside and outside electrophysiological environment of cells is much different. Considering the controllability and flexibility of cell membrane, the inner media of the cell membrane is assumed with memristive property. To mimic its characteristic in neural circuit, a memristor is used to connect two different capacitors, and the outputs are used to describe the membrane potential for the two-layer membranes, respectively. Accompanying with the C–M–C (capacitor–memristor–capacitor), an inductor, nonlinear resistor are used build a physical neural circuit. The neuron model with memristive cell membrane can mimic the biophysical properties of biological neurons, and energy function is defined to discern the dependence of firing mode on the energy level. Coherence resonance is induced under noisy disturbance on the neuron. Indeed, a

mode transition results from the large energy accommodation from external stimuli, and adaptive parameter growth is induced to keep certain energy level and firing patterns. This biophysical neuron is suitable to explore the self-organization and energy balance in neural networks, and appropriate regulation of capacitive parameter is effective to control the energy flow and firing patterns.

ACKNOWLEDGMENTS

This project was partially supported by National Natural Science Foundation of China (NNSFC) under Grant Nos. 12072139 and 12302070.

AUTHOR DECLARATIONS

Conflict of Interest

The authors have no conflicts to disclose.

Author Contributions

Yitong Guo: Data curation (equal); Formal analysis (equal); Investigation (equal); Resources (equal); Validation (equal). **Fuqiang Wu:** Data curation (equal); Formal analysis (equal); Investigation (equal); Methodology (equal); Software (equal); Validation (equal). **Feifei Yang:** Data curation (equal); Formal analysis (equal); Investigation (equal); Resources (equal); Validation (equal). **Jun Ma:** Formal analysis (lead); Funding acquisition (lead); Supervision (lead); Validation (lead); Visualization (lead); Writing – original draft (lead); Writing – review & editing (lead).

DATA AVAILABILITY

The data that support the findings of this study are available from the corresponding author upon request.

APPENDIX: VECTOR FORM FOR NEURON MODEL

$$\begin{aligned}
\begin{bmatrix} \dot{x} \\ \dot{y} \\ \dot{z} \\ \dot{\varphi}' \end{bmatrix} &= \begin{bmatrix} \alpha \left[(a' + b'\varphi'^2)(y - x) + x - \frac{1}{3}x^3 \right] \\ (a' + b'\varphi'^2)(x - y) + z \\ -\beta y - \gamma z \\ y - x \end{bmatrix} = F_c(x, y, z, \varphi') + F_d(x, y, z, \varphi') \\
&= \begin{bmatrix} \alpha(a' + b'\varphi'^2)y + z + \frac{1}{2}\alpha(a' + 3b'\varphi'^2) + \frac{\alpha}{4}(a'\varphi' + b'\varphi'^3)(3a' + 5b'\varphi'^2) \\ (2a' + 4b'\varphi'^2)x + z + \frac{\alpha}{4}(a'\varphi' + b'\varphi'^3)(3a' + 5b'\varphi'^2) - \frac{1}{2}(a' + 3b'\varphi'^2)y \\ -\beta y + \frac{\beta}{\alpha}x \\ y - x + \frac{1+\alpha}{2}(a'\varphi' + b'\varphi'^3) \end{bmatrix} \\
&+ \begin{bmatrix} \alpha \left[-x(a' + b'\varphi'^2) + x - \frac{1}{3}x^3 - \frac{1}{2}(a' + 3b'\varphi'^2) - \frac{1}{4}(a'\varphi' + b'\varphi'^3)(3a' + 5b'\varphi'^2) \right] - z \\ -(a' + b'\varphi'^2)y - (a' + 3b'\varphi'^2)x - \frac{\alpha}{4}(a'\varphi' + b'\varphi'^3)(3a' + 5b'\varphi'^2) + \frac{1}{2}(a' + 3b'\varphi'^2)y \\ -\gamma z - \frac{\beta}{\alpha}x \\ -\frac{1+\alpha}{2}(a'\varphi' + b'\varphi'^3) \end{bmatrix} \\
&= \begin{bmatrix} 0 & A & \beta & -\alpha \\ -A & 0 & \beta & -1 \\ -\beta & -\beta & 0 & 0 \\ \alpha & 1 & 0 & 0 \end{bmatrix} \begin{bmatrix} -\frac{1}{\alpha}x - \frac{1}{2}(a'\varphi' + b'\varphi'^3) \\ y + \frac{1}{2}(a'\varphi' + b'\varphi'^3) \\ \frac{1}{\beta}z \\ \frac{1}{2}(a' + 3b'\varphi'^2)(y - x) \end{bmatrix} + \begin{bmatrix} A_{11} & 0 & 0 & 0 \\ 0 & A_{22} & 0 & 0 \\ 0 & 0 & A_{33} & 0 \\ 0 & 0 & 0 & A_{44} \end{bmatrix} \begin{bmatrix} -\frac{1}{\alpha}x - \frac{1}{2}(a'\varphi' + b'\varphi'^3) \\ y + \frac{1}{2}(a'\varphi' + b'\varphi'^3) \\ \frac{1}{\beta}z \\ \frac{1}{2}(a' + 3b'\varphi'^2)(y - x) \end{bmatrix}, \\
A_{11} &= \frac{\alpha \left[-x(a' + b'\varphi'^2) + x - \frac{1}{3}x^3 - \frac{1}{2}(a' + 3b'\varphi'^2) - \frac{1}{4}(a'\varphi' + b'\varphi'^3)(3a' + 5b'\varphi'^2) \right] - z}{-\frac{1}{\alpha}x - \frac{1}{2}(a'\varphi' + b'\varphi'^3)}, \\
A_{22} &= \frac{-(a' + b'\varphi'^2)y - (a' + 3b'\varphi'^2)x - \frac{\alpha}{4}(a'\varphi' + b'\varphi'^3)(3a' + 5b'\varphi'^2) + \frac{1}{2}(a' + 3b'\varphi'^2)y}{y + \frac{1}{2}(a'\varphi' + b'\varphi'^3)}, \\
A_{33} &= \frac{-\beta\gamma z - \frac{\beta^2}{\alpha}x}{z}, \quad A_{44} = \frac{-(1+\alpha)(a'\varphi' + b'\varphi'^3)}{(a' + 3b'\varphi'^2)(y - x)}, \quad A = \frac{\alpha}{2}(3a' + 5b'\varphi'^2).
\end{aligned}$$

According to the criterion in Eq. (6), the same energy function in Eq. (5) is obtained by using Helmholtz theorem, and similar approach of energy function for other models can refer to Refs. 8, 11, and 82.

REFERENCES

- ¹H. Lin, C. Wang, F. Yu *et al.*, “A review of chaotic systems based on memristive Hopfield neural networks,” *Mathematics* **11**, 1369 (2023).
- ²K. H. Wood, M. D. Wheelock, J. R. Shumen *et al.*, “Controllability modulates the neural response to predictable but not unpredictable threat in humans,” *NeuroImage* **119**, 371–381 (2015).
- ³T. M. Karrer, J. Z. Kim, J. Stiso *et al.*, “A practical guide to methodological considerations in the controllability of structural brain networks,” *J. Neural Eng.* **17**, 026031 (2020).
- ⁴F. Su, J. Wang, H. Li *et al.*, “Analysis and application of neuronal network controllability and observability,” *Chaos* **27**, 023103 (2017).
- ⁵J. Jiang and Y. C. Lai, “Irrelevance of linear controllability to nonlinear dynamical networks,” *Nat. Commun.* **10**, 3961 (2019).
- ⁶Y. Xie, Z. Yao, and J. Ma, “Phase synchronization and energy balance between neurons,” *Front. Inf. Technol. Electron. Eng.* **23**, 1407–1420 (2022).
- ⁷L. M. Zeltser, R. J. Seeley, and M. H. Tschöp, “Synaptic plasticity in neuronal circuits regulating energy balance,” *Nat. Neurosci.* **15**, 1336–1342 (2012).
- ⁸G. Sun, F. Yang, G. Ren *et al.*, “Energy encoding in a biophysical neuron and adaptive energy balance under field coupling,” *Chaos Solitons Fractals* **169**, 113230 (2023).
- ⁹L. Gautron, J. K. Elmquist, and K. W. Williams, “Neural control of energy balance: Translating circuits to therapies,” *Cell* **161**, 133–145 (2015).
- ¹⁰X. Yu, H. Bao, M. Chen *et al.*, “Energy balance via memristor synapse in Morris-Lecar two-neuron network with FPGA implementation,” *Chaos Solitons Fractals* **171**, 113442 (2023).
- ¹¹F. Yang, Y. Xu, and J. Ma, “A memristive neuron and its adaptability to external electric field,” *Chaos* **33**, 023110 (2023).
- ¹²Y. Xie, Y. Xu, and J. Ma, “Desynchronization and energy diversity between neurons,” *Nonlinear Dyn.* **111**, 11521–11541 (2023).
- ¹³F. Yang, Y. Wang, and J. Ma, “Creation of heterogeneity or defects in a memristive neural network under energy flow,” *Commun. Nonlinear Sci. Numer. Simul.* **119**, 107127 (2023).
- ¹⁴Y. Xie, Z. Yao, and J. Ma, “Formation of local heterogeneity under energy collection in neural networks,” *Sci. China Technol. Sci.* **66**, 439–455 (2023).
- ¹⁵H. Zhang, L. Y. Wang, P. J. Zhang *et al.*, “Estimation of biophysical properties of cell exposed to electric field,” *Chin. Phys. B* **30**, 038702 (2021).
- ¹⁶X. Zhang and J. Ma, “Wave filtering and firing modes in a light-sensitive neural circuit,” *J. Zhejiang Univ. Sci. A* **22**, 707–720 (2021).
- ¹⁷Y. Ge, J. Li, W. Jiang *et al.*, “A spintronic memristive circuit on the optimized RBF-MLP neural network,” *Chin. Phys. B* **31**, 110702 (2022).
- ¹⁸A. Bahramian, S. S. Jamal, F. Parastesh *et al.*, “Collective behavior of cortico-thalamic circuits: Logic gates as the thalamus and a dynamical neuronal network as the cortex,” *Chin. Phys. B* **31**, 028901 (2022).
- ¹⁹Y. Xie, Z. Yao, X. Hu *et al.*, “Enhance sensitivity to illumination and synchronization in light-dependent neurons,” *Chin. Phys. B* **30**, 120510 (2021).
- ²⁰Y. Xu and J. Ma, “Control of firing activities in thermosensitive neuron by activating excitatory autapse,” *Chin. Phys. B* **30**, 100501 (2021).
- ²¹Y. Xie and J. Ma, “How to discern external acoustic waves in a piezoelectric neuron under noise?,” *J. Biol. Phys.* **48**, 339–353 (2022).
- ²²Y. Xie, P. Zhou, Z. Yao *et al.*, “Response mechanism in a functional neuron under multiple stimuli,” *Physica A* **607**, 128175 (2022).
- ²³S. He, K. Rajagopal, A. Karthikeyan *et al.*, “A discrete Huber-Braun neuron model: From nodal properties to network performance,” *Cogn. Neurodyn.* **17**, 301–310 (2023).
- ²⁴K. Rajagopal, J. Ramadoss, S. He *et al.*, “Obstacle induced spiral waves in a multilayered Huber-Braun (HB) neuron model,” *Cogn. Neurodyn.* **17**, 277–291 (2023).
- ²⁵X. Wang, X. Zhang, M. Zheng *et al.*, “Noise-induced coexisting firing patterns in hybrid-synaptic interacting networks,” *Physica A* **615**, 128591 (2023).
- ²⁶H. Lin, C. Wang, Q. Deng *et al.*, “Review on chaotic dynamics of memristive neuron and neural network,” *Nonlinear Dyn.* **106**, 959–973 (2021).
- ²⁷F. Parastesh, S. Jafari, H. Azarnoush *et al.*, “Chimeras,” *Phys. Rep.* **898**, 1–114 (2021).
- ²⁸S. Majhi, M. Perc, and D. Ghosh, “Dynamics on higher-order networks: A review,” *J. R. Soc. Interface* **19**(188), 20220043 (2022).
- ²⁹S. D. Vijay, K. Thamilmaran, and A. I. Ahamed, “Superextreme spiking oscillations and multistability in a memristor-based Hindmarsh–Rose neuron model,” *Nonlinear Dyn.* **111**, 789–799 (2023).
- ³⁰H. Shen, F. Yu, C. Wang *et al.*, “Firing mechanism based on single memristive neuron and double memristive coupled neurons,” *Nonlinear Dyn.* **110**, 3807–3822 (2022).
- ³¹P. Zhou, X. Zhang, X. Hu *et al.*, “Energy balance between two thermosensitive circuits under field coupling,” *Nonlinear Dyn.* **110**, 1879–1895 (2022).
- ³²J. T. Fossi, V. Deli, Z. T. Njitacke *et al.*, “Phase synchronization, extreme multistability and its control with selection of a desired pattern in hybrid coupled neurons via a memristive synapse,” *Nonlinear Dyn.* **109**, 925–942 (2022).
- ³³A. Karthikeyan, M. E. Cimen, A. Akgul *et al.*, “Persistence and coexistence of infinite attractors in a fractal Josephson junction resonator with unharmonic current phase relation considering feedback flux effect,” *Nonlinear Dyn.* **103**, 1979–1998 (2021).
- ³⁴Y. Zhang, Y. Xu, Z. Yao *et al.*, “A feasible neuron for estimating the magnetic field effect,” *Nonlinear Dyn.* **102**, 1849–1867 (2020).
- ³⁵A. Marino, G. G. Genchi, V. Mattoli *et al.*, “Piezoelectric nanotransducers: The future of neural stimulation,” *Nano Today* **14**, 9–12 (2017).
- ³⁶X. Zhang, X. Cui, D. Wang *et al.*, “Piezoelectric nanotopography induced neuron-like differentiation of stem cells,” *Adv. Funct. Mater.* **29**, 1900372 (2019).
- ³⁷Y. Liu, W. Xu, J. Ma *et al.*, “A new photosensitive neuron model and its dynamics,” *Front. Inf. Technol. Electron. Eng.* **21**, 1387–1396 (2020).
- ³⁸I. Hussain, S. Jafari, D. Ghosh *et al.*, “Synchronization and chimeras in a network of photosensitive FitzHugh–Nagumo neurons,” *Nonlinear Dyn.* **104**, 2711–2721 (2021).
- ³⁹X. F. Zhang, J. Ma, Y. Xu *et al.*, “Synchronization between FitzHugh–Nagumo neurons coupled with phototube,” *Acta Phys. Sin.* **70**, 090502 (2021).
- ⁴⁰Z. Yang, Y. Zhang, and F. Wu, “Memristive magnetic coupling feedback induces wave-pattern transition,” *Nonlinear Dyn.* **100**, 647–658 (2020).
- ⁴¹F. Wu, X. Hu, and J. Ma, “Estimation of the effect of magnetic field on a memristive neuron,” *Appl. Math. Comput.* **432**, 127366 (2022).
- ⁴²Z. Li, Z. Guo, M. Wang *et al.*, “Firing activities induced by memristive autapse in FitzHugh–Nagumo neuron with time delay,” *AEU Int. J. Electron. Commun.* **142**, 153995 (2021).
- ⁴³W. Fan, X. Chen, H. Wu *et al.*, “Firing patterns and synchronization of Morris-Lecar neuron model with memristive autapse,” *AEU Int. J. Electron. Commun.* **158**, 154454 (2023).
- ⁴⁴S. Zhang, J. Zheng, X. Wang *et al.*, “Multi-scroll hidden attractor in memristive HR neuron model under electromagnetic radiation and its applications,” *Chaos* **31**, 011101 (2021).
- ⁴⁵I. Hussain, S. Jafari, M. Perc *et al.*, “Chimera states in a multi-weighted neuronal network,” *Phys. Lett. A* **424**, 127847 (2022).
- ⁴⁶M. Shafiei, S. Jafari, F. Parastesh *et al.*, “Time delayed chemical synapses and synchronization in multilayer neuronal networks with ephaptic inter-layer coupling,” *Commun. Nonlinear Sci. Numer. Simul.* **84**, 105175 (2020).
- ⁴⁷B. Yan, F. Parastesh, S. He *et al.*, “Interlayer and intralayer synchronization in multiplex fractional-order neuronal networks,” *Fractals* **30**, 2240194 (2022).
- ⁴⁸M. Lü, C. N. Wang, J. Tang *et al.*, “Collapse of synchronization in a memristive network,” *Commun. Theor. Phys.* **64**, 659 (2015).
- ⁴⁹T. Remi, P. A. Subha, and K. Usha, “Collective dynamics of neural network with distance dependent field coupling,” *Commun. Nonlinear Sci. Numer. Simul.* **110**, 106390 (2022).
- ⁵⁰F. Wu, Y. Guo, and J. Ma, “Reproduce the biophysical function of chemical synapse by using a memristive synapse,” *Nonlinear Dyn.* **109**, 2063–2084 (2022).
- ⁵¹M. Perc, “Optimal spatial synchronization on scale-free networks via noisy chemical synapses,” *Biophys. Chem.* **141**(2–3), 175–179 (2009).
- ⁵²Z. Wei, F. Parastesh, H. Azarnoush *et al.*, “Nonstationary chimeras in a neuronal network,” *Europhys. Lett.* **123**, 48003 (2018).
- ⁵³M. Xing, Z. Yang, and Y. Chen, “Bursting types and bifurcation analysis of the temperature-sensitive Purkinje neuron,” *Nonlinear Dyn.* **111**, 1819–1834 (2023).
- ⁵⁴L. Duan, T. Liang, Y. Zhao *et al.*, “Multi-time scale dynamics of mixed depolarization block bursting,” *Nonlinear Dyn.* **103**, 1043–1053 (2021).
- ⁵⁵Z. Lü, M. Liu, and L. Duan, “Dynamical analysis of dendritic mixed bursting within the pre-Bötzinger complex,” *Nonlinear Dyn.* **103**, 897–912 (2021).

- ⁵⁶D. Chen, J. Li, W. Zeng *et al.*, “Topology identification and dynamical pattern recognition for Hindmarsh–Rose neuron model via deterministic learning,” *Cogn. Neurodyn.* **17**, 203–220 (2023).
- ⁵⁷Q. Xu, Z. Ju, S. Ding *et al.*, “Electromagnetic induction effects on electrical activity within a memristive Wilson neuron model,” *Cogn. Neurodyn.* **16**, 1221–1231 (2022).
- ⁵⁸B. Cao, H. Gu, and K. Ma, “Complex dynamics of hair bundle of auditory nervous system (I): Spontaneous oscillations and two cases of steady states,” *Cogn. Neurodyn.* **16**, 917–940 (2022).
- ⁵⁹B. Cao, H. Gu, and R. Wang, “Complex dynamics of hair bundle of auditory nervous system (II): Forced oscillations related to two cases of steady state,” *Cogn. Neurodyn.* **16**, 1163–1188 (2022).
- ⁶⁰Z. Wang and L. Duan, “The combined effects of the thalamic feed-forward inhibition and feed-back inhibition in controlling absence seizures,” *Nonlinear Dyn.* **108**, 191–205 (2022).
- ⁶¹M. R. Islam, X. Zhao, Y. Miao *et al.*, “Epileptic seizure focus detection from interictal electroencephalogram: A survey,” *Cogn. Neurodyn.* **17**, 1–23 (2023).
- ⁶²B. Sarvi Zargar, M. R. Karami Mollaei, F. Ebrahimi *et al.*, “Generalizable epileptic seizures prediction based on deep transfer learning,” *Cogn. Neurodyn.* **17**, 119–131 (2023).
- ⁶³M. Du, J. Li, W. Ying *et al.*, “A dynamics model of neuron-astrocyte network accounting for febrile seizures,” *Cogn. Neurodyn.* **16**, 411–423 (2022).
- ⁶⁴J. Ma, “Biophysical neurons, energy, and synapse controllability: A review,” *J. Zhejiang Univ. Sci. A* **24**, 109–129 (2023).
- ⁶⁵M. Lv, C. Wang, G. Ren *et al.*, “Model of electrical activity in a neuron under magnetic flow effect,” *Nonlinear Dyn.* **85**, 1479–1490 (2016).
- ⁶⁶M. Sparvoli, J. S. Marma, G. F. Nunes *et al.*, “Operation of neuronal membrane simulator circuit for tests with memristor based on graphene and graphene oxide,” in *Advances in Computational Intelligence: 16th International Work-Conference on Artificial Neural Networks, IWANN 2021, Virtual Event, June 16–18, 2021, Proceedings, Part II 16* (Springer International Publishing, 2021). pp. 93–102.
- ⁶⁷X. Zhang, W. Wang, Q. Liu *et al.*, “An artificial neuron based on a threshold switching memristor,” *IEEE Electron Device Lett.* **39**, 308–311 (2018).
- ⁶⁸R. K. Budhathoki, M. P. Sah, S. P. Adhikari *et al.*, “Composite behavior of multiple memristor circuits,” *IEEE Trans. Circuits Syst. I Regul. Pap.* **60**, 2688–2700 (2013).
- ⁶⁹A. Yeşil, Y. Babacan, and F. Kaçar, “A new DDCC based memristor emulator circuit and its applications,” *Microelectronics J.* **45**, 282–287 (2014).
- ⁷⁰G. Innocenti, M. Di Marco, A. Tesi *et al.*, “Memristor circuits for simulating neuron spiking and burst phenomena,” *Front. Neurosci.* **15**, 681035 (2021).
- ⁷¹P. Ji, J. Ye, Y. Mu *et al.*, “Signal propagation in complex networks,” *Phys. Rep.* **1017**, 1–96 (2023).
- ⁷²F. Parastesh, M. Mehrabbeik, K. Rajagopal *et al.*, “Synchronization in Hindmarsh–Rose neurons subject to higher-order interactions,” *Chaos* **32**, 013125 (2022).
- ⁷³E. Vasilyeva, A. Kozlov, K. Alfaro-Bittner *et al.*, “Multilayer representation of collaboration networks with higher-order interactions,” *Sci. Rep.* **11**, 5666 (2021).
- ⁷⁴T. Palabas, J. J. Torres, M. Perc *et al.*, “Double stochastic resonance in neuronal dynamics due to astrocytes,” *Chaos Solitons Fractals* **168**, 113140 (2023).
- ⁷⁵A. V. Andreev, V. V. Makarov, A. E. Runnova *et al.*, “Coherence resonance in stimulated neuronal network,” *Chaos Solitons Fractals* **106**, 80–85 (2018).
- ⁷⁶C. Wang, J. Tang, and J. Ma, “Minireview on signal exchange between nonlinear circuits and neurons via field coupling,” *Eur. Phys. J. Spec. Top.* **228**, 1907–1924 (2019).
- ⁷⁷M. Chen, A. Wang, C. Wang *et al.*, “DC-offset-induced hidden and asymmetric dynamics in memristive Chua’s circuit,” *Chaos Solitons Fractals* **160**, 112192 (2022).
- ⁷⁸A. Ishaq Ahamed and M. Lakshmanan, “Nonsmooth bifurcations, transient hyperchaos and hyperchaotic beats in a memristive Murali-Lakshmanan-Chua circuit,” *Int. J. Bifurcat. Chaos* **23**, 1350098 (2013).
- ⁷⁹W. Marszalek and H. Podhaisky, “2D bifurcations and Newtonian properties of memristive Chua’s circuits,” *Europhys. Lett.* **113**, 10005 (2016).
- ⁸⁰M. E. Sahin, A. S. Demirkol, H. Guler *et al.*, “Design of a hyperchaotic memristive circuit based on wien bridge oscillator,” *Comput. Electr. Eng.* **88**, 106826 (2020).
- ⁸¹C. K. Volos, A. Akgul, V. T. Pham *et al.*, “Antimonotonicity, crisis and multiple attractors in a simple memristive circuit,” *J. Circuits Syst. Comput.* **27**, 1850026 (2018).
- ⁸²J. Jia, F. Yang, and J. Ma, “A bimembrane neuron for computational neuroscience,” *Chaos Solitons Fractals* **173**, 113689 (2023).
- ⁸³Q. Xu, Y. Wang, H. H. C. Iu *et al.*, “Locally active memristor-based neuromorphic circuit: Firing pattern and hardware experiment,” *IEEE Trans. Circuits Syst. I Regul. Pap.* **70**, 3130–3141 (2023).
- ⁸⁴Q. Xu, Y. Wang, B. Chen *et al.*, “Firing pattern in a memristive Hodgkin–Huxley circuit: Numerical simulation and analog circuit validation,” *Chaos Solitons Fractals* **172**, 113627 (2023).
- ⁸⁵K. Yang, J. Joshua Yang, R. Huang *et al.*, “Nonlinearity in memristors for neuromorphic dynamic systems,” *Small Sci.* **2**, 2100049 (2022).



How to define energy function for memristive oscillator and map

Yitong Guo · Ying Xie · Jun Ma 

Received: 29 July 2023 / Accepted: 15 October 2023
© The Author(s), under exclusive licence to Springer Nature B.V. 2023

Abstract During the release and propagation of intracellular and extracellular ions, electromagnetic field is induced accompanying with propagation of energy flow. The firing mode is dependent on the energy level, and external energy injection will induce distinct mode transition. Exact energy function for a neuron developed from a neural circuit can be obtained directly by applying scale transformation for the physical field energy. For generic neuron models, dimensionless Hamilton energy function can be obtained by using Helmholtz theorem, and this energy function can be considered as a specific Lyapunov function. In this review, approach of energy function for memristive neuron is discussed by designing equivalent neural circuit coupled by two kinds of memristors, which are dependent on the magnetic flux and charge flux, respectively. A scheme is suggested to get equivalent energy function for memristive neuron in the form of map by

introducing a scale parameter. The memristive map reduced from the memristive neuron can produce similar attractors and firing modes under applying the same parameters, and the average Hamilton energy for the map neuron is decreased because of regulation from the scale parameter. On the other hand, a memristive map is replaced by an equivalent memristive oscillator for finding an equivalent Hamilton energy function according to the Helmholtz theorem. The energy scheme can be helpful for further investigating energy property of artificial neurons, maps and discrete memristors. It also provides evidence that maps are more suitable for investigating neural activities than neuron oscillators.

Keywords Hamilton energy · Memristive neuron · Neural circuit · Memristor

Y. Guo · J. Ma (✉)
College of Electrical and Information Engineering,
Lanzhou University of Technology, Lanzhou 730050,
China
e-mail: hyperchaos@163.com

Y. Guo · J. Ma
Department of Physics, Lanzhou University of
Technology, Lanzhou 730050, China

Y. Xie · J. Ma
School of Science, Chongqing University of Posts and
Telecommunications, Chongqing 430065, China

1 Introduction

The occurrence of chaos and chaos in nonlinear circuits depends on the involvement of electric components, and one nonlinear component with nonlinear relation between voltage and channel current is required at least. When these circuits are activated, capacitive energy is shunted to inductive channels and memristive channels based on memristors [1–5]. A simple nonlinear circuit requires the

combination and connection to capacitor, inductor, negative resistor and even external signal source, and appropriate setting in parameters will develop chaos in these nonlinear circuits [6–10]. In particular, some nonlinear circuits can be tamed and improved to present bursting, spiking patterns, and neural circuits are obtained to propose equivalent neuron models. Indeed, piezoelectric ceramic [11], Josephson junction [12, 13], photocell [14, 15], thermistor [16, 17], memristor can be connected to some neural circuits for building reliable neural circuits for further considering the physical effect during activating neural activities in biophysical neurons [18–22].

From physical aspect, energy is exchanged and propagated when biological neurons present different firing modes and patterns. For nonlinear circuits, continuous oscillation needs stable energy supply and shunting between different electric components. The physical energy in nonlinear circuits can be obtained by considering the energy in the capacitive, inductive and memristive channels, and then the physical field energy can be converted into equivalent dimensionless energy function [23–25] by applying scale transformation on the variables and parameters in the field energy function. On the other hand, suitable Hamilton energy function can be confirmed in a nonlinear oscillator by using Helmholtz theorem [26–28]. However, it keeps open for discrete systems and maps to get energy function, and the involvement of discrete memristor makes the question become more interesting and worthy of investigation.

In this review, based on a memristive map [29, 30], a scheme is used to estimate the energy function in theoretical way. A scale parameter is introduced to build a equivalent continuous dynamical system for getting the Hamilton energy function and then the value for the scale parameter is confirmed by bifurcation analysis, which the memristive oscillator has the same maximal value or phase space with the memristive oscillator. This scheme can be further used to calculate energy for more maps and energy level will be switched to control the chaos in maps.

2 Energy in nonlinear circuit and continuous oscillator

Quiescent biological neurons develop static distribution of electric field, and the membrane potential keeps

certain constants for keeping propagation balance of intracellular and extracellular ions. In presence of external stimulus beyond the threshold, certain firing mode is triggered to present continuous firing patterns accompanying with jumping between energy levels. That is, distinct physical effect becomes distinct and it can be reproduced in some equivalent neural circuits by considering the main physical properties. The capacitive energy can be described by the capacitors and charge-controlled memristor [31–34], the inductive energy can be mimicked by inductors and magnetic-flux dependent memristor [35–38], nonlinear resistor in parallel with the inductive channel can be used to bridge connection to the magnetic field and electric field. In addition, involvement of constant voltage sources into the inductive channel or memristive channel is suitable to represent the resting potentials of ion channels. Biological neurons can induce electrical field and magnetic field, and ion channels are important for exchange and propagation of ions including calcium, potassium and sodium. Therefore, a capacitor and its output voltage are used to mimic the electric field and membrane potential, inductor and its channel current can describe the magnetic field and the transmembrane current. Additive memristors are used to estimate the physical field effect and special property of ion channels, such as detecting external field and self-adaption and controllability. In Fig. 1, a simple neural circuit is built by connecting one capacitor, two different kinds of memristors, one nonlinear resistor with cubic relation between channel current and across voltage, and

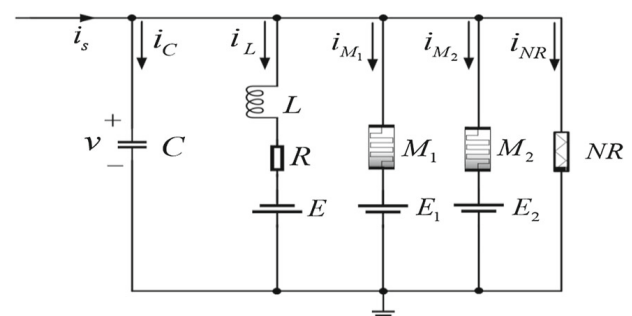


Fig. 1 Memristive neural circuit coupled by memristors. C , L , M_1 , M_2 , and NR describe capacitor, inductor, magnetic flux-dependent memristor, charge-controlled memristor, nonlinear resistor, respectively. Constant E denotes reverse potential, i_s represents external forcing current, the output voltage for capacitor is v

external stimulus can be time-varying or sampled from specific signal source within specific frequency band.

In Fig. 1, three different constant voltage sources are introduced to mimic the effect of reverse voltage in these ion channels. The involvement of NR is used to describe the nonlinear relation of energy flow between capacitive and inductive field. The channel current across the two memristors and nonlinear resistor is respectively estimated,

$$\begin{cases} i_{NR} = -\frac{1}{\rho} \left(v - \frac{1}{2} \frac{v^2}{V_0} - \frac{1}{3} \frac{v^3}{V_0^2} \right); \\ i_{M1} = M(\varphi)(v - E_1) = (a + 3b\varphi^2)(v - E_1); \\ i_{M2} = \frac{(v - E_2)}{W(q)} = (c + dq^2)(v - E_2); \end{cases} \quad (1)$$

where the physical parameters (ρ, V_0) , (a, b) , (c, d) are relative to the material properties of the NR, M_1 and M_2 , respectively. The parameters (ρ, V_0) can be discerned from the i - v (current and voltage across the nonlinear resistor) curve when the nonlinear resistor is connected to a simple circuit. φ and q describe the magnetic flux and charges across the two kinds of memristors. v and i_L measure the voltage across the capacitor and channel current across the inductor. Furthermore, the field energy in each electric component, and the total energy function are respectively calculated by

$$\begin{cases} W_C = \frac{1}{2} C v^2; \quad W_L = \frac{1}{2} L i_L^2; \\ W_{M1} = \frac{1}{2} L_M i_{M1}^2 = \frac{1}{2} \varphi i_{M1} = \frac{1}{2} (a + 3b\varphi^2)(v - E_1)\varphi; \\ W_{M2} = \frac{1}{2} C_M v_{M2}^2 = \frac{1}{2} q v_{M2} = \frac{1}{2} (v - E_2)q; \\ W = \frac{1}{2} C v^2 + \frac{1}{2} L i_L^2 + \frac{1}{2} (a + 3b\varphi^2)(v - E_1)\varphi + \frac{1}{2} (v - E_2)q; \end{cases} \quad (2)$$

An equivalent Hamilton energy function H in dimensionless form can be obtained by

$$\begin{aligned} H &= \frac{W}{CV_0^2} = \frac{1}{CV_0^2} \left[\frac{1}{2} C v^2 + \frac{1}{2} L i_L^2 + \frac{1}{2} (a + 3b\varphi^2)(v - E_1)\varphi + \frac{1}{2} (v - E_2)q \right] \\ &= \frac{W}{W_0} = \frac{1}{2} x^2 + \frac{1}{2\alpha} y^2 + \frac{1}{2} (a' + b'z^2)(x - e_1)z + \frac{1}{2} (x - e_2)w; \end{aligned} \quad (3)$$

As a result, any changes of the variables and memristive parameters will trigger shift of energy level, and energy is shunted between capacitive, inductive and memristive types. The normalized parameters and dimensionless variables for physical variables and intrinsic parameters are defined by

$$\begin{cases} x = \frac{v}{V_0}, y = \frac{\rho i_L}{V_0}, z = \frac{\varphi}{\rho C V_0}, w = \frac{q}{C V_0}, \tau = \frac{t}{\rho C}, \\ \alpha = \frac{\rho^2 C}{L}, \xi = \frac{R}{\rho}, \\ a' = \rho a, b' = 3b\rho^3 C^2 V_0^2, W_0 = C V_0^2, e = \frac{E}{V_0}, \\ e_1 = \frac{E_1}{V_0}, e_2 = \frac{E_2}{V_0}; \end{cases} \quad (4)$$

According to Eq. (3), the neuron shows jump between energy levels when the electric activities are switched from periodical, spiking, bursting to chaotic patterns. The memristive oscillator regulates its energy value close to certain energy level in presenting sole firing mode. In presence of multiple firing modes, energy level is switched with time. External stimulus can inject energy flux and external electromagnetic field can change the energy shunting between the capacitive and inductive channels, and it explains the mode transition in excitable media under continuous polarization and magnetization.

The circuit equation for Fig. 1 can be obtained as follows

$$\begin{cases} C \frac{dv}{dt} = i_s - i_L - i_{M1} - i_{M2} - i_{NR}; \\ L \frac{di_L}{dt} = v + E - R i_L; \\ \frac{d\varphi}{dt} = v - E_1; \\ \frac{dq}{dt} = i_{M2} = (c + dq^2)(v - E_2); \end{cases} \quad (5)$$

Indeed, the dynamics of the neuron with double memristive channels can be described by equivalent and dimensionless form as follows

$$\begin{cases} \frac{dx}{d\tau} = i'_s - y - (a' + b'z^2)(x - e_1) \\ \quad - (c' + d'w^2)(x - e_2) + x - \frac{1}{2}x^2 - \frac{1}{3}x^3; \\ \frac{dy}{d\tau} = \alpha(x - \xi y + e); \\ \frac{dz}{d\tau} = x - e_1; \\ \frac{dw}{d\tau} = (c' + d'w^2)(x - e_2); \end{cases} \quad (6)$$

By applying and taming the normalized parameters and external forcing current, the firing mode and patterns in the memristive oscillator in Eq. (6) can be

controlled effectively. From Eq. (5) to Eq. (6), scale transformation Eq. (4) is required, and additive scale transformation is used as follows

$$i'_s = \frac{\rho i_s}{V_0}, \quad \xi = \frac{\rho}{R}, \quad e = \frac{E}{V_0}, \quad c' = \rho c, \quad d' = \rho d C^2 V_0^2; \quad (7)$$

The neural circuit contains magnetic field and electric field energy, and its dynamics can be replaced by equivalent vector form. According to the Helmholtz theorem [39, 40], the solution for the Hamilton energy H of generic nonlinear oscillator in vector form and its derivative of time meets the criterion as follows

$$\begin{cases} \frac{dX}{d\tau} = F_c(X) + F_d(X), \quad X \in R^n; \\ \nabla H^T F_c(X) = 0; \\ \nabla H^T F_d(X) = \frac{dH}{d\tau}; \end{cases} \quad (8)$$

The physical field is composed of gradient term $F_d(X)$ and curl field term $F_c(X)$, which corresponds to the electric field in the capacitor and magnetic field in inductor of nonlinear circuit, respectively. By the way, the memristive system in Eq. (6) is updated for getting suitable Hamilton energy function, see appendix. An identical energy function as the form in Eq. (3) can be obtained to confirm the reliability of this scheme. The memristive oscillator in Eq. (6) can be approached by discrete form with suitable time step, which is considered as scale parameter ε , and it is defined by

$$\begin{cases} x_{n+1} = x_n + \varepsilon [i'_s - y_n - (a' + b'z_n^2)(x_n - e_1) \\ \quad - (c' + d'w_n^2)(x_n - e_2) + x_n - \frac{1}{2}x_n^2 - \frac{1}{3}x_n^3]; \\ y_{n+1} = y_n + \varepsilon \alpha (x_n - \xi y_n + e); \\ z_{n+1} = z_n + \varepsilon (x_n - e_1); \\ w_{n+1} = w_n + \varepsilon (c' + d'w_n^2)(x_n - e_2); \end{cases} \quad (9)$$

In addition, the energy function in discrete form is updated as follows

$$H_n = \varepsilon \left[\frac{1}{2}x_n^2 + \frac{1}{2\alpha}y_n^2 + \frac{1}{2}(a' + b'z_n^2)(x_n - e_1)z_n + \frac{1}{2}(x_n - e_2)w_n \right]; \quad (10)$$

The scale parameter ε has similar role as the time step to discretize memristive oscillator presenting in differential equations into a simple map, and its value can be detected by matching the maximal value for

variable x in Eq. (6) and x_n in Eq. (9). That is, all the corresponding parameters are selected the same value, and the scale parameter ε is changed carefully until the two systems cover the same region and maximal value in the phase space. That is, introducing suitable value for the scale parameter ε , the memristive oscillator in Eq. (6) and memristive map in Eq. (9) should have the same dynamical properties including attractors, attraction domain, maximal Lyapunov exponent and same size of phase portrait. When it is considered as a memristive neuron, both of them can present complete spiking, bursting and even chaotic patterns. In this way, the energy function in Eq. (10) with suitable value for ε can measure the energy level for memristive neuron in the form of map. In particular, the memristive map will keep low energy level than the memristive oscillator because the scale parameter ε is often selected with low value ($\varepsilon < 1$). In practical way, memristive map requires low energy than memristive oscillator in signal processing and showing the same dynamical properties. It is important to clarify the approach of energy for some maps by developing equivalent oscillator model so that Helmholtz theorem can be applied for theoretical analysis and prediction for the energy function under periodic stimulus $i'_s = I_0 + A \cos(\omega\tau)$.

It is interesting to discuss the scheme for energy approach for Eqs. (6) and (9) by setting the same group of parameters as $a = 0.01$, $b = 0.01$, $c = 0.01$, $d = 0.01$, $e = 0.05$, $e_1 = 0.05$, $e_2 = 0.06$, $\alpha = 1.21$; $\xi = 0.15$, $A = 1.0$, $I_0 = 0.9$, and same initials setting are selected for the variables $(x, y, z, w) = (x_n, y_n, z_n, w_n) = (0.2, 0.1, 0.01, 0.01)$. The bifurcation analysis and average energy are plotted in Fig. 2.

The firing mode, profile of attractors and average energy of the memristive neuron will be controlled by external stimulus with changing the angular frequency. To confirm the consistence and similarity of attractors and firing patterns between the memristive neuron and map, scale parameter is adjusted to track the maximal value for membrane potential and average energy in Fig. 3.

From Fig. 3, the memristive neuron in Eq. (6) can be reproduced the same firing patterns and attractors in the memristive map in Eq. (9) by setting suitable value for scale parameter ε . The energy level and firing mode in the neuron in Eq. (6) are dependent on the angular frequency of external stimulus. From Eqs. (3)–(10), the discrete neuron is endowed with scale parameter ε ,

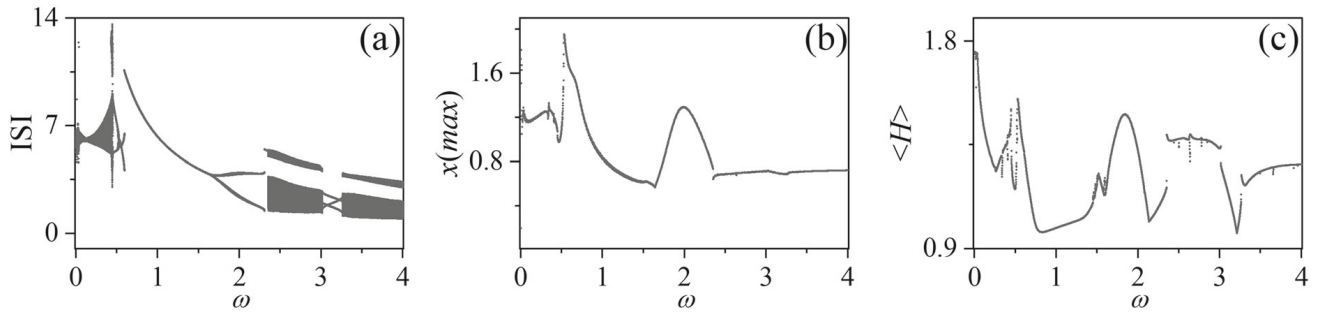


Fig. 2 Bifurcation of ISI (interspike interval) from membrane potential, $x_{max} = x(max)$ for maximal value of membrane potential, and average Hamilton energy $\langle H \rangle$ with changing frequency ω in Eq. (6)

as a result, its average energy $\langle H_n \rangle$ becomes less than $\langle H \rangle$ because $\varepsilon < 1$. Therefore, it is suitable to reproduce similar firing patterns and attractors of nonlinear oscillators in some equivalent maps by setting appropriate value for the scale parameter when they are selected with the same parameters. Particularly, the energy level in the equivalent map is decreased greatly than the memristive oscillator. In a word, scale parameter can be introduced into the discrete energy function for the equivalent map reduced from the memristive oscillator with the same parameters setting. It is important to calculate the energy function for a memristive map by developing similar memristive oscillator, and then the energy function will be discretized by removing the scale parameter directly.

3 Energy descriptions in memristive map

From dynamical viewpoint, discrete systems and maps can be considered as discretized forms for continuous dynamical systems by applying Euler algorithm approach with suitable time step. For a generic dynamical system expressed by differential equations,

$$\begin{cases} \frac{dx}{d\tau} = f(x, y, z); \\ \frac{dy}{d\tau} = g(x, y, z); \\ \frac{dz}{d\tau} = h(x, y, z); \end{cases} \quad (11)$$

Its equivalent discrete form is obtained by

$$\begin{cases} x_{n+1} = x_n + \varepsilon f(x_n, y_n, z_n); \\ y_{n+1} = y_n + \varepsilon g(x_n, y_n, z_n); \\ z_{n+1} = z_n + \varepsilon h(x_n, y_n, z_n); \end{cases} \quad (12)$$

where the parameter ε denotes the time scale, Eq. (12) will match with Eq. (11) in dynamical characteristic by setting suitable values for ε . Based on Helmholtz theorem, the Hamilton energy function for dynamical systems similar to Eq. (11) can be obtained theoretically. From Eq. (3), the continuous energy function is dependent on some intrinsic parameters and all the variables in the memristive system, and any changes in the firing patterns will induce fluctuations in the energy levels. For discrete systems, energy function becomes discrete as well. Indeed, appropriate scale parameter with time can be applied to convert discrete systems into equivalent continuous system for obtaining energy function.

$$\begin{cases} x_{n+1} = F(x_n, y_n, z_n); \\ y_{n+1} = G(x_n, y_n, z_n); \\ z_{n+1} = W(x_n, y_n, z_n); \end{cases} \Rightarrow \begin{cases} \frac{1}{\varepsilon} [x_{n+1} - x_n] = \frac{1}{\varepsilon} [F(x_n, y_n, z_n) - x_n]; \\ \frac{1}{\varepsilon} [y_{n+1} - y_n] = \frac{1}{\varepsilon} [G(x_n, y_n, z_n) - y_n]; \\ \frac{1}{\varepsilon} [z_{n+1} - z_n] = \frac{1}{\varepsilon} [W(x_n, y_n, z_n) - z_n]; \end{cases} \\ \Rightarrow \begin{cases} \frac{dx}{d\tau} = \frac{1}{\varepsilon} [F(x, y, z) - x]; \\ \frac{dy}{d\tau} = \frac{1}{\varepsilon} [G(x, y, z) - y]; \\ \frac{dz}{d\tau} = \frac{1}{\varepsilon} [W(x, y, z) - z]; \end{cases} \quad (13)$$

According to the criterion in Eq. (8), the Hamilton energy for the discrete system in Eq. (13) can be expressed in generic form

$$\begin{cases} H = H(\varepsilon, x, y, z); \\ H_n = H(x_n, y_n, z_n); \end{cases} \quad (14)$$

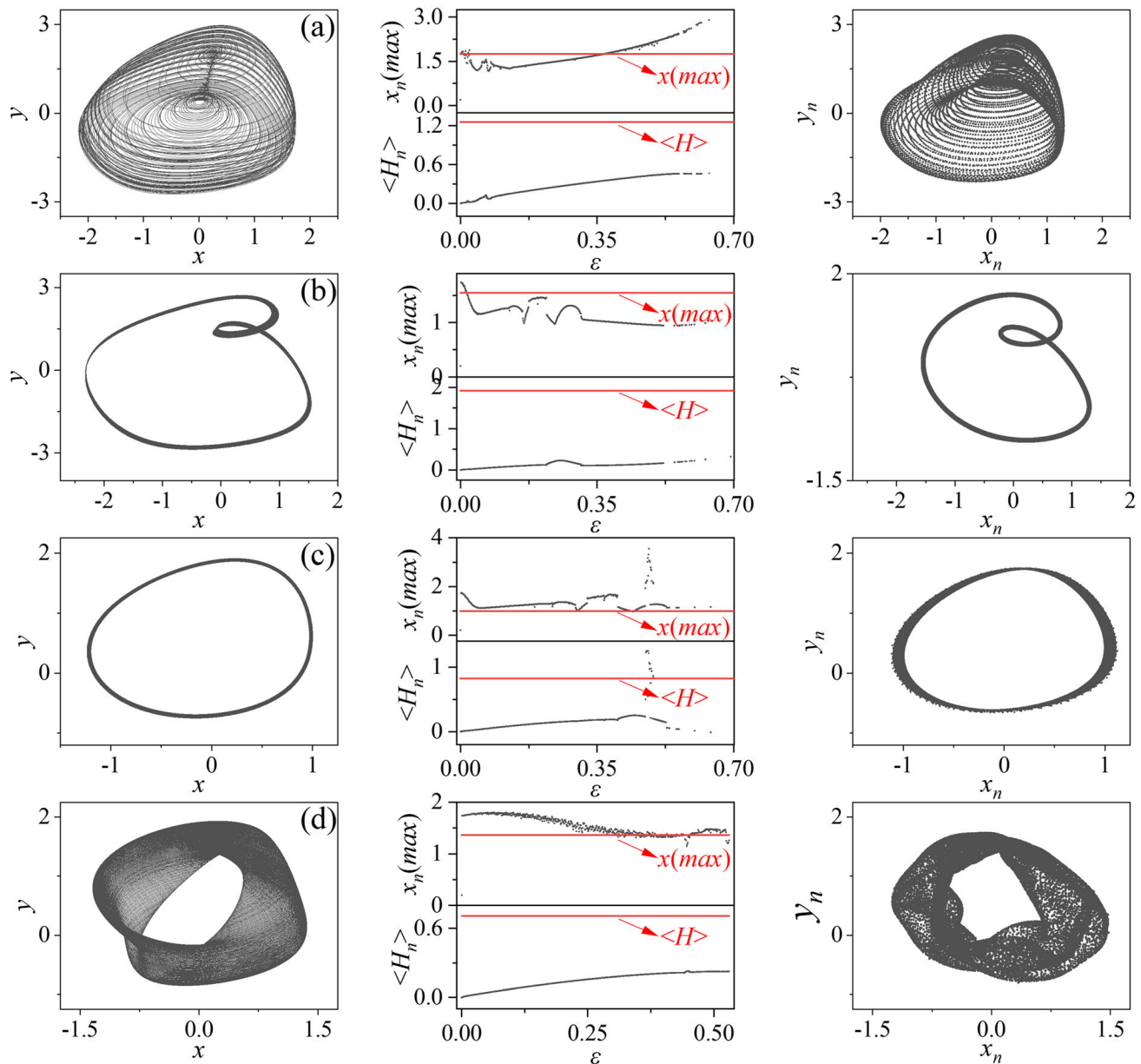


Fig. 3 Different attractors for the memristive neuron/map in Eqs. (6) and (9) under suitable scale parameter ε , and the average energy $\langle H_n \rangle$ and $x_n(\max)$ in memristive discrete neuron via

scale parameter ε . For **a** bursting $\omega = 0.035$, $\varepsilon = 0.104$; **b** spiking $\omega = 0.53$, $\varepsilon = 0.29$; **c** periodic $\omega = 1.0$, $\varepsilon = 0.0013$; **d** chaotic $\omega = 2.9$, $\varepsilon = 0.5$

For a memristive map developed from Hénon map,

$$\begin{cases} x_{n+1} = 1 + by_n - ax_n^2 - (\alpha + 3\beta\varphi_n^2)x_n; \\ y_{n+1} = x_n; \\ \varphi_{n+1} = \varphi_n + cx_n; \end{cases} \quad (15)$$

By introducing appropriate scale parameter, it obtains equivalent memristive oscillator as follows

$$\begin{cases} \frac{dx}{d\tau} = \frac{1}{\varepsilon} [1 + by - ax^2 - (\alpha + 1 + 3\beta\varphi^2)x]; \\ \frac{dy}{d\tau} = \frac{1}{\varepsilon} (x - y); \\ \frac{d\varphi}{d\tau} = \frac{c}{\varepsilon} x; \end{cases} \quad (16)$$

From dynamical viewpoint, appropriate setting for the scale parameter in Eq. (16) will reproduce similar dynamical characteristic as in Eq. (15) under setting the same parameters. In practical way, appropriate

electric components can be combined to reproduce similar signals in the analog circuit by applying suitable physical parameters for these potential electric components. Based on the Helmholtz theorem, the energy function for Eq. (16) can be defined and obtained in theoretical way. It can be expressed in the vector form containing two kinds of physical fields as follows

$$\begin{pmatrix} \dot{x} \\ \dot{y} \\ \dot{\varphi} \end{pmatrix} = F_c + F_d = \begin{pmatrix} -\frac{by}{\varepsilon} - \frac{bc}{2\varepsilon}(\alpha + 3\beta\varphi^2)x \\ \frac{x}{\varepsilon} - \frac{1}{\varepsilon}b\beta\varphi^3 \\ \frac{cx}{\varepsilon} + \frac{b\varphi y}{\varepsilon x} + \frac{bc}{2\varepsilon}(\alpha\varphi + \beta\varphi^3) \end{pmatrix} \\ + \begin{pmatrix} \frac{1}{\varepsilon}[1 + 2by - ax^2 - (\alpha + 1 + 3\beta\varphi^2)x + \frac{bc}{2}(\alpha + 3\beta\varphi^2)x] \\ -\frac{y}{\varepsilon} + \frac{1}{\varepsilon}b\beta\varphi^3 \\ -\frac{b\varphi y}{\varepsilon x} - \frac{bc}{2\varepsilon}(\alpha\varphi + \beta\varphi^3) \end{pmatrix} \\ = \begin{pmatrix} 0 & -b & -bc \\ b & 0 & -\frac{b\varphi}{x} \\ bc & \frac{b\varphi}{x} & 0 \end{pmatrix} \begin{pmatrix} \frac{x}{\varepsilon b} + \frac{1}{2\varepsilon}(\alpha\varphi + \beta\varphi^3) \\ \frac{y}{\varepsilon} \\ \frac{x}{2\varepsilon}(\alpha + 3\beta\varphi^2) \end{pmatrix} \\ + \begin{pmatrix} A_{11} & 0 & 0 \\ 0 & A_{22} & 0 \\ 0 & 0 & A_{33} \end{pmatrix} \begin{pmatrix} \frac{x}{\varepsilon b} + \frac{1}{2\varepsilon}(\alpha\varphi + \beta\varphi^3) \\ \frac{y}{\varepsilon} \\ \frac{x}{2\varepsilon}(\alpha + 3\beta\varphi^2) \end{pmatrix}; \quad (17)$$

The coefficient for the matrix in Eq. (17) is defined by

$$\begin{cases} A_{11} = \frac{1 - ax^2 - (\alpha + 1 + 3\beta\varphi^2)x + \frac{bc}{2}(\alpha + 3\beta\varphi^2)x}{\frac{1}{b}x + \frac{1}{2}(\alpha\varphi + \beta\varphi^3)}; \\ A_{22} = \frac{-y + \beta\varphi^3}{y}; \quad A_{33} = \frac{-\frac{2b\varphi y}{x} - bc(\alpha\varphi + \beta\varphi^3)}{(\alpha + 3\beta\varphi^2)x}; \end{cases} \quad (18)$$

The solution for Hamilton energy function can be suggested as follows

$$H = \frac{1}{\varepsilon}[\frac{1}{2b}x^2 + \frac{1}{2}y^2 + \frac{1}{2}(\alpha\varphi + \beta\varphi^3)x]; \quad (19)$$

As a result, the discrete energy function for Eq. (15) is updated by

$$H_n = H_1 + H_2 + H_M \\ = \frac{1}{2b}x_n^2 + \frac{1}{2}y_n^2 + \frac{1}{2}(\alpha\varphi_n + \beta\varphi_n^3)x_n; \quad (20)$$

Compared to Eq. (15), and additive scale parameter ε is introduced into Eq. (16), bifurcation analysis can be applied to detect the region for ε when other parameters are fixed the same setting for the memristive map in Eq. (15). Three terms including H_1 , H_2 and H_M mark the capacitive, inductive energy and memristive energy, respectively. To cover the same phase space, the parameter ε is changed from 0.001 to a finite threshold, and the maximal value (x_{max}) for the variable x is selected to match the maximal value $x_{max}(n)$ and then the suitable value for parameter ε will be confirmed. By taming the value for the scale parameter ε , the dynamics of the memristive map in Eq. (15) will be reproduced by memristive oscillator in Eq. (16) completely by showing the same attractor, sampled time series, maximal Lyapunov exponent, size of phase portrait in the phase space. In simple way, both the continuous and discrete systems have the same maximal value for the first variables, and it can be confirmed via bifurcation analysis with changing the parameter ε carefully. As a result, the energy function in Eq. (19) with exact parameter ε will address the energy property for the memristive map in Eq. (15) well.

In fact, there are three terms for energy sources kept in certain channels or components, and the oscillatory state is dependent on the energy shunting between these channels. Any changes of parameters in Eq. (15) will modify the oscillatory mode and the energy level in Eq. (20) will be adjusted synchronously. As a result, energy ration between the three terms will be adjusted when oscillation is changed. The energy ratio is defined in

$$\begin{cases} p_1 = \frac{H_1}{H_n} = \frac{\frac{1}{2b}x_n^2}{\frac{1}{2b}x_n^2 + \frac{1}{2}y_n^2 + \frac{1}{2}(\alpha\varphi_n + \beta\varphi_n^3)x_n}; \\ p_2 = \frac{H_2}{H_n} = \frac{\frac{1}{2}y_n^2}{\frac{1}{2b}x_n^2 + \frac{1}{2}y_n^2 + \frac{1}{2}(\alpha\varphi_n + \beta\varphi_n^3)x_n}; \\ p_3 = \frac{H_M}{H_n} = \frac{\frac{1}{2}(\alpha\varphi_n + \beta\varphi_n^3)x_n}{\frac{1}{2b}x_n^2 + \frac{1}{2}y_n^2 + \frac{1}{2}(\alpha\varphi_n + \beta\varphi_n^3)x_n}; \end{cases} \quad (21)$$

In fact, H_1 and H_2 can present capacitive and inductive energy, and the ratio $H_1:H_2$ is also effective to predict mode transition in the oscillatory states. Similar energy proportion $P_1=H_1/H$, $P_2=(H_2+H_M)/H$ can be

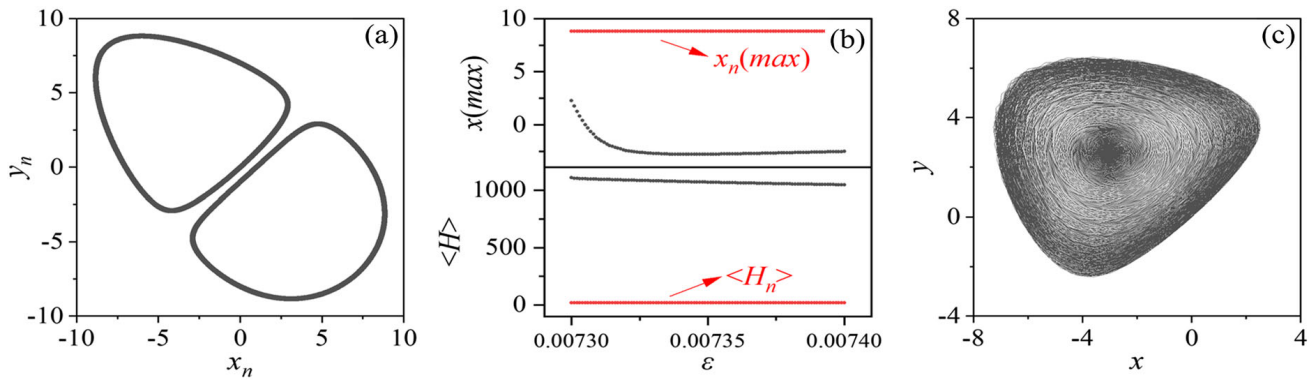


Fig. 4 **a** Attractor in memristive map in Eq. (15); **b** average energy $\langle H \rangle$ and x_{max} versus with scale parameter ε ; **c** chaotic attractor in Eq. (16) at $\varepsilon = 0.0073$. Equations (15) and (16)

defined to estimate the regulation on dynamics from capacitive and inductive energy, respectively. From the memristive map in Eq. (15) and memristive oscillator in Eq. (16), parameters can be adjusted to trigger periodic or chaotic behaviors. The involvement of scale parameter into energy function in Eq. (19) can increase the energy level directly during the conversion from memristive map to nonlinear oscillator. In Fig. 4, parameters are selected to develop chaotic attractors in the memristive map, and the same parameters and suitable scale parameter are endowed to mimic the oscillatory characteristic in the memristive map. The scale parameter is also adjusted to track the evolution of the average energy and maximal value for the variable x in the memristive oscillator in Eq. (16) as well.

Two chaotic rings are formed in the phase space for the memristive map, while chaotic attractors are induced in the memristive oscillator in Eq. (16) by taming the scale parameter $\varepsilon=0.0073$. The maximal value for the memristive map and memristive oscillator has similar oscillation, while their average energy has distinct diversity because of the involvement of scale parameter. Indeed, the scale parameter is adjusted carefully but the maximal values still show some difference even they can present similar oscillatory characteristic with time. It indicates that the

select the same parameters as $b = 1.0$, $a = 0.05$, $\alpha = 0$, $\beta = 0$, $c = 0.1$; initials $(x, y, \varphi) = (x_n, y_n, \varphi_n) = (0.02, 0.01, 0.01)$

memristive oscillator has no bridge to potential equivalent nonlinear circuits.

On the other hand, the same parameters setting for memristive map in Eq. (15) and memristive oscillator in Eq. (16) can be applied, the scale parameter ε can be adjusted to keep them in same energy level as $H=H_n$ synchronously even they can present different attractors and firing patterns. In fact, the weight for each energy term is crucial for selecting the firing patterns and mode, and the introduction of scale parameter ε seldom changes the energy proportion among the capacitive, inductive and memristive energy terms. In this way, most of the maps can be updated with equivalent oscillators, which the corresponding Hamilton energy functions are obtained by using Helmholtz theorem, the suitable energy function for the maps can be obtained by removing the scale parameters for the Hamilton energy function for the nonlinear oscillators. In Fig. 5, the scale parameter is adjusted to keep the memristive map and memristive oscillator with the same energy level by changing the scale parameter carefully and parameters for the two memristive systems are different.

When the memristive map and memristive oscillator are endowed with different parameters setting, appropriate selection of scale parameter can ensure two memristive systems keep the same energy level and same oscillatory state. In fact, the Hamilton

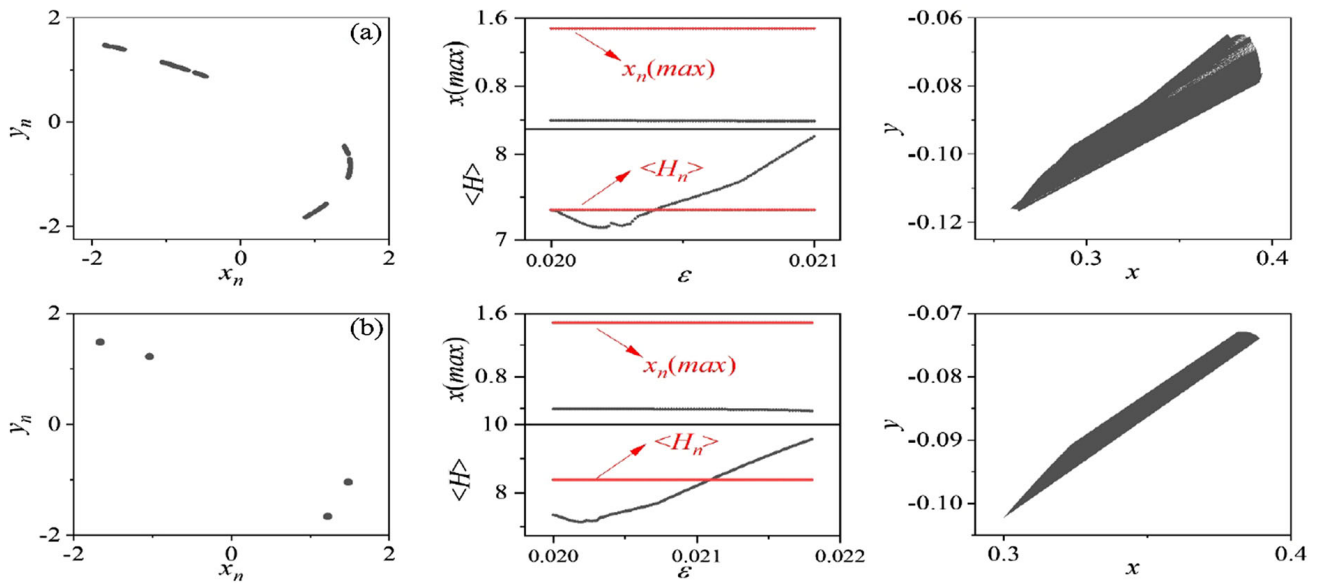


Fig. 5 Attractors in Eqs. (15) and (16) with the same energy level, average energy $\langle H \rangle$ and x_{max} versus under different value for ϵ . For **a** chaotic map, $\beta = 0.002$, $\epsilon = 0.0204$, $\beta' = 0.154$; **b** periodic map, $\beta = 0.08$, $\epsilon = 0.02109$, $\beta' = 0.154$. Setting $b = 0.1$, $a = 0.62$, $\alpha = 0.1$, $\beta = 0.01$,

$c = 0.2$ in Eq. (15); $b' = 0.102$, $a' = 1.725$, $\alpha' = 2.05$, $\beta' = 0.154$, $c' = 0.0009$ in Eq. (16); same initials $(x, y, \varphi) = (x_n, y_n, \varphi_n) = (0.02, 0.01, 0.01)$. In the figures, $x_{max} = x(max)$, $x_n(max)$ denote the maximal value in the sampled time series for two memristive systems

energy function is a kind of Lyapunov function and restricts the cooperation between different variables of the system. For physical oscillators converted from nonlinear circuits, the sole Hamilton energy is derived from the field energy including inductive, capacitive and memristive components. The weight for each term of the energy function is decided by the normalized parameters after scale transformation for all physical variables and parameters. As a result, these weights are more important in the energy function than the scale parameter. From a nonlinear oscillator to a map, continuous energy function is replaced by discrete energy function with suitable scale parameter. From a map to a continuous oscillator, the weight for each energy term can be confirmed and energy function for the map has no scale parameter, but the discrete energy function is helpful to predict the mode transition accompanying with shift in energy level.

From physical viewpoint, most of the nonlinear oscillators in mathematical form can be derived from equivalent circuit equations and mechanical systems. The activation and exchange of energy flow are

dominated by the physical properties of physical elements, which also govern the nonlinear terms in the dynamical equations and mathematical models. For most of the nonlinear circuits, the field energy can be obtained by summing the energy in each electric component, and they can be converted into dimensionless energy function after scale transformation. For generic nonlinear oscillators, the application of Helmholtz theorem provides help to get the Hamilton energy function, which is considered as a kind of Lyapunov function, and specific terms for energy terms means special electric components should be used in this circuit. Memristor is a functional electric competent, and its memristive properties throw lights for activating self-adaptive property of nonlinear terms in the physical systems and network, and energy flow can be controlled in adaptive way in presence of external field. As a result, the involvement of memristive term into dynamical systems can explain the self-controllability and adaption greatly [41–43]. Energy characteristic of nervous and neural circuits is very important [44], and physical energy in neural

circuits can be obtained in theoretical way, which Helmholtz theorem can confirm its correctness when the physical energy is converted into dimensionless Hamilton energy. In experimental way, the transient performances of the circuit should be considered [45] in the realization of analog circuits, and so the reliability of the neural circuits can be verified and evaluated.

For discrete systems and maps, scale parameter is introduced to build an equivalent nonlinear oscillator in the form of ODEs (Ordinary differential equations) and its energy function also contains the same scale parameter. Based on the Helmholtz theorem, energy function for the nonlinear oscillator is obtained and then it is discretized to denote the energy function without scale parameter for the map. In the phase space, the nonlinear oscillator will cover the same phase size and maximal value as the map when the scale parameter is adjusted carefully. For some specific maps defined in mathematical form, there are some differences in the maximal value for variables in the map and nonlinear oscillator. Referring to the energy characteristic of the known electric components, the generic form of the Hamilton energy function can be suggested, and scale parameter is introduced to confirm its exact value when the nonlinear oscillator model matches with the map in phase space completely. The scheme can be further used to explore the formation of defects and heterogeneity [46, 47] in discrete networks when energy function for each node is estimated exactly.

For obtaining exact energy function for generic maps, equivalent nonlinear oscillators can be designed by defining appropriate transformation for the parameters and discrete variables as follows.

$$\begin{cases} x_{n+1} = f(x_n, \lambda) \Rightarrow \frac{dy}{d\tau} = f(y, p), y = \{y_1, y_2, \dots, y_n, \dots\}; \\ \lambda = \lambda(p, h), x_n = x_n(y_n, h, p); \text{ or} \\ p = p(\lambda, h), y_n = y_n(x_n, h, \lambda); h \text{ is time step} \end{cases} \quad (22)$$

where the map and continuous oscillator has the same local kinetics but the parameters and variables have certain relevance, that is, the parameter p differs from λ for presenting the same dynamics. For

example, the Logistic map can be described by a Logistic oscillator by using the transformation in Eq. (22) [48].

4 Conclusions

In this work, field energy for a memristor-coupled circuit is defined and its equivalent dimensionless Hamilton energy for the memristive oscillator is obtained by applying scale transformation. The approach of energy function is also confirmed by using Helmholtz theorem. The memristive oscillator is reduced into discrete map and its equivalent energy form is obtained by setting suitable scale parameter. Keeping the same dynamical characteristics, memristive map shows lower energy level than the memristive oscillator. In addition, a memristive map developed from Hénon map added with memristive term is integrated into equivalent continuous oscillator by introducing suitable scale parameter, and its energy function is approached in theoretical way. Furthermore, discrete energy function is confirmed to describe the energy characteristic of the memristive Hénon map. This scheme can be further used to estimate the energy function for other discrete systems even discrete memristor is coupled. That is, maps are updated with equivalent nonlinear oscillators for getting theoretical energy function with scale parameter, and the generic energy function for the map can be obtained by removing the scale parameter for the energy function of its equivalent nonlinear oscillator.

Acknowledgements This project is supported by the National Natural Science Foundation of China under Grant Nos. 12072139.

Funding The authors have not disclosed any funding.

Data availability The data are available upon reasonable request.

Declarations

Conflict of interest The authors declare that they have no conflict of interest with this publication.

Appendix

$$\begin{cases} A_{11} = \frac{i'_s + (a' + b'z^2)(x - e_1) - (c' + d'w^2)(x - e_2) + x - \frac{1}{2}x^2 - \frac{1}{3}x^3 + \frac{1}{2}(x - e_1)(a' + 3b'z^2) + \frac{1}{2}c'(x - e_2)}{x + \frac{1}{2}(a'z + b'z^3) + \frac{1}{2}w} \\ A_{22} = \frac{\alpha^2[e - \xi y - \frac{1}{2}(a'z + b'z^3) - \frac{1}{2}w - \frac{3b'}{2a'}z^2(x - e_1) - \frac{1}{2}(e_2 - e_1)]}{-2e_1 - (a'z + b'z^3) - w + 2\frac{y}{a'}} \\ A_{33} = \frac{(x - e_1)(a' + 3b'z^2)}{-2c'e_2 + 2d'w^2(x - e_2) - c'(a'z + b'z^3) - c'w - 2y} \\ A_{44} = \frac{(x - e_2)}{(x - e_2)} \end{cases} \quad (A1)$$

$$\begin{pmatrix} \dot{x} \\ \dot{y} \\ \dot{z} \\ \dot{w} \end{pmatrix} = F_c + F_d = \begin{pmatrix} -y - \frac{1}{2}(x - e_1)(a' + 3b'z^2) - \frac{1}{2}c'(x - e_2) \\ \alpha x + \frac{1}{2}\alpha(a'z + b'z^3) + \frac{1}{2}\alpha w + \frac{3\alpha b'}{2a'}z^2(x - e_1) + \frac{1}{2}\alpha(e_2 - e_1) \\ x + \frac{1}{2}(a'z + b'z^3) + \frac{1}{2}w - \frac{y}{a'} \\ c'x + \frac{1}{2}c'a'z + b'z^3 + \frac{1}{2}c'w + y \end{pmatrix} \\ + \begin{pmatrix} i'_s + (a' + b'z^2)(x - e_1) - (c' + d'w^2)(x - e_2) + x - \frac{1}{2}x^2 - \frac{1}{3}x^3 + \frac{1}{2}(x - e_1)(a' + 3b'z^2) + \frac{1}{2}c'(x - e_2) \\ \alpha e - \alpha\xi y - \frac{1}{2}\alpha(a'z + b'z^3) - \frac{1}{2}\alpha w - \frac{3\alpha b'}{2a'}z^2(x - e_1) - \frac{1}{2}\alpha(e_2 - e_1) \\ -e_1 - \frac{1}{2}(a'z + b'z^3) - \frac{1}{2}w + \frac{y}{a'} \\ -c'e_2 + d'w^2(x - e_2) - \frac{1}{2}c'(a'z + b'z^3) - \frac{1}{2}c'w - y \end{pmatrix}; \\ = \begin{pmatrix} 0 & -\alpha & -1 & -c' \\ \alpha & 0 & \frac{\alpha}{a'} & -\alpha \\ 1 & -\frac{\alpha}{a'} & 0 & 0 \\ c' & \alpha & 0 & 0 \end{pmatrix} \begin{pmatrix} x + \frac{1}{2}(a'z + b'z^3) + \frac{1}{2}w \\ \frac{y}{a'} \\ \frac{1}{2}(x - e_1)(a' + 3b'z^2) \\ \frac{1}{2}(x - e_2) \end{pmatrix} + \begin{pmatrix} A_{11} & 0 & 0 & 0 \\ 0 & A_{22} & 0 & 0 \\ 0 & 0 & A_{33} & 0 \\ 0 & 0 & 0 & A_{44} \end{pmatrix} \begin{pmatrix} x + \frac{1}{2}(a'z + b'z^3) + \frac{1}{2}w \\ \frac{y}{a'} \\ \frac{1}{2}(x - e_1)(a' + 3b'z^2) \\ \frac{1}{2}(x - e_2) \end{pmatrix}; \quad (A2)$$

References

1. Kavehei, O., Iqbal, A., Kim, Y.S., et al.: The fourth element: characteristics, modelling and electromagnetic theory of the memristor. *Proc. Royal Soc. A: Math. Phys. Eng. Sci.* **466**, 2175–2202 (2010)
2. Yeşil, A., Babacan, Y., Kaçar, F.: A new DDCC based memristor emulator circuit and its applications. *Microelectron. J.* **45**, 282–287 (2014)
3. Zidan, M.A., Fahmy, H.A.H., Hussain, M.M., et al.: Memristor-based memory: the sneak paths problem and solutions. *Microelectron. J.* **44**, 176–183 (2013)
4. Wang, L., Yang, C.H., Wen, J., et al.: Overview of emerging memristor families from resistive memristor to spintronic memristor. *J. Mater. Sci.: Mater. Electron.* **26**, 4618–4628 (2015)
5. Goswami, S., Pramanick, R., Patra, A., et al.: Decision trees within a molecular memristor. *Nature* **597**, 51–56 (2021)
6. Kuznetsov, N., Mokaev, T., Ponomarenko, V., et al.: Hidden attractors in Chua circuit: mathematical theory meets physical experiments. *Nonlinear Dyn.* **111**, 5859–5887 (2023)
7. Wang, E., Yan, S., Sun, X., et al.: Analysis of bifurcation mechanism of new hyperchaotic system, circuit

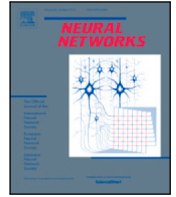
- implementation, and synchronization. *Nonlinear Dyn.* **111**, 3869–3885 (2023)
8. Vijay, S.D., Thamilaran, K., Ahamed, A.I.: Superextreme spiking oscillations and multistability in a memristor-based Hindmarsh-Rose neuron model. *Nonlinear Dyn.* **111**, 789–799 (2023)
 9. Xu, H., Zhang, Z., Peng, M.: Novel bursting patterns and the bifurcation mechanism in a piecewise smooth Chua's circuit with two scales. *Nonlinear Dyn.* **108**, 1755–1771 (2022)
 10. Zhang, X., Ma, J.: Wave filtering and firing modes in a light-sensitive neural circuit. *J. Zhejiang Univ. Sci. A* **9**, 707–720 (2021)
 11. Guan, M.J., Liao, W.H.: On the equivalent circuit models of piezoelectric ceramics. *Ferroelectrics* **386**, 77–87 (2009)
 12. Karthikeyan, A., Cimen, M.E., Akgul, A., et al.: Persistence and coexistence of infinite attractors in a fractal Josephson junction resonator with unharmonic current phase relation considering feedback flux effect. *Nonlinear Dyn.* **103**, 1979–1998 (2021)
 13. Zhang, Y., Xu, Y., Yao, Z., et al.: A feasible neuron for estimating the magnetic field effect. *Nonlinear Dyn.* **102**, 1849–1867 (2020)
 14. Xie, Y., Yao, Z., Hu, X., et al.: Enhance sensitivity to illumination and synchronization in light-dependent neurons. *Chin. Phys. B* **30**, 120510 (2021)
 15. Liu, Y., Xu, W., Ma, J., et al.: A new photosensitive neuron model and its dynamics. *Front. Informa. Technol. Electron. Eng.* **21**, 1387–1396 (2020)
 16. Ibrahim, O., Hassan, S.M., Abdulkarim, A., et al.: Design of wheatstone bridge based thermistor signal conditioning circuit for temperature measurement. *J. Eng. Sci. Technol. Rev.* **12**, 12–17 (2019)
 17. Naveen Kumar, V., Lakshmi Narayana, K.V.: Development of thermistor signal conditioning circuit using artificial neural networks. *IET Sci. Meas. Technol.* **9**, 955–961 (2015)
 18. Groschner, L.N., Malis, J.G., Zuidinga, B., et al.: A biophysical account of multiplication by a single neuron. *Nature* **603**, 119–123 (2022)
 19. Ma, J.: Biophysical neurons, energy, and synapse controllability: a review. *J. Zhejiang Univ. Sci. A* **24**, 109–129 (2023)
 20. Wu, F., Hu, X., Ma, J.: Estimation of the effect of magnetic field on a memristive neuron. *Appl. Math. Comput.* **432**, 127366 (2022)
 21. Wu, F., Ma, J., Zhang, G.: A new neuron model under electromagnetic field. *Appl. Math. Comput.* **347**, 590–599 (2019)
 22. Di Maio, V., Santillo, S., Ventriglia, F.: Synaptic dendritic activity modulates the single synaptic event. *Cogn. Neurodyn.* **15**, 279–297 (2021)
 23. Wang, C., Yao, Z., Xu, W., et al.: Phase synchronization between nonlinear circuits by capturing electromagnetic field energy. *Mod. Phys. Lett. B* **34**, 2050323 (2020)
 24. Zhou, P., Ma, J., Tang, J.: Clarify the physical process for fractional dynamical systems. *Nonlinear Dyn.* **100**, 2353–2364 (2020)
 25. Zhou, P., Zhang, X., Hu, X., et al.: Energy balance between two thermosensitive circuits under field coupling. *Nonlinear Dyn.* **110**, 1879–1895 (2022)
 26. Ren, L., Lin, M.H., Abdulwahab, A., et al.: Global dynamical analysis of the integer and fractional 4D hyperchaotic Rabinovich system. *Chaos, Solit. Fract.* **169**, 113275 (2023)
 27. Leutcho, G.D., Khalaf, A.J.M., Njitacke Tabekoueng, Z., et al.: A new oscillator with mega-stability and its Hamilton energy: infinite coexisting hidden and self-excited attractors. *Chaos* **30**, 033112 (2020)
 28. Njitacke, Z.T., Takembo, C.N., Awrejcewicz, J., et al.: Hamilton energy, complex dynamical analysis and information patterns of a new memristive FitzHugh-Nagumo neural network. *Chaos, Solit. Fract.* **160**, 112211 (2022)
 29. Rong, K., Bao, H., Li, H., et al.: Memristive Hénon map with hidden Neimark-Sacker bifurcations. *Nonlinear Dyn.* **108**, 4459–4470 (2022)
 30. Peng, Y., Sun, K., He, S.: A discrete memristor model and its application in Hénon map. *Chaos, Solitons Fractals* **137**, 109873 (2020)
 31. Fouda, M.E., Radwan, A.G.: Charge controlled memristor-less memcapacitor emulator. *Electron. Lett.* **48**, 1454–1455 (2012)
 32. Petrović, P.B.: Charge-controlled grounded memristor emulator circuits based on Arbel-Goldminz cell with variable switching behaviour. *Analog Integr. Circ. Sig. Process* **113**, 373–381 (2022)
 33. Yang, F., Xu, Y., Ma, J.: A memristive neuron and its adaptability to external electric field. *Chaos* **33**, 023110 (2023)
 34. Lin, R., Shi, G., Qiao, F., et al.: Research progress and applications of memristor emulator circuits. *Microelectron. J.* **133**, 105702 (2023)
 35. Yao, Z., Zhou, P., Alsaedi, A., et al.: Energy flow-guided synchronization between chaotic circuits. *Appl. Math. Comput.* **374**, 124998 (2020)
 36. Bao, B., Hu, J., Cai, J., et al.: Memristor-induced mode transitions and extreme multistability in a map-based neuron model. *Nonlinear Dyn.* **111**, 3765–3779 (2023)
 37. Vijayakumar, M.D., Natiq, H., Meli, M.I.T., et al.: Hamiltonian energy computation of a novel memristive mega-stable oscillator (MMO) with dissipative, conservative and repelled dynamics. *Chaos, Solit. Fract.* **155**, 111765 (2022)
 38. Wang, G., Xu, Y., Ge, M., et al.: Mode transition and energy dependence of FitzHugh-Nagumo neural model driven by high-low frequency electromagnetic radiation. *AEU-Int. J. Electron. Commun.* **120**, 153209 (2020)
 39. Xie, Y., Zhou, P., Ma, J.: Energy balance and synchronization via inductive-coupling in functional neural circuits. *Appl. Math. Model.* **113**, 175–187 (2023)
 40. Kobe, D.H.: Helmholtz's theorem revisited. *Am. J. Phys.* **54**, 552–554 (1986)
 41. Song, F., Liu, Y., Shen, D., et al.: Learning control for motion coordination in wafer scanners: toward gain adaptation. *IEEE Trans. Industr. Electron.* **69**, 13428–13438 (2022)
 42. Zhang, C., Kordestani, H., Shadabfar, M.: A combined review of vibration control strategies for high-speed trains and railway infrastructures: challenges and solutions. *J. Low Freq. Noise Vib. Active Control* **42**, 272–291 (2023)
 43. Li, D., Yu, H., Tee, K.P., et al.: On time-synchronized stability and control. *IEEE Trans. Syst. Man Cyber. Syst.* **52**, 2450–2463 (2021)

44. Wang, R., Wang, Y., Xu, X., et al.: Brain works principle followed by neural information processing: a review of novel brain theory. *Artif. Intell. Rev.* (2023). <https://doi.org/10.1007/s10462-023-10520-5>
45. Xia, C., Zhu, Y., Zhou, S., et al.: Simulation study on transient performance of a marine engine matched with high-pressure SCR system. *Int. J. Engine Res.* **24**, 1327–1345 (2023)
46. Yang, F., Wang, Y., Ma, J.: Creation of heterogeneity or defects in a memristive neural network under energy flow. *Commun. Nonlinear Sci. Numer. Simul.* **119**, 107127 (2023)
47. Xie, Y., Yao, Z., Ma, J.: Formation of local heterogeneity under energy collection in neural networks. *Sci. China Technol. Sci.* **66**, 439–455 (2023)
48. Shen, B. W., Pielke, R. A. Sr, Zeng, X.: The 50th Anniversary of the Metaphorical Butterfly Effect since

Lorenz (1972): Multistability, Multiscale Predictability, and Sensitivity in Numerical Models. *Atmosphere*, 14(8): 1279 (2023)

Publisher's Note Springer Nature remains neutral with regard to jurisdictional claims in published maps and institutional affiliations.

Springer Nature or its licensor (e.g. a society or other partner) holds exclusive rights to this article under a publishing agreement with the author(s) or other rightsholder(s); author self-archiving of the accepted manuscript version of this article is solely governed by the terms of such publishing agreement and applicable law.



Full Length Article

Energy controls wave propagation in a neural network with spatial stimuli

Yitong Guo^a, Mi Lv^b, Chunni Wang^{c,*}, Jun Ma^{a,c}^a College of Electrical and Information Engineering, Lanzhou University of Technology, Lanzhou, 730050, Gansu, PR China^b Faculty of Engineering, China University of Petroleum-Beijing at Karamay, Karamay, 834000, Xinjiang, PR China^c Department of Physics, Lanzhou University of Technology, Lanzhou, 730050, Gansu, PR China

ARTICLE INFO

Keywords:

Coherence resonance
Neural circuit
Hamilton energy
Synaptic growth
Energy balance

ABSTRACT

Nervous system has distinct anisotropy and some intrinsic biophysical properties enable neurons present various firing modes in neural activities. In presence of realistic electromagnetic fields, non-uniform radiation activates these neurons with energy diversity. By using a feasible model, energy function is obtained to predict the growth of synaptic connections of these neurons. Distribution of average value of the Hamilton energy function vs. intensity of noisy disturbance can predict the occurrence of coherence resonance, which the neural activities show high regularity by applying noisy disturbance with moderate intensity. From physical viewpoint, the average energy value has similar role average power for the neuron. Non-uniform spatial disturbance is applied and energy is injected into the neural network, statistical synchronization factor is calculated to predict the network synchronization stability and wave propagation. The intensity for field coupling is adaptively controlled by energy diversity between adjacent neurons. Local energy balance will terminate further growth of the coupling intensity; otherwise, heterogeneity is formed in the network due to energy diversity. Furthermore, memristive channel current is introduced into the neuron model for perceiving the effect of electromagnetic induction and radiation, and a memristive neuron is obtained. The circuit implement of memristive circuit depends on the connection to a magnetic flux-controlled memristor into the mentioned neural circuit in an additive branch circuit. The connection and activation of this memristive neural network are controlled under external spatial electromagnetic radiation by capturing enough field energy. Continuous energy collection and exchange generate energy diversity and synaptic connection is created to regulate the synchronous firing patterns and energy balance.

1. Introduction

Neural activities require continuous energy supply and mode transition in neurons means switch in energy levels. Biological neurons have certain diversity in the excitability and they can present different firing patterns under external excitations. The collective electrical behaviors of nervous system can be expressed by using neural networks applying with different biophysical settings. Gradient stimuli can inject different energy flow into the neurons, and wave propagation is activated to keep local energy balance between adjacent neurons. The synaptic intensity is controlled by the energy diversity between adjacent neurons, and they can reach high synchronization level by increasing the coupling intensity adaptively. Biological neurons have distinct biophysical characteristics and their electrical activities can be reproduced by some equivalent neural circuits, which can be further developed to obtain reliable neuron models (Druckmann et al., 2011; Kepecs & Wang, 2000; Lengler, Jug, & Steger, 2013; Lim et al., 2015; Pakdaman, Tanabe, & Shimokawa, 2001). The physical property of inner and outer cell

membranes can be similar to an ideal capacitor, and the propagation of ions along the channels embedded into the cell membrane is the same as channel current across an induction coil. The intracellular ions can generate electric field and any pumping of these ions and channel current can induce magnetic field. Therefore, energy between magnetic field and electric field is converted bidirectionally and nonlinear relation enables its nonlinear oscillation in the membrane potentials. In practical way, a generic simple RLC (nonlinear resistor, inductor, and capacitor) circuit can be built and adjusted to reproduce similar firing patterns as biological neurons. The circuit equations and field energy can be described by equivalent theoretical models (Aberra, Peterchev, & Grill, 2018; Gerstner & Naud, 2009; Herz et al., 2006; Kafraj, Parastesh, & Jafari, 2020; Van Geit, De Schutter, & Achard, 2008) and Hamilton energy functions (Njitacke et al., 2022, 2021; Wang et al., 2017; Yang et al., 2021; Zhang et al., 2023), respectively.

In fact, biological neurons have developed different biophysical functions for perceiving a variety of external signals. For example,

* Corresponding author.

E-mail address: wangcn05@163.com (C. Wang).<https://doi.org/10.1016/j.neunet.2023.11.042>

Received 7 September 2023; Received in revised form 16 October 2023; Accepted 19 November 2023

Available online 30 November 2023

0893-6080/© 2023 Elsevier Ltd. All rights reserved.

visual neurons (Butts, 2019; Gabbiani et al., 2002; Wang et al., 2018) can encode external lights into electric signals and its equivalent circuit realization accounts for photoelectric conversion via phototube or photocell (Hussain et al., 2021; Xie et al., 2021). Auditory neurons (Cao, Gu, & Ma, 2022; Cao, Gu, & Wang, 2022; Demanez & Demanez, 2003) can discern voice by converting sounds and mechanical vibration into electric signals and its effective acoustoelectric conversion resembles activation of piezoelectric elements (Guo et al., 2021; Wang et al., 2021) connecting to a neural circuit. Realistic neurons and artificial neurons can be capable for perceiving more physical signals including electromagnetic field and keeping silence to some signals via wave filtering. In particular, electromagnetic induction and radiation (EMIR) in neurons should be estimated and clarified in theoretical way. That is, combination of suitable electric components including memristor (Babacan, Kaçar, & Gürkan, 2016; Lin et al., 2020; Tan & Wang, 2020; Yi et al., 2018) and Josephson junction (Dana, Sengupta, & Hu, 2006; Foka et al., 2021) can build some functional circuits and then they are mapped into equivalent biophysical neurons (Clark et al., 2022; Gjorgjieva, Drion, & Marder, 2016; Mondal et al., 2019; Yu, Sejnowski, & Cauwenberghs, 2011) to discuss the physical effects on neural activities in possible way. In general way, bifurcation analysis and nonlinear resonance can be analyzed within these mathematical or biophysical neurons, and these oscillator-like neurons can also be connected in different networks for developing spatial patterns, and multiple firing modes are induced under noise (Bao et al., 2022; Wojewoda et al., 2021; Yuan et al., 2022). When the local kinetics is described the same neuron, the competition between identical neurons and controllability in coupling channels (synaptic connections) are crucial for taming the pattern formation. When the clustered neurons from different community networks are connected and controlled, the cooperation between neurons from different functional regions (Yao & Wang, 2021, 2022) can be investigated.

Noisy disturbances on the neurons can be described by imposing suitable excitations including noise on the membrane potential or magnetic flux variables. The activation of biological neurons needs enough metabolizable energy, from physical viewpoint, the capacitive and inductive energy are very important for supporting continuous neural activities during the diffusion and propagation of intracellular and extracellular ions. When a biophysical neuron is mimicked by an equivalent neural circuit, the energy function for the neuron can be mapped from the field energy for the neural circuit. Similar coherence resonance can be found, and the average energy can discern the occurrence of coherence resonance in the neuron under noise. By applying suitable stimulus, logistic and chaotic resonance can be induced in most of the neuron models (Yao et al., 2021; Yu et al., 2023). The appearance of spiral wave, Turing patterns in the neural networks and excitable media shows adaptive self-organization of cells (Chen et al., 2018, 2019; Ding et al., 2023; Hu et al., 2023). The formation of spatial patterns are controlled by the distribution of energy levels of neurons, adaptive local energy balance via synaptic coupling or field coupling is helpful to develop special patterns when energy flow is propagated in the neural network. From physical viewpoint, energy level in each neuron controls the network patterns by adjusting the coupling intensity adaptively. Any external energy injection can change the energy level to keep energy balance with adjacent neurons.

Electromagnetic radiation and external stimuli can inject energy into the nervous system and the neural activities are regulated under polarization and magnetization (Lu, Yi, & Liu, 2022). Therefore, control of energy flow is effective to control the firing patterns in neurons and networks (Zhang et al., 2021), for example, changes of energy level in neurons account for adaptive parameter shift and energy diversity supports desynchronization between neurons (Hou, Zhou, Ren, et al., 2023; Wu, Guo, & Ma, 2023; Xie, Xu, & Ma, 2023; Yang, Xu, & Ma, 2023). Inspired by the specific physical property of memristors, memristive

term and magnetic flux variable are introduced to describe the effect of electromagnetic induction on a neuron, and the memristive neuron is suitable for detecting electromagnetic radiation and energy function is defined to explain the self-adaption of field coupling under energy flow. In this paper, we will consider the cooperation and competition in a neural network exposed to non-uniform electromagnetic radiation; synaptic coupling is activated between neurons without considering electromagnetic induction the coupling intensity is increased before reaching local energy balance between neurons. Furthermore, a memristive neuron is suggested and used to explore the pattern formation and synchronization by activating field coupling in an adaptive way, the energy function is also calculated and the energy diversity between adjacent neurons controls the adaptive growth of coupling intensity.

2. Model and scheme

The main biophysical property in a biological neuron can be reproduced in a simple neural circuit by incorporating appropriate electric components. A capacitor can describe the capacitance property of cell intima and outer membrane, an inductor can represent the inductance property of ion channel, and a constant voltage into a branch circuit connected with inductor denotes the property of reverse potential. In particular, nonlinear resistor bridges nonlinear relation between the magnetic field and electric field energy. As a result, spiking, bursting and even chaotic firing patterns can be generated in most of the nonlinear circuits. Furthermore, the components such as memristor, thermistor, piezoelectric ceramics, phototube and Josephson junction are connected to optimize the physical function of the neural circuits and the distinct self-adaption can be explained and understood. In the recent work, a similar Hindmarsh–Rose (HR) neuron model is suggested and its potential physical property is clarified (Xie, Yao, Ren, et al., 2023). The simple neuron composing two variables is described by

$$\begin{cases} \frac{dx}{d\tau} = \dot{x} = -w - ax^3 + bx^2 + I_{ext}; \\ \frac{dw}{d\tau} = \dot{w} = -c + dx^2 + rs(x - \lambda) - rw; \end{cases} \quad (1)$$

where the variables (x, w) represent the membrane potential and channel current, respectively. I_{ext} denotes equivalent transmembrane current, λ estimates the resting potential for ion channel, and (a, b, c, r, s) are normalized parameters. For a two-variable neuron, periodic form for $I_{ext} = A \cos(\omega\tau)$ can be applied to induce mode transition and present chaotic patterns by taming the amplitude or angular frequency. It shows some difference from the previous HR family because a voltage-controlled electric component (VCEC) is used to control the channel current. The current across the nonlinear resistor (NR), VCEC and constant voltage in the neural circuit is defined as follows

$$\begin{cases} V_M = -\frac{d}{rsV_0} V^2; \\ E = \frac{c}{rs} V_0 + \lambda V_0; \\ i_{NR} = -\frac{1}{\rho} \left(\frac{bV^2}{V_0} - \frac{aV^3}{V_0^2} \right); \end{cases} \quad (2)$$

where ρ and V_0 are intrinsic parameters in NR passing with channel current i_{NR} , V and V_M represent output voltage for the capacitor and VCEC, respectively. When these ions are diffused in neuron or pumped across the cell membrane for a biological neuron, the energy in the neuron is exchanged and distribution of electromagnetic field is regulated. Therefore, the energy level accounts for the mode selection in neural activities. By applying the Helmholtz theorem (Kobe, 1986), the energy function H satisfies the following criterion

$$\begin{cases} \nabla H^T F_c(X) = 0; \\ \frac{dH}{d\tau} = \nabla H^T F_d(X); \\ \frac{dX}{d\tau} = F_c(X) + F_d(X), X \in \mathbb{R}^N; \end{cases} \quad (3)$$

The neuron model in Eq. (1) can be presented in a vector form

$$\begin{aligned} \begin{pmatrix} \dot{x} \\ \dot{w} \end{pmatrix} &= \begin{pmatrix} -w - ax^3 + bx^2 + I_{ext} \\ -c + dx^2 - rw + rs(x - \lambda) \end{pmatrix} = F_c + F_d \\ &= \begin{pmatrix} -w - dx^2 \\ rsx + 2dxw \end{pmatrix} + \begin{pmatrix} -ax^3 + (b+d)x^2 + I_{ext} \\ dx^2 - rs\lambda - c - rw - 2dxw \end{pmatrix} \\ &= \begin{pmatrix} 0 & -1 \\ 1 & 0 \end{pmatrix} \begin{pmatrix} 2dxw + rsx \\ w + dx^2 \end{pmatrix} \\ &+ \begin{pmatrix} \frac{-ax^3 + (b+d)x^2 + I_{ext}}{dx^2 + rsx} & 0 \\ 0 & \frac{dx^2 - rs\lambda - c - rw - 2dxw}{w} \end{pmatrix} \begin{pmatrix} 2dxw + rsx \\ w + dx^2 \end{pmatrix}; \end{aligned} \quad (4)$$

The Hamilton energy H is obtained under the criterion in Eq. (3)

$$\begin{cases} (-w - dx^2) \frac{\partial H}{\partial x} + (w + dx^2) \frac{\partial H}{\partial w} = 0; \\ H = H_C + H_L + H_M = \frac{1}{2}rsx^2 + \frac{1}{2}w^2 + dx^2w; \end{cases} \quad (5)$$

HR neuron discards channel property and the function Hamilton energy has many forms. Indeed, the Hamilton energy becomes sole when it is converted from the physical field energy in the equivalent neural circuit. In the previous works (Bao et al., 2018; Cai et al., 2022, 2021; Heidarpur, Ahmadi, & Kandalaf, 2017; Ochs & Jenderny, 2021), different schemes are suggested to reproduce the dynamical properties in the HR model by setting a variety of neural circuits, memristor is also coupled to improve the physical property of these equivalent neural circuits and memristive effect is estimated (Etémé et al., 2021; Li & Zhou, 2021; Usha & Subha, 2019; Vijay, Thamilmaran, & Ahamed, 2022). Considering the physical property VCEC, energy is consumed and exchanged in this specific component. Any changes in the parameters (r, s, d) will control the energy flow in this neuron, and the firing activities will be changed synchronously (Xie, Yao, Ren, et al., 2023). Simple mathematical neuron just encodes finite information and appropriate firing mode can be selected in presence of external stimuli and parameter shift. Under noisy disturbance, coherence resonance and even stochastic resonance can be induced in Eq. (1). Showing in the recent works (Hou, Ma, & Yang, 2023; Wang, Sun, & Ren, 2023; Xie, Yao, & Ma, 2022; Xie, Zhou, & Ma, 2023; Zhou, Zhang, & Ma, 2022), each neuron contains certain inner electromagnetic energy approached by equivalent Hamilton energy, and energy diversity will force the synaptic connections to clustered neurons until reach energy balance. Therefore, more neurons are guided to connect adjacent neurons for fast energy exchange and energy balance by increasing the coupling intensity adaptively. In particular, parameter shifts can be induced and heterogeneity is created to keep local energy balance in the neural networks (Xie, Yao, & Ma, 2023; Yang, Wang, & Ma, 2023). It is worthy of exploring the self-organization in the neural network under two different cases. Most of the neurons show certain diversity in the biophysical properties and these functional regions are regulated to cooperate for processing signals in the brain. In addition, electromagnetic radiation and spatial stimuli can be non-uniform. Therefore, each neuron in the network will suffer from different stimuli defined by using a spatial function. External noisy disturbance often results from the uncertain changes in field and energy injection will induce equivalent current in the channel and disturbance on the membrane potential.

Case 1 Collective activities and energy balance in neural network without electromagnetic induction.

For simplicity, we consider a chain network and adjacent neurons are forced to couple two adjacent neurons under energy diversity and the spatial stimulus $I_{ext} = A \cos(\omega\tau + i\alpha)$ is applied on the i th neuron, the constant α is relative to the media property of the neuron. The dynamics is described by

$$\begin{cases} \frac{dx_i}{d\tau} = -w_i - ax_i^3 + bx_i^2 + A \cos(\omega\tau + i\alpha) + k_i(x_{i+1} - 2x_i + x_{i-1}) + \eta(\tau); \\ \frac{dw_i}{d\tau} = -c + dx_i^2 + rs(x_i - \lambda) - rw_i; \\ \frac{dk_i}{d\tau} = \sigma \cdot k_i \vartheta(\Delta H_i - \varepsilon), \vartheta(p) = 1, p \geq 0, \vartheta(p) = 0, p < 0; \end{cases} \quad (6)$$

where the coupling intensity k_i is controlled by the energy diversity between adjacent neurons and it increases to constant value under local energy balance. The statistical property of the membrane noise with intensity D on the i th neuron is approached by $\langle \eta(\tau)\eta(\tau') \rangle = 2D\delta(\tau - \tau')$, the gain σ restricts the growth ratio for k_i . The constant α is relative to the media property, $\alpha = 0.5\pi$, π will make spatial stimuli present periodic type, and neurons show difference in the firing modes and excitability. For identical oscillators, further increasing the coupling intensity can enable realization of complete synchronization and homogeneous state in the network. However, gradient stimuli will inject energy with diversity and neurons become different under shape deformation, and some neurons just reach local energy balance rather than stabilizing synchronization. For statistical estimation, synchronization factor (SF) is defined to predict the synchronization degree,

$$SF = \frac{\langle F^2 \rangle - \langle F \rangle^2}{\frac{1}{N} \sum_{i=1}^N (\langle x_i^2 \rangle - \langle x_i \rangle^2)}; \quad F = \frac{1}{N} \sum_{i=1}^N x_i; \quad (7)$$

The symbol $\langle * \rangle$ estimates the average value of any variable within a transient period (running time in numerical approach), and lower value for SF means pattern formation in the network composed of N nodes. A higher value for SF confirms occurrence of perfect synchronization in the network. The energy diversity between adjacent neurons to the i th neuron is given in

$$\begin{aligned} \Delta H_i &= |H_{i+1} - H_i| + |H_{i-1} - H_i| \\ &= \left| \frac{1}{2}rsx_{i+1}^2 + \frac{1}{2}w_{i+1}^2 + dx_{i+1}^2w_{i+1} - \frac{1}{2}rsx_i^2 - \frac{1}{2}w_i^2 - dx_i^2w_i \right| \\ &+ \left| \frac{1}{2}rsx_{i-1}^2 + \frac{1}{2}w_{i-1}^2 + dx_{i-1}^2w_{i-1} - \frac{1}{2}rsx_i^2 - \frac{1}{2}w_i^2 - dx_i^2w_i \right|; \end{aligned} \quad (8)$$

It indicates that the adjacent neurons reach local energy balance and the intensity of synaptic coupling will get a saturation value when a few neurons are synchronized completely. On the other hand, stable complete synchronization in the network means all the neurons reach energy balance. Therefore, global energy balance is helpful for keeping complete synchronization while local energy balance can support the property diversity and formation of regular patterns generated by local defects or heterogeneity in the network. Therefore, electric synapses are created and the synaptic intensity for each pair of neurons is regulated by the energy diversity when the neural network is suffered from spatial excitations. In fact, the parameters (A, α) in the spatial stimuli can be adjusted to detect the collective responses in the neural network. Furthermore, noisy disturbance with different intensities can be imposed to predict whether regular patterns can be developed by calculating the distribution for SF.

Case 2 Collective activities and energy balance in memristive network with electromagnetic induction

As reported in Ge, Wang, and Jia (2021), Lin, Wang, Deng, et al. (2021), Ma (2023), Takembo et al. (2019), Wan et al. (2022), memristive term can be introduced into some neuron models for describing the effect of electromagnetic induction and radiation, and these memristive neurons can be controlled by field coupling via exchange of magnetic flux between neurons. In an experimental way, magnetic flux-controlled memristor (MFCM) can be connected to the neural circuit by adding a new branch circuit in parallel with the capacitor. A similar neural circuit coupled by MFCM (Ding et al., 2023) can be designed in Fig. 1.

Considering a generic form for the MFCM containing magnetic flux ϕ , the channel current and its field energy can be described by

$$\begin{cases} i_{MFCM} = M(\phi)V_M = (\gamma + 3\beta\phi^2)V; \\ W_{MFCM} = \frac{1}{2}\phi i_{MFCM} = \frac{1}{2}(\gamma\phi + 3\beta\phi^3)V; \end{cases} \quad (9)$$

The relation for physical variables in this memristive circuit in Xie, Yao, Ren, et al. (2023) is given in

$$\begin{cases} C \frac{dV}{dt} = i_{ext} - i_L - i_{NR} - i_{MFCM}; \\ L \frac{di_L}{dt} = V - E - Ri_L - V_M; \\ \frac{d\phi}{dt} = V; \end{cases} \quad (10)$$

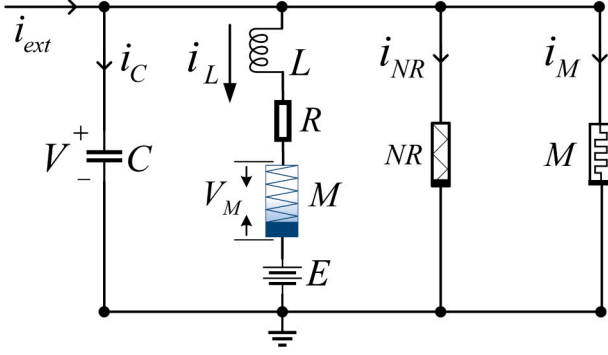


Fig. 1. Schematic diagram for memristive neural circuit. Setting neural circuit composed of a MFCM and voltage-controlled electric component (M) with voltage V_M . NR is a nonlinear resistor and constant voltage E defines a resting potential for the ion channel. The physical relation for the electric components is presented in Eq. (2), respectively.

By using similar scale transformation for the variables in the last two equations

$$\begin{cases} V = xV_0, i_L = \frac{wV_0}{\rho}, \tau = \frac{t}{\rho C}, i_{ext} = \frac{I_{ext}V_0}{\rho}, r = \frac{\rho RC}{L}, \\ s = \frac{R}{\rho}, \varphi' = \frac{\varphi}{\rho CV_0}; \gamma' = \gamma\rho, \beta' = \beta\rho^3 C^2 V_0^2; \end{cases} \quad (11)$$

A new memristive HR neuron is obtained by

$$\begin{cases} \frac{dx}{d\tau} = -w - ax^3 + bx^2 - (\gamma' + 3\beta'\varphi'^2)x + I_{ext}; \\ \frac{dw}{d\tau} = dx^2 - c + rs(x - \lambda) - rw; \\ \frac{d\varphi'}{d\tau} = x \end{cases} \quad (12)$$

where external forcing current I_{ext} can select similar periodic form for the neuron in Eq. (1). Its equivalent Hamilton energy in this memristive channel is mapped from Eq. (9) and it is rewritten by

$$H_{MFCM} = \frac{W_{MFCM}}{CV_0^2} = \frac{1}{2} \frac{(\gamma' + 3\beta'\varphi'^2)\varphi V}{CV_0^2} = \frac{1}{2} (\gamma'\varphi'x + 3\beta'\varphi'^3x); \quad (13)$$

The membrane potential can switch to some negative values and the Hamilton energy for the memristive synapse can be activated to select negative values, which means energy can be emitted and shunted from the memristive synapse. Therefore, the Hamilton energy for the memristive neuron in Eq. (12) is approached by

$$H = H_C + H_L + H_M + H_{MFCM} = \frac{1}{2}rsx^2 + \frac{1}{2}w^2 + dx^2w + \frac{1}{2}(\gamma'\varphi'x + 3\beta'\varphi'^3x); \quad (14)$$

The involvement of magnetic flux and induction current in the memristive channel can well address the effect of electromagnetic induction. As a result, magnetic field superposition becomes inevitable among the clustered neurons accompanying with energy flow between adjacent neurons. In presence of external spatial energy injection accompanied with spatial current $I_{ext} = A \cos(\omega\tau + i\alpha)$, synaptic connections are created to propagate energy for reaching fast energy balance in the memristive network. The growth of intensity for field coupling and collective dynamics in the neural network composed of memristive neurons can be calculated by

$$\begin{cases} \frac{dx_i}{d\tau} = -w_i - ax_i^3 + bx_i^2 + A \cos(\omega\tau + i\alpha) - (\gamma' + 3\beta'\varphi_i'^2)x_i; \\ \frac{dw_i}{d\tau} = dx_i^2 - c + rs(x_i - \lambda) - rw_i; \\ \frac{d\varphi_i'}{d\tau} = x_i + D_i(\varphi_{i+1}' - 2\varphi_i' + \varphi_{i-1}'); \\ \frac{dD_i}{d\tau} = \sigma \cdot D_i \vartheta(\Delta H_i - \epsilon); \end{cases} \quad (15)$$

where D_i measures the intensity for field coupling between two adjacent neurons to the i th neuron. That is, field coupling between adjacent neurons in the chain network is controlled by the energy diversity, which can be controlled by the spatial stimuli, and it is updated by using Eq. (14)

$$\Delta H_i = |H_{i+1} - H_i| + |H_{i-1} - H_i| \quad (16)$$

Any diversity in initials generates energy difference, and then synaptic connection is created to shunt energy for reaching possible energy balance. In case of complete synchronization, energy diversity is decreased zero while phase lock will support continuous energy changes and some neurons can reach local energy balance in the network.

3. Numerical results and discussion

A suitable neuron can present various firing activities when external stimulus is changed in the amplitude or frequency carefully. In practical way, bifurcation analysis can predict the mode transition and changes of the neural activities. Then external forcing current is adjusted to detect the mode transition by calculating the ISI (interspike interval) in Fig. 2. Setting parameters as $r = 0.119, s = 0.05, \lambda = -1.6, a = 0.41, b = 4.01, c = 2.4, d = 0.79$, and the initials (0.02, 0.03) for Eq. (1).

From Fig. 2, it is demonstrated that the firing mode is dependent on the amplitude and frequency of external stimulus closely. Furthermore, the membrane potential for neuron presenting in different firing patterns are plotted in Fig. 3 by selecting the same amplitude value in external forcing current I_{ext} in Fig. 2.

When forcing intensity is fixed, continuously taming the forcing frequency can switch mode changes of the oscillatory states. On the other hand, continuous enhancement of the forcing intensity can suppress bursting and chaotic patterns for developing periodic oscillation completely. Therefore, the new two-variable neuron model reproduces the main firing modes as those biological or biophysical neurons. A single neuron can process finite information and adjacent coupling can be combined into external stimuli. It is worthy of investigating the cooperation and competition between more neurons in a network, and the effect of adaptive regulation in synaptic coupling should be clarified.

To explore the collective behaviors of neurons in a chain network, the distribution of membrane potential and corresponding energy levels are calculated when the local kinetics is presented with four different firing modes in Fig. 4, for simplicity, $N = 200$ neurons are placed in this network with non-flux boundary condition. Constant parameter $\alpha = 0.01$ is fixed in $I_{ext} = A \cos(\omega\tau + i * \alpha)$ to discern the spatial excitation, and $\sigma = 0.003$ is used to control adaptive growth of the synaptic connection intensity during wave propagation in the neural network.

Due to diversity in spatial forcing on the network, changeable coupling intensity seldom controls the network to reach complete synchronization and spatial patterns are developed even all the nodes are activated from the same initials. The SF for the network often obtains lower value and it indicates the synchronization degree is low (non-perfect). In fact, distributed stimuli enable diversity of excitability of these neurons, and complete synchronization is blocked even the coupling is further increased. In Fig. 5, the changes of energy level between adjacent neurons are tracked by adjusting synaptic intensity.

The coupling intensity for each neuron keeps continuous growth synchronously because of uncertain energy diversity between adjacent neuron in the network. Spatial disturbance on the network can induce wave propagation and energy flow is propagated to enhance further growth of the coupling intensity, and then local energy balance can be reached in the network before reaching homogeneous states in the network. During the wave propagation, the coupling intensity for some neurons keeps further increase because of local energy balance is disturbed. From Fig. 5, the oscillatory type of each neuron is changed due to adjacent coupling and spatial excitation with diversity, so the

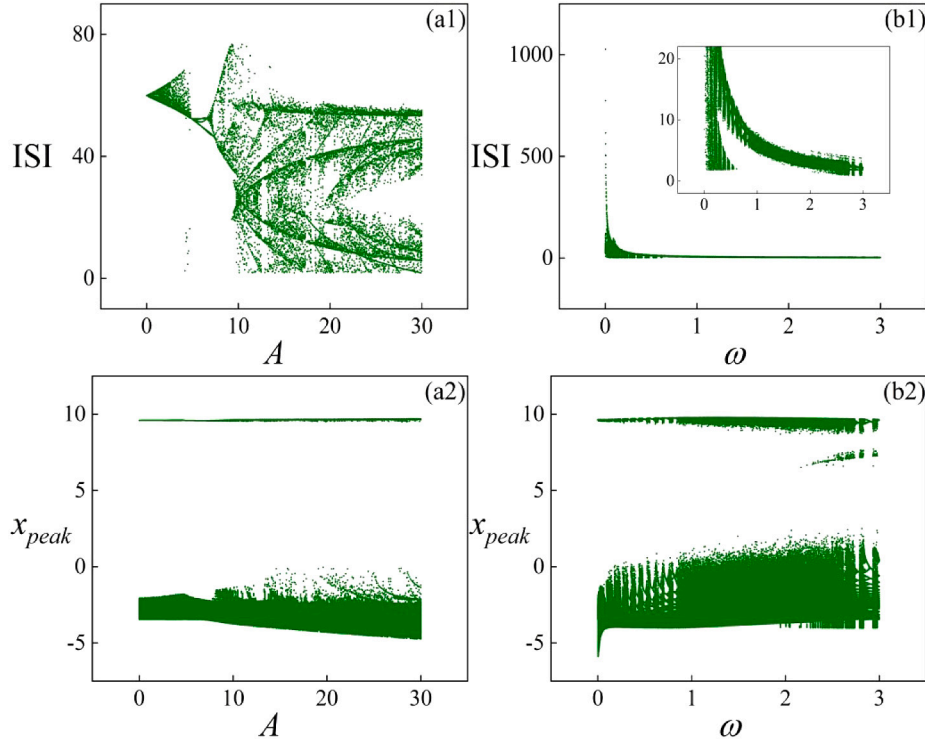


Fig. 2. Effects of different external stimuli on neuronal firing patterns by changing A , ω . For (a1, a2) $\omega = 0.12$; (b1, b2) $A = 14$. x_{peak} defines the peak value for the membrane potential.

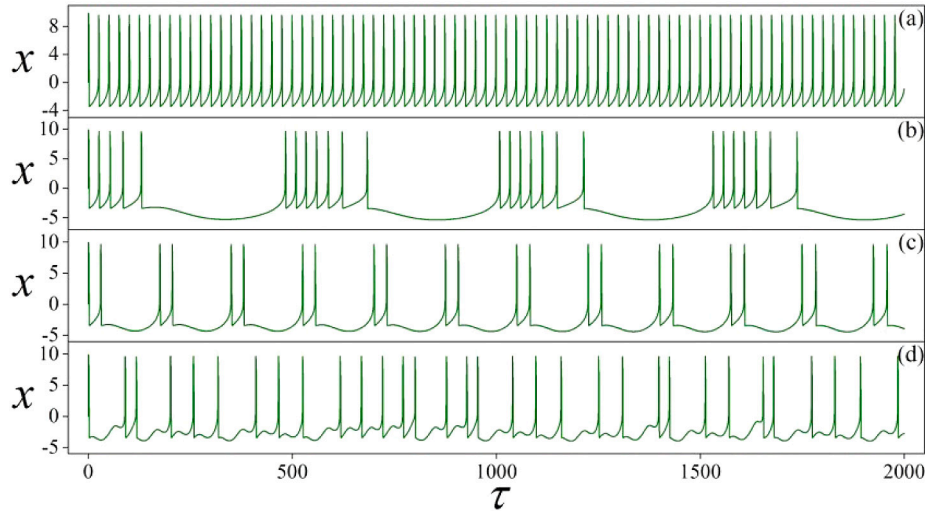


Fig. 3. Four kinds of firing modes in neural activities in single neuron by selecting different frequencies ω at $A = 14$. For (a) spiking $\omega = 0.0001$; (b) bursting $\omega = 0.012$; (c) periodic firing $\omega = 0.036$; (d) chaotic firing $\omega = 0.12$.

firing patterns for the 100th neurons are tracked to show the transition of energy level and selection of firing patterns in the chain network with adaptive synaptic intensity in Fig. 6.

In presenting periodic patterns, the neurons show transition of energy level within wide range, and energy range is decreased in the bursting and chaotic neurons of the chain network. The local kinetics is also controlled by the amplitude of external forcing, and then the forcing intensity is adjusted to control the wave propagation and pattern formation in the network in Fig. 7.

From Fig. 7, most of the region of the network can keep energy balance while some local areas hold distinct energy difference and then

heterogeneity is developed. Therefore, wave propagation is activated in local area and then is blocked by some neurons under synchronization. Similar investigation is carried out, and the distribution of synaptic intensity is plotted in Fig. 8.

These neurons keep synchronous growth of coupling intensity because of continuous spatial excitation and energy diversity in the network. As shown in Figs. 5, and 8, the coupling intensity still keeps low value within 1000 time units, and it is below the threshold for stabilizing complete synchronization in the network. Readers and researchers may suggest using higher initial value or gain for the coupling intensity, indeed, these neurons show sparse connection because they

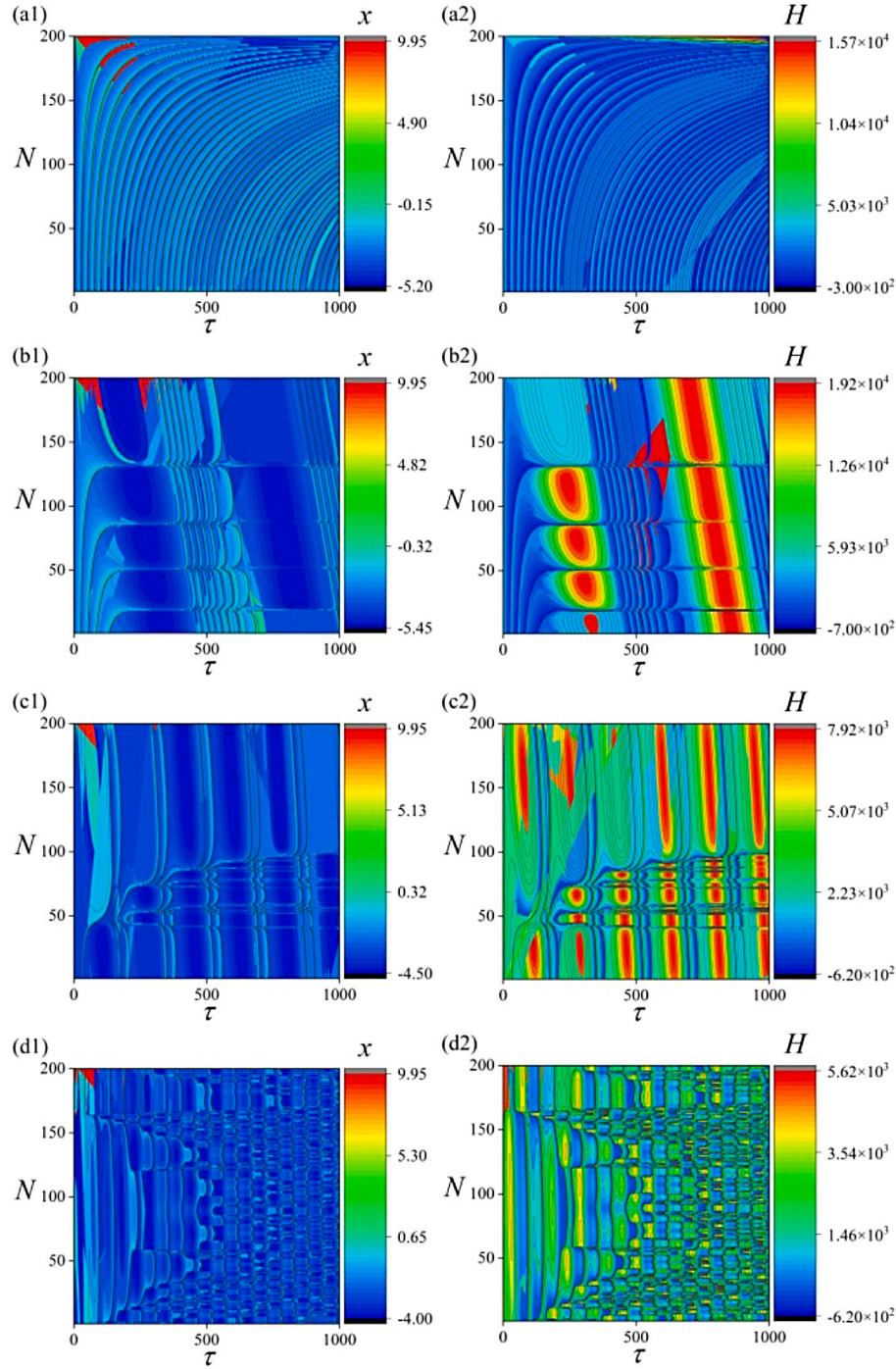


Fig. 4. Formation of spatial pattern and evolution of Hamilton energy in the chain network under spatial stimulus $I_{ext} = 14 \cos(\omega\tau + i * \alpha)$. For (a1, a2) $\omega = 0.0001$; (b1, b2) $\omega = 0.012$; (c1, c2) $\omega = 0.036$; (d1, d2) $\omega = 0.12$. The same initials for variables (0.02, 0.03) and gain $k = 10^{-5}$ are fixed, and $\alpha = 0.01$.

have slight diversity in initial energy by setting the same initial values. By applying distributed stimuli, spatial energy flow is injected to different neurons and energy diversity can be increased to enhance possible growth of coupling intensity for realizing fast local energy balance. Within a finite time, then the growth of coupling intensity is terminated. Therefore, complete synchronization is blocked because some adjacent neurons just keep intermittent energy balance. For a clear illustration, the distribution of SF is calculated by modifying the amplitude and angular frequency in Fig. 9, respectively.

From Fig. 9, the synchronization factor is kept low value when the angular frequency is increased within 0.0001 to 3.0. By setting $\omega = 0.12$, the SF is further decreased because the diversity from

spatial diversity is increased and approach of synchronization becomes more difficult for neurons with high parameter mismatch (excitability diversity).

In fact, electromagnetic induction has important impact on the mode selection of neural activities, the nonlinear resonance in memristive neuron shown in Eq. (12) is discussed and initials are fixed at (0.02, 0.03, 0.01). $a = 0.52, b = 4.02, \gamma' = 0.1, \beta' = 0.02, c = 2.2, d = 0.83, r = 0.206, s = 4, \lambda = -1.6$. Similar bifurcation analysis is provided, and relation of firing mode to the external stimuli is calculated in Fig. 10.

The memristive neuron still presents a variety of firing patterns and its mode transition in electrical activities are controlled by external stimulus in the amplitude or frequency completely. When memristive

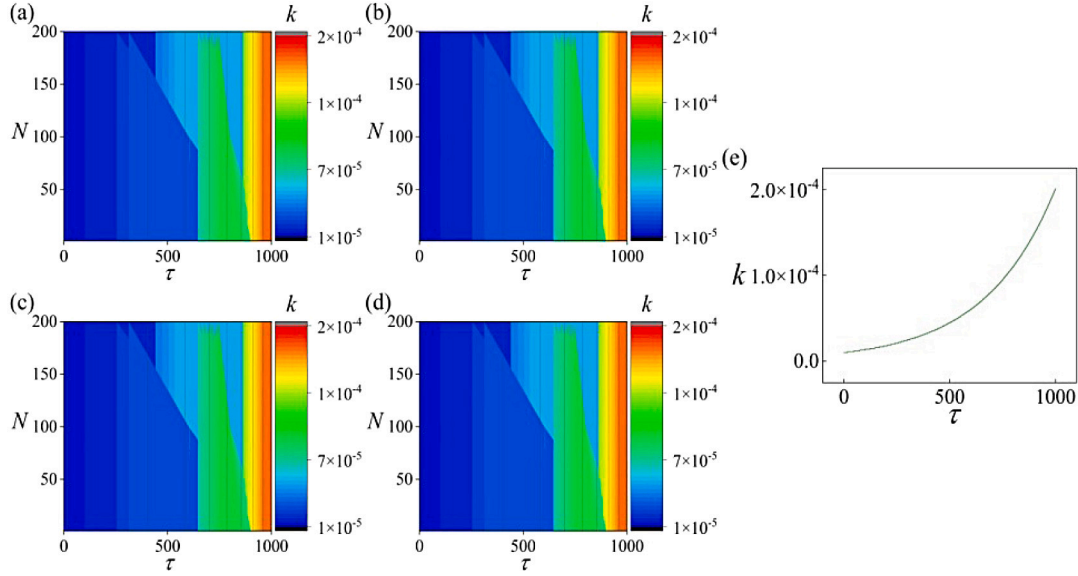


Fig. 5. Evolution of coupling intensity k in the chain network composed of $N = 200$ neurons. For (a) $\omega = 0.0001$; (b) $\omega = 0.012$; (c) $\omega = 0.036$; (d) $\omega = 0.12$; (e) growth of k for the 100th neuron. Spatial stimuli with intensity $A = 14$, and $\alpha = 0.01$.

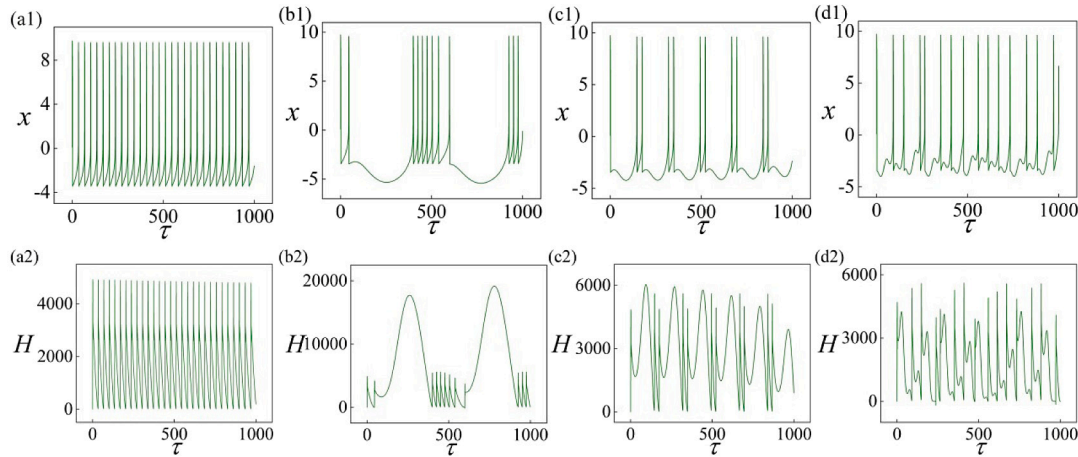


Fig. 6. Transition of firing patterns and energy level for the 100th neuron. For (a1, a2) $\omega = 0.0001$; (b1, b2) $\omega = 0.012$; (c1, c2) $\omega = 0.036$; (d1, d2) $\omega = 0.12$. Setting $A = 14$, $\alpha = 0.01$.

term is involved to discern the effect of electromagnetic induction, additive memristive current also keep against the external stimulus during the regulation of excitability. Therefore, the transition of neural activities becomes complex and the neuron prefer to keep chaotic states. In Fig. 11, the firing patterns in the memristive neurons are plotted to show the competition between memristive current and external stimulus.

The firing patterns including spiking, bursting and chaotic types are some different from the generic neuron because of the involvement of memristive current into the neuron. Similar firing patterns can be induced by adjusting the amplitude when the angular frequency of external stimulus is fixed. With further increasing the amplitude and frequency of external exciting, the memristive neuron is guided to present chaotic patterns. It is important to clarify the dependence of firing modes on the energy proportion in the neuron, and the ratio for each kind of energy (H_C , H_L , H_M , H_{MFCM}) in Eq. (14) to total energy H is calculated in Fig. 12 within a transient period about 2000 time units.

It is found that capacitive energy H_C holds a tiny proportion in the energy level. In Fact, H_M also stores electric field energy because

this electric component is controlled by voltage (membrane potential). The magnetic field used to hold higher energy proportion than the electric field, and thus continuous oscillation enables mode transition in the electric activities. Due to the modulation from memristive current, which accounts for the EMI and EMR (electromagnetic induction and radiation), the energy flow mainly keeps in the magnetic field and thus neuron can maintain distinct firing mode. The energy proportion of the memristive channel can explain the selection of firing modes in neural activities. The neuron will present chaotic state when energy in the memristive channel keeps high proportion. On the other hand, the neuron keeps bursting when energy proportion in memristive channel is low. In fact, the memristive channel shunts the energy under electromagnetic induction, and then the firing modes of the memristive neuron are controlled during energy exchange between different capacitive and inductive channels. Similarly, the pattern formation and wave propagation in the chain network composed of memristive neurons can be calculated and plotted when the local kinetics is described by different neurons, respectively. The same parameter $\alpha = 0.01$ is fixed in spatial excitation $I_{ext} = A \cos(\omega\tau + i * \alpha)$, and the coupling

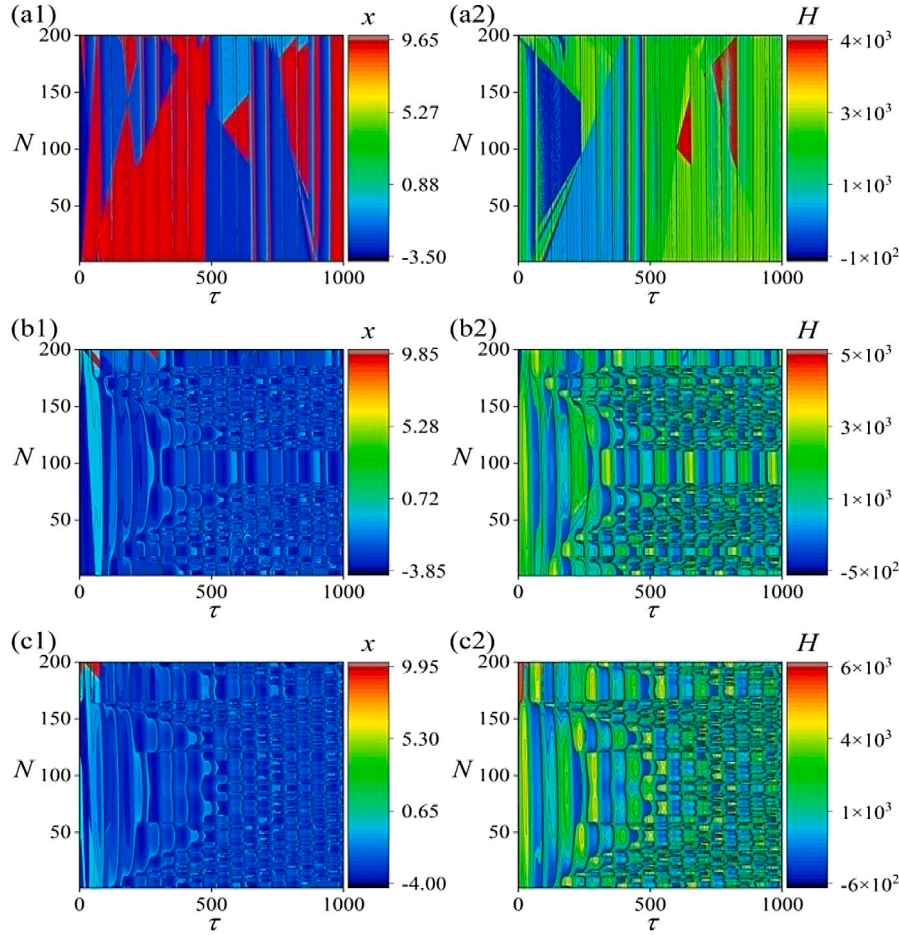


Fig. 7. Development of spatial pattern and Hamilton energy are plotted by changing $I_{ex} = A \cos(0.12\tau + i * \alpha)$. For (a1, a2) $A = 2.2$; (b1, b2) $A = 11.3$; (c1, c2) $A = 14$. The same initials (0.02, 0.03) and gain $k = 10^{-5}$ are fixed, $\alpha = 0.01$, snapshots are plotted in color scale.

intensity is adaptively increased with a gain $\sigma = 0.003$ in the neural network during wave propagation. In presence of spatial excitation and disturbance, all neurons are injected energy with diversity and these non-identical neurons are connected with growing coupling intensity before reaching complete synchronization and energy balance. For simplicity, the distribution of SF is plotted in Fig. 13.

It shows distinct difference from Fig. 9 when memristive current is introduced into the neuron. It is found that memristive network has higher SF values than the neural network in Eq. (6) because the memristive current can suppress the spatial diversity, as a result, these memristive neurons will be coupled with growing intensity for keeping high synchronization degree and local energy balance.

Energy flow is shunted in the network and neurons are coupled to show bursting patterns when spatial excitation induces energy diversity into the neural network. Therefore, adjacent neurons change the energy level and the transient period for reaching local energy balance becomes longer. It also means synchronous patterns are blocked and it has application to prevent the seizure by suppressing bursting synchronization.

Neurons can be excited to present stochastic resonance and coherence resonance in presence of noisy excitation. As a result, energy is injected to change the energy level of the neuron for presenting firing modes. Continuous energy injection from periodic stimulus and noisy disturbance can develop high regularity in the neural activities when noise intensity is carefully adjusted. In a word, a biophysical neuron model should meet the characteristic of coherence resonance or

stochastic resonance under noisy stimulus. It is also worthy of confirming emergence of stochastic resonance in an isolated memristive neuron shown in Eq. (12) when additive noisy disturbance is imposed on the membrane potential and magnetic flux, respectively. For simplicity, Gaussian white noise is changed the intensity D and the corresponding coefficient variability (CV) of ISI series is estimated.

$$CV = \frac{\sqrt{(\langle T^2 \rangle - \langle T \rangle^2)}}{\langle T \rangle}; \quad (17)$$

where T measures the ISI from membrane potentials, and lower CV value predicates occurrence of coherence resonance and higher regularity in the neural activities. In Fig. 14, distribution for CV vs. noise intensity is approached in presence of noisy disturbance from electric field and magnetic field, respectively.

In presence of noisy electric field, an additive noise is imposed to affect the membrane potential directly. When external magnetic field is fluctuated in stochastic way, additive noise has direct impact on the channel current. From Fig. 14, lowest value for CV is consistent with highest average energy value for Hamilton energy, and it means that the neuron keeps high average energy level to present periodic firing patterns under coherence resonance. On the other hand, the noise threshold for inducing coherence resonance has different thresholds when noise is imposed on the membrane patch and ion channel, respectively. Stochastic disturbance resulting from noisy electric field on membrane patch requires a lower noise threshold than noisy disturbance resulting from uncertain magnetic field on ion channels to induce coherence resonance.

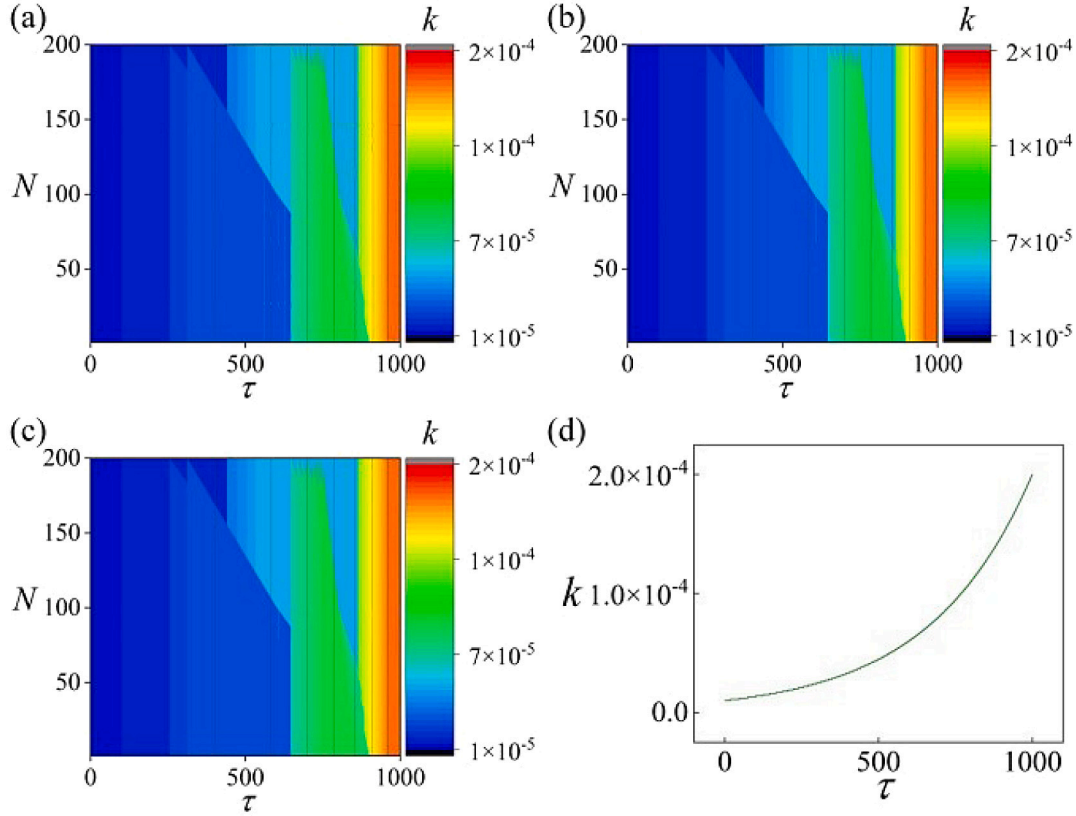


Fig. 8. Evolution of coupling intensity k in the chain network composed of $N = 200$ neurons. For (a) $A = 2.2$; (b) $A = 11.3$; (c) $A = 14.0$. (d) growth of k for the 100th neuron. Spatial stimuli with angular frequency $\omega = 0.12$, $\alpha = 0.01$.

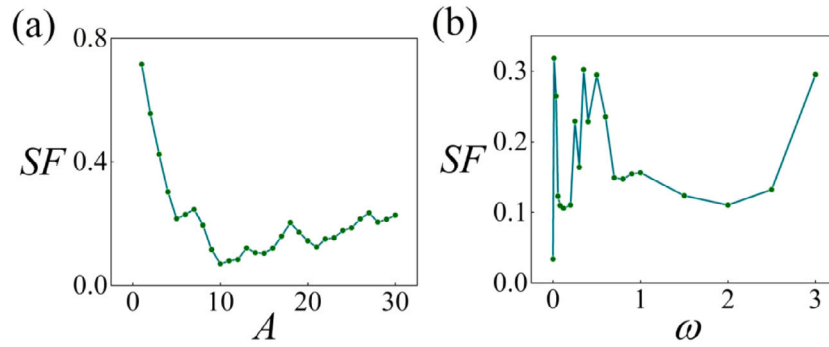


Fig. 9. Distribution of synchronization factors (SFs) in the network driven by periodic signals. For (a) $\omega = 0.12$; (b) $A = 14$. Spatial stimulus $I_{ext} = A \cos(\omega\tau + i * \alpha)$, $\alpha = 0.01$.

In absence of external periodic stimulus, the time-varying memristive current regulate the neural activities and similar coherence resonance is induced when the intensity of membrane noise is adjusted. It means stochastic excitation from external electric field can enhance regular firing when EMI is considered. On the other hand, periodic forcing keeps against the memristive current by changing the excitability. Two kinds of stochastic disturbance, which adds noisy term on the first and third formula respectively, modify the effect of memristive current and then the energy proportion between electric field and magnetic field is adjusted to trigger different firing modes. The memristive neuron keeps distinct periodic states for lower CV values; otherwise, chaotic patterns are induced to prevent the synchronization approach.

In a summary, clear definition and clarification of physical characteristics in neural circuits are crucial to build reliable biophysical

neurons. In particular, the energy level and its dependence on firing mode should be clarified. EMI and EMR provide effective energy exchange in physical field and memristive current well addresses the physical effect on neural activities. Noisy disturbance can affect the membrane potential directly or indirectly. For clustered neurons, continuous energy shunting and spatial energy injection support gradient distribution of energy, and then flexible synapses are guided to grow the intensity with time. In fact, local energy balance enables these non-identical neurons coexist with multiple firing patterns and bursting synchronization is blocked to prevent the emergence of seizure in the nervous system. The involvement of memristor into neural circuit enables its ability for discerning the effect of electromagnetic induction, and field coupling accounts for the exchange of magnetic flux and energy flow. As a result, the coupling intensity is controlled by energy diversity, and adaptive regulation of biological neurons can be understood from energy aspect.

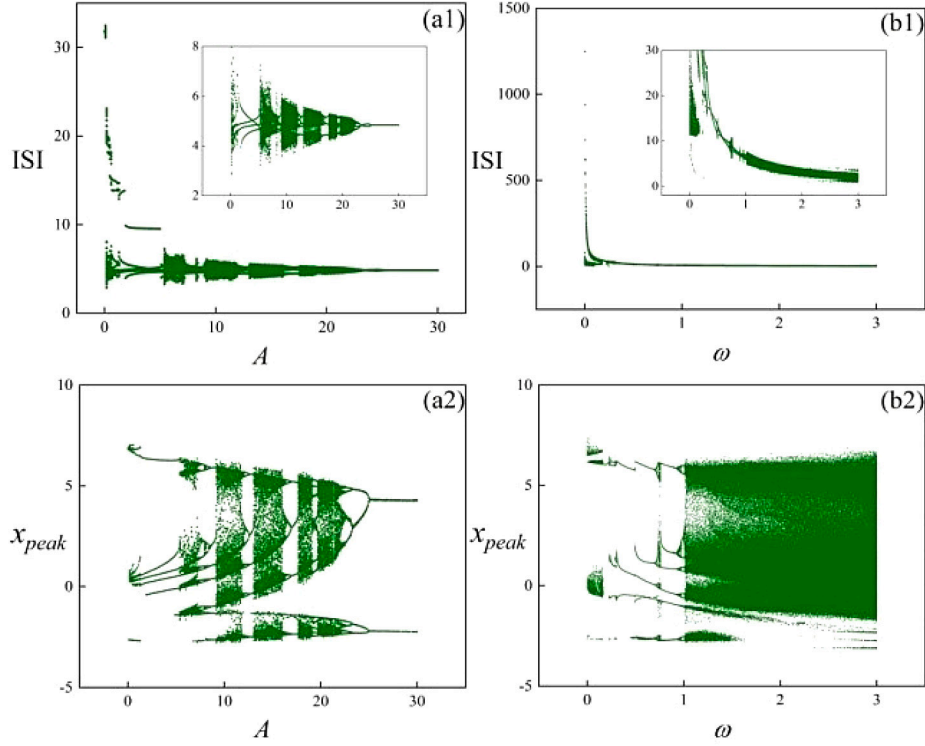


Fig. 10. Selection of firing modes in neural activities in an isolated memristive neuron driven by periodic stimulus. For (a1, a2) $\omega = 1.3$; (b1, b2) $A = 10$. Parameters select $a = 0.52, b = 4.02, \gamma' = 0.1, \beta' = 0.02, c = 2.2, d = 0.83, r = 0.206, s = 4, \lambda = -1.6$.

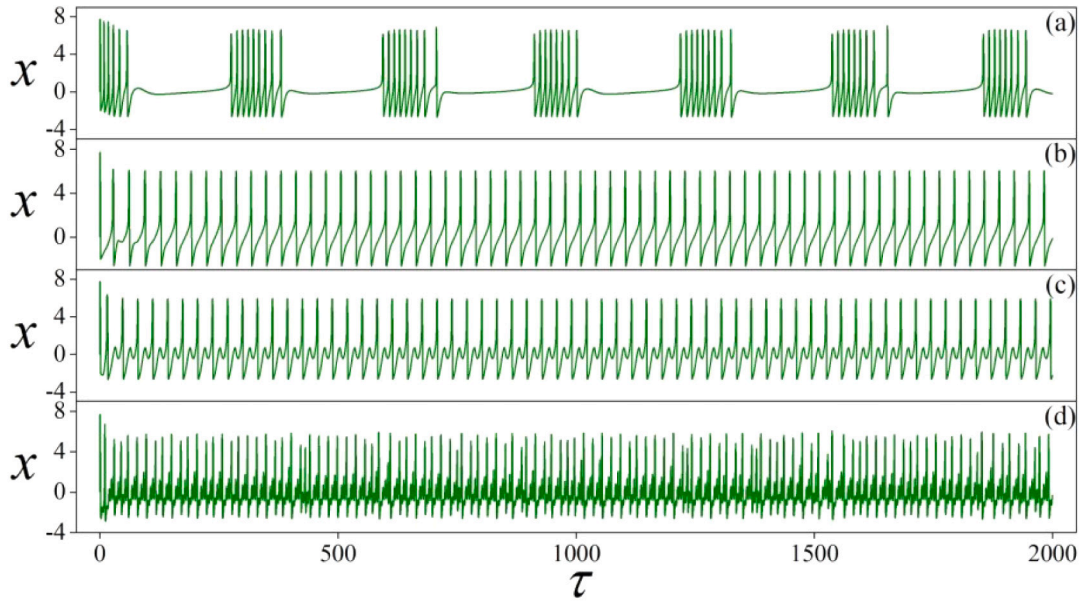


Fig. 11. Different firing modes in neural activities of memristive neuron under different frequencies ω . For (a) bursting $\omega = 0.02$; (b) spiking $\omega = 0.2$; (c) periodic firing $\omega = 0.4$; (d) chaotic firing $\omega = 1.3$. Setting $a = 0.52, b = 4.02, \gamma' = 0.1, \beta' = 0.02, c = 2.2, d = 0.83, r = 0.206, s = 4, \lambda = -1.6, A = 10$, and initials (0.02, 0.03, 0.01).

4. Conclusions

In this work, a MFCM is connected to a simple neural circuit for describing the effect of electromagnetic induction on neural activities. The memristive neuron can present similar stochastic resonance, which high regularity in the electric activities of neuron can be detected. The Hamilton energy function is defined and mapped from physical field energy. The curve for average energy $\langle H \rangle$ vs. noise intensity can be effective to predict the emergence of coherence resonance, which

the neuron prefers to keep highest energy level (average value) and periodic firing patterns. Considering the intrinsic diversity in biophysical neurons, spatial disturbances are imposed to control the collective behaviors of the neural network. In presence of EMIR, the memristive currents also activate the neurons as spatial disturbance, and electric activities become more complex and regularity is destroyed. The coupling intensity for adjacent neurons is adaptively increased in exponential way before reaching local energy balance. When energy diversity keeps alive, heterogeneity is created and local energy

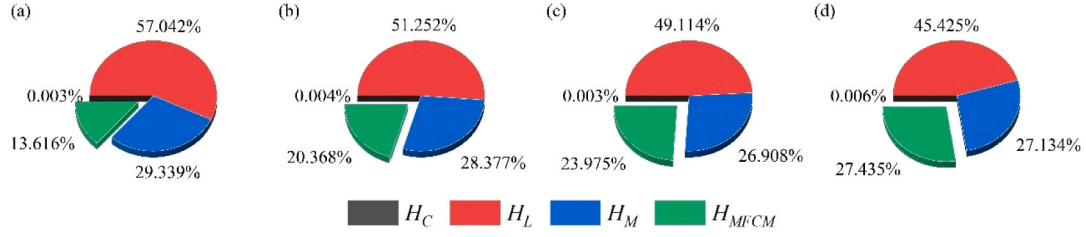


Fig. 12. Energy proportion of four kinds of field energy to total energy of a memristive neuron. For (a) bursting $A = 10, \omega = 0.02$; (b) periodic firing $A = 10, \omega = 0.4$; (c) spiking $A = 10, \omega = 0.2$; (d) chaotic firing $A = 10, \omega = 1.3$.

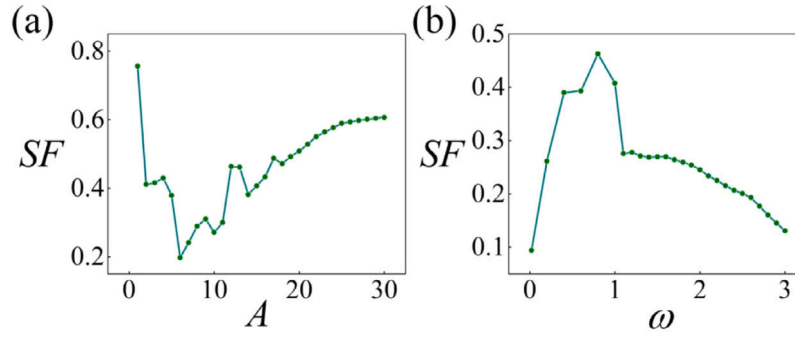


Fig. 13. Distribution of synchronization factors (SFs) in the network driven by periodic signals. For (a) $\omega = 1.3$; (b) $A = 10$. Spatial stimulus $I_{ext} = A \cos(\omega\tau + i * \alpha)$, $\alpha = 0.01$.

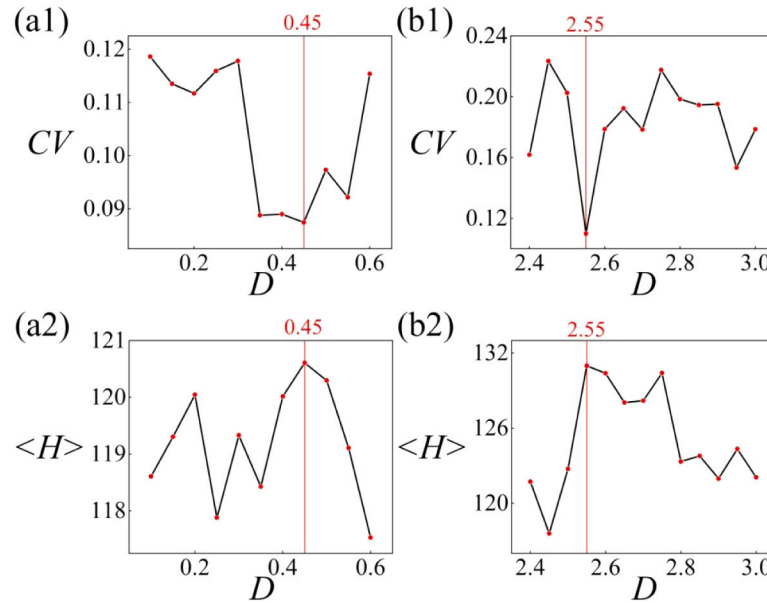


Fig. 14. Distribution of synchronization factors and average Hamilton energy in the memristive neuron. (a1, b1) CV distribution and (a2, b2) average Hamilton energy $\langle H \rangle$ on noise intensity. For (a1, a2) noisy electric field and $I_{ext} = 10 \cos 1.3\tau$; (b1, b2) noisy magnetic field and $I_{ext} = 10 \cos 1.3\tau$. Setting parameters $a = 0.52, b = 4.02, c = 2.2, d = 0.83, r = 0.206, s = 4, \lambda = -1.6, \gamma' = 0.1, \beta' = 0.02$, and initials $(0.02, 0.03, 0.01)$.

balance is broken. These spatial disturbances and excitation prevent the occurrence of complete synchronization even local energy balance can be obtained in the network.

Declaration of competing interest

The authors declare that they have no known competing financial interests or personal relationships that could have appeared to influence the work reported in this paper.

Data availability

Data will be made available on request.

Acknowledgments

This project is supported by National Natural Science Foundation of China under Grant No. 62361037.

References

- Abera, A. S., Peterchev, A. V., & Grill, W. M. (2018). Biophysically realistic neuron models for simulation of cortical stimulation. *Journal of Neural Engineering*, 15, Article 066023.
- Babacan, Y., Kaçar, F., & Gürkan, K. (2016). A spiking and bursting neuron circuit based on memristor. *Neurocomputing*, 203, 86–91.

- Bao, H., Chen, Z. G., Cai, J. M., et al. (2022). Memristive cyclic three-neuron-based neural network with chaos and global coexisting attractors. *Science China Technological Sciences*, 65, 2582–2592.
- Bao, B., Hu, A., Xu, Q., et al. (2018). AC-induced coexisting asymmetric bursters in the improved Hindmarsh–Rose model. *Nonlinear Dynamics*, 92, 1695–1706.
- Butts, D. A. (2019). Data-driven approaches to understanding visual neuron activity. *Annual Review of Vision Science*, 5, 451–477.
- Cai, J., Bao, H., Chen, M., et al. (2022). Analog/digital multiplierless implementations for nullcline- characteristics-based piecewise linear Hindmarsh–Rose neuron model. *IEEE Transactions on Circuits and Systems. I. Regular Papers*, 69, 2916–2927.
- Cai, J., Bao, H., Xu, Q., et al. (2021). Smooth nonlinear fitting scheme for analog multiplierless implementation of Hindmarsh–Rose neuron model. *Nonlinear Dynamics*, 104, 4379–4389.
- Cao, B., Gu, H., & Ma, K. (2022). Complex dynamics of hair bundle of auditory nervous system (I): spontaneous oscillations and two cases of steady states. *Cognitive Neurodynamics*, 16, 917–940.
- Cao, B., Gu, H., & Wang, R. (2022). Complex dynamics of hair bundle of auditory nervous system (II): forced oscillations related to two cases of steady state. *Cognitive Neurodynamics*, 16, 1163–1188.
- Chen, J. X., Xiao, J., Qiao, L. Y., et al. (2018). Dynamics of scroll waves with time-delay propagation in excitable media. *Communications in Nonlinear Science and Numerical Simulation*, 59, 331–337.
- Chen, J. X., Zhan, S., Qiao, L. Y., et al. (2019). Collective dynamics of self-propelled nanomotors in chemically oscillating media. *Europhysics Letters*, 125, 26002.
- Clark, R., Fuller, L., Platt, J. A., et al. (2022). Reduced-dimension, biophysical neuron models constructed from observed data. *Neural Computation*, 34, 1545–1587.
- Dana, S. K., Sengupta, D. C., & Hu, C. K. (2006). Spiking and bursting in josephson junction. *IEEE Transactions on Circuits and Systems II: Express Briefs*, 53, 1031–1034.
- Demanez, J. P., & Demanez, L. (2003). Anatomophysiology of the central auditory nervous system: basic concepts. *Acta oto-rhino-laryngologica belgica*, 57, 227–236.
- Ding, Q., Wu, Y., Hu, Y., et al. (2023). Tracing the elimination of reentry spiral waves in defibrillation: Temperature effects. *Chaos, Solitons & Fractals*, 174, Article 113760.
- Druckmann, S., Berger, T. K., Schürmann, F., et al. (2011). Effective stimuli for constructing reliable neuron models. *PLoS Computational Biology*, 7, Article e1002133.
- Étémé, A. S., Tabi, C. B., Beyala Ateba, J. F., et al. (2021). Chaos break and synchrony enrichment within Hindmarsh–Rose-type memristive neural models. *Nonlinear Dynamics*, 105, 785–795.
- Foka, N. F. F., Ramakrishnan, B., Tchamda, A. R., et al. (2021). Dynamical analysis of josephson junction neuron model driven by a thermal signal and its digital implementation based on microcontroller. *The European Physical Journal B*, 94, 234.
- Gabbiani, F., Krapp, H. G., Koch, C., et al. (2002). Multiplicative computation in a visual neuron sensitive to looming. *Nature*, 420, 320–324.
- Ge, M. Y., Wang, G. W., & Jia, Y. (2021). Influence of the Gaussian colored noise and electromagnetic radiation on the propagation of subthreshold signals in feedforward neural networks. *Science China Technological Sciences*, 64, 847–857.
- Gerstner, W., & Naud, R. (2009). How good are neuron models? *Science*, 326(5951), 379–380.
- Gjorgjieva, J., Drion, G., & Marder, E. (2016). Computational implications of biophysical diversity and multiple timescales in neurons and synapses for circuit performance. *Current Opinion in Neurobiology*, 37, 44–52.
- Guo, Y., Zhou, P., Yao, Z., et al. (2021). Biophysical mechanism of signal encoding in an auditory neuron. *Nonlinear Dynamics*, 105, 3603–3614.
- Heidarpur, M., Ahmadi, A., & Kandalaf, N. (2017). A digital implementation of 2D Hindmarsh–Rose neuron. *Nonlinear Dynamics*, 89, 2259–2272.
- Herz, A. V. M., Gollisch, T., Machens, C. K., et al. (2006). Modeling single-neuron dynamics and computations: a balance of detail and abstraction. *Science*, 314(5796), 80–85.
- Hou, B., Ma, J., & Yang, F. (2023). Energy-guided synapse coupling between neurons under noise. *Journal of Biological Physics*, 49, 49–76.
- Hou, B., Zhou, P., Ren, G., et al. (2023). Energy flow controls synchronization in a network coupled with memristive synapses. *European Physical Journal Plus*, 138, Article 293.
- Hu, Y., Ding, Q., Wu, Y., et al. (2023). Polarized electric field-induced drift of spiral waves in discontinuous cardiac media. *Chaos, Solitons & Fractals*, 175, Article 113957.
- Hussain, I., Jafari, S., Ghosh, D., et al. (2021). Synchronization and chimeras in a network of photosensitive FitzHugh–Nagumo neurons. *Nonlinear Dynamics*, 104, 2711–2721.
- Kafraj, M. S., Parastesh, F., & Jafari, S. (2020). Firing patterns of an improved Izhikevich neuron model under the effect of electromagnetic induction and noise. *Chaos, Solitons & Fractals*, 137, Article 109782.
- Kepecs, A., & Wang, X. J. (2000). Analysis of complex bursting in cortical pyramidal neuron models. *Neurocomputing*, 32, 181–187.
- Kobe, D. H. (1986). Helmholtz's theorem revisited. *American Journal of Physics*, 54, 552–554.
- Lengler, J., Jug, F., & Steger, A. (2013). Reliable neuronal systems: the importance of heterogeneity. *PLoS One*, 8, Article e80694.
- Li, Z., & Zhou, H. (2021). Regulation of firing rhythms in a four-stable memristor-based Hindmarsh–Rose neuron. *Electronics Letters*, 57, 715–717.
- Lim, H., Kornijuk, V., Seok, J. Y., et al. (2015). Reliability of neuronal information conveyed by unreliable neuristor-based leaky integrate-and-fire neurons: a model study. *Scientific Reports*, 5, 09776.
- Lin, H., Wang, C., Deng, Q., et al. (2021). Review on chaotic dynamics of memristive neuron and neural network. *Nonlinear Dynamics*, 106, 959–973.
- Lin, H., Wang, C., Hong, Q., et al. (2020). A multi-stable memristor and its application in a neural network. *IEEE Transactions on Circuits and Systems II: Express Briefs*, 67, 3472–3476.
- Lu, L. L., Yi, M., & Liu, X. Q. (2022). Energy-efficient firing modes of chay neuron model in different bursting kinetics. *Science China Technological Sciences*, 65, 1661–1674.
- Ma, J. (2023). Biophysical neurons, energy, and synapse controllability: a review. *Journal of Zhejiang University-Science A*, 24, 109–129.
- Mondal, A., Upadhyay, R. K., Ma, J., et al. (2019). Bifurcation analysis and diverse firing activities of a modified excitable neuron model. *Cognitive Neurodynamics*, 13, 393–407.
- Njitacke, Z. T., Awrejcewicz, J., Ramakrishnan, B., et al. (2022). Hamiltonian energy computation and complex behavior of a small heterogeneous network of three neurons: circuit implementation. *Nonlinear Dynamics*, 107, 2867–2886.
- Njitacke, Z. T., Koumetio, B. N., Ramakrishnan, B., et al. (2021). Hamiltonian energy and coexistence of hidden firing patterns from bidirectional coupling between two different neurons. *Cognitive Neurodynamics*, 16, 899–916.
- Ochs, K., & Jenderny, S. (2021). An equivalent electrical circuit for the Hindmarsh–Rose model. *International Journal of Circuit Theory and Applications*, 49, 3526–3539.
- Pakdaman, K., Tanabe, S., & Shimokawa, T. (2001). Coherence resonance and discharge time reliability in neurons and neuronal models. *Neural Networks*, 14(6–7), 895–905.
- Takembo, C. N., Mvogo, A., Ekobena Fouda, H. P., et al. (2019). Effect of electromagnetic radiation on the dynamics of spatiotemporal patterns in memristor-based neuronal network. *Nonlinear Dynamics*, 95, 1067–1078.
- Tan, Y., & Wang, C. (2020). A simple locally active memristor and its application in HR neurons. *Chaos*, 30, Article 053118.
- Usha, K., & Subha, P. A. (2019). Hindmarsh–Rose neuron model with memristors. *Biosystems*, 178, 1–9.
- Van Geit, W., De Schutter, E., & Achard, P. (2008). Automated neuron model optimization techniques: a review. *Biological Cybernetics*, 99, 241–251.
- Vijay, S. D., Thamilaran, K., & Ahamed, A. I. (2022). Superextreme spiking oscillations and multistability in a memristor-based Hindmarsh–Rose neuron model. *Nonlinear Dynamics*, 111, 789–799.
- Wan, Q., Yan, Z., Li, F., et al. (2022). Multistable dynamics in a hopfield neural network under electromagnetic radiation and dual bias currents. *Nonlinear Dynamics*, 109, 2085–2101.
- Wang, Y., Sun, G. P., & Ren, G. D. (2023). Diffusive field coupling-induced synchronization between neural circuits under energy balance. *Chinese Physics B*, 32, Article 040504.
- Wang, H., Wang, J., Cai, G., et al. (2021). A physical perspective to the inductive function of myelin-A missing piece of neuroscience. *Frontiers in Neural Circuits*, 14, Article 562005.
- Wang, G., Wang, R., Kong, W., et al. (2018). Simulation of retinal ganglion cell response using fast independent component analysis. *Cognitive Neurodynamics*, 12, 615–624.
- Wang, Y., Wang, C., Ren, G., et al. (2017). Energy dependence on modes of electric activities of neuron driven by multi-channel signals. *Nonlinear Dynamics*, 89, 1967–1987.
- Wojewoda, J., Rajagopal, K., Pham, V. T., et al. (2021). Chimera state in a network of nonlocally coupled impact oscillators. *Journal of Zhejiang University-Science A*, 22, 235–244.
- Wu, F. Q., Guo, Y. T., & Ma, J. (2023). Energy flow accounts for adaptive property of functional synapse. *Science China Technological Science*, 66, 3139–3152.
- Xie, Y., Xu, Y., & Ma, J. (2023). Desynchronization and energy diversity between neurons. *Nonlinear Dynamics*, 111, 11521–11541.
- Xie, Y., Yao, Z., Hu, X., et al. (2021). Enhance sensitivity to illumination and synchronization in light-dependent neurons. *Chinese Physics B*, 30, Article 120510.
- Xie, Y., Yao, Z., & Ma, J. (2022). Phase synchronization and energy balance between neurons. *Frontiers of Information Technology and Electronic Engineering*, 23, 1407–1420.
- Xie, Y., Yao, Z., & Ma, J. (2023). Formation of local heterogeneity under energy collection in neural networks. *Science China Technological Sciences*, 66, 439–455.
- Xie, Y., Yao, Z., Ren, G. D., et al. (2023). Estimate physical reliability in Hindmarsh–Rose neuron. *Physics Letters. A*, 464, Article 128693.
- Xie, Y., Zhou, P., & Ma, J. (2023). Energy balance and synchronization via inductive-coupling in functional neural circuits. *Applied Mathematical Modelling*, 113, 175–187.
- Yang, Y., Ma, J., Xu, Y., et al. (2021). Energy dependence on discharge mode of Izhikevich neuron driven by external stimulus under electromagnetic induction. *Cognitive Neurodynamics*, 15, 265–277.
- Yang, F., Wang, Y., & Ma, J. (2023). Creation of heterogeneity or defects in a memristive neural network under energy flow. *Communications in Nonlinear Science and Numerical Simulation*, 119, Article 107127.
- Yang, F., Xu, Y., & Ma, J. (2023). A memristive neuron and its adaptability to external electric field. *Chaos. An Interdisciplinary Journal of Nonlinear Science*, 33, Article 023110.

- Yao, Y., Ma, J., Gui, R., et al. (2021). Enhanced logical chaotic resonance. *Chaos. An Interdisciplinary Journal of Nonlinear Science*, 31, Article 023103.
- Yao, Z., & Wang, C. (2021). Control the collective behaviors in a functional neural network. *Chaos, Solitons & Fractals*, 152, Article 111361.
- Yao, Z., & Wang, C. (2022). Collective behaviors in a multiple functional network with hybrid synapses. *Physica A. Statistical Mechanics and its Applications*, 605, Article 127981.
- Yi, W., Tsang, K. K., Lam, S. K., et al. (2018). Biological plausibility and stochasticity in scalable VO₂ active memristor neurons. *Nature Communications*, 9, Article 4661.
- Yu, T., Sejnowski, T. J., & Cauwenberghs, G. (2011). Biophysical neural spiking, bursting, and excitability dynamics in reconfigurable analog VLSI. *IEEE Transactions on Biomedical Circuits and Systems*, 5, 420–429.
- Yu, D., Zhan, X., Yang, L., et al. (2023). Theoretical description of logical stochastic resonance and its enhancement: Fast Fourier transform filtering method. *Physical Review E*, 108, Article 014205.
- Yuan, Y., Yang, H., Han, F., et al. (2022). Traveling chimera states in locally coupled memristive hindmarsh -rose neuronal networks and circuit simulation. *Science China Technological Sciences*, 65, 1445–1455.
- Zhang, L., Xiong, L., An, X., et al. (2023). Hamilton energy balance and synchronization behaviors of two functional neurons. *Cognitive Neurodynamics*, 17, 1683–1702.
- Zhang, S., Zheng, J., Wang, X., et al. (2021). Multi-scroll hidden attractor in memristive HR neuron model under electromagnetic radiation and its applications. *Chaos*, 31, Article 011101.
- Zhou, P., Zhang, X., & Ma, J. (2022). How to wake up the electric synapse coupling between neurons? *Nonlinear Dynamics*, 108, 1681–1695.



Energy and synchronization between two neurons with nonlinear coupling

Yitong Guo¹ · Ying Xie² · Chunni Wang² · Jun Ma^{2,3}

Received: 30 August 2023 / Revised: 26 October 2023 / Accepted: 26 November 2023
© The Author(s), under exclusive licence to Springer Nature B.V. 2023

Abstract

Consensus and synchronous firing in neural activities are relative to the physical properties of synaptic connections. For coupled neural circuits, the physical properties of coupling channels control the synchronization stability, and transient period for keeping energy diversity. Linear variable coupling results from voltage coupling via linear resistor by consuming certain Joule heat, and electric synapse coupling between neurons derives from gap junction connection under special electrophysiological condition. In this work, a voltage-controlled electric component with quadratic relation in the $i-v$ (current–voltage) is used to connect two neural circuits composed of two variables. The energy function obtained by using Helmholtz theorem is consistent with the Hamilton energy function converted from the field energy in the neural circuit. Chaotic signals are encoded to approach a mixed signal within certain frequency band, and then its amplitude is adjusted to excite the neuron for detecting possible occurrence of nonlinear resonance. External stimuli are changed to trigger different firing modes, and nonlinear coupling activates changeable coupling intensity. It is confirmed that nonlinear coupling behaves functional regulation as hybrid synapse, and the synchronization transition between neurons can be controlled for reaching possible energy balance. The nonlinear coupling is helpful to keep energy diversity and prevent synchronous bursting because positive and negative feedback is switched with time. As a result, complete synchronization is suppressed and phase lock is controlled between neurons with energy diversity.

Keywords Hamilton energy · Nonlinear coupling · Energy balance · Synchronization · Neuron

Introduction

For a biological neuron, inner electric field energy and magnetic field energy is exchanged during the propagation of intracellular and extracellular ions, and membrane potential is adjusted under external stimuli. For a couple or more neurons, diversity in electromagnetic field energy forces the creation and growth of synaptic connections and thus they can reach fast energy balance in the neural network (Torrealdea et al. 2006; Zhou et al. 2022a; Xie et al.

2022, 2023; Wang et al. 2022). For example, Zhou et al. (2022a) claimed that adaptive growth of electric synapse results from energy diversity between neurons. The electric synapse (Curti and O'Brien 2016; Bennett 1997; Xie et al. 2021a; Bennett and Zukin 2004; Zandi-Mehran et al. 2020) activates its coupling regulation under special condition and it becomes transient because continuous consumption of Joule heat can induce temperature effect on neural activities. Bidirectional coupling via electric synapses often provides a fast energy balance by applying variables error on the nonlinear oscillators in the form of negative feedback. From a dynamical viewpoint, the electric synapse coupling just induces linear variable coupling of membrane potentials (Bennett 2000; Zhou et al. 2021a; Velazquez and Carlen 2000; Gerasimova et al. 2015). On the other hand, the chemical synapse coupling (Balenzuela and García-Ojalvo 2005; Shafiei et al. 2020; Smith and Pereda 2003; Kundu et al. 2019; Hu and Cao 2016) keeps continuous regulation on the collective electric activities in

✉ Chunni Wang
wangcn05@163.com

¹ College of Electrical and Information Engineering, Lanzhou University of Technology, Lanzhou 730050, China

² Department of Physics, Lanzhou University of Technology, Lanzhou 730050, China

³ School of Science, Chongqing University of Posts and Telecommunications, Chongqing 430065, China

neurons and it is approached by equivalent memristive synapse connecting two neurons (Wu et al. 2022a). Smith and Pereda (2003) confirmed that chemical synapse has impact on the activation of nearby electric synapse. From physical viewpoint, the release of neurotransmitter and activation of Calcium accounts for the functional regulation from chemical synapse, and field coupling is triggered to connect neurons for reaching energy balance between neurons. Therefore, synchronous firing patterns can be controlled under chemical synapse coupling, which is accompanied with field coupling via electromagnetic field (Yao and Wang 2022, 2021; Yao et al. 2021; Zhou et al. 2022b; Xu et al. 2019). For example, Yao and Wang (2022, 2021), Yao et al. (2021) suggested that hybrid synapse coupling can be approached by activating capacitive and inductive field coupling, which is realized by connecting capacitor, inductor and even memristor in parallel or in series. In fact, the field coupling can be considered as nonlinear coupling via hybrid synapse (Sun et al. 2013; Yu et al. 2017; Calim et al. 2020; Uzuntarla 2019; Xu et al. 2021) and it has certain advantage than the simple electric synapse coupling by consuming large Joule heat during the energy propagation along the coupling channels. Considering the physical approach and circuit implement, these hybrid synapses can be considered a kind of field coupling. In a practical way, the circuit realization and implement of hybrid synapse can be designed by using combination of capacitor, inductor, resistor and memristor and even nonlinear resistor, and nonlinear coupling is activated to connect the equivalent neural circuits. In presence of resistance of artificial synapse, the nonlinear electric component in the coupling channels can consume a little Joule heat and it also emits energy flow because it can be considered as an active component. Therefore, the channel current becomes nonlinear, and nonlinear coupling (Gieseler et al. 2014; Wang et al. 2010; Petereit and Pikovsky 2017; Wei et al. 2019; Chithra and Raja 2017) is switched to regulate the synchronous behaviors between chaotic oscillators. As reported in Wei et al. (2019), the coupling intensity is regulated in adaptive way and the stability of synchronization in the network is controllable.

Reliable neural circuits coupled by specific electric components can reproduce certain biophysical function of biological neurons in nervous system. For example, a phototube is activated to excite a simple RLC circuit (resistor–inductor–capacitor), this neural circuit is sensitive to light and can be considered as an artificial light-sensitive neuron as visual neuron (Xie et al. 2021a, b). The involvement of thermistor into nonlinear circuit can perceive external temperature because the channel current across the thermistor is dependent on the temperature and this shunted current can regulate the charge and discharge of capacitor in this circuit (Xu et al. 2020; Xu and Ma

2021). Furthermore, activation of memristive channel can enhance the biophysical function of neurons (Wu et al. 2022b, 2020) and electromagnetic field energy can be defined theoretically. In particular, electric field variable (Wu et al. 2019) is supplied into the Hindmarsh–Rose neuron model (González-Miranda 2007; Ochs and Jenderny 2021; Cai et al. 2021) and external electric field is applied to control the mode selection in electric activities. In Ref. (Cai et al. 2021), an equivalent neural circuit is proposed to mimic the dynamical property of electric activities produced in the HR neuron. A special current can well explain the enhanced firing along with seizure induced by inhibitory interneuron (Wang et al. 2023), and it is helpful to avoid seizure. The memristive neurons show distinct controllability because the external magnetic field can be captured by regulating the memristive current and the firing modes are controlled effectively (Zhang et al. 2018; Bao et al. 2021; Chen et al. 2021; Pu et al. 2021; Rajagopal et al. 2019). For example, Zhang et al. (2018) suggested a scheme to design memristive neuron with lower energy consumption. Rajagopal et al. (2019) presented a new memristive neuron with fractional order and the effect of electromagnetic induction is estimated. In addition, Josephson junction (JJ) can perceive external magnetic field, and its involvement into neural circuit can be used to control the neural behaviors and similar stochastic resonance can be induced under noisy disturbance in the magnetic field (Zhang et al. 2020a, b; Dana et al. 2006; Njitacke et al. 2022a). Considering the distinct physical properties of JJ and memristors, more additive branch circuits are connected to the neural circuits to enhance the ability for perceiving physical signals, and then these biophysical neurons become more controllable because external physical stimuli can be converted into equivalent channel currents, which regulate the membrane potential and firing modes synchronously. For more neurons, these specific components can be used as functional synapse to connect neural circuits, and the coupling channels are controllable because of nonlinear relation for the voltage and current.

Continuous energy supply and exchange are crucial for neurons in presenting kinds of firing patterns, and stable energy balance is helpful to keep synchronous electric activities (Moujahid et al. 2011; Torrealdea et al. 2009). For generic neuron model and nonlinear oscillators, Zhou et al. (2021b) explained how to approach the sole Hamilton energy function and used as appropriate Lyapunov function. For more guidance about neurodynamics from physical viewpoint, readers can refer to the recent reviews (Ma et al. 2019; Ma 2023). In this paper, a kind of nonlinear coupling is used to couple two feasible neurons, the Hamilton energy is derived and physical property of the neural circuit is explained. Two neurons are coupled via

nonlinear coupling via a hybrid synapse, and the synchronization stability is discussed.

Model and scheme

For generic neuron models composed of quadratic term for membrane potentials, the combination of simple and ideal capacitor, inductor, and shunted current across nonlinear resistor with nonlinear relation between channel current and output voltage is effective to build a controllable neural circuit. To facilitate the enhancement of biophysical function of neural circuit, specific electric components are embedded into the branch circuits of *RLC* circuit (Resistor–inductor–capacitor) (Kyprianidis et al. 2012), see the recent review (Ma 2022, 2023). When higher order terms are included into the neuron model, it needs the involvement of similar voltage-controlled component and memristor, and energy is also shunted in these electric components. For simplicity, an improved *RLC* circuit is suggested in Fig. 1.

The external stimulus i_{ext} is generated from a voltage source and it is shunted into three branch circuits. The circuit equations for Fig. 1 are obtained to bridge the voltage V and channel current i_L as follows

$$\begin{cases} C \frac{dV}{dt} = i_{ext} - i_L - i_{NR}; \\ L \frac{di_L}{dt} = V - E - Ri_L - V_M; \end{cases} \quad (1)$$

The functional component M can be considered as voltage-controlled, and its voltage V_M is defined by

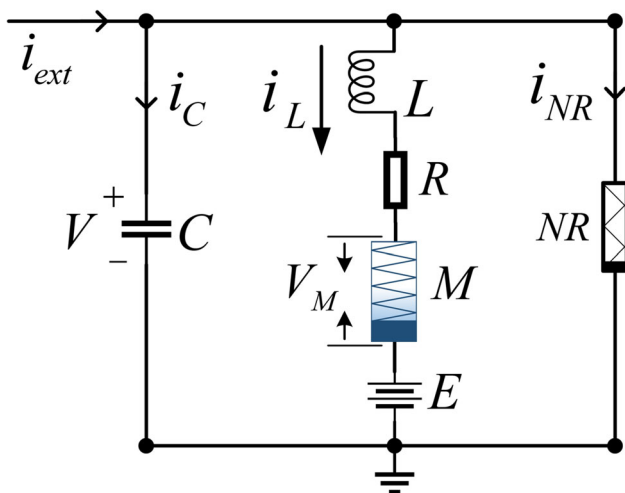


Fig. 1 Schematic diagram for a *RLC* circuit. V_M denotes the voltage for the electric component M with quadratic operation on the voltage V for the capacitor, NR is a nonlinear resistor and its current is described in Eq. (3). C , L , defines capacitance for capacitor, and inductance for inductor, respectively

$$V_M = -\frac{d}{rsV_0}V^2, \quad E = \frac{c}{rs}V_0 + \lambda V_0; \quad (2)$$

where the constant E is used to describe the reverse potential in the ion channel current. The normalized parameters (c , d , r , s , λ) are the same parameters in the Hindmarsh–Rose (HR) neuron model (Hindmarsh and Rose 1982, 1984). Inspired by the i – v relation with quadratic term for nonlinear component in Ref. (Kyprianidis et al. 2012; Rajasekar and Lakshmanan 1988), the relation of current and voltage across the *NR* is defined by

$$i_{NR} = -\frac{1}{\rho} \left(\frac{bV^2}{V_0} - \frac{aV^3}{V_0^2} \right); \quad (3)$$

where ρ and V_0 are the resistance in the linear region and cut-off voltage in the i – v curve for *NR*. a and b are same as the parameters in the HR model (Hindmarsh and Rose 1982, 1984). V_0 in Eqs. (2) and (3) is the same. The electromagnetic field energy in the neural circuit, and average energy cost per time unit in the electric component M can be estimated by

$$\begin{cases} W = W_C + W_L - W_M = \frac{1}{2}CV^2 + \frac{1}{2}Li_L^2 + \frac{d}{rsV_0}V^2i_L\rho C; \\ W_M = i_MV_M\rho C = -\frac{d}{rsV_0}V^2i_L\rho C; \end{cases} \quad (4)$$

That is, the field energy in the neuron is kept in capacitive and inductive forms. In this simple neuron with one capacitive variable and one inductive variable, the involvement of voltage-controlled component M into the ion channel occupies partial electric field energy in capacitive form. Capacitive energy is pumped and shunted into the voltage-controlled channel, so W_M has opposite direction of energy flow from W_C . Furthermore, these physical variables and parameters in Eqs. (1–4) are mapped into dimensionless variables by using the following scale transformation

$$\begin{cases} x = \frac{V}{V_0}, \quad w = \frac{i_L\rho}{V_0}, \quad \tau = \frac{t}{\rho C}, \quad I_{ext} = \frac{\rho}{V_0}i_{ext}, \\ r = \frac{\rho RC}{L}, \quad s = \frac{\rho}{R}; \end{cases} \quad (5)$$

As a result, an equivalent neuron model is obtained by

$$\begin{cases} \dot{x} = -w - ax^3 + bx^2 + I_{ext}; \\ \dot{w} = -c + dx^2 + rs(x - \lambda) - rw; \end{cases} \quad (6)$$

From dynamical viewpoint, the external current I_{ext} can be adjusted to trigger mode transition in the electric activities, and external field is also helpful to change the effect of reverse potential λ for regulating the firing modes. According to the definition for dimensionless variables and

parameters, these normalized parameters (a, b, c, d, r, s) are associated with the properties of ion channel, and λ accounts for the resting potential of one ion channel for the neuron. In addition, the equivalent Hamilton energy H can be mapped from the field energy W by using the same scale transformation on Eq. (4), and it is defined by

$$\begin{aligned} W &= \frac{1}{2} CV_0^2 x^2 + \frac{1}{2} \frac{L}{\rho^2 C} w^2 + \frac{d}{rs} x^2 w CV_0^2 \\ &= \frac{CV_0^2}{rs} \left[\frac{1}{2} rsx^2 + \frac{1}{2} w^2 + dx^2 w \right] \\ &= \frac{CV_0^2}{rs} H; \\ H &= \frac{1}{2} rsx^2 + \frac{1}{2} w^2 + dx^2 w; \end{aligned} \quad (7)$$

Guided by the Helmholtz theorem (Kobe 1986), the Hamilton energy for the neuron asks for the criterion

$$\begin{cases} \nabla H^T F_c = 0; \nabla H^T F_d = \frac{dH}{d\tau}; \\ \frac{dX}{d\tau} = F(X) = F_c(X) + F_d(X); X \in \mathbb{R}^N \end{cases} \quad (8)$$

Surely, the neuron in Eq. (6) has much similarity to the previous two-variable HR model proposed by Hindmarsh and Rose (1982). Considering the characteristic of inner field of neuron, the equivalent vector for Eq. (6) is updated by

$$H = \frac{1}{2} rsx^2 + \frac{1}{2} w^2 + dx^2 w = H_C + H_L - H_M; \quad (11)$$

This energy form in Eq. (11) is consistent with the energy function in Eq. (7), which is mapped from physical field energy after scale transformation. The changes of the Hamilton energy with time is confirmed by

$$\begin{aligned} \frac{dH}{d\tau} &= \nabla H^T F_d = x^4 (d^2 - 2adw - ars) + x^3 [(b+d)(2dw + rs) \\ &\quad - 2d^2 w] - dx^2 (rs\lambda + c + rw - w) - w^2 (r + 2dx) \\ &\quad - w(rs\lambda + c) + (rsx + 2dxw)I_{ext}; \end{aligned} \quad (12)$$

Changes in the parameters (r, s, d) have direct impact on the energy flow, which can also be controlled by external stimulus. According to Eq. (11), the Hamilton energy of the neuron is relative to the firing mode, membrane potential and the normalized parameters (r, s, d, w) directly. As defined in Eq. (11), the first term H_C and the second term H_L define electric field energy and magnetic field energy, and any changes in the excitability will modify the ratio between the two kinds of field energy.

$$H_L = \frac{1}{2} w^2, \quad H_C = \frac{1}{2} rsx^2, \quad P = \frac{H_C}{H_L} = \frac{rsx^2}{w^2}; \quad (13)$$

Periodic stimulus, chaotic series and even noise can be applied to regulate the neural activities and energy flow is shunted between magnetic field and electric field. It is

$$\begin{aligned} \begin{pmatrix} \dot{x} \\ \dot{w} \end{pmatrix} &= \begin{pmatrix} -w - ax^3 + bx^2 + I_{ext} \\ -c + dx^2 - rw + rs(x - \lambda) \end{pmatrix} = [J(x, w) + R(x, w)] \nabla H = F_c + F_d \\ &= \begin{pmatrix} -w - dx^2 \\ rsx + 2dxw \end{pmatrix} + \begin{pmatrix} -ax^3 + (b+d)x^2 + I_{ext} \\ dx^2 - rs\lambda - c - rw - 2dxw \end{pmatrix} \\ &= \begin{pmatrix} 0 & -1 \\ 1 & 0 \end{pmatrix} \begin{pmatrix} 2dxw + rsx \\ w + dx^2 \end{pmatrix} + \begin{pmatrix} \frac{-ax^3 + (b+d)x^2 + I_{ext}}{2dxw + rsx} & 0 \\ 0 & \frac{dx^2 - rs\lambda - c - rw - 2dxw}{w + dx^2} \end{pmatrix} \begin{pmatrix} 2dxw + rsx \\ w + dx^2 \end{pmatrix}; \end{aligned} \quad (9)$$

The energy function H for Eq. (9) follows the criterion as follows

$$(-w - dx^2) \frac{\partial H}{\partial x} + (rsx + 2dxw) \frac{\partial H}{\partial w} = 0; \quad (10)$$

As a result, an appropriate solution for the Hamilton energy is obtained by

interesting to discuss the mode transition when the energy proportion P is selected with different values. For two neurons, the synchronization stability is dependent on the biophysical properties of the coupling channel. Here, we consider the synchronization control for the two neurons connected by a nonlinear resistor, which the channel current has the form in Eq. (3). The coupled neural circuits are described by

$$\begin{cases} C \frac{dV}{dt} = i_{ext} - i_L - i_{NR} - i_{coupling}; \\ L \frac{di_L}{dt} = V - E - Ri_L - V_M; \\ C \frac{dV'}{dt} = i_{ext} - i'_L - i'_{NR} + i_{coupling}; \\ L \frac{di'_L}{dt} = V' - E - Ri'_L - V'_M; \\ i_{coupling} = -\frac{1}{\rho} \left[\frac{b(V - V')^2}{V_0} - \frac{a(V - V')^3}{V_0^2} \right] \end{cases} \quad (14)$$

By using the similar scale transformation, the dynamics for two coupled neurons can be given in the form

$$\begin{cases} \dot{x} = -w - ax^3 + bx^2 + I_{ext} + b(x - x')^2 - a(x - x')^3; \\ \dot{w} = -c + dx^2 + rs(x - \lambda) - rw; \\ \dot{x}' = -w' - ax'^3 + bx'^2 + I_{ext} - b(x - x')^2 + a(x - x')^3; \\ \dot{w}' = -c + dx'^2 + rs(x' - \lambda) - rw'; \end{cases} \quad (15)$$

The last two terms in the first and third formulas in Eq. (15) denote the equivalent dimensionless current across the coupling channel. The error function for states and Hamilton energy is defined respectively,

$$\begin{cases} \theta(e_x, e_w) = \sqrt{(x - x')^2 + (w - w')^2}; \\ \Delta H = |H_1 - H_2| = \left| \frac{1}{2}rsx^2 + \frac{1}{2}w^2 + dx^2w - \frac{1}{2}rsx'^2 - \frac{1}{2}w'^2 - dx'^2w' \right|; \end{cases} \quad (16)$$

In addition, phase series can be obtained by applying Hilbert transformation on the sampled time series for membrane potentials of two neurons, and then phase synchronization and phase lock between two neurons can be further verified when external stimuli are controlled to trigger different firing modes in the neurons. It is important to discuss the dynamical property of the coupling channels. In presence of linear coupling via ideal resistor with resistance R_k , the coupling intensity for two different cases (linear and nonlinear coupling) can be expressed by

$$\begin{cases} i_{coupling} = k(x' - x), \quad k = \frac{\rho}{R_k}, & \text{linear coupling via } R_k; \\ i'_{coupling} = b(x - x')^2 - a(x - x')^3, & \text{nonlinear coupling via } NR; \\ k' = b(x - x') - a(x - x')^2, & \text{nonlinear coupling via } NR; \end{cases} \quad (17)$$

That is, nonlinear coupling introduces time-varying coupling intensity k' and it terminates to zero adaptively under complete synchronization or balance between membrane potentials. As described in Eq. (6), the external stimulus I_{ext} can be derived from periodic signal source, and the deterministic model can be excited to present different firing modes. Indeed, realistic signal source may be more complex

and the neuron will be excited by mixed signals, which can be filtered from a chaotic system. For simplicity, signals from Pikovskii-Rabinovich (PR) oscillator (Pikovskii and Rabinovich 1978) are encoded to stimulate the neuron, and it is defined by

$$\begin{cases} \frac{dx'}{d\tau} = y' - \delta z'; \\ \frac{dy'}{d\tau} = -x' + 2\gamma y' + \alpha z' + \beta; \\ \frac{dz'}{d\tau} = \mu(x' + z' - z'^3); \\ I_{ext} = E_0 \sin(x'); \end{cases} \quad (18)$$

where x' , y' , z' are dimensionless variables mapped from the output voltage and current in the nonlinear circuit, and it presents chaotic state at $\alpha = 0.165$, $\beta = 0$, $\gamma = 0.201$, $\delta = 0.66$, $\mu = 1/0.047$. E_0 is a positive constant and considered as gain for control of the amplitude of the filtered chaotic signals, and similar chaotic signal from Lorenz, Rössler or other chaotic systems can be encoded for I_{ext} , which is effective to activate mode transition and nonlinear resonance in the electric activities. That is, the sampled time series for variable x' are chaotic and further encoding in sine function as $I_{ext} = E_0 \sin(x')$ will introduce irregular stimulus on the neuron. The coefficient variability (CV) is estimated to judge the coherence degree as follows

$$CV = \frac{\sqrt{\langle T^2 \rangle - \langle T \rangle^2}}{\langle T \rangle}; \quad (19)$$

where T denotes the interspike interval in the sampled time series for membrane potential, and the symbol $\langle * \rangle$ represents an average of the variable within certain transient period. Lower value for CV means higher coherence resonance in the neuron.

Results and discussion

The fourth order Runge–Kutta algorithm is used to approach numerical solution with time step $h = 0.01$. To present different firing patterns, the amplitude and angular frequency in the external stimulus $u_s = A \cos \omega \tau$ are adjusted to control the neuron in Eq. (6) with initial value (0.02, 0.01). The parameters are selected as $a = 0.52$, $b = 4.23$, $c = 2.6$, $d = 0.92$, $r = 0.119$, $s = 0.05$, $\lambda = -1.6$. For coupling synchronization, the initial values for two neurons are fixed at (0.02, 0.01, 0.03, 0.02). In Fig. 2, bifurcation analysis is supplied to confirm the appearance of different firing modes.

By adjusting the external stimulus, this neuron is suitable to produce a variety of firing patterns including chaotic, bursting and spiking, and it means this neuron has

Fig. 2 Bifurcation of ISI for membrane potential x vs. parameters A , ω . For **a** $\omega = 0.12$; **b** $A = 8.0$

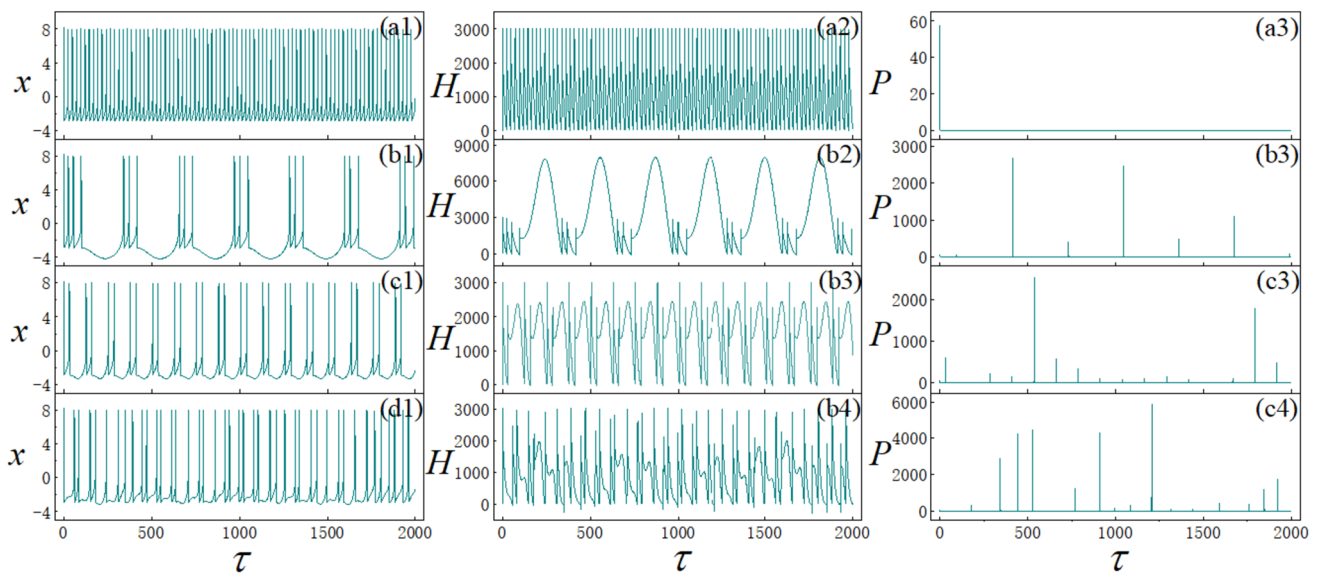
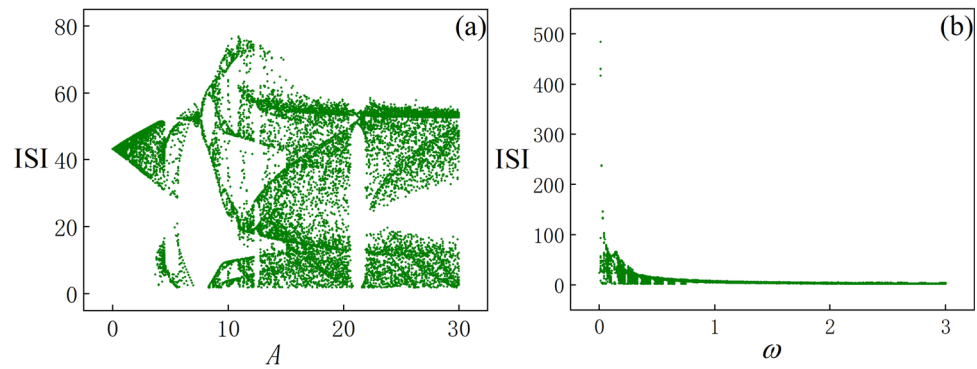
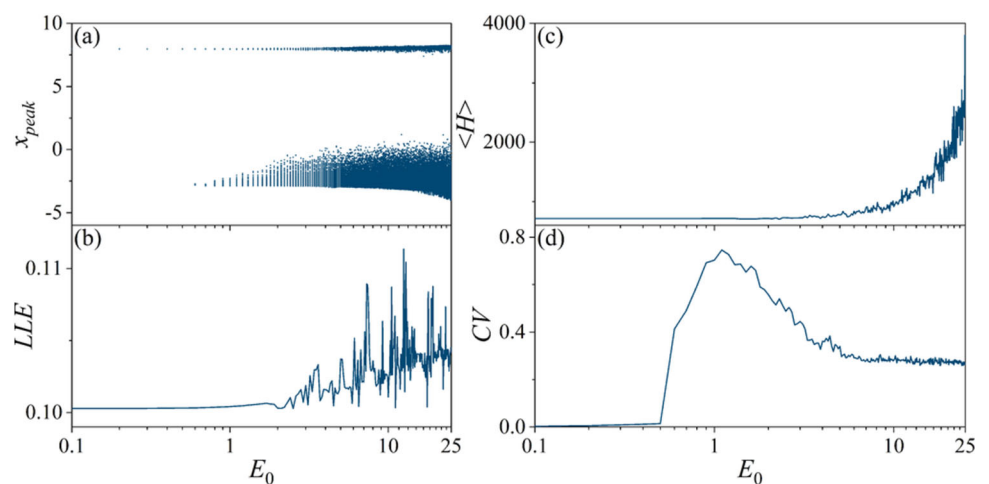


Fig. 3 Firing patterns of membrane, Hamilton energy H in Eq. (11), energy ratio P between H_C and H_L in Eq. (13), at $A = 8$. For **a1–a3** spiking patterns $\omega = 0.0001$; **b1–b3** bursting patterns $\omega = 0.02$; **c1–c3** periodic patterns $\omega = 0.05$; **d** chaotic patterns $\omega = 0.08$

Fig. 4 **a** Bifurcation of peaks for membrane potential x vs. E_0 in $I_{\text{ext}} = E_0 \sin(x')$; **b** average energy dependence on E_0 ; **c** Largest Lyapunov exponent vs. E_0 ; **d** CV distribution versus E_0



the main dynamical characteristic as those biological neurons. Extensive numerical results confirmed that noisy disturbance accompanying periodic stimuli can generate stochastic resonance by changing the noise intensity

carefully. For better showing, the electric activities are plotted and corresponding energy function is calculated to discern mode dependence on the firing modes in Fig. 2.

From Fig. 3, the energy in a single neuron is changed with the transition of firing modes, and further increasing the angular frequency of external stimulus can induce chaotic states. In presence of spiking patterns, the neuron used to keep higher energy level, while chaotic activities supports a lower average value in the Hamilton energy. Except the spiking condition, transient switch in the energy ratio is detected, and it means a fast energy release and exchange between magnetic field and electric field.

Realistic stimuli on neurons are not distinct periodic type, it is worthy of investigating the nonlinear response when mixed signals is applied. For simplicity, chaotic signals from PR in Eq. (18) are encoded to excite the neuron by applying different amplitudes for $I_{\text{ext}} = E_0 \sin(x')$, the Largest Lyapunov exponent, average energy $\langle H \rangle$, peak values from membrane potential and distribution for CV in Eq. (19) are calculated in Fig. 4.

From Fig. 4, the encoded chaotic signals $E_0 \sin(x')$ can inject stimuli as mixed signals and the excitability of the neuron can be regulated by the gain E_0 effectively, so mode transition can be controlled completely. Indeed, $E_0 \sin(x')$ can be considered as combination of periodic and stochastic disturbance, and appropriate setting for the gain E_0 can induce coherence resonance-like behavior in the neural activities. Further increasing the value for the gain E_0 prefers to impose chaotic stimulus and the neuron is excited to present chaotic firing patterns. The curve for CV distribution in Fig. 4d has no lowest value and it is in some difference from the previous curve for CV versus noise intensity, which moderate noise intensity supports

coherence resonance accompanying with lowest CV value. It is interesting to clarify the energy characteristic of the neuron excited by this stimulus, and the results are illustrated in Fig. 5.

In fact, $I_{\text{ext}} = E_0 \sin(x')$ can excite the neuron as quasi-periodic signals and the neuron prefers to trigger chaotic states and it keeps lower Hamilton energy because of fast discharge. During the firing of neural activities, electric field energy will keep a lower value than the magnetic field energy except some transient period. It indicates that the channel current in the neuron is fluctuated quickly and membrane potential is regulated to release energy quickly as well.

Synaptic connection can propagate energy effectively by regulating the synaptic current, and the time-varying coupling is dependent on the energy diversity. Linear electric synapse coupling requires special electrophysiological condition and consumption of Joule heat becomes inevitable. Indeed, biological neurons prefer to trigger field coupling and nonlinear coupling by activating hybrid synapse. In Fig. 6, the synchronous response between two neurons under the same periodic stimulus is calculated.

In presence of nonlinear coupling via hybrid synapse defined in Eq. (17), two identical neurons have difficult to reach complete synchronization. However, they can reach phase lock when the external stimulus is adjusted, and it indicates that the two neurons can guided to present some suitable firing modes in the neural activities. Furthermore, the energy diversity between two coupled neurons is calculated in Fig. 7.

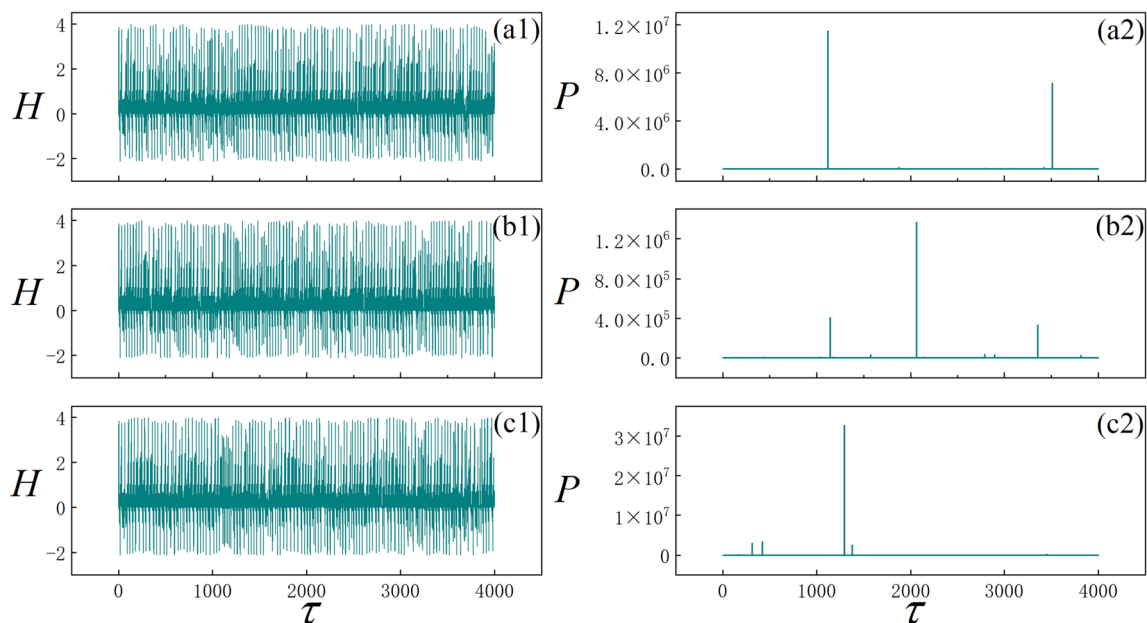
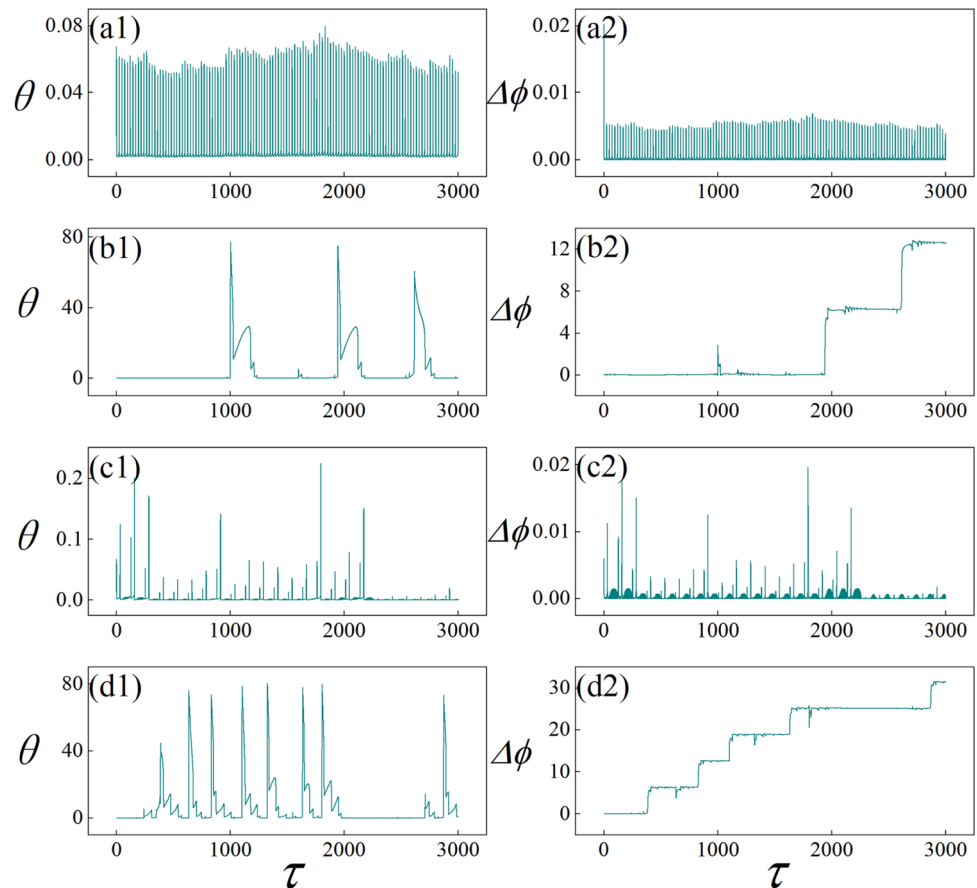


Fig. 5 Evolution of Hamilton energy H and changes in the ratio P between H_C and H_L is plotted in presence of mixed signals $I_{\text{ext}} = E_0 \sin(x')$. For **a1, a2** $E_0 = 1.0$; **b1, b2** $E_0 = 6.0$; **c1, c2** $E_0 = 20.0$

Fig. 6 Evolution of error function θ in Eq. (16) and phase error $\Delta\phi$ for two coupled neurons in presence of periodic stimulus. For **a1, a2** $A = 8.0$, $\omega = 0.0001$; **b1, b2** $A = 8.0$, $\omega = 0.02$; **c1, c2** $A = 8.0$, $\omega = 0.05$; **d1, d2** $A = 8.0$, $\omega = 0.08$. Phase series ϕ_1 and ϕ_2 are obtained by applying Hilbert transformation on the sampled time series for the variables (x, x'), and $\Delta\phi = \phi_1 - \phi_2$



Two identical neurons have the same distinct period and synchronization between periodic neurons becomes easy. When neurons reach complete synchronization, energy diversity is reduced to zero and energy balance is stabilized. This nonlinear coupling just activates subthreshold coupling because the gain in the coupling term is relative to some intrinsic parameters in the neuron. Therefore, they can reach transient synchronization rather than stable complete synchronization, and energy diversity will be changeable with time. In addition, the changes of coupling term and synaptic intensity in Eq. (17) is estimated when neurons are excited to present different modes.

From Fig. 8, in presence of four different firing modes, the synaptic current becomes time-varying, and it means that two neurons keep certain diversity of membrane potential. Therefore, complete synchronization is blocked, and it is helpful to prevent bursting synchronization and the occurrence of seizure in the nervous system. Considering the difference in excitability in biological neurons, two neurons connected via hybrid synapse are excited by encoded chaotic signals with different intensities, and the results are plotted in Fig. 9.

When the mixed signals are encoded with lower gain and intensity, phase synchronization between two neurons becomes available and it means this hybrid synapse is effective to trigger synchronous firing patterns. With further increase of the gain in the mixed signals, neurons prefer to present chaotic patterns and complete synchronization becomes difficult and phase lock is also broken with time. The energy diversity between neurons driven by encoded chaotic signals is also obtained to predict whether energy balance can be realized in Fig. 10.

It is found that the two neurons show time-varying energy diversity with time, and thus energy propagation along the hybrid synapse is continued, it is helpful to find coexisting different firing patterns in the nervous systems. Furthermore, the coupling intensity for nonlinear coupling is also estimated in Fig. 11 to predict whether the two neurons keep its nonlinear coupling all the time.

From Fig. 11a, it means the synaptic current is terminated because two neurons have the same membrane potentials and nonlinear coupling is switched off within a transient period. Therefore, two neurons keep their own firing modes and they can reach partial synchronization. From Fig. 11b, c, the synaptic current fluctuates with time

Fig. 7 Evolution of energy error for two coupled neurons driven by periodic signals. For **a** spiking neurons, $A = 8.0$, $\omega = 0.0001$; **b** bursting neurons, $A = 8.0$, $\omega = 0.02$; **c** periodic neurons, $A = 8.0$, $\omega = 0.05$; **d** chaotic neurons, $A = 8.0$, $\omega = 0.08$

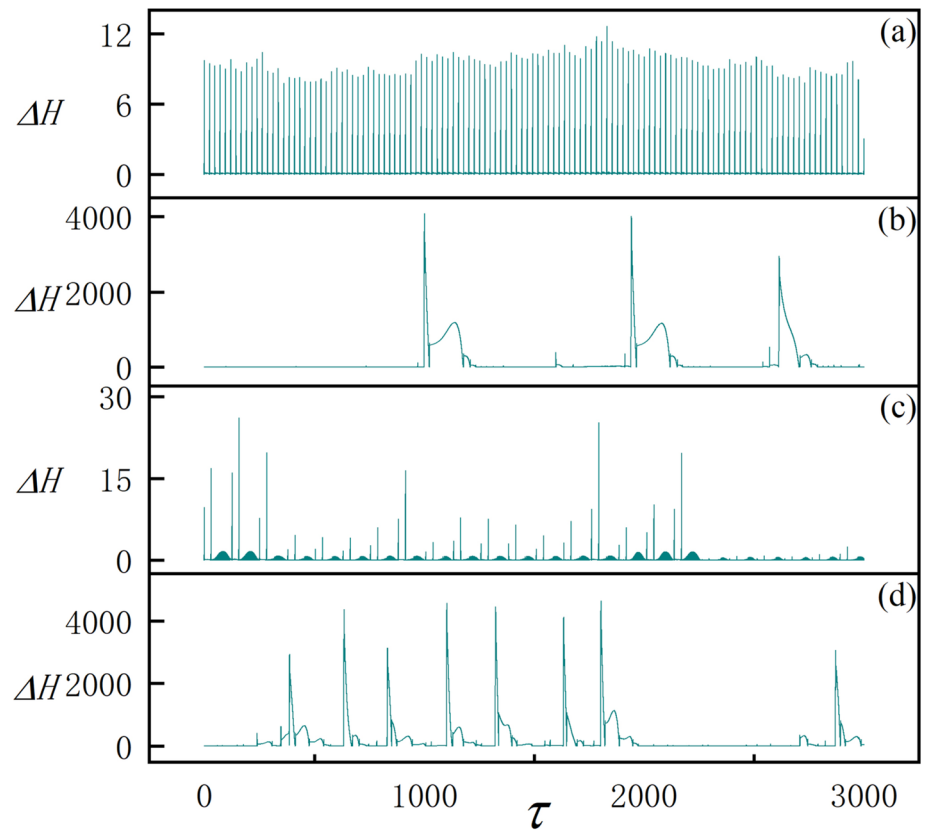


Fig. 8 Changes in synaptic intensity k' along the hybrid synapse for two coupled neurons in Eq. (18). For **a** $A = 8.0$, $\omega = 0.0001$; **b** $A = 8.0$, $\omega = 0.02$; **c** $A = 8.0$, $\omega = 0.05$; **d** $A = 8.0$, $\omega = 0.08$

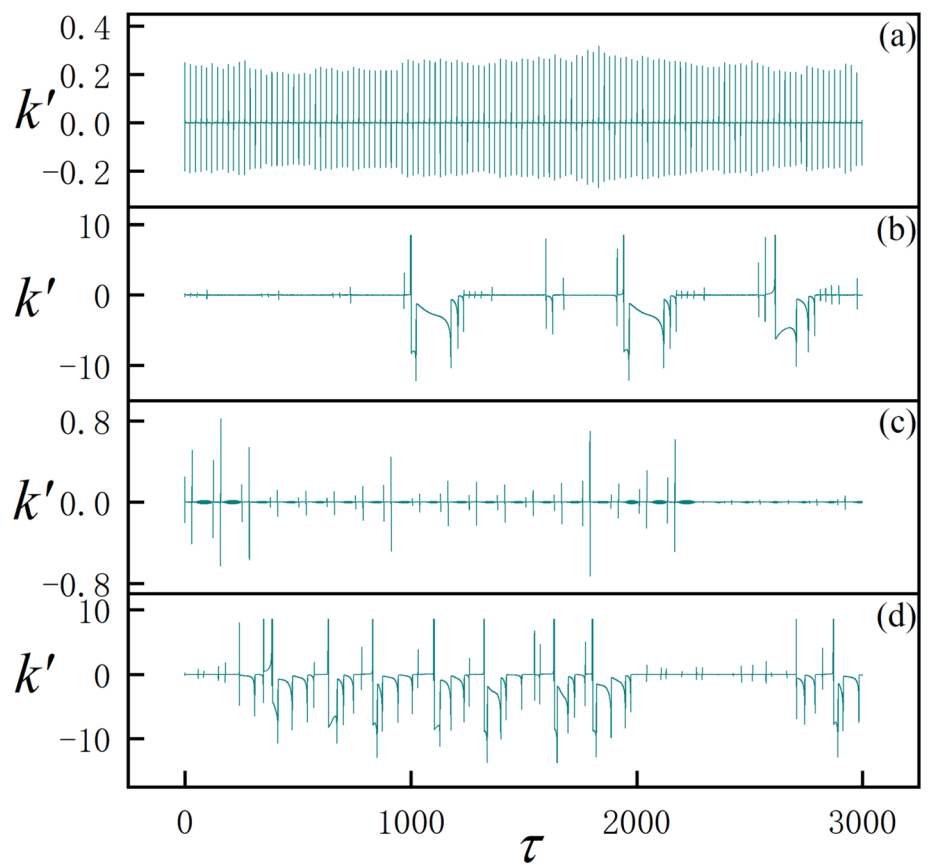


Fig. 9 Evolution of error function for two coupled neurons presented in different firing modes and phase error diagram by mixed signals $I_{\text{ext}} = E_0 \sin(x')$. For **a1, a2** $E_0 = 1.0$; **b1, b2** $E_0 = 6.0$; **c1, c2** $E_0 = 20.0$

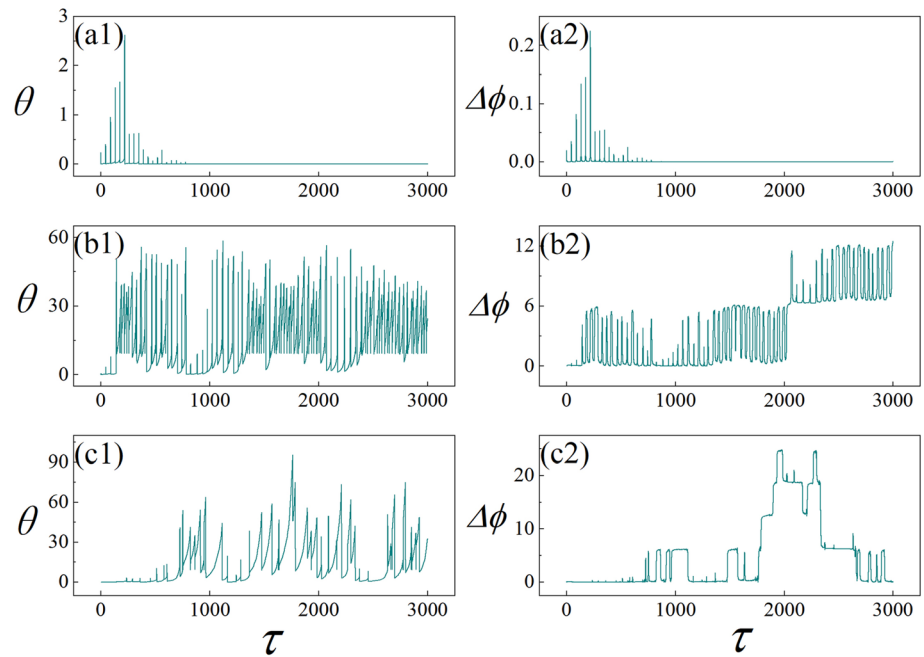
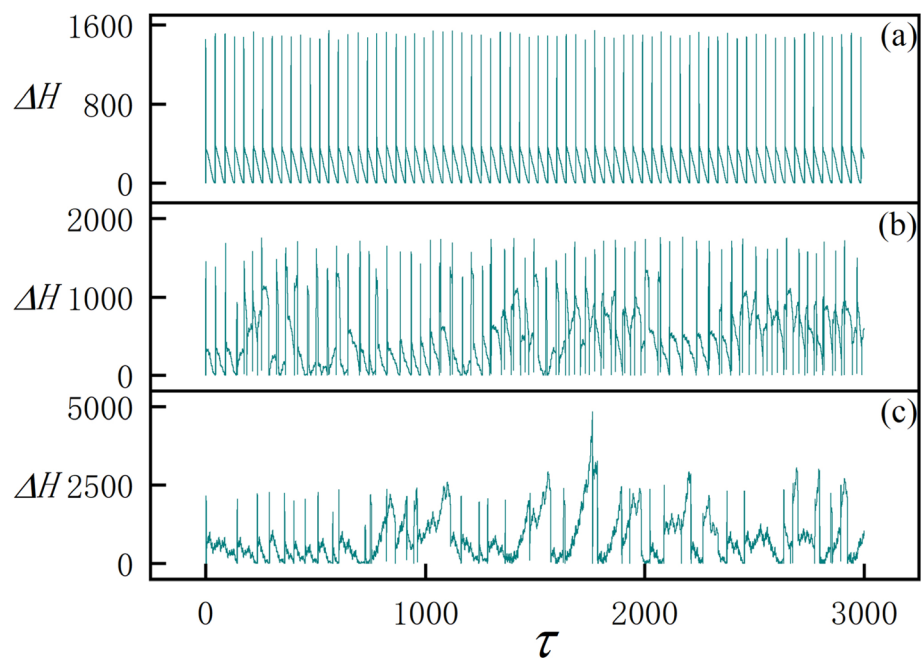


Fig. 10 Evolution of energy error for two coupled neurons driven by mixed signals $I_{\text{ext}} = E_0 \sin(x')$. For **a** $E_0 = 1.0$; **b** $E_0 = 6.0$; **c** $E_0 = 20.0$

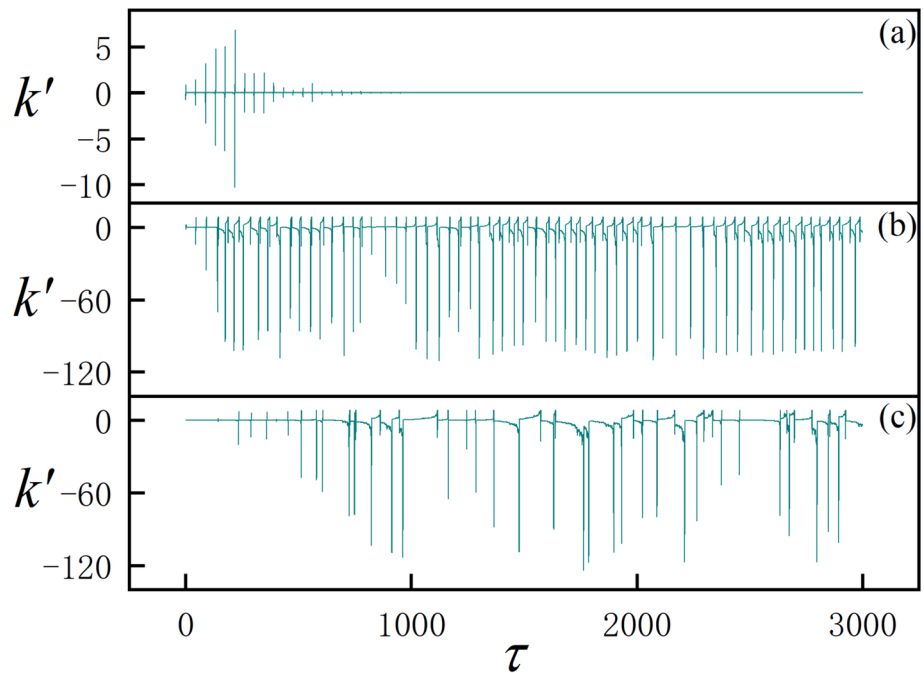


and it means the hybrid synapse keeps working for continuous energy propagation and exchange because of distinct diversity in the two neurons. In particular, appearance of negative value for the coupling intensity k' indicates this nonlinear coupling activates positive feedback on each neuron, therefore, energy diversity and firing modes are regulated with time.

In summary, realistic biological neurons often receive mixed signals from external stimulus and neurons in the

neural networks will capture more signals from other neurons. Furthermore, these multi-channels injections are detected to compose an encoded signal within certain frequency band. When two or more neurons are excited, hybrid synapses rather than sole and ideal synapses are activated to propagate energy between neurons, transition from synchronization and desynchronization is switched when the coupling intensity along the nonlinear channel is changed between negative and positive values. As a result,

Fig. 11 Changes in synaptic intensity k' along the hybrid synapse for two coupled neurons driven by $I_{\text{ext}} = E_0 \sin(x')$. For **a** $E_0 = 1.0$; **b** $E_0 = 6.0$; **c** $E_0 = 20.0$



two neurons can present different firing patterns and modes in the neural activities. Hybrid synapse plays an important role to keep energy diversity and these neurons are blocked to reach synchronous firing patterns, which can prevent the occurrence of seizure. In fact, hybrid synapse accounts for nonlinear coupling and it is suitable to approach close biophysical property and physical effect of realistic synapses for biological neurons. In a practical way, combination of functional electric components including memristor, nonlinear resistor, thermistor, phototube, piezoelectric component and Josephson junction can enhance the sensitivity and controllability of synaptic connection and coupling channels, the main advantage of these functional synapse is its intensity can be regulated adaptively and external stimuli can control the coupling channel directly. The energy definition within this work is defined and confirmed from physical viewpoint (Njitacke et al. 2022b), it is different from the previous energy description in Wang and Zhu (2016), Zhu et al. (2019), Wang et al. (2021) for neurons. As mentioned in our recent works, continuous energy injection and absorption will induce shape deformation, some neurons will show parameter shift to keep pace with other neurons for showing synchronous firing or desynchronization, as a result, self-adaption of biological neurons are released. Nonlinear coupling provides possible intermittent positive and negative regulation on two neurons, and this scheme can be further used to induce and control chimera in neural networks Yang et al. (2022), Kanagaraj et al. (2023), Feng et al. (2023) by developing coexistence of synchronization and non-synchronization.

Conclusions

Based on the Helmholtz theorem, an energy function for a two-variable neuron is defined from physical viewpoint and it is also confirmed by applying scale transformation on the field energy in the neural circuit composed of a voltage-controlled component. Filtered chaotic signals are used to excite the neuron for mimicking realistic stimulus. It indicates that biological neurons can be excited to present regular patterns under mixed signal matching with realistic signals within certain frequency band, and average energy and CV distributions are calculated to discern mode transition in electrical activities. Furthermore, two neural circuits are coupled by the same nonlinear resistor, and synchronization stability and phase lock are controlled by the nonlinear coupling. Under some firing modes, the coupling intensity is decreased to zero and nonlinear coupling is terminated with the same membrane potentials. In other cases, continuous nonlinear coupling contributes to phase lock or phase synchronization, and possible bursting synchronization is prevented. That is, nonlinear coupling provides effective energy exchange and supports coexistence of multiple firing modes in neurons under energy diversity. To activate the self-adaption of biological neurons, shape deformation accompanying with parameter shift becomes inevitable and then the hybrid synapse is controlled to adjust the coupling intensity for reaching next energy balance between neurons.

Acknowledgements This project is partially supported by National Natural Science Foundation of China under Grant No. 62361037. The authors thank Dr. Yao Zhao for the help in numerical verification.

Data availability Data available on appropriate request from the authors.

Declarations

Conflict of interest The authors declare no any interest conflict with publication of this work.

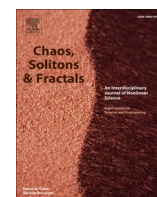
References

- Balenzuela P, García-Ojalvo J (2005) Role of chemical synapses in coupled neurons with noise. *Phys Rev E* 72:021901
- Bao BC, Zhu YX, Ma J et al (2021) Memristive neuron model with an adapting synapse and its hardware experiments. *Sci China Technol Sci* 64:1107–1117
- Bennett MVL (1997) Gap junctions as electrical synapses. *J Neurocytol* 26:349–366
- Bennett MVL (2000) Electrical synapses, a personal perspective (or history). *Brain Res Rev* 32:16–28
- Bennett MVL, Zukin RS (2004) Electrical coupling and neuronal synchronization in the mammalian brain. *Neuron* 41:495–511
- Cai J, Bao H, Xu Q et al (2021) Smooth nonlinear fitting scheme for analog multiplierless implementation of Hindmarsh–Rose neuron model. *Nonlinear Dyn* 104:4379–4389
- Calim A, Torres JJ, Ozer M et al (2020) Chimera states in hybrid coupled neuron populations. *Neural Netw* 126:108–117
- Chen B, Xu Q, Chen M et al (2021) Initial-condition-switched boosting extreme multistability and mechanism analysis in a memcapacitive oscillator. *Front Inf Technol Electron Eng* 22:1517–1531
- Chithra A, Raja MI (2017) Synchronization and chaotic communication in nonlinear circuits with nonlinear coupling. *J Comput Electron* 16:833–844
- Curti S, O'Brien J (2016) Characteristics and plasticity of electrical synaptic transmission. *BMC Cell Biol* 17:59–70
- Dana SK, Sengupta DC, Hu CK (2006) Spiking and bursting in Josephson junction. *IEEE Trans Circuits Syst II Express Briefs* 53:1031–1034
- Feng P, Yang J, Wu Y (2023) Chimera state in a feed-forward neuronal network. *Cogn Neurodyn* 17:1119–1130
- Gerasimova SA, Gelikonov GV, Pisarchik AN et al (2015) Synchronization of optically coupled neural-like oscillators. *J Commun Technol Electron* 60:900–903
- Gieseler J, Spasenović M, Novotny L et al (2014) Nonlinear mode coupling and synchronization of a vacuum-trapped nanoparticle. *Phys Rev Lett* 112:103603
- González-Miranda JM (2007) Complex bifurcation structures in the Hindmarsh–Rose neuron model. *Int J Bifurc Chaos* 17:3071–3083
- Hindmarsh JL, Rose RM (1982) A model of the nerve impulse using two first-order differential equations. *Nature* 296:162–164
- Hindmarsh JL, Rose RM (1984) A model of neuronal bursting using three coupled first order differential equations. *Proc R Soc Lond Ser B Biol Sci* 221:87–102
- Hu D, Cao H (2016) Stability and synchronization of coupled Rulkov map-based neurons with chemical synapses. *Commun Nonlinear Sci Numer Simul* 35:105–122
- Kanagaraj S, Moroz I, Durairaj P et al (2023) Imperfect chimera and synchronization in a hybrid adaptive conductance based exponential integrate and fire neuron model. *Cogn Neurodyn*. <https://doi.org/10.1007/s11571-023-10000-0>
- Kobe DH (1986) Helmholtz's theorem revisited. *Am J Phys* 54:552–554
- Kundu S, Majhi S, Ghosh D (2019) Chemical synaptic multiplexing enhances rhythmicity in neuronal networks. *Nonlinear Dyn* 98:1659–1668
- Kyprianidis IM, Papachristou V, Stouboulos IN et al (2012) Dynamics of coupled chaotic Bonhoeffer–van der Pol oscillators. *WSEAS Trans Syst* 11:516–526
- Ma J (2022) Dynamics and model approach for functional neurons. *J Guangxi Normal Univ (Nat Sci Edn)* 40:307–323 (in Chinese)
- Ma J (2023) Biophysical neurons, energy and synapse controllability: a review. *J Zhejiang Univ Sci A* 24:109–129
- Ma J, Yang Z, Yang L et al (2019) A physical view of computational neurodynamics. *J Zhejiang Univ Sci A* 20:639–659
- Moujahid A, d'Anjou A, Torrealdea FJ et al (2011) Energy and information in Hodgkin–Huxley neurons. *Phys Rev E* 83:031912
- Njitacke ZT, Ramakrishnan B, Rajagopal K et al (2022a) Extremely rich dynamics of coupled heterogeneous neurons through a Josephson junction synapse. *Chaos Solitons Fractals* 164:112717
- Njitacke ZT, Koumetio BN, Ramakrishnan B et al (2022b) Hamiltonian energy and coexistence of hidden firing patterns from bidirectional coupling between two different neurons. *Cogn Neurodyn* 16:899–916
- Ochs K, Jenderny S (2021) An equivalent electrical circuit for the Hindmarsh–Rose model. *Int J Circuit Theory Appl* 49:3526–3539
- Peterit J, Pikovsky A (2017) Chaos synchronization by nonlinear coupling. *Commun Nonlinear Sci Numer Simul* 44:344–351
- Pikovskii AS, Rabinovich MI (1978) A simple autogenerator with stochastic behavior. *Soviet Phys Dokl* 23:183–185
- Pu Y, Yu B, He Q et al (2021) Fractional-order memristive neural synaptic weighting achieved by pulse-based fracmemristor bridge circuit. *Front Inf Technol Electron Eng* 22:862–876
- Rajagopal K, Nazarimehr F, Karthikeyan A et al (2019) Dynamics of a neuron exposed to integer-and fractional-order discontinuous external magnetic flux. *Front Inf Technol Electron Eng* 20:584–590
- Rajasekar S, Lakshmanan M (1988) Period-doubling bifurcations, chaos, phase-locking and devil's staircase in a Bonhoeffer–van der Pol oscillator. *Phys D* 32:146–152
- Shafiei M, Jafari S, Parastesh F et al (2020) Time delayed chemical synapses and synchronization in multilayer neuronal networks with ephaptic inter-layer coupling. *Commun Nonlinear Sci Numer Simul* 84:105175
- Smith M, Pereda AE (2003) Chemical synaptic activity modulates nearby electrical synapses. *Proc Natl Acad Sci* 100:4849–4854
- Sun J, Deng B, Liu C et al (2013) Vibrational resonance in neuron populations with hybrid synapses. *Appl Math Model* 37:6311–6324
- Torrealdea FJ, d'Anjou A, Graña M et al (2006) Energy aspects of the synchronization of model neurons. *Phys Rev E* 74:011905
- Torrealdea FJ, Sarasola C, d'Anjou A (2009) Energy consumption and information transmission in model neurons. *Chaos Solitons Fractals* 40:60–68
- Uzuntarla M (2019) Firing dynamics in hybrid coupled populations of bistable neurons. *Neurocomputing* 367:328–336
- Velazquez JLP, Carlen PL (2000) Gap junctions, synchrony and seizures. *Trends Neurosci* 23:68–74
- Wang R, Zhu Y (2016) Can the activities of the large scale cortical network be expressed by neural energy? A brief review. *Cognit Neurodyn* 10:1–5
- Wang CN, Li SR, Ma J et al (2010) Synchronization transition in degenerate optical parametric oscillators induced by nonlinear coupling. *Appl Math Comput* 216:647–654
- Wang Y, Xu X, Wang R (2021) Energy features in spontaneous up and down oscillations. *Cogn Neurodyn* 15:65–75

- Wang C, Sun G, Yang F et al (2022) Capacitive coupling memristive systems for energy balance. *AEU Int J Electron Commun* 153:154280
- Wang XJ, Gu HG, Jia YB (2023) Relationship between threshold and bifurcation for paradoxical responses of spiking along with seizure induced by inhibitory modulation. *Europhys Lett* 142:50002
- Wei B, Xiao F, Shi Y (2019) Fully distributed synchronization of dynamic networked systems with adaptive nonlinear couplings. *IEEE Trans Cybern* 50:2926–2934
- Wu F, Ma J, Zhang G (2019) A new neuron model under electromagnetic field. *Appl Math Comput* 347:590–599
- Wu FQ, Ma J, Zhang G (2020) Energy estimation and coupling synchronization between biophysical neurons. *Sci China Technol Sci* 63:625–636
- Wu F, Guo Y, Ma J (2022a) Reproduce the biophysical function of chemical synapse by using a memristive synapse. *Nonlinear Dyn* 109:2063–2084
- Wu F, Hu X, Ma J (2022b) Estimation of the effect of magnetic field on a memristive neuron. *Appl Math Comput* 432:127366
- Xie Y, Yao Z, Hu X et al (2021a) Enhance sensitivity to illumination and synchronization in light-dependent neurons. *Chin Phys B* 30:120510
- Xie Y, Zhu ZG, Zhang XF et al (2021b) Control of firing mode in nonlinear neuron circuit driven by photocurrent. *Acta Phys Sin* 70:210502
- Xie Y, Yao Z, Ma J (2022) Phase synchronization and energy balance between neurons. *Front Inf Technol Electron Eng* 23:1407–1420
- Xie Y, Zhou P, Ma J (2023) Energy balance and synchronization via inductive-coupling in functional neural circuits. *Appl Math Model* 113:175–187
- Xu Y, Ma J (2021) Control of firing activities in thermosensitive neuron by activating excitatory autapse. *Chin Phys B* 30:100501
- Xu Y, Jia Y, Wang H et al (2019) Spiking activities in chain neural network driven by channel noise with field coupling. *Nonlinear Dyn* 95:3237–3247
- Xu Y, Liu M, Zhu Z et al (2020) Dynamics and coherence resonance in a thermosensitive neuron driven by photocurrent. *Chin Phys B* 29:098704
- Xu K, Maidana JP, Orio P (2021) Diversity of neuronal activity is provided by hybrid synapses. *Nonlinear Dyn* 105:2693–2710
- Yang Y, Xiang C, Dai X et al (2022) Chimera states and cluster solutions in Hindmarsh–Rose neural networks with state resetting process. *Cogn Neurodyn* 16:215–228
- Yao Z, Wang C (2021) Control the collective behaviors in a functional neural network. *Chaos Solitons Fractals* 152:111361
- Yao Z, Wang C (2022) Collective behaviors in a multiple functional network with hybrid synapses. *Phys A* 605:127981
- Yao Z, Wang C, Zhou P et al (2021) Regulating synchronous patterns in neurons and networks via field coupling. *Commun Nonlinear Sci Numer Simul* 95:105583
- Yu H, Guo X, Wang J (2017) Stochastic resonance enhancement of small-world neural networks by hybrid synapses and time delay. *Commun Nonlinear Sci Numer Simul* 42:532–544
- Zandi-Mehran N, Jafari S, Hashemi Golpayegani SM et al (2020) Different synaptic connections evoke different firing patterns in neurons subject to an electromagnetic field. *Nonlinear Dyn* 100:1809–1824
- Zhang Y, He W, Wu Y et al (2018) Highly compact artificial memristive neuron with low energy consumption. *Small* 14(51):1802188
- Zhang Y, Xu Y, Yao Z et al (2020a) A feasible neuron for estimating the magnetic field effect. *Nonlinear Dyn* 102:1849–1867
- Zhang Y, Wang CN, Tang J et al (2020b) Phase coupling synchronization of FHN neurons connected by a Josephson junction. *Sci China Technol Sci* 63:2328–2338
- Zhou P, Yao Z, Ma J et al (2021a) A piezoelectric sensing neuron and resonance synchronization between auditory neurons under stimulus. *Chaos Solitons Fractals* 145:110751
- Zhou P, Hu X, Zhu Z et al (2021b) What is the most suitable Lyapunov function? *Chaos Solitons Fractals* 150:111154
- Zhou P, Zhang X, Ma J (2022a) How to wake up the electric synapse coupling between neurons? *Nonlinear Dyn* 108:1681–1695
- Zhou P, Zhang X, Hu X et al (2022b) Energy balance between two thermosensitive circuits under field coupling. *Nonlinear Dyn* 110:1879–1895
- Zhu F, Wang R, Pan X et al (2019) Energy expenditure computation of a single bursting neuron. *Cogn Neurodyn* 13:75–87

Publisher's Note Springer Nature remains neutral with regard to jurisdictional claims in published maps and institutional affiliations.

Springer Nature or its licensor (e.g. a society or other partner) holds exclusive rights to this article under a publishing agreement with the author(s) or other rightsholder(s); author self-archiving of the accepted manuscript version of this article is solely governed by the terms of such publishing agreement and applicable law.



Review article

Model approach of electromechanical arm interacted with neural circuit, a minireview

Jun Ma^{a,b,c,*}, Yitong Guo^{a,b}^a College of Electrical and Information Engineering, Lanzhou University of Technology, Lanzhou 730050, China^b Department of Physics, Lanzhou University of Technology, Lanzhou 730050, China^c School of Science, Chongqing University of Posts and Telecommunications, Chongqing 430065, China

ARTICLE INFO

Keywords:

Neural circuit
Scale transformation
Neuron
Artificial arm
Synchronization

ABSTRACT

Artificial neurons can be designed and excited to produce similar smart responses as biological neurons driven by electromagnetic excitations. The interaction between cell membrane and ion channels accounts for the mode transition in membrane potentials and the changes of inner field energy during continuous diffusion and propagation of ions in the neuron. The external stimuli just speed up the mode selection by changing the gradient distribution of electromagnetic field of the cell. The propagated electric pulses are affected by the Calcium wave and concentration, and muscle is controlled to behave suitable body gaits. In this review, a neural circuit-coupled electromechanical device is suggested to clarify how neural signals drive the artificial arms. The pre-placed neural circuit can be regarded as a wave filter, and the encoded signals are guided to excite one electromechanical arm, and then a pair of arms connected with a spring is controlled to simulate the motion of two arms. The circuit and motion equations for the artificial arms are presented with exact definition of energy function. Scale transformation is applied to obtain an equivalent dimensionless dynamical model and the dimensionless Hamilton energy. Finally, an adaptive control law is presented to control the neural circuit and the load circuit in the electromechanical device. This work provides possible guidance for designing artificial arms or legs under electric stimuli, readers can find clues for further investigation under complete dynamical analysis.

1. Introduction

Nervous system can perceive a variety of external stimuli, and then suitable firing modes in electrical activities are induced to propagate the encoded signals among neurons. When more biological neurons are excited, the Calcium concentrations of cells are increased and tamed to control the body muscle [1,2], and then appropriate gaits are stabilized. In presence of external stimuli, most of the neurons in the same functional regions are waken for developing possible synaptic connection under energy flow, and even neurons from other functional regions are affected to build multi-layer network. As a result, the body keeps suitable and safe gaits to give smart response to the multiple-channels excitation. The time series for membrane potential of a biological neuron are often available due to the application of patch clamp technology, while the channel currents are often fit with different functions composed of the membrane potential with suitable parameters. In fact, model setting and model improvement of biological neurons should consider the main physical property during the occurrence of neural

activities. At least, one capacitive variable is useful for the membrane potential and its inner electric field, another inductive variable becomes crucial to measure the channel current and its effect of magnetic field. Considering the distribution and interaction between different kinds of ion channels, some additive nonlinear terms are required to describe the effect of ion channels during the energy conversion between magnetic field and electric field when neurons are excited. From physical aspect, both capacitor and charge-controlled memristor (CCM) [3–5] have capacitive variables when the output voltage or charges flow are detectable. On the other hand, inductor and magnetic-flux controlled memristor (MFCM) [6–8] present inductive variables when the induced current or magnetic flux can be measured in reliable way.

Indeed, a generic neuron model [9,10] requires two variables including the membrane potential and recovery variable for channel current. As a result, a simple neural circuit composed of a capacitor, an inductor and a nonlinear resistor can be tamed to present similar firing patterns as mathematical neurons or biological neurons by developing similar spiking, bursting or chaotic states. To approach the effect of

* Corresponding author at: Department of Physics, Lanzhou University of Technology, Lanzhou 730050, China.

E-mail addresses: hyperchaos@163.com, hyperchaos@lut.edu.cn (J. Ma).

<https://doi.org/10.1016/j.chaos.2024.114925>

Received 21 March 2024; Received in revised form 7 April 2024; Accepted 21 April 2024

Available online 24 April 2024

0960-0779/© 2024 Elsevier Ltd. All rights reserved.

complex ion channels, more branch circuits are created in the generic RLC (resistor-inductor-capacitor) for introducing different kinds of channel current terms. Therefore, these neuron models present more than three variables, and some of them can describe the effect of electromagnetic induction [11–13], temperature, electric and magnetic field, and even photoelectric conversion in the neurons. The effect of electromagnetic induction in the neuron and neural circuits is often described by introducing memristive current and magnetic flux variable in the models [14,15]. During circuit implement, memristor, Josephson junction, piezoelectric ceramic, thermistor, photocell and voltage-controlled devices can be incorporated into the branch circuits of a neural circuit, and then the controlled circuit can be effective to discern or detect external physical signals [16–18]. For example, phototube is connected to a neural circuit for building a light-sensitive neuron [19], and Josephson junction is used to detect external magnetic field when it is incorporated into a neural circuit [20]. After scale transformation, these neural circuits can be converted into dimensionless neuron models with different current terms, and they are called as functional biophysical neurons. In fact, the Hopfield neural network is considered as an effective network model for generic signal processing, and the involvement of memristive function into it [21–23] can measure the effect of electromagnetic induction and radiation. Furthermore, similar memristive regulation is applied to the Chialvo neuron [24,25] and Hindmarsh-Rose neuron models [26–28], the complete dynamical analysis, energy definition and synchronization control provide helpful comments on understanding the relation between modes selection and energy levels. Besides the common analysis, circuit implement and fractional order approach of the neuron model pave new ways for neurodynamics [29,30].

From mathematical viewpoint, two variables are necessary for building an oscillator-like neuron model, one variable for the membrane potential and another variable for the channel current. To present chaotic firing patterns, suitable external stimulus including noise or periodic forcing becomes indispensable. As a result, the physical property of the cell membrane is missed because all external stimuli are regarded as equivalent transmembrane current terms. Some recent works [31–33] claimed that reliable neuron models should involve two capacitive variables, one for the outer membrane and another for the inner membrane when the cell membrane has two sides supporting different distribution of electromagnetic field. Surely, map neuron models [34–37] are also effective to reproduce the main dynamical property and physical effect when the map neuron is clarified with exact energy function. That is, it is crucial to clarify the energy characteristic and self-adaptive property before suggesting and confirming any new neuron models. Most of the oscillator-like neuron model can obtain their energy function by using the Helmholtz theorem, while the energy function definition of map neurons becomes a challenge. The author of this work suggested a scheme to define energy function for many maps, and it also provides a clue to check the reliability of maps from energy aspect [38–40]. When the energy function is obtained in exact form, an adaptive law can be suggested to control the intrinsic parameter growth and adaptive regulation of synaptic intensity when the energy level is beyond a threshold [41,42]. For two or more neurons, the synaptic connections keep adaptive growth in the synapse intensity when the energy diversity is beyond a threshold, therefore, the neurons can keep energy balance and phase synchronization or desynchronization [43–46]. Furthermore, continuous energy accumulation can develop heterogeneity [47,48] while energy release can create defects in the neural network when the synaptic bridges are controlled by energy diversity in a local area of the network.

By now, dynamical analysis in many neuron models has been investigated extensively. Based on these neuron models, collective behaviors and self-organization under noise have been discussed by connecting different neural networks. As is known, the arms and legs can behave different gaits when the nervous system is guided with suitable commands. To discard the complex freedoms of arm and leg, a moving

beam driven by electromechanical force [49–51] can mimic the dynamical characteristic of moving arm or leg. In generic way, the load circuit composed of coils with N turns is banded to one end of a beam, which is placed into a magnetic field, the Ampere force generated in the load circuit will drive the beam to move when external forcing current is injected into the coils of the load circuit. On the other hand, the coils of the load circuit will generate a dynamic electromotive force (DEF) to change the channel current, and then induced electromotive force (IEF) is generated during the moving of the beam. As a result, both DEF and IEF will apply feedback to the terminal of neural circuit, which its output voltage is used to excite the load circuit. That is, the neural circuit interacts with the load circuit adhere to the moving beam by changing the current across the coupling channel when DEF and IEF are generated. The neural circuits can be described by oscillator neuron models, and it is important to convert the physical variables including displacement and velocity into dimensionless variables for dynamical analysis. For example, Wadden et al. [52] proposed a neuro-mechanical model and the motion of single leg is controlled. Mbeunga et al. [53] analyzed the nonlinear response in an array of electromechanical systems driven by an electrical line of Fitzhugh-Nagumo neurons. Ngongiah et al. [54] explored the motion of myriapods by using an array of mechanical arms coupled to an array of Fitzhugh-Nagumo neuron circuits. Furthermore, Ngongiah et al. [55] designed a bioinspired electromechanical system, which that Fitzhugh-Nagumo neuron circuits are combined to drive synchronically an array of mechanical legs, and driving-response of the array of legs are discussed. Kouami et al. [56] investigated an array of nanoelectromechanical beams driven by an electrical line of Josephson junctions equivalent models, and the motion of the beams is dependent on the junction current. Wang et al. [57] designed a four-bar linkage bionic knee joint structure with a variable axis and a double closed-loop servo position control strategy based on computed torque control is used to improve anthropomorphic characteristics and the dynamic performance of the bionic mechanical leg powered by servo pneumatic muscle (SPM). In Ref. [58], analytical and numerical investigations of Josephson junction neuron circuits actuating a mechanical arm and the array are provided.

In this paper, the interaction between neural circuit and electromechanical devices is discussed, and this study is helpful to design artificial arm and leg, and it also provides an example for the application of neural circuits. The circuit equations for the neural circuit are approached, the dependence of displacement of the moving beam on the electromechanical force is defined, and then scale transformation is used to obtain a dimensionless model for describing the relation between neural activities and mechanical motion. Section 2 contains five subsections, Section 2.1 presents generic description for a generic neural circuit and its energy function. Section 2.2 explained the working mechanism of an artificial arm/leg under electromagnetic force. Section 2.3 presented discussion about cooperation between two artificial arms. Section 2.4 supplied complete discussion about how memristor-based neural circuit drive an artificial arm developed from an electromechanical device. Section 2.5 suggested an adaptive law for control the neural circuit and the moving arm. Section 3 gave the conclusion and suggestions for this field.

2. Model and scheme

For most of the neurons, periodic stimulus seldom triggers the same firing patterns only when the external forcing current is endowed with high intensity. Sometimes, chaotic stimuli on the neuron just develop spiking or bursting patterns rather than chaotic behaviors in membrane potential because the biological and biophysical neurons encode the external signal in nonlinear way. That is, artificial and biological neurons can be considered as effective wave filter and signal generator because the outputs often are different from the exciting signals.

2.1. Signal encoding and wave filtering in a neural circuit

As shown in Fig. 1, external physical signal i_s across a resistor R_s , which induces a voltage drop, is interacted with the output terminal of the RC circuit and the filtered signal i_{out} often has a different frequency band from the injected signal i_s .

When the nonlinear electric component NM is not activated by cutting off the switch S , the forcing current i_s across the linear resistor R_s imposed a voltage excitation on the capacitor C and also shunted a current to excite the inductor L . As a result, the charged capacitor generates a channel current and the induction coil in the LC circuit creates an induced electromotive force (IEF), the interaction between the inductor and capacitor will impose a feedback to the injected forcing current i_s , and the output signals i_{out} shows some diversity from the original input signal i_s . In an experimental way, activation of the nonlinear electric device NM , for example, NM can be a nonlinear resistor or a memristor, the LC circuit is excited to present continuous oscillation even without applying external forcing current i_s because the nonlinear electric element can be regarded as exciting source. The emitted current i_e from the output terminal will interact with the injected current i_e , and combination of two channels currents will control the amplitude and frequency of final output signals i_{out} . From physical viewpoint, the outputs i_e from the LC circuit can suppress finite frequency band of the injected signal and then wave filtering is realized. According to the Kirchhoff's theorem, the relation between physical variables in Fig. 1 can be obtained by

$$\begin{cases} C \frac{dV}{dt} = i_e - i_L - i_{NM}; \\ L \frac{di_L}{dt} = V; \quad i_{out} = i_s + i_e. \end{cases} \quad (1)$$

The channel current along the electric component NM often shows nonlinear relation between the voltage and current as follows

$$\begin{cases} i_{NM} = -\frac{1}{\rho} \left(V - \frac{1}{3} \frac{V^3}{V_0^2} \right), \text{nonlinear resistor}; \\ i_{NM} = (\alpha + 3\beta\phi^2)V, \text{MFCM}. \end{cases} \quad (2)$$

That is, when the switch S in Fig. 1 is closed, the nonlinear current or memristive current in Eq. (2) is effective to support continuous oscillation in the neural circuit and then the firing patterns are controlled. Furthermore, the output signal i_{out} becomes dependent on the load circuit when it is connected to drive another neural circuit or

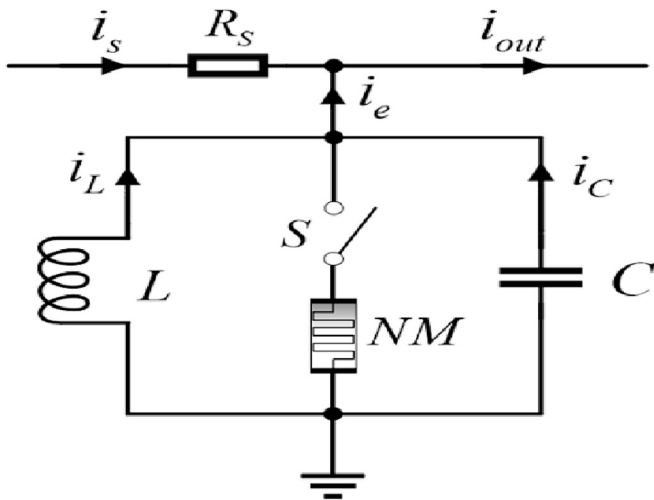


Fig. 1. Schematic diagram for neural circuit. L , C , NM represents an inductor, capacitor and nonlinear resistor including memristor, phototube and piezoelectric ceramic, respectively.

electromechanical device.

2.2. Electromechanical arm and leg driven by neural circuit

The current carrying coil is subjected to Ampere force in a magnetic field, and it is powerful to drive a electromechanical beam (EEB) when the coil is enwound to the end of the beam (for simplicity, $i_{out} = i_{EM}$), as shown in Fig. 2.

According to Fig. 2, the spring generates a damping force, which controls the stability of the moving beam. A motional electromotive force is evoked when the coils adhere to the moving beam continues to cut the magnetic field lines, while no induced electromotive force occurs when the channel current i_{EM} is kept as a constant. On the other hand, the coils of the load circuit connecting to the moving beam are linked to a voltage source will build a close loop, and the time-varying i_{EM} will produce an induced electromotive force as well. The external magnetic field with intensity B generates an ampere force F_A on the coils with N turns. As a result, the U shaped rod connected to the moving beam will be driven by the Ampere's force $F_A (=2NB l_0 i_{EM})$ in an external stable magnetic field. The coils adhere to the U shaped rod with N rounds, and the displacement changes of the moving beam with total quality m_0 can be estimated by

$$\begin{cases} \frac{dx}{dt} = y; \\ \frac{dy}{dt} = \frac{2NB l_0 i_{EM}}{m_0} - \frac{\eta}{m_0} y - \frac{K}{m_0} x. \end{cases} \quad (3)$$

The gains (η , K) in Eq. (3) the damping coefficient and elastic coefficient of spring, respectively. The displacement variable x has distinct physical unit, and moving equation can be converted into dimensionless form by applying suitable scale transformation. The motional electromotive force along the coil in Fig. 2 is approached by $\varepsilon_{MB1} = 2NB l_0 dx/dt$ when the moving beam pass through the field, and the induced electromotive force $\varepsilon_{MB2} = L_{EM} di_{EM}/dt$ is dependent on the changes of channel current i_{EM} . Some physical parameters (V_0 , C , ρ) in the neural circuit can be used as reference values when the neural circuit in Fig. 1 is used to excite the load circuit of electromechanical arm in Fig. 2.

$$\begin{cases} \tau = \frac{t}{\rho C}, \hat{x} = \frac{x}{l_0}, \hat{y} = \frac{\rho C}{l_0} y, \hat{i}_{EM} = \frac{\rho i_{EM}}{V_0}; \\ a = \frac{2\rho C^2 NB V_0}{m_0}, b = \frac{\rho C \eta}{m_0}, k_1 = \frac{\rho^2 C^2 K}{m_0}. \end{cases} \quad (4)$$

In a dimensionless space, the moving beam is described by

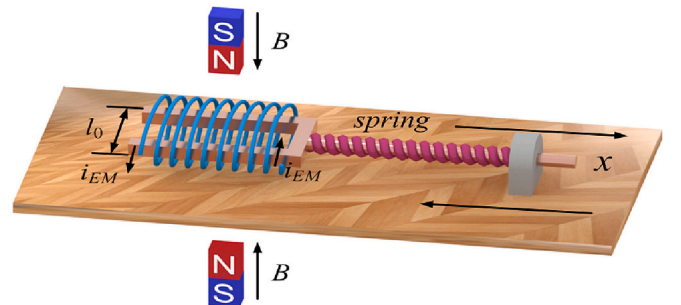


Fig. 2. Schematic diagram for electromechanical arm/leg. The section length of the N rounds coil has a length l_0 , which measures the distance between two rods of the left end of the beam. B represents the external magnetic field, and x denotes the displacement of the moving beam along the horizontal plane. The spring has an elastic coefficient K and i_{EM} denotes the channel current across the coils of the load circuit.

$$\begin{cases} \frac{d\hat{x}}{d\tau} = \hat{y}; \\ \frac{d\hat{y}}{d\tau} = ai_{EM}' - b\hat{y} - k_1\hat{x}. \end{cases} \quad (5)$$

The dimensionless current i_{EM}' comes from the output end of the neural circuit. In a practical way, it can be selected as different forms including spiking, bursting and even chaotic series. For dynamical analysis, the signal series for i_{EM}' can be derived from the membrane potential of a neuron, which can be stimulated to stabilize suitable firing patterns. The field energy W_1 in the neural circuit and the mechanical energy W_2 for the moving beam are defined in Eq. (6a) and the equivalent dimensionless forms are updated in Eq. (6b).

$$\begin{cases} W_1 = \frac{1}{2}CV^2 + \frac{1}{2}Li_L^2 + \frac{1}{2}L_{EM}i_{EM}^2; \\ W_2 = \frac{1}{2}Kx^2 + \frac{1}{2}m_0y^2. \end{cases} \quad (6a)$$

$$\begin{cases} u = \frac{V}{V_0}, \quad v = \frac{i_L\rho}{V_0}, \quad \mu_1 = \frac{\rho^2C}{L}; \\ \mu_2 = \frac{\rho^2C}{L_{EM}}, \quad \mu_3 = \frac{KI_0^2}{CV_0^2}, \quad \mu_4 = \frac{m_0I_0^2}{\rho^2C^3V_0^2}; \\ H_1 = \frac{W_1}{CV_0^2} = \frac{1}{2}u^2 + \frac{1}{2}\frac{v^2}{\mu_1} + \frac{1}{2}\frac{i_{EM}^2}{\mu_2}; \\ H_2 = \frac{W_2}{CV_0^2} = \frac{1}{2}\mu_3\hat{x}^2 + \frac{1}{2}\mu_4\hat{y}^2. \end{cases} \quad (6b)$$

L_{EM} defines the inductance coefficient for the coil of the load circuit in the mechanical arm. The neural circuit can present periodic and/or chaotic firing modes during the shift of energy levels, as a result, the load circuit is controlled in the channel current and the motion of the moving beam is regulated with synchronous changes of the mechanical energy. The beam begins to move when the electric field energy is converted to mechanical energy. For simplicity, the output signal i_{out} from Fig. 1 is applied to excite the EEB in Fig. 2, the coils adhere to the moving beam can be considered as load circuit. As a result, the i_{out} will equal to the channel current i_{EM} and then the neural circuit will suffer from feedback from the load circuit embedded to the moving beam. A complete diagram in Fig. 3 for the neural circuit coupled with electromechanical arm can be approached by combing Figs. 1 and 2 as follows.

Therefore, the correlation between variables for the coupled circuit and moving beam can be measured by

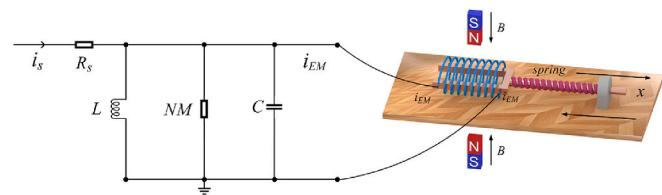


Fig. 3. Schematic diagram for neural circuit interacting with the load circuit of the electromechanical arm. The current across the inductor L , nonlinear element NM and capacitor C is described by i_L , i_{NM} , i_C , respectively.

$$\begin{cases} C \frac{dV}{dt} = i_s - i_L - i_{NM} - i_{EM}; \\ L \frac{di_L}{dt} = V; \\ L_{EM} \frac{di_{EM}}{dt} = V - 2NB l_0 y; \\ \frac{dx}{dt} = y; \\ \frac{dy}{dt} = \frac{2N}{m_0} B l_0 i_{EM} - \frac{\eta}{m_0} y - \frac{K}{m_0} x. \end{cases} \quad (7)$$

The coefficients (L , L_{EM} , C) describes the inductance coefficient for the coils in the neural circuit and load circuit, capacitance of the capacitor of the neural circuit, respectively. When the channel current across the NM is given in the form as the first formula in Eq. (2), the interaction between the neural circuit and the moving beam can be explored in the dynamical model in a new group of dynamical equations. Apply similar the scale transformation presented in Eq. (4), and other variables and parameters in dimensionless forms are redefined as follows.

$$i_s = \frac{\rho}{V_0} i_s, \quad \lambda_1 = \frac{\rho^2C}{L}, \quad \lambda_2 = \frac{\rho^2C}{L_{EM}}, \quad \lambda_3 = \frac{2NB l_0^2}{L_{EM} V_0}. \quad (8)$$

Inserting the variable and parameters into Eq. (7), it obtains a group of nonlinear equations as follows

$$\begin{cases} \frac{du}{d\tau} = i_s' - v + u - \frac{1}{3}u^3 - i_{EM}'; \\ \frac{dv}{d\tau} = \lambda_1 u; \\ \frac{di_{EM}'}{d\tau} = \lambda_2 u - \lambda_3 \hat{y}; \\ \frac{d\hat{x}}{d\tau} = \hat{y}; \\ \frac{d\hat{y}}{d\tau} = ai_{EM}' - b\hat{y} - k_1\hat{x}. \end{cases} \quad (9)$$

By taming the external forcing current i_s and its equivalent dimensionless form i_s' , the neuron will switch two different firing modes and then the channel current in the load circuit is changed to control the moving the beam under Ampere's force. Therefore, combination of Figs. 1 and 2 can be discussed in Eq. (9) by exploring the response relation between input current and displacement of the moving beam. It is interesting to discuss similar case when two beams are connected with another spring, and it is helpful to discern the cooperation between two arms when the muscle is excited by electrical signals.

2.3. Double electromechanical arms and legs

Two identical electromechanical arms in Fig. 2 are coupled with a spring, and a pair of beams is driven by electromagnetic force for behaving the cooperation of two artificial arms in Fig. 4.

From Fig. 4, any dislocation of the two moving beams will apply restoring force on each beam. For simplicity, the load circuits of the double EEB can be excited by using the same forcing current i_{EM} . The displacements for the two moving beams are marked as x_1 and x_2 , the distance between two moving beams is fixed as L_0 . Therefore, the spring connects two moving beams and applies a feedback force as $k(x_1 - x_2)$ along the direction of the moving beams. Therefore, the displacements for the two moving beams are approached by

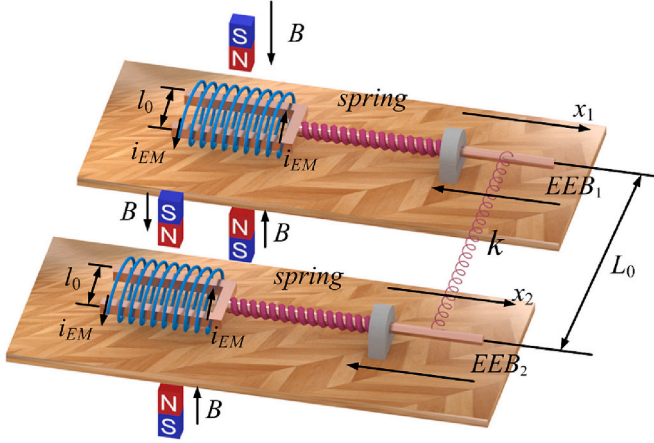


Fig. 4. Schematic diagram for double electromechanical arms. EEB₁ and EEB₂ denote two moving beams and they are connected with an ideal spring with elastic coefficient k .

$$\begin{cases} \frac{dx_1}{dt} = y_1; \\ \frac{dy_1}{dt} = \frac{2N}{m_0}Bl_0i_{EM} - \frac{\eta}{m_0}y_1 - \frac{K}{m_0}x_1 - \frac{k}{m_0}(x_1 - x_2); \\ \frac{dx_2}{dt} = y_2; \\ \frac{dy_2}{dt} = \frac{2N}{m_0}Bl_0i_{EM} - \frac{\eta}{m_0}y_2 - \frac{K}{m_0}x_2 - \frac{k}{m_0}(x_2 - x_1). \end{cases} \quad (10)$$

In fact, any changes of the channel current (i_{EM}) relative to the outputs from the neural circuit can induce displacement diversity between two moving beams, and the connecting spring will stretch to impose feedback force to the beam for reaching possible synchronous motion. When the same exciting current (channel current) i_{EM} is applied to the two moving beams, the motional and induced electromotive force in the load circuit will be half of the output voltage from the neural circuit. By applying similar scale transformation for a single beam, the dynamics of the double moving beams can be described by

$$\begin{cases} \frac{du}{d\tau} = i_s - v + u - \frac{1}{3}u^3 - i_{EM}; \\ \frac{dv}{d\tau} = \lambda_1 u; \\ \frac{di_{EM}}{d\tau} = \frac{1}{2}\lambda_2 u - \frac{1}{2}\lambda_3 \hat{y}; \\ \frac{d\hat{x}_1}{d\tau} = \hat{y}_1; \\ \frac{d\hat{y}_1}{d\tau} = ai_{EM} - b\hat{y}_1 - k_1\hat{x}_1 - k'(\hat{x}_1 - \hat{x}_2); \\ \frac{d\hat{x}_2}{d\tau} = \hat{y}_2; \\ \frac{d\hat{y}_2}{d\tau} = ai_{EM} - b\hat{y}_2 - k_1\hat{x}_2 - k'(\hat{x}_2 - \hat{x}_1). \end{cases} \quad (11)$$

The dimensionless coefficient defines as $k' = k\rho^2C^2/m_0$. By taming the external forcing current, the neural circuit is regulated in the firing patterns, and its coupling to the load circuit will drive the moving beam in different states. By tracking the trajectories of the coupled beams, phase synchronization and complete synchronization between the two moving beams can be discussed. Similar to the definition in Eqs. (6a) and (6b), the energy function for the coupled two electromechanical beams can be obtained. When the external forcing current i_s is adjusted, which the signal source can be voice applied on a piezoelectric ceramic or illumination imposed on a photocell, the encoded electric signal is encoded to excite the load circuit for driving the coupled beams. As a

result, this device can simulate the linear motion of arms. Considering a noisy disturbance relative to external electromagnetic field, noise term can be applied to the formula for the membrane potential in the neuron-coupled beam system, and the motion of the beam can be affected. When the nonlinear component NM in Figs. 1 and 3 is selected with memristor, an additive constant voltage V_0 in the branch circuit is required to set reference voltage for further scale transformation.

2.4. Electromechanical arm and leg driven by memristive circuit

The involvement of MFCM can describe the inner electromagnetic induction during the propagation of ions along the branch circuit and channels. The injected and perceived signals are encoded via the memristive channel, and energy exchanges are continued between electric field and magnetic field accompanying with changes of the capacitive and inductive variables. In Fig. 5, a simple memristor-based neural circuit is designed, and its outputs are used to excite the load circuit via the coupling capacitor C_M .

The constant voltage V_0 can be considered as resting potential of the ion channel, V_s is relative to signal source for mimicking the acoustic electric conversion via a piezoelectric ceramic and photoelectric conversion via a phototube. The component C_M connected with a constant resistor is used to keep balance the output voltage from the neural circuit and the electromotance generated from the load circuit. The physical variables for Fig. 5 can be confirmed in the following equations

$$\begin{cases} C \frac{dV}{dt} = i_s - i_L - i_{NM} - i_{EM}; \\ L \frac{di_L}{dt} = V; \quad i_{NM} = (\alpha + 3\beta\phi^2)(V - V_0); \\ L_{EM} \frac{di_{EM}}{dt} = V - V_m - i_{EM}R_m - 2NBl_0y; \\ C_M \frac{dV_m}{dt} = i_{EM}; \\ \frac{d\phi}{dt} = V - V_0; \quad \frac{dx}{dt} = y; \\ \frac{dy}{dt} = \frac{2N}{m_0}Bl_0i_{EM} - \frac{\eta}{m_0}y - \frac{K}{m_0}x. \end{cases} \quad (12)$$

Magnetic field energy is shunted into the inductive and memristive channels when channel current is passed along the memristive channel. Indeed, the memristor can be considered as an equivalent inductor and then its field energy $W_M = 0.5\phi i_{NM}$ can be converted into dimensionless form H_M by applying suitable scale transformation on the variables and parameters in the field energy function W_M .

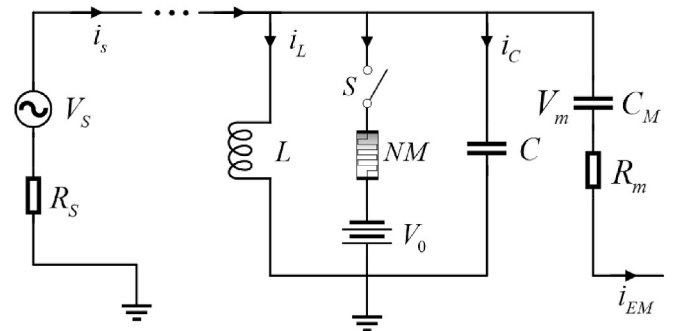


Fig. 5. Schematic diagram for electromechanical arm/leg driven by memristive circuit.

$$\begin{cases} u = \frac{V}{V_0}, v = \frac{i_L R_m}{V_0}, \varphi = \frac{\phi}{R_m C V_0}, \tau = \frac{t}{R_m C}, i_{EM} = \frac{R_m i_{EM}}{V_0}; \\ i_s' = \frac{i_s R_m}{V_0}, V_m' = \frac{V_m}{V_0}, \alpha' = \alpha R_m, \beta' = \beta R_m^3 C^2 V_0^2, \delta_1 = \frac{R_m^2 C}{L}; \\ \delta_2 = \frac{R_m^2 C}{L_{EM}}, \delta_3 = \frac{2NR_m B l_0^2}{L_{EM} V_0}, \delta_4 = \frac{C}{C_m}, \delta_5 = \frac{2R_m N B V_0 C^2}{m_0}; \\ \delta_6 = \frac{R_m C \eta}{m_0}, \delta_7 = \frac{R_m^2 C^2 K}{m_0}, \hat{x} = \frac{x}{l_0}, \hat{y} = \frac{R_m C}{l_0} y. \end{cases} \quad (13)$$

The energy function for these electric components in the neural circuit and load circuit are described by

$$\begin{cases} W_1 = \frac{1}{2} C V^2 + \frac{1}{2} L i_L^2 + \frac{1}{2} L_{EM} i_{EM}^2 + \frac{1}{2} C_m V_m^2 + \frac{1}{2} \phi i_{NM}; \\ H_1 = \frac{W_1}{C V_0^2}, \\ = \frac{1}{2} u^2 + \frac{1}{2} \frac{v^2}{\mu_1} + \frac{1}{2} \frac{i_{EM}^2}{\mu_2} + \frac{1}{2} \frac{V_m^2}{\delta_4} + \frac{1}{2} (\alpha' \varphi + 3\beta' \varphi^3)(u-1); \\ \mu_1 = \frac{\rho^2 C}{L}, \mu_2 = \frac{\rho^2 C}{L_{EM}}, \delta_4 = \frac{C}{C_m}, \alpha' = \alpha R_m. \end{cases} \quad (14)$$

The moving beam has the same mechanical energy shown in the second formulas in Eqs. (6a) and (6b). Furthermore, the dynamics of the memristive neural circuit coupled with the load circuit and the moving beam is described by

$$\begin{cases} \frac{du}{d\tau} = i_s' - v - (\alpha' + 3\beta' \varphi^2)(u-1) - i_{EM}'; \\ \frac{dv}{d\tau} = \delta_1 u; \\ \frac{di_{EM}}{d\tau} = \delta_2 (u - V_m' - i_{EM}') - \delta_3 \hat{y}; \\ \frac{dV_m'}{d\tau} = \delta_4 i_{EM}'; \\ \frac{d\varphi}{d\tau} = u - 1; \\ \frac{d\hat{x}}{d\tau} = \hat{y}; \\ \frac{d\hat{y}}{d\tau} = \delta_5 i_{EM}' - \delta_6 \hat{y} - \delta_7 \hat{x}. \end{cases} \quad (15)$$

In presence of external electromagnetic radiation, noisy or periodic forms can be applied to the right side for the formula in the fifth formula in Eq. (15), and energy injection enables shift of the inner energy level of the neural circuit and the load circuit. As a result, the firing modes and the coupling channel current i_{EM} (and its dimensionless form i_{EM}') are changed to guide the motion of the beam/arm under electromagnetic force.

2.5. Adaptive control of neural circuit and moving beam under energy flow

According to Eqs. (14) and (6b), most of the energy terms have quadratic power of variables except the energy term for memristive component. When all the parameters are known and all the variables are available, the energy function can be discerned with exact value all the time. In some recent works, a generic adaptive growth law for intrinsic parameters of the neurons is suggested to control mode transition and the intensity of synaptic coupling between neurons [59,60]. The continuous growth of intrinsic parameters can be controlled by Heaviside function when the energy level or energy proportion is beyond certain threshold. For example, the parameter $\delta_4 = C/C_m$ accounts for the ratio for two capacitive elements, and any shape deformation of these components will induce parameter shift during energy injection and release. Therefore, a group of adaptive law can be suggested to

control the growth or decrease of the parameters until it reaches a saturation value.

$$\begin{cases} \frac{d\delta_4}{d\tau} = \sigma \cdot \delta_4 \Theta(H_1 - \kappa_1), \Theta(P) = 1, P \geq 0, \Theta(P) = 0, P < 0; \\ \frac{d\delta_4}{d\tau} = \sigma \cdot \delta_4 \Theta\left(\frac{H_L}{H_1} - \kappa_2\right); \\ \frac{d\delta_4}{d\tau} = \sigma \cdot \delta_4 \Theta\left(\frac{H_C}{H_1} - \kappa_3\right). \end{cases} \quad (16)$$

Positive value for the gain σ supports continuous growth while negative value for σ just induces decrease of the parameter. H_1 denotes the total dimensionless energy (Hamilton energy) for the neuron and it can be mapped from the field energy for the neural circuit. H_C and H_L represent the dimensionless capacitive and inductive energy for the neuron, respectively. κ_1 , κ_2 and κ_3 are selected thresholds. Other bifurcation parameters can be applied with the similar control law in Eq. (16) no matter the models are presented in oscillator-like form or maps.

In fact, most of the variables for channel current are not detectable in synchronous way except the time series for voltages. As mentioned above, the field energy in these ideal capacitive components accounts for energy terms quadratic form, therefore, voltage function can be used to replace the energy terms in the growth law in Eq. (16), and it can be updated with a reliable form as follows.

$$\begin{cases} \frac{d\delta_4}{d\tau} = \sigma \cdot \delta_4 \Theta\left(\frac{V_m^2}{u^2} - \kappa_1\right), \Theta(P) = 1, P \geq 0, \Theta(P) = 0, P < 0; \\ \frac{d\delta_4}{d\tau} = \sigma \cdot \delta_4 \Theta(V_m^2 - \kappa_2); \\ \frac{d\delta_4}{d\tau} = \sigma \cdot \delta_4 \Theta(u^2 - \kappa_3). \end{cases} \quad (17)$$

In circuit implement, the variables in Eq. (17) can be replaced with the corresponding physical variables, and additive branch circuit can be designed to control the neural circuit and moving beam in adaptive way. From mathematical aspect, researchers can write hundreds of models and the parameters can be adjusted to produce similar spiking and bursting patterns as biological neurons. Furthermore, these neuron models can be simulated on many equivalent nonlinear circuits. However, the most important thing is to clarify its intrinsic working mechanism and release its self-adaptive property, in particular, the energy function should be provide with exact physical explanation. From my understanding, the intrinsic energy flow controls all the target and desired states when suitable adaptive control law is discovered and confirmed. In this way, more neural circuits and combined arrays can be built to control the complex motion of artificial arms/legs and electro-mechanical devices freely. Finally, the author honestly expects this minireview can provide possible guidance for readers in this field, and these suggestions can be helpful to explore the application of artificial neural circuits. Complete dynamical analysis on the suggested models can be finished by readers.

3. Conclusions

In this review, a generic neural circuit is proposed and its energy function is defined. The working principle of a simple electromechanical beam is explained and the moving beam under electromagnetic force (Ampere force) can mimic the motion of artificial arms. Appropriate scale transformation is provided to obtain dimensionless energy for the neural circuit-coupled electromechanical beam, and the dynamical equations are expressed in exact form. Furthermore, two electromechanical beams are connected with a spring, and the outputs from the neural circuit are used to excite the load circuit adhere to the moving beams, and this device can simulate the gaits cooperation between two artificial arms. Finally, an adaptive control law under energy flow is suggested to control the neural circuit, and thus the moving beam can be

guided to target gaits freely. This review provides possible clues to design reliable neural circuits, and the interaction between neural circuits and artificial arms developed from mechanical devices is explained from physical and dynamical aspect. The suggestions and clarification in this review provides clues for application of computational neuroscience and intelligent control of dynamical systems.

Data statement

No new data are created in this work.

CRediT authorship contribution statement

Jun Ma: Writing – review & editing, Writing – original draft, Visualization, Project administration, Funding acquisition, Formal analysis.
Yitong Guo: Visualization, Validation, Investigation, Formal analysis.

Declaration of competing interest

The authors declare that they have no known competing financial interests or personal relationships that could have appeared to influence the work reported in this paper.

Data availability

Data will be made available on request.

Acknowledgement

This project is supported by the National Natural Science Foundation of China under the Grant No. 12072139. The authors thank Dr. Ying Xie for her help for plotting Figs. 1 and 5.

References

- [1] Wisloff U, Loennechen JP, Falck G, et al. Increased contractility and calcium sensitivity in cardiac myocytes isolated from endurance trained rats. *Cardiovasc Res* 2001;50:495–508.
- [2] Valentim MA, Brahmabhatt AN, Tupling AR. Skeletal and cardiac muscle calcium transport regulation in health and disease. *Biosci Rep* 2022;42:BSR20211997.
- [3] Petrović PB. Charge-controlled grounded memristor emulator circuits based on Arbel-Goldminz cell with variable switching behaviour. *Analog Integr Circuits Signal Process* 2022;113:373–81.
- [4] Bhardwaj K, Srivastava M. Compact charge-controlled memristance simulator with electronic/resistive tunability. *Journal of Circuits, Systems and Computers* 2022;31:2250094.
- [5] Fang ZY, Zhang CK, Wang YM, et al. Construction, dynamic analysis and DSP implementation of a novel 3D discrete memristive hyperchaotic map. *Chaos, Solitons & Fractals* 2023;177:114303.
- [6] Raj N, Ranjan RK, Khateb F. Flux-controlled memristor emulator and its experimental results. *IEEE Transactions on Very Large Scale Integration (VLSI) Systems* 2020;28:1050–61.
- [7] Shen SP, Shang DS, Chai YS, et al. Realization of a flux-driven memtransistor at room temperature. *Chinese Physics B* 2016;25:027703.
- [8] Wu HG, Bao BC, Chen M. Threshold flux-controlled memristor model and its equivalent circuit implementation. *Chinese Physics B* 2014;23:118401.
- [9] Xie Y, Yao Z, Ren G, et al. Estimate physical reliability in Hindmarsh-Rose neuron. *Physics Letters A* 2023;464:128693.
- [10] Wang H, Lu Q, Wang Q. Generation of firing rhythm patterns and synchronization in the Morris-Lecar neuron model. *International Journal of Nonlinear Sciences and Numerical Simulation* 2005;6:7–12.
- [11] Kafraj MS, Parastesh F, Jafari S. Firing patterns of an improved Izhikevich neuron model under the effect of electromagnetic induction and noise. *Chaos, Solitons & Fractals* 2020;137:109782.
- [12] Baysal V, Yilmaz E. Effects of electromagnetic induction on vibrational resonance in single neurons and neuronal networks. *Physica A: Statistical Mechanics and its Applications* 2020;537:122733.
- [13] Xu Q, Ju Z, Ding S, et al. Electromagnetic induction effects on electrical activity within a memristive Wilson neuron model. *Cognitive Neurodynamics* 2022;16:1221–31.
- [14] Ramasamy M, Devarajan S, Kumarasamy S, et al. Effect of higher-order interactions on synchronization of neuron models with electromagnetic induction. *Appl Math Comput* 2022;434:127447.
- [15] Wang G, Yang L, Zhan X, et al. Chaotic resonance in Izhikevich neural network motifs under electromagnetic induction. *Nonlinear Dynamics* 2022;107:3945–62.
- [16] Shi QQ, Zhang L, An XL, et al. Dynamic exploration of a controllable thermosensitive neuron model and its applications. *International Journal of Bifurcation and Chaos* 2022;32:2250198.
- [17] Hussain I, Ghosh D, Jafari S. Chimera states in a thermosensitive FitzHugh-Nagumo neuronal network. *Appl Math Comput* 2021;410:126461.
- [18] Zhu Z, Zhang X, Wang Y, et al. Functional responses of autaptic neural circuits to acoustic signals. *International Journal of Bifurcation and Chaos* 2023;33:2330009.
- [19] Xie Y, Yao Z, Hu X, et al. Enhance sensitivity to illumination and synchronization in light-dependent neurons. *Chinese Physics B* 2021;30:120510.
- [20] Njitacke ZT, Ramakrishnan B, Rajagopal K, et al. Extremely rich dynamics of coupled heterogeneous neurons through a Josephson junction synapse. *Chaos, Solitons & Fractals* 2022;164:112717.
- [21] Wan Q, Yan Z, Li F, et al. Multistable dynamics in a Hopfield neural network under electromagnetic radiation and dual bias currents. *Nonlinear Dynamics* 2022;109:2085–101.
- [22] Ding S, Wang N, Bao H, et al. Memristor synapse-coupled piecewise-linear simplified Hopfield neural network: dynamics analysis and circuit implementation. *Chaos, Solitons & Fractals* 2023;166:112899.
- [23] Lin H, Wang C, Yu F, et al. A review of chaotic systems based on memristive Hopfield neural networks. *Mathematics* 2023;11:1369.
- [24] Vivekanandhan G, Natiq H, Merrikhi Y, et al. Dynamical analysis and synchronization of a new memristive Chialvo neuron model. *Electronics* 2023;12:545.
- [25] Cao H, Wang Y, Banerjee S, et al. A discrete Chialvo-Rulkov neuron network coupled with a novel memristor model: Design, Dynamical analysis, DSP implementation and its application. *Chaos, Solitons & Fractals* 2024;179:114466.
- [26] Alexander P, Natiq H, Ghasemi M, et al. Hamilton energy variations in memristive Hindmarsh-Rose neurons under attractive and repulsive couplings. *European Physical Journal Plus* 2024;139:133.
- [27] Mehrabbeik M, Ahmadi A, Bakouie F, et al. The impact of higher-order interactions on the synchronization of Hindmarsh-Rose neuron maps under different coupling functions. *Mathematics* 2023;11:2811.
- [28] Liu Y, Shen Y, Zhang H, et al. Periodic firing evolution of a Hindmarsh-Rose neuron model and FPGA circuit implementation. *European Physical Journal Plus* 2024;139:235.
- [29] Hariharan S, Suresh R, Chandrasekar VK. Noise-induced extreme events in integer and fractional-order memristive Hindmarsh-Rose neuron models: a comprehensive study. *European Physical Journal Plus* 2024;139:292.
- [30] Vivekanandhan G, Abdolmohammadi HR, Natiq H, et al. Dynamic analysis of the discrete fractional-order Rulkov neuron map. *Math Biosci Eng* 2023;20:4760–81.
- [31] Yang F, Ma J, Ren G. A Josephson junction-coupled neuron with double capacitive membranes. *J Theor Biol* 2024;578:111686.
- [32] Guo Y, Wu F, Yang F, et al. Physical approach of a neuron model with memristive membranes. *Chaos: An Interdisciplinary. Journal of Nonlinear Science* 2023;33:113106.
- [33] Yang F, Guo Q, Ma J. A neuron model with nonlinear membranes. *Cognitive Neurodynamics* 2023. <https://doi.org/10.1007/s11571-023-10017-5>.
- [34] Bao B, Wang Z, Hua Z, et al. Regime transition and multi-scroll hyperchaos in a discrete neuron model. *Nonlinear Dynamics* 2023;111:13499–512.
- [35] Bao B, Hu J, Cai J, et al. Memristor-induced mode transitions and extreme multistability in a map-based neuron model. *Nonlinear Dynamics* 2023;111:3765–79.
- [36] Guo Y, Xie Y, Ma J. How to define energy function for memristive oscillator and map. *Nonlinear Dynamics* 2023;111:21903–15.
- [37] Ibarz B, Casado JM, Sanjuán MAF. Map-based models in neuronal dynamics. *Phys Rep* 2011;501(1–2):1–74.
- [38] Li Y, Lv M, Ma J, et al. A discrete memristive neuron and its adaptive dynamics. *Nonlinear Dynamics* 2024. <https://doi.org/10.1007/s11071-024-09361-w>.
- [39] Yang F, Zhou P, Ma J. An adaptive energy regulation in a memristive map linearized from circuit with two memristive channels. *Communications in Theoretical Physics* 2024;76:035004.
- [40] Guo YT, Ma J, Zhang XF, et al. Memristive oscillator to memristive map, energy characteristic. *Science China Technological Science* 2024. <https://doi.org/10.1007/s11431-023-2637-1>.
- [41] Wu FQ, Guo YT, Ma J. Energy flow accounts for the adaptive property of functional synapses. *Science China Technological Sciences* 2023;66:3139–52.
- [42] Hou B, Hu X, Guo Y, et al. Energy flow and stochastic resonance in a memristive neuron. *Physica Scripta* 2023;98:105236.
- [43] Xie Y, Xu Y, Ma J. Desynchronization and energy diversity between neurons. *Nonlinear Dynamics* 2023;111:11521–41.
- [44] Torrealdea FJ, d'Anjou A, Graña M, et al. Energy aspects of the synchronization of model neurons. *Physical Review E* 2006;74:011905.
- [45] Wang Y, Sun G, Ren G. Diffusive field coupling-induced synchronization between neural circuits under energy balance. *Chinese Physics B* 2023;32:040504.
- [46] Sun G, Yang F, Ren G, et al. Energy encoding in a biophysical neuron and adaptive energy balance under field coupling. *Chaos, Solitons & Fractals* 2023;169:113230.
- [47] Xie Y, Yao Z, Ma J. Formation of local heterogeneity under energy collection in neural networks. *Science China Technological Sciences* 2023;66:439–55.
- [48] Yang F, Wang Y, Ma J. Creation of heterogeneity or defects in a memristive neural network under energy flow. *Communications in Nonlinear Science and Numerical Simulation* 2023;119:107127.
- [49] Ngongiah IK, Balamurali R., Kuatie GF, et al. Mechanical arm (s) driven by Josephson junction circuit (s), mimicking the movement pattern of myriapods. *Physica Scripta* 2023;98:045221.
- [50] Dietz V, Fouad K, Bastiaanse CM. Neuronal coordination of arm and leg movements during human locomotion. *European Journal of Neuroscience* 2001;14:1906–14.

- [51] Nkomidio AM, Noubissie S, Wofo P. Dynamics of arrays of legs powered by a discrete electrical model of nerve. *Physics Letters A* 2014;378(11–12):857–62.
- [52] Wadden T, Ekeberg Ö. A neuro-mechanical model of legged locomotion: single leg control. *Biol Cybern* 1998;79:161–73.
- [53] Mbeunga NK, Nana B, Wofo P. Dynamics of array mechanical arms coupled each to a Fitzhugh-Nagumo neuron. *Chaos, Solitons & Fractals* 2021;153:111484.
- [54] Ngongiah IK, Ramakrishnan B, Kuia GF, et al. Actuating mechanical arms coupled to an array of FitzHugh-Nagumo neuron circuits. *European Physical Journal Special Topics* 2023;232:285–99.
- [55] Ngongiah IK, Sriram S, Dongmo ED, et al. Analysis of a network of FitzHugh-Nagumo neuron circuit coupled to an array of mechanical leg to mimic the locomotion of a multi-legged organism. *Waves in Random and Complex Media* 2024. <https://doi.org/10.1080/17455030.2023.2301091>.
- [56] Kouami NM, Nana B, Wofo P. Analysis of array nanoelectromechanical beams driven by an electrical line of Josephson junctions. *Physica C: Superconductivity and its Applications* 2020;574:1353658.
- [57] Wang B, Wang Y, Huang J, et al. Computed torque control and force analysis for mechanical leg with variable rotation axis powered by servo pneumatic muscle. *ISA Trans* 2023;140:385–401.
- [58] Ngongiah IK, Vivekanandan G, Kuia GF, et al. Theoretical investigation of an array of Josephson junction neuron circuits actuating a mechanical leg and the array in mimicking a multi-legged locomotion. *Pramana* 2023;97(3):135.
- [59] Li YN, Wang CN, Hu XK, et al. Characterize electric activity in a light-sensitive membrane. *Chinese Journal of Physics* 2024;88:967–81.
- [60] Jia JE, Wang CN, Zhang XF, et al. Energy and self-adaption in a memristive map neuron. *Chaos, Solitons & Fractals* 2024;182:114738.

Memristive oscillator to memristive map, energy characteristic

GUO YiTong^{1,2}, MA Jun^{1,2,3*}, ZHANG XiaoFeng² & HU XiKui³

¹ College of Electrical and Information Engineering, Lanzhou University of Technology, Lanzhou 730050, China;

² Department of Physics, Lanzhou University of Technology, Lanzhou 730050, China;

³ School of Science, Chongqing University of Posts and Telecommunications, Chongqing 400065, China

Received December 22, 2023; accepted March 12, 2024; published online April 22, 2024

Most of nonlinear oscillators composed of capacitive and inductive variables can obtain the Hamilton energy by using the Helmholtz theorem when the models are rewritten in equivalent vector forms. The energy functions for biophysical neurons can be obtained by applying scale transformation on the physical field energy in their equivalent neural circuits. Realistic dynamical systems often have exact energy functions, while some mathematical models just suggest generic Lyapunov functions, and the energy function is effective to predict mode transition. In this paper, a memristive oscillator is approached by two kinds of memristor-based nonlinear circuits, and the energy functions are defined to predict the dependence of oscillatory modes on energy level. In absence of capacitive variable for capacitor, the physical time t and charge q are converted into dimensionless variables by using combination of resistance and inductance (L, R), e.g., $\tau = t \times R/L$. Discrete energy function for each memristive map is proposed by applying the similar weights as energy function for the memristive oscillator. For example, energy function for the map is obtained by replacing the variables and parameters of the memristive oscillator with corresponding variables and parameters for the memristive map. The memristive map prefers to keep lower average energy than the memristive oscillator, and chaos is generated in a discrete system with two variables. The scheme is helpful for energy definition in maps, and it provides possible guidance for verifying the reliability of maps by considering the energy characteristic.

Hamilton energy, memristor, Helmholtz theorem, scale transformation, memristive circuit

Citation: Guo Y T, Ma J, Zhang X F, et al. Memristive oscillator to memristive map, energy characteristic. *Sci China Tech Sci*, 2024, 67: 1567–1578, <https://doi.org/10.1007/s11431-023-2637-1>

1 Introduction

Nonlinear circuits are often used as signal sources and further filtering of the output signals can match with some realistic signals within specific frequency band. High order nonlinear terms account for complexity and specific function in electric components, which are crucial for supporting chaotic states and field energy savage. By taming some intrinsic parameters, chaos and hyperchaos are induced in the nonlinear circuits [1–4], which are often described by equivalent nonlinear oscillators, and these chaotic systems have potential application in image encryption [5–8]. The

bionics throws light on the achievements of artificial intelligence [9,10] and functional enhancements of artificial neurons and setting on biophysical neurons [11–15]. For further clues about model approach of neural activities from physical aspect, readers can explore suggestions in the recent review and the references therein [16].

The reliability of nonlinear circuits depends on the controllability. It means that most of the intrinsic parameters can be controllable in wide range. External stimuli accompanying with energy injection can be encoded to guide the outputs to reach target levels. The cell membrane and synapse of a biological neuron have distinct flexibility, as a result, gradient energy and external stimuli including forcing current, depolarized field will change the energy level and firing

*Corresponding author (email: hyperchaos@163.com)

modes in neural activities in adaptive way. Therefore, the synaptic intensity is regulated under the energy flow [17,18]. For example, an adaptive law [17,18] is suggested to control the growth of synaptic intensity in two kinds of memristive neurons, which are developed from neural circuits connecting with memristive channels. Furthermore, two or more neurons can be connected by synapses with a growth of the synaptic intensity until reaching energy balance, while heterogeneity [19,20] can be created in the neural network due to continuous energy collection from the adjacent neurons.

Most of the nonlinear circuits can present periodic or chaotic states. A few nonlinear circuits can be tamed to present similar firing patterns derived from biological neurons. Some neural circuits are designed and their dimensionless forms are used as neuron models [21–25]. It is crucial to consider the physical property of biological neurons before building an equivalent simple neural circuit. Static distribution of intracellular ions induces electric field in the cell membrane, stochastic diffusion and propagation of ions across the cell membrane induce magnetic field due to current effect. Continuous exchange of energy flow will change the distribution of intracellular and extracellular ions, and thus the relation between membrane potential and channel current becomes nonlinear dependence. Therefore, capacitor, inductor, nonlinear resistor and constant voltage source are four necessary elements for building a simple neural network. The capacitor accounts for the capacitive property of cell membrane, an inductor mimics the magnetic field effect because of propagation and diffusion of ions, constant voltage results from the resting potential in an ion channel. In a neural circuit, a constant voltage source is often connected to the inductor in series, and the nonlinear resistor is used as additive channel to shunt energy flow. When piezoelectric ceramics, phototube and thermistor are incorporated into the neural circuit, the neurons become sensitive to external voice, illumination and temperature [26–30]. In particular, the involvement of memristive current and magnetic flux variable into the neuron models can estimate the electromagnetic induction and radiation [31–35]. Based on these memristive neurons, the collective neural activities can be controlled under field coupling even synaptic coupling is suppressed greatly.

Oscillator-like models can be derived from circuit equations by applying scale transformation on the physical variables and parameters in the neural circuits. The energy function composed of capacitive, inductive and memristive terms can be mapped from the field energy for the electric components with distinct field effect including capacitor, inductor and memristor. The energy function can also be derived and verified by using the Helmholtz theorem when the formulas for the neuron model are updated with vector forms. The emergence of chaos in an autonomous oscillator requires involvement of three variables at least in absence of

noisy disturbance and time delay. However, a map can produce chaotic series even one variable is regulated. To produce chaotic behaviour in the neural activities, three-variable neurons and two-variable models driven by external periodic current in the form of nonlinear oscillators have been investigated extensively. However, discrete systems and maps (discrete neurons) [36–38] are effective to mimic the main firing modes in some biological neurons, and the involvement of memristive term is helpful to estimate the electromagnetic induction as well [39,40]. Memsitor shows great application in neural circuits and synapse implement for neuromorphic computing see recent review works [41–44]. Most of the memristive oscillators can be approached by setting equivalent memristor-based circuits and the energy characteristic is clear. However, many works about discrete memristor and memristive maps are discussed from mathematical definition and field programmable gate array (FPGA) simulation [39,45–49], and how to describe the energy characteristic keeps open. Therefore, it is a challenge to define and estimate the energy function for map neurons, and the energy level dependence on firing modes keeps open.

In this paper, a memristive oscillator is expressed by two different kinds of nonlinear circuits coupled by magnetic flux-controlled memristor (MFCM) and charge-controlled memristor (CCM), respectively. CCM and a voltage-controlled element are used to couple the inductor when capacitor is not available. After scale transformation, two kinds of memristor-based circuits are described by similar memristive oscillators and energy functions are defined. Applying linear transformation on the variables and intrinsic parameters, each memristive oscillator is replaced by a memristive map under covariation. For example, $dy/dt = A \times y(1-y)$ to $x_{n+1} = B \times x_n(1-x_n)$. Then the energy function for the memristive oscillator is referred to define a discrete energy function for the map with the same weights. Bifurcation analysis is carried out, and the average energy is calculated to predict coherence resonance in the memristive maps.

2 Model and scheme

Reliable algorithm is crucial to obtain numerical solutions for nonlinear equations, e.g., the fourth order Runge-Kutta algorithm is effective to find solve numerical results for nonlinear oscillators described by differential equations, which are often discretized in exact forms. In particular, the involvement of noisy excitations and disturbances makes a stochastic dynamical system, and the approach of numerical results depends on reliable algorithms [50,51]. On the other hand, map modelling of complex systems can avoid and reduce the difficulty during numerical approach. In ref. [52], energy function for memristive devices is defined and estimation of energy for some maps is discussed. It is assumed

that the same weights can be applied for the energy function of a map by exploring the Hamilton energy function for an equivalent nonlinear oscillator, which has distinct covariation with the map. In ref. [53], linear transformation is applied to bridge connection to two nonlinear oscillators and their equivalent maps. The capacitive energy $0.5C \times V^2$ for a capacitor and inductive energy $0.5L \times i^2$ for an inductor can be mapped into equivalent forms as $0.5A \times x^2$ and $0.5B \times y^2$, where V, i are physical variables, x, y are corresponding dimensionless variables, and A, B are normalized gains for the energy terms. Both MFCM [54–56] and CCM [57–59] can save and contain field energy when they are incorporated into a linear or nonlinear circuit. The energy property in an MFCM and CCM can be described by suitable energy function in an equivalent inductor and capacitor, respectively. In fact, the energy description for memristive devices often presents a high order term. That is, scale transformation bridges connection between the circuit equations and the nonlinear oscillator, field energy and Hamilton energy completely [60].

For a nonlinear oscillator with a few variables, the dynamics can be investigated in its equivalent nonlinear circuit. It is a challenge to verify the numerical results during selecting and combining these potential electric components. For example, the variables (x, y, z, \dots) for a nonlinear oscillator can be described by the output voltage for a capacitor, induction current along an induction coil, and a constant term often means involvement of constant voltage source in the branch circuit. Is it possible to build more equivalent nonlinear circuits for mimicking the dynamics for the same nonlinear oscillator? From physical viewpoint, continuous oscillation in a nonlinear circuit requires the involvement of capacitive and inductive components synchronously. In ref. [53], the author suggested a memristive oscillator with two variables, and scale transformation is applied to obtain an equivalent map for further energy estimation.

2.1 Linear transformations between memristive oscillator and memristive map

The memristive oscillator is given in the form as follows:

$$\begin{cases} \frac{dy}{d\tau} = ry(1-y) - (\alpha' + 3\beta'\phi'^2)y, \\ \frac{d\phi'}{d\tau} = a\phi' + by, \end{cases} \quad (1)$$

where r, a, b, α', β' are dimensionless parameters, and y, ϕ' are dimensionless variables. Indeed, the eq. (1) is autonomous and it seldom presents chaotic series without external stimulus or noisy disturbance. The Hamilton energy for the memristive oscillator is described by

$$H = \frac{1}{2}y^2 + \frac{1}{2}(\alpha'\phi' + 3\beta'\phi'^3)y. \quad (2)$$

When the variable y is mapped from a voltage variable, the two energy terms are relative to capacitive and memristive field, respectively. By applying the following linear transformation in eq. (3), the memristive oscillator in eq. (1) is replaced by a memristive map with similar form in discrete type in eq. (4).

$$\begin{cases} \lambda = 1 + r\Delta\tau, \quad \alpha' = \frac{\alpha}{\varepsilon}, \quad \beta' = \frac{\beta\Delta\tau^2}{(1+r\Delta\tau)^2}, \quad b = \frac{\varepsilon}{\Delta\tau}, \\ \phi_n = \frac{r\Delta\tau}{(1+r\Delta\tau)}\phi'_n, \quad x_n = \frac{r\Delta\tau}{1+r\Delta\tau}y_n, \quad a = \frac{(k-1)}{\Delta\tau}, \end{cases} \quad (3)$$

where the variables (y_n, ϕ'_n) are sampled time series for the variables (y, ϕ') in eq. (1), $\Delta\tau$ is the time step for numerical approach of eq. (1).

$$\begin{cases} x_{n+1} = \lambda x_n(1-x_n) - (\alpha + 3\beta\phi_n^2)x_n, \\ \phi_{n+1} = k\phi_n + \varepsilon x_n. \end{cases} \quad (4)$$

The memristive map in eq. (4) can be regulated in the parameters for developing different firing patterns. The memristive oscillator in eq. (1) can be verified by designing two equivalent circuits by incorporating different memristors. Case 1: Capacitor, nonlinear resistor and MFCM are connected in the neural circuit. Case 2: Inductor, a voltage-dependent element and CCM are connected in the neural circuit.

2.2 Approach of memristive oscillator by using MFCM

To verify the reliability of eq. (1), a nonlinear circuit in Figure 1 is plotted to match with the energy property in eq. (2). It is helpful to predict the physical properties of electric components involved in this circuit.

The channel current i_{NR} across the nonlinear resistor and memristive current i_M are respectively described by [60]

$$\begin{cases} i_{NR} = -\frac{r}{\rho}(V - \frac{V^2}{V_0}); \\ i_M = \frac{dq}{dt} = M(\phi)V = (\alpha_1 + 3\beta_1\phi^2)V, \end{cases} \quad (5)$$

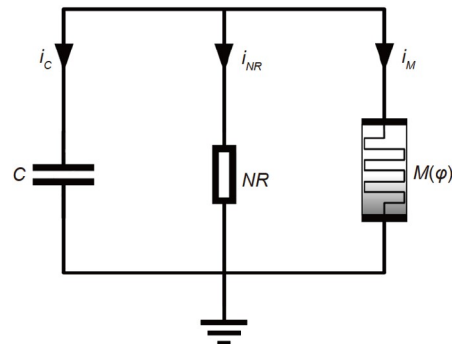


Figure 1 Schematic diagram for a neural circuit coupled by MFCM. A memristive circuit composed of one capacitor, nonlinear resistor (NR) and one MFCM.

where V estimates the output voltage for the capacitor with capacitance C , ϕ is the magnetic flux variable across the memristor with physical parameters (α, β) . V_0 is constant, and the gains (r, b) are the same parameters in eq. (1). Under the Kirchhoff's theorem, the relations between physical variables for Figure 1 are defined by

$$\begin{cases} C \frac{dV}{dt} = -i_{NR} - i_M, \\ \frac{d\phi}{dt} = A\phi + bV, \end{cases} \quad (6)$$

where the normalized parameter b has no physical unit, and the parameter A has physical unit. The physical variables and parameters in eq. (6) are rewritten in a dimensionless form [61]:

$$\begin{cases} y = \frac{V}{V_0}, \quad \phi' = \frac{\phi}{\rho C V_0}, \quad \tau = \frac{t}{\rho C}, \\ \alpha' = \rho \alpha, \beta' = \rho^3 C^2 V_0^2 \beta, a = A \rho C. \end{cases} \quad (7)$$

Inserting the variables and parameters for eq. (7) into the eq. (6), it has the same form as presented in eq. (1). That is, eq. (6) can produce similar behaviors in the memristive oscillator in eq. (1). The capacitive and memristive energy W_1 and the dimensionless form for eq. (6) are estimated by [61]

$$\begin{cases} W_1 = \frac{1}{2} C V^2 + \frac{1}{2} L M i_M^2 = \frac{1}{2} C V^2 + \frac{1}{2} \phi i_M, \\ H_1 = \frac{W_1}{C V_0^2} = \frac{1}{2} y^2 + \frac{1}{2} (\alpha' \phi' + 3\beta' \phi'^3) y. \end{cases} \quad (8)$$

That is, the field energy in eq. (8) is consistent with the energy description in eq. (2), and the Hamilton energy is verified by using the Helmholtz theorem when the memristive oscillator is rewritten in a vector form. Therefore, combination of a capacitor and an MFCM accompanying with a nonlinear resistor is effective to reproduce similar dynamical behaviors in the nonlinear oscillator in eq. (1). The potential mechanism is that continuous oscillation in nonlinear system requires continuous exchange between capacitive and inductive field.

2.3 Approach of memristive oscillator by using CCM

A CCM has similar physical property as capacitor by keeping capacitive property in field and energy characteristic. It is interesting to investigate whether combination of inductor and CCM can develop similar dynamics in eq. (1), and the circuit implement is plotted in Figure 2.

According to Figure 2, the dimensionless variables (y, ϕ') in eq. (1) can link to the channel current across the inductor and charge for the CCM. The relation between variables in Figure 2 is defined as follows:

$$\begin{cases} L \frac{di_L}{dt} = V_{i_L} - V_M, \\ \frac{dq}{dt} = Bq + di_L. \end{cases} \quad (9)$$

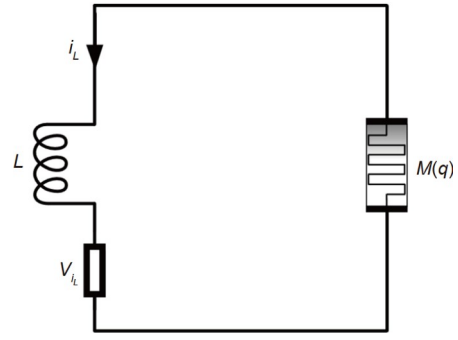


Figure 2 Schematic diagram for a neural circuit coupled by CCM. A memristive circuit connected by one inductor, nonlinear resistor (NR) and one CCM.

The parameter B is relative to the physical property of the CCM, and it is approached by $B = \sigma/C_0$, which C_0 measures the capacitive ability in the CCM and σ is a constant conductance. The physical characteristic for the CCM and channel current for NR are defined by

$$\begin{cases} V_{i_L} = \rho(i_L - \frac{\rho i_L^2}{V_0}), \\ V_M = M(q)i_L = (\alpha_2 + 3\beta_2 q^2)i_L. \end{cases} \quad (10)$$

By applying similar scale transformation for the variables and parameters in eqs. (9) and (10), a group of new variables and parameters are obtained by

$$\begin{cases} z' = \frac{\rho i_L}{V_0}, \quad q' = \frac{q}{C_0 V_0}, \quad \tau = \frac{t}{\rho C_0}, \quad \gamma = \frac{\rho^2 C_0}{L}, \\ \alpha' = \frac{\rho C_0}{L} \alpha_2, \beta' = \frac{\rho C_0^3 V_0^2}{L} \beta_2, c = \sigma \rho. \end{cases} \quad (11)$$

As a result, the eq. (9) is updated in a dimensionless form as follows:

$$\begin{cases} \frac{dz'}{d\tau} = \gamma z'(1 - z') - (\alpha' + 3\beta' q'^2)z', \\ \frac{dq'}{d\tau} = cq' + dz'. \end{cases} \quad (12)$$

It has the identical form shown in eq. (1) even the symbols for variables and parameters show some differences. Therefore, the two memristive systems in eqs. (1) and (12) can present similar oscillatory characteristic by applying suitable parameters. It is important to identify the energy for the nonlinear circuit in Figure 2 and the field energy and its dimensionless energy form are given in

$$\begin{cases} W_2 = \frac{1}{2} L i_L^2 + \frac{1}{2} C_M V_M^2 = \frac{1}{2} L i_L^2 + \frac{1}{2} q V_M, \\ H_2 = \frac{W_2}{C_0 V_0^2} = \frac{1}{2} \gamma z'^2 + \frac{1}{2} \gamma (\alpha' q' + 3\beta' q'^3) z'. \end{cases} \quad (13)$$

By using similar linear transformation, the dynamics in eq. (12) can be presented in a map form.

$$\begin{cases} w_{n+1} = \eta w_n (1 - w_n) - (\alpha + 3\beta q_n^2) w_n, \\ q_{n+1} = \delta q_n + \mu w_n. \end{cases} \quad (14)$$

From eq. (12) to eq. (14), it requires the following criterion for redefining the parameters and variables.

$$\begin{cases} \eta = 1 + \gamma\Delta\tau, \quad \alpha' = \frac{\alpha}{\Delta\tau}, \quad \beta' = \frac{\beta\Delta\tau\gamma^2}{(1+\gamma\Delta\tau)^2}, \quad d = \frac{\mu}{\Delta\tau}, \\ q_n = \frac{\gamma\Delta\tau}{(1+\gamma\Delta\tau)}q'_n, \quad w_n = \frac{\gamma\Delta\tau}{1+\gamma\Delta\tau}z'_n, \quad c = \frac{\delta-1}{\Delta\tau}, \end{cases} \quad (15)$$

where the variables (z'_n, q'_n) are discretized from the variables (z', q') in eq. (12). Both eqs. (4) and (14) have the similar form even these dimensionless variables are mapped from different physical variables. However, their energy functions in eqs. (8) and (13) are much different because the physical field energy can be kept in different types. It means that combination of different electronic components will have different energy thresholds and ranges. Indeed, circuit implement of the same nonlinear oscillator is dependent on the combination of electric components greatly. A capacitive component is crucial to keep electric field, and then discharge will pump energy into inductive components for inducing continuous oscillation. When a capacitor is not available, a CCM is effective to save and propagate charges in continuous way. As a result, changes of the channel current passed in the inductor or induction coil generate an induced electromotive force. Therefore, capacitive components are indispensable elements to build nonlinear circuits, and specific component dependent on charge flow similar as the form of eq. (10) becomes indispensable.

2.4 Scale transformation for physical parameters and units

In generic way, standard physical time unit is available when both intrinsic parameters including capacitance and resistance (C, R) or capacitive and inductance (C, L) are known, and then the physical time is converted into dimensionless time variable as $\tau=t/RC$, or $\tau=t/(LC)^{1/2}$. In fact, when the intrinsic parameter C is not known, another time factor can be used as reference value

$$\begin{cases} \eta = 1 + \gamma\Delta\tau, \quad \alpha' = \frac{\alpha}{\Delta\tau}, \quad \beta' = \frac{\beta\Delta\tau\gamma^2}{(1+\gamma\Delta\tau)^2}, \quad d = \frac{\mu}{\Delta\tau}, \\ q_n = \frac{\gamma\Delta\tau}{(1+\gamma\Delta\tau)}q'_n, \quad w_n = \frac{\gamma\Delta\tau}{1+\gamma\Delta\tau}z'_n, \quad c = \frac{\delta-1}{\Delta\tau}. \end{cases} \quad (16)$$

Therefore, replacing the variables in eq. (9) can develop the memristive circuit in another form without clarifying $B=\sigma/C_0$. A group of new variables and parameters are defined by

$$\begin{cases} z' = \frac{\rho i_L}{V_0}, \quad q' = \frac{\rho^2}{LV_0}q, \quad \tau = \frac{\rho t}{L}, \\ \alpha' = \frac{1}{\rho}\alpha_2, \beta' = \frac{L^2V_0^2}{\rho^5}\beta_2, k_2 = \frac{BL}{\rho}. \end{cases} \quad (17)$$

The memristive circuit in eq. (9) is updated with a new form as follows:

$$\begin{cases} \frac{dz'}{d\tau} = z'(1-z') - (\alpha' + 3\beta'q'^2)z', \\ \frac{dq'}{d\tau} = k_2q' + dz'. \end{cases} \quad (18)$$

It presents similar form as shown in eq. (12). As a result, similar dynamics can be reproduced by taming the parameters in eq. (18). As a result, similar discrete system for eq. (18) can be obtained in the form as presented in eq. (14). The energy function for eq. (18) is given in the form as follows:

$$\begin{cases} W_3 = \frac{1}{2}Li_L^2 + \frac{1}{2}C_MV_M^2 = \frac{1}{2}Li_L^2 + \frac{1}{2}qV_M, \\ H_3 = \frac{W_2}{V_0^2(L/\rho^2)} = \frac{W_2\rho^2}{LV_0^2} = \frac{1}{2}z'^2 + \frac{1}{2}(\alpha'q' + 3\beta'q'^3)z'. \end{cases} \quad (19)$$

Indeed, scale transformation seldom changes the energy function for the memristive circuit. Therefore, eq. (18) has the same form of energy function defined in eq. (13) accompanying the gain $p=1/\gamma$. It is interesting to discuss the energy approach for the memristive maps in possible way. Eq. (8) presents exact calculation of energy for the memristive eq. (1). Considering relation between these parameters for the oscillator and map, a discrete energy function for eq. (4) is estimated as follows:

$$H_n = \frac{1}{2}x_n^2 + \frac{1}{2}(\alpha\varphi_n + 3\beta\varphi_n^3)x_n. \quad (20)$$

For the memristive map in eq. (14), the energy function is suggested as follows:

$$H_n = p[\frac{1}{2}w_n^2 + \frac{1}{2}(\alpha q_n + 3\beta q_n^3)w_n]. \quad (21)$$

The weight or gain for the energy function in eq. (14) can be selected with $p=1$, and it has no distinct impact on the exchange between capacitive and inductive energy terms. The discrete energy function in eq. (21) is consistent with a discrete form from eq. (19), and it indicates that the dimensionless energy function is independent of the scale transformation because the energy function can be mapped from the sole field energy function for the memristive circuit completely.

Appearance and emergence of chaos in an autonomous nonlinear oscillator requires three variables at least. In absence of external periodic forcing or noisy excitation, the memristive oscillator in eqs. (1), (12), (18) just contains two variables. Therefore, periodic oscillatory states can be developed rather than inducing any chaotic series. As is known, chaos can be induced one-variable map and two-variable map. Therefore, the memristive maps shown in eqs. (4) and (14) can be tamed to present chaotic states by setting appropriate values for the dimensionless parameters for supporting a positive Lyapunov exponent. The potential mechanism is that the discretization operation for the nonlinear oscillators introduces time factor for the variables into the new developed maps, and the sampled time series in

periodic type are encoded in the amplitude and interval synchronously. Therefore, these mapped discrete systems can present chaos or new periodic characteristic. In this case, the memristive maps have distinct advantage than the memristive oscillators for producing similar firing activities as biological neurons.

2.5 Adaptive growth law controlled by energy level

Biological neurons often show controllable properties during the polarization and magnetization, and even shape deformation is induced by specific mechanical stimuli. As a result, some intrinsic parameters for ion channel, capacitive and inductive properties are changed. Indeed, we can use a similar control law as in refs. [17,18] for the memristive parameters in eqs. (1), (12) and (18), and then the memristive oscillators can experience different firing modes and the average value for the energy function will show corresponding jump between different energy levels. To keep the same form for variables, the growth of intrinsic parameter is controlled with exponential form smoothly. For maps, the growth criterion is considered as saturation form restricted by a Heaviside function. For simplicity, we consider the adaptive growth of one memristive parameter for the memristive map as follows:

$$\begin{cases} \alpha = \alpha_0 + \Delta\alpha \cdot \text{int}\left(\frac{n}{N_0}\right) \mathfrak{H}(H_n - \kappa), \\ \mathfrak{H}(P) = 1, P \geq 0, \mathfrak{H}(P) = 0, P < 0, \end{cases} \quad (22)$$

where α_0 is the initial value for memristive parameter, $\Delta\alpha$ is the growth step, n denotes iterations, N_0 measures the interval for next growth, κ is the energy threshold and the Heaviside function in eq. (22) controls its growth when the energy level is beyond a threshold. On the other hand, average energy value often predicts high regularity in the neural activities. Adaptive reduction in some parameters is also effective to control the mode transition. For example,

$$\begin{cases} \alpha = \alpha_0 - \Delta\alpha \cdot \text{int}\left(\frac{n}{N_0}\right) \mathfrak{H}(\kappa - H_n), \\ \mathfrak{H}(P) = 1, P \geq 0, \mathfrak{H}(P) = 0, P < 0. \end{cases} \quad (23)$$

In the next section for numerical approach, the case defined in eq. (22) will be discussed. $\Delta\alpha > 0$ means positive growth of the memristive parameter from a small value, $\Delta\alpha < 0$ can calculate the case for reduction of memristive parameter from a high value.

3 Results and discussion

The memristive neuron can be presented in similar form in eqs. (1), (12) and (18) and parameters can be adjusted to trigger similar dynamical behaviors. The fourth order Runge-Kutta algorithm can be applied to explore the dynamics by finding the numerical solutions for the memristive oscillator even different symbols are used for the variables and parameters. Bifurcation parameters are changed to present different firing patterns, and the corresponding energy function is calculated as well. Our main aim is to investigate the dynamics and energy characteristic of the memristive map, and nonlinear response under the suggested adaptive law in eq. (23). At first, we calculated the mode selection in eq. (4) by changing one parameter carefully, and the distribution of variable series is plotted in Figure 3.

From Figure 3, it is demonstrated that the memristive map shows distinct transition between different firing modes by changing one intrinsic parameter carefully. Complete firing patterns including spiking, bursting and chaotic states are induced by taming a single parameter in continuous way. To discern the dynamics and energy characteristic of this memristive oscillator, formation of attractors and energy evolution are plotted for the neuron presenting different neural activities in Figure 4.

The profile of the attractor is relative to the firing mode and energy level. From chaotic state to periodic firing patterns, chaotic attractor is suppressed and the average energy value is increased. The similar case for memristive map in eq. (14) is explored, and the bifurcation diagram is plotted in Figure 5.

Complete firing modes are found in the memristive map in eq. (14) by adjusting one normalized parameter carefully,

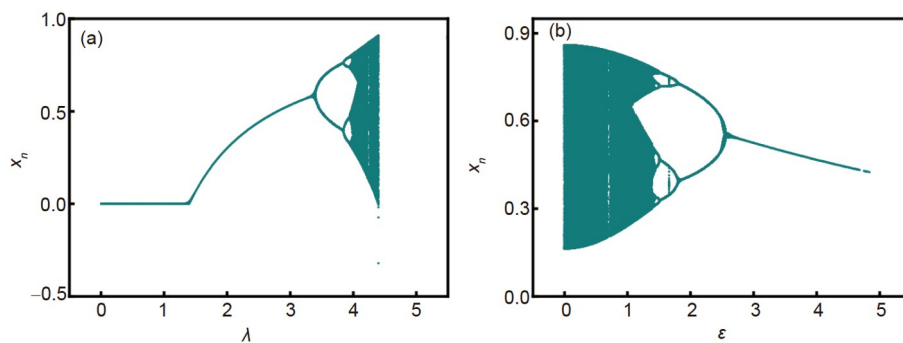


Figure 3 Bifurcation diagram of X_n vs. parameter λ (a) and parameter ϵ (b). (a) $\epsilon=0.15$; (b) $\lambda=4.2$. Setting parameters $\alpha=0.4$, $\beta=0.02$, $k=0.5$ and initials (0.2, 0.1).

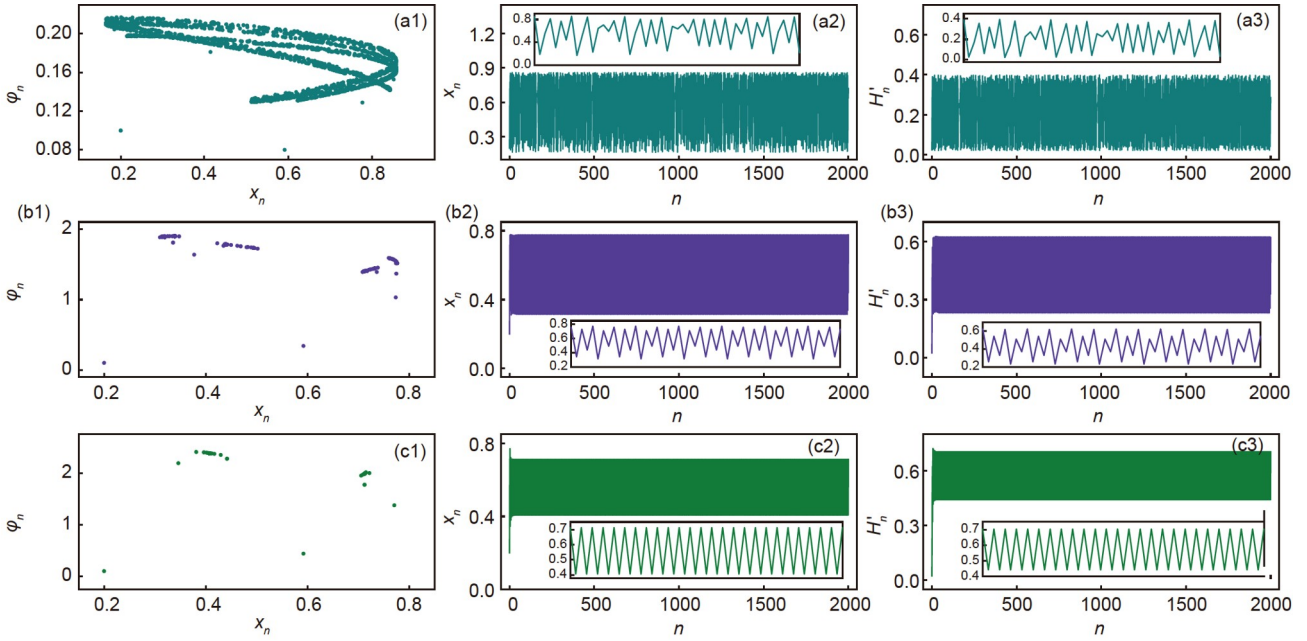


Figure 4 Developed attractors, evolution of variable x_n and energy level. (a1, a2, a3) $\varepsilon=0.15$; (b1, b2, b3) $\varepsilon=1.45$; (c1, c2, c3) $\varepsilon=1.95$. The other parameters are fixed at $\lambda=4.2$. (a3) $\langle H'_n \rangle = 0.214$; (b3) $\langle H'_n \rangle = 0.435$; (c3) $\langle H'_n \rangle = 0.572$. The enlarged images show the situation with iterations between 500 and 550.

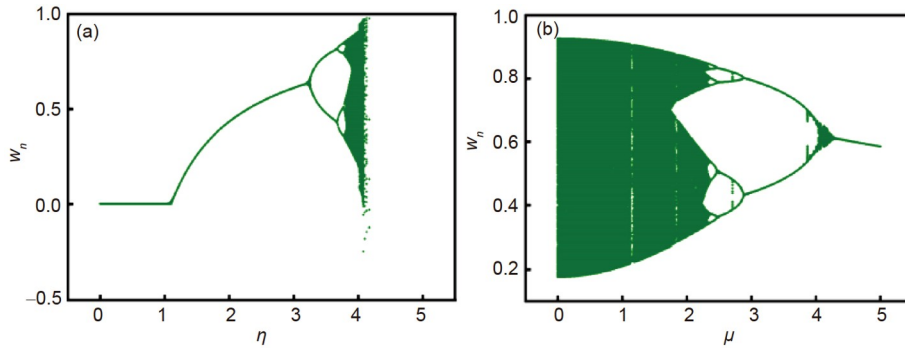


Figure 5 Bifurcation of variable W_n vs. parameter η (a) and parameter μ (b). (a) $\mu=1.75$; (b) $\eta=3.9$. Setting parameters $\alpha=0.1$, $\beta=0.01$, and $\delta=0.3$.

and the mode transition in Figure 5 is some different from the distribution in eq. (3). Furthermore, the formation of attractor, changes of variable and energy function for the map are calculated in Figure 6. Shift in the average energy and changes of attractor profile predict mode transition in the memristive map.

By changing a single parameter in eq. (14), chaotic attractor is guided to show periodic type, and the average energy for the map also shows slight increase. Furthermore, it is interesting to discuss the formation of attractors and mode transition when the memristive map neuron in eq. (14) is regulated by the adaptive law in eq. (22), and changes of attractors are shown in Figure 7. Form simplicity, $\alpha_0=0.1$, $\Delta\alpha=0.005$, $\kappa=0.5$, $N_0=40$ are used for the control law and map attractors are presented.

The shape of attractors is changed with adaptive growth of one memristive parameter in the map, chaotic and periodic attractors can be formed as well. For better clarification, the

transition in the membrane potential, energy level and growth of memristive parameter is shown in Figure 8.

Distinct changes are observed in the series for membrane potential and energy function during the growth of memristive parameter with constant footstep. Similar to the growth criterion in eq. (22), one memristive parameter can be regulated with negative growth in eq. (23), which begins from a higher value to a lower value. Similar mode transition can be detected. By changing other parameters with the same control law, similar mode transition and jump between energy levels can be found as well.

By setting higher value for the gain $\Delta\alpha$ or smaller interval N_0 , the memristive parameter encounters rapid growth and mode transition becomes more distinct. Furthermore, the case for $\mu=1.58$, 2.85 is calculated in Figures 9 and 10.

From Figure 8 to Figure 10, the average energy is increased from 0.142 to 0.607, and the firing mode is also switched from chaotic to periodic oscillation. For most of the

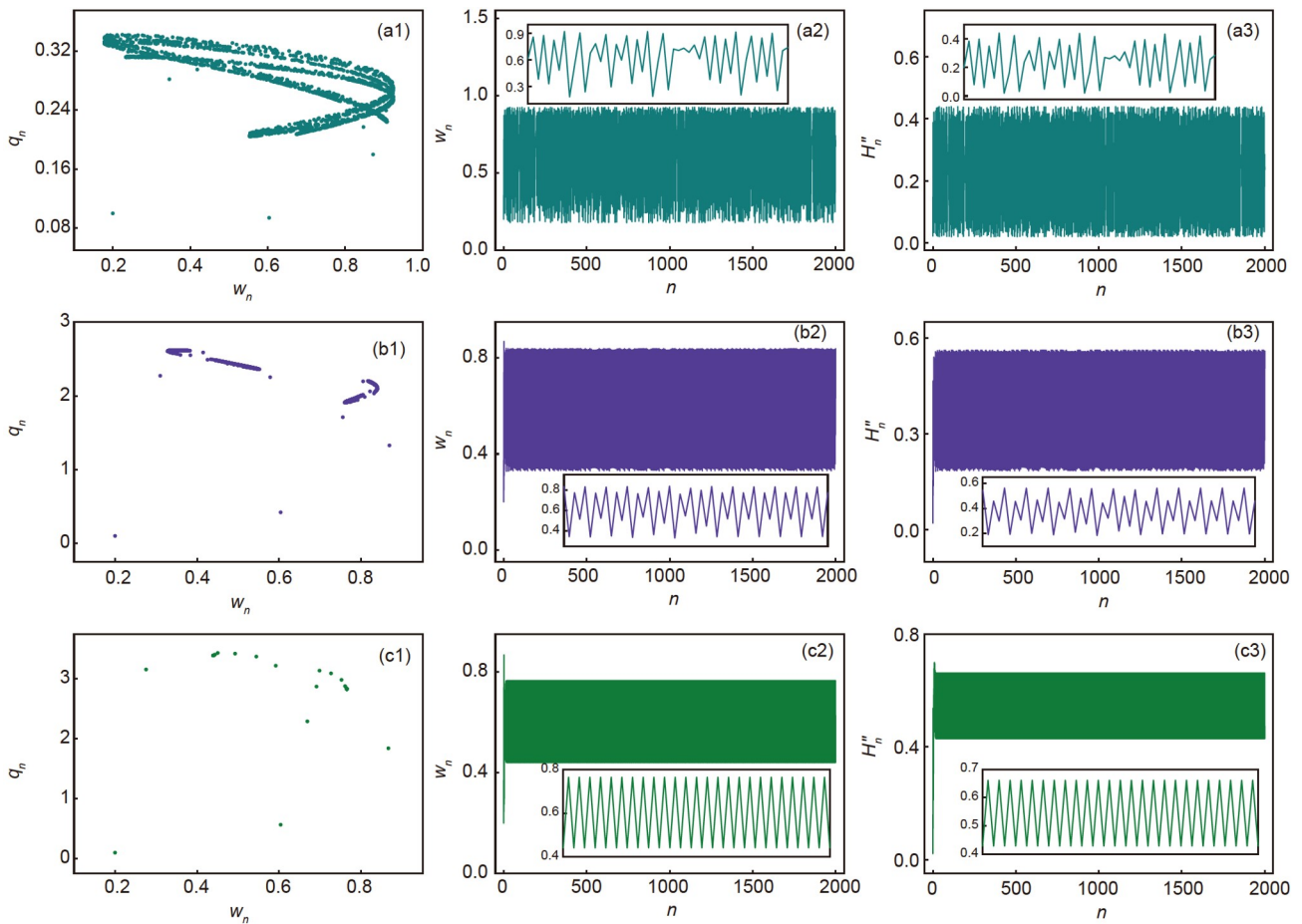


Figure 6 Developed attractors, evolution of variable w_n and energy level. (a1, a2, a3) $\mu=0.22$; (b1, b2, b3) $\mu=1.85$; (c1, c2, c3) $\mu=2.58$. Setting parameters $\eta=3.9$, $p=1$. The average energy for (a3) $\langle H_n'' \rangle = 0.233$, (b3) $\langle H_n'' \rangle = 0.379$, (c3) $\langle H_n'' \rangle = 0.544$. Enlarged images show the situation with iterations between 500 and 550.

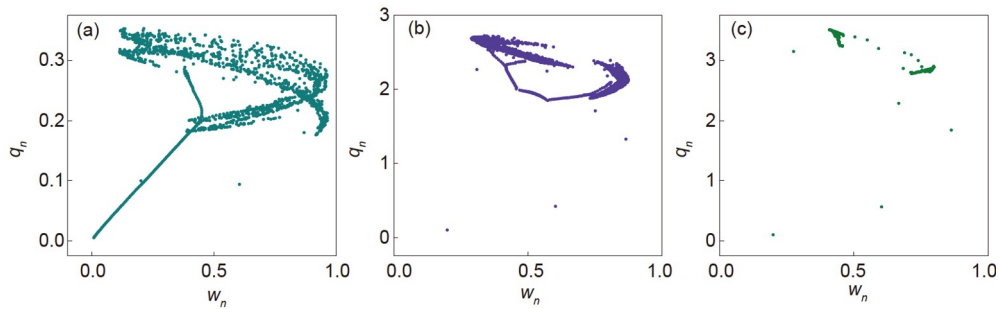


Figure 7 Developed attractors by changing parameter μ . (a) $\mu=0.22$; (b) $\mu=1.85$; (c) $\mu=2.58$. Setting parameters $\alpha_0=0.1$, $\Delta\alpha=0.005$, $\kappa=0.5$, $N_0=40$, $\beta=0.01$, $\eta=3.9$, and the initial values select (0.2, 0.1).

neuron models, the distributions of peak value, interspike intervals (ISI), discrete variable vs. bifurcation parameter seldom show continuous changes, and the firing modes in neural activities are modified when one parameter is changed continuously. That is, one bifurcation parameter can select different values to support the same firing activities such as chaotic, periodic spiking and bursting, and quiescent state. By extensive approach the average Hamilton energy of a neuron with similar firing mode, four distinct energy levels

or footsteps can be detected when a neuron is excited to present four different firing activities [51]. A chaotic pattern often occupies a lower energy level, and periodic pattern often occupies a higher energy level. Both spiking and bursting can be considered as similar to quasi-periodic state, because distinct periodicity often requires higher energy level for keeping periodic oscillation.

For complete showing the dynamics of neural activities in a neuron model, oscillator like or map type, reproduction of

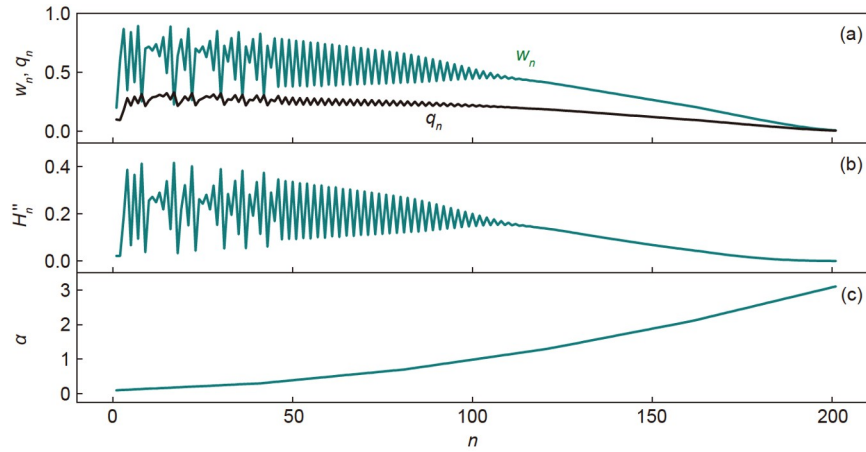


Figure 8 Evolution of variable $w_n q_n$ (a), Hamiltonian energy (b), and growth of memristive parameter α (c). Setting parameters $\alpha_0=0.1$, $\beta=0.01$, $\kappa=0.5$, $\eta=3.9$, $p=1$, $\mu=0.22$. Average energy value finds 0.142.

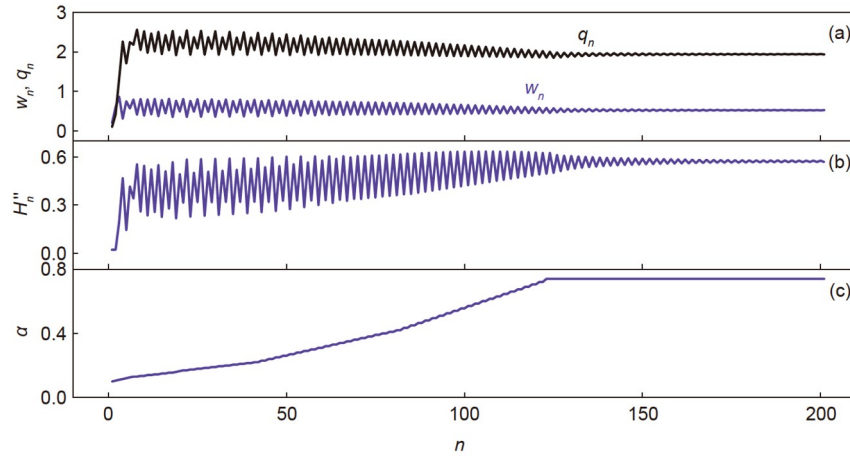


Figure 9 Evolution of variable $w_n q_n$ (a), Hamiltonian energy (b), and growth of memristive parameter α (c). Setting parameters $\alpha_0=0.1$, $\beta=0.01$, $\kappa=0.5$, $\eta=3.9$, $p=1$, $\mu=1.85$. Average energy value finds 0.502.

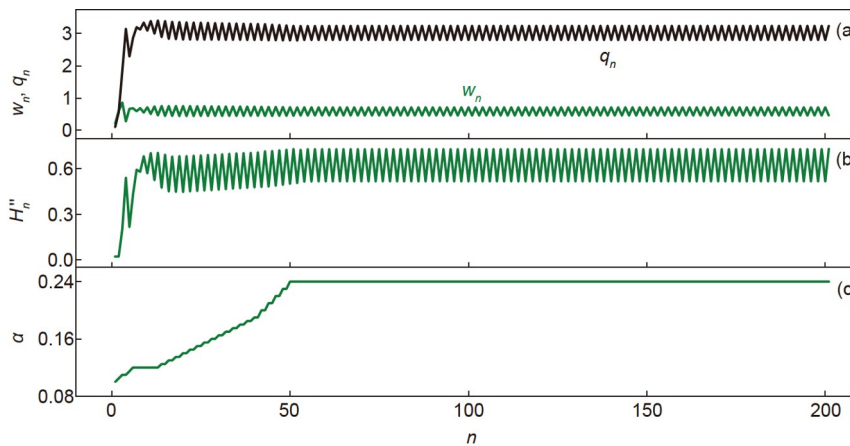


Figure 10 Evolution of variable $w_n q_n$ (a), Hamiltonian energy (b), and growth of memristive parameter α (c). Setting parameters $\alpha_0=0.1$, $\beta=0.01$, $\kappa=0.5$, $\eta=3.9$, $p=1$, $\mu=2.58$. Average energy value finds 0.607.

complete firing modes is the main characteristic. In presence of noisy excitation, nonlinear resonances can be induced by taming the intensity of noisy disturbance. Besides the calculation of SNR (signal to noise ratio) and CV (coefficient

variability) vs. noise intensity, the distribution of average Hamilton energy $\langle H \rangle$ with different noise intensities provides a more effective way to predict the emergence of coherence resonance. Within a transient period or iterations N ,

average energy $\langle H \rangle$ prefers to estimate the average power of the neuron or nonlinear oscillator, and high energy level is effective to keep distinct periodic state. Therefore, noise excitation can be applied on the right side of the first formula in eqs. (4) and (14). By taming the noise intensity, similar coherence resonance can be induced and confirmed by estimating the distribution of CV values or $\langle H_n \rangle$ for eqs. (21) and (22). The Hamilton energy function H can be used as Lyapunov function, $dH/d\tau$ often means energy release and the system becomes stable within finite transient period. The discrete energy function H_n is effective to restrict the stability in a map. When energy is released in stable way, H_n is decreased in each iteration, and then

$$\frac{H_{n+1} - H_n}{H_n - H_{n-1}} < 1. \quad (24)$$

In the last decades, more interesting works about computational neuroscience have been finished on neuron models presented in nonlinear oscillators [62–65], some of which are included with biophysical effects, and numerical approach of membrane potentials for neurons and further statistical analysis often involves reliability of numerical algorithm in presence of noisy disturbance. Based on these oscillator-like models, coupling channels and links are tamed to control the collective behaviors in networks with linear, hybrid and higher order interaction [66–70], respectively. Map approach from equivalent nonlinear oscillator and nonlinear circuits, and reliability verification of the proposed maps can find clues from the scheme in this paper. In particular, energy definition for maps becomes helpful to discern the dependence of oscillatory modes on energy level provides new insights to predict occurrence of nonlinear resonance and further control under energy flow.

4 Conclusions

In this work, physical approach of an oscillator neuron with memristive term is discussed, and the equivalent nonlinear circuits are suggested to mimic the nonlinear terms and neural activities in the memristive neuron. It suggests two kinds of neural circuits by using different functional electric components. That is, a memristive oscillator can be implemented in some equivalent circuits composed of different electric components. When capacitive component as capacitor is not available, a CCM can behave similar role for supporting energy exchange between magnetic field and electric field. In particular, linear transition of sampled variables from the memristive oscillator and accompanying with time scale (such as time step for the nonlinear oscillator) can define a group of new variables, which are combined to build function maps. It provides theoretical evidence and guidance to design functional maps rather than giving

mathematical maps arbitrarily. The obtained functional maps have good covariant feature with the original functional oscillators. For example, removing the subscript for the variables in the map will show the same form in the formula for nonlinear oscillator. As a result, a suitable energy function with the same weight for capacitive, inductive and memristive terms can be obtained for the memristive map in theoretical way. We also suggest an adaptive law to control one memristive parameter in the map under energy flow, mode transition occurs accompanying with energy shift during the mode transition. It explains the self-adaption property in map neurons from energy aspect. For further application of digital circuits and intelligent computation based on maps, readers can refer to this work and then some feasible maps can be designed from physical aspect. The suggested functional maps can be used for exploring pattern stability and wave propagation in the networks composed of maps [71–74]. The scheme throws insights on the study the maps coupled with discrete memristor [75–80]. The scheme is also helpful for presenting reliable map neurons and further application of setting map networks. Memristive terms accounts for the emergence of multistability and coexistence of more attractors, and it also provides energy source for some controllable neural circuits and biological neurons [81,82]. It is worthy of investigating the collective behaviors and self-organization of networks composed of reliable neurons, and thus researchers can find bridges to discover the potential dynamical mechanism for some neural disease [83,84].

This work was supported by the National Natural Science Foundation of China (Grant No. 12072139).

- 1 Heinrich M, Dahms T, Flunkert V, et al. Symmetry-breaking transitions in networks of nonlinear circuit elements. *New J Phys*, 2010, 12: 113030
- 2 Kenkel S W, Straley J P. Percolation theory of nonlinear circuit elements. *Phys Rev Lett*, 1982, 49: 767–770
- 3 Sivaganesh G, Srinivasan K, Arulgnanam A. Analytical studies on the dynamics of higher-dimensional nonlinear circuit systems. *Pramana*, 2022, 96: 185
- 4 Ardila V, Ramirez F, Suarez A. Analytical and numerical bifurcation analysis of circuits based on nonlinear resonators. *IEEE Trans Microwave Theor Techn*, 2021, 69: 4392–4405
- 5 Gao X, Mou J, Xiong L, et al. A fast and efficient multiple images encryption based on single-channel encryption and chaotic system. *Nonlinear Dyn*, 2022, 108: 613–636
- 6 Xin J, Hu H, Zheng J. 3D variable-structure chaotic system and its application in color image encryption with new Rubik's Cube-like permutation. *Nonlinear Dyn*, 2023, 111: 7859–7882
- 7 Ning X, Dong Q, Zhou S, et al. Construction of new 5D Hamiltonian conservative hyperchaotic system and its application in image encryption. *Nonlinear Dyn*, 2023, 111: 20425–20446
- 8 Liu X, Tong X, Wang Z, et al. Construction of controlled multi-scroll conservative chaotic system and its application in color image encryption. *Nonlinear Dyn*, 2022, 110: 1897–1934
- 9 Wang R, Wang Y, Xu X, et al. Brain works principle followed by neural information processing: A review of novel brain theory. *Artif Intell Rev*, 2023, 56: 285–350
- 10 Quaranta G, Lacarbonara W, Masri S F. A review on computational

- intelligence for identification of nonlinear dynamical systems. *Nonlinear Dyn*, 2020, 99: 1709–1761
- 11 Groschner L N, Malis J G, Zuidinga B, et al. A biophysical account of multiplication by a single neuron. *Nature*, 2022, 603: 119–123
 - 12 Tagluk M E, Isik I. Communication in nano devices: Electronic based biophysical model of a neuron. *Nano Commun Netw*, 2019, 19: 134–147
 - 13 Wu F Q, Ma J, Zhang G. Energy estimation and coupling synchronization between biophysical neurons. *Sci China Tech Sci*, 2020, 63: 625–636
 - 14 Clark R, Fuller L, Platt J A, et al. Reduced-dimension, biophysical neuron models constructed from observed data. *Neural Comput*, 2022, 34: 1545–1587
 - 15 Sotero R C, Trujillo-Barreto N J. Biophysical model for integrating neuronal activity, EEG, fMRI and metabolism. *NeuroImage*, 2008, 39: 290–309
 - 16 Ma J. Biophysical neurons, energy, and synapse controllability: A review. *J Zhejiang Univ Sci A*, 2023, 24: 109–129
 - 17 Wu F Q, Guo Y T, Ma J. Energy flow accounts for the adaptive property of functional synapses. *Sci China Tech Sci*, 2023, 66: 3139–3152
 - 18 Yang F, Xu Y, Ma J. A memristive neuron and its adaptability to external electric field. *Chaos-An Interdisciplinary J Nonlinear Sci*, 2023, 33: 023110
 - 19 Xie Y, Yao Z, Ma J. Formation of local heterogeneity under energy collection in neural networks. *Sci China Tech Sci*, 2023, 66: 439–455
 - 20 Yang F, Wang Y, Ma J. Creation of heterogeneity or defects in a memristive neural network under energy flow. *Commun Nonlinear Sci Numer Simul*, 2023, 119: 107127
 - 21 Real E, Asari H, Gollisch T, et al. Neural circuit inference from function to structure. *Curr Biol*, 2017, 27: 189–198
 - 22 Pan Y, Monje M. Activity shapes neural circuit form and function: A historical perspective. *J Neurosci*, 2020, 40: 944–954
 - 23 Davis F P, Nern A, Picard S, et al. A genetic, genomic, and computational resource for exploring neural circuit function. *eLife*, 2020, 9: e50901
 - 24 Sussillo D. Neural circuits as computational dynamical systems. *Curr Opin Neurobiol*, 2014, 25: 156–163
 - 25 Wu F, Yao Z. Dynamics of neuron-like excitable Josephson junctions coupled by a metal oxide memristive synapse. *Nonlinear Dyn*, 2023, 111: 13481–13497
 - 26 Xie Y, Yao Z, Hu X, et al. Enhance sensitivity to illumination and synchronization in light-dependent neurons. *Chin Phys B*, 2021, 30: 120510
 - 27 Zhou P, Yao Z, Ma J, et al. A piezoelectric sensing neuron and resonance synchronization between auditory neurons under stimulus. *Chaos Solitons Fractals*, 2021, 145: 110751
 - 28 Xu Y, Liu M, Zhu Z, et al. Dynamics and coherence resonance in a thermosensitive neuron driven by photocurrent. *Chin Phys B*, 2020, 29: 098704
 - 29 Tagne J F, Edima H C, Njitacke Z T, et al. Bifurcations analysis and experimental study of the dynamics of a thermosensitive neuron conducted simultaneously by photocurrent and thermistance. *Eur Phys J Spec Top*, 2022, 231: 993–1004
 - 30 Zhu Z, Ren G, Zhang X, et al. Effects of multiplicative-noise and coupling on synchronization in thermosensitive neural circuits. *Chaos Solitons Fractals*, 2021, 151: 111203
 - 31 Shen H, Yu F, Wang C, et al. Firing mechanism based on single memristive neuron and double memristive coupled neurons. *Nonlinear Dyn*, 2022, 110: 3807–3822
 - 32 Wu F, Hu X, Ma J. Estimation of the effect of magnetic field on a memristive neuron. *Appl Math Comput*, 2022, 432: 127366
 - 33 Wen Z, Wang C, Deng Q, et al. Regulating memristive neuronal dynamical properties via excitatory or inhibitory magnetic field coupling. *Nonlinear Dyn*, 2022, 110: 3823–3835
 - 34 Xu Q, Ju Z, Ding S, et al. Electromagnetic induction effects on electrical activity within a memristive Wilson neuron model. *Cogn Neurodyn*, 2022, 16: 1221–1231
 - 35 Kafraj M S, Parastesh F, Jafari S. Firing patterns of an improved Izhikevich neuron model under the effect of electromagnetic induction and noise. *Chaos Solitons Fractals*, 2020, 137: 109782
 - 36 Narayanan R, Johnston D. Functional maps within a single neuron. *J Neurophysiol*, 2012, 108: 2343–2351
 - 37 Ibarz B, Casado J M, Sanjuán M A F. Map-based models in neuronal dynamics. *Phys Rep*, 2011, 501: 1–74
 - 38 Muni S S, Fatoyinbo H O, Ghosh I. Dynamical effects of electromagnetic flux on chialvo neuron map: Nodal and network behaviors. *Int J Bifurcation Chaos*, 2022, 32: 2230020
 - 39 Ramakrishnan B, Mehrabbeik M, Parastesh F, et al. A new memristive neuron map model and its network's dynamics under electrochemical coupling. *Electronics*, 2022, 11: 153
 - 40 Bao H, Li K X, Ma J, et al. Memristive effects on an improved discrete Rulkov neuron model. *Sci China Tech Sci*, 2023, 66: 3153–3163
 - 41 Li Y, Wang Z, Midya R, et al. Review of memristor devices in neuromorphic computing: Materials sciences and device challenges. *J Phys D-Appl Phys*, 2018, 51: 503002
 - 42 Khalid M. Review on various memristor models, characteristics, potential applications, and future works. *Trans Electr Electron Mater*, 2019, 20: 289–298
 - 43 Thakkar P, Gosai J, Gogoi H J, et al. From fundamentals to frontiers: A review of memristor mechanisms, modeling and emerging applications. *J Mater Chem C*, 2024, 12: 1583–1608
 - 44 Lin H, Wang C, Deng Q, et al. Review on chaotic dynamics of memristive neuron and neural network. *Nonlinear Dyn*, 2021, 106: 959–973
 - 45 Lai Q, Lai C. Design and implementation of a new hyperchaotic memristive map. *IEEE Trans Circuits Syst II*, 2022, 69: 2331–2335
 - 46 Liu X, Sun K, Wang H, et al. A class of novel discrete memristive chaotic map. *Chaos Solitons Fractals*, 2023, 174: 113791
 - 47 Ramadoss J, Almatroud O A, Momani S, et al. Discrete memristance and nonlinear term for designing memristive maps. *Symmetry*, 2022, 14: 2110
 - 48 Rong K, Bao H, Li H, et al. Memristive Hénon map with hidden Neimark–Sacker bifurcations. *Nonlinear Dyn*, 2022, 108: 4459–4470
 - 49 Bao B, Zhao Q, Yu X, et al. Complex dynamics and initial state effects in a two-dimensional sine-bounded memristive map. *Chaos Solitons Fractals*, 2023, 173: 113748
 - 50 Fox R F, Gatland I R, Roy R, et al. Fast, accurate algorithm for numerical simulation of exponentially correlated colored noise. *Phys Rev A*, 1988, 38: 5938–5940
 - 51 Li X, Xu Y. Energy level transition and mode transition in a neuron. *Nonlinear Dyn*, 2024, 112: 2253–2263
 - 52 Mantegna R N. Fast, accurate algorithm for numerical simulation of Lévy stable stochastic processes. *Phys Rev E*, 1994, 49: 4677–4683
 - 53 Guo Y, Xie Y, Ma J. How to define energy function for memristive oscillator and map. *Nonlinear Dyn*, 2023, 111: 21903–21915
 - 54 Ma J. Energy function for some maps and nonlinear oscillators. *Appl Math Comput*, 2024, 463: 128379
 - 55 Isah A, Bilbault J M. Review on the basic circuit elements and memristor interpretation: Analysis, technology and applications. *J Low Power Electron Appl*, 2022, 12: 44
 - 56 Abraham I. The case for rejecting the memristor as a fundamental circuit element. *Sci Rep*, 2018, 8: 10972
 - 57 Ramakrishnan B, Durdu A, Rajagopal K, et al. Infinite attractors in a chaotic circuit with exponential memristor and Josephson junction resonator. *AEU-Int J Electron Commun*, 2020, 123: 153319
 - 58 Isah A, Nguetcho A S T, Binczak S, et al. Dynamics of a charge-controlled memristor in master–slave coupling. *Electron Lett*, 2020, 56: 211–213
 - 59 Sun J, Yang J, Liu P, et al. Design of general flux-controlled and charge-controlled memristor emulators based on hyperbolic functions. *IEEE Trans Comput-Aided Des Integr Circuits Syst*, 2022, 42: 956–967
 - 60 Sharma P K, Ranjan R K, Khateb F, et al. Charged controlled mem-

- element emulator and its application in a chaotic system. *IEEE Access*, 2020, 8: 171397–171407
- 61 Wang C, Tang J, Ma J. Minireview on signal exchange between nonlinear circuits and neurons via field coupling. *Eur Phys J Spec Top*, 2019, 228: 1907–1924
 - 62 Wang X, Yu D, Wu Y, et al. Effects of potassium channel blockage on inverse stochastic resonance in Hodgkin-Huxley neural systems. *J Zhejiang Univ Sci A*, 2023, 24: 735–748
 - 63 Huang W, Yang L, Zhan X, et al. Synchronization transition of a modular neural network containing subnetworks of different scales. *Front Inform Technol Electron Eng*, 2023, 24: 1458–1470
 - 64 Xie Y, Yao Z, Ma J. Phase synchronization and energy balance between neurons. *Front Inform Technol Electron Eng*, 2022, 23: 1407–1420
 - 65 Wu F, Gu H, Jia Y. Bifurcations underlying different excitability transitions modulated by excitatory and inhibitory memristor and chemical autapses. *Chaos Solitons Fractals*, 2021, 153: 111611
 - 66 Majhi S, Perc M, Ghosh D. Dynamics on higher-order networks: A review. *J R Soc Interface*, 2022, 19: 20220043
 - 67 Li X, Ghosh D, Lei Y. Chimera states in coupled pendulum with higher-order interaction. *Chaos Solitons Fractals*, 2023, 170: 113325
 - 68 Parastesh F, Mehrabbeik M, Rajagopal K, et al. Synchronization in Hindmarsh–Rose neurons subject to higher-order interactions. *Chaos-An Interdiscipl J Nonlinear Sci*, 2022, 32: 013125
 - 69 Ramasamy M, Devarajan S, Kumarasamy S, et al. Effect of higher-order interactions on synchronization of neuron models with electromagnetic induction. *Appl Math Comput*, 2022, 434: 127447
 - 70 Kundu S, Ghosh D. Higher-order interactions promote chimera states. *Phys Rev E*, 2022, 105: L042202
 - 71 Atay F M, Jost J, Wende A. Delays, connection topology, and synchronization of coupled chaotic maps. *Phys Rev Lett*, 2004, 92: 144101
 - 72 Koronovskii A A, Moskalenko O I, Shurygina S A, et al. Generalized synchronization in discrete maps. New point of view on weak and strong synchronization. *Chaos Solitons Fractals*, 2013, 46: 12–18
 - 73 Winkler M, Sawicki J, Omelchenko I, et al. Relay synchronization in multiplex networks of discrete maps. *Europhys Lett*, 2019, 126: 50004
 - 74 Muni S S, Rajagopal K, Karthikeyan A, et al. Discrete hybrid Izhi-kevich neuron model: Nodal and network behaviours considering electromagnetic flux coupling. *Chaos Solitons Fractals*, 2022, 155: 111759
 - 75 Ma M, Yang Y, Qiu Z, et al. A locally active discrete memristor model and its application in a hyperchaotic map. *Nonlinear Dyn*, 2022, 107: 2935–2949
 - 76 Peng Y, He S, Sun K. A higher dimensional chaotic map with discrete memristor. *AEU-Int J Electron Commun*, 2021, 129: 153539
 - 77 Zhong H, Li G, Xu X. A generic voltage-controlled discrete memristor model and its application in chaotic map. *Chaos Solitons Fractals*, 2022, 161: 112389
 - 78 Ren L, Mou J, Banerjee S, et al. A hyperchaotic map with a new discrete memristor model: Design, dynamical analysis, implementation and application. *Chaos Solitons Fractals*, 2023, 167: 113024
 - 79 Bao H, Hua Z Y, Liu W B, et al. Discrete memristive neuron model and its interspike interval-encoded application in image encryption. *Sci China Tech Sci*, 2021, 64: 2281–2291
 - 80 Li C, Yang Y, Yang X, et al. Application of discrete memristors in logistic map and Hindmarsh–Rose neuron. *Eur Phys J Spec Top*, 2022, 231: 3209–3224
 - 81 Bao H, Chen Z G, Cai J M, et al. Memristive cyclic three-neuron-based neural network with chaos and global coexisting attractors. *Sci China Tech Sci*, 2022, 65: 2582–2592
 - 82 Lu L L, Yi M, Liu X Q. Energy-efficient firing modes of chay neuron model in different bursting kinetics. *Sci China Tech Sci*, 2022, 65: 1661–1674
 - 83 Yuan Y Y, Yang H, Han F, et al. Traveling chimera states in locally coupled memristive Hindmarsh–Rose neuronal networks and circuit simulation. *Sci China Tech Sci*, 2022, 65: 1445–1455
 - 84 Yu Y, Fan Y B, Han F, et al. Transcranial direct current stimulation inhibits epileptic activity propagation in a large-scale brain network model. *Sci China Tech Sci*, 2023, 66: 3628–3638



RESEARCH

Control electromechanical arms by using a neural circuit

Yitong Guo · Xinlin Song · Jun Ma

Received: 11 July 2024 / Accepted: 28 August 2024 / Published online: 2 September 2024
© The Author(s), under exclusive licence to Springer Nature B.V. 2024

Abstract Neural electrical signals forced the muscle tissue to behave effective body gait. When neural activities are measured in a neural circuit, artificial electromechanical arm and leg can be controlled to mimic the movement and even vibration of limbs. In this paper, a simple neural circuit is used to drive an electromechanical arm (EMA) device by activating Ampere's force via the load circuit adhered to the moving beam, and the load circuit is coupled with the neural circuit for energy conversion. The circuit equations, field energy and moving equation of the beam are obtained for dynamical analysis. Furthermore, two EMAs are coupled via a spring for mimicking the cooperation between two arms or legs during synchronous movement, and then the same electrical signal is used to control the moving states of the coupled EMAs. This processing can describe the synchronous movements of two arms along horizontal linear motion under neural stimuli. Noisy disturbance

is applied to detect and predict occurrence of stochastic resonance in the moving beams by calculating signal to noise ratio, and the average Hamilton energy vs. time is effective to predict the emergence of nonlinear stochastic and coherence resonance by approach the average power from physical aspect. The results provide helpful guidance to design complex electromechanical device for behaving complex gaits. That is, neural signals can be used to excite the electromechanical devices as muscles and then the body gaits are controlled effectively.

Keywords Neural circuit · Artificial arm · Electromechanical coupling · Hamilton energy · Resonance

1 Introduction

Neural activities in nervous system depend on the activation of neurons and interaction with astrocyte [1–5], and the contraction of muscle tissue can be controlled by Calcium current [6–10]. When the propagation of electrical signal and information exchange in the nervous system are broken, some neural diseases [11–15] occur and behaving normal and safe body gaits become difficult. Besides experimental approach and detection, setting theoretical models for measuring neural activities become helpful for predicting mode transition in electrical activities

Y. Guo · J. Ma (✉)
College of Electrical and Information Engineering,
Lanzhou University of Technology, Lanzhou 730050,
China
e-mail: hyperchaos@163.com; hyperchaos@lut.edu.cn

X. Song
School of Science, Xi'an University of Science and
Technology, Xi'an 710054, China

J. Ma
Department of Physics, Lanzhou University of
Technology, Lanzhou 730050, China

[16–20] and these neuron models [21, 22] can be connected in networks for exploring the collective behaviors [23–26], self-organization and creation of heterogeneity and defects [27–30].

The researchers can create and propose a variety of mathematical neuron models only when their sampled time series for one capacitive variable can present similar spiking, bursting behaviors by adjusting one or more bifurcation parameters, and the external excitations including noisy disturbance. In fact, it is worthy of clarifying the biophysical property and reliability of these suggested neuron models even all the mathematical neurons can be implemented in suitable analog circuits via circuit platform or digital signal processing devices. On the other hand, some researchers prefer to build a variety of nonlinear circuits by incorporating capacitor, inductor, memristor [31–35], Josephson junction [36–38], thermistor [39–41], piezoelectric ceramic [42–44] and phototube [45–47] into the branch circuit, and these nonlinear circuits are tamed to present similar firing patterns as observed in the biological neuron, and the reliability of these models can be confirmed in the recent review [22].

A single capacitive variable is helpful to measure the electrical activities in cell membrane and the material property will be left out even more linear term and nonlinear terms are introduced to estimate the regulation and interaction from ion channel currents. During equivalent circuit approach, one capacitor in parallel with other branch circuits composed of the elements such as induction coil, constant voltage source, resistor and other nonlinear elements. As a result, sampled time series for the output voltage from the capacitor will be detected to keep pace with the experimental data from biological neurons. Indeed, considering the material property and layer size, two sides of the cell membrane have different distribution of electromagnetic field and the membrane potential. Therefore, it is important to involve the membrane property on the energy regulation and mode transition in neurons by introducing two capacitive variables in the neuron model [48–51], one for the outer membrane and another variable for the inner membrane of the biological neurons. During circuit approach for double capacitive variables in a neural circuit, two capacitors connected via a functional component are effective to mimic the physical property of the double-layer cell membrane [52, 53]. Clear definition of energy function for neurons is crucial to explore and discover the

potential mechanism for adaptive growth of intrinsic parameters and mode transition in neural activities of functional neurons [54–56].

From neural signal driving to muscle response accompanying with suitable body gait, energy is propagated and converted from electrical energy to mechanical energy. In practical way, load circuit adhered to the beam or jointed compound pendulum can be excited by Ampere force when the electromechanical arm or legs [57–60] are exposed to external magnetic field. In the recent works [61–64], neural circuit and its coupled array are activated to control the movements of artificial arms and legs. For a brief guidance, please see our recent review and comments [65]. When human arms or legs are disabled, it is worthy of designing reliable electromechanical device to provide possible aids for keeping normal body gaits. Neural signals control the muscles, and relaxation and contraction of muscles are crucial to regulate the skeletal movement including horizontal moving and rotation via the joint. Complex body gaits require the cooperation of two arms (or two legs), which are also connected and coupled via body tissue and skeletons. For simplicity, we just discussed the simple horizontal movement of a single arm and synchronous movements of two coupled arms by applying neural signals on the load circuit of the electromechanical arm(s). In this work, we proposed a simple neural circuit to drive a couple of electromechanical arms, and the cooperation between two arms/legs can be simulated and explored in dynamical aspect. Noisy disturbance is applied to detect stochastic resonance of the neural circuit-coupled electromechanical device and synchronization stability between two coupled arms. Electric signals from the neural circuit is used to couple the load circuit of the electromechanical arm by generating Ampere's force, and the moving beam behaves similar gait as arm(s) following horizontal reciprocating motion.

2 Model and scheme

Considering the energy characteristic in biological neurons, capacitive variable derived from a capacitor and inductive variable accounting for channel current across an inductor are used to build neuron models composed of high order nonlinear terms. The capacitive variable bridges connection to membrane

potential of a neuron and it is approach by the output voltage of capacitor in the branch circuit, inductive variable links to the current due to ions propagation in the cell. Involvement of nonlinear term results from the estimation of complex energy exchange and interaction between magnetic field and electric field of the neuron during ions diffusion and exchange. Therefore, a simple neural circuit presented in Fig. 1 is used to explore the neural activities and energy level in a neuron under external stimulus.

A cubic term for the voltage variable of capacitor is defined to simulate the channel current across the nonlinear resistor NM, and standard circuit equations can be obtained to discern the relation between physical variables (V_C , i_L) following the Kirchhoff theorem. The voltage dependence on the current in Fig. 1 are restricted by

$$\begin{cases} i_{NM} = -\frac{1}{\rho} \left(V_C - \frac{1}{3} \frac{V_C^3}{V_0^2} \right) \\ C \frac{dV_C}{dt} = i_S - i_L - i_{NM} \\ L \frac{di_L}{dt} = V_C. \end{cases} \quad (1)$$

The intrinsic parameters (V_0 , ρ) relative to the NR can be detected in experiment way by measuring the i - v curve. The physical variables are replaced with dimensionless variables under the scale transformation,

$$u = \frac{V_C}{V_0}, v = \frac{i_L \rho}{V_0}, \tau = \frac{t}{\rho C}, i'_S = \frac{\rho i_S}{V_0}, \lambda_1 = \frac{\rho^2 C}{L}. \quad (2)$$

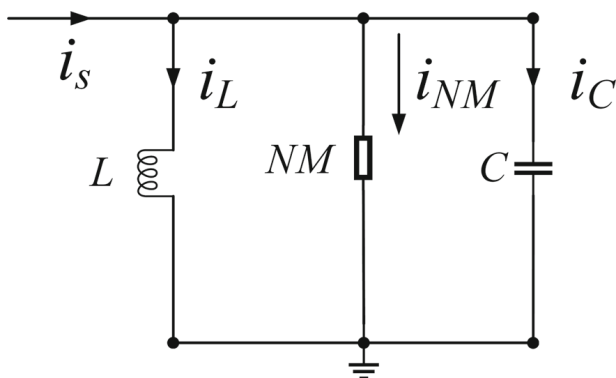


Fig. 1 Neural circuit driven by forcing current i_S . Inductor L , nonlinear element NM and capacitor C correlate the variables i_L , i_{NM} , i_C , respectively. NM can be selected as nonlinear resistor, memristor, Josephson junction or other functional electric components

Inserting the new variables (u , v) and parameters in Eq. (2) into Eq. (1), an equivalent neuron model is obtained by

$$\begin{cases} \frac{du}{d\tau} = i'_S - v + u - \frac{1}{3} u^3; \\ \frac{dv}{d\tau} = \lambda_1 u. \end{cases} \quad (3)$$

In generic way, the external stimulus i'_S can be imposed with different values for changing the excitability of the neuron, and then distinct mode transition from periodic to chaotic patterns can be induced accompanying with emergence of spiking and bursting states. Noisy disturbance on the membrane potential u will induce coherence, stochastic resonance, and chaotic resonance by taming the noise intensity and external forcing current carefully.

2.1 Single electromechanical arm (leg) driven by neural circuit

The neural circuit presented in Fig. 1 is used to couple the load circuit adhered to the electromechanical arm (EMA). According to Fig. 2, the output voltage from the capacitor excites the load circuit and the Ampere force drives the motion of the beam, and the movement is also controlled by the spring and damping force in this device. The clarification of working principle of Fig. 2 can refer to our recent review [65].

When the external magnetic field is fixed, any switch of the channel current i_{EM} across the load circuit will change the Ampere's force, and then the EMA will modify its moving states including the velocity and direction. The coils adhere to the U shaped rod/beam has N rounds, and the moving beam measures its quality m_0 . The displacement x and moving velocity y for the driven beam are controlled by

$$\begin{cases} \frac{dx}{dt} = y; \\ \frac{dy}{dt} = \frac{2N}{m_0} B l_0 i_{EM} - \frac{\eta}{m_0} y - \frac{K}{m_0} x. \end{cases} \quad (4)$$

Where the parameter η represents damping gain, K is the elastic coefficient for the spring, l_0 is the coil size (width for the U bracket). The dynamics in the EMA and moving beam is described by

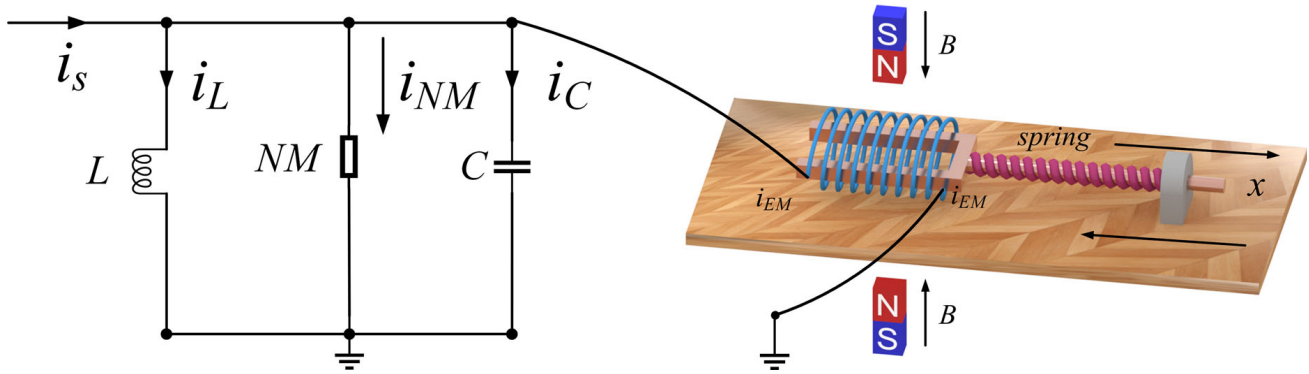


Fig. 2 Schematic diagram for neural circuit interacted with the electromechanical arm (EMA). B locates the external magnetic field, and the variable x denotes displacement of the moving

beam. The driving current i_{EM} derived from the left neural circuit generates Ampere's force in the load circuit of the EMA

$$\begin{cases} C \frac{dV_C}{dt} = i_s - i_L - i_{NM} - i_{EM}; \\ L \frac{di_L}{dt} = V_C; \\ L_{EM} \frac{di_{EM}}{dt} = V_C - 2NB l_0 y; \\ \frac{dx}{dt} = y; \\ \frac{dy}{dt} = \frac{2N}{m_0} B l_0 i_{EM} - \frac{\eta}{m_0} y - \frac{K}{m_0} x. \end{cases} \quad (5)$$

These physical variables are replaced with dimensionless variables under scale transformation as follows

$$\begin{aligned} u &= \frac{V_C}{V_0}, v = \frac{i_L \rho}{V_0}, \tau = \frac{t}{\rho C}, i'_{EM} \\ &= \frac{\rho i_{EM}}{V_0}, i'_s = \frac{\rho i_s}{V_0}, \lambda_1 = \frac{\rho^2 C}{L}, \lambda_2 = \frac{\rho^2 C}{L_{EM}}; \\ \lambda_3 &= \frac{2NB l_0^2 \rho}{L_{EM} V_0}, \hat{x} = \frac{x}{l_0}, \hat{y} = \frac{\rho C}{l_0} y, \\ a &= \frac{2\rho C^2 NB V_0}{m_0}, b = \frac{\rho C \eta}{m_0}, k_1 = \frac{\rho^2 C^2 K}{m_0}. \end{aligned} \quad (6)$$

Inserting the defined variables and parameters in Eq. (6) into Eq. (5), the dynamics is calculated by

$$\begin{cases} \frac{du}{d\tau} = i'_s - v + u - \frac{1}{3}u^3 - i'_{EM}; \\ \frac{dv}{d\tau} = \lambda_1 u; \\ \frac{di'_{EM}}{d\tau} = \lambda_2 u - \lambda_3 \hat{y}; \\ \frac{d\hat{x}}{d\tau} = \hat{y}; \\ \frac{d\hat{y}}{d\tau} = a i'_{EM} - b \hat{y} - k_1 \hat{x}. \end{cases} \quad (7)$$

From dynamical viewpoint, external stimulus i'_s , which can be derived from physical signals including acoustic wave, illumination and even electromagnetic excitation, controls the excitability of the neuron. The firing modes are controlled by the external excitation and feedback regulation from the load circuit in the EMA. Within physical level, external stimulus injects energy into the neural circuit, and a part of energy is converted into mechanical energy for supporting continuous movement of the beam (artificial arm). The field energy W_1 in the left circuit and the mechanical energy W_2 for the moving beam are defined by

$$\begin{cases} W_1 = \frac{1}{2} C V_C^2 + \frac{1}{2} L i_L^2 + \frac{1}{2} L_{EM} i_{EM}^2; \\ W_2 = \frac{1}{2} K x^2 + \frac{1}{2} m_0 y^2; \end{cases} \quad (8)$$

The total energy value for the coupled neural circuit and EMA gives $W = W_1 + W_2$. By applying scale transformation on the physical energy in Eq. (8), the dimensionless parameters and Hamilton energy are given in for obtaining dimensionless energy in the neuron H_1 , load circuit H_2 and total energy H .

$$\begin{cases} \mu_1 = \frac{\rho^2 C}{L}, \mu_2 = \frac{\rho^2 C}{L_{EM}}, \mu_3 = \frac{K l_0^2}{C V_0^2}, \mu_4 = \frac{m_0 l_0^2}{\rho^2 C^3 V_0^2}; \\ H = H_1 + H_2; \\ H_1 = \frac{W_1}{C V_0^2} = \frac{1}{2} u^2 + \frac{1}{2} \frac{v^2}{\mu_1} + \frac{1}{2} \frac{i_{EM}^2}{\mu_2}; \\ H_2 = \frac{W_2}{C V_0^2} = \frac{1}{2} \mu_3 \hat{x}^2 + \frac{1}{2} \mu_4 \hat{y}^2. \end{cases} \quad (9)$$

The neural circuit can receive and perceive external noisy excitation due to uncertain fluctuation of electric field. In presence of stochastic force on the moving beam, its displacement will be controlled by noisy disturbance. Therefore, two kinds of noisy disturbances are applied to affect the dynamical response in this activated EMA as follows

$$\begin{cases} \frac{du}{d\tau} = i'_S - v + u - \frac{1}{3}u^3 - i'_{EM} + \xi_1(\tau); \\ \frac{dv}{d\tau} = \lambda_1 u; \\ \frac{di'_{EM}}{d\tau} = \lambda_2 u - \lambda_3 \hat{y}; \\ \frac{d\hat{x}}{d\tau} = \hat{y} + \xi_2(\tau); \\ \frac{d\hat{y}}{d\tau} = ai'_{EM} - b\hat{y} - k_1 \hat{x}. \end{cases} \quad (10)$$

For simplicity, two kinds of noisy excitations including $\xi_1(\tau)$ and $\xi_2(\tau)$ are considered as Gaussian white noise, and the statistical characteristic with zero average value for the noise at intensity D is measured by

$$\langle \xi(\tau) \rangle = 0, \langle \xi(\tau)\xi(s) \rangle = 2D\delta(\tau - s); \quad (11)$$

By changing the noise intensity carefully, stochastic can be induced by measuring the signal-to-noise ratio (SNR) or the average energy function $\langle H \rangle$ or $\langle H_1 \rangle$ within a transient period. The symbol $\langle * \rangle$ indicates an average calculation of variables or function within the running time during numerical approach. SNR is approached by detecting the peak value in the power spectrum by applying Fast Fourier Transform (FFT) on the variable series, and it defines as follows [66]

$$SNR = 10 \log 10 \frac{S}{B} = P_{peak} \frac{f_{peak}}{\Delta f} \quad (12)$$

where P_{peak} is the maximal value in the power spectrum at certain noise intensity, f_{peak} and Δf describe the corresponding frequency for and half peak width for this peak value P_{peak} , respectively. In presence of stochastic resonance [67–70], the driven system captures enough energy and then SNR and $\langle H \rangle$ will keep highest value to support high regulation, for example, the neural activities show periodic oscillation. In the following numerical approach, the sampled time series for variable u will be used to

calculate the distribution of SNR when noisy disturbance is imposed on the neural circuit by regulating the membrane potential/voltage. On the other hand, the sampled time series \hat{x} are used to estimate the SNR when different noisy excitation is applied to control the displacement directly.

2.2 Double electromechanical arms and legs driven by neural circuit

A bird has a pair of wings and a health human has a pair of arms and legs, therefore, perfect cooperation between the arms, wings and legs are crucial to keep safe body gaits. As presented in Fig. 2, a couple of EMAs are driven by the same electrical signals from the neural circuit.

When the left neural circuit in Fig. 3 is activated by applying external forcing current i_s , the output current i_{EM} is regulated accompanying with different firing patterns in the neural circuit. The same parameter setting in the load circuits generate identical Ampere's force on the EMAs and then they prefer to keep synchronous movement under bidirectional coupling via the connection spring. The correlation between the physical variables of Fig. 3 is expressed by

$$\begin{cases} C \frac{dV_C}{dt} = i_s - i_L - i_{NM} - i_{EM}; \\ L \frac{di_L}{dt} = V_C; \\ L_{EM} \frac{di_{EM}}{dt} = V_C - 2NBl_0(y_1 + y_2); \\ \frac{dx_1}{dt} = y_1; \\ \frac{dy_1}{dt} = \frac{2N}{m_0}Bl_0i_{EM} - \frac{\eta}{m_0}y_1 - \frac{K}{m_0}x_1 - \frac{k}{m_0}(x_1 - x_2); \\ \frac{dx_2}{dt} = y_2; \\ \frac{dy_2}{dt} = \frac{2N}{m_0}Bl_0i_{EM} - \frac{\eta}{m_0}y_2 - \frac{K}{m_0}x_2 - \frac{k}{m_0}(x_2 - x_1). \end{cases} \quad (13)$$

where (x_1, x_2) and (y_1, y_2) denote the displacements and velocities for two moving arms/ beams. Complete scale transformation is applied on the variables and parameters in Eq. (13) and a new group of dimensionless variables and parameters are updated by

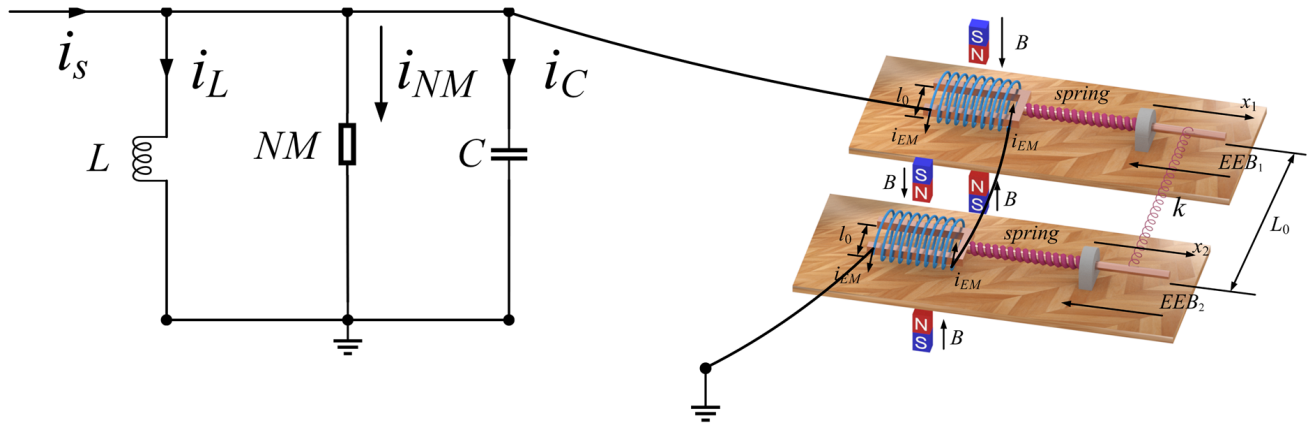


Fig. 3 Schematic diagram for neural circuit coupled with double electromechanical arms. Two moving beams (arms) are coupled via a spring with the spring coefficient k . The load circuits of the two EMAs are driven by the same channel current

and they are exposed to the same magnetic field. Spring connection between two EMAs is similar to the connection between two arms by using muscle and skeleton, so that they can keep synchronous cooperation

$$\begin{aligned}
 u &= \frac{V_C}{V_0}, v = \frac{i_L \rho}{V_0}, \tau = \frac{t}{\rho C}, \\
 i'_{EM} &= \frac{\rho i_{EM}}{V_0}, i'_S = \frac{\rho i_S}{V_0}, \lambda_1 = \frac{\rho^2 C}{L}, \lambda_2 = \frac{\rho^2 C}{L_{EM}}, \\
 \lambda_3 &= \frac{2NB l_0^2 \rho}{L_{EM} V_0}, \\
 \hat{x}_1 &= \frac{x_1}{l_0}, \hat{x}_2 = \frac{x_2}{l_0}, \hat{y}_1 = \frac{\rho C}{l_0} y_1, \\
 \hat{y}_2 &= \frac{\rho C}{l_0} y_2, a = \frac{2\rho C^2 NB V_0}{m_0}, b = \frac{\rho C \eta}{m_0}, \\
 k_1 &= \frac{\rho^2 C^2 K}{m_0}, k' = \frac{\rho^2 C^2 k}{m_0}.
 \end{aligned} \quad (14)$$

Similar to Eq. (6) for single EMA, the dynamics in the two coupled EMAs are approached by inserting the definitions in Eq. (14) into Eq. (13). When two EMA are endowed with the same spring, their spring coefficients keep the identical value k and the dynamics is calculated in Eq. (15a). Considering the diversity and difference between two EMAs, setting different spring coefficients for the two moving beams, for example, the spring coefficient for each EMA is marked as k_1 and k_2 , the cooperation between two moving arms can be explored in the dynamical model in Eq. (15b).

$$\begin{cases}
 \frac{du}{d\tau} = i'_S - v + u - \frac{1}{3}u^3 - i'_{EM}; \\
 \frac{dv}{d\tau} = \lambda_1 u; \\
 \frac{di'_{EM}}{d\tau} = \lambda_2 u - \lambda_3(\hat{y}_1 + \hat{y}_2); \\
 \frac{d\hat{x}_1}{d\tau} = \hat{y}_1; \\
 \frac{d\hat{y}_1}{d\tau} = ai'_{EM} - b\hat{y}_1 - k_1\hat{x}_1 - k'(\hat{x}_1 - \hat{x}_2); \\
 \frac{d\hat{x}_2}{d\tau} = \hat{y}_2; \\
 \frac{d\hat{y}_2}{d\tau} = ai'_{EM} - b\hat{y}_2 - k_1\hat{x}_2 - k'(\hat{x}_2 - \hat{x}_1).
 \end{cases} \quad (15a)$$

$$\begin{cases}
 \frac{du}{d\tau} = i'_S - v + u - \frac{1}{3}u^3 - i'_{EM}; \\
 \frac{dv}{d\tau} = \lambda_1 u; \\
 \frac{di'_{EM}}{d\tau} = \lambda_2 u - \lambda_3(\hat{y}_1 + \hat{y}_2); \\
 \frac{d\hat{x}_1}{d\tau} = \hat{y}_1; \\
 \frac{d\hat{y}_1}{d\tau} = ai'_{EM} - b\hat{y}_1 - k_1\hat{x}_1 - k'(\hat{x}_1 - \hat{x}_2); \\
 \frac{d\hat{x}_2}{d\tau} = \hat{y}_2; \\
 \frac{d\hat{y}_2}{d\tau} = ai'_{EM} - b\hat{y}_2 - k_2\hat{x}_2 - k'(\hat{x}_2 - \hat{x}_1).
 \end{cases} \quad (15b)$$

For two coupled EMAs, the field energy is given in similar form presented in Eq. (16),

$$\begin{cases} W_1 = \frac{1}{2}CV_C^2 + \frac{1}{2}Li_L^2 + \frac{1}{2}L_{EM}i_{EM}^2 + \frac{1}{2}L_{EM}i_{EM}^2; \\ W_2 = \frac{1}{2}K_1\hat{x}_1^2 + \frac{1}{2}K_2\hat{x}_2^2 + \frac{1}{2}m_0(\hat{y}_1^2 + \hat{y}_2^2). \end{cases} \quad (16)$$

For two identical EMAs, $K_1 = K_2 = K$, the energy function ($W = W_1 + W_2$) in Eq. (16) is simplified and the two EMAs can be driven to present synchronous movement. Furthermore, dimensionless energy for two coupled EMAs are updated as follows

$$\begin{cases} \mu_1 = \frac{\rho^2 C}{L}, \mu_2 = \frac{\rho^2 C}{L_{EM}}, \mu_3 = \frac{K_1 l_0^2}{CV_0^2}, \mu'_3 = \frac{K_2 l_0^2}{CV_0^2}, \mu_4 = \frac{m_0 l_0^2}{\rho^2 C^3 V_0^2}, \mu_5 = \frac{kl_0^2}{CV_0^2}; \\ H_1 = \frac{W_1}{CV_0^2} = \frac{1}{2}u^2 + \frac{1}{2}\mu_1 v^2 + \frac{i_{EM}^2}{\mu_2}; \\ H_2 = \frac{W_2}{CV_0^2} = \frac{1}{2}\mu_3 \hat{x}_1^2 + \frac{1}{2}\mu'_3 \hat{x}_2^2 + \frac{1}{2}\mu_4 (\hat{y}_1^2 + \hat{y}_2^2). \end{cases} \quad (17)$$

When the two EMAs select the same spring coefficient as $K_1 = K_2 = K$, the dimensionless parameter $\mu_3 = \mu'_3$ and energy function $H = H_1 + H_2$ in Eq. (17) is simplified because the gain for the spring energy is the same. Applying noisy forcing on the moving beam and membrane, the dynamics is calculated by

$$\begin{cases} \frac{du}{d\tau} = i'_S - v + u - \frac{1}{3}u^3 - i'_{EM} + \xi_1(\tau); \\ \frac{dv}{d\tau} = \lambda_1 u; \\ \frac{di'_{EM}}{d\tau} = \lambda_2 u - \lambda_3(\hat{y}_1 + \hat{y}_2); \\ \frac{d\hat{x}_1}{d\tau} = \hat{y}_1 + \xi_2(\tau); \\ \frac{d\hat{y}_1}{d\tau} = ai'_{EM} - b\hat{y}_1 - k_1\hat{x}_1 - k'(\hat{x}_1 - \hat{x}_2); \\ \frac{d\hat{x}_2}{d\tau} = \hat{y}_2 + \xi_2(\tau); \\ \frac{d\hat{y}_2}{d\tau} = ai'_{EM} - b\hat{y}_2 - k_2\hat{x}_2 - k'(\hat{x}_2 - \hat{x}_1). \end{cases} \quad (18)$$

The same stochastic forcing is applied to affect the movement of the two coupled beams. In presence of parameter mismatch, the two coupled EMAs are blocked by different damping forces even they are forced by the same Ampere force, and then phase lock is induced between two moving EMAs. From dynamical aspect, the external current can be adjusted to control the neural circuit showing different firing patterns, and the channel current across the EMAs will select different values for inducing suitable Ampere force. Interaction between the Ampere force, damping

force and bidirectional coupling via spring connection will control the synchronous movements of the coupled EMAs completely.

3 Numerical results and discussion

The fourth order Runge-Kutta algorithm can be applied to find numerical solutions for the variable series from the oscillator-like dynamical models in Eqs. (7), (9) and (18). In presence of stochastic disturbance, Euler forward algorithm is effective to describe the statistical analysis from the sampled time series for the variables. In Fig. 4, the time series for membrane potential are calculated for common bifurcation analysis and the mode dependence on the external stimulus $A\cos(\omega\tau)$, which is imposed on the membrane variable in Eq. (5).

From Fig. 4, the two-variable neuron can be controlled to present different firing modes, and the appearance of positive Lyapunov exponent indicates that this neuron can be excited to generate chaos in the electrical activities. For better illustration, the formation of attractors and membrane series are plotted in Fig. 5.

That is, changes of the angular frequency of external forcing can develop different attractors and the firing patterns are controlled completely. When the neural circuit is activated to excite the load circuit in the electromechanical arm (EMA) presented in Eq. (7), the beam is forced to change its displacement in Fig. 6.

From Fig. 6, the EMA shows its displacement between positive and negative values, it means that the beam move forward and backward in continuous way. Changeable channel current in the load circuit adhered to the moving beam controls the motion of the beam or EMA. It is interesting to clarify the energy characteristic of neural circuit and moving beam defined in Eq. (9), and the results are shown in Fig. 7.

In fact, external stimulus injects energy into the neural circuit, and a part of field energy is shunted to flow across the load circuit and then converted to mechanical energy. On the other hand, the moving beam generates electromotive force via the load circuit and feedback is applied to regulate the driving in the neural circuit accompanying with energy interaction. The driving neural circuit shows periodic firing mode and then the moving beam prefers to show similar

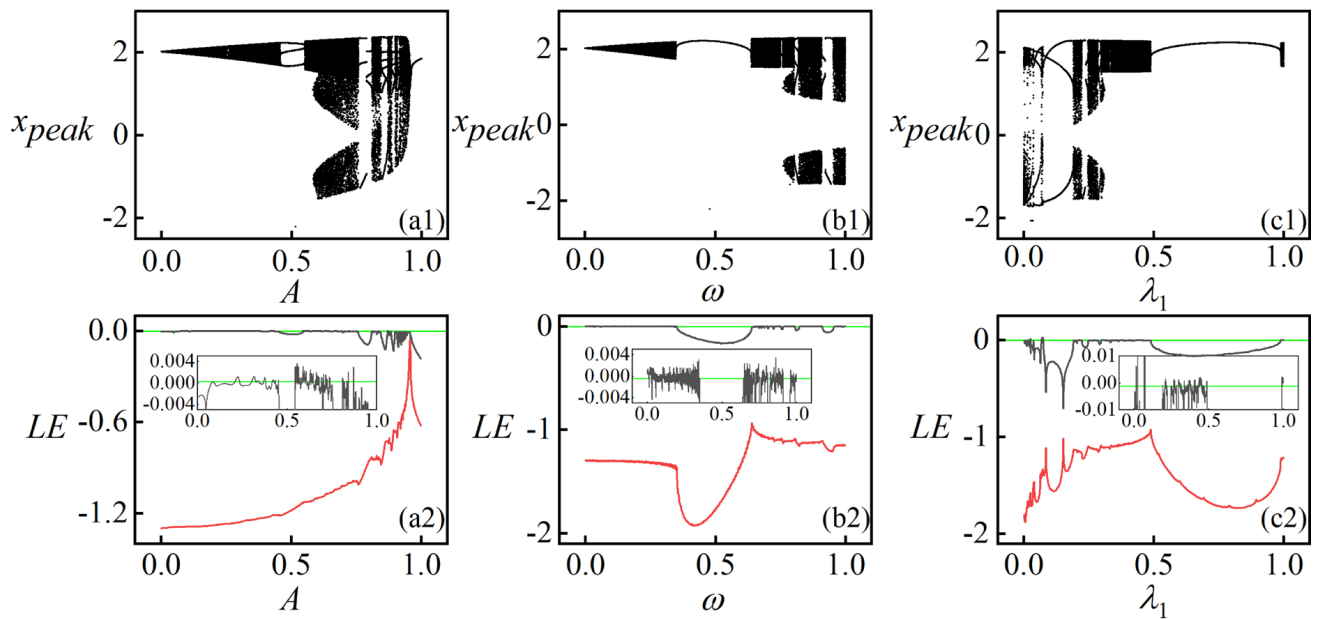
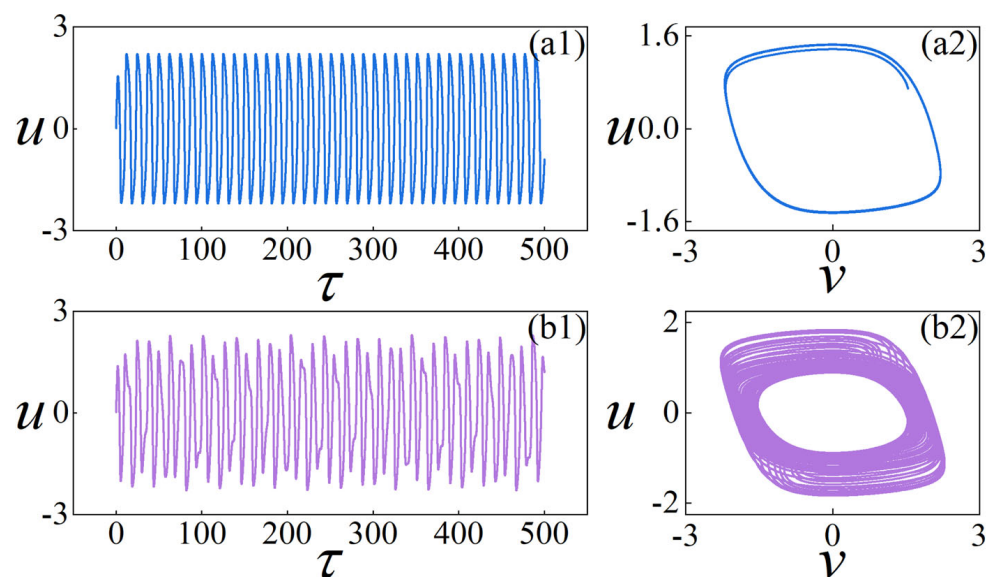


Fig. 4 Distribution of peak values for membrane potential (**a1**, **b1**, **c1**) and Lyapunov exponent (LE) (**a2**, **b2**, **c2**) by applying periodic stimulus on the neural circuit. For (**a1**, **a2**) $\omega = 0.8$,

$\lambda_1 = 0.3$; **b1**, **b2** $A = 0.6$, $\lambda_1 = 0.3$; **c1**, **c2** $A = 0.6$, $\omega = 0.8$. Setting initials (0.02, 0.01)

Fig. 5 Evolution of membrane potential and formation of attractors in the neural circuit under different forcing currents. For **a1**, **a2** spiking $\omega = 0.5$; **b1**, **b2** chaotic firing $\omega = 0.8$. Setting $A = 0.6$ and $\lambda_1 = 0.3$



periodic firing patterns. In Fig. 8, the motion of the EMA is calculated.

The EMA keeps periodic motion even the neuron is activated to present chaotic patterns, the potential mechanism is that the load circuit imposed effective feedback on the driving neural circuit. In Fig. 9, the energy exchange and changes in the EMA and driving circuit are plotted.

The neural activities in the driving neural circuit show chaotic states while the load circuit keeps

periodic firing accompanying with periodic moving in the beam. $H_1 - H_2$ keeps positive value, and it indicates that the neural can release enough energy to excite the EMA. Furthermore, the energy proportion is calculated in Fig. 10 when the driving neural circuit is excited to present in periodic and chaotic modes, respectively.

The mechanical energy term keeps lower proportion in the total energy H . In presence of periodic firing, the neural circuit keeps higher proportion for

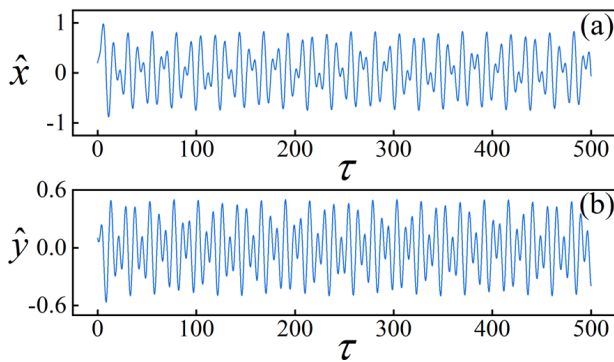


Fig. 6 Changes of displacement and velocity in the moving beam. Setting parameters as $a = 0.2$, $b = 0.3$, $k_1 = 0.1$, $\lambda_1 = 0.3$, $\lambda_2 = 0.4$, $\lambda_3 = 0.3$, $A = 0.6$, $\omega = 0.5$, and the initials $(0.02, 0.01, 0.01, 0.2, 0.1)$.

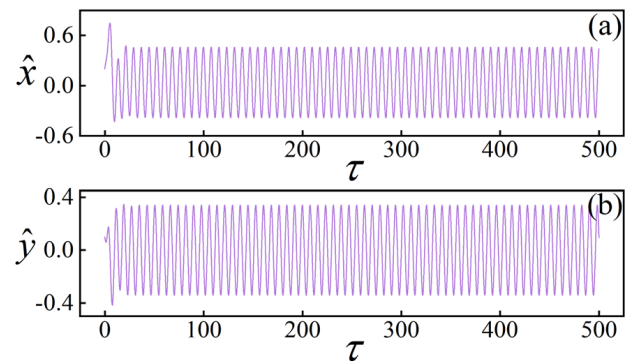


Fig. 8 Changes of displacement of EMA **a** and velocity evolution **b**. Setting parameters $a = 0.2$, $b = 0.3$, $k_1 = 0.1$, $\lambda_1 = 0.3$, $\lambda_2 = 0.4$, $\lambda_3 = 0.3$, $A = 0.6$, $\omega = 0.8$

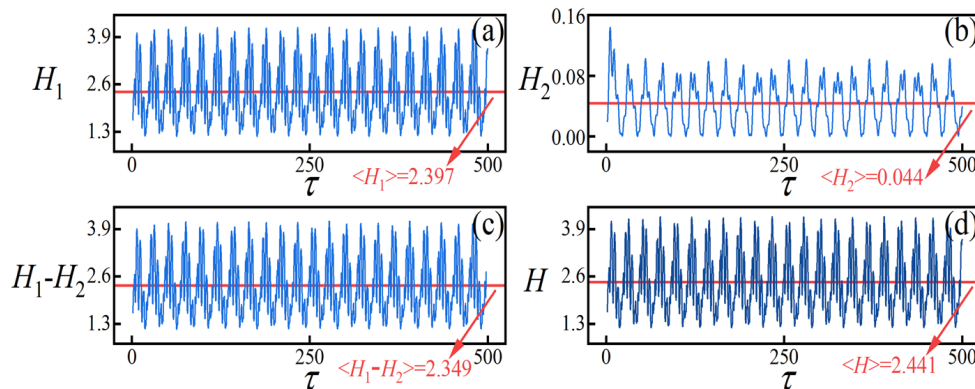


Fig. 7 Energy evolution of the neural circuit and moving beam. Setting parameters $a = 0.2$, $b = 0.3$, $k_1 = 0.1$, $\lambda_1 = 0.3$, $\lambda_2 = 0.4$, $\lambda_3 = 0.3$, $A = 0.6$, $\omega = 0.5$. For **a** energy function

for the driving neuron; **b** energy for load circuit; **c** energy diversity between neural circuit and load circuit; **d** total energy H for neuron and EMA

the capacitive terms and the energy in the load circuit also keeps a higher proportion than the case that the neuron is excited to show chaotic states. It is interesting to discuss the case under noisy excitation. When the moving beam is excited by noisy disturbance, which noisy excitation is imposed to excite the fourth variable in Eq. (10). In presence of noisy disturbance on the membrane potential, the noisy driving is applied to excite the first variable in Eq. (10). Based on the sampled time series for membrane potentials, energy function is calculated and the distribution of SNR values and average energy $\langle H \rangle$ is respectively plotted in Fig. 11. When noisy excitation is applied to affect the membrane potential u , the SNR is calculated by using the sampled time series for variable u when noise intensity is changed carefully. On the other hand, direct stochastic excitation on the moving beam by adding noisy excitation on the displacement will obtain the SNR values by using

the sampled time series for the displacement variable \hat{x} .

From Fig. 11, it is demonstrated that distinct peak is detected in the curve for SNR and average energy under moderate noise intensity. However, it requires different threshold in the noise intensity for inducing stochastic resonance when noise is imposed on different positions in the neural circuit-coupled EMA. Noisy disturbance on the first membrane variable accounts for the stochastic excitation from external electrical field, while noisy excitation on the displacement variable results from external stochastic force on the moving beam.

Above all, we discussed the driving and response in the EMA with single arm and it is worthy of exploring the synchronous motion for double arms in the EMA. As presented in Fig. 3, the load circuits for the two EMA are excited by an identical current. When the two EMAs are endowed with identical parameters,

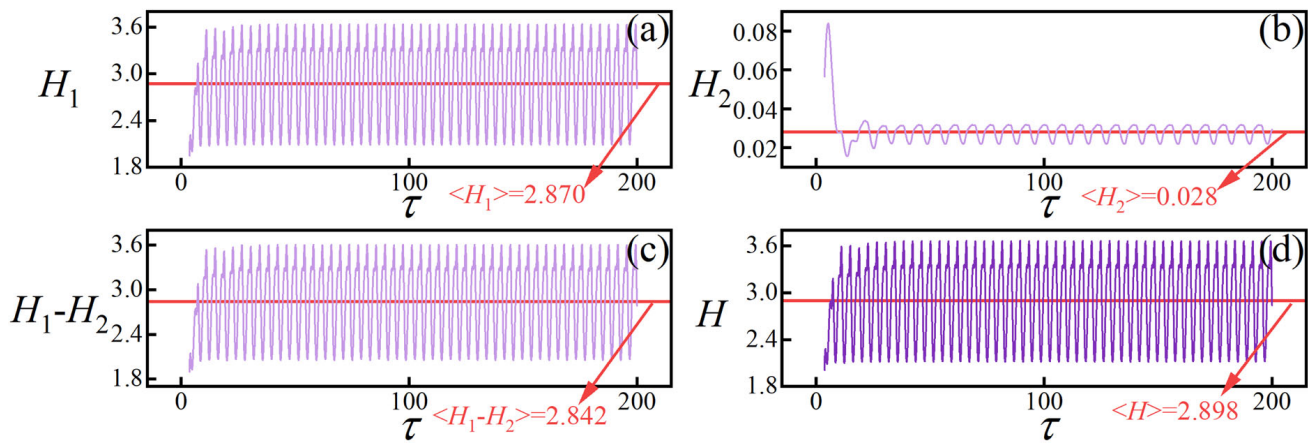


Fig. 9 Energy evolution of the neural circuit and moving beam. Setting parameters $a = 0.2$, $b = 0.3$, $k_1 = 0.1$, $\lambda_1 = 0.3$, $\lambda_2 = 0.4$, $\lambda_3 = 0.3$, $\mu_1 = 0.3$, $\mu_2 = 0.4$, $\mu_3 = 0.3$, $\mu_4 = 0.5$, $A = 0.6$, $\omega = 0.8$. For

a energy function for the driving neuron; **b** mechanical energy; **c** energy diversity between neural circuit and load circuit; **d** total energy H for neuron and EMA

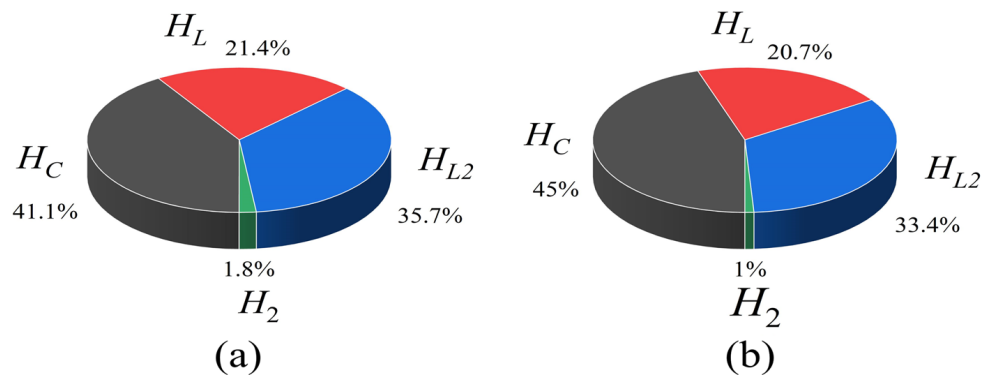
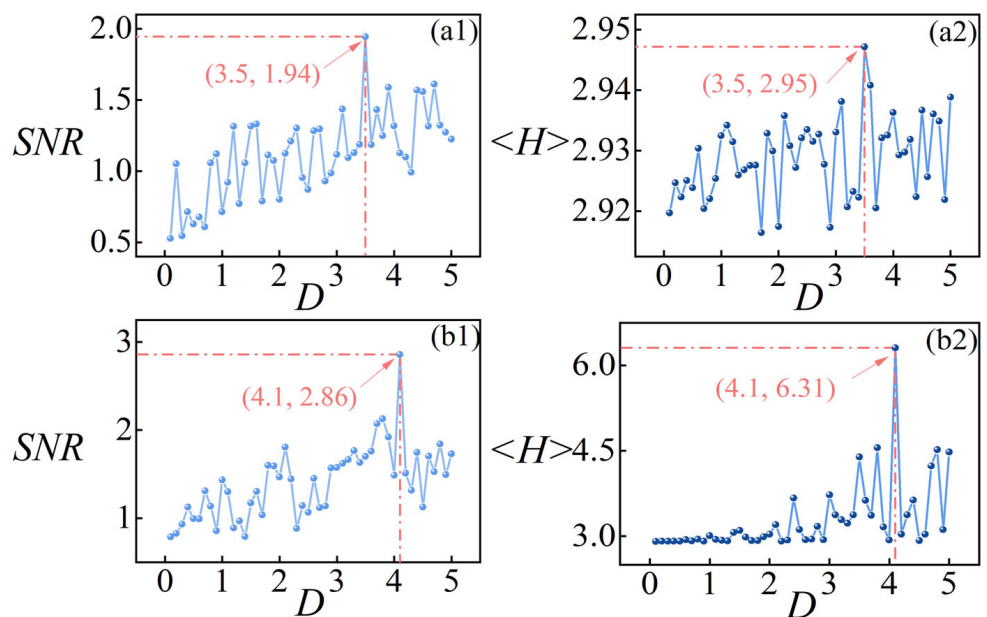


Fig. 10 Energy proportion in the neuron coupled EMA. H_C and H_L for capacitive and inductive terms in the neural circuit, H_{L2} for inductive energy in load circuit, H_2 for the mechanical

energy in the moving beam. Setting parameters $a = 0.2$, $b = 0.3$, $k_1 = 0.1$, $\lambda_1 = 0.3$, $\lambda_2 = 0.4$, $\lambda_3 = 0.3$, $\mu_1 = 0.3$, $\mu_2 = 0.4$, $\mu_3 = 0.3$, $\mu_4 = 0.5$, $A = 0.6$. For **a** $\omega = 0.5$; **b** $\omega = 0.8$

Fig. 11 Dependence of SNR and $\langle H \rangle$ on noise intensity D . For **a1**, **a2**, noise excites the variable u ; **b1**, **b2** noise excites the variable for displacement. Setting parameters $a = 0.2$, $b = 0.3$, $k_1 = 0.1$, $\lambda_1 = 0.3$, $\lambda_2 = 0.4$, $\lambda_3 = 0.3$, $\mu_1 = 0.3$, $\mu_2 = 0.4$, $\mu_3 = 0.3$, $\mu_4 = 0.5$, $A = 0.6$, $\omega = 0.8$



they will behave synchronous motion all the time. However, any parameter diversity in the two EMAs will induce parameter mismatch in the parameters, and complete synchronization becomes difficult for the two coupled EMAs. For simplicity, we consider the case that two EMA has some difference in the spring coefficient, and then dimensionless parameters (k_1, k_2) are selected with different values. Without applying external noise, numerical series can be obtained from Eq. (15b). The difference between displacement and velocity for the two EMAs are plotted in Fig. 12.

When two EMAs are selected with different parameters, complete synchronization is broken. As a result, and the interaction between two EMAs is regulated via the connection spring for possible energy balance. In Fig. 13, the energy evolution in the driving neuron and EMA is respectively calculated, and the energy definition is given in Eq. (17).

The energy functions for the driving neuron (presented in periodic firing mode) and the moving beams/EMAs become time-varying during the interaction between the neural circuit and EMAs. From Fig. 13c, the energy from the driving neuron H_1 is larger than the mechanical energy in the moving beam at $H_1 > H_2$, it indicates that the neural circuit shunted energy to the EMA and then the moving beam is controlled effectively. Furthermore, the error evolution for displacement and velocity diversity is respectively calculated in Fig. 14 when the neural circuit is excited in chaotic mode.

The displacement error between two moving EMAs/beams shows periodical oscillation and they seldom keep synchronous motion even the connection

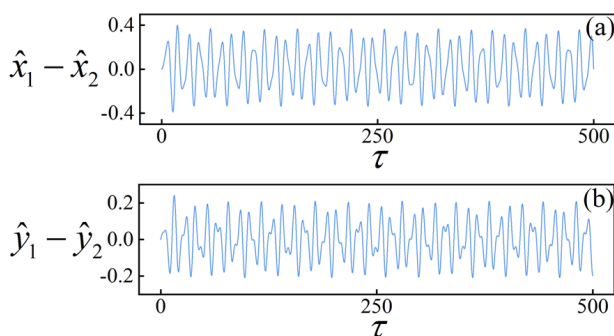


Fig. 12 Evolution of displacement error and velocity error for two coupled EMAs. Setting parameters $a = 0.2$, $b = 0.3$, $k_1 = 0.1$, $k_2 = 0.2$, $k' = 0.1$, $\lambda_1 = 0.3$, $\lambda_2 = 0.4$, $\lambda_3 = 0.3$, $A = 0.6$, $\omega = 0.5$. For **a** displacement error; **b** velocity difference between two coupled EMAs

spring between two beams keeps active regulation. Furthermore, energy changes are estimated in Fig. 15 when chaotic signals from the neuron are used to excite the coupled EMAs.

Compared the results in Fig. 15 with the results in Fig. 13, the driving neuron prefers to keep higher average energy $\langle H_1 \rangle$ and the average energy diversity is increased when the neural circuit is excited in chaos than the case for periodic firing mode in the neural circuit. The average value for mechanical energy $\langle H_2 \rangle$ showed slight decrease than the case presented in Fig. 13b. However, the average of total energy function $\langle H \rangle$ presented slight increase under chaotic excitation, and it is different from the case in Fig. 13. Similarly, the energy proportion is calculated in Fig. 16 when the two coupled EMAs are excited by periodic or chaotic signals from the neural circuit, respectively.

The energy proportion in Fig. 16 is some different from the distribution map in Fig. 10. Desynchronization between the two coupled EMAs applied different feedback regulation on the load coils and it channel current is changed with time. The load circuits adhered to the moving beam keep higher energy proportion than the energy terms in the neural circuit. That is, non-synchronous motions in the two coupled EMAs cost high energy flow and more energy from the driving neural circuit is pumped into the load circuits. Similar stochastic resonance is explored by adding noisy excitation on the neural circuit and the moving beams, defined in Eq. (18), and the results are plotted in Fig. 17.

When two EMAs are coupled, similar stochastic resonance is induced and the average energy can obtain peak values under moderate noise intensity. It requires a different threshold of noise intensity supporting the stochastic resonance presented in Fig. 11. Figure 11 discussed the case for single EMA driven by a neural circuit, and it is found that stochastic resonance can be induced no matter whether noisy excitation is applied to control the neural circuit or the moving beam directly. Fig. 17 explored the case about stochastic resonance in two coupled EMAs with parameter mismatch, and it is confirmed that noisy excitation is effective to induce similar stochastic resonance by taming the intensity of noise intensity. Both Figs. 11 and 17 show that the maximal values for SNR show some diversity when noisy disturbance is applied to excite the membrane potential variable u

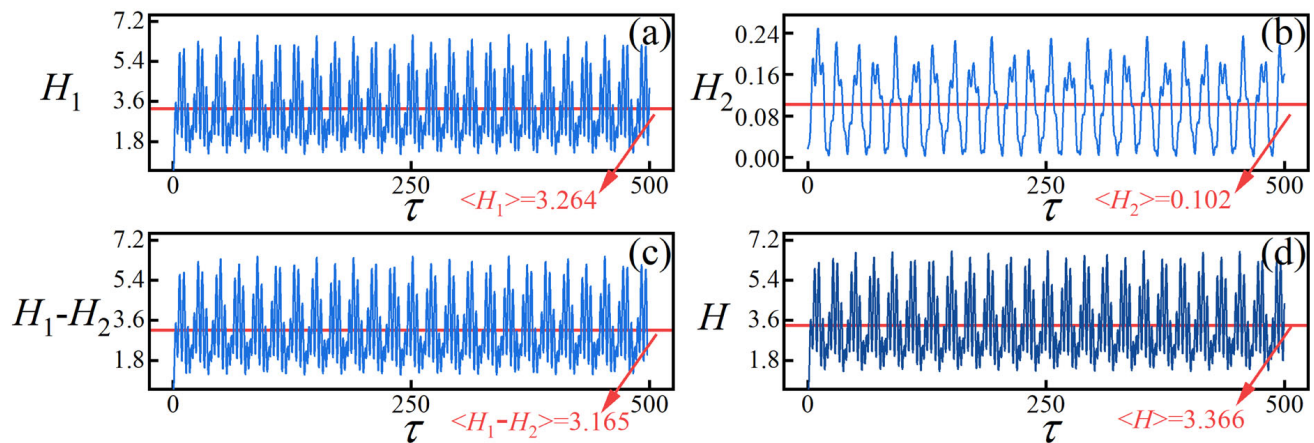


Fig. 13 Energy evolution of the neural circuit and moving beam. Setting parameters $a = 0.2$, $b = 0.3$, $k_1 = 0.1$, $k_2 = 0.2$, $k' = 0.1$, $\lambda_1 = 0.3$, $\lambda_2 = 0.4$, $\lambda_3 = 0.3$, $\mu_1 = 0.3$, $\mu_2 = 0.4$, $\mu_3 = 0.3$, $\mu_4 = 0.5$, $\mu_5 = 0.4$, $A = 0.6$, $\omega = 0.5$. For **a** energy function for the

driving neuron; **b** mechanical energy for two coupled EMAs; **c** energy diversity between neural circuit and load circuit; **d** total energy H for neuron and two coupled EMAs

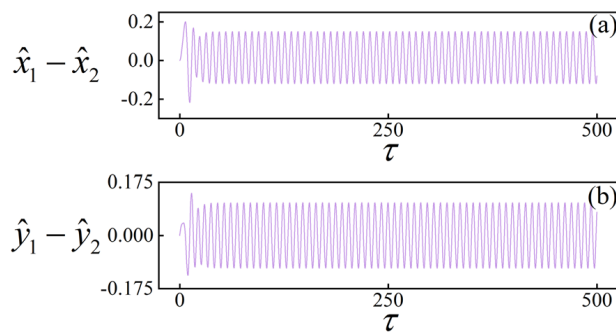


Fig. 14 Evolution of displacement error and velocity error for two coupled EMAs. Setting parameters $a = 0.2$, $b = 0.3$, $k_1 = 0.1$, $k_2 = 0.2$, $k' = 0.1$, $\lambda_1 = 0.3$, $\lambda_2 = 0.4$, $\lambda_3 = 0.3$, $A = 0.6$, $\omega = 0.8$. For **a** displacement error; **b** velocity difference between two coupled EMAs

and the displacement variable \hat{x} , respectively. From physical viewpoint, any noisy disturbance can inject some energy into the mechanical or physical systems. Noisy excitation on the displacement variable means that direct energy injection into the moving beam and mechanical energy is regulated under the external Ampere's force and damping force, as a result, regular moving state can be induced. Noisy disturbance on the membrane potential variable u just modified the firing modes in the neural activities, and a part of energy flow is shunted to the EMA for keep regular moving states. SNR has similar roles as average power and $\langle H \rangle$, direct energy injection is more effective to keep

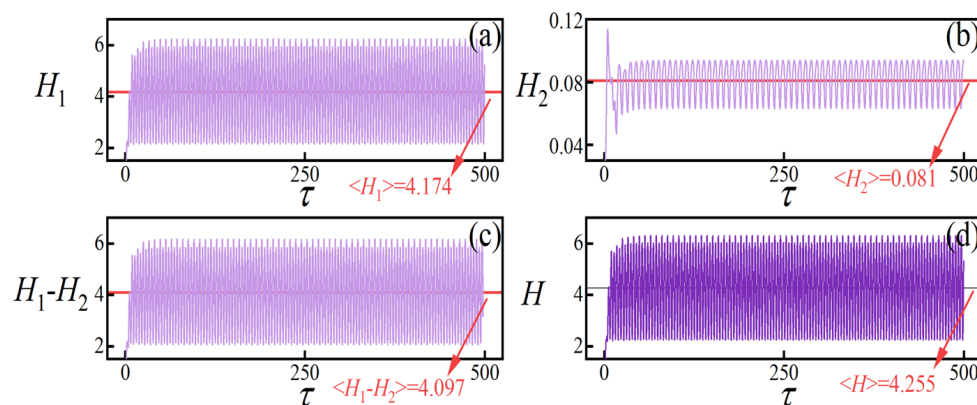


Fig. 15 Energy evolution of the neural circuit and moving beams. Setting parameters $a = 0.2$, $b = 0.3$, $k_1 = 0.1$, $k_2 = 0.2$, $k' = 0.1$, $\lambda_1 = 0.3$, $\lambda_2 = 0.4$, $\lambda_3 = 0.3$, $\mu_1 = 0.3$, $\mu_2 = 0.4$, $\mu_3 = 0.3$, $\mu_4 = 0.5$, $\mu_5 = 0.4$, $A = 0.6$, $\omega = 0.8$. For **a** energy function for the

driving neuron; **b** mechanical energy for two coupled EMAs; **c** energy diversity between neural circuit and load circuit; **d** total energy H for neuron and two coupled EMAs

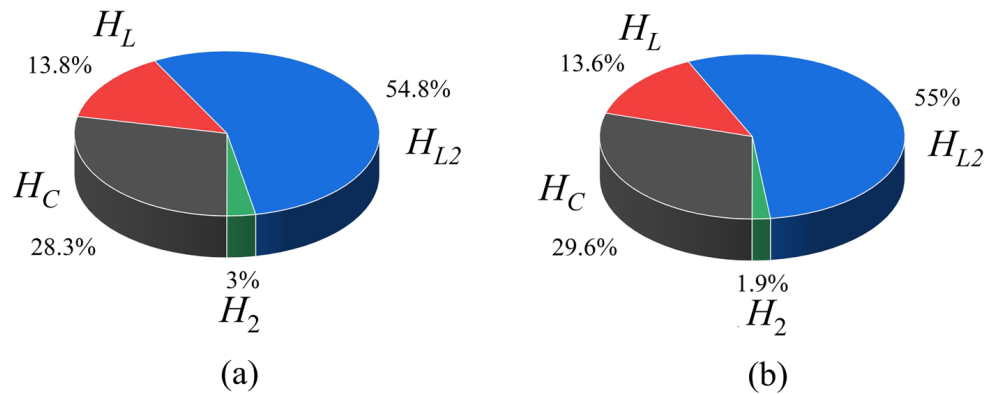
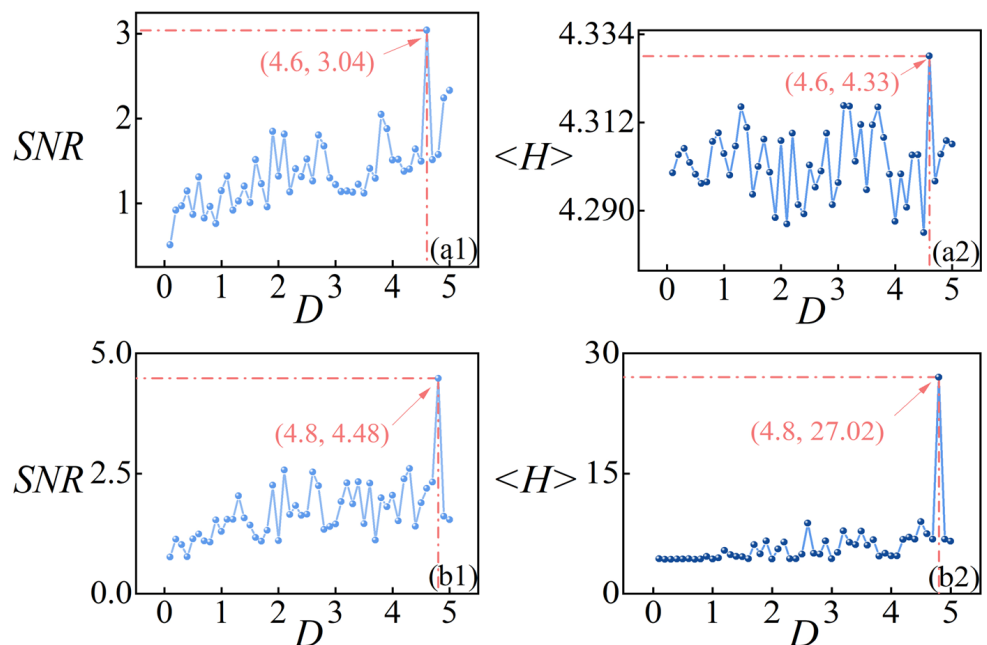


Fig. 16 Energy proportion in the neuron coupled EMAs. H_C and H_L for capacitive and inductive terms in the neural circuit, H_{L2} for inductive energy in load circuit, H_2 for the total energy in

the two moving beams. Setting parameters $a = 0.2$, $b = 0.3$, $k_1 = 0.1$, $k_2 = 0.2$, $k' = 0.1$, $\lambda_1 = 0.3$, $\lambda_2 = 0.4$, $\lambda_3 = 0.3$, $\mu_1 = 0.3$, $\mu_2 = 0.4$, $\mu_3 = 0.3$, $\mu_4 = 0.5$, $A = 0.6$. For **a** $\omega = 0.5$; **b** $\omega = 0.8$

Fig. 17 Dependence of SNR and $\langle H \rangle$ on noise intensity D . For **a1, a2**, noise excites the variable u ; **b1, b2** noise excites the displacement variables (fourth and sixth variable in Eq. (18)). Setting parameters $a = 0.2$, $b = 0.3$, $k_1 = 0.1$, $k_2 = 0.2$, $k' = 0.1$, $\lambda_1 = 0.3$, $\lambda_2 = 0.4$, $\lambda_3 = 0.3$, $\mu_1 = 0.3$, $\mu_2 = 0.4$, $\mu_3 = 0.3$, $\mu_4 = 0.5$, $A = 0.6$, $\omega = 0.8$



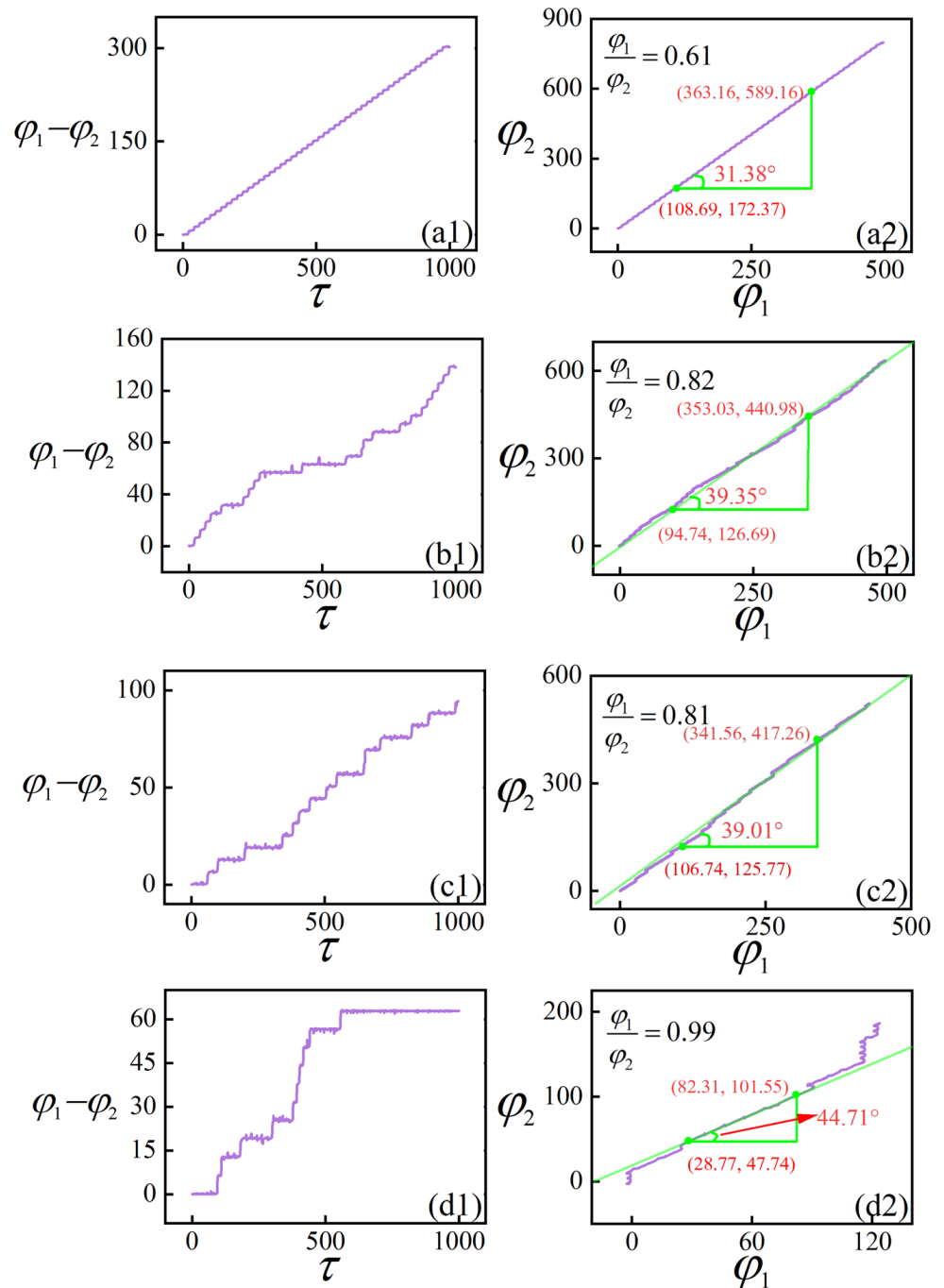
regular states under noisy excitation. Surely, we can use the time series for the same variable to calculate the distribution of SNR no matter whether noisy disturbance is applied to affect the displacement variable or the membrane potential variable directly, and appearance of stochastic resonance, coherence resonance can be predicted and detected effectively.

For realistic systems, two arms/legs often have parameter difference because of material property diversity in the muscles. For example, the left arm and right arm can lift different heavy objects and they also can behave different body gaits. However, they can be guided to present synchronous movement under the electric signals from nervous system by control the

muscles [71–74]. For clear illumination, the phase error is calculated in Fig. 18 by taming the noise intensity carefully.

By taming the noise intensity, the two coupled EMAs can show phase lock and phase synchronization due to continuous excitation from noise and chaotic signals from the neural circuit. Linear fitting for the phase portrait in Fig. 18(a2, b2, c2, d2), phase lock $\varphi_1:\varphi_2$ can be estimated at different levels (0.61, 0.82, 0.81, 0.99) and it is confirmed that involvement of noisy excitation can change the phase lock between two coupled EMAs. Indeed, similar cases can be explored when two EMS are driven by two different neural circuits, which can be connected with a resistor

Fig. 18 Evolution of phase errors between two moving beams/coupled EMAs. For **a1, a2** $D = 0$; **b1, b2** $D = 2.5$; **c1, c2** $D = 4.8$; **d1, d2** $D = 5.0$. Setting parameters $a = 0.2$, $b = 0.3$, $k_1 = 0.1$, $k_2 = 0.2$, $k' = 0.1$, $\lambda_1 = 0.3$, $\lambda_2 = 0.4$, $\lambda_3 = 0.3$, $\mu_1 = 0.3$, $\mu_2 = 0.4$, $\mu_3 = 0.3$, $\mu_4 = 0.5$, $A = 0.6$, $\omega = 0.8$



or a memristor. In this way, any breakdown in one driving neural circuit still controls the coupled EMAs effectively.

In a summary, neural circuit can be excited to force the motion of single EMA and two coupled EMAs by pumping field energy into the load circuit, and a part of energy is converted to mechanical energy. On the other hand, the moving beam/arms have distinct feedback on the neural circuit via the channel current

across the load circuit. Involvement of noisy disturbance or excitation can regulate the moving state of the EMA and phase lock between two coupled EMAs. The results in this work provides possible guidance to design a array of coupled neural circuits for driving more coupled EMAs, and thus the EMAs can behave more complex and flexible body gaits. For simplicity, the external forcing currents imposed on the neural circuits in Figs. 2 and 3 are selected with periodic

forms. Indeed, the neural circuit can be excited by realistic signals, which are filtered or converted from acoustic wave, photoelectric signal and even chemical signals by incorporating specific electric components into the additive branch circuit of the neural circuit. For example, a phototube can convert external illumination into photocurrent for discerning the changes of external optical field. A piezoelectric ceramic can perceive external acoustic wave by converting voice into acoustic and electrical signals. A gas sensor can detect and convert external odor or chemical signal into voltage-controlled signal. In practical way, thermistor can also be connected to the neural circuit and thus the output voltage becomes dependent on temperature. That is, by incorporating specific components into the neural circuit, the EMAs will be controlled by the physical or chemical signals effectively. In our study, the EMAs are connected in series and their load circuits keep the same channel current. In fact, two neural circuits can be coupled to drive the two coupled EMAs and it prevents possible breakdown in the control of the coupled EMAs, for example, the motion of the EMAs can be controlled by another neural circuit when any damage occurs in one neural circuit. To behave complex gaits similar human arms, more elements/beams can be jointed and an array of neural circuits can be used to control the beams directly and synchronously. This work just discussed simple movement of arms under horizontal direction, and the movement of EMAs depends on the activation of Ampere's force. In fact, jointed pendulums are more effective to mimic the moving states and body gaits when artificial muscles are excited by neural signals, and arm movements can be reproduced with similar mechanical characteristics [75–78]. For example, gear driving, electronic motor winds flexible ropes can be used to simulate the processing of muscle relaxation and contraction, readers can explore these topics under the mentioned suggestions. Our discussion prefers to the dynamical property of electromechanical arm(s), while jointed pendulums can exhibit the main static mechanical property of artificial mechanical arms. Readers can replace the neural circuit in Fig. 1 by using different functional electronic components, and electronic motor can be used to generate continuous force so that external magnetic field can be removed without using Ampere's force.

4 Conclusions

In this paper, a simple neural circuit-coupled EMA device is proposed for dynamical analysis in artificial arms. Stochastic resonance is induced by applying noisy excitation on the neural circuit and moving beam, respectively. Noisy excitation on the displacement of the moving beam and the driving neural circuit has different working mechanism accompanying with energy injection into the electromechanical coupling system composed of artificial arm and neural circuit. It is helpful to mimic the processing of muscle driven by electrical signal and provides clues to design artificial arm or leg to aid disabled animals. The moving states of the beam/arms along horizontal direction depend on the interaction and competition between damping force and Ampere's force, and the electromechanical arm prefer to keep periodic movements when neural signals are propagated to excite the load circuit of the EMAs. Furthermore, a couple of EMAs with parameter mismatch are excited by the neural circuit, and safe signal propagation from the neural circuit is effective to synchronize two identical EMAs. Considering the parameter diversity in two coupled EMAs, for example, spring coefficients have slight differences, and the two EMAs can be controlled to keep synchronization stability or phase lock. External stochastic excitation on the moving beams coupled by a simple spring can enhance the occurrence of phase synchronization. It provides insights to design coupled EMAs to behave more complex body gaits and states.

Acknowledgements The authors thank Dr. Feifei Yang for his helpful discussion and proof verification.

Author contributions Yitong Guo finished the proof of model approach, formal analysis and numerical calculation. Xinlin Song presented formal analysis and model proof. Jun Ma suggested this investigation, presented formal analysis, writing the draft and edited the final version of this paper.

Funding This project is supported by National Natural Science Foundation of China under Grant No. 12072139.

Data availability No datasets were generated or analysed during the current study. The numerical data or code can be provided under reasonable request.

Declarations

Conflict of interest The authors declare no competing interests.

References

- Durkee, C., Kofuji, P., Navarrete, M., et al.: Astrocyte and neuron cooperation in long-term depression. *Trends Neurosci.* **44**, 837–848 (2021)
- Schipke, C.G., Kettenmann, H.: Astrocyte responses to neuronal activity. *Glia* **47**, 226–232 (2004)
- Ben Achour, S., Pascual, O.: Astrocyte–neuron communication: functional consequences. *Neurochem. Res.* **37**, 2464–2473 (2012)
- Paixão, S., Klein, R.: Neuron–astrocyte communication and synaptic plasticity. *Curr. Opin. Neurobiol.* **20**, 466–473 (2010)
- Ricci, G., Volpi, L., Pasquali, L., et al.: Astrocyte–neuron interactions in neurological disorders. *J. Biol. Phys.* **35**, 317–336 (2009)
- Flucher, B.E., Tuluc, P.: How and why are calcium currents curtailed in the skeletal muscle voltage-gated calcium channels? *J. Physiol.* **595**, 1451–1463 (2017)
- Berridge, M.J.: Smooth muscle cell calcium activation mechanisms. *J. Physiol.* **586**, 5047–5061 (2008)
- Bers, D.M.: Calcium fluxes involved in control of cardiac myocyte contraction. *Circul. Res.* **87**, 275–281 (2000)
- Bers, D.M., Perez-Reyes, E.: Ca channels in cardiac myocytes: structure and function in Ca influx and intracellular Ca release. *Cardiovasc. Res.* **42**, 339–360 (1999)
- Bers, D.M.: Calcium and cardiac rhythms: physiological and pathophysiological. *Circ. Res.* **90**, 14–17 (2002)
- Liu, Z., Han, F., Wang, Q.: A review of computational models for gamma oscillation dynamics: from spiking neurons to neural masses. *Nonlinear Dyn.* **108**, 1849–1866 (2022)
- Yang, C., Liu, Z., Wang, Q., et al.: Epilepsy as a dynamical disorder orchestrated by epileptogenic zone: a review. *Nonlinear Dyn.* **104**, 1901–1916 (2021)
- Wang, Z., Yang, Y., Duan, L.: Control effects of electromagnetic induction on epileptic seizures. *Nonlinear Dyn.* **112**, 6615–6628 (2024)
- Zhao, J., Yu, Y., Han, F., et al.: Dynamic modeling and closed-loop modulation for absence seizures caused by abnormal glutamate uptake from astrocytes. *Nonlinear Dyn.* **112**, 3903–3916 (2024)
- Islam, M.R., Zhao, X., Miao, Y., et al.: Epileptic seizure focus detection from interictal electroencephalogram: a survey. *Cogn. Neurodyn.* **17**, 1–23 (2023)
- Cek, M.E., Uludag, I.F.: Spectral resonance in Fitzhugh-Nagumo neuron system: relation with stochastic resonance and its role in EMG signal characterization. *Cogn. Neurodyn.* **18**, 1779–1787 (2024)
- Li, D., Li, S., Pan, M., et al.: The role of extracellular glutamate homeostasis dysregulated by astrocyte in epileptic discharges: a model evidence. *Cogn. Neurodyn.* **18**, 485–502 (2024)
- Yu, Y., Fan, Y.B., Han, F., et al.: Transcranial direct current stimulation inhibits epileptic activity propagation in a large-scale brain network model. *Sci. China Technol. Sci.* **66**, 3628–3638 (2023)
- Lu, L.L., Yi, M., Liu, X.Q.: Energy-efficient firing modes of chay neuron model in different bursting kinetics. *Sci. China Technol. Sci.* **65**, 1661–1674 (2022)
- Yuan, Y., Yang, H., Han, F., et al.: Traveling chimera states in locally coupled memristive Hindmarsh-Rose neuronal networks and circuit simulation. *Sci. China Technol. Sci.* **65**, 1445–1455 (2022)
- Wang, X., Yu, D., Wu, Y., et al.: Effects of potassium channel blockage on inverse stochastic resonance in Hodgkin-Huxley neural systems. *J. Zhejiang Univ. Sci. A* **24**, 735–748 (2023)
- Ma, J.: Biophysical neurons, energy, and synapse controllability: a review. *J. Zhejiang Univ. Sci. A* **24**, 109–129 (2023)
- Liu, Z.L., Yu, Y., Wang, Q.Y.: Functional modular organization unfolded by chimera-like dynamics in a large-scale brain network model. *Sci. China Technol. Sci.* **65**, 1435–1444 (2022)
- Kanagaraj, S., Moroz, I., Durairaj, P., et al.: Imperfect chimera and synchronization in a hybrid adaptive conductance based exponential integrate and fire neuron model. *Cogn. Neurodyn.* **18**, 473–484 (2023)
- Tang, J., Zhang, J., Ma, J., et al.: Noise and delay sustained chimera state in small world neuronal network. *Sci. China Technol. Sci.* **62**, 1134–1140 (2019)
- Huang, W., Yang, L., Zhan, X., et al.: Synchronization transition of a modular neural network containing subnetworks of different scales. *Front. Inf. Technol. Electron. Eng.* **24**, 1458–1470 (2023)
- Liang, B., Wang, X., Wang, L.: Impact of heterogeneity on network embedding. *IEEE Trans. Netw. Sci. Eng.* **9**, 1296–1307 (2022)
- Xie, Y., Yao, Z., Ma, J.: Formation of local heterogeneity under energy collection in neural networks. *Sci. China Technol. Sci.* **66**, 439–455 (2023)
- Yang, F., Wang, Y., Ma, J.: Creation of heterogeneity or defects in a memristive neural network under energy flow. *Commun. Nonlinear Sci. Numer. Simul.* **119**, 107127 (2023)
- Meirom, E.A., Mannor, S., Orda, A.: Strategic formation of heterogeneous networks. *IEEE J. Sel. Areas Commun.* **35**, 751–763 (2017)
- Bao, B., Hu, J., Cai, J., et al.: Memristor-induced mode transitions and extreme multistability in a map-based neuron model. *Nonlinear Dyn.* **111**, 3765–3779 (2023)
- Bao, B., Chen, L., Bao, H., et al.: Bifurcations to bursting oscillations in memristor-based FitzHugh-Nagumo circuit. *Chaos Solitons Fractals* **181**, 114608 (2024)
- Sun, J., Han, J., Wang, Y., et al.: Memristor-based neural network circuit of operant conditioning accorded with biological feature. *IEEE Trans. Circuits Syst. I Regular Papers* **69**, 4475–4486 (2022)
- Yu, F., Kong, X., Yao, W., et al.: Dynamics analysis, synchronization and FPGA implementation of multiscroll Hopfield neural networks with non-polynomial memristor. *Chaos Solitons Fractals* **179**, 114440 (2024)
- Yi, W., Tsang, K.K., Lam, S.K., et al.: Biological plausibility and stochasticity in scalable VO₂ active memristor neurons. *Nat. Commun.* **9**, 4661 (2018)
- Mishra, A., Ghosh, S., Kumar Dana, S., et al.: Neuron-like spiking and bursting in Josephson junctions: a review chaos: an Interdisciplinary. *J. Nonlinear Sci.* **31**, 052101 (2021)

37. Chalkiadakis, D., Hizanidis, J.: Dynamical properties of neuromorphic Josephson junctions. *Phys. Rev. E* **106**, 044206 (2022)
38. Njitacke, Z.T., Ramakrishnan, B., Rajagopal, K., et al.: Extremely rich dynamics of coupled heterogeneous neurons through a Josephson junction synapse. *Chaos Solitons Fractals* **164**, 112717 (2022)
39. Shi, Q.Q., Zhang, L., An, X.L., et al.: Dynamic exploration of a controllable thermosensitive neuron model and its applications. *Int. J. Bifurc. Chaos* **32**, 2250198 (2022)
40. Yao, Z., Wang, C.: Control the collective behaviors in a functional neural network. *Chaos Solitons Fractals* **152**, 111361 (2021)
41. Ramakrishnan, B., Foka, N.F.F., Akgül, A., et al.: Coexisting attractors in neuronal circuit based on Josephson junction under the effects of light and temperature: analysis and microcontroller implementation. *Iran. J. Sci.* **48**, 487–496 (2024)
42. Xie, Y., Ma, J.: How to discern external acoustic waves in a piezoelectric neuron under noise? *J. Biol. Phys.* **48**, 339–353 (2022)
43. Zhang, X., Cui, X., Wang, D., et al.: Piezoelectric nanotopography induced neuron-like differentiation of stem cells. *Adv. Funct. Mater.* **29**, 1900372 (2019)
44. Pinho, T.S., Silva, D., Ribeiro, J.C., et al.: Enhanced neuronal differentiation by dynamic piezoelectric stimulation. *J. Biomed. Mater. Res. Part A* **111**, 35–44 (2023)
45. Xie, Y., Yao, Z., Hu, X., et al.: Enhance sensitivity to illumination and synchronization in light-dependent neurons. *Chin. Phys. B* **30**, 120510 (2021)
46. Zhang, X., Ma, J.: Wave filtering and firing modes in a light-sensitive neural circuit. *J. Zhejiang Univ. Sci. A* **22**, 707–720 (2021)
47. Li, F., Li, X., Ren, L.: Noise-induced collective dynamics in the small-world network of photosensitive neurons. *J. Biol. Phys.* **48**, 321–338 (2022)
48. Yang, F., Ma, J., Ren, G.: A Josephson junction-coupled neuron with double capacitive membranes. *J. Theor. Biol.* **578**, 111686 (2024)
49. Li, Y., Ma, J., Xie, Y.: A biophysical neuron model with double membranes. *Nonlinear Dyn.* **112**, 7459–7475 (2024)
50. Guo, Y., Wu, F., Yang, F., et al.: Physical approach of a neuron model with memristive membranes. *Chaos Interdiscip. J. Nonlinear Sci.* **33**, 113106 (2023)
51. Wang, B., Lv, M., Zhang, X., et al.: Dynamics in a light-sensitive neuron with two capacitive variables. *Phys. Scr.* **99**, 055225 (2024)
52. Yang, F., Guo, Q., Ma, J.: A neuron model with nonlinear membranes. *Cogn. Neurodyn.* **18**, 673–684 (2024)
53. Jia, J., Yang, F., Ma, J.: A bimembrane neuron for computational neuroscience. *Chaos Solitons Fractals* **173**, 113689 (2023)
54. Wu, F.Q., Guo, Y.T., Ma, J.: Energy flow accounts for the adaptive property of functional synapses. *Sci. China Technol. Sci.* **66**, 3139–3152 (2023)
55. Yang, F., Ren, L., Ma, J., et al.: Two simple memristive maps with adaptive energy regulation and digital signal process verification. *J. Zhejiang Univ. Sci. A* **25**, 382–394 (2024)
56. Guo, Y.T., Ma, J., Zhang, X.F., et al.: Memristive oscillator to memristive map, energy characteristic. *Sci. China Technol. Sci.* **67**, 1567–1578 (2024)
57. Isabelle, M., Sylvie, Q.B., Chantal, P.: Electromechanical assessment of ankle stability. *Eur. J. Appl. Physiol.* **88**, 558–564 (2003)
58. Ngongiah, I.K., Balamurali, R., Kuiate, G.F., et al.: Mechanical arm(s) driven by Josephson junction circuit (s), mimicking the movement pattern of myriapods. *Phys. Scr.* **98**, 045221 (2023)
59. Ngongiah, I.K., Vivekanandan, G., Kuiate, G.F., et al.: Theoretical investigation of an array of Josephson junction neuron circuits actuating a mechanical leg and the array in mimicking a multi-legged locomotion. *Pramana* **97**, 135 (2023)
60. Mehrholz, J., Hädrich, A., Platz, T., et al.: Electromechanical and robot-assisted arm training after stroke: updated review. *Stroke* **43**, e172–e173 (2012)
61. Ngongiah, I.K., Ramakrishnan, B., Kuiate, G.F., et al.: Actuating mechanical arms coupled to an array of Fitz-Hugh–Nagumo neuron circuits. *Eur. Phys. J. Special Topics* **232**, 285–299 (2023)
62. Notué Kadjie, A., Nwagoum Tuwa, P.R., Wofo, P.: An electromechanical pendulum robot arm in action: dynamics and control. *Shock. Vib.* **2017**, 3979384 (2017)
63. Kouam Tagne, R., Wofo, P., Awrejcewicz, J.: Dynamics of the rotating arm of an electromechanical system subjected to the action of circularly placed magnets: numerical study and experiment. *Int. J. Bifurc. Chaos* **33**, 2350052 (2023)
64. Mbeunga, N.K., Nana, B., Wofo, P.: Dynamics of array mechanical arms coupled each to a Fitzhugh–Nagumo neuron. *Chaos Solitons Fractals* **153**, 111484 (2021)
65. Ma, J., Guo, Y.: Model approach of electromechanical arm interacted with neural circuit, a minireview. *Chaos Solitons Fractals* **183**, 114925 (2024)
66. Lee, S.G., Kim, S.: Parameter dependence of stochastic resonance in the stochastic Hodgkin–Huxley neuron. *Phys. Rev. E* **60**, 826 (1999)
67. Longtin, A.: Stochastic resonance in neuron models. *J. Stat. Phys.* **70**, 309–327 (1993)
68. McDonnell, M.D., Abbott, D.: What is stochastic resonance? Definitions, misconceptions, debates, and its relevance to biology. *PLoS Comput. Biol.* **5**, e1000348 (2009)
69. Harmer, G.P., Davis, B.R., Abbott, D.: A review of stochastic resonance: Circuits and measurement. *IEEE Trans. Instrum. Meas.* **51**, 299–309 (2002)
70. Balenzuela, P., Braun, H., Chialvo, D.R.: The ghost of stochastic resonance: an introductory review. *Contemp. Phys.* **53**, 17–38 (2012)
71. Kurita, Y., Ishikawa, T., Tsuji, T.: Stiffness display by muscle contraction via electric muscle stimulation. *IEEE Robot. Autom. Lett.* **1**, 1014–1019 (2016)
72. Schauer, T.: Sensing motion and muscle activity for feedback control of functional electrical stimulation: ten years of experience in Berlin. *Annu. Rev. Control.* **44**, 355–374 (2017)
73. Son, C., Kim, S., Kim, S., et al.: Detection of muscle activation through multi-electrode sensing using electrical stimulation. *Sens. Actuators A Phys.* **275**, 19–28 (2018)

74. Jain, R.K., Datta, S., Majumder, S.: Design and control of an IPMC artificial muscle finger for micro gripper using EMG signal. *Mechatronics* **23**, 381–394 (2013)
75. Sharghi, H., Bilgen, O.: Dynamics of pendulum-based systems under human arm rotational movements. *Mech. Syst. Signal Process.* **183**, 109630 (2023)
76. Donner, P., Christange, F., Lu, J., et al.: Cooperative dynamic manipulation of unknown flexible objects: joint energy injection based on simple pendulum fundamental dynamics. *Int. J. Social Robot.* **9**, 575–599 (2017)
77. Lampart, M., Zapoměl, J.: Dynamics of a non-autonomous double pendulum model forced by biharmonic excitation with soft stops. *Nonlinear Dyn.* **99**, 1909–1921 (2020)
78. Chung, C.Y.: Balancing of an inverted pendulum with a kinematically redundant robot. *Int. J. Gen. Syst.* **31**, 1–15 (2002)

Publisher's Note Springer Nature remains neutral with regard to jurisdictional claims in published maps and institutional affiliations.

Springer Nature or its licensor (e.g. a society or other partner) holds exclusive rights to this article under a publishing agreement with the author(s) or other rightsholder(s); author self-archiving of the accepted manuscript version of this article is solely governed by the terms of such publishing agreement and applicable law.



Letter

Model approach of artificial muscle and leg movements

Yitong Guo^a, Chunni Wang^b, Jun Ma^{a,b,*}^a College of Electrical and Information Engineering, Lanzhou University of Technology, Lanzhou, 730050, China^b Department of Physics, Lanzhou University of Technology, Lanzhou, 730050, China

ARTICLE INFO

Communicated By Matjaz Perc

Keywords:

Neural circuit
Electronic motor
Muscle movements
Leg gait
Jointed pendulums

ABSTRACT

In this work, two flexible ropes are wound to an electronic motor in opposite directions and the other terminal ends are pinned to two jointed points for mimicking the artificial muscles. Electrical signals from a neural circuit are used to control the rotation of electronic motor(s), and the pulling forces along the flexible ropes control the rotation angles of the jointed pendulums as legs. The leg gaits are investigated in dynamics by changing the channel current shunted from the neural circuit, and the electronic motor-controlled flexible ropes behave as artificial muscles. A single neural circuit and two coupled neural circuits are used to control the electromechanical legs by adjusting the forcing current. The neural circuit drives the electronic motor and then jointed pendulums are controlled. The circuit equations, rotation equations and energy description are presented. It provides possible guidance to design artificial muscles for aiding disabled legs and arms.

1. Introduction

When neural signals are propagated to the leg muscles, contraction and relaxation of gluteus maximus muscle (GMM), biceps femoris muscle (BFM), lateral thigh muscle (LTM) and tensor fascia lata muscle (TFLM) will control the rotation and movements of femur, tibia and fibula. As a result, different leg gaits are activated to keep body balance. Any damage or disability in these muscles will affect the leg gaits and keeping safe body gaits becomes difficult. From mechanical viewpoint, the femur, tibia and fibula are connected to generate similar dynamical behaviors as two jointed pendulums. When a flexible rope or string is wound to an electronic motor, clockwise and counterclockwise rotation of the electronic motor will relax or contract the length of the rope as muscle movement. Muscle contraction [1–5] is a fundamental characteristic of muscle tissue, referring to the mechanical response that occurs in muscle fibers after receiving stimulation. The maintenance of body posture, spatial movement, complex movements, and respiratory movements are all achieved through muscle contraction activities [6–10]. According to the theory of muscle filament sliding, the basic process of muscle contraction is: muscle cells generate action potentials, causing an increase in calcium concentration in the muscle plasma, which binds to troponin C. Troponin undergoes conformational changes, weakening the binding between troponin I and actin. Protomyosin undergoes conformational changes, exposing binding sites on actin [11–15]. The transverse bridge binds to actin, causing the transverse

bridge to twist and drag the thin muscle filament towards the center of the thick muscle filament. Through the transverse bridge cycle formed by the binding, twisting, dissociation, and re binding and re twisting of the transverse bridge and actin, the fine filaments continuously slide and the muscle segments shorten. The energy source during muscle contraction is the energy released by ATP hydrolysis [16–20].

Heartbeat results from continuous relaxation and contraction of cardiac tissue accompanying with blood pumping [21–25], and electrical signals are propagated in the cardiac tissue by generating target waves [26–30]. However, breakup of these target waves will induce new spiral waves, which can block normal propagation of electrical signals in the cardiac tissue, and emergence of spiral waves in the cardiac tissue predicts emergence of arrhythmia and further breakup of spiral waves will induce rapid death of the heart due to fibrillation [31–35]. On the other hand, safe body gaits are crucial for working and it is dependent on the flexible muscles, which are controlled by different neural signals from the nervous systems. That is, continuous electrical stimuli can control the muscle contraction and relaxation, and then the bones are pulled and guided to keep suitable body gaits including legs and arms, and then movements are activated.

A simple nonlinear circuit can be controlled to present similar spiking and bursting patterns as those biological neurons, and these spiking or bursting circuits are considered as neural circuits. By applying scale transformation on the circuit equations, a dimensionless nonlinear oscillator can be approached as generic neuron model. By adding

* Corresponding author.

E-mail addresses: hyperchaos@lut.edu.cn, hyperchaos@163.com (J. Ma).<https://doi.org/10.1016/j.physleta.2024.130069>

Received 17 September 2024; Received in revised form 8 November 2024; Accepted 13 November 2024

0375-9601/© 2024 Elsevier B.V. All rights are reserved, including those for text and data mining, AI training, and similar technologies.

specific terms into the neuron model, functional description is enhanced to propose more functional biophysical neuron models, see recent reviews and reference therein [36,37]. Besides these oscillator-like neuron models, map neurons [38–42] can produce similar firing patterns and for further dynamical analysis in the field of computational neuroscience. To check the reliability of these neuron models, exact and clear definition of energy functions become crucial for further understanding the controllability and self-adaptive properties of biophysical neurons [43–45].

The dynamics of human gaits shows complexity, and short continuous recordings of the human locomotory apparatus possess properties typical of deterministic chaotic systems [46]. Ashkenazy et al. [47] proposed a stochastic model for exploring the dynamics in human gaits. For dynamical analysis and control, more theoretical models have been proposed for identifying the mechanical characteristic of body gaits [48–52]. Stability and movement control are two main research topics about body gaits. It is a challenge to design auxiliary electromechanical devices to aid the movement of disabled arms and legs. Therefore, a variety of manipulators have been proposed to control muscle movements and joint motions [53–56]. Indeed, the activation of artificial arms/ legs and mechanical arms depends on the electromechanical device greatly, which can provide powerful forces and torques to control the muscle movements. In practical way, hydraulic drive [57–59], artificial muscles [60–63], electromechanical drive [64–67] can be used to control the body gaits for keeping stability or appropriate movements. In fact, the electromechanical devices can be controlled by electric signals from a neural circuit or coupled neural circuits, and the nervous signal regulation on body gaits can be explored in the electromechanical-coupled neural circuit, see recent works and references therein [68–70].

In this work, two jointed pendulums driven by a neural circuit and coupled neural circuits are proposed to mimic the movements of legs controlled by muscles. The contraction and relaxation of muscles are replaced by using flexible ropes winded to an electronic motor, and changes of the flexible ropes can generate different tensions to the jointed pendulums. The electronic motor is controlled by the output electrical signals from the neural circuit. It designs a kind of artificial muscle by building suitable electromechanical device including neural circuit, flexible ropes, and electronic motor and jointed pendulums. The suggested scheme is helpful to aid those disabled legs for keeping safe body gaits and further application of robot arms and legs.

In the second section, the movements of femur and fibula are described by two jointed beams, which are controlled by artificial muscles. Flexible ropes are used to mimic the muscle relation and the pulling force from muscle is controlled by an electronic motor, which is controlled by the electric signals from neural circuits. The movement of the electromechanical devices and changes in the neural circuit are described in detail. In the third section, numerical results are provided to show the mode transition in the neuron and neural circuits, rotation movement of the electromechanical device. In the last section, conclusion and suggestions are supplied for further investigation with this topic.

2. Model description and discussion

Muscle contraction is the phenomenon of muscle contraction response to external physical and chemical stimuli. It usually means the contraction of vertebrate skeletal muscles through the transmission of activity potentials. A single action potential produces a single contraction, while repeated activity potentials will generate a rigid contraction. Muscle contractions that do not occur through activity potentials are mostly caused by non transmissible depolarization. If depolarization is limited to local muscles and is transient, it is called local contraction. Depolarization, if it is sustained throughout the muscle, is called constrictive contraction [71,72]. The sustained contractions observed in smooth muscles are generally referred to as spasms, but many ones are

still accompanied by repeated activity potentials or sustained depolarization [73,74]. However, the sustained contractions observed in the adductor muscles of bivalves seldom show any changes in electrical potential, and this contraction is due to a gated structure. The three forms of muscle contraction are shortening contraction, elongating contraction, and isometric contraction [75–77]. Shortening contraction finds cardiac contraction, including two forms: isotonic and isokinetic contraction [78]. Isotonic contraction [79] accounts for the state of movement in which muscles no longer increase in tension when resisting constant resistance, such as lifting a barbell. Isokinetic contraction [80] refers to the constant speed that the muscles resist external resistance, producing maximum tension, and is a mutual adaptation of forces. For example, stretching and contracting are centrifugal contractions, which are caused by muscle tension being lower than external resistance, such as actions like placing heavy objects. Isometric contraction refers to movements where muscle tension is equal to external resistance and muscle length remains unchanged, such as plank support, inversion, and so on.

As shown in Fig. 1, the leg gaits are controlled by the muscles and then the femur is jointed with the tibia and fibula for behaving different gaits.

In fact, the mechanic characteristic of the femur, tibia and fibula can be described by the movements in a pair of jointed pendulums as shown in Fig. 2.

Supposing the length for two pendulums as $OA=l_1$, $AB=l_2$, the velocity relation is approached by

$$\begin{cases} \frac{d\theta_1}{dt} = \omega_1 = \frac{v_A}{l_1}, \\ \frac{d\theta_2}{dt} = \omega_2 = \frac{v_{BA}}{l_2} = \frac{v_{B1}}{l_2}, \\ v_B \cos\theta_2 = v_A \sin(\theta_1 + \theta_2). \end{cases} \quad (1)$$

Any rotations of the pendulum OA will drag the jointed beam AB and the object B . On the other hand, horizontal driving or excitation on the B object/point will force continuous rotation of the jointed pendulums AB and OA synchronously. To mimic the contraction and relaxation of leg muscles in Fig. 1, flexible ropes are wrapped around an electronic motor (EM) as shown in Fig. 3. The rotation direction and rotation frequency of the EM are dependent on the intrinsic current along the rotor coils with N turns, and the coils of the EM can be considered as load circuit, which shunts current from a neural circuit. This processing mimics the neural regularity on muscles movement. The artificial tissue keeps constant tension when the EM is controlled in static state, and clockwise rotation or anticlockwise rotation will regulate the length and tension (or pulling force) of the flexible ropes effectively, and this processing is similar to the relaxation and contraction of muscles.

As shown in Fig. 3, the two points (O , A) decrease its length when the electronic motor is activated with clockwise rotation, and it indicates that the muscle is contracted. On the other hand, counterclockwise rotation of the EM will increase the distance between the two points (O , A) and it means that the muscle is relaxed. The EM controlled flexible rope OA can behave similar contraction and relaxation property as muscles as LTM and BFM when the two ends of the ropes are pinned to femur and tibia, respectively. In practical realization, the device in Fig. 3 should be encapsulated and adhered to the legs. When the same device in Fig. 3 is adhered to the two jointed pendulums (OA , AB) in Fig. 2, the intrinsic tension will be activated to control the rotation and leg gait as shown in Fig. 1. Supposing the EM can generate a moment \vec{M} , and the EM has a radius r_0 , and then the tension/force T along the artificial muscle is estimated by

$$\begin{cases} \vec{M} = \vec{P}_M \times \vec{B} = I_{Motor} S \hat{e} \times \vec{B}, \quad M = |\vec{M}| = |\vec{M}|, \\ T = \frac{M}{2r_0} = \frac{NSBI_{Motor}}{2r_0} \sin(\hat{e}, \vec{B}) = KI_{Motor} \sin(\omega_0 t + \phi_0) = KI_{Motor}(t). \end{cases} \quad (2)$$

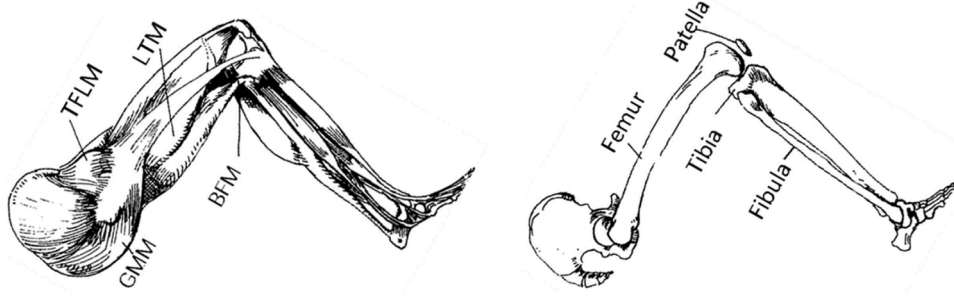


Fig. 1. Anatomy diagram of leg (left) and leg skeleton diagram (right). Gluteus maximus muscle (GMM), biceps femoris muscle (BFM), lateral thigh muscle (LTM), tensor fascia lata muscle (TFLM).

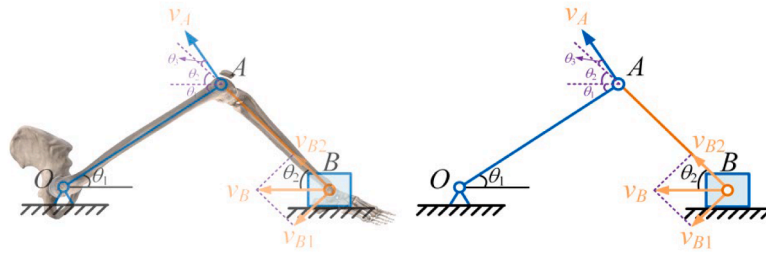


Fig. 2. Coupled pendulums for jointed femur and tibia (leg). O, A, B denotes jointed points, and the beam OA, AB rotates against the points O, A, B respectively. The terminal end B moves along horizontal direction. Rotation of OA and AB mimic the movement of femur, tibia and fibula, respectively.

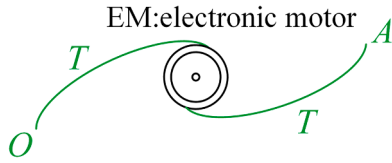


Fig. 3. Artificial muscle is mimicked by enwinding flexible strings/ropes to an electronic motor (EM). T denotes the tension/pulling force along the strings. Clockwise or anticlockwise rotation in EM will change the length for OA , muscle contraction or relaxation is realized.

Within the EM, it has N -turns coils and S denotes its size, B is the intensity of magnetic field surrounded the coils, and \hat{e} defines the normal direction of coil plane. The parameter ω_0 is the angular frequency of the EM, and φ_0 denotes the initial phase value of the motor. I_{motor} represents the channel current of the motor coils and it is shunted from a signal source or neural circuit. To keep a stable leg gait, it indicates that the EM must present a constant moment and the intrinsic tension T becomes a constant as well. Vertical to the length direction of the pendulums (OA, AB), the components of stress can force the two pendulums to rotate against the jointed points (O, A) by generating suitable moments. As a result, the jointed pendulums will change their angles (θ_1, θ_2) to keep appropriate leg gaits.

$$\begin{cases} M_{OA} \propto T_1 l_1 = k_1 T_1 l_1, & M_{AB} \propto T_2 l_2 = k_2 T_2 l_2, \\ l_2 \sin \theta_2 = l_1 \sin \theta_1, \\ J_1 \frac{d^2 \theta_1}{dt^2} = k_1 T_1 l_1 + k_2 T_2 l_2 + N l_2 \cos \theta_2 - P_1 \frac{l_1}{2} \cos \theta_1 - P_2 \frac{l_2}{2} \cos \theta_2, \\ J_2 \frac{d^2 \theta_2}{dt^2} = \frac{1}{3} \frac{P_2 l_2}{g} \frac{d^2 \theta_2}{dt^2} = k_2 T_2 l_2 + N l_2 \cos \theta_2 - P_2 \frac{l_2}{2} \cos \theta_2. \end{cases} \quad (3)$$

The gravities for the two jointed pendulums (OA, AB) are marked as (P_1, P_2), N denotes the vertical supporting force on point B . When the intrinsic tension T_1 (or T_2) along the artificial muscles has an angle Ω_1 (or Ω_2) against the pendulum OA (or AB), $k_1 = \sin \Omega_1$, $k_2 = \sin \Omega_2$. The moment (torque) of inertia for the jointed pendulum OAB is described by

$J_1 = (P_1 l_1^2 / 3 + P_2 l_2^2 / 3 + P_2 l_1^2) / g = m_1 l_1^2 / 3 + m_2 l_2^2 / 3 + m_2 l_1^2$. When external load force is applied to the point B , the artificial muscle is regulated adaptively and thus the jointed pendulums will keep static gait. In presence of keeping stable body gait under torque balance, the angles (θ_1, θ_2) are stabilized at some constant values as follows

$$\begin{cases} \cos \theta_1 = 2k_1 \frac{T_1}{P_1}, \\ \cos \theta_2 = \frac{2k_2 T_2}{P_2 - 2N}. \end{cases} \quad (4)$$

On the other hand, time-varying contraction and relaxation of the leg muscles will change the intrinsic tensions and then the leg gaits will be regulated by changing the angles (θ_1, θ_2). As presented in Eq.(2), the tensions (T_1, T_2) can be selected with time-varying functions, which can present distinct periodic signals, chaotic signals and even spiking or bursting series as the membrane potentials from some neurons developed from many neural circuits. Selecting time-varying tension (T_1, T_2) for Eq.(3), it indicates that the artificial muscles will contract or relax with time, and then different leg gaits can be presented accompanying with the changes of the angles (θ_1, θ_2). The third formula in Eq. (3) is much complex, and the two gait angles (θ_1, θ_2) are restricted by the second formula in Eq. (3). Therefore, Eq. (3) is rewritten in equivalent forms by updating the second and fourth formulas in Eq.(3) as follows

$$\begin{cases} l_2 \sin \theta_2 = l_1 \sin \theta_1, \\ \frac{d^2 \theta_2}{dt^2} = \frac{3gk_2 T_2 + 3Ng \cos \theta_2}{P_2 l_2} - \frac{3g}{2l_2} \cos \theta_2. \end{cases} \quad (5)$$

It indicates the end point B of the coupled pendulums can move in free way (left to right, up and down) when the vertical supporting $N = 0$. The complete diagram for the leg gait controlled by artificial muscles via the tension (T_1, T_2) can be presented in Fig. 4.

According to Fig. 4, any changes of the current across the EM1 and EM2 will modify the rotational torques and the flexible rope OA or AB will adjust its length and the intrinsic tension along the ropes. Furthermore, additive moments for the jointed pendulums combined of OA and AB are applied to change the gait stability. In this way, leg movement is realized. In fact, when the electrical signals activated the

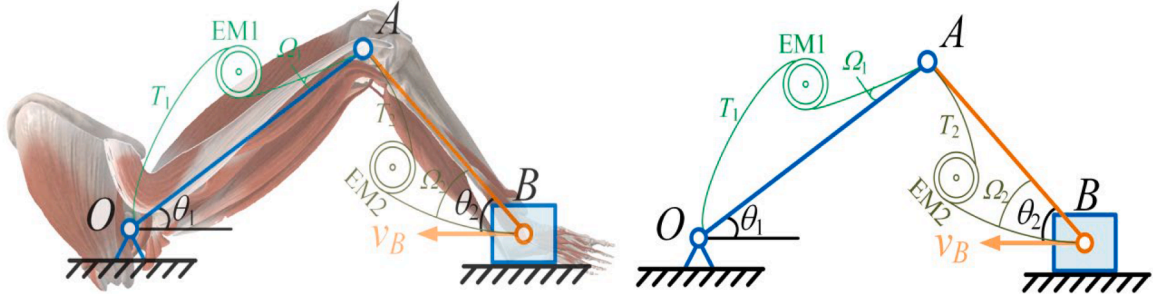


Fig. 4. Jointed pendulums driven by artificial muscles, which the electronic motor controls the contraction and relaxation of the flexible ropes. EM1 and EM2 are controlled by external electrical signals.

EM1 and EM2 are generated from a stable signal source, the effect of load effect of N-turns coils in the electronic motor can be ignored. Surely, short beam can also be connected to the jointed point B to mimic the foot gait. Supposing the load circuit of the EM has an intrinsic resistor R_0 , and the two EMs are excited by the same channel current from a simple neural circuit shown in Fig. 5.

The output voltage from the capacitor controls the channel current across NR, and it is approached by

$$i_{NR} = -\frac{1}{\rho} \left(V - \frac{1}{2} \frac{V^2}{V_0} - \frac{1}{3} \frac{V^3}{V_0^2} \right). \quad (6)$$

The intrinsic parameters (V_0, ρ) are relative to the material property of NR and they can be approached from experimental way. For simplicity, the same output channel current is applied to driven two EMs and the circuit is plotted in Fig. 6.

The physical variables in Fig. 6 can be described by the circuit equations as follows

$$\begin{cases} C \frac{dV}{dt} = i_s + i_L + \frac{1}{\rho} \left(V - \frac{V^2}{2V_0} - \frac{V^3}{3V_0^2} \right) - i_{MT}, \\ L \frac{di_L}{dt} = E - i_L R - V, \\ L_{MT} \frac{di_{MT}}{dt} = \frac{1}{2} V - i_{MT} R_0. \end{cases} \quad (7)$$

These physical variables and parameters can be rewritten in dimensionless forms as follows

$$\begin{cases} x = \frac{V}{V_0}, y = \frac{i_L \rho}{V_0}, z = \frac{i_{MT} \rho}{V_0}, i_s = \frac{i_s \rho}{V_0}, \tau = \frac{t}{\rho C}, \\ a = \frac{E}{V_0}, b = \frac{\rho^2 C}{L}, c = \frac{R}{\rho}, d = \frac{\rho^2 C}{L_{MT}}, \beta = \frac{R_0}{\rho}. \end{cases} \quad (8)$$

Inserting the parameters and variables into Eq.(9), the coupled neuron and muscles are described by

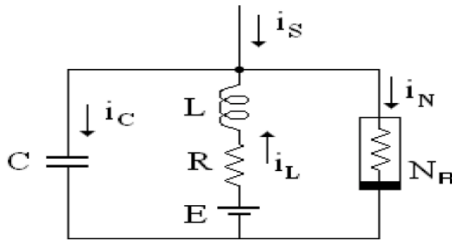


Fig. 5. (RLC) Neural circuit is composed of capacitor C, inductor L, nonlinear resistor NR. Constant voltage E denotes reverse potential of ion channel, R is a constant resistor, i_s represents external forcing current.

$$\begin{cases} \frac{dx}{d\tau} = i_s + y + \left(x - \frac{x^2}{2} - \frac{x^3}{3} \right) - z, \\ \frac{dy}{d\tau} = b(a - cy - x), \\ \frac{dz}{d\tau} = d \left(\frac{1}{2} x - \beta z \right). \end{cases} \quad (9)$$

From biophysical viewpoint, external forcing current i_s modifies the excitability by inserting energy into the neuron, and the firing patterns are changed during the changes of membrane potentials for the variable x . According to Eq.(2), the channel current $i_{motor} = i_{MT}$, and it is proportional to the dimensionless variable z by setting appropriate gain k for the tension T including T_1 and T_2 , here, $T_1 = T_2 = T$. By taming the intrinsic parameters (a, b, c, d, β) and the external current i_s , the neuron can present different firing modes during the changes of membrane potentials. When the neuron generates constant voltage or membrane potential, the artificial muscles keeps constant tension values and the variable z becomes stable. On the other hand, Continuous changes of membrane potential will modify the channel current z and then the tension for artificial muscles becomes time-varying, it predicts that the artificial muscles keeps contraction and relaxation accompanying with switch in the leg gaits.

When the two EMs in Fig. 4 are controlled by two different channel currents, the jointed pendulums and artificial muscles will behave their gaits freely, and the circuit is plotted in Fig. 7.

As shown in Fig. 4, the load circuits for the two electronic motors in the artificial muscles are controlled by two coupled neural circuits, and the current across each load circuit (L_{MT1}, L_{MT2}) is affected by the external stimulus and other electric components by shunting the energy flow. Similarly giving circuit equations for the physical variables and the neural circuits are coupled to control the artificial muscles as follows

$$\begin{cases} C \frac{dV_1}{dt} = i_s + i_{L1} + \frac{1}{\rho} \left(V_1 - \frac{V_1^2}{2V_0} - \frac{V_1^3}{3V_0^2} \right) - i_{MT1} + \frac{(V_2 - V_1)}{R}, \\ L \frac{di_{L1}}{dt} = E - i_{L1} R - V_1, \\ L_{MT1} \frac{di_{MT1}}{dt} = V_1 - i_{MT1} R_0, \\ C \frac{dV_2}{dt} = i_s + i_{L2} + \frac{1}{\rho} \left(V_2 - \frac{V_2^2}{2V_0} - \frac{V_2^3}{3V_0^2} \right) - i_{MT2} + \frac{(V_1 - V_2)}{R}, \\ L \frac{di_{L2}}{dt} = E - i_{L2} R - V_2, \\ L_{MT2} \frac{di_{MT2}}{dt} = V_2 - i_{MT2} R_0. \end{cases} \quad (10)$$

The variables including voltage and channel currents for the left side circuit are marked with subscript 1, while the variables for right side circuit in Fig. 7 are discerned by adding subscript 2, and the same electric components for two sides of the coupled neural circuits are

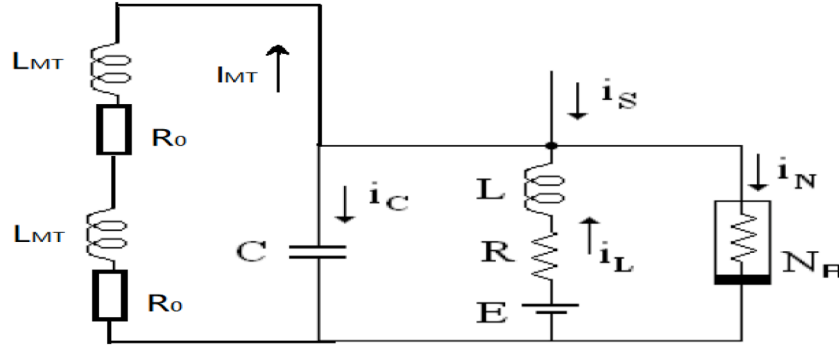


Fig. 6. Neural circuit excites the EMs for mimicking the artificial muscles. L_{MT} and R_0 denote the intrinsic inductance and resistance for the load coils in the EM. The current across the EM coils $I_{MT}=I_{motor}$ in Eq.(2).

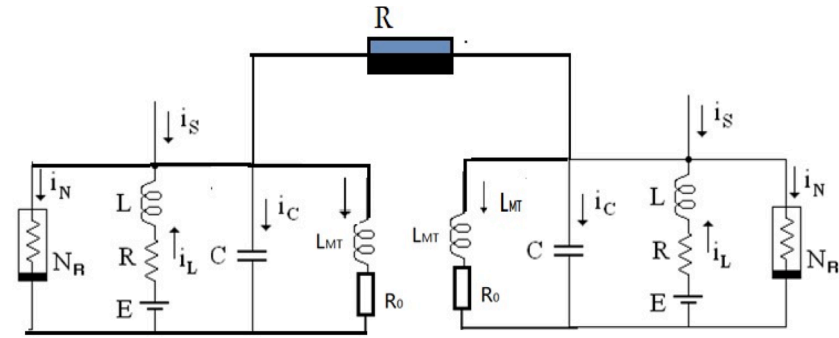


Fig. 7. Two coupled neural circuits are activated to driven the load circuits for the artificial muscles. The coupling channel is built by connecting two neural circuits via a linear resistor with the same resistance R .

selected identical parameter value, for example, $L_1=L_2=L$, $C_1=C_2=C$, $L_{MT1}=L_{MT2}=L_{MT}$, $E_1=E_2=E$, $R_1=R_2=R$, $R_{01}=R_{02}=R$, $i_{s1}=i_{s2}=i_s$. By applying similar definition in Eq.(8) on the physical variables and parameters in Eq.(10), the coupled neurons interacted with feedback modulation from the artificial muscles are described by

$$\begin{cases} \frac{dx_1}{d\tau} = i_s + y_1 + \left(x_1 - \frac{x_1^2}{2} - \frac{x_1^3}{3}\right) - z_1 + \frac{1}{c}(x_2 - x_1), \\ \frac{dy_1}{d\tau} = b(a - cy_1 - x_1), \\ \frac{dz_1}{d\tau} = d(x_1 - \beta z_1), \\ \frac{dx_2}{d\tau} = i_s + y_2 + \left(x_2 - \frac{x_2^2}{2} - \frac{x_2^3}{3}\right) - z_2 + \frac{1}{c}(x_1 - x_2), \\ \frac{dy_2}{d\tau} = b(a - cy_2 - x_2), \\ \frac{dz_2}{d\tau} = d(x_2 - \beta z_2). \end{cases} \quad (11)$$

When the artificial muscles adhered to the two jointed pendulums are controlled by two separate neural circuits, the tensions for the artificial muscles can select different values by inducing different torques. For example, T_1 is controlled by the series for variable z_1 and T_2 is controlled by the series for variable z_2 . As a result, the leg can behave different gaits freely. Involvement of coupling between two neural circuits can regulate the cooperation between the two jointed pendulums and then the leg gaits are controlled. On the other hand, breakdown in one of the neural circuit still excites the EMs and then the leg gaits can be controlled effectively. In fact, the leg gaits are mainly controlled by the criterion in Eq.(5) even the tensions for the artificial muscles can be adjusted to select different values.

When the jointed pendulums and the electronic motor are controlled by a single neural circuit shown in Fig. 6, the field energy W_1 is mainly

saved in the capacitor and three inductors, and then the field energy is replaced with dimensionless Hamilton energy as follows

$$\begin{cases} W_1 = \frac{1}{2}CV^2 + \frac{1}{2}Li_L^2 + L_{MT}i_{MT}^2, \\ H_1 = \frac{W_1}{CV_0^2} = \frac{1}{2}x^2 + \frac{1}{2b}y^2 + \frac{1}{2d}z^2. \end{cases} \quad (12)$$

For two coupled neural circuits in Fig. 7, the field energy W_2 is obtained as well and its dimensionless energy function H_2 is given in

$$\begin{cases} W_2 = \frac{1}{2}CV_1^2 + \frac{1}{2}Li_{L1}^2 + \frac{1}{2}L_{MT1}i_{MT1}^2 + \frac{1}{2}CV_2^2 + \frac{1}{2}Li_{L2}^2 + \frac{1}{2}L_{MT2}i_{MT2}^2, \\ H_2 = \frac{W_2}{CV_0^2} = \frac{1}{2}(x_1^2 + x_2^2) + \frac{1}{2b}(y_1^2 + y_2^2) + \frac{1}{2d}(z_1^2 + z_2^2). \end{cases} \quad (13)$$

When the legs or jointed pendulums suffer from external load bearing, the muscles contract to keep enough tension for keeping gait balance. For the neural circuit-coupled jointed pendulum via artificial muscle, contraction or relaxation of the ropes enwinding to the electronic motor will change the leg gaits and feedback is activated to regulate the neural circuit by generating induced electromotive force in the N -turns coils in the load circuit of the electronic motor. For numerical verification, the fourth order Runge-Kutta algorithm can be applied to find solutions for Eq.(9) and its energy evolution in Eq.(12) can be detected when two EMs are driven by the same channel current from the neural circuit. Similarly, numerical solutions can be obtained for Eq.(11) and its energy function in Eq.(13) when the two EMs are driven by a couple coupled neural circuits. According to Eq.(2) and Eq. (5), the rotation angles (θ_1, θ_2) for the two jointed pendulums can also be estimated and different leg gaits are formed in stable way. For dynamical analysis, external forcing current can be selected with photocurrent across a phototube or piezoelectric current converted from an acoustic wave via piezoelectric ceramic. In addition, noisy disturbance can also

be applied to detect the response in the leg gaits and energy conversion between capacitive and inductive energy when the leg and artificial muscles are controlled in static states.

Based on the simple neural circuit in Fig. 5, the neural signals are derived to excite the electronic motor, and the flexible ropes connected to the jointed pendulums are adjusted, as a result, the jointed femur, tibia and fibula are guided to present different leg gaits. Combination of other functional electronic components including memristor, phototube, piezoelectric ceramic and thermistor into the neural circuit in Fig. 5 can enhance the physical perceptive function of the neural circuit. In particular, involvement of memristor into neural circuit can induce multi-stability [81,82] and controllability to external electromagnetic radiation because external physical stimuli inject energy into the memristive channel.

From control aspect, external stimuli inject energy into the neural circuits, and a part of field energy is shunted into the load circuits of the EMs for generating strong torques to control the tension in the ropes, which connect to the skeleton. As a result, the leg gaits can be controlled effectively within short transient period. As is known, neural signals are propagated to the leg muscles and then the leg behave suitable gaits by generating appropriate muscle tensions (pulling force) during continuous movements. In fact, the leg gaits can be discerned by detecting the detectable rotation angles (θ_1, θ_2). On the other hand, detection of the moving velocity of jointed point B provides another way to measure the reciprocating motion of the leg, which is similar to the rehabilitation training for disabled legs. When the physical parameters for the load circuits of the EMs are fixed, activation of adaptive law depends on the regulation of the channel current across the EMs coils synchronously. By applying larger channel current in the load circuit, the EMs torques and rope tensions are increased to speed the rotation movement of the jointed pendulums, and the leg moves quickly. Otherwise, the leg and jointed pendulums move slowly. The field energy in the neural circuit and EMs are converted to mechanical energy due to the coupling between EMs and neural circuit. That is, changes of the energy ratio between capacitive energy and inductive energy will control the movement state the jointed pendulums and the EMs. Similar to the parameter growth law for a single neural circuit [38,80], an adaptive control law for controllable parameters can be suggested as follows

$$\begin{cases} \frac{dc}{dt} = \delta \cdot c \cdot \vartheta(H - H_0), \vartheta(U) = 1, U \geq 0, \vartheta(U) = 0, U < 1, \\ H = \frac{1}{2}x^2, \text{ for Fig.6,} \\ H = \frac{1}{2}(x_1^2 + x_2^2), \text{ for Fig.7.} \end{cases} \quad (14)$$

In Eq.(14), the gain δ controls the growth intensity of the parameter c , H measures the capacitive energy in the neuron or neural circuit, and H_0 is the threshold for the energy. The energy level can be calculated when all variables are available. In practical way, the kernel variable of the Heaviside function in Eq.(14) can be replaced by using detectable voltage variable. Therefore, the adaptive growth law in Eq.(14) is updated by

$$\begin{cases} \frac{dc}{dt} = \delta \cdot c \cdot \vartheta(x - x_0), \vartheta(U) = 1, U \geq 0, \vartheta(U) = 0, U < 1, \\ \frac{db}{dt} = \delta \cdot b \cdot \vartheta(x - x_0), x = x_1, \text{ or } x_2 \text{ for Fig.7.} \end{cases} \quad (15)$$

When the membrane potential or the capacitor voltage is beyond the threshold x_0 , the parameter c or b can keep continuous growth, and the total energy function H_1 in Eq.(12) or H_2 in Eq.(13) will be modified. Positive value for the δ will apply negative regulation to decrease the variable y or variables (y_1, y_2), and inductive energy in the neural circuits is decreased synchronously. As a result, the load circuit of the EMs will share more energy flow to control the EMs effectively, and then the jointed pendulums are guided to behave suitable gaits. For static state,

the angles can be estimated from Eq.(4) when the tension and torques generated by the artificial tissue in Eq.(2) are invariable. In presence of time-varying stimulus, the channel current across the load circuit of the EMs will generate different torques and tensions, and the rotation movement of the jointed pendulum can be explored by finding numerical results from Eq.(3).

Indeed, electronic motors can be used to contract or relax the length of flexible ropes, and simple artificial muscles can be mimicked to control the body gaits. Two jointed pendulums can be controlled to mimic the movement and rotation of arms and legs, and activation of artificial muscles are helpful to aid the disabled legs. By taming the electrical activities in the neural circuits, the output voltage and current from the neural circuit can be used to control the electronic motors and then the jointed pendulums and even robot arms and legs can be controlled to keep stable gaits. This scheme provides some clues to design and control artificial legs, and it is helpful to keep safe body gaits for those people with disabled legs. Damage of body muscles can ignore the electrical stimuli and then the body gaits are out of control from the neural signals simultaneously. Therefore, gaits stability and normal muscle movements are disturbed to behave suitable states. On the other hand, blocking the regulation from neural signals due to different nervous disorders [83–85] also disables muscle movements and auxiliary neural circuits can be designed to control the muscle relaxation for behaving safe body gaits.

3. Numerical results and discussion

According to the stability condition in Eq.(4), the jointed beams/pendulums can keep appropriate angles and gaits when the pulling forces from the EMs are applied to balance the intrinsic gravitational moments. In fact, the jointed beams can also keep stability even only one EM is activated because the jointed point A supports them at suitable angles by adjusting the pulling force from one EM via the ropes. Any changes of the horizontal displacement for free end B ($X = x_{OB} = OA \cos(\theta_1) + AB \cos(\theta_2) = l_1 \cos(\theta_1) + l_2 \cos(\theta_2)$) will modify the leg gaits and rotation angles (θ_1, θ_2), which depend on the pulling forcing from the EMs. In numerical approach, the gains (k_1, k_2) can select maximal value 1, and different constant values for T_1 and T_2 can be applied to detect the static gait angles (θ_1, θ_2).

Considering the continuous movements of the jointed pendulums as shown in Eq.(5), for simplicity, $P_1 = P_2$, $T_1 = T_2 = T$, $k_1 = k_2 = 1.0$. The internationally recognized normal ratio of thighs to calves is: the ideal size of thighs is height multiplied by 0.341, and the ideal size of calves is height multiplied by 0.21. The vertical supporting force N can be selected as zero or other positive value less than P_2 . Here, $l_1 = 0.6$ m, $l_2 = 0.4$ m, $g = 10.0$ N/kg, $P_1 = 2.5$ kg, $P_2 = 2.5$ kg, $N = 1$ kg, and then the Eq.(5) is updated by

$$\begin{cases} \frac{d\theta_2}{dt} = \omega_2, \\ \frac{d\omega_2}{dt} = \frac{3gk_2T_2 + 3Ng\cos\theta_2}{P_2l_2} - \frac{3g}{2l_2}\cos\theta_2 \\ = 30T_2 - 7.5\cos\theta_2, \\ \sin\theta_1 = \frac{l_2}{l_1}\sin\theta_2 = \frac{2}{3}\sin\theta_2. \end{cases} \quad (16)$$

By setting different constant values for T , the numerical solutions for Eq.(6) can discern the movements of the jointed pendulums/legs. As shown in Eq.(2), the pulling force T is proportional to the channel current across the motor coils, which shunts current from the driving neural circuits. Therefore, the force T can also be selected with a specific function, constants or periodic series for keeping static balance or continuous movement in the legs. For example, $T = k'z$ from Eq.(9) or $T_2 = k'z_2$ from Eq.(11), that is, the artificial muscle produces tension proportional to the channel current in the coils of the EM. The coefficient is mainly decided by the coils in the EM. The neuron in Eq.(9) and the

coupled neurons in Eq.(11) can be excited to present periodic, spiking, bursting activities, and then the movements of the jointed pendulums can be explored by finding numerical solutions from Eq.(16). When the anticlockwise torques are not balanced by the clockwise torques in the second formula in Eq.(16), the jointed pendulums or legs keep continuous rotation, as a result, the gait angles (θ_1, θ_2) will be beyond safe thresholds and the electromechanical legs are destroyed.

In practical way, the angles (θ_1, θ_2) are restricted within a scope less than $\pi/2$ during the changes of tension T including T_1 and T_2 , which should be adjusted in adaptive way. The channel current of the coils in the EMs, which are shunted from the neural circuit, can select negative or positive values; it indicates that the EM can switch its rotation directions following the changes of channel current. On the other hand, $T > 0$ means muscle contracts/shrinks while $T < 0$ means muscle relaxation. Therefore, a diode can be incorporated into the branch circuit connecting to the load circuit (EM), so that the channel current across the coils of the EM becomes unidirectional. During numerical approach, larger initial value for θ_2 means the muscle is contracted with high tension (pulling force), while smaller initial value for θ_2 means the muscle is relaxed with lower tension. In Fig. 8, the artificial muscle is activated with different tensions, and the values for T_2 in Eq.(16) are changed to detect the gait angles (θ_1, θ_2) under torques balance ($30T_2 = 7.5\cos\theta_2$), and the vertical axis is represented in radians.

From Fig. 8, appropriate setting for the muscle tensions can keep suitable leg gaits, and smaller values for the muscle tensions T_1 and T_2 will break the gait balance, as a result, the gait angles (θ_1, θ_2) will obtain negative values. As mentioned above, the channel current for the variable z and (z_1, z_2) can be regulated to keep negative or positive values, therefore, the EM generates clockwise or anticlockwise torques, which means the artificial muscles will present relaxation or contraction state with time, and the muscle tension T will select negative or positive values with the changes of channel currents in the EMs. In Fig. 9, the muscle tension T is controlled by the channel current as $T_2 = kz = 0.4z$ (switch between negative and positive values), and the evolution of gait angles and displacement x_B are plotted in Fig. 9.

From the results in Fig. 9, it is demonstrated that gait angles (θ_1, θ_2) can present values beyond the safe threshold $\pi/2$ when the electromechanical leg is controlled by the artificial muscles, which is regulated by the output signals from the neural circuit. Therefore, the channel current of the EMs should be controlled to keep positive values for the pulling forces (muscle tensions) T_1 and T_2 . As suggested above, $T = |kz|$, absolute value supports positive value for the pulling force in the artificial muscles. During circuit control, a diode can be used in the branch circuit connecting the coils of EMs (load circuit). For adaptive control, the

external forcing or one intrinsic parameter can be adjusted following the growth law in Eqs. (14) and (15), so that the EMs produce positive/anticlockwise torques to balance the clockwise tensions, as a result, the leg gaits are controlled in safe state.

In a summary, an artificial muscle device is proposed by regulating the length of the ropes winded to an EM, which is controlled by the electrical signals from a neural circuit. The coils of the EM is considered as load circuit (branch circuit) of the neural circuit, and the EMs produce suitable torques to control the contraction and relaxation of the muscles during changes of the length of flexible ropes. By taming the neural circuit, the channel current shunted from the neural circuit is modified to induce different torques and then the electromechanical leg keeps appropriate gaits.

4. Conclusions

In this paper, we suggested a simple model for artificial muscle by enwinding flexible ropes on an electronic motor, and the artificial muscles control the leg gaits by regulating the tensions (pulling forces). The leg gait is approached by using a pair of jointed pendulums and the electronic motor is driven by a neural circuit. The N-turns coils in the electronic motor are considered as a load circuit to the driving neural circuit. The neural circuit controls the rotation of electronic motor and the length of the winded rope is changed to mimic the contraction and relaxation of the muscles, as a result, the tensions and torques are modified to regulate the gait angles (θ_1, θ_2) for the jointed pendulums. In this way, the leg gaits are controlled effectively. This scheme can be further used to design and control artificial arms/legs, and complex body gaits can be controlled completely. It also provides clues to suppress movement disorders in presence of neural diseases including seizure, Parkinson's disease and Alzheimer's disease [86–90].

Data statements

No numerical data are used in this study.

CRediT authorship contribution statement

Yitong Guo: Visualization, Validation, Software, Formal analysis, Conceptualization. **Chunni Wang:** Writing – original draft, Visualization, Methodology, Investigation, Funding acquisition. **Jun Ma:** Writing – review & editing, Supervision, Project administration, Investigation.

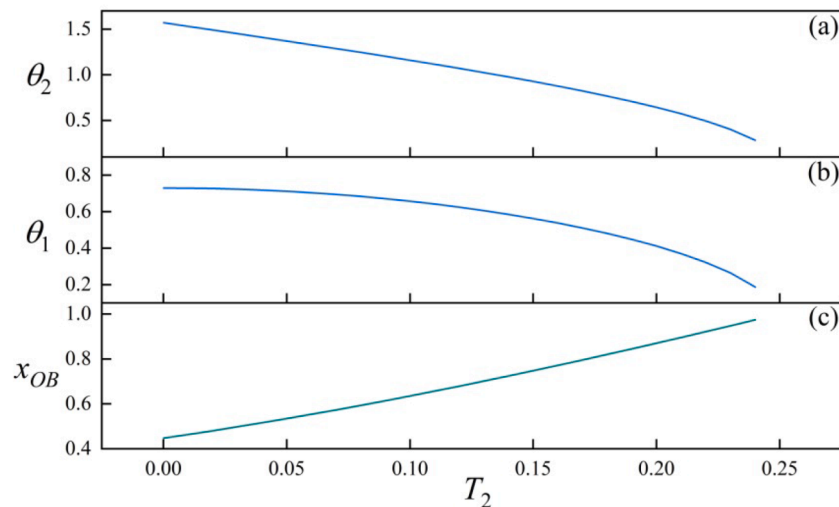


Fig. 8. Dependence of gait angles (θ_1, θ_2) and displacement x_B on muscle tension T_2 . For (a) θ_2 ; (b) θ_1 ; (c) displacement x_{OB} .

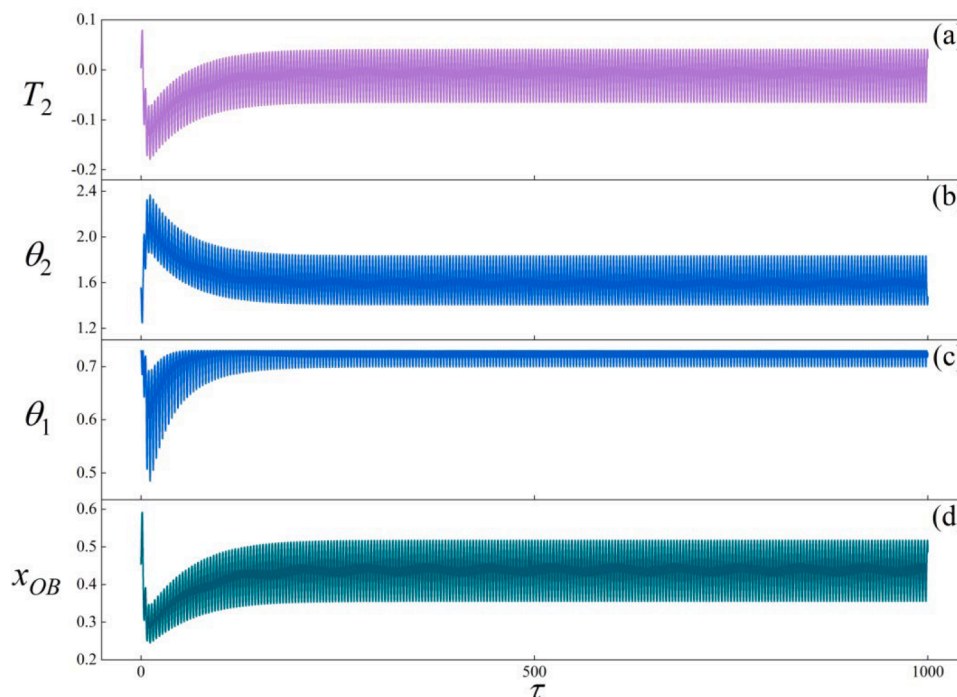


Fig. 9. Evolution of gait angles, muscle tension and displacement for point B vs. time. For (a) $T_2 = 0.4z$; (b) θ_2 ; (c) θ_1 ; (d) displacement x_{OB} . The series for variable z are generated from Eq.(9), setting parameters $A = 3.5$, $\omega = 1.6$, $\alpha = 0.3$, $b = 0.2$, $c = 0.3$, $d = 0.2$, $\beta = 0.1$, $i_s = A \cos(\omega \tau)$, initials (0.02, 0.01, 0.01).

Declaration of competing interest

The authors declare that they have no known competing financial interests or personal relationships that could have appeared to influence the work reported in this paper

Acknowledgements

This project is supported by National Natural Science Foundation of China under the Grant No. 62361037.

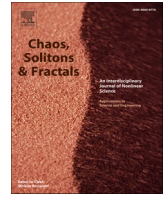
Data availability

No data was used for the research described in the article.

References

- [1] H.L. Sweeney, D.W. Hammers, Muscle contraction, *Cold Spring Harb Perspect Biol* 10 (2018) a023200.
- [2] A.V. Gomes, J.D. Potter, D. Szczesna-Cordary, The role of troponins in muscle contraction, *IUBMB Life* 54 (2002) 323–333.
- [3] W. Herzog, K. Powers, K. Johnston, et al., A new paradigm for muscle contraction, *Front. Physiol.* 6 (2015) 174.
- [4] T.A.J. Duke, Molecular model of muscle contraction, in: *Proceedings of the National Academy of Sciences* 96, 1999, pp. 2770–2775.
- [5] W. Herzog, T.R. Leonard, V. Joumaa, et al., Mysteries of muscle contraction, *J. Appl. Biomech.* 24 (2008) 1–13.
- [6] M. Caruel, L. Truskinovsky, Physics of muscle contraction, *Rep. Progr. Phys.* 81 (2018) 036602.
- [7] W. Herzog, R. Ait-Haddou, Considerations on muscle contraction, *J. Electromyogr. Kinesiol.* 12 (2002) 425–433.
- [8] D.E. Rassier, W. Herzog, Considerations on the history dependence of muscle contraction, *J. Appl. Physiol.* 96 (2004) 419–427.
- [9] A. Horowitz, C.B. Menice, R. Laporte, et al., Mechanisms of smooth muscle contraction, *Physiol. Rev.* 76 (1996) 967–1003.
- [10] W. Herzog, G. Schappacher-Tilp, Molecular mechanisms of muscle contraction: a historical perspective, *J. Biomech.* 155 (2023) 111659.
- [11] H. Rasmussen, Y. Takuwa, S. Park, Protein kinase C in the regulation of smooth muscle contraction, *FASEB J.* 1 (1987) 177–185.
- [12] J. Li, N.C. King, L.I. Sinoway, ATP concentrations and muscle tension increase linearly with muscle contraction, *J. Appl. Physiol.* 95 (2003) 577–583.
- [13] L. Marcucci, L. Truskinovsky, Muscle contraction: a mechanical perspective, *Eur. Phys. J. E* 32 (2010) 411–418.
- [14] S.J. Gunst, W. Zhang, Actin cytoskeletal dynamics in smooth muscle: a new paradigm for the regulation of smooth muscle contraction, *Am. J. Physiol.-Cell Physiol.* 295 (2008) C576–C587.
- [15] Z. Wang, S. Raunser, Structural biochemistry of muscle contraction, *Annu. Rev. Biochem.* 92 (2023) 411–433.
- [16] J.A. Rall, Mechanism of Muscular Contraction, Springer, New York, 2014.
- [17] L.J. Bhargava, M.G. Pandey, F.C. Anderson, A phenomenological model for estimating metabolic energy consumption in muscle contraction, *J. Biomech.* 37 (2004) 81–88.
- [18] A. Guillot, F. Lebon, D. Rouffet, et al., Muscular responses during motor imagery as a function of muscle contraction types, *Int. J. Psychophysiol.* 66 (2007) 18–27.
- [19] S. Puetz, L.T. Lubomirov, G. Pfister, Regulation of smooth muscle contraction by small GTPases, *Physiology* 24 (2009) 342–356.
- [20] D.A. Smith, M.A. Geeves, J. Sleep, et al., Towards a unified theory of muscle contraction. I: foundations, *Ann. Biomed. Eng.* 36 (2008) 1624–1640.
- [21] H. Jawad, N.N. Ali, A.R. Lyon, et al., Myocardial tissue engineering: a review, *J. Tissue Eng. Regen. Med.* 1 (2007) 327–342.
- [22] G. Karreman, C. Prood, Heart muscle contraction oscillation, *Int. J. Biomed. Comput.* 38 (1995) 49–53.
- [23] U. Freyschuss, Elicitation of heart rate and blood pressure increase on muscle contraction, *J. Appl. Physiol.* 28 (1970) 758–761.
- [24] V.F. Gladwell, J.H. Coote, Heart rate at the onset of muscle contraction and during passive muscle stretch in humans: a role for mechanoreceptors, *J. Physiol.* 540 (2002) 1095–1102.
- [25] E. Brunello, L. Fusi, A. Ghisleni, et al., Myosin filament-based regulation of the dynamics of contraction in heart muscle, in: *Proceedings of the National Academy of Sciences* 117, 2020, pp. 8177–8186.
- [26] J.M. Galvez, J.P. Alonso, L.A. Sangrador, et al., Effect of muscle mass and intensity of isometric contraction on heart rate, *J. Appl. Physiol.* 88 (2000) 487–492.
- [27] R.D. Vaughan-Jones, Excitation and contraction in heart: the role of calcium, *Br. Med. Bull.* 42 (1986) 413–420.
- [28] O. Berenfeld, A.V. Zaitsev, S.F. Mironov, et al., Frequency-dependent breakdown of wave propagation into fibrillatory conduction across the pectinate muscle network in the isolated sheep right atrium, *Circ. Res.* 90 (2002) 1173–1180.
- [29] J. Duclay, A. Martin, Evoked H-reflex and V-wave responses during maximal isometric, concentric, and eccentric muscle contraction, *J. Neurophysiol.* 94 (2005) 3555–3562.
- [30] J.L. Beckham, R. van Venrooy A, S. Kim, et al., Molecular machines stimulate intercellular calcium waves and cause muscle contraction, *Nat. Nanotechnol.* 18 (2023) 1051–1059.
- [31] C.R.C. Wyndham, Atrial fibrillation: the most common arrhythmia, *Tex. Heart. Inst. J.* 27 (2000) 257.
- [32] R.S. Wijesurendra, B. Casadei, Mechanisms of atrial fibrillation, *Heart.* 105 (2019) 1860–1867.
- [33] C. Gutierrez, D.G. Blanchard, Atrial fibrillation: diagnosis and treatment, *Am. Fam. Physician.* 83 (2011) 61–68.
- [34] K.M. Ryder, E.J. Benjamin, Epidemiology and significance of atrial fibrillation, *Am. J. Cardiol.* 84 (1999) 131–138.

- [35] P. Verdecchia, G.P. Reboldi, R. Gattobigio, et al., Atrial fibrillation in hypertension: predictors and outcome, *Hypertension* 41 (2003) 218–223.
- [36] J. Ma, Biophysical neurons, energy, and synapse controllability: a review, *J. Zhejiang Univ. Sci. A* 24 (2023) 109–129.
- [37] J. Ma, Z. Yang, L. Yang, et al., A physical view of computational neurodynamics, *J. Zhejiang Univ. Sci. A* 20 (2019) 639–659.
- [38] F. Yang, L. Ren, J. Ma, et al., Two simple memristive maps with adaptive energy regulation and digital signal process verification, *J. Zhejiang Univ. Sci. A* 25 (2024) 382–394.
- [39] Y. Li, M. Lv, J. Ma, et al., A discrete memristive neuron and its adaptive dynamics, *Nonlinear Dyn.* 112 (2024) 7541–7553.
- [40] H. Bao, K.X. Li, J. Ma, et al., Memristive effects on an improved discrete Rulkov neuron model, *Sci. China Technol. Sci.* 66 (2023) 3153–3163.
- [41] B. Ramakrishnan, M. Mehrabbeik, F. Parastesh, et al., A new memristive neuron map model and its network's dynamics under electrochemical coupling, *Electronics* (Basel) 11 (2022) 153.
- [42] N. Zandi-Mehran, S. Panahi, Z. Hosseini, et al., One dimensional map-based neuron model: a phase space interpretation, *Chaos, Soliton. Fractals* 132 (2020) 109558.
- [43] J. Jia, C. Wang, X. Zhang, et al., Energy and self-adaption in a memristive map neuron, *Chaos, Soliton. Fractal.* 182 (2024) 114738.
- [44] Y.T. Guo, J. Ma, X.F. Zhang, et al., Memristive oscillator to memristive map, energy characteristic, *Sci. China Technol. Sci.* 67 (2024) 1567–1578.
- [45] F. Wu, Y. Guo, J. Ma, Energy flow accounts for the adaptive property of functional synapses, *Sci. China Technol. Sci.* 66 (2023) 3139–3152.
- [46] M. Perc, The dynamics of human gait, *Eur. J. Phys.* 26 (2005) 525.
- [47] Y. Ashkenazy, J.M. Hausdorff, P.C. Ivanov, et al., A stochastic model of human gait dynamics, *Physica A: Stat. Mech. Appl.* 316 (2002) 662–670.
- [48] N. Scafetta, D. Marchi, B.J. West, Understanding the complexity of human gait dynamics, *Chaos: An Interdisciplinary Journal of Nonlinear Science* 19 (2009) 026108.
- [49] C. Vimieiro, E. Andrada, H. Witte, et al., A computational model for dynamic analysis of the human gait, *Comput. Methods Biomech. Biomed. Engin.* 18 (2015) 799–804.
- [50] S.M. Bruijn, J.H. Van Dieën, Control of human gait stability through foot placement, *J. R. Soc. Interf.* 15 (2018) 20170816.
- [51] M. Ezati, B. Ghannadi, J. McPhee, A review of simulation methods for human movement dynamics with emphasis on gait, *Multibody Syst. Dyn.* 47 (2019) 265–292.
- [52] J. Sun, S. Wu, P.A. Voglewede, Dynamic simulation of human gait model with predictive capability, *J. Biomech. Eng.* 140 (2018) 031008.
- [53] T. Kashima, Y. Isurugi, M. Shima, Analysis of a muscular control system in human movements, *Biol. Cybern.* 82 (2000) 123–131.
- [54] G.J.V.I. Schenau, From rotation to translation: constraints on multi-joint movements and the unique action of bi-articular muscles, *Hum Mov Sci* 8 (1989) 301–337.
- [55] G.F. Koshland, J.C. Galloway, C.J. Nevoret-Bell, Control of the wrist in three-joint arm movements to multiple directions in the horizontal plane, *J. Neurophysiol.* 83 (2000) 3188–3195.
- [56] C.J. Ketcham, N.V. Dounskaia, G.E. Stelmach, Multijoint movement control: the importance of interactive torques, *Prog. Brain Res.* 143 (2004) 207–218.
- [57] H. Kimura, M. Kataoka, S. Suzuki, et al., A flexible robotic arm with hydraulic skeleton, *J. Adv. Mech. Des. Syst. Manuf.* 6 (2012) 1107–1120.
- [58] A. Kargov, T. Werner, C. Pylatiuk, et al., Development of a miniaturised hydraulic actuation system for artificial hands, *Sensor. Actuator. A: Phys.* 141 (2008) 548–557.
- [59] M. Feng, J. Dai, W. Zhou, et al., Kinematics analysis and trajectory planning of 6-DOF hydraulic robotic arm in driving side pile, *Machines* 12 (2024) 191.
- [60] Y. Qiu, E. Zhang, R. Plamthottam, et al., Dielectric elastomer artificial muscle: materials innovations and device explorations, *Acc. Chem. Res.* 52 (2019) 316–325.
- [61] S.M. Mirvakili, I.W. Hunter, Artificial muscles: mechanisms, applications, and challenges, *Adv. Mater.* 30 (2018) 1704407.
- [62] D.R. Higuera-Ruiz, K. Nishikawa, H. Feigenbaum, et al., What is an artificial muscle? A comparison of soft actuators to biological muscles, *Bioinspir. Biomim.* 17 (2021) 011001.
- [63] K.C. Wickramatunge, T. Leephakpreeda, Study on mechanical behaviors of pneumatic artificial muscle, *Int. J. Eng. Sci.* 48 (2010) 188–198.
- [64] J. Mehrholz, A. Hädrich, T. Platz, et al., Electromechanical and robot-assisted arm training after stroke: updated review, *Stroke* 43 (2012) e172–e173.
- [65] A. Notué Kadjie, P.R. Nwagoum Tuwa, P. Wofo, An electromechanical pendulum robot arm in action: dynamics and control, *Shock Vib.* 2017 (2017) 3979384.
- [66] R. Kouam Tagne, P. Wofo, J. Awrejcewicz, Dynamics of the rotating arm of an electromechanical system subjected to the action of circularly placed magnets: numerical study and experiment, *Int. J. Bifurcat. Chaos* 33 (2023) 2350052.
- [67] N.K. Mbeunga, B. Nana, P. Wofo, Dynamics of array mechanical arms coupled each to a Fitzhugh-Nagumo neuron, *Chaos Soliton. Fractals* 153 (2021) 111484.
- [68] J. Ma, Y. Guo, Model approach of electromechanical arm interacted with neural circuit, a minireview, *Chaos Soliton. Fractal.* 183 (2024) 114925.
- [69] Y. Guo, X. Song, J. Ma, Control electromechanical arms by using a neural circuit, *Nonlinear Dyn.* (2024), <https://doi.org/10.1007/s11071-024-10260-3>.
- [70] L. Zhang, W. Jin, Simulating the motion of a mechanical arm driven by neural circuit, *Phys. Scr.* 99 (2024) 115213.
- [71] N.C. Heer, A.C. Martin, Tension, contraction and tissue morphogenesis, *Development* 144 (2017) 4249–4260.
- [72] A. Rachev, K. Hayashi, Theoretical study of the effects of vascular smooth muscle contraction on strain and stress distributions in arteries, *Ann. Biomed. Eng.* 27 (1999) 459–468.
- [73] Y.Y. Mei, M.H. Lee, T.C. Cheng, et al., NMDA receptors sustain but do not initiate neuronal depolarization in spreading depolarization, *Neurobiol. Dis.* 145 (2020) 105071.
- [74] A. Kitamura, H. Ishibashi, M. Watanabe, et al., Sustained depolarizing shift of the GABA reversal potential by glutamate receptor activation in hippocampal neurons, *Neurosci. Res.* 62 (2008) 270–277.
- [75] W. Herzog, Mechanisms of enhanced force production in lengthening (eccentric) muscle contractions, *J. Appl. Physiol.* 116 (2014) 1407–1417.
- [76] N.D. Reeves, M.V. Narici, Behavior of human muscle fascicles during shortening and lengthening contractions in vivo, *J. Appl. Physiol.* 95 (2003) 1090–1096.
- [77] B. Pasquet, A. Carpentier, J. Duchateau, Specific modulation of motor unit discharge for a similar change in fascicle length during shortening and lengthening contractions in humans, *J. Physiol.* 577 (2006) 753–765.
- [78] A.A. Jones, G.A. Power, W. Herzog, History dependence of the electromyogram: implications for isometric steady-state EMG parameters following a lengthening or shortening contraction, *J. Electromyogr. Kinesiol.* 27 (2016) 30–38.
- [79] R. De Vita, R. Grange, P. Nardinocchi, et al., Mathematical model for isometric and isotonic muscle contractions, *J. Theor. Biol.* 425 (2017) 1–10.
- [80] B.M. Baroni, C.M.A. Stoccheri, R.C. do Espírito Santo, et al., The effect of contraction type on muscle strength, work and fatigue in maximal isokinetic exercise, *Isokinet. Exerc. Sci.* 19 (2011) 215–220.
- [81] H. Bao, Y. Gu, Q. Xu, et al., Parallel bi-memristor hyperchaotic map with extreme multistability, *Chaos Soliton. Fractal.* 160 (2022) 112273.
- [82] J. Zhang, H. Bao, J. Gu, et al., Multistability and synchronicity of memristor coupled adaptive synaptic neuronal network, *Chaos, Soliton. Fractals* 185 (2024) 115157.
- [83] Y. Yu, Y. Fan, S. Hou, et al., Optogenetic stimulation of primary motor cortex regulates beta oscillations in the basal ganglia: a Computational study, *Commun. Nonlinear Sci. Numer. Simul.* 117 (2023) 106918.
- [84] D. Fan, Y. Wang, J. Wu, et al., The preview control of a corticothalamic model with disturbance, *Electron. Res. Arch.* 32 (2024) 812–835.
- [85] J. Zhao, Y. Yu, F. Han, et al., Dynamic modeling and closed-loop modulation for absence seizures caused by abnormal glutamate uptake from astrocytes, *Nonlinear Dyn.* 112 (2024) 3903–3916.
- [86] D. Fan, H. Wu, G. Luan, et al., The potential scale-free network mechanism underlying the formation of focal epilepsy, *Europhys. Lett.* 141 (2023) 32002.
- [87] C.A. Davie, A review of Parkinson's disease, *Br. Med. Bull.* 86 (2008) 109–127.
- [88] S. Fanning, D. Selkoe, U. Dettmer, Parkinson's disease: proteinopathy or lipidopathy? *NPJ. Parkinsons. Dis.* 6 (2020) 3.
- [89] A. Monsonego, H.L. Weiner, Immunotherapeutic approaches to Alzheimer's disease, *Science* (1979) 302 (2003) 834–838.
- [90] R.B. Maccioni, L.E. Rojo, J.A. Fernandez, et al., The role of neuroimmunomodulation in Alzheimer's disease, *Ann. N. Y. Acad. Sci.* 1153 (2009) 240–246.



Jointed pendulums driven by a neural circuit, electromechanical arm model approach

Yitong Guo^{a,c}, Chunni Wang^b, Jun Ma^{a,b,*}

^a College of Electrical and Information Engineering, Lanzhou University of Technology, Lanzhou 730050, China

^b Department of Physics, Lanzhou University of Technology, Lanzhou 730050, China

^c Department of Mathematics, North University of China, Taiyuan 030051, Shanxi, China

ARTICLE INFO

Keywords:

Neural circuit
Hamilton energy
Electromechanical arm
Gear drive
Stability

ABSTRACT

The mechanical characteristic of an arm can be investigated in a two-stage cascade pendulum, which two jointed pendulums rotate to a jointed point and move forward for keeping stable gaits. The arm gaits and stability are controlled by the electrical signal interacted with the muscle. In this paper, two short beams are jointed to mimic the motion and stability of an arm driven by electromechanical force, which is generated from the gear or friction interaction between a beam and electromotor activated by electric signals from a neural circuit. On end of the artificial arm is jointed to a fixed point, another end is connected to a moving beam along horizontal direction. An electrical motor is driven by the output signals from a neural circuit, and it generates effective horizontal force to control the stability and gaits in the coupled pendulums via a gear interaction. When the electrical motor (EM) is activated, it has a feedback on the driving neural circuit by changing the firing activities because the load circuit of the EM generates induced electromotive force as an additive branch circuit of the neural circuit, and this interaction is similar to the processing that athletic training can modify the mentality by training the neural activities. External physical signal is applied and changed to control the neural circuit, and then the moving beam can impose time-varying force to control the stability of the jointed pendulums. In presence of noisy excitation, similar nonlinear resonance can be induced in the neural circuit. The dynamics in the neural circuit-coupled pendulums is explored in detail. That is, the neural circuit regulates the EM for generating electromechanical force and then the jointed pendulums are controlled in the arm gaits. This mechanical process is similar to the rehabilitation training for disabled arms with movement disorders. The results provide helpful clues to design artificial electromechanical arm and application of arm rehabilitation for muscular injuries.

1. Introduction

Skeletal muscles are controlled by electrical signals from nervous system [1–5] and different body gaits depend on the muscle contraction and relaxation. After a stroke [6–8], the body gaits are corrupted and the arms seldom behave normal behaviors. Movement related impairments and limitations in walking are common long-term after stroke. On the other hand, trembling arms [9–13] is considered as disability in body gaits due to impairments in the arm and abnormality in nervous system. Therefore, it is worthy of investigating approach of electromechanical arms and legs [14–19], and jointed pendulums [20–24] can be driven by circuit array or neural circuits [25–29], which can encode external physical signals including light and voice, and then these biophysical neurons [30–34] derived from functional neural circuits [35–39] can be

used to control the artificial arms or legs.

A generic neuron model can present distinct firing patterns including quiescent, spiking, bursting and even chaotic characteristic by applying appropriate external stimulus, and noisy excitation can induce a kind of nonlinear resonance including stochastic resonance and coherence resonance [40–44], logical resonance [45–49] and chaotic resonance occurs by applying filtered signals [50–54]. The simple neuron models can be described by nonlinear oscillator [55–58] or maps [59–62], and functional description can be enhanced by introducing more specific nonlinear terms into the mathematical neurons or biological neurons for proposing some functional neurons [63–67], which can perceive external illumination, temperature changes, acoustic wave and electromagnetic field by incorporating different electronic components into the neural circuits. For example, the memristive neurons developed

* Corresponding author at: College of Electrical and Information Engineering, Lanzhou University of Technology, Lanzhou 730050, China.

E-mail addresses: hyperchaos@lut.edu.cn, hyperchaos@163.com (J. Ma).

<https://doi.org/10.1016/j.chaos.2024.115739>

Received 5 August 2024; Received in revised form 12 October 2024; Accepted 1 November 2024

0960-0779/© 2024 Elsevier Ltd. All rights are reserved, including those for text and data mining, AI training, and similar technologies.

from neural circuit composed of memristors [68–70] can be controlled to show multistability [71,72] and intrinsic electromagnetic induction and even radiation can be estimated in theoretical way [73–76]. Based on these memristive neurons [77–81], self-organization and collective behaviors can be explored in the memristive neural networks [82–85], and spatial electromagnetic radiation [86,87] has distinct impact on the wave propagation in the networks. That is, involvement of memristor enhances the controllability of neural circuit and self-adaptive property of biophysical neurons can be released by the energy flow [88,89]. For a brief guidance, readers can find clues in the recent reviews and the references therein [90,91].

Arm gaits can be simulated by using a paired jointed pendulums connecting to a fixed point, and the contraction and relaxation of an arm in a plane produce similar rotation and movements in the jointed pendulums driven by an external force. The movements of biological arms are controlled by muscles, and relaxation and contraction of muscles adhered to the skeleton are adjusted by the neural signals. As a result, disabled arms/legs due to muscles disability seldom present normal movements, and necessary rehabilitation training becomes important by applying continuous forcing on the arm end [92]. On the other hand, smart mechanical arms of robots often depend on the involvement of artificial tissue for generating more freedom degrees in motion. Two-degree-of-freedom robotic manipulators [93–97] have been investigated in the past twenty years. For reliable control, neural networks are proposed to stabilize the robotic manipulators [98–100]. Indeed, the shape memory enables alloys to represent muscles and tendons [101–105]. In fact, electromagnetic brakes in joints [106–110] are important for the gaits control and thus the artificial arms can behave complex gaits and movements. On the other hand, magnetorheological fluids are effective for designing brakes in joints [111–115] and thus the robot gaits can be controlled effectively. From mechanical aspect, the movement and rotation of electromechanical device including arms and legs depend on active driving and excitation for electromechanical forces, which can be generated from electric motors or pneumatic systems [116–120], the involvement of neural circuit interacting with the control device can guide the robots to present smart responses and actions.

In this paper, two pendulums are jointed to mimic the motion of an arm, one end of the jointed pendulums is hanged to a rotating point and another end is jointed to a moving beam geared with an electrical motor. The torques of the electrical motor is dependent on the electrical signal from a neural circuit composed of a magnetic flux-controlled memristor (MFCM). The jointed pendulums-coupled with moving beam is considered as an electromechanical device for mimicking the dynamical property of artificial arm driven by neural signals generated from a neural circuit. The kinetics relation, mechanical interaction between the jointed pendulums and moving beam (excitation source), circuit equation and energy characteristic are defined and discussed. The scheme is helpful to design reliable artificial arms and further dynamical control in the electromechanical devices.

2. Model and control strategy

An arm can behave different gaits due to the interaction between muscles and nervous electrical signals. Contraction exercise can train the muscle and arm flexibility, and the motion of arms can be controlled by the electrical signals from nervous system. When the palm suffers from external mechanical force, the movement of the arms can be estimated by the measuring the movements and stability of two jointed pendulums in a plane space. The external applied torques keeps against the muscle contraction and intrinsic gravity of skeleton, and then appropriate arm gaits are stabilized synchronously.

2.1. Simulation of an arm with jointed cascade pendulums

The mechanical characteristic of an arm can be investigated when

the arm is considered as cascade pendulums shown in Fig. 1.

The cascade pendulums suffered to two different gravitational moments and an external moment activated by a horizontal force $F(t)$ via a beam with length l . The cascade pendulums can rotate to the hanging points O and A_0 in Fig. 1. Horizontal force to the right can generate counterclockwise torques to be against the clockwise gravitational torques, and the two jointed pendulums can be controlled to keep balance. On the other hand, applying Horizontal force to the left long a beam is also effective to control stability in the jointed pendulums when the horizontal beam is jointed to the connecting point B_0 . To keep static balance and stability in the jointed cascade pendulums, the torques equation meets the following criterion in Eq. (1).

$$\begin{cases} P_1 \cdot \frac{l_1}{2} \cos \theta_1 + P_2 \cdot \left(l_1 \cos \theta_1 + \frac{l_2}{2} \cos \theta_2 \right) = F \cdot (l_1 \sin \theta_1 + l_2 \sin \theta_2), \\ P_2 \cdot \frac{l_2}{2} \cos \theta_2 = F \cdot l_2 \sin \theta_2. \end{cases} \quad (1)$$

When the jointed pendulums are used to mimic the mechanical response, the force $F(t)$ can be considered as a mechanical control from the muscle. Furthermore, correlation in Eq. (1) can be updated to present a simple form as follows

$$\begin{cases} P_1 \cdot \frac{l_1}{2} \cos \theta_1 + P_2 \cdot l_1 \cos \theta_1 = F \cdot l_1 \sin \theta_1, \\ P_2 \cdot \frac{l_2}{2} \cos \theta_2 = F \cdot l_2 \sin \theta_2. \end{cases} \quad (2)$$

When external forcing $F(t)$ is fixed, the compound pendulums control their correlated angles in stable state.

$$\begin{cases} \tan \theta_1 = \frac{P_1 + 2P_2}{2F}, \\ \tan \theta_2 = \frac{P_2}{2F}. \end{cases} \quad (3)$$

Indeed, any changes of the forcing value $F=F(t)$ can modify the gait of the two jointed pendulums, which will rotate to a new pairs of angles for keeping stable gaits. Therefore, the angle relation between θ_1 and θ_2 is dependent on the applied force F with time. In a practical way, the beam forcing along horizontal direction can be selected with a pulse form, periodic and even chaotic type, and the coupled pendulums will keep different gaits by changing the angles (θ_1, θ_2) synchronously. According to the stability criterion in Eq. (3) and Fig. 1, the jointed pendulums keep stability at $\theta_1 > \theta_2$ and instability occurs at $\theta_1 = \theta_2$. For example, it means damage of the arms at $\theta_2 > \theta_1$. On the other hand, direction switch of horizontal forcing F along horizontal axis positive direction to the left direction also can supports dynamical stability and balance of the two pendulums as well because of jointed interaction via point B_0 , and this case $\theta_1 < \theta_2$ just occurs for jointed pendulums. In a generic way, periodic $F(t)$ can break the gait stability of the two jointed pendulums.

In fact, when the end point of the jointed pendulums B_0 is activated by a continuous forcing without connecting a horizontal beam (no jointed interaction), the jointed pendulums can keep dynamical balance during changes of the angles (θ_1, θ_2). For example, the force $F(t)$ in Eq. (3) can be selected with periodic or chaotic signals from a nonlinear circuit or neuron oscillator, in a simple way, the output voltage series equal to the value for $F(t)$, the gaits for the jointed pendulums will be controlled completely.

2.2. Horizontal reciprocating motion of a moving beam

As shown in Fig. 1, applying a horizontal force to the right direction can keep stable state in the jointed pendulums and switch of horizontal force to the left will break the stability of the coupled pendulums. Therefore, time-varying force $F(t)$ will change the arm gait and stability in the jointed pendulums accompanying with changes in the angles ($\theta_1,$

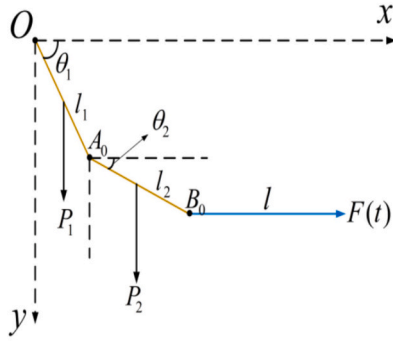


Fig. 1. Schematic diagram for a pair of cascade pendulums. P_1 and P_2 represent the gravity for the pendulum with a length l_1 and l_2 , respectively. The time-varying force $F(t)$ is applied along the horizontal direction via a beam with a length l , which is jointed to the coupled pendulums.

θ_2). In practice, the moving beam with a length l can be driven by an electrical motor via gear or friction as shown in Fig. 2.

According to Fig. 2, the horizontal beam is forced to keep reciprocating motion via gears interaction when the gear adhered to the electric motor is driven the motor. When one end of the moving beam in Fig. 2 is jointed to the end terminal B_0 of the coupled pendulums in Fig. 1, continuous forcing will generate time-varying torques, which is effective to change the movement and rotation of the two jointed pendulums. The electrical motor has an N-turns coil and its electric torques is measured by

$$\begin{cases} \vec{M} = \vec{P}_m \times \vec{B} = N I_s S \hat{n} \times \vec{B}, \\ M = N \cdot I_s \cdot S \cdot B \cdot \sin(\hat{n}, \vec{B}) = NS I_s B \sin(\hat{n}, \vec{B}). \end{cases} \quad (4)$$

where the parameters (B, S, I_s) denote the magnetic field intensity, coil area and current intensity across the N-turns coil in the electrical motor, respectively. That is, the electric torques is mainly controlled by the current I_s across the coil, and this current will be generated from a neural circuit in subsection 2.3. The N-turns coil is considered as an additive branch circuit or load circuit of the driving neural circuit. By applying larger value for the current I_s across the electric motor, a stronger torques is generated to speed up the moving beam and the jointed pendulums will be controlled with a larger force $F(t)$. Periodical change in the current I_s can generate clockwise and counterclockwise torques, respectively, and then the moving beam will move to opposite directions intermittently. As a result, the joint pendulums will keep different rotation directions, and this processing is similar to the stretching and relaxing movement of arms. As shown in Fig. 2, the electromagnetic torques can impose tangential force on the moving beam via gear interaction, the motor has a radius r and the tangential force from the EM can be approached by

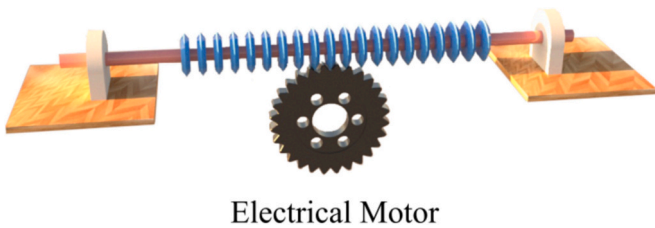
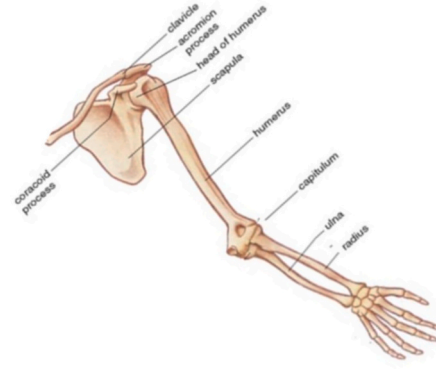


Fig. 2. Reciprocating motion of a beam driven by an electrical motor (EM). The rotation of the motor can be driven by electrical signals from a neural circuit, and switch of the output voltage from negative to positive value will control the rotation direction of the motor and the moving beam is switched in the directions.



$$F = F(t) = \frac{NS I_s B}{r} \sin(\hat{n}, \vec{B}) = \frac{NS I_s(t) B}{r} \sin(\omega_0 t). \quad (5)$$

The parameter ω_0 measures the angular frequency of the electrical motor and it is relative to the external load driven by the motor because of resistive torques. The moving beam can apply load damping to the electrical motor via gear interaction because the two jointed pendulums can apply feedback via jointed point B_0 to the beam, and then the motor can keep continuous rotation under fixed angular frequency, which is also restricted by the velocity of the moving beam as $\omega_0 r = dx/dt$. The variable x measures the displacement of the moving beam. For animal arms or legs, the modulation of body gaits is controlled by the muscle via electrical signals from nervous system. On the other hand, continuous muscle training has positive feedback on the nervous system and the neural activities can be tamed effectively. Supposing the moving beam interacted with the electrical motor has a quality m , and its dynamics of displacement x is measured by

$$\begin{cases} m \frac{d^2 x}{dt^2} + \eta \frac{dx}{dt} = F(t) = \frac{NS I_s(t) B}{r} \sin(\omega_0 t), \\ \frac{dx}{dt} = \omega_0 r = v. \end{cases} \quad (6)$$

The second term in the first formula of Eq. (6) denotes the damping modulation due to constraint from the jointed pendulums, and it is proportional to the moving velocity with a constant gain η . Eq. (6) can be replaced by an equivalent couple of first order differential equations as follow

$$\begin{cases} \frac{dx}{dt} = v, \\ \frac{dv}{dt} = \frac{NS I_s(t) B}{mr} \sin(\omega_0 t) - \frac{\eta}{m} v. \end{cases} \quad (7a)$$

Or

$$\begin{cases} \frac{dx}{dt} = v, \\ \frac{dv}{dt} = \frac{NS I_s(t) B}{mr} \sin\left(\frac{v}{r} t\right) - \frac{\eta}{m} v. \end{cases} \quad (7b)$$

Furthermore, the current variable I_s in Eqs. (7a) and (7b) can be converted to dimensionless variable for obtaining a dimensionless oscillator model for the displacement and velocity. Reciprocating motion of a moving beam will apply time-varying force to the jointed pendulums to rotate the jointed points and their mechanical energy is mainly kept as rotational kinetic energy (W_{P1} , W_{P2}), and the moving beam keeps a translational kinetic energy (W_I).

$$\begin{cases} W_{P1} = \frac{1}{2}J_1\omega_1^2 = \frac{1}{2}\left(\frac{1}{3}\frac{P_1l_1^2}{g}\right)\omega_1^2 = \frac{1}{6g}P_1l_1^2\left(\frac{d\theta_1}{dt}\right)^2, \\ W_{P2} = \frac{1}{2}J_2\omega_2^2 = \frac{1}{2}\left(\frac{1}{3}\frac{P_2l_2^2}{g}\right)\omega_2^2 = \frac{1}{6g}P_2l_2^2\left(\frac{d\theta_2}{dt}\right)^2, \\ W_l = \frac{1}{2}m\left(\frac{dx}{dt}\right)^2 = \frac{1}{2}mv^2. \end{cases} \quad (8)$$

From Eq. (3), the evolution of rotation angles (θ_1, θ_2) for the coupled pendulums can be obtained by

$$\begin{cases} \frac{d\theta_1}{dt} = \omega_1 = \frac{P_1 + 2P_2}{2}\cos^2\theta_1 \frac{d}{dt}\left(\frac{1}{F(t)}\right) \\ \quad = -\frac{r(P_1 + 2P_2)\cos^2\theta_1}{2NBSI_s^2(t)\sin^2(\omega_0 t)} \left[\frac{dI_s(t)}{dt}\sin(\omega_0 t) + \omega_0 I_s(t)\cos(\omega_0 t) \right], \\ \frac{d\theta_2}{dt} = \omega_2 = \frac{P_2}{2}\cos^2\theta_2 \frac{d}{dt}\left(\frac{1}{F(t)}\right) \\ \quad = -\frac{rP_2\cos^2\theta_2}{2NBSI_s^2(t)\sin^2(\omega_0 t)} \left[\frac{dI_s(t)}{dt}\sin(\omega_0 t) + \omega_0 I_s(t)\cos(\omega_0 t) \right]. \end{cases} \quad (9)$$

During the time-varying modulation from $F(t)$, the angular velocities for the two jointed pendulums have distinct ratio at $\omega_1:\omega_2 = (P_1+P_2)\cos^2(\theta_1)/(P_2\cos^2(\theta_2))$. For simple case $P_1=P_2$, it obtains $\omega_1:\omega_2 = 2\cos^2\theta_1/\cos^2\theta_2$. As shown in Eq. (6), the mechanical forcing $F(t)$ is dependent on the product of two time variables, and the angular velocity in Eq. (9) and rotational kinetic energy in Eq. (8) can be estimated by numerical approach. Similar to Eq. (7b), the variable ω_0 in Eq. (9) can be replaced with $\omega_0 = v/r$ and rotation frequency of electrical motor can be approached synchronously. In fact, during continuous rotation of the two jointed-pendulums, the angles (θ_1, θ_2) are modified synchronously to satisfy the stability criterion in Eq. (3) and the ration for angular frequency ($\omega_1:\omega_2$) is dependent of external force $F(t)$. Referring to the hanging point (original point) O , the displacement or jointed points position (x, y) is given in

$$\begin{cases} x_{B0} = l_1\cos\theta_1 + l_2\cos\theta_2, & y_{B0} = l_1\sin\theta_1 + l_2\sin\theta_2, \\ x_{A0} = l_1\cos\theta_1, & y_{A0} = l_1\sin\theta_1. \end{cases} \quad (10)$$

When the position (x, y) or (x_{B0}, y_{B0}) for the jointed point B_0 is detected, the jointed point A_0 is predicted simultaneously. That is, the jointed pendulums keep two freedoms when a horizontal forcing is

applied to the terminal end B_0 . According to Fig. 2, the jointed point B_0 is driven by the left terminal end of the moving beam forced by the EM, that is, the displacement x can obtained under the constraint condition in Eq. (7b). Therefore, numerical solutions from Eq. (7) obtains the evolution of displacement variable $x = x_{B0}$, and then the change relations can be detected from the first formula in Eq. (10). When the two jointed pendulums are forced, the torque constraint for the jointed point B_0 is derived by

$$M = J \frac{d^2\theta_2}{dt^2} = F \cdot l_2 \sin\theta_2 - P_2 \cdot \frac{l_2}{2} \cos\theta_2 = \frac{P_2 l_2^2}{3g} \frac{d^2\theta_2}{dt^2}. \quad (11)$$

where $J = P_2 l_2^2/3g$ represents the moment of inertia for the pendulum A_0B_0 against to the jointed point B_0 . The angle series θ_2 can be obtained from Eq. (11), and available series for displacement $x = x_{B0}$ support the solution for the evolution of angle series θ_1 according to the displacement condition in Eq. (10) when the force $F=F(t)$ is detected or known. Indeed, scale transformation should be applied to the variables in Eqs. (7a)–(11) to obtain equivalent dimensionless forms during numerical approach when the force $F=F(t)$ is generated from EM driven by the neural circuit. A complete dynamical description for movement of the jointed pendulums is shown in Eq. (12) for any known force $F=F(t)$, which is applied to the point B_0 .

$$\begin{cases} \frac{dx}{dt} = v, \\ \frac{dv}{dt} = \frac{F(t)}{m} - \frac{\eta}{m}v, \\ \frac{d\theta_2}{dt} = \omega_2, \\ \frac{d\omega_2}{dt} = \frac{3g}{2P_2 l_2} [2F(t)\sin\theta_2 - P_2\cos\theta_2], \\ \cos\theta_1 = \frac{1}{l_1}(x_{B0} - l_2\cos\theta_2) = \frac{x - l_2\cos\theta_2}{l_1}, \\ \text{or, } \theta_1 = \arccos\left(\frac{x - l_2\cos\theta_2}{l_1}\right). \end{cases} \quad (12)$$

That is, the angles (θ_1, θ_2) and displacement x can obtain the numerical solutions from Eq. (12), and the jointed point B_0 also detect its displacement $y = y_{B0}$ along y -axis direction following the criterion in Eq. (10). Therefore, the position for jointed A_0 can also be detected

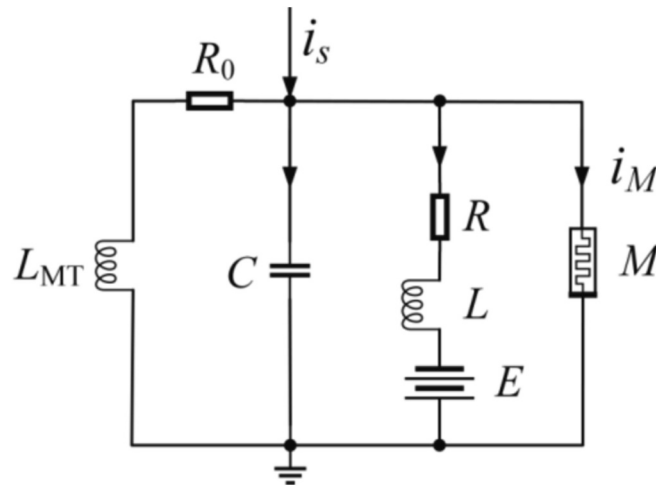


Fig. 3. Schematic diagram for the electrical motor-coupled neural circuit. L_{MT} denotes the inductance of the N -turns coil in the electric motor, C, L, M represents the capacitor, inductor and memristor, R_0 is the intrinsic resistance of the electric motor, R and E represents the resistance and reverse voltage in the ion channel. External physical signal i_s is applied to excite the neural circuit.

according to Eq. (10) when the numerical solutions for (θ_1, θ_2) are available from Eq. (12) by setting any constant value or periodic value for $F(t)$.

2.3. Electromechanical arm coupled with a neural circuit

The electrical motor forced the moving beam to control the jointed pendulums, and the electromagnetic torques is dependent on the output voltage and current from the driving neural circuit, which is controlled by external physical signals, for example, acoustic wave or illumination can be converted to equivalent electrical signals applied to the neural circuit. The electromagnetic induction in the electric motor has distinct feedback on the driving neural circuit via a linear resistor R_0 , and the driving-response neural circuit and motor circuit are presented in Fig. 3.

The electric motor adhered to the moving beam can mimic the interaction between muscle and neural electrical signals, and the electromechanical coupling between jointed pendulums and neural circuits is approached by applying load circuit to the driving neural circuit. For simplicity, a magnetic flux-controlled memristor (MFCM) is considered in the branch circuit of the neural circuit in Fig. 3. The channel current across the MFCM is approached by

$$i_M = M(\phi)V = (\alpha + 3\beta\phi^2)V. \quad (13)$$

where the variable V represents the voltage for the capacitor and memristor, and the parameters (α, β) are relative to the material property of the MFCM. In presence of external magnetic field, the magnetic flux ϕ for the memristive channel will be affect and then the memristive current across the memristor has distinct modulation on the capacitive channel, which is also controlled by external forcing i_s and inductive channel current i_L as well. The correlation between the physical variables in Fig. 3 can be described by the circuit equations according to the Kirchhoff's theorem, and dynamics of the voltage, induction current and magnetic flux variables for the Fig. 3 are given in

$$\begin{cases} C \frac{dV}{dt} = i_s - I_s - i_M - i_L, \\ L_{MT} \frac{di_s}{dt} = V - I_s R_0, \\ L \frac{di_L}{dt} = V + E - i_L R, \\ \frac{d\phi}{dt} = V + k_1 \phi. \end{cases} \quad (14)$$

where the variables (V, I_s, i_L) indicates the voltage across the capacitor, channel current for the load coil with inductance L_{MT} and the inductor L , respectively. When the equivalent load inductor in Fig. 3 is removed, it indicates that the neural circuit cuts connection to the electromechanical device and the electric motor is switched off excitation from the neural circuit. The physical parameter k_1 is relative to the material property of the memristor and high value for k_1 means that intracellular ions in the memristor are active to support the occurrence of magnetic field. High order term associated with the memristive current i_M in Eq. (13) and Eq. (14) seldom supports an exact analytical solution for the neural circuit. Therefore, scale transformation is applied to the physical variables in Eq. (14), and a group of new dimensionless variables and parameters are obtained by

$$\begin{cases} u_1 = \frac{V}{E}, \quad u_2 = \frac{I_s R}{E}, \quad u_3 = \frac{i_L R}{E}, \quad \varphi = \frac{\phi}{RCE}, \\ \tau = \frac{t}{RC}, \quad i'_s = \frac{Ri_s}{E}, \quad \alpha' = \alpha R, \quad \beta' = \beta R^3 C^2 E^2, \\ k = R C k_1, \quad \lambda_1 = \frac{R^2 C}{L_{MT}}, \quad \lambda_2 = \frac{R R_0 C}{L_{MT}}, \quad \lambda_3 = \frac{R^2 C}{L}. \end{cases} \quad (15)$$

Furthermore, the dynamics of the neural circuit in Eq. (14) can be explored in a dimensionless memristive neuron by inserting the new

variables and parameters in Eq. (15) into Eq. (14) as follows

$$\begin{cases} \frac{du_1}{d\tau} = i'_s - u_2 - u_3 - (\alpha' + 3\beta'\varphi^2)u_1, \\ \frac{du_2}{d\tau} = \lambda_1 u_1 - \lambda_2 u_2, \\ \frac{du_3}{d\tau} = \lambda_3(u_1 + 1 - u_3), \\ \frac{d\varphi}{d\tau} = u_1 + k\varphi. \end{cases} \quad (16)$$

In generic way, the sampled time series for the membrane potential u_1 can be calculated by applying the fourth order Runge-Kutta algorithm with a suitable time step, and then the changes of energy function in the memristive neuron in Eq. (16) can be calculated according to the definition in Eq. (17). Furthermore, external membrane noise and even electromagnetic radiation can be imposed to control the mode transition in the neural activities. In fact, mode transition and changes in the membrane potential in Eq. (16) will adjust the current variable u_2 for the load circuit, and then the torques is modified to control the movement of the beam and jointed pendulums. The field energy functions kept in the capacitive, inductive and memristive elements in Fig. 3 are defined, and the corresponding dimensionless forms are respectively presented by

$$\begin{cases} W = \frac{1}{2}CV^2 + \frac{1}{2}L_{MT}I_s^2 + \frac{1}{2}Li_L^2 + \frac{1}{2}\phi i_M, \\ H = \frac{W}{CE^2} = \frac{1}{2}u_1^2 + \frac{1}{2\lambda_1}u_2^2 + \frac{1}{2\lambda_3}u_3^2 + \frac{1}{2}(\alpha'\varphi + 3\beta'\varphi^3)u_1. \end{cases} \quad (17)$$

In an effective way, the average value $\langle H \rangle$ for the Hamilton energy in Eq. (17) can be estimated within a transient period (running time for numerical approach), and it is effective to predict energy shift, mode transition and nonlinear resonance. Furthermore, the distribution of $\langle H \rangle$ vs. noise intensity can be used to predict the occurrence of coherence resonance and stochastic resonance when a maximal value is detected in the curve for $\langle H \rangle$ vs. noise intensity D . For simplicity, additive Gaussian white noise with zero average is considered, and its statistical property is $\langle \xi(\tau)\xi(s) \rangle = 2D\delta(\tau-s)$. Applying similar scale transformation for the physical variables (displacement and velocity) and parameters in Eq. (7b) and kinetic energy of the moving beam W_l in Eq. (8), an equivalent dimensionless moving equation and energy function H_l are obtained in Eqs. (18a) and (18b).

$$\begin{cases} \frac{dx'}{d\tau} = v', \\ \frac{dv'}{d\tau} = \lambda_4 u_2 \sin(\lambda_5 v' \tau) - \lambda_6 v', \\ H_l = \frac{W_l}{CE^2} = \frac{1}{2} \frac{mv^2}{CE^2} = \frac{1}{2} \lambda_7 v'^2. \end{cases} \quad (18a)$$

$$\begin{cases} x' = \frac{x}{l_1}, \quad v' = \frac{v}{l_1} RC, \quad \lambda_4 = \frac{NRC^2 ESB}{m l_1 r}, \\ \lambda_5 = \frac{l_1}{r}, \quad \lambda_6 = \frac{\eta RC}{m}, \quad \lambda_7 = \frac{m l_1^2}{C^3 E^2 R^2}. \end{cases} \quad (18b)$$

The variables (x', v') represent the dimensionless displacement and velocity. In fact, the mechanical energy including the kinetic energy in the coupled pendulums and moving beam, field energy in the electrical motor are mainly converted from the field energy in the neural circuit in presence of external continuous electrical stimulus. Higher energy value for H in Eq. (17) indicates that the memristive neuron in Eq. (16) can generate continuous oscillation and then energy is pumped to drive the motor and the jointed pendulums. On the other hand, continuous rotation of the jointed pendulums will apply mechanical feedback on the moving beam and the motor, and then the current in the motor coils is changed to regulate the electrical activities in the neural circuit. That is, the coils in the EM can be considered as load circuit, which can shunt energy flow and apply feedback on the driving neural circuit as additive

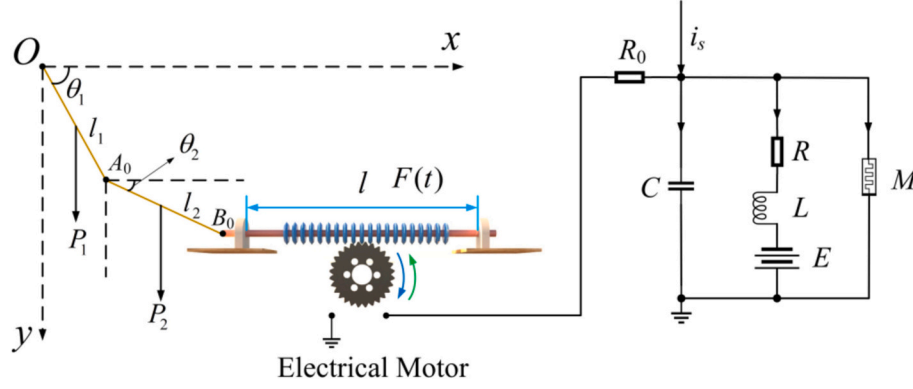


Fig. 4. Schematic diagram for jointed pendulums-coupled with moving beam and neural circuit. The N-turns coils in the electrical motor mark an inductance L_{MT} , and it is a load circuit to the driving neural circuit.

branch circuit.

As shown in Eq. (9), calculation of the angular velocities of the coupled pendulums (ω_1, ω_2) still involves physical units. Inserting the second formula in Eq. (14) into Eq. (9), and then applying the same scale transformation on the variables and parameters, the dimensionless angular velocities for the jointed pendulums can be estimated by finding the solutions for the following equations.

$$\begin{cases} \frac{d\theta_1}{d\tau} = \omega'_1 \\ \frac{d\theta_2}{d\tau} = \omega'_2 \end{cases} = \frac{RCrE(P_1 + 2P_2)\cos^2\theta_1}{2NBSI^2_S(\tau)\sin^2(\omega'\tau)} \left[\left(\frac{u_1}{L_{MT}} - \frac{R_0}{RL_{MT}}u_2 \right) \sin(\omega'\tau) + \frac{\omega'}{R^2C}u_2\cos(\omega'\tau) \right],$$

$$\begin{cases} \frac{d\theta_2}{d\tau} = \omega'_2 \\ \frac{\omega'}{R^2C}u_2\cos(\omega'\tau) \end{cases} = \frac{RCrEP_2\cos^2\theta_2}{2NBSI^2_S(\tau)\sin^2(\omega'\tau)} \left[\left(\frac{u_1}{L_{MT}} - \frac{R_0}{RL_{MT}}u_2 \right) \sin(\omega'\tau) + \frac{\omega'}{R^2C}u_2\cos(\omega'\tau) \right]. \quad (19)$$

where angular frequency $\omega_0 t = \omega'\tau$, $\omega' = \lambda_5 v'$ and $\tau = t/RC$. A group of physical parameters are included in the Eq. (19), and its numerical solution is relative to the values of the physical variables. The parameters in Eq. (16) and Eqs. (18a) and (18b) are defined without physical units for obtaining numerical results. In experimental way, all the parameters should be endowed with standard international physical units. For simple estimation, all the physical parameters can be selected with 1, and then all the dimensionless parameters or coefficients in Eq. (16), Eq. (18a), Eq. (18b), Eq. (19) can be simplified to select a parameter value 1 as well. Furthermore, the rotational kinetics energy for the jointed pendulum can also be estimated in the first and second formulas in Eq. (8) as well. In fact, the displacement x has direct relation to the angle θ_1 and θ_2 in Eq. (10) no matter whether the force $F(t)$ is applied freely or results from the driving from the electromechanical device coupled with the neural circuit. According to Eqs. (18) and (18b), the constraint relation in Eq. (10) can be replaced with dimensionless variables as well, and then the positions for the jointed points (A_0, B_0) and angles (θ_1, θ_2) are also obtained by updating Eq. (12) in dimensionless forms. Both Eq. (2) and Eq. (3) defines the constraint relationship of torques for any static balance and stability, and it is helpful to keep normal or safe arm gait. If so, Eq. (9) and Eq. (19) provides a numerical estimation for the angular frequency for the jointed pendulums. For simplicity, setting $l_1 = l_2$ and $P_1 = P_2$, the frequency ratio between two pendulums is estimated at $\omega_1:\omega_2 = 2\cos^2\theta_1/\cos^2\theta_2$, or $d\theta_1/d\theta_2 = 2\cos^2\theta_1/\cos^2\theta_2$. To keep safe arm gaits, the two angular frequencies for the jointed pendulums should comply with the constraint relationship in Eq. (3), otherwise, two parts of the jointed pendulums will rotate its jointed point freely. As a result,

the artificial arm developed from the electromechanical arms seldom keeps stability and breakdown occurs under external load bearing. When the external force $F(t)$ is generated from the moving beam, which is interacted with the rotating EM, the tangential force from generated from EM excites the jointed point B_0 along the moving beam. As a result, the jointed pendulums began to rotate under the torques generated by the force $F(t)$ and their gravitational moments. According to Eq. 5 and Eq. (7b), the constraint relations for the angles and displacement in Eq. (12) can be updated as follows

$$\begin{cases} \frac{dx}{dt} = v, \\ \frac{dv}{dt} = \frac{NSI_S(t)B}{mr} \sin\left(\frac{v}{r}t\right) - \frac{\eta}{m}v, \\ \frac{d\theta_2}{dt} = \omega_2, \\ \frac{d\omega_2}{dt} = \frac{3g}{2P_2l_2} \left[2 \frac{NSI_S(t)B}{r} \sin\left(\frac{v}{r}t\right) \sin\theta_2 - P_2\cos\theta_2 \right], \\ \cos\theta_1 = \frac{1}{l_1} (x_{B0} - l_2\cos\theta_2) = \frac{x - l_2\cos\theta_2}{l_1}, \\ \text{or, } \theta_1 = \arccos\left(\frac{x - l_2\cos\theta_2}{l_1}\right). \end{cases} \quad (20)$$

The channel current $I_S(t)$ can be obtained from Eq. (14), and the movements of the jointed pendulums can be calculated from Eq. (20). For numerical approach, similar scale transformation can be used to convert the physical variables including velocity, displacement and physical time into dimensionless variables (v', x', ω'). In fact, Eq. (20) assumed that the jointed point B_0 can move in the x - y plane and the force $F(t)$ is kept along horizontal direction, and the jointed pendulums have two freedoms in the plane space. However, in a practical way, as shown in Fig. 4, the jointed point B_0 is restricted to move along horizontal direction because the electromechanical device (moving beam and EM) is fixed on the experimental platform, and the jointed point B_0 can't move along y -axis direction. As a result, the jointed point A_0 can move with two freedoms and the constraint relation in Eq. (20) is updated by removing the third and fourth formulas because the jointed point B_0 presents linear motion without rotation movement.

The work flow in Fig. 4 is summarized, external physical signals including acoustic wave encoded by piezoelectric ceramics, illumination via phototubes, filtered signal via thermistor or Josephson junction are applied to control the firing activities. The time-varying neural signal from the neural circuit drives the electrical motor, and its rotation directions are controlled by the channel current across the resistor R_0 . Switch of negative and positive voltage for the capacitor will control the rotation direction and frequency of the electrical motor, and then the horizontal beam is activated to keep reciprocating motion via gear coupling to the electrical motor. Reciprocating motion of the moving

beam applies force and moment to the jointed pendulums via the jointed point B_0 , and then the gait stability of the jointed pendulums is controlled. In this way, the relation between the angles (θ_1, θ_2) and the displacement for point B_0 is given in

$$\begin{cases} y = y_{B_0} = l_1 \sin \theta_1 + l_2 \sin \theta_2 = \text{Constant} = l_0, \\ x = x_{B_0} = l_1 \cos \theta_1 + l_2 \cos \theta_2, \quad l_1 \leq l_0 \leq l_1 + l_2. \end{cases} \quad (21)$$

The constant l_0 in Eq. (21) is the initial value for point B_0 along y-axis in the jointed pendulums. The correlation between the angles (θ_1, θ_2) can be estimated from Eq. (21) when the displacement x is detected. The movement of the jointed point B_0 is calculated in Eq. 7b and its dimensionless form in Eq. (18a) by measuring its displacement $x' = x/l_1$ with time. The transcendental equation is updated with dimensionless form to find numerical solutions of the angles.

$$\begin{cases} y' = y'_{B_0} = \frac{y}{l_1} = \sin \theta_1 + \frac{l_2}{l_1} \sin \theta_2 = \frac{l_0}{l_1}, \\ x' = x'_{B_0} = \frac{x}{l_1} = \cos \theta_1 + \frac{l_2}{l_1} \cos \theta_2 = x'. \end{cases} \quad (22)$$

From Eq. (22), a stable and specific solution can be confirmed as $\theta_1 = \theta_2 = \pi/2$ at $l_1 = l_2 = l_0/2$ and it indicates the moving beam is stabilized at $x' = x = 0$. Usually, the upper arm length of adults is about 30–40 cm, and the forearm length is about 20–30 cm. Therefore, the ratio l_2/l_1 can be selected values from 0.5 to 1.0, and the ratio l_0/l_1 can select values from 1.0 to 2.0. During numerical approach in next section, the parameters can be selected as $l_2/l_1 = 0.8$ and $l_0/l_1 = 1.2$ (or, $l_2/l_1 = 0.8$ and $l_0/l_1 = 1.5$; $l_2/l_1 = 1.0$ and $l_0/l_1 = 1.5$). The second formula in Eq. (22) indicates the displacement x' varies within the scope $(-l_2/l_1 - 1)$ to $(1 + l_2/l_1)$. It means that the jointed pendulums are restricted in the angles, and it also applied feedback to the moving beam via the jointed pointed B_0 . Combing the dynamical description in Eq. (16) and Eq. (18a), the correlation between dimensionless displacement and variables for Fig. 4 are described by

$$\begin{cases} \frac{du_1}{d\tau} = i'_s - u_2 - u_3 - (\alpha' + 3\beta'\varphi^2)u_1, \\ \frac{du_2}{d\tau} = \lambda_1 u_1 - \lambda_2 u_2, \\ \frac{du_3}{d\tau} = \lambda_3(u_1 + 1 - u_3), \\ \frac{d\varphi}{d\tau} = u_1 + k\varphi, \\ \frac{dx'}{d\tau} = v', \\ \frac{dv'}{d\tau} = \lambda_4 u_2 \sin(\lambda_5 v'\tau) - \lambda_6 v'. \end{cases} \quad (23)$$

From dynamical viewpoint, external stimulus i'_s modifies the excitability of the neuron, and different firing patterns are activated accompany with suitable channel current u_2 , which controls the moving beam via the gear meshing from electrical motor, and then the jointed pendulums are excited via the jointed point B_0 . That is, any changes of the exciting current i'_s will modify the variable u_1 , and then u_2 is adjusted to control the displacement x' and moving velocity v' , as a result, the coupled pendulums rotate against the jointed point (A_0, O). For effective numerical approach of angle θ_2 and θ_1 , the time series x' from the fifth formula in Eq. (23) can be used in Eq. (22), and the two constraint equations enable numerical finding for θ_1 and θ_2 . There are nine parameters in Eq. (9), the neural circuit can be tamed to present different firing activities, and the displacement x' for the moving beam is controlled. Indeed, parameter setting should be selected carefully so that the constraint criteria in Eq. (22) can be satisfied, otherwise, the

displacement x' will obtain large values and the jointed pendulums are destroyed. From physical aspect, external excitation injects energy into the neural circuit, and a part of energy is converted to mechanical energy of the moving beam and the jointed pendulums. For potential application, continuous forcing to the jointed pendulums via the moving beam can be considered as a kind of rehabilitation training on disabled arms.

3. Dynamical analysis and discussion

As shown in Fig. 4 and Eq. (23), the fourth order Runge-Kutta algorithm can be applied to find numerical solutions for the dimensionless variables. Furthermore, the changes of angles (θ_1, θ_2) can be detected from Eq. (22) and the movement of the coupled pendulums can be discussed. In this way, the driving and response in the neural circuit-coupled electromechanical arms can be analyzed. For clear illumination, it is interesting to clarify the dynamics of the jointed pendulums, neural circuit, respectively. As presented in Eq. (3), the stability of the coupled pendulums is dependent on the excitation $F(t)$, which can be selected with different kinds of signals. For example, external mechanical force can be applied to the end point B_0 along the horizontal direction. In numerical way, we can select one variable from the Lorenz system as external force $F(t)$, and the response of the rotation can be obtained by

$$\begin{cases} \frac{dX}{d\tau} = a(Y - X), \\ \frac{dY}{d\tau} = bX - Y - XZ, \\ \frac{dZ}{d\tau} = XY - cZ, \\ \theta_1 = \arctg \frac{P_1 + 2P_2}{2F} = \arctg \frac{P_1 + 2P_2}{2X}, \\ \theta_2 = \arctg \frac{P_2}{2F} = \arctg \frac{P_2}{2X}. \end{cases} \quad (24)$$

Setting parameters (a, b, c) to suitable values will develop periodic or chaotic states in the Lorenz system. For example, $a = 10$, $b = 28$, $c = 2.667$ will induce chaos in the Lorenz oscillator. For simplicity, the jointed pendulums can select the same gravity as $P_1 = P_2 = P$, and the angular frequency of the coupled pendulums under any stability can be estimated by

$$\begin{cases} \omega_1 = \frac{d\theta_1}{dt} = -\frac{3P}{2X^2} \cos^2 \theta_1 \frac{dX}{dt} = -\frac{3aP \cos^2 \theta_1}{2X^2} (Y - X), \\ \omega_2 = \frac{d\theta_2}{dt} = -\frac{P}{2X^2} \cos^2 \theta_2 \frac{dX}{dt} = -\frac{aP \cos^2 \theta_2}{2X^2} (Y - X). \end{cases} \quad (25)$$

In chaotic states, the angular frequencies for the jointed pendulums will present chaotic changes while applying periodic forcing can make the rotation of coupled pendulums produce periodic changes in the angular frequencies. However, time-varying angular frequencies in the jointed pendulums still support dynamical balance between the two coupled pendulums. Most of the chaotic systems can be controlled to present periodic states and the sampled time series will keep distinct period. Therefore, the parameters in Lorenz system and Eq. (24) can be adjusted to apply periodic signals for $F(t) = X(t)$, and the jointed pendulums will be controlled to present periodical motion. On the other hand, generic and mathematical neuron models can be excited to present spiking and bursting patterns, and a neuron model can be used to replace the Lorenz system in Eq. (24). As a result, similar neural signals can be applied to drive the coupled pendulums for predicting the mechanical and dynamical response in presence of neural stimulus.

For the neural circuit without considering load coils of the electrical

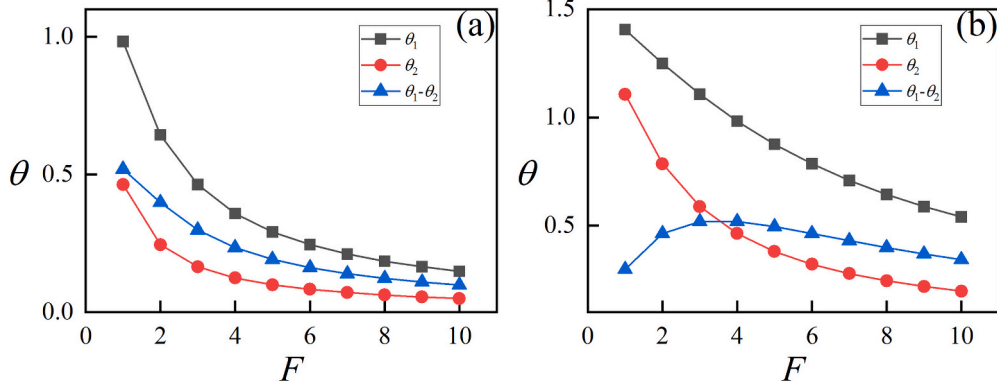


Fig. 5. Distribution of rotation angles vs. external force F . For (a) $P_1 = P_2 = 1$, (b) $P_1 = P_2 = 4$.

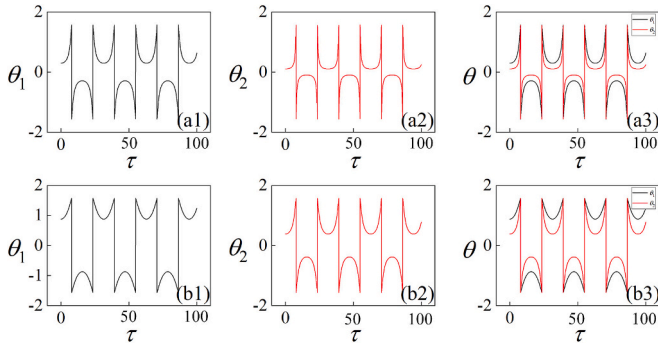


Fig. 6. Distribution of rotation angles vs. external force $F(t) = 0.5\cos(0.2t)$. For (a1, a2, a3) $P_1 = P_2 = 1$, (b1, b2, b3) $P_1 = P_2 = 4$.

motor (EM), its electrical activities can be estimated by simplifying Eq. (16) and the correlation between three variables is shown in Eq. (26).

$$\begin{cases} \frac{du_1}{d\tau} = i_s - u_3 - (\alpha' + 3\beta'\varphi^2)u_1, \\ \frac{du_3}{d\tau} = \lambda_3(u_1 + 1 - u_3), \\ \frac{d\varphi}{d\tau} = u_1 + k\varphi. \end{cases} \quad (26)$$

Its intrinsic Hamilton energy can be derived from Eq. (17), and it meets the following form

$$H = \frac{1}{2}u_1^2 + \frac{1}{2\lambda_3}u_3^2 + \frac{1}{2}(\alpha'\varphi + 3\beta'\varphi^3)u_1. \quad (27)$$

Any adjustment of the external stimulus and noisy excitation on the neuron in Eq. (26), the excitability will be modified to induce suitable firing modes in the electrical activities. According to Eq. (27), the energy values for the memristive neuron are changed synchronously, and continuous change of the intrinsic parameters of the memristive neuron will induce shift between the average energy levels. For example, the average energy for the Hindmarsh-Rose has four distinct levels and taming one bifurcation parameter can induce energy shift between the four levels for the average energy [121] accompanying mode transition. From physical viewpoint, average energy $\langle H \rangle$ within a transient period estimates the average power and it has similar role as signal to noise ratio (SNR) in predicting the occurrence of nonlinear resonance. Indeed, its energy function can be further verified by using the Helmholtz theorem when the neuron model in Eq. (26) is rewritten in a vector form as follows

$$\begin{aligned} \begin{bmatrix} \frac{du_1}{d\tau} \\ \frac{du_3}{d\tau} \\ \frac{d\varphi}{d\tau} \end{bmatrix} &= F_c(u_1, u_3, \varphi) + F_d(u_1, u_3, \varphi) \\ &= \begin{bmatrix} i_s - u_3 - (\alpha' + 3\beta'\varphi^2)u_1 \\ \lambda_3(u_1 + 1 - u_3) \\ u_1 + k\varphi \end{bmatrix} \\ &= \begin{bmatrix} -u_3 - (\alpha' + 9\beta'\varphi^2)u_1 \\ \lambda_3u_1 - 3\beta'\lambda_3\varphi^3 \\ 2u_1 + \varphi(\alpha' + 3\beta'\varphi^2 + \frac{u_3}{u_1}) \end{bmatrix} \\ &+ \begin{bmatrix} i_s + 6\beta'\varphi^2u_1 \\ \lambda_3(1 - u_3 + 3\beta'\varphi^3) \\ k\varphi - u_1 - \varphi(\alpha' + 3\beta'\varphi^2 + \frac{u_3}{u_1}) \end{bmatrix} \\ &= \begin{bmatrix} 0 & -\lambda_3 & -2 \\ \lambda_3 & 0 & -\lambda_3\frac{\varphi}{u_1} \\ 2 & \lambda_3\frac{\varphi}{u_1} & 0 \end{bmatrix} \begin{bmatrix} u_1 + \frac{1}{2}(\alpha'\varphi + 3\beta'\varphi^3) \\ \frac{u_3}{\lambda_3} \\ \frac{1}{2}(\alpha' + 9\beta'\varphi^2)u_1 \end{bmatrix} \\ &+ \begin{bmatrix} a_{11} & 0 & 0 \\ 0 & a_{22} & 0 \\ 0 & 0 & a_{33} \end{bmatrix} \begin{bmatrix} u_1 + \frac{1}{2}(\alpha'\varphi + 3\beta'\varphi^3) \\ \frac{u_3}{\lambda_3} \\ \frac{1}{2}(\alpha' + 9\beta'\varphi^2)u_1 \end{bmatrix}, \\ a_{11} &= \frac{i_s + 6\beta'\varphi^2u_1}{u_1 + \frac{1}{2}(\alpha'\varphi + 3\beta'\varphi^3)}, \quad a_{22} = \lambda_3^2(1 - u_3 + 3\beta'\varphi^3)u_3, \\ a_{33} &= \frac{-2u_1 - 2\varphi(\alpha' + 3\beta'\varphi^2 + \frac{u_3}{u_1} - k)}{(\alpha' + 9\beta'\varphi^2)u_1}. \end{aligned} \quad (28)$$

The energy function H for Eq. (26) is the same as the form in Eq. (27) because it meets the criterion as follows

$$\begin{aligned} &[-u_3 - (\alpha' + 9\beta'\varphi^2)u_1] \frac{\partial H}{\partial u_1} + (\lambda_3u_1 - 3\beta'\lambda_3\varphi^3) \frac{\partial H}{\partial u_3} \\ &+ \left[2u_1 + \varphi(\alpha' + 3\beta'\varphi^2 + \frac{u_3}{u_1}) \right] \frac{\partial H}{\partial \varphi}. \end{aligned} \quad (29)$$

And its derivatives to time is verified by

$$\begin{aligned} \frac{dH}{d\tau} &= \nabla H^T F_d(u_1, u_3, \varphi) = [\dot{u}_1 + 6\beta' \varphi^2 u_1] \frac{\partial H}{\partial u_1} + \\ &[\lambda_3(1 - u_3 + 3\beta' \varphi^3)] \frac{\partial H}{\partial u_3} + \left[-u_1 - \varphi \left(\alpha' + 3\beta' \varphi^2 + \frac{u_2 + u_3}{u_1} - k \right) \right] \frac{\partial H}{\partial \varphi}. \end{aligned} \quad (30)$$

In presence of noisy excitation, the isolated neuron can be tamed to present coherence resonance accompanying with high regularity in the neural activities. In practical way, the average energy $\langle H \rangle$ in Eq. (27) can be calculated to predict the emergence of coherence resonance. That is, $\langle H \rangle$ obtains a highest value within a transient period and it means that the average power reaches the maximal values. It provides a better way rather than calculating the common distribution for CV (coefficient of variability) and signal to noise ratio. Similarly, the energy function H for Eq. (16) can also be verified by using Helmholtz theorem when it is rewritten with an equivalent vector form as follows.

Indeed, the energy function in Eq. (17) is the sole exact solution in Eq. (32), and the energy evolution vs. time is calculated by

$$\begin{aligned} \frac{dH}{d\tau} &= \nabla H^T F_d(u_1, u_2, u_3, \varphi) = [\dot{u}_1 + 6\beta' \varphi^2 u_1] \frac{\partial H}{\partial u_1} \\ &+ (-\lambda_2 u_2 + 3\lambda_1 \beta' \varphi^3) \frac{\partial H}{\partial u_2} + \lambda_3(1 - u_3 + 3\beta' \varphi^3) \frac{\partial H}{\partial u_3} \\ &+ \left[-u_1 + k\varphi - \left(\alpha' + 3\beta' \varphi^2 + \frac{u_2 + u_3}{u_1} \right) \varphi \right] \frac{\partial H}{\partial \varphi}. \end{aligned} \quad (33)$$

It should be emphasized that the mechanical energy for the moving beam and the jointed pendulums are not associated with field energy because it seldom meets the applicable conditions for Helmholtz theorem. Therefore, the total energy for Eq. (23) can be approached by using the Helmholtz theorem, and then the mechanical energy can be obtained by using physical scheme defined in Eq. (8) when the angular frequency for the jointed pendulums are available.

In experimental way, external electrical stimulus controls the output voltage of the neural circuit, and then the channel current in the load

$$\begin{aligned} \begin{bmatrix} \frac{du_1}{d\tau} \\ \frac{du_2}{d\tau} \\ \frac{du_3}{d\tau} \\ \frac{d\varphi}{d\tau} \end{bmatrix} &= F_c(u_1, u_2, u_3, \varphi) + F_d(u_1, u_2, u_3, \varphi) = \begin{bmatrix} \dot{u}_1 - u_2 - u_3 - (\alpha' + 3\beta' \varphi^2) u_1 \\ \lambda_1 u_1 - \lambda_2 u_2 \\ \lambda_3(u_1 + 1 - u_3) \\ u_1 + k\varphi \end{bmatrix} \\ &= \begin{bmatrix} -u_2 - u_3 - (\alpha' + 9\beta' \varphi^2) u_1 \\ \lambda_1(u_1 - 3\beta' \varphi^3) \\ \lambda_3(u_1 - 3\beta' \varphi^3) \\ 2u_1 + \left(\alpha' + 3\beta' \varphi^2 + \frac{u_2 + u_3}{u_1} \right) \varphi \end{bmatrix} + \begin{bmatrix} \dot{u}_1 + 6\beta' \varphi^2 u_1 \\ -\lambda_2 u_2 + 3\lambda_1 \beta' \varphi^3 \\ \lambda_3(1 - u_3 + 3\beta' \varphi^3) \\ -u_1 + k\varphi - \left(\alpha' + 3\beta' \varphi^2 + \frac{u_2 + u_3}{u_1} \right) \varphi \end{bmatrix} \\ &= \begin{bmatrix} 0 & -\lambda_1 & -\lambda_3 & -2 \\ \lambda_1 & 0 & 0 & -\frac{\lambda_1}{u_1} \varphi \\ \lambda_3 & 0 & 0 & -\frac{\lambda_3}{u_1} \varphi \\ 2 & \frac{\lambda_1}{u_1} \varphi & \frac{\lambda_3}{u_1} \varphi & 0 \end{bmatrix} \begin{bmatrix} u_1 + \frac{1}{2}(\alpha' \varphi + 3\beta' \varphi^3) \\ \frac{u_2}{\lambda_1} \\ \frac{u_3}{\lambda_3} \\ \frac{1}{2}(\alpha' + 9\beta' \varphi^2) u_1 \end{bmatrix} + \begin{bmatrix} a_{11} & 0 & 0 & 0 \\ 0 & a_{22} & 0 & 0 \\ 0 & 0 & a_{33} & 0 \\ 0 & 0 & 0 & a_{44} \end{bmatrix} \begin{bmatrix} u_1 + \frac{1}{2}(\alpha' \varphi + 3\beta' \varphi^3) \\ \frac{u_2}{\lambda_1} \\ \frac{u_3}{\lambda_3} \\ \frac{1}{2}(\alpha' + 9\beta' \varphi^2) u_1 \end{bmatrix}, \\ a_{11} &= \frac{\dot{u}_1 + 6\beta' \varphi^2 u_1}{u_1 + \frac{1}{2}(\alpha' \varphi + 3\beta' \varphi^3)}, \quad a_{22} = \frac{\lambda_1(-\lambda_2 u_2 + 3\lambda_1 \beta' \varphi^3)}{u_2}, \\ a_{33} &= \frac{\lambda_3^2(1 - u_3 + 3\beta' \varphi^3)}{u_3}, \quad a_{44} = \frac{-2u_1 + 2k\varphi - 2\left(\alpha' + 3\beta' \varphi^2 + \frac{u_2 + u_3}{u_1} \right) \varphi}{(\alpha' + 9\beta' \varphi^2) u_1}. \end{aligned} \quad (31)$$

The new energy function for the memristive neuron considering load regulation in Eq. (16) and Eq. (31) can be approached by the theoretical solution for the following formula

$$\begin{aligned} &[-u_2 - u_3 - (\alpha' + 9\beta' \varphi^2) u_1] \frac{\partial H}{\partial u_1} + \lambda_1(u_1 - 3\beta' \varphi^3) \frac{\partial H}{\partial u_2} + \\ &\lambda_3(u_1 - 3\beta' \varphi^3) \frac{\partial H}{\partial u_3} + \left[2u_1 + \left(\alpha' + 3\beta' \varphi^2 + \frac{u_2 + u_3}{u_1} \right) \varphi \right] \frac{\partial H}{\partial \varphi}. \end{aligned} \quad (32)$$

circuit of the electrical motor is changed to control the velocity of the moving beam via gear interaction. Continuous impact or pull to the jointed point B_0 , which connects the end and terminal of the moving beam and the pendulum, will control the gait of the coupled pendulums completely. In this way, neural signals are propagated to control the electromechanical arms effectively. For generic dynamical analysis, numerical solutions for Eq. (22) and Eq. (23) can be obtained by taming the external stimulus even noisy disturbance is applied. For energy analysis, Eq. (17) presents complete description for the neuron-

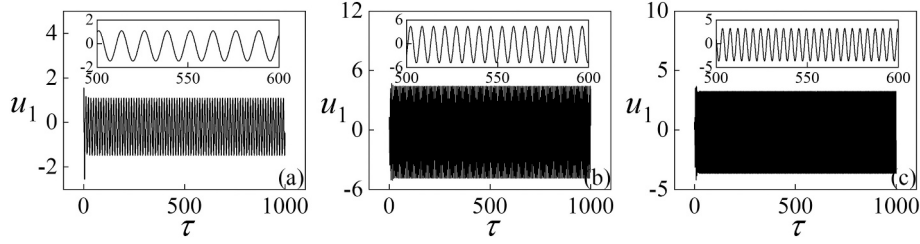


Fig. 7. Evolution of membrane potential vs. time. For (a) $\omega = 0.5$; (b) $\omega = 1.0$; (c) $\omega = 1.5$. Setting parameters $\alpha = 0.01$, $\beta = 0.001$, $A = 2.3$, $k = -0.3$, $\lambda_1 = 0.8$, $\lambda_2 = 0.2$, $\lambda_3 = 0.6$, $\lambda_4 = 0.3$, $\lambda_5 = 0.2$, $\lambda_6 = 0.5$, and external periodic forcing $i_s = A\cos(\omega\tau)$. Inserted figures are enlarged version within finite period 500 to 600 time units.

electromechanical arms developed from the neural circuit coupled with jointed pendulums. For energy dependence on firing modes in the memristive neuron, Eq. (17) and Eq. (27) denote exact energy functions and the distribution of average value $\langle H \rangle$ vs. noise intensity provides a feasible way for predicting the coherence resonance and stochastic resonance under noisy driving. Following our study and suggestions in this work, assistive wearable devices can be adhered to the arms and electrical signals from miniature neural circuits can be activated to control the skeletal muscles, and then the disabled arms can be trained to present normal gait.

For clear understanding the relation between the neural circuit, moving beam and movement of the coupled pendulums, numerical results are provided by setting different mechanical forces, and then the neural activities are also calculated during the interaction between the electromechanical device and the neural circuits. According to stability criterion for jointed pendulums in Eq. (3), setting different external forces can keep stability in the jointed pendulum, and the results are plotted in Fig. 5.

By applying different constant forces on the jointed pendulums, the two rotation angles are modified to keep static body gaits. That is, under the stability restraints from Eq. (3), any external forces will adjust the two rotation angles synchronously and adaptively. In fact, we assumes

that the external force can produce anticlockwise torques to balance the clockwise torques resulting from gravities of the pendulums and Eq. (3) is obtained. In fact, applying horizontal left-direction force can generate clockwise torques while the gravities of the pendulum will generate anticlockwise torques, and then the jointed pendulums can also keep dynamical stability. Furthermore, time-varying force is applied to track the stability in the jointed pendulums, and the results are plotted in Fig. 6.

When periodic force is applied to control the jointed pendulums, the rotation angles also show symmetrical changes with time. In particular, any changes of one rotation angle will trigger synchronous change of another rotation angle so that the jointed pendulums keep stability completely. Extensive numerical results for $F(t) = A + B\cos(0.2t)$ can confirm similar results by setting different values for the amplitudes (A , B). According to Eq. (24), chaotic series can be selected for external force $F(\tau)$, stability criterion in Eq. (3) supports adaptive regulation of the angles for presenting chaotic changes with time as well. Fig. 5 and Fig. 6 discussed the case that the jointed pendulums are controlled by external mechanical force. Following the stability criterion in Eq. (3), the two angles changes synchronously to keep balance in the torques. From Eq. (23), external electric stimulus control the neural circuit (and neuron) to present periodic or chaotic state, and then the shunted current across the

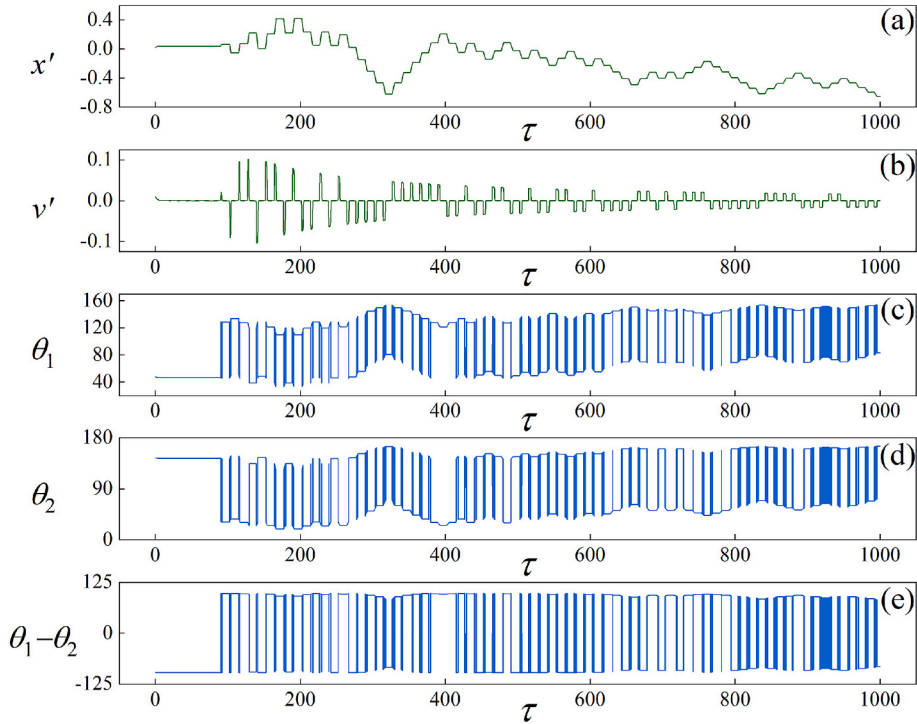


Fig. 8. Evolution of displacement (a), (b) velocity of moving beam, (c, d) rotation angles and (e) angle error for the jointed pendulums driven by neural circuit. Setting parameters $\alpha = 0.01$, $\beta = 0.001$, $A = 2.3$, $\omega = 0.5$, $k = -0.3$, $\lambda_1 = 0.8$, $\lambda_2 = 0.2$, $\lambda_3 = 0.6$, $\lambda_4 = 0.3$, $\lambda_5 = 0.2$, $\lambda_6 = 0.5$, and external periodic forcing $i_s = A\cos(\omega\tau)$. Scale on the vertical axis is marked with degree angle (not radian).

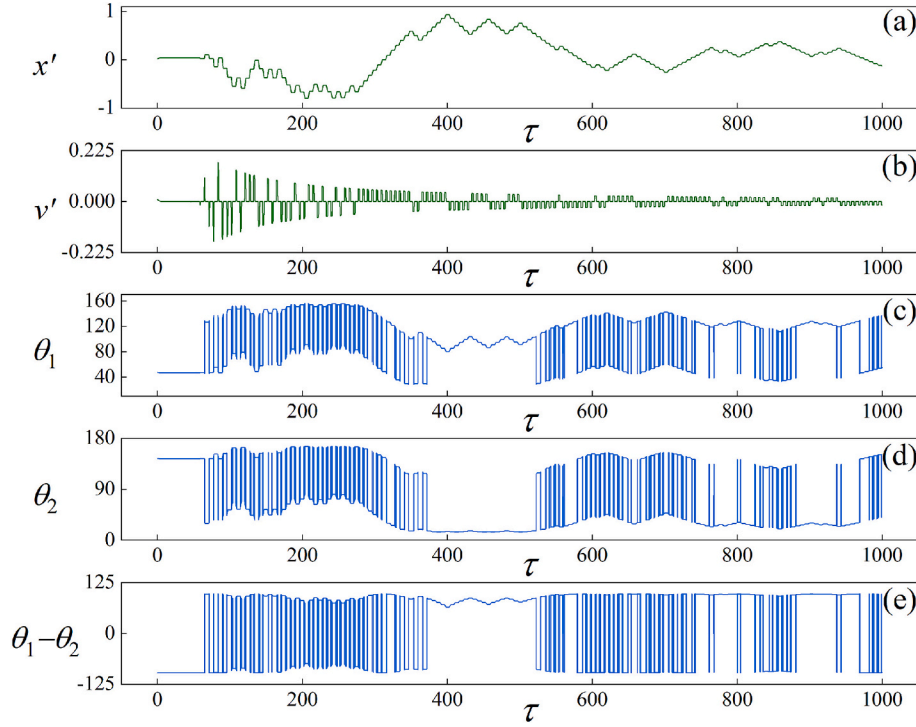


Fig. 9. Evolution of displacement (a), (b) velocity of moving beam, (c, d) rotation angles and (e) angle error for the jointed pendulums driven by neural circuit. Setting parameters $\alpha = 0.01$, $\beta = 0.001$, $A = 2.3$, $\omega = 1.0$, $k = -0.3$, $\lambda_1 = 0.8$, $\lambda_2 = 0.2$, $\lambda_3 = 0.6$, $\lambda_4 = 0.3$, $\lambda_5 = 0.2$, $\lambda_6 = 0.5$, and external periodic forcing $i_s' = A \cos(\omega\tau)$. Scale on the vertical axis is marked with degree angle (not radian).

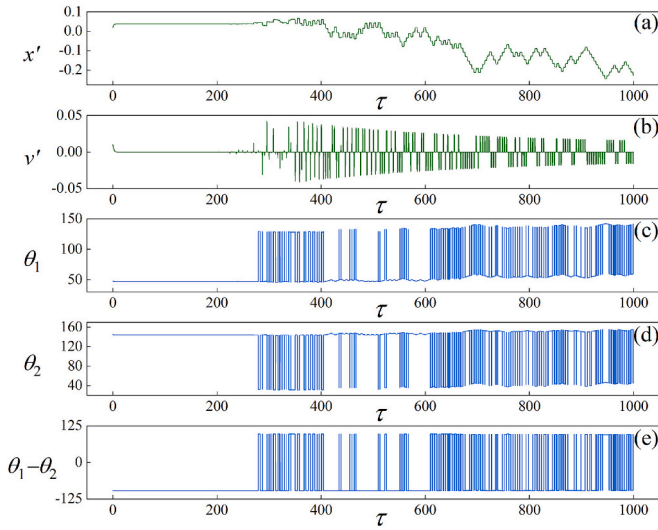


Fig. 10. Evolution of displacement (a), (b) velocity of moving beam, (c, d) rotation angles and (e) angle error for the jointed pendulums driven by neural circuit. Setting parameters $\alpha = 0.01$, $\beta = 0.001$, $A = 2.3$, $\omega = 1.5$, $k = -0.3$, $\lambda_1 = 0.8$, $\lambda_2 = 0.2$, $\lambda_3 = 0.6$, $\lambda_4 = 0.3$, $\lambda_5 = 0.2$, $\lambda_6 = 0.5$, and external periodic forcing $i_s' = A \cos(\omega\tau)$. Scale on the vertical axis is marked with degree angle (not radian).

electric motor will produce different torques and then the jointed pendulums are controlled to present different movements. The changes of three variables of the neurons are plotted in Fig. 7 when the neuron is excited by periodic signal $i_s' = A \cos(\omega\tau)$. Furthermore, modification of the displacement, velocity of the moving beam, rotation angle against the jointed point O is presented in Fig. 8 following the criterion for angles in Eq. (22).

In presence of periodic excitation on the neuron, it is used to present

periodic firing patterns and the channel current across the load circuit adhered to the electronic motor also keeps periodic signals to induce periodic force, which controls the stability of the jointed pendulums. Furthermore, setting the corresponding forcing frequency, the changes of displacement, velocity and angles are calculated in Fig. 8, Fig. 9 and Fig. 10, respectively.

From Fig. 8 and Fig. 9, the displacement and velocity show switch between positive and negative values, it indicates that the moving beam and jointed point B_0 keep continuous reciprocating motion, and then the rotation angles are controlled with appropriate gaits. Further increasing the forcing frequency of external electric stimulus on the neural circuit as shown in Fig. 10, periodic neuron controls the electromechanical beam and the jointed pendulums to move along negative direction, which the displacement x' becomes negative within a transient period about 500 time units. From Fig. 10(b), the velocity keeps transition between negative and positive values, and it means that reciprocating motion still occurs for the moving beam and coupled pendulums.

When the neuron is excited to present periodic activities, the periodic channel current in the load circuit of EM seldom supports periodic displacement and velocity of the moving beam. That is, both of the electromechanical devices including the moving beams and the jointed pendulums move in non-periodic way. When the displacement and velocity of the moving beam are fixed a constant, the rotation angle is stabilized. On the other hand, irregular changes in the displacement of the moving beam means switch of the moving velocity, and then the rotation angle becomes irregular synchronously. In fact, the jointed pendulums interacted with the moving beam and the EM is controlled by the damping force, and then the neural circuit is controlled due to the feedback via the load circuit. Therefore, the neural activities prefer to keep periodic types. On the other hand, it also means external mechanical force and training via EM can suppress chaos in the neural circuit.

In a summary, skeletal muscles control the arms/legs via neural electric signals and thus the body can keep safe gaits. On the other hand, activation of body gaits has positive feedback to the nervous system due

to electromechanical coupling. Therefore, the neurons in the nervous system can present mode transition in the neural activities. The arm motion can be considered as a kind of jointed pendulums stimulated by external excitation from a neural circuit, which suffers a feedback modulation via the equivalent induced current across the electrical motor or inductor in the feedback loop by adding an additive branch circuit of the driving neural circuit. That is, the external stimulus activates the neural circuit, and the electrical signals applied a mechanical forcing on the jointed pendulums, while the rotation of the coupled pendulums generates suitable feedback current via electromechanical coupling as muscle contraction. As a result, the interaction between muscle and neural electrical signals is explored in a couple jointed pendulums coupled by a neural circuit. The moving beam driven by electrical motor and the neural signals from the neural circuit plays similar role as muscle in the body. We just discussed the case that the jointed pendulums and the moving beam are controlled to move or rotate in the same plane space. It is worthy of investigating the case when the coupled pendulums and moving beam are connected by using spherical joints, and then the jointed pendulums can present different arm gaits in three-dimensionless space. In extensive studies, springs can be introduced to connect the jointed pendulums, and further involvement of electrical signals from neural circuit can be effective to control the elastic force via these springs. That is, electrical signals-controlled springs can be used to control the stability and dynamical states of the jointed pendulums and artificial arms can be designed to give help to animals with disabled arms or legs. Appearance of neural diseases [122–124] is harmful for activating normal body gaits, and clarification of oscillatory characteristic of brain electric activities [125–127] are helpful to propose possible schemes to aid neural regulation. Furthermore, electromechanical devices can be designed to aid the stability of body gaits and movement. This work just used a neural circuit to control the movements of the jointed pendulums, the complex movements of jointed pendulums with higher freedom requires activation of more neural circuits, and the synchronous control of neural networks [128] can be helpful to control the cooperative movements of the artificial manipulators and electromechanical arm/legs.

4. Conclusions

In this paper, a simple electromechanical coupling device is proposed to explore the interaction between muscle and nervous signals. A couple of jointed pendulums are forced by a moving beam driven by an electrical motor, which the current is shunted from a neural circuit. Any physical stimuli applied to the neural circuit will regulate the output voltage and channel current across the electric motor adhered to the moving beam, which can impose continuous force and suitable moment to the jointed pendulums. On the other hand, changes of the gait in the jointed pendulums will impose force feedback on the moving beam and the connected motor, in which the coils is considered as a load branch circuit, and then the channel current across the motor coils will apply feedback to the driving neural circuit. This processing is similar to the interaction between skeletal muscles and electrical signals from the nervous system because muscle contraction can regulate the neural signals. The correlation between physical variables for the jointed pendulums, moving beam and neural circuit are described and exact energy functions are defined, furthermore, dimensionless models and Hamilton energy/kinetics energy are obtained by applying scale transformation on the variables and parameters in the physical definitions. The driving-response processing in the electromechanical device provides possible clues to design and control artificial arms for those disabled animals or humans. It also indicates that mechanical training is helpful to control the neural activities and then the nervous system can be guided to behave suitable firing patterns.

Data statement

No numerical data are used in this study and the figures have not been used in other papers.

CRediT authorship contribution statement

Yitong Guo: Visualization, Validation, Investigation, Formal analysis, Data curation. **Chunni Wang:** Writing – original draft, Validation, Methodology, Investigation, Funding acquisition, Formal analysis, Conceptualization. **Jun Ma:** Writing – review & editing, Methodology, Investigation, Formal analysis, Conceptualization.

Declaration of competing interest

The authors declare that they have no known competing financial interests or personal relationships that could have appeared to influence the work reported in this paper.

Acknowledgments

This project is supported by the National Natural Science Foundation of China under Grant No. 62361037.

Data availability

Data will be made available on request.

References

- [1] Mehrholz J, Hädrich A, Platz T, et al. Electromechanical and robot-assisted arm training after stroke: updated review. *Stroke* 2012;43:e172–3.
- [2] Ma J, Guo Y. Model approach of electromechanical arm interacted with neural circuit, a minireview. *Chaos, Solitons Fractals* 2024;183:114925.
- [3] Notué Kadjie A, Nwagoum Tuwa PR, Wofo P. An electromechanical pendulum robot arm in action: dynamics and control. *Shock Vib* 2017;2017:3979384.
- [4] Kouam Tagne R, Wofo P, Awrejcewicz J. Dynamics of the rotating arm of an electromechanical system subjected to the action of circularly placed magnets: numerical study and experiment. *International Journal of Bifurcation and Chaos* 2023;33:2350052.
- [5] Feathers DJ, Paquet VL, Drury CG. Measurement consistency and three-dimensional electromechanical anthropometry. *Int J Ind Ergon* 2004;33:181–90.
- [6] Palmcrantz S, Wall A, Vreede KS, et al. Impact of intensive gait training with and without electromechanical assistance in the chronic phase after stroke—a multi-arm randomized controlled trial with a 6 and 12 months follow up. *Front Neurosci* 2021;15:660726.
- [7] Mehrholz J, Platz T, Kugler J, et al. Electromechanical and robot-assisted arm training for improving arm function and activities of daily living after stroke. *Stroke* 2009;40:e392–3.
- [8] Mehrholz J. Is electromechanical and robot-assisted arm training effective for improving arm function in people who have had a stroke?: a cochrane review summary with commentary. *Am J Phys Med Rehabil* 2019;98:339–40.
- [9] Karthik PN, Sundaresan R. Detecting an odd restless Markov arm with a trembling hand. *IEEE Trans Inf Theory* 2021;67:5230–58.
- [10] Tahayori B, Riley ZA, Mahmoudian A, et al. Rambling and trembling in response to body loading. *Mot Control* 2012;16:144–57.
- [11] Shin S, Motl RW, Sosnoff JJ. A test of the rambling and trembling hypothesis: multiple sclerosis and postural control. *Mot Control* 2011;15:568–79.
- [12] Slomka K, Juras G, Sobota G, et al. The reliability of a rambling–trembling analysis of center of pressure measures. *Gait Posture* 2013;37:210–3.
- [13] Shin S, Sosnoff JJ. Spinal cord injury and seated postural control: a test of the rambling and trembling hypothesis. *Mot Control* 2017;21:443–56.
- [14] Alışverişçi GF, Bayıroğlu H, Felix JLP, et al. A nonlinear electromechanical pendulum arm with a nonlinear energy sink control (NES) approach. *J Theor Appl Mech* 2016;54:975–86.
- [15] Kitio Kwuimy CA, Wofo P. Dynamics, chaos and synchronization of self-sustained electromechanical systems with clamped-free flexible arm. *Nonlinear Dynamics* 2008;53:201–13.
- [16] de Araújo RC, Junior FL, Rocha DN, et al. Effects of intensive arm training with an electromechanical orthosis in chronic stroke patients: a preliminary study. *Arch Phys Med Rehabil* 2011;92:1746–53.
- [17] Ebanda ALA, Tchakui MV, Wofo P. Nonlinear dynamics of two electromechanical arms acting discontinuously on a balloon under the action of a sinusoidal excitation. *Heliyon* 2024;10:e32990.
- [18] Zhang L, Jin WY. Simulating the motion of a mechanical arm driven by neural circuit. *Physica Scripta* 2024;99:115213.

- [19] Astudillo Roblero H, Gallardo Arancibia J, Ayala Bravo C. Comparative study of classical PID control algorithms for the angular control of an electromechanical arm. *Revista chilena de ingeniería* 2021;28:612–28.
- [20] Drewniak EI, Jay GD, Fleming BC, et al. Comparison of two methods for calculating the frictional properties of articular cartilage using a simple pendulum and intact mouse knee joints. *J Biomech* 2009;42:1996–9.
- [21] Galan J, Fraser WB, Acheson DJ, et al. The parametrically excited upside-down rod: an elastic jointed pendulum model. *J Sound Vib* 2005;280:359–77.
- [22] Lampart M, Zapoměl J. Dynamics of a non-autonomous double pendulum model forced by biharmonic excitation with soft stops. *Nonlinear Dynamics* 2020;99:1909–21.
- [23] Song H, Park H, Park S. A springy pendulum could describe the swing leg kinetics of human walking. *J Biomech* 2016;49:1504–9.
- [24] Awrejcewicz J, Kudra G, Wasilewski G. Experimental and numerical investigation of chaotic regions in the triple physical pendulum. *Nonlinear Dynamics* 2007;50:755–66.
- [25] Yang F, Guo Q, Ma J. A neuron model with nonlinear membranes. *Cogn Neurodyn* 2024;18:673–84.
- [26] Liu J, Zhou Y, Duan S, et al. Memristive neural network circuit implementation of associative learning with overshadowing and blocking. *Cogn Neurodyn* 2023;17:1029–43.
- [27] Lu Q, Wang X, Tian J. A new biological central pattern generator model and its relationship with the motor units. *Cogn Neurodyn* 2022;16:135–47.
- [28] Selmi K, Bouallegue K, Soufi Y. A new class of chaotic attractors using different activation functions in neuron with multi dendrites. *Cogn Neurodyn* 2024. <https://doi.org/10.1007/s11571-024-10124-x>.
- [29] Chen Y, Yang F, Ren G, et al. Setting a double-capacitive neuron coupled with Josephson junction and piezoelectric source. *Cogn Neurodyn* 2024. <https://doi.org/10.1007/s11571-024-10145-6>.
- [30] Wu F, Ma J, Zhang G. Energy estimation and coupling synchronization between biophysical neurons. *SCIENCE CHINA Technol Sci* 2020;63:625–36.
- [31] Gjorgjieva J, Drion G, Marder E. Computational implications of biophysical diversity and multiple timescales in neurons and synapses for circuit performance. *Curr Opin Neurobiol* 2016;37:44–52.
- [32] Ye J, Rozdeba PJ, Morone UI, et al. Estimating the biophysical properties of neurons with intracellular calcium dynamics. *Phys Rev E* 2014;89:062714.
- [33] Groschner LN, Malis JG, Zuidinga B, et al. A biophysical account of multiplication by a single neuron. *Nature* 2022;603:119–23.
- [34] Li Y, Ma J, Xie Y. A biophysical neuron model with double membranes. *Nonlinear Dynamics* 2024;112:7459–75.
- [35] Tagluk ME, Isik I. Communication in nano devices: electronic based biophysical model of a neuron. *Nano Communication Networks* 2019;19:134–47.
- [36] Clark R, Fuller L, Platt JA, et al. Reduced-dimension, biophysical neuron models constructed from observed data. *Neural Comput* 2022;34:1545–87.
- [37] Schwemmer MA, Fairhall AL, Denève S, et al. Constructing precisely computing networks with biophysical spiking neurons. *J Neurosci* 2015;35:10112–34.
- [38] Marom S, Marder E. A biophysical perspective on the resilience of neuronal excitability across timescales. *Nat Rev Neurosci* 2023;24:640–52.
- [39] Wu F, Kang T, Shao Y, et al. Stability of Hopfield neural network with resistive and magnetic coupling. *Chaos, Solitons Fractals* 2023;172:113569.
- [40] Yu H, Galán RF, Wang J, et al. Stochastic resonance, coherence resonance, and spike timing reliability of Hodgkin–Huxley neurons with ion-channel noise. *Physica A: Statistical Mechanics and its Applications* 2017;471:263–75.
- [41] Andreev AV, Makarov VV, Runkova AE, et al. Coherence resonance in stimulated neuronal network. *Chaos, Solitons Fractals* 2018;106:80–5.
- [42] Chiu AWL, Bardakjian BL. Stochastic and coherence resonance in an in silico neural model. *Ann Biomed Eng* 2004;32:732–43.
- [43] Liu Y, Xu X. Stochastic and coherence resonance in a dressed neuron model. *International Journal of Bifurcation and Chaos* 2014;24:1450052.
- [44] Calim A, Palabas T, Uzuntarla M. Stochastic and vibrational resonance in complex networks of neurons. *Phil Trans R Soc A* 2021;379:20200236.
- [45] Deng H, Gui R, Yao Y. Temperature-induced logical resonance in the Hodgkin–Huxley neuron. *Chinese Physics B* 2023;32:120501.
- [46] Yao Y. Logical chaotic resonance in the FitzHugh–Nagumo neuron. *Nonlinear Dynamics* 2022;107:3887–901.
- [47] Yu D, Yang L, Zhan X, et al. Logical stochastic resonance and energy consumption in stochastic Hodgkin–Huxley neuron system. *Nonlinear Dynamics* 2023;111:6757–72.
- [48] Yao Y, Yao C. Autapse-induced logical resonance in the FitzHugh–Nagumo neuron. *Nonlinear Dynamics* 2023;111:4807–21.
- [49] Murali K, Rajasekar S, Aravind MV, et al. Construction of logic gates exploiting resonance phenomena in nonlinear systems. *Phil Trans R Soc A* 2021;379:20200238.
- [50] Nobukawa S, Nishimura H, Yamanishi T, et al. Analysis of chaotic resonance in Izhikevich neuron model. *PLoS One* 2015;10:e0138919.
- [51] Baysal V, Saraç Z, Yilmaz E. Chaotic resonance in Hodgkin–Huxley neuron. *Nonlinear Dynamics* 2019;97:1275–85.
- [52] Baysal V, Solmaz R, Ma J. Investigation of chaotic resonance in type-I and type-II Morris–Lecar neurons. *Appl Math Comput* 2023;448:127940.
- [53] Nobukawa S, Shibata N. Controlling chaotic resonance using external feedback signals in neural systems. *Sci Rep* 2019;9:4990.
- [54] Baysal V, Erkan E, Yilmaz E. Impacts of autapse on chaotic resonance in single neurons and small-world neuronal networks. *Phil Trans R Soc A* 2021;379:20200237.
- [55] Stiefel KM, Ermentrout GB. Neurons as oscillators. *J Neurophysiol* 2016;116:2950–60.
- [56] Rinberg A, Taylor AL, Marder E. The effects of temperature on the stability of a neuronal oscillator. *PLoS Comput Biol* 2013;9:e1002857.
- [57] Lytvyn V, Vysoitska V, Peleshchak I, et al. Time dependence of the output signal morphology for nonlinear oscillator neuron based on Van der Pol model. *International Journal of Intelligent Systems and Applications* 2018;10:8–17.
- [58] Laing CR. Phase oscillator network models of brain dynamics. *Computational models of brain and Behavior* 2017:505–17.
- [59] Luo L, Flanagan JG. Development of continuous and discrete neural maps. *Neuron* 2007;56:284–300.
- [60] Li Y, Lv M, Ma J, et al. A discrete memristive neuron and its adaptive dynamics. *Nonlinear Dynamics* 2024;112:7541–53.
- [61] He S, Rajagopal K, Karthikeyan A, et al. A discrete Huber–Braun neuron model: from nodal properties to network performance. *Cogn Neurodyn* 2023;17:301–10.
- [62] Guo YT, Ma J, Zhang XF, et al. Memristive oscillator to memristive map, energy characteristic. *SCIENCE CHINA Technol Sci* 2024;67:1567–78.
- [63] Narayanan R, Johnston D. Functional maps within a single neuron. *J Neurophysiol* 2012;108:2343–51.
- [64] Meinertzhagen IA, Takemura S, Meinertzhagen IA, et al. From form to function: the ways to know a neuron. *J Neurogenet* 2009;23:68–77.
- [65] Yu K, Niu X, Krook-Magnuson E, et al. Intrinsic functional neuron-type selectivity of transcranial focused ultrasound neuromodulation. *Nat Commun* 2021;12:2519.
- [66] Pan Y, Monje M. Activity shapes neural circuit form and function: a historical perspective. *J Neurosci* 2020;40:944–54.
- [67] Mizusaki BEP, O'Donnell C. Neural circuit function redundancy in brain disorders. *Curr Opin Neurobiol* 2021;70:74–80.
- [68] Bao B, Rong K, Li H, et al. Memristor-coupled logistic hyperchaotic map. *IEEE Trans Circuits Syst II Express Briefs* 2021;68:2992–6.
- [69] Bao B, Chen L, Bao H, et al. Bifurcations to bursting oscillations in memristor-based FitzHugh–Nagumo circuit. *Chaos, Solitons Fractals* 2024;181:114608.
- [70] Bao B, Hu J, Bao H, et al. Memristor-coupled dual-neuron mapping model: initials-induced coexisting firing patterns and synchronization activities. *Cogn Neurodyn* 2024;18:539–55.
- [71] Bao B, Hu J, Cai J, et al. Memristor-induced mode transitions and extreme multistability in a map-based neuron model. *Nonlinear Dynamics* 2023;111:3765–79.
- [72] Zhang J, Bao H, Gu J, et al. Multistability and synchronicity of memristor coupled adaptive synaptic neuronal network. *Chaos, Solitons Fractals* 2024;185:115157.
- [73] Baysal V, Yilmaz E. Effects of electromagnetic induction on vibrational resonance in single neurons and neuronal networks. *Physica A: Statistical Mechanics and its Applications* 2020;537:122733.
- [74] Kafraj MS, Parastesh F, Jafari S. Firing patterns of an improved Izhikevich neuron model under the effect of electromagnetic induction and noise. *Chaos, Solitons Fractals* 2020;137:109782.
- [75] Xu Q, Ju Z, Ding S, et al. Electromagnetic induction effects on electrical activity within a memristive Wilson neuron model. *Cogn Neurodyn* 2022;16:1221–31.
- [76] Yuan ZX, Feng PH, Du MM, et al. Dynamical response of a neuron–astrocyte coupling system under electromagnetic induction and external stimulation. *Chinese Physics B* 2020;29:030504.
- [77] Wang R, Fan Y, Wu Y. Spontaneous electromagnetic induction promotes the formation of economical neuronal network structure via self-organization process. *Sci Rep* 2019;9:9698.
- [78] Rostami Z, Jafari S. Defects formation and spiral waves in a network of neurons in presence of electromagnetic induction. *Cogn Neurodyn* 2018;12:235–54.
- [79] Xu Q, Wang K, Shan Y, et al. Dynamical effects of memristive electromagnetic induction on a 2D Wilson neuron model. *Cogn Neurodyn* 2024;18:645–57.
- [80] Ramasamy M, Devarajan S, Kumarasamy S, et al. Effect of higher-order interactions on synchronization of neuron models with electromagnetic induction. *Appl Math Comput* 2022;434:127447.
- [81] Wan Q, Yan Z, Li F, et al. Complex dynamics in a Hopfield neural network under electromagnetic induction and electromagnetic radiation. *Chaos: An Interdisciplinary Journal of Nonlinear Science* 2022;32:073107.
- [82] Hu X, Ding Q, Wu Y, et al. Dynamical rewiring promotes synchronization in memristive FitzHugh–Nagumo neuronal networks. *Chaos, Solitons Fractals* 2024;184:115047.
- [83] Kiani F, Yin J, Wang Z, et al. A fully hardware-based memristive multilayer neural network. *Sci Adv* 2021;7:eabj4801.
- [84] Liu H, Ma L, Wang Z, et al. An overview of stability analysis and state estimation for memristive neural networks. *Neurocomputing* 2020;391:1–12.
- [85] He S, Liu J, Wang H, et al. A discrete memristive neural network and its application for character recognition. *Neurocomputing* 2023;523:1–8.
- [86] Guo Y, Lv M, Wang C, et al. Energy controls wave propagation in a neural network with spatial stimuli. *Neural Netw* 2024;171:1–13.
- [87] Guo Y, Xie Y, Ma J. Nonlinear responses in a neural network under spatial electromagnetic radiation. *Physica A: Statistical Mechanics and its Applications* 2023;626:129120.
- [88] Yang F, Ren L, Ma J, et al. Two simple memristive maps with adaptive energy regulation and digital signal process verification. *Journal of Zhejiang University-Science A* 2024;25:382–94.
- [89] Wu FQ, Guo YT, Ma J. Energy flow accounts for the adaptive property of functional synapses. *SCIENCE CHINA Technol Sci* 2023;66:3139–52.
- [90] Ma J. Biophysical neurons, energy, and synapse controllability: a review. *Journal of Zhejiang University-Science A* 2023;24:109–29.
- [91] Lin H, Wang C, Deng Q, et al. Review on chaotic dynamics of memristive neuron and neural network. *Nonlinear Dynamics* 2021;106:959–73.
- [92] Guo YT, Song XL, Ma J. Control electromechanical arms by using a neural circuit. *Nonlinear Dynamics* 2024. <https://doi.org/10.1007/s11071-024-10260-3>.

- [93] Feliu V, Rattan KS, Brown HB. Control of a two-degree-of-freedom lightweight flexible arm with friction in the joints. *J Robot Syst* 1995;12:1–17.
- [94] Oh S, Kong K. Two-degree-of-freedom control of a two-link manipulator in the rotating coordinate system. *IEEE Trans Ind Electron* 2015;62:5598–607.
- [95] Faieghi MR, Delavari H, Baleanu D. A novel adaptive controller for two-degree of freedom polar robot with unknown perturbations. *Commun Nonlinear Sci Numer Simul* 2012;17:1021–30.
- [96] Osypiuk R, Finkemeyer B, Skoczowski S. Simple two degree of freedom structures and their properties. *Robotica* 2006;24:365–72.
- [97] Huang H, Dong E, Xu M, et al. Mechanism design and kinematic analysis of a robotic manipulator driven by joints with two degrees of freedom (DOF). *Industrial Robot: An International Journal* 2018;45:34–43.
- [98] Jin L, Li S, Yu J, et al. Robot manipulator control using neural networks: a survey. *Neurocomputing* 2018;285:23–34.
- [99] Liu Z, Peng K, Han L, et al. Modeling and control of robotic manipulators based on artificial neural networks: a review. *Iran J Sci Technol Trans Mech Eng* 2023;47:1307–47.
- [100] Truong TN, Vo AT, Kang HJ. Neural network-based sliding mode controllers applied to robot manipulators: a review. *Neurocomputing* 2023;562:126896.
- [101] Shinjo N, Swain GW. Use of a shape memory alloy for the design of an oscillatory propulsion system. *IEEE J Ocean Eng* 2004;29:750–5.
- [102] Gilardi G, Haslam E, Bundhoo V, et al. A shape memory alloy based tendon-driven actuation system for biomimetic artificial fingers, part II: modelling and control. *Robotica* 2010;28:675–87.
- [103] Park HB, Kim DR, Kim HJ, et al. Design and analysis of artificial muscle robotic elbow joint using shape memory alloy actuator. *Int J Precis Eng Manuf* 2020;21:249–56.
- [104] Hamid QY, Hasan WZW, Hanim MAA, et al. Shape memory alloys actuated upper limb devices: A review. *Sensors and Actuators Reports* 2023;5:100160.
- [105] Park SJ, Kim U, Park CH. A novel fabric muscle based on shape memory alloy springs. *Soft robotics* 2020;7:321–31.
- [106] Yasa Y, Sincar E, Ertugrul BT, et al. A multidisciplinary design approach for electromagnetic brakes. *Electr Power Syst Res* 2016;141:165–78.
- [107] Li P, Tang M, Lyu C, et al. Design and analysis of a novel active screw-drive pipe robot. *Advances in Mechanical Engineering* 2018;10. 1687814018801384.
- [108] Wang K, Ju H, Yang Y, et al. An optimized permanent magnet brake mechanism in robot joints. *IEEE Access* 2021;9:18278–86.
- [109] Tan R, Zheng J, Yu B, et al. Design and analysis of a hollow-ring permanent magnet brake for robot joints. *Mechanical Sciences* 2022;13:687–99.
- [110] Achille Ecladore TT, Bobo YE, Mbaka NE. Design and realization of a controlled electromagnetic breaking system. *J Eng* 2023;2023:1426506.
- [111] Eshgarf H, Nadooshan AA, Raisi A. An overview on properties and applications of magnetorheological fluids: dampers, batteries, valves and brakes. *Journal of Energy Storage* 2022;50:104648.
- [112] Jinaga R, Thimmaiah J, Kolekar S, et al. Design, fabrication and testing of a magnetorheologic fluid braking system for machine tool application. *SN Applied Sciences* 2019;1:328.
- [113] Agrawal A, Ciocanel C, Martinez T, et al. A bearing application using magnetorheological fluids. *J Intell Mater Syst Struct* 2002;13:667–73.
- [114] Skalski P, Kalita K. Role of magnetorheological fluids and elastomers in today's world. *Acta Mechanica et Automatica* 2017;11:267–74.
- [115] Hu G, Wu L, Li L, et al. Performance analysis of rotary magnetorheological brake with multiple fluid flow channels. *IEEE Access* 2020;8:173323–35.
- [116] Rouzbeh B, Bone GM, Ashby G, et al. Design, implementation and control of an improved hybrid pneumatic-electric actuator for robot arms. *IEEE access* 2019;7:14699–713.
- [117] Shi Y, Cai M, Xu W, et al. Methods to evaluate and measure power of pneumatic system and their applications. *Chin J Mech Eng* 2019;32:42.
- [118] Pustavrh J, Hočevan M, Podražaj P, et al. Comparison of hydraulic, pneumatic and electric linear actuation systems. *Sci Rep* 2023;13:20938.
- [119] Beater P. Modelling and control of pneumatic vane motors. *International Journal of Fluid Power* 2004;5:7–16.
- [120] Kazama T. Comparison of power density of transmission elements in hydraulic, pneumatic, and electric drive systems. *Mechanical Engineering Letters* 2019;5:19–00139.
- [121] Li XD, Xu Y. Energy level transition and mode transition in a neuron. *Nonlinear Dynamics* 2024;112:2253–63.
- [122] Fan D, Qi L, Hou S, et al. The seizure classification of focal epilepsy based on the network motif analysis. *Brain Res Bull* 2024;207:110879.
- [123] Zhao J, Yu Y, Han F, et al. Dynamic modeling and closed-loop modulation for absence seizures caused by abnormal glutamate uptake from astrocytes. *Nonlinear Dynamics* 2024;112:3903–16.
- [124] Yin L, Yu Y, Han F, et al. Unveiling serotonergic dysfunction of obsessive-compulsive disorder on prefrontal network dynamics: a computational perspective. *Cereb Cortex* 2024;34:bhae258.
- [125] Liu Z, Han F, Wang Q. A review of computational models for gamma oscillation dynamics: from spiking neurons to neural masses. *Nonlinear Dynamics* 2022;108:1849–66.
- [126] Liu ZL, Yu Y, Wang QY. Functional modular organization unfolded by chimera-like dynamics in a large-scale brain network model. *SCIENCE CHINA Technol Sci* 2022;65:1435–44.
- [127] Yu Y, Fan YB, Han F, et al. Transcranial direct current stimulation inhibits epileptic activity propagation in a large-scale brain network model. *SCIENCE CHINA Technol Sci* 2023;66:3628–38.
- [128] Huang W, Yang L, Zhan X, et al. Synchronization transition of a modular neural network containing subnetworks of different scales. *Front Inf Technol Electron Eng* 2023;24:1458–70.

An electromechanical arm model controlled by artificial muscles

Yitong GUO^{1,2,3} & Jun MA^{1,2*}

¹ College of Electrical and Information Engineering, Lanzhou University of Technology, Lanzhou 730050, China

² Department of Physics, Lanzhou University of Technology, Lanzhou 730050, China

³ Department of Mathematics, North University of China, Taiyuan, 030051, China

Received August 6, 2024; accepted November 26, 2024; published online March 5, 2025

Abstract An effective and rapid response of muscle contraction and relaxation is crucial for performing appropriate body gaits, including movements of the arms and legs. Any deformation in the muscles can disrupt gait stability, making muscle movement difficult. The arm, consisting of the radius, ulna, and humerus, can be modeled as mechanically jointed pendulums, with tensions from the arm muscles varying during contraction and relaxation. In a static state, the muscles maintain constant tension and length, even when external gravitational force is applied to the hand. This study presents a system in which a pair of jointed pendulums is driven by artificial muscles, represented by flexible ropes wound around the edge of an electronic motor's wheel. Muscle movement is simulated through the adjustment of the length of the flexible ropes attached to the motor. Switching between the clockwise and counterclockwise rotation of the motor modifies the length of the flexible ropes, thereby altering the intrinsic tensions to control arm movements. Electrical signals from a simple neural circuit are used to control the rotation of the electronic motor, enabling the regulation of muscle movement in the arm model by adjustable flexible ropes. The stability criterion for the electromechanical arm is derived, and the interactions among the neural circuit, electronic motor, and jointed pendulums are examined in detail. The results and proposed scheme can contribute to the design of controllable artificial arms, providing potential assistance to disabled arms by incorporating auxiliary artificial muscles.

Keywords jointed pendulums, muscle relaxation and contraction, neural signal, artificial muscle, control

Citation: Guo Y T, Ma J. An electromechanical arm model controlled by artificial muscles. *Sci China Tech Sci*, 2025, 68(4): 1420403, <https://doi.org/10.1007/s11431-024-2855-3>

1 Introduction

A continuous heartbeat maintains stable blood pumping, resulting from the ongoing relaxation and contraction of cardiac tissue controlled by electrical signals emitted from the sinoatrial node, which generates stable target waves [1–5]. Specifically, the sinoatrial node produces impulses that coordinate the heartbeat as these pulses propagate through the cardiac tissue. Any ischemic defects in the cardiac tissue can obstruct the propagation of target waves, potentially inducing arrhythmia and leading to the formation of spiral waves in the heart. These spiral waves, which exhibit a higher rotation frequency, can suppress target waves

and block signal propagation [6–10]. In severe cases, the breakup of these spiral waves can lead to fibrillation, making sudden cardiac death inevitable [11–14]. Therefore, continuous and robust regulation of cardiac tissue through electrical signals is essential for effective blood pumping, hemoglobin, and oxygen exchange, and maintaining a healthy metabolism. Conversely, the brain cortex plays a critical role in signal processing, body movement control, and decision-making. For example, the selection and control of body muscles are mainly governed by neural signals originating from the brain and spinal cord.

Stable body gaits and safe body movements mainly rely on the adaptive regulation and control of muscles, including those in the arms and legs. The relaxation and contraction of muscles in various limbs are governed by electrical signals

* Corresponding author (email: hyperchaos@163.com)

from the nervous system [13–17]. Damage to the arm or leg muscles can significantly restrict limb movement. Consequently, designing electromechanical devices can provide valuable assistance to disabled animals and humans [18], enabling disabled arms or legs to perform appropriate body movements and maintain safe gaits. The movements of jointed skeletons are constrained and depend on the tension of the attached muscles. Many movement disorders are associated with the disruption of neural signal propagation, resulting in muscles losing control of the neural signals originating in the brain. To address this, electromechanical devices can be utilized to assist body movements, enabling disabled arms and legs to perform appropriate gaits. The driving forces for robotic arms, legs, or manipulators can be achieved through the use of hydraulic devices, electric motors, and artificial muscles, with movement freedom being a critical factor for robotic manipulators. The instantaneous motion state should be monitored, allowing rapid feedback to adjust the manipulator and electric motor accordingly. For example, neural networks can be trained to control robotic manipulators [19–22], enabling the detection of potential faults to prevent incorrect movements. Alloys with distinct shape memory properties exhibit material and mechanical characteristics similar to those of muscles and tendons [23–26], making them suitable for fabricating flexible manipulators, as discussed in recent reviews [27]. Additionally, joint braking mechanisms can be activated using magnetorheological fluids [28–31]; for further guidance, refer to the reviews and references therein [32–34]. Two-degree-of-freedom robotic manipulators [35–38] control movement within a plane, and their characteristics can be emulated using jointed pendulums [39]. The nervous system exhibits highly self-adaptive properties, enabling the body to maintain stable and safe gaits. However, artificial electromagnetic devices and manipulators are subject to inevitable stochastic disturbances or excitations. For example, a flying bird can adaptively control its wings even in complex wind conditions. Refs. [40,41] discuss the impact of stochastic disturbances on airfoils in hypersonic flows and outline potential control strategies. Beyond nonlinear vibration, complex movements such as rolling motion under stochastic disturbances merit further study, with relevant insights and guidance found in recent works, such as in ref. [42].

In this study, two jointed pendulums are used to simulate the mechanical properties and movements of disabled arms. The disabled arm muscles are replaced with an artificial muscle device, implemented using flexible ropes attached to an electronic motor, with tension adjustments made by changing the rope length. The rotation of the electronic motor is regulated by current diverted from a neural circuit, which is controlled by external electrical stimuli. Consequently, the tensions applied to the jointed pendulums are

modified to maintain balance with the external weight/load and the intrinsic weight of the arm simultaneously. The torques and tensions produced by the artificial muscles are controlled by electrical signals from two coupled neural circuits. The stability conditions for the electromechanical arm driven by artificial muscles are analyzed through dynamical equations, and the energy characteristics of the neural circuit are also clarified. The suggestions and discussions presented in this work offer valuable insights for designing artificial arms and provide potential assistance for disabled arms and legs.

2 Model description and control discussion

The movement of muscles is controlled by neural electrical signals, enabling muscles to relax, contract, or maintain a fixed shape. Specifically, the length and cross-sectional area of muscles can be adjusted to maintain different body gaits, which depend on the propagation of electrical signals and external forces. Muscles control the movements of the arms, legs, and even the heartbeat, with electrical signals emitted from the sinoatrial node to generate target waves in cardiac tissue. Running and walking rely on the movement of leg and arm muscles, which are controlled by neural signals from the brain. Additionally, the heartbeat is associated with continuous contraction and relaxation in cardiac tissue, regulated by calcium flow and modulated by electrical signals from the sinoatrial node during wave propagation in the heart. As illustrated in Figure 1, arm extension and bending can be controlled by the arm muscles. According to the anatomical structure of the arm, the upper and lower arms can be modeled as a pair of jointed pendulums, as illustrated in Figure 2. The rotation angles relative to the horizontal or vertical direction can be adjusted by activating muscle tensions or applying external forces.

As illustrated in Figure 1, an electrical stimulus to the muscles or external gravity will alter the arm's gait during muscle movement. From a mechanical perspective, the arm's skeletal structure is similar to the movement of two jointed pendulums, as illustrated in Figure 2.

As illustrated in Figure 2, the point where the scapula hangs and the connection between the humerus and ulna (and radius) can be considered as two jointed points for a pair of connected pendulums. The muscle tensions in the arm can be modeled by applying an equivalent external force $F(t)$ at the terminal end B_0 of the jointed pendulums. Consequently, the jointed pendulums can be treated as an artificial arm, with their movement and stability depending on the intrinsic gravitational forces of the pendulums (P_1, P_2) and the external force $F(t)$ under torque balance.

According to the jointed pendulums model in Figure 2, the stability criterion is derived by

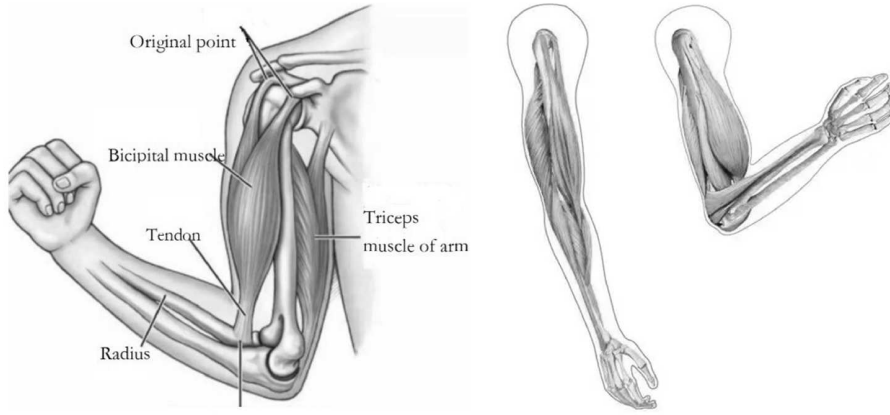


Figure 1 (Color online) Arm gaits and movements controlled by the arm muscles.

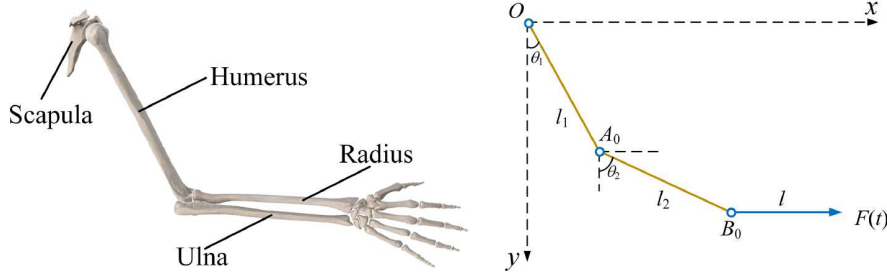


Figure 2 (Color online) Jointed arms vs. coupled pendulums. O , A_0 , and B_0 denote the joint points. The lengths of the humerus and ulna are represented by l_1 and l_2 , respectively. An external force $F(t)$ is applied via a beam with length l .

$$\begin{cases} F(t) \cdot l_2 \cos \theta_2 = P_2 \cdot \frac{l_2}{2} \sin \theta_2, \\ F(t) \cdot (l_2 \cos \theta_2 + l_1 \cos \theta_1) \\ = P_1 \cdot \frac{l_1}{2} \sin \theta_1 + P_2 \cdot \left(l_1 \sin \theta_1 + \frac{l_2}{2} \sin \theta_2 \right). \end{cases} \quad (1)$$

In the stable state, the rotation angles (θ_1 , θ_2) remain stable due to the balance between the clockwise torques generated by P_1 and P_2 and the counterclockwise torques induced by the external force $F(t)$, as follows:

$$\begin{cases} \tan \theta_2 = \frac{2F(t)}{P_2}, \\ \tan \theta_1 = \frac{2F(t)}{P_1 + 2P_2}. \end{cases} \quad (2)$$

From eq. (2), any change in the external force $F(t)$ or the muscle tensions will modify the arm gaits by simultaneously adjusting the rotation angles. Considering the flexibility of the arm muscles, as illustrated in Figure 3, flexible ropes are wound around the electronic motors (EM1 and EM2) to simulate the relaxation and contraction of the arm muscles. The intrinsic tensions produced by EM1 and EM2 are denoted as T_1 and T_2 , and the corresponding angles relative to their pendulum lengths will remain constant when the jointed pendulums maintain static stability.

Suppose EM1 and EM2 have the same physical config-

uration, with N -turn coils and intrinsic resistance R_0 . When an external current $I_S = I_{motor}$ is applied to the EMs, the rotational torque and tangential force along the wheel edge are given by

$$\begin{cases} \vec{M} = \vec{P}_M \times \vec{B}, \\ T = \frac{|\vec{M}|}{2r_0} = \frac{NSBI_{motor}}{2r_0} \sin(\vec{e}, \vec{B}) = kI_S(t) \sin(\omega_0 t). \end{cases} \quad (3)$$

The current through the electronic motor (EM) can be shunted from a neural circuit, with the coils in the EM functioning as a branch circuit that serves as a load for the driving neural circuit. Here, r_0 represents the motor radius,

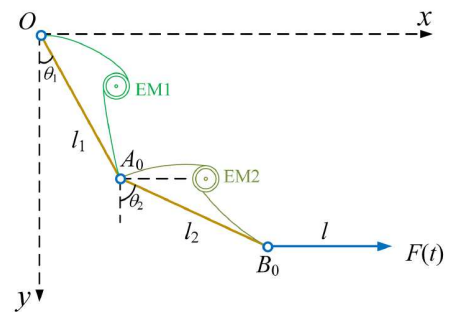


Figure 3 (Color online) Static jointed pendulums for stable arm gaits under the tensions of the artificial tissue without external load bearing. EM1 and EM2 represent electronic motors wound with flexible ropes.

and the gain k is related to the coil size and the internal magnetic field intensity B when the EM is activated by the current $I_S(t)$. The rotational frequency ω_0 is controlled by the external load and becomes constant once the system reaches a stable state. When EM1 and EM2 are endowed with the same physical parameters, the tension $T_1 = T_2 = T$, and this value is proportional to the current $I_S(t)$ flowing through the motor coils. Similar to the situation depicted in Figure 2, the torque balance between the jointed pendulums is described by

$$\overline{M}_{P1} + \overline{M}_{P2} = \overline{M}_{T1} + \overline{M}_{T2} + \overline{M}_F. \quad (4)$$

That is, the clockwise torques generated by P_1 and P_2 will balance against the counterclockwise torques generated by $F(t)$, T_1 , and T_2 . Specifically, the external force $F(t)$ provides additional support for the counterclockwise torques and can be set to zero when the two intrinsic tensions in the artificial muscles (flexible ropes via the EM) are sufficient to control the arm gaits. For simplicity, let $F(t) = 0$, and the criterion for torque balance is expressed as

$$\begin{cases} T_2 \cdot l_2 \sin \Omega_2 = P_2 \cdot \frac{l_2}{2} \sin \theta_2, \\ T_2 \cdot [l_2 \sin \Omega_2 + l_1 \sin(\theta_1 - \theta_2 + \Omega_2)] + T_1 \cdot l_1 \cdot \sin \Omega_1 \\ = P_2 \cdot \frac{l_2}{2} \sin \theta_2 + P_1 \cdot \frac{l_1}{2} \sin \theta_1. \end{cases} \quad (5)$$

The relationship between torque and force arm is provided in the Appendix. As a result, the rotation angles are given by

$$\begin{cases} \sin \theta_2 = \frac{2T_2 \sin \Omega_2}{P_2}, \\ \sin \theta_1 = \frac{2T_2 \sin(\theta_1 - \theta_2 + \Omega_2) + 2T_1 \sin \Omega_1}{P_1}. \end{cases} \quad (6)$$

The rotation angle θ_1 for pendulum OA depends on the interaction between the tensions T_1 , T_2 , and the gravity P_1 . Similarly, the rotation angle θ_2 , controlled by the gravity P_2 , also influences the changes in angle θ_1 . Once the rotation angles (θ_1 , θ_2) are obtained numerically, the corresponding angular velocities can be derived synchronously as $\omega = d\theta/dt$. According to the law of rigid body rotation, the relationship between angular acceleration and external torque for the jointed points (O , A_0) is expressed by

$$\begin{cases} J_O \frac{d^2 \theta_1}{dt^2} = J_O \frac{d\omega_1}{dt} \\ = \left(\frac{1}{3} \frac{P_1}{g} l_1^2 + \frac{1}{3} \frac{P_2}{g} l_2^2 + \frac{P_2}{g} l_1^2 \right) \frac{d^2 \theta_1}{dt^2} \\ = T_2 [l_2 \sin \Omega_2 + l_1 \sin(\theta_1 - \theta_2 + \Omega_2)] +_1 \\ T_1 \cdot l_1 \cdot \sin \Omega_1 - \left[P_2 \cdot \frac{l_2}{2} \sin \theta_2 + P_1 \cdot \frac{l_1}{2} \sin \theta_1 \right], \\ J_{AO} \frac{d^2 \theta_2}{dt^2} = J_{AO} \frac{d\omega_2}{dt} = \frac{1}{3} \frac{P_2}{g} l_2^2 \frac{d^2 \theta_2}{dt^2} \\ = T_2 l_2 \sin \Omega_2 - P_2 \frac{l_2}{2} \sin \theta_2. \end{cases} \quad (7)$$

Eq. (7) reduces to the same form as eq. (5) when the jointed pendulums are stabilized and not rotating over time. In the two-dimensional space, the positions of the jointed points (A_0 , B_0) can be determined by

$$\begin{cases} x_{A_0} = l_1 \sin \theta_1, y_{A_0} = l_1 \cos \theta_1, \\ x_{B_0} = l_1 \sin \theta_1 + l_2 \sin \theta_2, y_{B_0} = l_1 \cos \theta_1 + l_2 \cos \theta_2. \end{cases} \quad (8)$$

In the presence of gravitational disturbance, a gravity force P is applied at the endpoint B_0 , similar to the case where the hand is holding a weight P , as illustrated in Figure 4.

The torque balance for the jointed pendulums in Figure 4 can be expressed as

$$\begin{cases} T_2 \cdot l_2 \sin \Omega_2 + F(t) \cdot l_2 \cos \theta_2 \\ = P_2 \cdot \frac{l_2}{2} \sin \theta_2 + P \cdot l_2 \cdot \sin \theta_2, \\ T_2 \cdot [l_2 \sin \Omega_2 + l_1 \sin(\theta_1 - \theta_2 + \Omega_2)] + T_1 \cdot l_1 \cdot \sin \Omega_1 \\ + F(t) \cdot [l_2 \cos \theta_2 + l_1 \cos \theta_1] \\ = P_2 \cdot \frac{l_2}{2} \sin \theta_2 + P_1 \cdot \frac{l_1}{2} \sin \theta_1 + P \cdot [l_2 \sin \theta_2 + l_1 \sin \theta_1]. \end{cases} \quad (9)$$

When the external force $F(t)$ is removed, the relationship between the rotation angles is given by

$$\begin{cases} \sin \theta_2 = \frac{2T_2 \sin \Omega_2}{P_2 + 2P}, \\ \sin \theta_1 = \frac{2T_2 \sin(\theta_1 - \theta_2 + \Omega_2) + 2T_1 \sin \Omega_1}{P_1 + 2P}. \end{cases} \quad (10)$$

The involvement of the external weight P alters the angular frequencies in (θ_1 , θ_2), while the artificial muscles are regulated to generate varying tensions (T_1 , T_2) to maintain dynamic balance in the jointed pendulums. In this manner, the arm gaits are adjusted in synchrony with changes in the external weight P . As shown in eq. (3), the tension values (T_1 , T_2) are proportional to the channel current $I_{motor} = I_S$ flowing through the N-turn coils in EM1 and EM2. Theoretically, the stimulus I_S can be generated by a piezoelectric ceramic through the capture of acoustic waves [43, 44] or by photocurrent generated across a phototube through the conversion of external illumination. In practice, the forcing current I_S can be derived from a simple neural circuit consisting of a capacitor, inductor, nonlinear resistor, and a voltage source. As a result, the N-turn coils in EM1 and EM2 can be treated as additive load circuits to the neural circuit. Assuming the load coils have an inductance denoted as L_{MT} , and both EMs are selected with the same inductance, $L_{MT1} = L_{MT2} = L_{MT}$. In Figure 5, external illumination is applied to activate the phototubes, generating photocurrents. These photocurrents are then used to excite the two coupled neural circuits via a resistor with resistance R . The shunted currents across the load circuits with intrinsic inductance L_{MT} will activate the electronic motors EM1 and EM2.

The relationship between the physical variables in Figure 5 can be expressed as

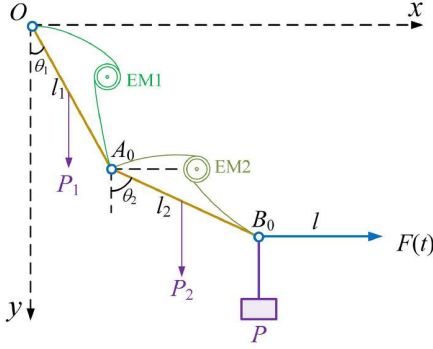


Figure 4 (Color online) Static jointed pendulums for stable arm gaits in the presence of an external gravitational load P . P_1 , P_2 , and P represent the gravitational forces acting on the pendulum OA_0 , A_0B_0 , and the external weight, respectively. EM1 and EM2 apply intrinsic tensions along the flexible ropes, marked as T_1 and T_2 , respectively.

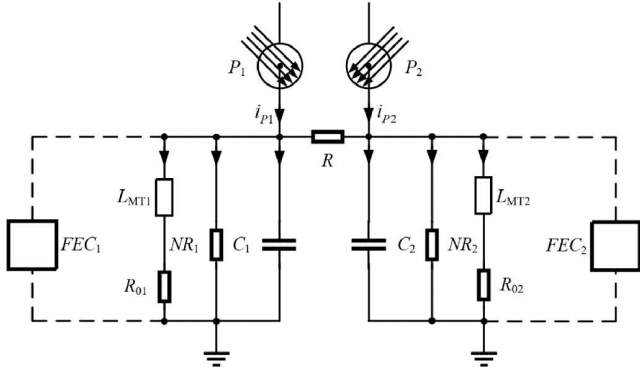


Figure 5 (Color online) Schematic diagram of the coupled neural circuits driving the EMs. The photocurrents i_{p1} and i_{p2} are generated in the phototubes under external illumination. R_0 represents the intrinsic resistance in the load circuit, and R is the resistance of the resistor in the coupling channel. NR is a nonlinear resistor, and the functional electronic component (FEC) can be chosen from options such as a memristor, induction coil, Josephson junction, thermistor, or piezoelectric ceramic.

$$\begin{cases} C_1 \frac{dV_1}{dt} = i_{p1} - i_{MT1} - i_{NR1} + \frac{V_2 - V_1}{R}, \\ L_{MT1} \frac{di_{MT1}}{dt} = V_1 - R_0 i_{MT1}, \\ C_2 \frac{dV_2}{dt} = i_{p2} - i_{MT2} - i_{NR2} + \frac{V_1 - V_2}{R}, \\ L_{MT2} \frac{di_{MT2}}{dt} = V_2 - R_0 i_{MT2}. \end{cases} \quad (11)$$

For simplicity, the channel current through the nonlinear resistor (NR) is given by

$$\begin{cases} i_{NR1} = -\frac{1}{\rho} \left(V_1 + \frac{V_1^2}{E} - \frac{V_1^3}{E^2} \right), \\ i_{NR2} = -\frac{1}{\rho} \left(V_2 + \frac{V_2^2}{E} - \frac{V_2^3}{E^2} \right). \end{cases} \quad (12)$$

The intrinsic parameters (E, ρ) are related to the material

properties of NR and can be estimated by measuring the i - v curve in the experimental circuit. The field energy (W) is mainly stored in the capacitive and inductive components, including capacitors and induction coils, in the neural circuit illustrated in Figure 5.

$$W = \frac{1}{2} C_1 V_1^2 + \frac{1}{2} L_{MT1} i_{MT1}^2 + \frac{1}{2} C_2 V_2^2 + \frac{1}{2} L_{MT2} i_{MT2}^2. \quad (13)$$

For the numerical approach and dynamical analysis, the physical variables in eq. (10) can be redefined as dimensionless variables using a scale transformation [39, 45] as follows:

$$\begin{cases} x_1 = \frac{V_1}{E}, y_1 = \frac{\rho i_{MT1}}{E}, \tau = \frac{t}{\rho C_1}, x_2 = \frac{V_2}{E}, \\ y_2 = \frac{\rho i_{MT2}}{E}, i'_{p1} = \frac{\rho i_{p1}}{E}, i'_{p2} = \frac{\rho i_{p2}}{E}, \\ a = \frac{\rho^2 C_1}{L_{MT}}, b = \frac{R_0}{\rho}, c = \frac{C_1}{C_2}, \delta = \frac{\rho}{R}. \end{cases} \quad (14)$$

As a result, the dynamics of the coupled neural and artificial muscle model are described by

$$\begin{cases} \frac{dx_1}{d\tau} = i'_{p1} - y_1 + x_1 + x_1^2 - x_1^3 + \delta(x_2 - x_1), \\ \frac{dy_1}{d\tau} = a(x_1 - by_1), \\ \frac{dx_2}{d\tau} = c(i'_{p2} - y_2 + x_2 + x_2^2 - x_2^3) + c\delta(x_1 - x_2), \\ \frac{dy_2}{d\tau} = a(x_2 - by_2). \end{cases} \quad (15)$$

Additionally, the field energy W is replaced by an equivalent Hamilton energy H , as follows:

$$H = \frac{W}{C_1 E^2} = \frac{1}{2} x_1^2 + \frac{1}{2a} y_1^2 + \frac{1}{2} c x_2^2 + \frac{1}{2a} y_2^2. \quad (16)$$

When two capacitors are selected with the same value, $C_1 = C_2 = C$, eqs. (15) and (16) can be updated by setting the parameter $c = 1$. By varying the external photocurrents, the two load circuits are excited to drive EM1 and EM2, allowing the artificial muscles to effectively stabilize arm gaits. To further enhance the controllability of the neural circuit in Figure 5, memristors [46–50] can be added to the branch circuit. The memristive channels can perceive and capture external physical signals in the presence of an electromagnetic field, enabling the encoding of external field energy to excite the EMs, even when the external photocurrents are of low intensity. Eqs. (15) and (16) provide dimensionless definitions for the variables and the energy function. The current variables across EM1 and EM2 in Figure 5 and eq. (15) are denoted as i_{MT1} and i_{MT2} , which control the torques in the EMs and the tensions in the artificial muscles defined in eqs. (3) and (5). That is, $I_s(t) = I_{motor} = i_{MT}$. In conjunction with eq. (15), the tensions in the artificial muscles generated by the EMs in eq. (3) can be updated as follows:

$$\begin{cases} T_1 = \frac{|M_1|}{2r_0} = \frac{NSBi_{S1}}{2r_0} \sin(\bar{e}, \bar{B}) \\ = \frac{NSBi_{MT1}}{2r_0} \sin(\bar{e}, \bar{B}) = ki_{MT1}, \\ T_2 = \frac{|M_2|}{2r_0} = \frac{NSBi_{S2}}{2r_0} \sin(\bar{e}, \bar{B}) \\ = \frac{NSBi_{MT2}}{2r_0} \sin(\bar{e}, \bar{B}) = ki_{MT2}. \end{cases} \quad (17)$$

The coefficient k is related to the physical properties of the EM, and the dimensional tensions (T_1' , T_2') for the artificial muscles are expressed as follows:

$$\begin{cases} T_1' = \frac{T_1}{P_0} = \frac{T_1 r_0}{C_1 E^2} = \frac{NSBi_{MT1}}{2C_1 E^2} \sin(\bar{e}, \bar{B}) \\ = \frac{NSB}{2\rho C_1 E} \sin(\bar{e}, \bar{B}) y_1 = k' y_1, \\ T_2' = \frac{T_2}{P_0} = \frac{T_2 r_0}{C_1 E^2} = \frac{NSBi_{MT2}}{2C_1 E^2} \sin(\bar{e}, \bar{B}) \\ = \frac{NSB}{2\rho C_1 E} \sin(\bar{e}, \bar{B}) y_2 = k' y_2, \\ P_1' = \frac{P_1}{P_0}, P_2' = \frac{P_2}{P_0}, P' = \frac{P}{P_0}. \end{cases} \quad (18)$$

The dimensionless gain k' can be considered an intrinsic parameter for the artificial muscle. Furthermore, the torque balance criterion in eq. (6) is also updated as follows:

$$\begin{cases} \sin\theta_2 = \frac{2T_2' \sin\Omega_2}{P_2'}, \\ \sin\theta_1 = \frac{2T_2' \sin(\theta_1 - \theta_2 + \Omega_2) + 2T_1' \sin\Omega_1}{P_1'}. \end{cases} \quad (19)$$

Considering the tension properties of the artificial muscle, the maximum torque resulting from the muscle tension can be achieved by setting $\sin\Omega_1 = \sin\Omega_2 = 1$, where the tension directions are perpendicular to the pendulum length. In this case, eq. (19) can be simplified as follows:

$$\begin{cases} \sin\theta_2 = \frac{2T_2'}{P_2'} = \frac{2k' y_1}{P_2'}, \\ \sin\theta_1 = \frac{2T_2' \cos(\theta_2 - \theta_1) + 2T_1'}{P_1'} \\ = \frac{2k' y_2 \cos(\theta_2 - \theta_1) + 2k' y_1}{P_1'}. \end{cases} \quad (20)$$

According to the stability condition for the jointed pendulums in eq. (20), any change in the variable y_1 , generated from eq. (15), will simultaneously modify the rotation angles (θ_1 , θ_2), and the arm gaits will stabilize quickly. In the presence of external weight P , the torque balance criterion in eq. (10) can also be updated by setting $\sin\Omega_1 = \sin\Omega_2 = 1$ (or $\Omega_1 = \Omega_2 = \pi/2$) as follows:

$$\begin{cases} \sin\theta_2 = \frac{2T_2' \sin\Omega_2}{P_2' + 2P} = \frac{2T_2' \sin\Omega_2}{P_2' + 2P'} = \frac{2k' y_2}{P_2' + 2P'}, \\ \sin\theta_1 = \frac{2T_2' \sin(\theta_1 - \theta_2 + \Omega_2) + 2T_1' \sin\Omega_1}{P_1' + 2P} \\ = \frac{2k' y_2 \cos(\theta_2 - \theta_1) + 2k' y_1}{P_1' + 2P'}. \end{cases} \quad (21)$$

From eq. (21), any change in the external weight can induce a new dynamic stability in the jointed pendulums by adjusting the angles (θ_1 , θ_2) synchronously. That is, the artificial muscles can adjust the intrinsic tensions to generate appropriate torques that counteract changes in the external weight.

In the control circuit illustrated in Figure 5, two phototubes function like eyes, converting external illumination into photoelectric currents. These currents then control the EMs to maintain appropriate tensions and torques in the jointed pendulums. Capacitive components, such as capacitors and charge-controlled memristors, are effective at storing electric field energy under external electrical stimuli.

3 Numerical results and discussion

Using the fourth-order Runge–Kutta algorithm on eq. (15), the time series for membrane potentials, mapped from the output voltages of the coupled neural circuits, are obtained with a time step of 0.01. The transient period is set to 500 time units, and the initial values for the variables are selected as (0.2, 0.1, 0.2, 0.1). In Figure 6, the sampled membrane potentials for the first equation in eq. (15) are obtained for bifurcation analysis by varying the intensity of the photocurrent applied to the neuron, with both neurons receiving the same photocurrent.

As depicted in Figure 6, the coupled neurons exhibit distinct mode transitions in electrical activity as the intensity of the photocurrents increases. In this way, different firing modes can be induced to control the artificial muscles and arm movement. Additionally, the evolution of the variables

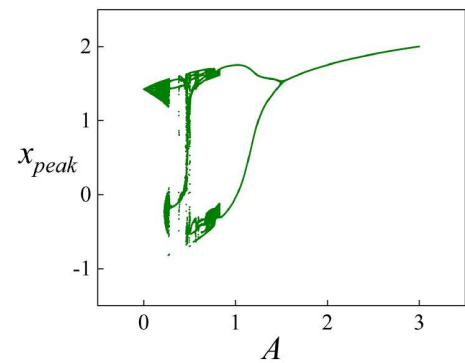


Figure 6 (Color online) Bifurcation diagram of membrane potential plotted by tracking the peak values of the variable x_1 . Parameters are set as $\delta = 0.2$, $a = 0.5$, $b = 0.3$, $c = 0.7$, $\omega_1 = \omega_2 = 1.3$.

and energy function for the coupled neurons is illustrated in Figures 7–9, with varying photocurrent intensities.

From Figures 7–9, the average energy $\langle H \rangle$ decreases from 2.04842 to 1.33887, followed by a slight increase as the intensity of the photocurrent increases. This change has a distinct impact on the excitability and firing patterns of the coupled neurons. The two neurons rarely maintain synchronization under bidirectional coupling during changes in the membrane potentials. It is interesting to examine the changes in the rotation angles of the arm under stable conditions when the neural signals are endowed with different intensities, as illustrated in Figure 10.

The two parts of the arm control their movements through the regulation of electrical signals, which activate the artificial muscles and ensure the arm maintains stability under external load bearing, as shown in eq. (21). The coupled neurons and neural circuits direct different currents along two distinct channels, while the movements of the upper arm and forearm are regulated synchronously due to the coupling between the two neural circuits. As a result, the arm can exhibit different gaits in response to neural stimuli, even when different load bearings are applied. That is, the movement or rotation of the upper arm and forearm is influenced during neural driving, allowing for the stabilization of appropriate gaits.

As shown in eq. (14), the capacitance C of a capacitor plays a crucial role in setting reference values for the time unit and energy unit, with $\tau = t/RC$, during the scale trans-

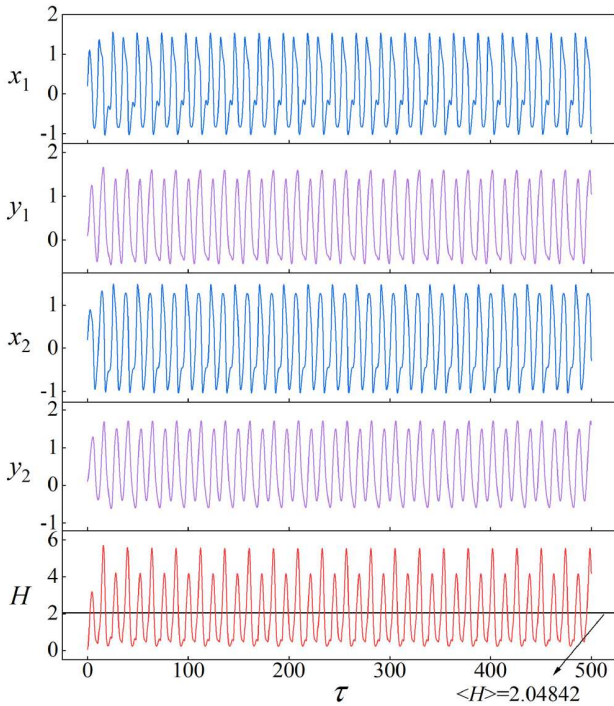


Figure 7 (Color online) Changes in membrane potential (x_1, x_2), channel current (y_1, y_2), and energy value over time. Parameters set as $\delta = 0.2$, $a = 0.5$, $b = 0.3$, $c = 0.7$, $\omega_1 = \omega_2 = 1.3$, $A = 0.3$.

formation of the physical variables. Additionally, inductive coils can be incorporated into the branch circuit in Figure 5,

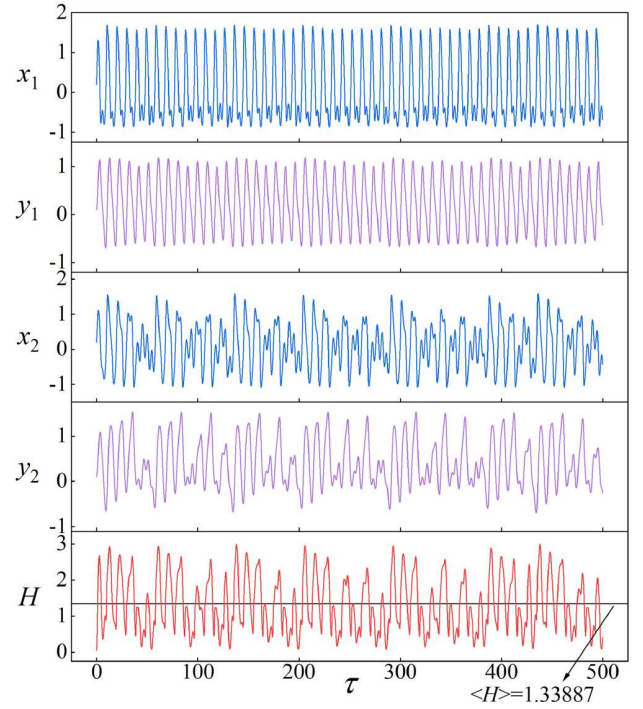


Figure 8 (Color online) Changes in membrane potential (x_1, x_2), channel current (y_1, y_2), and energy value over time. Parameters set as $\delta = 0.2$, $a = 0.5$, $b = 0.3$, $c = 0.7$, $\omega_1 = \omega_2 = 1.3$, $A = 0.7$.

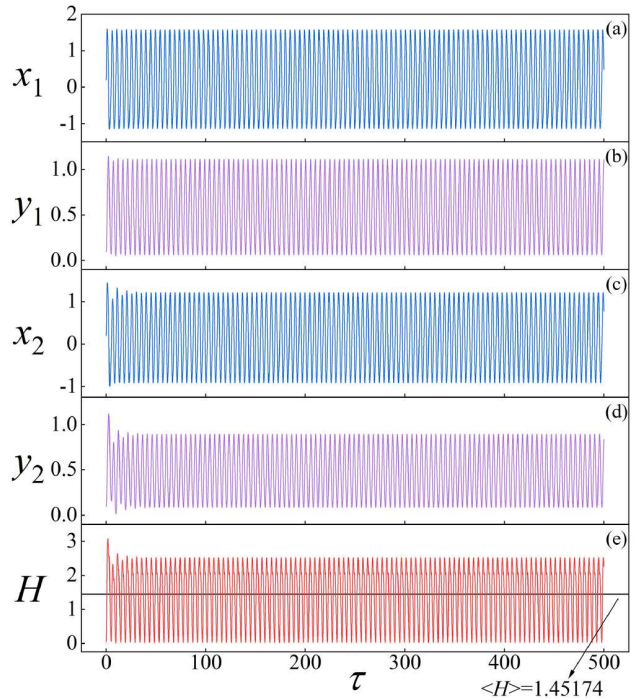


Figure 9 (Color online) Changes in membrane potential (x_1, x_2), channel current (y_1, y_2), and energy value over time. Parameters set as $\delta = 0.2$, $a = 0.5$, $b = 0.3$, $c = 0.7$, $\omega_1 = \omega_2 = 1.3$, $A = 1.6$.

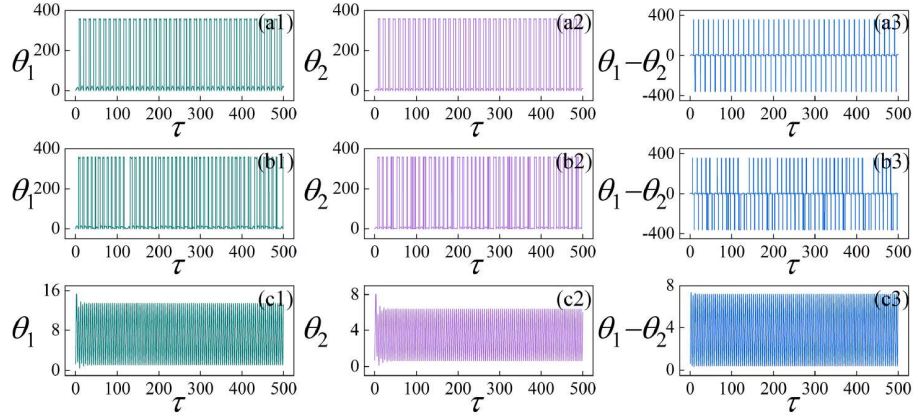


Figure 10 (Color online) Evolution of rotation angles and angle error over time. Parameters set as $\delta = 0.2$, $a = 0.5$, $b = 0.3$, $c = 0.7$, $\omega_1 = \omega_2 = 1.3$, $k' = 0.1$, $P' = 0.6$, $P_1' = 0.5$, $P_2' = 0.4$. For (a1, a2, a3), $A = 0.3$; (b1, b2, b3), $A = 0.7$; (c1, c2, c3), $A = 1.6$.

enabling the energy exchange between the magnetic field and the electric field, which in turn activates complex dynamics and firing patterns similar to those observed in biophysical neurons. The coupled neural circuits in Figure 5 serve as signal sources, stimulating the artificial muscles, which are mimicked by a combination of EMs and flexible ropes, to effectively control body and arm gaits. However, equivalent neural circuits can be constructed by replacing the capacitance C with a combination of resistance R and inductance L when a capacitor is unavailable. The dimensional transformation is described by

$$\begin{cases} [T] = \left[\frac{\varphi}{V} \right] = \left[\frac{LI}{RI} \right] = \left[\frac{L}{R} \right], \\ [RC] = [R] \left[\frac{Q}{V} \right] = \left[\frac{R}{V} \right] [IT] = \left[\frac{RI}{V} \right] [T] = [T], \\ [C] = \left[\frac{q}{V} \right] = \left[\frac{1}{V} \right] [I] \left[\frac{L}{R} \right] = \left[\frac{1}{RI} \right] [I] \left[\frac{L}{R} \right] = \left[\frac{L}{R^2} \right], \\ \tau = \frac{t}{T} = t \frac{R}{L} = \frac{t}{RC}, \quad q' = \frac{q}{CV_0} = \frac{R^2}{V_0 L} q. \end{cases} \quad (22)$$

The symbol $[*]$ represents dimensional operation, where t , q , v , I , and φ are physical variables. Without the use of capacitor components, effective nonlinear circuits can still be constructed to obtain equivalent neuron oscillators for further dynamic analysis. In summary, a simple artificial muscle approach is proposed by controlling the length and tension of flexible ropes wound around the EM. The stability of the jointed pendulums closely resembles the selection of arm gaits controlled by arm muscles. The tensions in the artificial muscles generate anticlockwise torques to counteract the clockwise torques caused by the weights in the coupled pendulums and the external weight. Electrical signals from the coupled neural circuits control the torques generated by the EMs, allowing the arm gaits and jointed pendulums to maintain stability synchronously.

Finally, it is interesting to discuss the implementation of adaptive dynamical stability in Figures 3 and 4 by regulating

the torques of the EM and the intrinsic tension along the flexible rope adaptively. The rotational torque generated by the EM depends on the channel current across its load circuits (L_{MT1} , L_{MT2}). According to eq. (15), the dimensionless parameters (a , b , δ) can be adjusted to detect the increase or decrease of the dimensionless current (y_1 , y_2). A larger value for parameter b can stabilize the second variable in eq. (15). When the external heavy load P is decreased, and a smaller rotational torque can maintain balance with the torques relative to the gravitational forces of the jointed pendulums and the heavy load. Alternatively, increasing the heavy load P requires stronger tensions and higher torques to balance the gravitational torques. The rotational torques are proportional to the channel current across the load circuit of the EM and are also dependent on the shunted currents along other channels and electronic components. The rotation angles (θ_1 , θ_2) are detectable and observable, and some parameters mapped from the physical parameters in the driving neural circuits can be regulated to control the current in the load circuit, tension, and rotational torque of the EM synchronously and adaptively. Following the adaptive growth criterion of parameters under energy flow, a Heaviside function composed of detectable kernel variables can be proposed [51–53]. For example, the parameter b can be regulated to control the rotation angle θ_1 as follows:

$$\begin{aligned} \frac{db}{d\tau} &= \sigma \cdot b \cdot \mathcal{G}(\theta_1 - \theta_0), \quad \mathcal{G}(X) = 1, X \geq 0, \\ \mathcal{G}(X) &= 0, X < 0. \end{aligned} \quad (23)$$

The gain σ can be selected to have either positive or negative values, and the parameter b is then increased or decreased to adjust the channel current across the load circuit. The threshold θ_0 in the Heaviside function in eq. (23) controls the initiation time for the growth of parameter b . As a result, the torque from the EM and the tension in the artificial muscle are regulated. From an energy perspective, a lower proportion of capacitive energy (energy stored in the capa-

citors in Figure 5) will support a higher proportion of inductive energy, allowing the load circuits to maintain higher energy and channel current. This, in turn, enables the EMs to generate stronger rotational torques. Consequently, higher torques lead to increased rotation angles (θ_1 , θ_2). Therefore, energy proportion can serve as the kernel variable in the Heaviside function in eq. (23), and an intrinsic parameter can be adaptively controlled to stabilize the arm gait and rotational angles.

Disabled muscles impede the body's ability to respond quickly and efficiently to neural electrical signals, thus restricting body gaits. Neurological diseases [54–57], such as Parkinson's and Alzheimer's, can negatively impact the stability of body gaits. In addition to potential neurogenic repair, the implementation of electromechanical systems under adaptive control may offer auxiliary support for safe body gaits and movement. Therefore, the proposed scheme, where muscle tension is controlled through the interaction of EMs with flexible ropes, can enable the regulation of skeletal movements to achieve suitable gaits. Building on the concepts discussed in this work, inverted and jointed pendulums can be further explored to investigate complex arm and leg gaits achieved through the activation of torques and tensions from artificial muscles or via gears.

4 Conclusion

In this work, the stability and movements of the arms are explored using a pair of jointed pendulums driven by artificial muscles, which are simulated by controlling the relaxation and contraction of flexible ropes via an electronic motor. The tensions in the artificial muscles can generate anticlockwise torques to counteract the clockwise torques produced by external weights. The rotation of EMs is controlled by the current from a couple of coupled neural circuit driven by photocurrents. In turn, the appropriate tensions and torques are adjusted to maintain stability in the electromechanical arm through torque balance. This scheme is useful for designing artificial arms and offers insights for repairing arms disabled due to muscle damage. The numerical solutions for these nonlinear equations can be obtained using the fourth-order Runge–Kutta algorithm, and the stability of the artificial arm under torque balance can be verified numerically, following the theoretical analysis outlined above. The electromechanical arm device provides valuable support for individuals with disabled arms.

Acknowledgements This work was supported by the National Natural Science Foundation of China (Grant Nos. 62361037, 12072139).

References

- Müllenbroich M C, Kelly A, Acker C, et al. Novel optics-based approaches for cardiac electrophysiology: A Review. *Front Physiol*, 2021, 12: 769586
- Cherubini C, Filippi S, Nardinocchi P, et al. An electromechanical model of cardiac tissue: Constitutive issues and electrophysiological effects. *Prog Biophys Mol Biol*, 2008, 97: 562–573
- Agladze K, Kay M W, Krinsky V, et al. Interaction between spiral and paced waves in cardiac tissue. *Am J Physiol-Heart Circulatory Physiol*, 2007, 293: H503–H513
- Sidorov V Y, Aliev R R, Woods M C, et al. Spatiotemporal dynamics of damped propagation in excitable cardiac tissue. *Phys Rev Lett*, 2003, 91: 208104
- Pinnell J, Turner S, Howell S. Cardiac muscle physiology. *Continuing Education Anaesthesia Crit Care Pain*, 2007, 7: 85–88
- Shajahan T K, Nayak A R, Pandit R, et al. Spiral-wave turbulence and its control in the presence of inhomogeneities in four mathematical models of cardiac tissue. *PLoS ONE*, 2009, 4: e4738
- Kim T Y, Woo S J, Hwang S, et al. Cardiac beat-to-beat alternations driven by unusual spiral waves. *Proc Natl Acad Sci USA*, 2007, 104: 11639–11642
- Bernus O, Verschelde H, Panfilov A V. Spiral wave stability in cardiac tissue with biphasic restitution. *Phys Rev E*, 2003, 68: 021917
- Rappel W J, Krummen D E, Baykaner T, et al. Stochastic termination of spiral wave dynamics in cardiac tissue. *Front Netw Physiol*, 2022, 2: 809532
- Kachalov V N, Kudryashova N N, Agladze K I. Spontaneous spiral wave breakup caused by pinning to the tissue defect. *Jetp Lett*, 2016, 104: 635–638
- Weiss J N, Qu Z, Chen P S, et al. The dynamics of cardiac fibrillation. *Circulation*, 2005, 112: 1232–1240
- Conte M, Petraglia L, Cabaro S, et al. Epicardial adipose tissue and cardiac arrhythmias: Focus on atrial fibrillation. *Front Cardiovasc Med*, 2022, 9: 932262
- Kuo I Y, Ehrlich B E. Signaling in muscle contraction. *Cold Spring Harb Perspect Biol*, 2015, 7: a006023
- Göktepe S, Wong J, Kuhl E. Atrial and ventricular fibrillation: Computational simulation of spiral waves in cardiac tissue. *Arch Appl Mech*, 2010, 80: 569–580
- Sweeney H L, Hammers D W. Muscle contraction. *Cold Spring Harb Perspect Biol*, 2018, 10: a023200
- Kato K, Muraoka T, Higuchi T, et al. Interaction between simultaneous contraction and relaxation in different limbs. *Exp Brain Res*, 2014, 232: 181–189
- Yotani K, Nakamoto H, Ikudome S, et al. Muscle contraction and relaxation-response time in response to on or off status of visual stimulus. *J Physiol Anthropol*, 2014, 33: 23
- Guo Y, Song X, Ma J. Control electromechanical arms by using a neural circuit. *Nonlinear Dyn*, 2025, 113: 1605–1622
- Liu Z, Peng K, Han L, et al. Modeling and control of robotic manipulators based on artificial neural networks: A review. *Iran J Sci Technol Trans Mech Eng*, 2023, 47: 1307–1347
- Eski I, Erkaya S, Savas S, et al. Fault detection on robot manipulators using artificial neural networks. *Robotics Comput-Integrated Manufacturing*, 2011, 27: 115–123
- Kim Y H, Lewis F L, Dawson D M. Intelligent optimal control of robotic manipulators using neural networks. *Automatica*, 2000, 36: 1355–1364
- Gupta P, Sinha N K. Intelligent control of robotic manipulators: Experimental study using neural networks. *Mechatronics*, 2000, 10: 289–305
- Aversa R, Tamburrino F, Petrescu R V V, et al. Biomechanically inspired shape memory effect machines driven by muscle like acting NiTi alloys. *Am J Appl Sci*, 2016, 13: 1264–1271
- Kujala S, Pajala A, Kallioinen M, et al. Biocompatibility and strength properties of nitinol shape memory alloy suture in rabbit tendon. *Biomaterials*, 2004, 25: 353–358
- Laurentis K J D, Mavroidis C. Mechanical design of a shape memory alloy actuated prosthetic hand. *THC*, 2002, 10: 91–106
- Hoh D J, Hoh B L, Amar A P, et al. Shape memory alloys. *Oper*

- Neurosurg, 2009, 64: 199–215
- 27 Rodrigue H, Wang W, Han M W, et al. An overview of shape memory alloy-coupled actuators and robots. *Soft Robotics*, 2017, 4: 3–15
 - 28 Jinaga R, Thimmaiah J, Kolekar S, et al. Design, fabrication and testing of a magnetorheologic fluid braking system for machine tool application. *SN Appl Sci*, 2019, 1: 1–2
 - 29 Hu G, Wu L, Li L, et al. Performance analysis of rotary magnetorheological brake with multiple fluid flow channels. *IEEE Access*, 2020, 8: 173323–173335
 - 30 Nakamura T, Midorikawa Y, Tomori H. Position and vibration control of variable rheological joints using artificial muscles and magnetorheological brake. *Int J Hum Robot*, 2011, 8: 205–222
 - 31 Sarkar C, Hirani H. Synthesis and characterization of nano-particles based magnetorheological fluids for brake. *Tribol Online*, 2015, 10: 282–294
 - 32 Eshgarf H, Ahmadi Nadooshan A, Raisi A. An overview on properties and applications of magnetorheological fluids: Dampers, batteries, valves and brakes. *J Energy Storage*, 2022, 50: 104648
 - 33 Hua D, Liu X, Li Z, et al. A review on structural configurations of magnetorheological fluid based devices reported in 2018–2020. *Front Mater*, 2021, 8: 640102
 - 34 Kumar J S, Paul P S, Raghunathan G, et al. A review of challenges and solutions in the preparation and use of magnetorheological fluids. *Int J Mech Mater Eng*, 2019, 14: 13
 - 35 Oh S, Kong K. Two-degree-of-freedom control of a two-link manipulator in the rotating coordinate system. *IEEE Trans Ind Electron*, 2015, 62: 5598–5607
 - 36 Faieghi M R, Delavari H, Baleanu D. A novel adaptive controller for two-degree of freedom polar robot with unknown perturbations. *Commun Nonlinear Sci Numer Simul*, 2012, 17: 1021–1030
 - 37 Osypiuk R, Finkemeyer B, Skoczowski S. Simple two degree of freedom structures and their properties. *Robotica*, 2006, 24: 365–372
 - 38 Ferrandy V, Indrawanto V, Ferryanto F, et al. Modeling of a two-degree-of-freedom fiber-reinforced soft pneumatic actuator. *Robotica*, 2023, 41: 3608–3626
 - 39 Ma J, Guo Y. Model approach of electromechanical arm interacted with neural circuit, a minireview. *Chaos Solitons Fractals*, 2024, 183: 114925
 - 40 Liu Q, Xu Y, Kurths J, et al. Complex nonlinear dynamics and vibration suppression of conceptual airfoil models: A state-of-the-art overview. *Chaos-An Interdisciplinary J Nonlinear Sci*, 2022, 32: 062101
 - 41 Guo W, Xu Y, Li Y, et al. Dynamic responses of a conceptual two-dimensional airfoil in hypersonic flows with random perturbations. *J Fluids Struct*, 2023, 121: 103920
 - 42 Zhao D, Li Y G, Xu Y, et al. Probabilistic description of extreme oscillations and reliability analysis in rolling motion under stochastic excitation. *Sci China Tech Sci*, 2023, 66: 2586–2596
 - 43 Chen Y, Yang F, Ren G, et al. Setting a double-capacitive neuron coupled with Josephson junction and piezoelectric source. *Cogn Neurodyn*, 2024, 18: 3125–3137
 - 44 Salim M, Salim D, Chandran D, et al. Review of nano piezoelectric devices in biomedicine applications. *J Intelligent Material Syst Struct*, 2018, 29: 2105–2121
 - 45 Yang F, Ren L, Ma J, et al. Two simple memristive maps with adaptive energy regulation and digital signal process verification. *J Zhejiang Univ Sci A*, 2024, 25: 382–394
 - 46 Corinto F, Forti M. Memristor circuits: Bifurcations without parameters. *IEEE Trans Circuits Syst I*, 2017, 64: 1540–1551
 - 47 Babacan Y, Yesil A, Tozlu O F, et al. Investigation of STDP mechanisms for memristor circuits. *AEU-Int J Electron Commun*, 2022, 151: 154230
 - 48 Olumodeji O A, Gottardi M. Arduino-controlled HP memristor emulator for memristor circuit applications. *Integration*, 2017, 58: 438–445
 - 49 Bao B, Chen L, Bao H, et al. Bifurcations to bursting oscillations in memristor-based FitzHugh-Nagumo circuit. *Chaos Solitons Fractals*, 2024, 181: 114608
 - 50 Bao B, Hu J, Cai J, et al. Memristor-induced mode transitions and extreme multistability in a map-based neuron model. *Nonlinear Dyn*, 2023, 111: 3765–3779
 - 51 Wu F Q, Guo Y T, Ma J. Energy flow accounts for the adaptive property of functional synapses. *Sci China Tech Sci*, 2023, 66: 3139–3152
 - 52 Yang F, Xu Y, Ma J. A memristive neuron and its adaptability to external electric field. *Chaos-An Interdisciplinary J Nonlinear Sci*, 2023, 33: 023110
 - 53 Guo Y, Lv M, Wang C, et al. Energy controls wave propagation in a neural network with spatial stimuli. *Neural Netws*, 2024, 171: 1–13
 - 54 Zhao J, Yu Y, Han F, et al. Dynamic modeling and closed-loop modulation for absence seizures caused by abnormal glutamate uptake from astrocytes. *Nonlinear Dyn*, 2024, 112: 3903–3916
 - 55 Wang X, Yu Y, Han F, et al. Dynamical mechanism of parkinsonian beta oscillation in a heterogenous subthalamopallidal network. *Nonlinear Dyn*, 2023, 111: 10505–10527
 - 56 Fan D, Yang Z, Yang C, et al. Clinically localized seizure focus maybe not exactly the position of abating seizures: A computational evidence. *Nonlinear Dyn*, 2021, 105: 1773–1789
 - 57 Yu Y, Fan Y B, Han F, et al. Transcranial direct current stimulation inhibits epileptic activity propagation in a large-scale brain network model. *Sci China Tech Sci*, 2023, 66: 3628–3638

Appendix

The relationship between torque and the force arm in the jointed pendulums is shown in Figures A1, A2, and A3.

According to Figure A1, the relationship between the torque and force arm at the joint points (O , A_0) can be described by

$$\begin{cases} O \text{ Joint : } T_1 l_1 \sin \Omega_1 + T_2 \sin \Omega_2 [l_2 + l_1 \cos(\theta_2 - \theta_1)] \\ \quad = P_1 \frac{l_1}{2} \sin \theta_1 + P_2 (l_1 \sin \theta_1 + \frac{l_2}{2} \sin \theta_2), \\ A_0 \text{ Joint : } T_2 l_2 \sin \Omega_2 = P_2 \frac{l_2}{2} \sin \theta_2. \end{cases} \quad (\text{a1})$$

Similarly, the case for $\theta_1 > \theta_2$ is illustrated in Figure A2 as follows:

The correlation between torque and force arm is described by

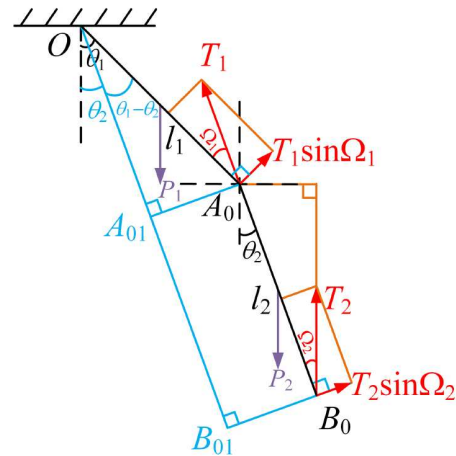


Figure A1 Stability in the jointed pendulums under torque balance for $\theta_1 > \theta_2$.

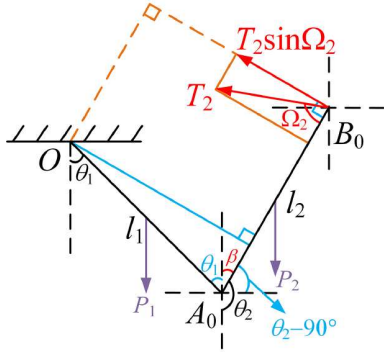


Figure A2 Stability in the jointed pendulums under torque balance when $\theta_1 < \theta_2$.

$$\begin{cases} O \text{ Joint : } T_1 l_1 \sin \Omega_1 + T_2 \sin \Omega_2 [l_2 - l_1 \cos(\pi - \theta_2 + \theta_1)] \\ \quad = P_1 \frac{l_1}{2} \sin \theta_1 + P_2 \left(\frac{l_2}{2} \sin \theta_2 + l_1 \sin \theta_1 \right), \\ A_0 \text{ Joint : } T_2 l_2 \sin \Omega_2 = P_2 \frac{l_2}{2} \sin \theta_2. \end{cases} \quad (\text{a2})$$

Eq. (a1) has the same form as eq. (a2). To better illustrate the force arm length, an arbitrary arm gait is illustrated in Figure A2.

The torque balance for the jointed points is expressed as

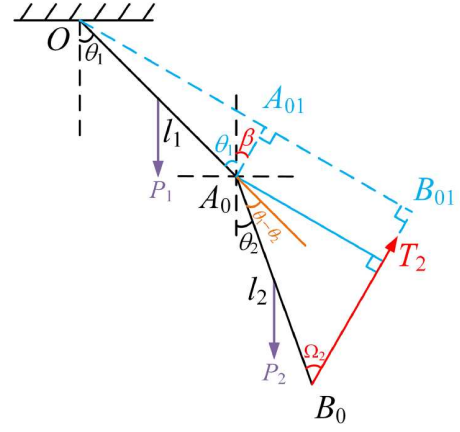


Figure A3 Stable jointed pendulums driven by EMs.

$$\begin{cases} O \text{ Joint : } T_1 l_1 \sin \Omega_1 + T_2 [l_2 \sin \Omega_2 + l_1 \cos(\theta_1 + \Omega_2 - \theta_2)] \\ \quad = P_1 \frac{l_1}{2} \sin \theta_1 + P_2 \left(\frac{l_2}{2} \sin \theta_2 + l_1 \sin \theta_1 \right), \\ A_0 \text{ Joint : } T_2 l_2 \sin \Omega_2 = P_2 \frac{l_2}{2} \sin \theta_2. \end{cases} \quad (\text{a3})$$

It is consistent with the stability constraint criterion in eqs. (a1) and (a2).